High–fidelity numerical modelling of ocean wave energy converters

Ollscoil
Mhá Nuad
Ollscoil na hÉireann
Má Nuad

Christian Windt

A thesis submitted for the degree of
Doctor of Philosophy

Maynooth University

Faculty of Science and Engineering, Electronic Engineering Department
Centre for Ocean Energy Research

October 2020

Head of the department: Prof. Ronan Farrell
Supervisor: **Prof. John V. Ringwood**

Abstract

The exploitation of ocean wave energy as a renewable energy source is a challenging task. However, once economically viable, wave energy can make a significant contribution to the global renewable energy mix and, thereby, aid the fight against climate change. To support this action, researchers and developers devise and optimise wave energy converters, employing complementary analysis in physical and numerical wave tanks, as well as during open ocean trials.

Compared to physical wave tanks, numerical wave tanks provide an excellent numerical test–bed, allowing the investigation of different device designs and scales, with the ability to passively measure relevant variables at arbitrary locations throughout the numerical domain.

Generally, numerical wave tanks can achieve different levels of fidelity, at different levels of computational cost. At the lower end of the fidelity spectrum, numerical wave tanks based on linear potential flow theory assume linear conditions (small wave amplitudes and body motions) and are computationally efficient tools for, e.g., early stage design. However, the linear assumptions are pushed beyond the limits of validity when large body motions or non–linear free surface deformations occur. In contrast, at the upper end of the fidelity spectrum, numerical wave tanks based on computational fluid dynamics can capture all relevant hydrodynamic non–linearities and produce high resolution data sets, but require substantially more computational resources.

Reviewing the available literature of high–fidelity numerical modelling of wave energy converters, knowledge gaps can be identified, hampering the exploitation of the fidelity of the computational fluids dynamics framework. Focusing on high–fidelity numerical modelling of wave energy converters, this thesis aims to fill some of the identified gaps. In particular, this thesis investigates the aspects of numerical wave generation and absorption, model validation, dynamic mesh motion methods, the flow field around devices, scaling effects, and the assessment of energy maximising controllers for wave energy converters within computational fluid dynamics based numerical wave tanks. Ultimately, this thesis highlights the potential of high–fidelity numerical models of wave energy converters to support device development, but also shows the complexity of this modelling framework. With the additional knowledge, gained through the work presented in this thesis, steps towards truly high–fidelity, wave–to–wire, models of wave energy converters can be taken to push devices towards commercial viability and, ultimately, transform wave energy from an untapped energy source to a significant contributor to the global renewable energy mix.

Zusammenfassung

Die Nutzung von Meereswellen als Quelle erneuerbarer Energien ist eine herausfordernde Aufgabe. Jedoch kann eine wirtschaftlich rentable Nutzung von Wellenenergie einen wesentlichen Beitrag zum globalen erneuerbaren Energiemix leisten und damit den Kampf gegen den Klimawandel unterstützen. Um diese Ziele zu erreichen, führen Forscher und Entwickler stetige Optimierungen an Wellenenergiekraftwerken mit Hilfe sich ergänzender Analysen in physikalischen und numerischen Wellentanks durch. Im Vergleich zu physikalischen Wellentanks bieten numerische Wellentanks einen hervorragenden Prüfstand für die Untersuchung verschiedener Anlagendesigns und –skalen mit der Möglichkeit der passiven Messung relevanter Variablen an beliebigen Stellen im gesamten numerischen Berechnungsgebiet.

Numerische Wellentanks können unterschiedliche Genauigkeitsstufen mit unterschiedlichen Rechenkosten erreichen. Am unteren Ende des Genauigkeitsspektrums liegen Wellentanks die auf der Theorie linearer Potentialströmung basieren. Unter der Annahme linearer Randbedingungen (kleine Wellenamplituden und Strukturbewegungen) dienen diese Verfahren als rechnerisch effiziente Werkzeuge in frühen Entwicklungsstadien. Die linearen Annahmen werden jedoch verletzt, wenn große Strukturbewegungen oder nichtlineare Verformungen der freien Wasseroberfläche auftreten. Im Gegensatz dazu können Wellentanks am oberen Ende des Genauigkeitsspektrums, durch die Berechung mittels numerischer Strömungsmechanik, alle relevanten hydrodynamischen Nichtlinearitäten erfassen. Diese erfordern jedoch wesentlich mehr Rechenressourcen.

In der Literatur finden sich jedoch erhebliche Wissenslücken im Bereich der numerischen Modellierung von Wellenenergiekraftwerken, welche die optimale Berechnung mittels numerischer Strömungsmechanik behindert. Vor diesem Hintergrund leistet diese Dissertation einen Beitrag, die identifizierten Wissenslücken im Bereich der hochauflösenden numerischen Modellierung von Wellenenergiekraftwerken zu schließen. Insbesondere befasst sich diese Arbeit mit den Aspekten der numerischen Wellenerzeugung und Absorption, Modellvalidierung, dynamischer Gitterbewegung, dem Strömungsfeld um Anlagen, Skalierungseffekten und der Bewertung von Regelungstechniken.

Letztendlich zeigt diese Dissertation das Potenzial hochauflösender numerischer Verfahren für die Forschung und Entwicklung von Wellenenergiekraftwerken, verdeutlicht allerdings auch die Komplexität dieser Berechnungsmethode. Das zusätzlichen Wissen, das durch die im Rahmen dieser Dissertation durchgeführten Studien gewonnen wurde, ermöglicht die Nutztung hochauflösender numerischer Verfahren um Wellenenergiekraftwerke in Richtung kommerzieller Nutzung zu treiben und mit der Nutzung von Wellenenergie einen wesentlichen Beitrag zum erneuerbarer Energienmix zu leisten.

Für Mama & Papa!

Declaration of authorship

I, Christian Windt, declare that this thesis titled 'High–fidelity numerical modelling of ocean wave energy converters' and the work presented in it are my own. I confirm that:

- This work was done wholly or mainly while in candidature for a research degree at this University.
- Where any part of this thesis has previously been submitted for a degree or any other qualification at this University or any other institution, this has been clearly stated.
- Where I have consulted the published work of others, this is always clearly attributed.
- Where I have quoted from the work of others, the source is always given. With the exception of such quotations, this thesis is entirely my own work.
- I have acknowledged all main sources of help.
- Where the thesis is based on work done by myself jointly with others, I have made clear exactly what was done by others and what I have contributed myself.

Date: 15/07/2020

Signature: Christian Windt

Acknowledgements

First and foremost, I would like to express my sincere gratitude to my supervisor, John V. Ringwood, for the opportunity to join the Centre for Ocean Energy Research as a PhD student, for his continuous support, and for his tireless dedication to improve my technical writing skills – I will always remember the Oxford comma.

I want to extend my gratitude to my co–supervisor Josh Davidson for all the OpenFOAM training, the incredibly valuable feedback, his effort to push the quality of our work, and all the thought–provoking CFD talk!

I also would like to say a special thank you to Pál Schmitt, who planted the wave energy seed in my head in 2014 and since then enabled so many fruitful collaborations. Furthermore, a big thank you to Edward Ransely for our collaboration on the CCP–WSI projects. I really enjoyed our intense discussions on professional topics and our not less intense unprofessional activities around the world. A special thanks also to my collaborators throughout my PhD, without whom a lot of my work would not have been possible: Deborah Greaves, Morten Kramer, Morten Jakobsen, Dominic Chandar, Francesco Ferri, Curtis Rusch, and Frederic Dias.

Thank you also to all members and alumni of the COER lab: Hasana Bagnal, Hakim Bouhali, Jake Cunningham, Francisco Dorespiuma, Andrei Ermakov, Marina García-Abril, Demián García-Violini, Bingyong Guo, Giuseppe Giorgi, Simone Giorgi, Fernando Jaramillo-Lopez, Tom Kelly, Alexis Mérigaud, Riccardo Novo, Francesco Paparella, Louis Papillon, Markel Penalba, Ahsan Said, and LiGuo Wang – It was truly grand!

A special thank you to 'my interns' Akram Benazzou, Jost Kemper, Alix Untrau, Leonardo Pio Pistillo, and Carl Hany, who did a tremendous job.

Particular shout–outs to my comrades in arms: Nicolás Faedo and Yerai Peña-Sanchez. It would not have been the same without you. I see you in Miami!

Many thanks also to the staff members of the EE Department, in particular Carrie Anne Barry, Ann Dempsey, Joanne Bredin, Denis Buckley, and John Malocco, for their continuous administrative and technical support.

Finally, I would like to express my gratitude to my parents, family, and friends. Without their support I would not be where I am now. Thank you!

Institutional

Gratitude is expressed to Science Foundation Ireland for supporting this work, under Grant no. 13/IA/1886. The author also wishes to acknowledge the DJEI/DES/SFI/HEA Irish Centre for High-End Computing (ICHEC) for the provision of computational facilities and support.

Contents

List of Figures

List of symbols

A	Wave amplitude
A_{HP}	Motion amplitude of the heave plate
A_{ss}	State–space matrix
$A_{\mathbf{a}_{wm}}$	Amplitude of the acceleration input in time domain
A_0	Peak amplitude of focused wave group
A_{CV}	Area of a control volume face
A_{PTO}	PTO force amplitude
A_s	Mass source surface area
$a_{\text{1/5th}}$	Distance between pivot and PTO attachment point
$\mathbf{a}_{wm}$	Acceleration input to the impulse source wave maker
$\hat{\mathbf{a}}_{wm}(j\omega)$	Frequency domain equivalent of $\mathbf{a}_{wm}$
α_p	Under–relaxation factor
α_{VF}	Volume fraction
$\alpha_{\text{VF},S}$	Sum of the volume fraction along a numerical wave probe
$\alpha_{\text{VF,target}}$	Target volume fraction
$\alpha_{\text{1/5th}}$	Angle between PTO anchor point and x–axis
$\mathcal{A}_{\eta_t}$	Amplitudes of η_t in frequency domain
$\mathcal{A}_{\eta_r}$	Amplitudes of η_r in frequency domain
$\mathcal{A}_{\mathbf{a}_{wm}}$	Amplitudes of $\mathbf{a}_{wm}$ in frequency domain
B	Bottom neighbouring node of central node P
b	bottom neighbouring face of central node P
B_{ss}	State–space vector
$b_{\text{1/5th}}$	Distance between pivot and PTO anchor point
b_{u}	Damping term in output–feedback controller
β	Modelling constant in the RNG $k-\varepsilon$ model
β_1	Modelling constant in the $k-\omega$ model

β_2	Modelling constant in the $k-\omega$ SST model
β^*	Modelling constant in the $k-\omega$ model
$\beta_{1/5\text{th}}$	Angle between arm and x–axis
C	Integration constant in the Bernoulli equation
C_{ss}	State–space vector
C_d	Viscous drag coefficient
C_r	Relative cell count
C_{SGS}	Modelling constant in the LES model
C_μ	Modelling constant in the $k-\varepsilon$ model
$C_{1\varepsilon}$	Modelling constant in the $k-\varepsilon$ model
$C_{2\varepsilon}$	Modelling constant in the $k-\varepsilon$ model
C_μ^*	] Modelling constant in the realizable $k-\varepsilon$ model
C_2	Modelling constant in the realizable $k-\varepsilon$ model
Co	Courant number
Co_{max}	Maximum Courant number
c	Wave celerity
c_0	User define coefficient for the Crank-Nicolson scheme
c_r	Interface compression factor
D	Cylinder diameter
D_{exp}	Experimental rotational damping coefficient
D_{num}	Numerical translational damping coefficient
D_{HP}	Diameter of the heave plate
$\mathcal{D}$	Rate of strain tensor
$\mathscr{D}$	Deviation rate
d	Water depth
d$\bar{H}_{\#i}$	Relative deviation in the mean phase averaged wave height between different grid layouts
Δ	Cut–off width
Δt	Time step
Δx	Spatial distance in the x direction
Δy	Spatial distance in the y direction

$\Delta\omega$	Angular frequency step
δ_{ij}	Kronecker delta
E	East neighbouring node of central node P
e	East neighbouring face of central node P
E	Model constant in the wall function
E_WEC	Absorbed energy
$E_\text{WEC,CFD}$	Absorbed energy in the CFD–based NWT
$E_\text{WEC,Lin}$	Absorbed energy in the Linear model
$\mathcal{E}$	Cumulative absorbed energy
ϵ_{H_m}	Relative deviation between the measured and initialised wave height
$\epsilon_{\bar{H}_\text{m}}$	Relative deviation between $\bar{H}_\text{m}$ and the theoretical wave height
$\epsilon_{\bar{H}_{r,i},H_t}$	Relative error between the target and resulting wave height
$\epsilon_{\bar{u}_\eta}(x_n, z_m)$	Relative error between measured and theoretical horizontal velocity
ε_t	Dissipation rate of the turbulent kinetic energy
F_s	Safety factor in convergence study
F_C	Blending function in the $k-\omega$ SST model
F_d	Drag force
F_i	Fourier transform of f_i
F_PTO	PTO force
$\bar{F}_z$	Mean heave force
Fr	Froude number
$\mathcal{F}$	Generic function identifier
$\digamma$	Predicted value in nRMSE
$\hat{\digamma}$	Reference value in nRMSE
f	Frequency
f_e	Excitation force
f_g	Gravity force
f_{in}	Inertia force
f_p	Peak wave frequency
f_PTO	PTO force frequency

f_{u}	Control force
$f_{\mathsf{u}}^{\mathsf{opt}}$	Optimal control force
f_v	Viscous force
$\mathbf{f}$	Force vector
$\mathbf{f}_b$	Vector of body forces
Φ	Velocity potential
ϕ	Generic fluid property
$\bar{\phi}$	Mean value of a generic fluid property
$\phi^{'}$	Fluctuation of a generic fluid property
ϕ_{computed}	Computed solution of ϕ
ϕ_{target}	Target solution of ϕ
φ	Wave phase
$\mathcal{G}$	Signal generator
g	Gravitational acceleration
Γ_{WEC}	WEC rotation angle around pivot point
Γ	Normalised rotational floater position
γ_1	Modelling constant in the $k-\omega$ model
γ_2	Modelling constant in the $k-\omega$ SST model
$\gamma_{1/5\mathsf{th}}$	Angle between reference point axis and x–axis
H	Wave height
H_{exp}	Experimentally measure wave height
H_{init}	Initialised wave height
H_{m}	Measured wave height
H_{m}^{*}	Wave height of the same wave in cyclic NWT
H_{msw}	Measured wave height of standing wave
H_{Theory}	Theoretical wave height
H_{tar}	Target wave height in wave maker controller
$\bar{H}_{\mathsf{m}}$	Mean phase averaged measured wave height
$\bar{H}_{\mathsf{msw}}$	Mean phase averaged measured wave height of standing wave
$\bar{H}_{\mathsf{m}}^{+}$	Upper bound of $\bar{H}_{\mathsf{m}}$
$\bar{H}_{\mathsf{m}}^{-}$	Lower bound of $\bar{H}_{\mathsf{m}}$

$\bar{H}_{\text{uf}}$	Phase averaged wave height from the uniform mesh
H_{PT}	Peak–to–trough wave height
$\bar{H}_r$	Mean wave height of the resulting wave
H_t	Wave height of the target wave
H_s	Significant wave height
$\underline{H}$	Empirical transfer function estimate
$\underline{\bar{H}}$	Average empirical transfer function estimate
$\underline{H}_{\mathbf{a},\eta,i}(j\omega)$	Transfer function from $\mathbf{a}_{wm,i}(j\omega)$ to $\eta_{r,i}(j\omega)$
$\mathscr{H}$	Optimal gain for output–feedback controller
h_s	Impulse source height
h_{Tank}	Height of the CFD–based NWT
η	Free surface elevation
$\eta^{(1)}$	First order free surface elevation
$\eta^{(2)}$	Second order free surface elevation
η_0	Modelling constant in the RNG $k-\varepsilon$ model
η_t	Target surface elevation
$\hat{\eta}_t(j\omega)$	Frequency domain equivalent of η_t
η_r	Resulting surface elevation
$\hat{\eta}_r(j\omega)$	Frequency domain equivalent of η_r
$\mathbf{I}$	Unit tensor
ι	User defined scalar value in the `limitedLinear` TVD scheme
K_{exp}	Experimental rotational spring stiffness
K_{num}	Numerical translational spring stiffness
KC	Keulegan–Carpenter number
Kl	Diffraction parameter
k	Wave number
k_{mooring}	Mooring line stiffness
k_t	Kinetic turbulent energy
k_{u}	Stiffness term in output–feedback controller
κ	Von Karman constant
$\varkappa$	Froude scaling factor

L	Characteristic length scale
L_{PTO}	Displacement of the PTO translator shaft
L_R	Length of the relaxation zone
$L_{R,a}$	Length of the absorption relaxation zone
$L_{R,g}$	Length of the generation relaxation zone
L_B	Length of the numerical beach
L_{SB}	Length of the sloped beach
L_{e}	Moment domain equivalent of f_{e}
L_{u}	Moment domain equivalent of f_{u}
l_{Device}	Distance between wave generation boundary and WEC
l_{Tank}	Length of the CFD–based NWT
l_{WP}	Distance between wave generation boundary and wave probe
ℓ	Turbulent length scale
Λ_{η_t}	Phases of η_t in frequency domain
Λ_{η_r}	Phases of η_r in frequency domain
$\Lambda_{\mathbf{a}_{wm}}$	Phases of $\mathbf{a}_{wm}$ in frequency domain
λ	Wave length
λ_p	Peak wave length
m	Mass
m_p	`nCorrectors`
m_{max}	Maximum number of `nCorrectors`
μ	Dynamic viscosity
μ_{air}	Dynamic viscosity of air
μ_{water}	Dynamic viscosity of water
μ_{SGS}	SGS turbulent viscosity
μ_t	Eddy viscosity
N	North neighbouring node of central node P
s	North neighbouring face of central node P
$\underline{N}$	Number of input signals
$\mathcal{N}$	Normalisation factor
$\mathbf{n}$	Normal vector

n_p	`nOuterCorrectors`
n	Number of samples
n_η	Number of wave components
n_{ss}	Order of the state–space model
n_{max}	Maximum number of `nOuterCorrectors`
ν	Kinematic viscosity
ν_{FS}	Full scale kinematic viscosity
ν_{MS}	Model scale kinematic viscosity
∇	Gradient
∇^2	Laplace operator
$\nabla\cdot$	Divergence
$\nabla\times$	Cross gradient
P	Central node P in a control volume
P_{WEC}	Instantaneous power
$\mathcal{P}$	Order of the accuracy from Richardson extrapolation
p	Pressure
$p_{\mathsf{atmospheric}}$	Atmospheric pressure
p^*	Guessed pressure
p^c	Pressure correction value
p^{new}	New pressure value in a SIMPLE iteration
Π	Solution from inviscid or viscous turbulent simulations
$\hat{\Pi}$	Solution from viscid laminar simulations
ϖ	Current value in nRMSD
$\hat{\varpi}$	Reference value in nRMSD
ϖ_l	Current value in nRMSD for a particular scale l
ϖ_k	Current value in nRMSD for a particular scale k
$\theta_{\mathsf{1/5th}}$	Angle between arm and reference point axis
q	Flux
R	Reflection coefficient
R_D	Discrimination ratio
R_{WEC}	WEC device radius

Re	Reynolds number
Re^*	Critical Reynolds number
$\mathcal{R}$	Refinement ratio
$\mathbb{R}$	Set of real numbers
ρ	Density
ρ_{air}	Density of air
ρ_{water}	Density of water
ϱ	Ratio between the upwind– and downwind–side gradients
r_s	Scalar value identifying the impulse source region
r_{WP}	Resolution of a numerical wave probe
S	South neighbouring node of central node P
s	South neighbouring face of central node P
S	Rate of strain
$\bar{S}$	Mean rate of strain
S'	Fluctuation of the rate of strain
$\bar{S}_{\text{rf}}$	Local rate of strain of the resolved flow
S_η	Wave spectrum
$S_{\eta,\text{Theory}}$	Theoretical wave spectrum
$S_{\mathcal{G}}$	Dynamic matrix within signal generator $\mathcal{G}$
$S_{\eta,\text{m}}$	Measured wave spectrum
$\bar{S}_{\eta,\text{m}}$	Mean measured wave spectrum
$\hat{S}_{\eta\,\text{I}}$	Peak value of the spectral density of the incident wave
$\hat{S}_{\eta\,\text{R}}$	Spectral density of the reflected wave at peak frequency of $\hat{S}_{\eta\text{I}}$
$\mathcal{S}_f$	Solution of the fine grid size
$\mathcal{S}_m$	Solution of the medium grid size
$\mathcal{S}_c$	Solution of the coarse grid size
s_m	Mass source term
s_b	Damping factor
$s_{b,\text{Max}}$	Maximum damping factor
Σ	WEC model
σ	Standard deviation

σ_k	Modelling constant in the $k-\varepsilon$ model
σ_ε	Modelling constant in the $k-\varepsilon$ model
σ_ω	Modelling constant in the $k-\omega$ model
$\sigma_{\omega,1}$	Modelling constant in the $k-\omega$ SST model
$\sigma_{\omega,2}$	Modelling constant in the $k-\omega$ SST model
T	Top neighbouring node of central node P
t	Top neighbouring face of central node P
$\mathbf{T}$	Stress tensor
T	Wave period
T_{HP}	Motion period of the heave plate
T_{ex}	Wave excitation torque
$T_{\text{ex,exp}}$	Experimental wave excitation torque
$T_{\text{ex,num}}$	Numerical wave excitation torque
T_{Hyd}	Hydrodynamic torque
T_{p}	Peak wave period
T_{PTO}	PTO force period
T_i	Turbulence intensity
$\mathcal{T}$	Energy maximisation time window
T'	Energy maximisation period
t	Time
t^*	Time window of the length of one wave period
t_r	Relative time
t_{run}	Simulation run time
$\hat{t}_{\text{run}}$	Relative simulation run time
$t_{\text{run,o}}$	Simulation run time for the overset grid method
$t_{\text{run,MM}}$	Simulation run time for the mesh morphing method
t_s	Simulated time
t_0	Temporal focal point
t^0	Current time step
t^1	Future time step
τ	Reynolds stresses

τ_{PTO}	PTO torque
τ_v	Viscous stresses
τ_w	Wall shear stress
$\mathcal{U}$	Relative grid uncertainty
$\mathcal{U}_a$	Absolute grid uncertainty
U_{ref}	Reference velocity in the $k-\varepsilon$ model
$\mathscr{U}$	Set of input signals
$\mathbf{u}$	Velocity vector
$\mathbf{u}^*$	Guessed velocity vector
$\mathbf{u}^c$	Velocity correction vector
$\mathbf{u_c}$	Correction velocity in the static boundary wave absorption method
$\mathbf{u_r}$	Compression velocity
$\mathbf{u}_{\text{target}}$	Target velocity vector
u	Velocity component in the Cartesian x coordinate
$\bar{u}$	Mean of u
$u^{'}$	Fluctuation of u
$\overline{\overline{u^{'}}}$	Variance of $u^{'}$
u_∞	Free stream velocity
u_η	Horizontal fluid velocity
$u_\eta^{(1)}$	First order horizontal fluid velocity
$u_\eta^{(2)}$	Second order horizontal fluid velocity
$\bar{u}_\eta$	Mean horizontal fluid velocity
u_τ	Friction velocity
u^+	Dimensionless velocity
Υ	Turbulent velocity scale
V	Volume of a control volume
V_d	Volume defect
v	Velocity component in the Cartesian y coordinate
$\bar{v}$	Mean of v
$v^{'}$	Fluctuation of v
$\overline{\overline{v^{'}}}$	Variance of $v^{'}$

$v_\eta^{(1)}$	First order horizontal velocity
$v_\eta^{(2)}$	Second order horizontal velocity
$\mathbf{v}_s$	Search vector
W	West neighbouring node of central node P
w	West neighbouring face of central node P
w	Velocity component in the Cartesian z coordinate
$\bar{w}$	Mean of w
$w^{'}$	Fluctuation of w
$\overline{\overline{w^{'}}}$	Variance of $w^{'}$
w_s	Impulse source width
w_{Tank}	Width of the CFD–based NWT
ω	Angular wave frequency
ω_0	Fundamental frequency
ω_p	Peak angular wave frequency
ω_t	Turbulent frequency
ω_{WEC}	Angular WEC velocity
ω_{wm}	Angular frequency of the acceleration input
x	Cartesian x coordinate.
x'	Sub–grid scale
x_0	Spatial focal point
x_b	Position within the numerical beach
x_c	PTO cylinder displacement
x_m	Specific location in the x–direction along the wave
x_n	Specific location in the x–direction along the NWT
x_{WP}	x coordinate of the wave probe position
$\mathbf{x}_{\mathsf{WP}}$	Vector of the wave probe position
$\mathbf{x}_{\mathsf{Eval}}$	Vector of the evaluation point
$\mathbf{x}_\eta$	Vector of the free surface elevation
ξ	Vector of experimental damping and stiffness coefficients
$\hat{\xi}$	Vector of estimated numerical damping and stiffness coefficients
$\xi_{\mathcal{G}}$	Solution vector within signal generator $\mathcal{G}$

$\dot{\xi}_{\mathcal{G}}$	Time derivative of the solution vector within signal generator $\mathcal{G}$
Ξ	Vector of PTO displacement and velocity data
χ_R	Weighting function in relaxation zone method
$\mathscr{Y}$	Set of output signals
Y_i	Fourier transform of y_i
y	Cartesian y coordinate
$\tilde{y}$	Output of the WEC system
y_i	System output, corresponding to f_i
y^+	Dimensionless distance to the wall
y_{WP}	y coordinate of the wave probe position
Ψ	Blending factor within the Crank–Nicolson scheme
ψ	Limiter function
z	Cartesian z coordinate
z_m	Specific location in the z–direction along the water column
z_{Max}	Maximum value in the z–direction of the domain bounding box
z_{WP}	z coordinate of the wave probe position
z_η	z coordinate of the free surface elevation

List of acronyms

1D	One–dimensional
2D	Two–dimensional
3D	Three–dimensional
AMETS	Atlantic Marine Energy Test Site
AMI	Arbitrary mesh interface
BEM	Boundary element method
BIMEP	Biscay Marine Energy Platform
CCP–WSI	Collaborative computational project in wave–structure interaction
CD	Central differencing
CFD	Computational fluid dynamics
CFL	Courant–Friedrichs–Lewy
CICSAM	Compressive interface capturing scheme for arbitrary meshes
CoM	Centre of mass
CPH	Cells per wave height
CPL	Cells per wave lengths
CV	Control volume
DBM	Dynamic boundary method
DExt	Down–wave extension
DNS	Direct numerical simulation
DoF	Degree of freedom
DSLR	Digital single–lens reflex
ETFE	Empirical transfer function estimate
EMCS	Energy maximising control system
EMEC	European marine energy centre
FAVOR	Fractional area–volume obstacle representation
FD	Finite–difference

FE	Finite–element
FFT	Fast Fourier transform
FS	Full scale
FSI	Fluid–structure interaction
FSPO	Floating storage production and offloading unit
FV	Finite–volume
GCI	Grid convergence index
gen	Generic device type
GUI	Graphical user interface
He	Heave
HiFi	High–fidelity
HRIC	High resolution interface capturing
ihWP	In–house wave probe implementation
isoWP	Iso–surface wave probe
ISM	Impulse source method
ISPH	Incompressible SPH
Ixx	Moment of inertia about the x–axis
Iyy	Moment of inertia about the y–axis
Izz	Moment of inertia about the z–axis
JONSWAP	Joint North Sea wave project
LCoE	Levelised cost of energy
LES	Large eddy simulation
MS	Full scale
MULES	Multi–dimensional limiter for explicit solution
MUSCL	Monotone upstream-centred schemes for conservation laws
nRMS	Normalised root–mean square
nRMSD	Normalised root–mean square deviation
nRMSE	Normalised root–mean square error
NWT	Numerical wave tank
OCP	Optimal control problem
OF	OpenFOAM

OFWP	Wave probe implementation in OpenFOAM
ola	OlaFlow
OpenFOAM	Open field operation and manipulation
OWC	Oscillating water column
OWSC	Oscillating wave surge converter
PG	Pressure gauge
Pi	Pitch
PIC	Particle–in–cell
PIMPEL	Pressure implicit for pressure linked equations
PISO	Pressure implicit split operator
PIV	Particle image velocimetry
PTO	Power take–off
QUICK	Quadratic upstream interpolation for convective kinetics
QP	Quadratic program
R&D	Research and development
RAM	Random access memory
RANS	Reynolds averaged Navier–Stokes
RAO	Response amplitude operator
RHPC	Receding-horizon pseudospectral optimal control
RMS	Root–mean square
RNG	Re–Normalisation group
Ro	Roll
RZM	Relaxation zone method
SBM	Static boundary method
SDF	Spectral density function
SEMREV	Central Nantes multi-function offshore test site
SGS	Sub–grid–scale
SID	System identification
SIMPLE	Semi–implicit method for pressure linked equations
SLERP	Spherical linear interpolation
spec	Specific device type

SPH	Smoothed particle hydrodynamics
SST	Shear stress transport
Su	Surge
Sw	Sway
SWENSE	Spectral wave explicit Navier–Stokes equations
SWL	Still water level
TRL	Technology readiness level
TVD	Total variation diminishing
UD	Upwind differencing
UExt	Up–wave extension
UK	United Kingdom
VOF	Volumne–of–fluid
WCSPH	Weakly compressible SPH
WEC	Wave energy converter
WECCCOMP	International WEC control competition
WP	Wave probe
WSI	Wave–structure interaction

1

Introduction

Contents

The undeniable increase of the atmospheric temperature (see Figure 1.1) and the widespread recognition of human–induced climate change have, in recent years, fuelled the research and development (R&D) into novel technologies to harness renewable energy sources. Amongst the available renewable energy sources, ocean wave energy, once economically viable, can make a valuable contribution towards a sustainable, global, energy mix [1].

However, researchers and developers face numerous challenges when devising novel concepts for wave energy conversion. The challenges comprise, amongst others, efficient conversion of relatively slow, reciprocating translational or rotary motion of the absorbing structure into unidirectional, relatively fast rotational motion within an electric generator[1]; integration into existing electrical gri ds; survivability of devices in harsh ocean environments; and extensive capital expenditure for offshore operations.

---

[1] Recently, efforts are made to bypass this challenge through the use of linear electric generators or flexible, dielectric membrane–type absorbers [2].

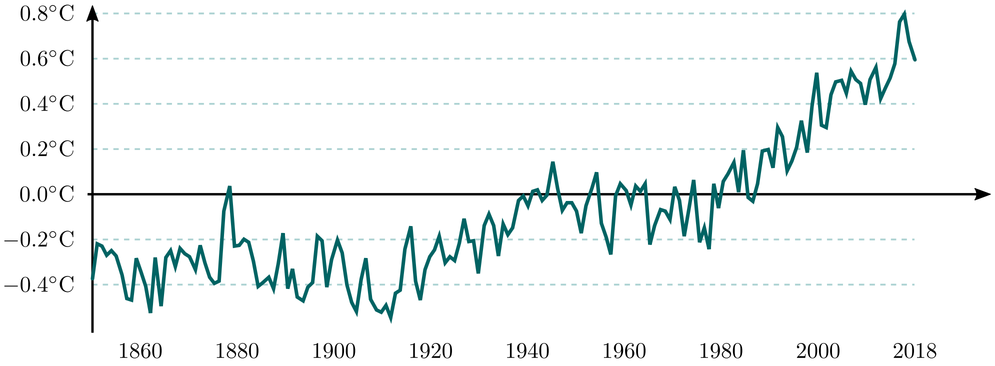

Figure 1.1: Global temperature anomaly relative to the 1961–1990 (adapted from [3])

An idealised schematic of different aspects (and their interrelationship), influencing the development and operation of wave energy converter (WEC) devices, is shown in Figure 1.2.

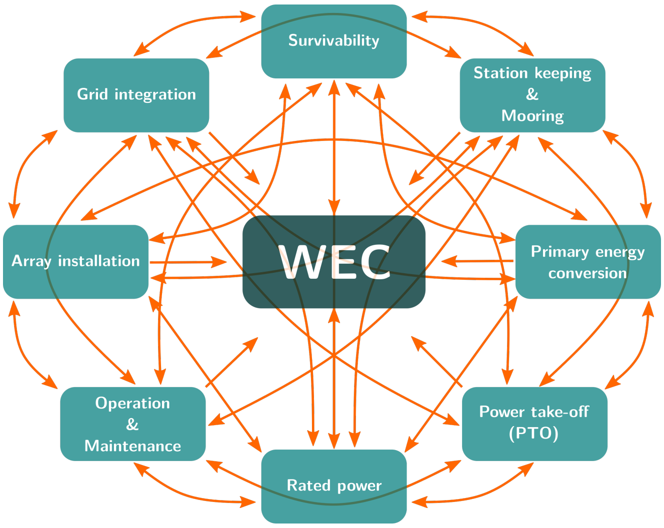

Figure 1.2: Influential aspects and their interrelationship of the overall performance and viability of a WEC (note that the visualisation does not claim to be complete).

The above mentioned aspects are commonly summarised by a single, monetary value: the levelised cost of energy (LCoE). The LCoE is defined as the ratio between the overall cost of an energy conversion device/array over its lifetime and the total generated electric energy over the lifetime. Example values of the LCoE of different energy sources are listed in Table 1.1.

From a hydrodynamic point of view, to drive down the LCoE, optimisation of the hydrodynamic response of the device is required, which can be achieved through optimisation of the shape, the operational degrees of freedom (DoFs), or implementation of energy maximising control systems (EMCSs). For the hydrodynamic optimisation and the synthesis and evaluation of EMCSs at low to mid technology readiness levels (TRLs) [6], researchers and developers rely on complementary experimental and numerical

Table 1.1: Levelised cost of energy for different energy sources

Energy source	LCoE [€/kWh]	Reference
Coal (Germany)	0.06 – 0.10	[4]
Onshore wind (Germany)	0.04 – 0.08	[4]
Offshore wind (Germany)	0.08 – 0.14	[4]
Solar photovoltaic (Germany)	0.04 – 0.12	[4]
Wave estimate (UK)	0.17	[5]

analysis, allowing experimentation in relatively controlled environments, compared to open ocean trials. However, given the interconnection between the different *WEC aspects* (see Figure 1.2), it is a challenging task to perform reliable experimental and numerical studies for the evaluation and optimisation of the WEC performance.

Generally, by testing in a real physical environment, physical wave tanks allow all the relevant wave–structure interaction (WSI) details to be captured. However, experimental test campaigns in physical wave tanks are generally constrained to a specific (small) scale, due to the dimensions and availability of test facilities. The scale constraint, in turn, presents difficulties for the representation of the WEC sub–systems, such as the power take–off (PTO) or the mooring system. In addition, the replication of the main WEC components (floater structure, joints, sub–structures) may also be difficult and induce undesired scaling effects, such as excessive mechanical friction. Furthermore, physical wave tank experiments are associated with high costs, when many design iterations are required. The main cost drivers are instrumentation, construction of the prototype, test facilities, and staff. Lastly, the accuracy of physical wave tank experiments potentially suffers from peculiarities of the test facility, such as reflections from the tank walls or measurement errors/noise.

Overcoming the drawbacks of high capital costs, measurement noise, mechanical friction and, to a great extent, scaling effects, numerical wave tanks (NWTs) provide powerful tools for the analysis of WECs. However, numerical testing environments also feature specific pros and cons, which inspire the main motivation of this thesis and are detailed in the following Section 1.1.

1.1 Thesis motivation

A NWT is the generic name for numerical simulators which model (non–)linear free surface waves, hydrodynamic forces, as well as floating body motions [7–9]. NWTs provide an excellent numerical tool for WEC R&D, allowing the investigation of different WEC designs and arbitrary, virtual, tank layouts, with the ability to passively measure relevant variables in all locations throughout the tank, thereby serving as an efficient test–bed for WSI analysis.

1.1.1 The model fidelity spectrum

The fluid dynamics within the NWT are governed by the Navier–Stokes equations (see Chapter 2). Following the continual increase in available computational power [10], different methods for the simulation of the fluid dynamics within a NWT have been developed over the years, with varying levels of fidelity and associated computational cost. The fidelity and associated computational cost spectrum of NWTs is schematically depicted in Figure 1.3.

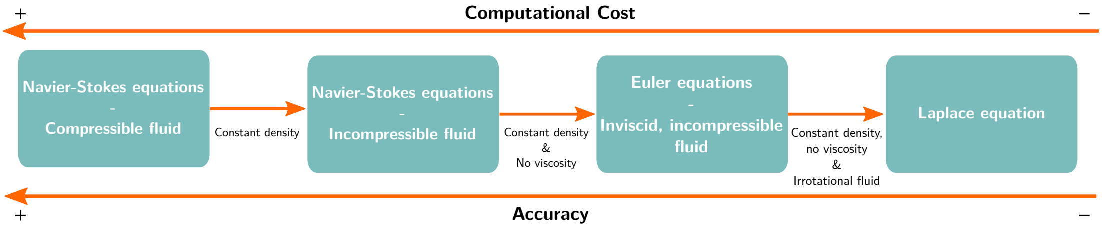

Figure 1.3: The fidelity and associated computational cost spectrum of NWTs (adapted from [11]). Based on the underlying assumptions for the fluid, the Navier-Stokes equations can be simplified, resulting in less costly but also less accurate simulation. An ideal NWT would deliver the highest possible accuracy at the lowest possible computational cost.

Historically, solving the Navier–Stokes equations for offshore engineering applications was computationally infeasible. Therefore, the governing equations were simplified to obtain linear potential flow theory, whereby solutions are efficiently computed by linearising the problem through assumptions of small amplitude oscillations, inviscid, irrotational, and incompressible flow (see Chapter 2). Although solution methods based on linear potential flow theory have been used successfully in many offshore engineering applications [12], the linearising assumptions are challenged by realistic WEC operation, where large amplitude motions may result from energetic waves or sustained wave/WEC resonance due to control action (see Figure 1.4).

While still assuming irrotational and inviscid fluid, non–linear, non–breaking free surface deformations (see Chapter 3) can be captured in fully non–linear potential flow solvers [13, 14]. Furthermore, potential flow models can be extended to approximate specific non-linear effects, such as viscous drag [15] or non-linear Froude–Krylov forces [16, 17]. At significantly greater computational expense, NWTs based on computational fluid dynamics (CFD) provide a more rigorous non–linear treatment of the Navier–Stokes equations[2]. Within the CFD–based NWT, the governing equations are solved

---

[2] A more detailed definition of the term *CFD*, as used throughout this thesis, is given in Chapter 4.

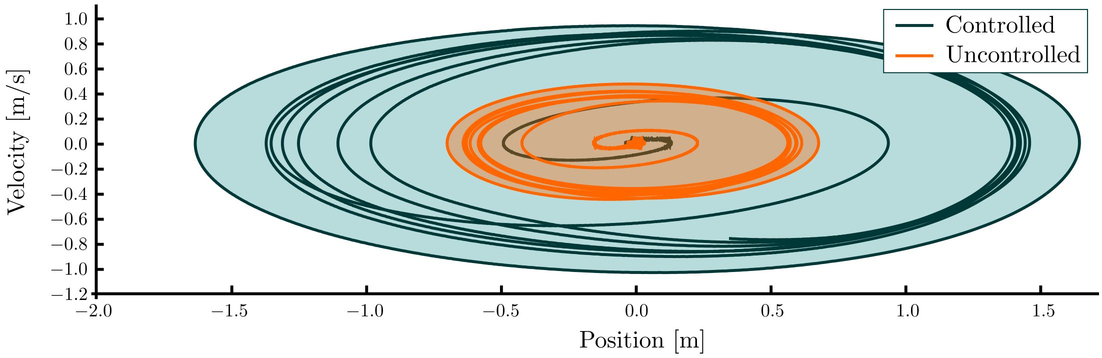

Figure 1.4: Operational space of an uncontrolled and controlled WEC device, with zero initial conditions and under regular wave excitation: The velocity of the WEC in the vertical direction is plotted over the WEC position in the vertical direction.

numerically by discretising the domain, in space and time, to form a system of linear algebraic equations (see Chapter 4). Compared to lower fidelity numerical tools, CFD–based NWTs have the advantage of inherently capturing all relevant hydrodynamic non-linearities, such as large surface deformation, viscous drag, or turbulence effects. The relative strengths and weaknesses of the available NWTs can be leveraged at different stages of the device R&D [18]. During early stage development, lower-fidelity models are suitable for parametric studies, where a vast number of simulations are required to cover a broad parameter space. Progressing in the development, the system under investigation becomes more refined and a higher level of accuracy is required to evaluate the performance of the system. The use of a high–fidelity, CFD–based NWTs can be particularly valuable for the:

- Examination of WEC responses under extreme loading,
- Generation of input data for data–driven system identification procedures,
- Generation of benchmark data for the assessment of lower–fidelity NWTs,
- Evaluation of the WEC performance under realistic conditions.

1.1.2 Holistic WEC modelling

To justify the additional computational cost of high–fidelity, CFD–based NWTs, a careful model setup is required, ensuring high–fidelity of the hydrodynamic model (numerical wave generation and absorption, accommodation of body motion, turbulence modelling, etc.) but, in addition, also high–fidelity of the involved WEC sub–system models, such as EMCSs, mooring, and PTO models (see Figure 1.5). Employing holistic CFD–based NWTs minimises the risk of undermining the overall NWT accuracy due to fidelity imbalances between the involved models.

In the available literature of CFD–based NWTs for WEC applications (see Chapter 5), some shortcomings regarding the hydrodynamic modelling, as well as an imbalance between (sub–)model fidelities can be observed. Motivated by the reviewed literature, this thesis tackles some of the observed shortcomings.

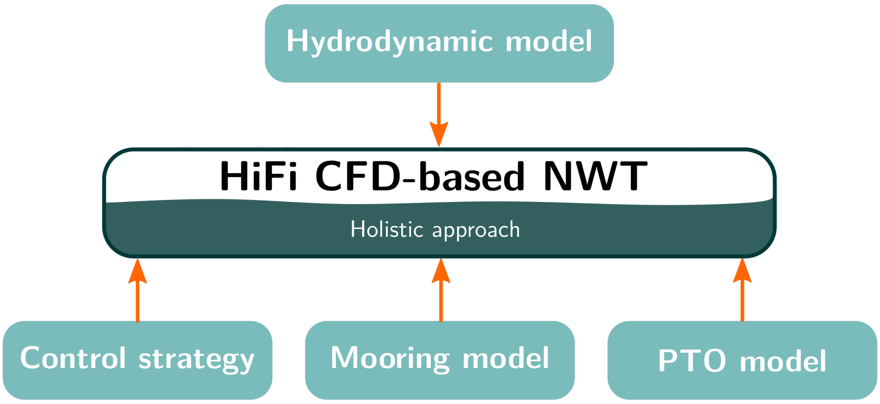

Figure 1.5: Schematic representation of a holistic, high–fidelity CFD–based NWT.

1.2 Objectives and contributions of the thesis

This section presents the objectives (see Section 1.2.1) and contributions of this thesis (see Section 1.2.2). The section also includes a list of publications associated with the contributions (see Section 1.2.3), as well as a list of publications offering supplementary material (see Section 1.2.4), indirectly supporting the main contributions[3].

1.2.1 Thesis objectives

The objectives of the present thesis are two–fold. Regarding the hydrodynamic model, the thesis aims to improve and assess various aspects of CFD–based NWTs, thereby ensuring highest possible accuracy of the hydrodynamic model. In particular, the considered aspects embrace numerical wave generation and absorption, model validation, dynamic mesh motion, turbulence modelling, and scaling. Furthermore, regarding the holistic WEC modelling, this thesis aims to perform sensitivity analysis of the WEC performance assessment framework on the level of complexity of its sub–models, in particular the control system. In this thesis, the C++ based Open field operation and manipulation (OpenFOAM) toolbox [19] will be used for the setup of all CFD–based NWTs.

---

[3] Note that, for clarity, the publications in Section 1.2.3 and 1.2.4 follow a different referencing system compared to the main reference system in this thesis.

1.2.2 Contributions of the thesis

The contributions of the present thesis can be divided into six categories, reflecting the six chapters in Part II of this thesis (see Section 1.3).

1. **Numerical wave generation and absorption:** This thesis presents advances in the implementation of an impulse source wave generation method. Furthermore, this thesis proposes a rigorous assessment procedure for numerical wave generation and absorption methods (see Chapter 6). The corresponding publications (see Section 1.2.3) are [CPA, JPD, JPE, SMF].

2. **Model validation:** This thesis presents comprehensive numerical model validation of four different WEC system models, highlighting the importance and influence of measurement uncertainty within the system parameters on the validation result (see Chapter 7). The corresponding publications are [CPC, CPF, CPG, JPG, JPH, JPJ, JPL].

3. **Dynamic mesh motion methods:** This thesis highlights the importance of advanced dynamic mesh motion methods for WEC control studies and delivers an assessment of recently released overset grid methods for single– and multi–phase problems in the OpenFOAM CFD framework (see Chapter 8). The corresponding publications are [CPB, CPD, JPF].

4. **Turbulence modelling:** This thesis investigates the ability and necessity of turbulence modelling within a CFD–based NWT for WEC applications. The considered case studies include the numerical analysis of the near flow field around an oscillating heave plate, as well as the excitation forces and dynamics of WECs under the influence of different turbulence models (see Chapter 9).

5. **Scaling effects:** This thesis presents a comprehensive analysis of the hydrodynamic scaling effects within a CFD–based NWT, based on two validated numerical models of a single device at different scales. By exploiting the capabilities of a CFD–based NWT, the presented analysis takes a closer look at the influence of the applied scaling law (Reynolds or Froude) on the numerical results (see Chapter 10). The corresponding publications is [JPN].

6. **Assessment of WEC controllers:** This thesis presents the assessment of the evaluation platform for EMCSs, based on two different WEC structures are three different EMCSs of varying aggressiveness (see Chapter 11). The corresponding publications are [CPE, JPM].

1.2.3 List of publications

Conference publications

[CPA] **C. Windt**, J. Davidson, P. Schmitt, J. V. Ringwood, *"Assessment of Numerical Wave Makers"*, Proceedings of the 12th European Wave and Tidal Energy Conference (EWTEC), Cork, Ireland, pages 707–(1-10), 2017.

[CPB] **C. Windt**, J. Davidson, B. Benazzou, J. V. Ringwood, *Performance Assessment of the Overset Grid Method for Numerical Wave Tank Experiments in the OpenFOAM Environment"*, Proceedings of the 37th International Conference on Ocean, Offshore & Arctic Engineering (OMAE), Madrid, Spain, pages 1-10, 2018.

[CPC] **C. Windt**, J. Davidson, E. J. Ransley, M. Jakobsen, M. Kramer, J. V. Ringwood, *"Validation of a CFD-based numerical wave tank of the Wavestar WEC"*, Proceedings of the 3rd International Conference on Renewable Energies Offshore (RENEW), Lisbon, Portugal, pages 439–446, 2018.

[CPD] **C. Windt**, J. Davidson, D. Chandar, J. V. Ringwood, *"On the Importance of Advanced Mesh Motion Models in CFD-based Numerical Wave Tanks for WEC Testing"*, Proceedings of the 8th International Conference on Computational Methods in Marine Engineering (MARINE), Gothenburg, Sweden, pages 145–156, 2019.

[CPE] **C. Windt**, N. Faedo, M. Penalba, J. V. Ringwood, *"Assessment of the Evaluation Framework for Energy Maximising Control Systems for the Wavestar Wave Energy Converter"*, Proceedings of the 2019 American Control Conference (ACC), Philadelphia, PA, USA, pages 4791–4796, 2019.

[CPF] **C. Windt**, J. Davidson, P. Schmitt, J. V. Ringwood, *"Contribution to the CCP-WSI Blind Test Series 3: Analysis of scaling effects of moored point-absorber wave energy converters in a CFD-based numerical wave tank"*, Proceedings of the 29th International Ocean and Polar Engineering Conference (ISOPE), Honolulu, HI, USA, pages 3051–3058, 2019.

[CPG] **C. Windt**, J. Davidson, P. Schmitt, J. V. Ringwood, *"Contribution to the CCP-WSI Blind Test Series 2: CFD-based numerical wave tank experiments employing an impulse source wave maker"*, Proceedings of the 13th European Wave and Tidal Energy Conference (EWTEC), Naples, Italy, pages 1265–(1-9), 2019.

Journal publications (published)

[JPA] M. Penalba, J. Davidson, **C. Windt**, J. V. Ringwood, *"A high-fidelity wave-to-wire simulation platform for wave energy converters: Coupled numerical wave tank and power take-off models"*, Applied Energy (*226*), pages 655–669, 2018.

[JPB] **C. Windt**, J. Davidson, J. V. Ringwood, *"High-fidelity numerical modelling of ocean wave energy systems: A review of computational fluid dynamics-based numerical wave tanks"*, Renewable and Sustainable Energy Reviews (*93*), pages 610–630, 2018.

[JPC] J. Davidson, **C. Windt**, G. Giorgi, R. Genest, J. V. Ringwood, *"Evaluation of energy maximising control systems for wave energy converters using OpenFOAM"*, in OpenFOAM – Selected papers from the 11th Workshop, Springer, 2018

[JPD] **C. Windt**, J. Davidson, P. Schmitt, J. V. Ringwood, *"On the assessment of numerical wave makers in CFD simulations"*, Journal of Marine Science and Engineering (*2*), 47, 2019.

[JPE] P. Schmitt, **C. Windt**, J. Davidson, J. V. Ringwood, *"The efficient application of an impulse source wavemaker to CFD simulations"*, Journal of Marine Science and Engineering (*3*), 71, 2019.

[JPF] **C. Windt**, J. Davidson, D. Chandar, J. V. Ringwood, *"Evaluation of the overset grid method for control studies of wave energy converters in OpenFOAM numerical wave tanks"*, Journal of Ocean Engineering and Marine Energy, pages 1–16, 2019.

[JPG] **C. Windt**, J. Davidson, E. J. Ransley, D. Greaves, M. Jakobsen, M. Kramer, J. V. Ringwood, *"Validation of a CFD-based numerical wave tank model for the power production assessment of the wavestar ocean wave energy converter"*, Renewable Energy (*146*), pages 2499–2516, 2020.

[JPH] **C. Windt**, J. Davidson, P. Schmitt, J. V. Ringwood, *"CCP-WSI blind test series 3: CFD-based numerical wave tank experiments employing an impulse source wave maker"*, International Journal of Offshore and Polar Engineering (*30*), pages 28–35, 2020.

[JPI] E. Ransley, S. Yan, S. Brown, M. Hann, D. Graham, **C. Windt**, P. Schmitt, J. Davidson, J. Ringwood, P. H. Musiedlak, J. Wang, J. Wang, Q. Ma, Z. Xie, N. Zhang, X. Zheng, G. Giorgi, H. Chen, Z. Lin, L. Qian, Z. Ma, W. Bai, Q. Chen, J. Zang, H. Ding, L. Cheng, J. Zheng, H. Gu, X. Gong, Z. Liu, Y. Zhuang, D. Wan, H. Bingham, D. Greaves, *"A blind comparative study of focused wave interactions with floating structures (CCP-WSI Blind Test Series 3)"*, International Journal of Offshore and Polar Engineering (*30*), pages 1–10, 2020.

[JPJ] **C. Windt**, J. Davidson, P. Schmitt, J. V. Ringwood, *"Wave–structure interaction of wave energy converters: A sensitivity analysis"*, accepted in the Proceedings of the Institution of Civil Engineers - Engineering and Computational Mechanics, n.d.

[JPK] E. Ransley, S. Brown, M. Hann, D. Greaves, **C. Windt**, J. Ringwood, J. Davidson, P. Schmitt, S. Yan, J. X. Wang,J. H. Wang, Q. Ma, Z. Xie, G. Giorgi, J. Hughes, A. Williams, I. Masters, Z. Lin, H. Chen, L. Qian, Z. Ma, Q. Chen, H. Ding, J. van Rij, Y. Yu, Z. Li, B. Bouscasse, G. Ducrozet, H. Bingham, *"Focused wave interactions with floating structures: A blind comparative study"*, accepted in the Proceedings of the Institution of Civil Engineers - Engineering and Computational Mechanics, n.d.

[JPL] **C. Windt**, N. Faedo, Y. Peña-Sanchez, D. Garcia Violini, J. Davidson, F. Ferri, J. V. Ringwood, *"Validation of a CFD-based numerical wave tank model of the 1/20th scale Wavestar wave energy converter"*, Fluids (*5*), 112, 2020

Journal publications (under review)

[JPM] **C. Windt**, N. Faedo, M. Penalba, F. Dias, J. V. Ringwood, *"Reactive control of wave energy devices – the modelling paradox"*, under review in Applied Ocean Research, n.d.

[JPN] **C. Windt**, J. Davidson, J. V. Ringwood, *"Numerical analysis of the hydrodynamic scaling effects for the Wavestar wave energy converter"*, under review in the Journal of Fluids and Structures, n.d.

Journal publications (in preparation)

[JPO] **C. Windt**, C. J. Rusch, J. Davidson, B. L. Polagye, B. D. Maurer, J. V. Ringwood, *"Numerical investigation of the near flow field around a heave plate of a wave energy converters"*, for Fluids and Structures.

[JPP] **C. Windt**, J. Davidson, D. Chandar, J. V. Ringwood, *"Turbulent or not: Flow field around wave energy converters"*, for Fluids and Structures.

1.2.4 Supplementary material

[SMA] **C. Windt**, J. Davidson, P. Schmitt, J. V. Ringwood, *"Development of an impulse–source–based wave–current interaction model"*, Proceedings of the 7th European Conference on Computational Fluid Dynamics (ECFD), Glasgow, UK, pages 3202–3212, 2018.

[SMB] Y. Peña-Sanchez, N. Faedo, M. Penalba, G. Giorgi, A. Mérigaud, **C. Windt**, D. Garcia Violini, L. Wang, J. V. Ringwood, *"Finite-Order hydrodynamic Approximation by Moment-Matching (FOAMM) toolbox for wave energy applications"*, Proceedings of the 13th European Wave and Tidal Energy Conference (EWTEC), Naples, Italy, pages 1448–(1-9), 2019.

[SMC] J. Kemper, **C. Windt**, K. Graf, J. V. Ringwood, *"Development towards a nested hydrodynamic model for the numerical analysis of ocean wave energy systems"*, Proceedings of the 13th European Wave and Tidal Energy Conference (EWTEC), Naples, Italy, pages 1414–(1-10), 2019.

[SMD] D. Garcia Violini, Y. Peña-Sanchez, N. Faedo, **C. Windt**, J. V. Ringwood, *"LTI energy-maximising control for the Wave Star wave energy converter: identification, design, and implementation"*, accepted in the 21st FAC World Congress, Berlin, Germany, 2020.

[SME] Y. Peña-Sanchez, **C. Windt**, J. Davidson, J. V. Ringwood, *"A Critical Comparison of Excitation Force Estimators for Wave Energy Devices"*, IEEE Transactions on Control Systems Technology (early access), 2019.

[SMF] P. Schmitt, **C. Windt**, J.Davidson, J. V. Ringwood, *"Beyond VoF – numerical wave tanks in OpenFOAM"*, Journal of Ocean Engineering and Marine Energy, pages 1—16, 2020

[SMG] D. Garcia Violini, Y. Peña-Sanchez, N. Faedo, **C. Windt**, J. V. Ringwood, *"Experimental implementation and validation of a broadband LTI energy-maximising control strategy for the Wavestar device"*, under review in IEEE Transactions on Control Systems Technology, n.d.

[SMH] **C. Windt**, J. Davidson, E. J. Ransley, D. Greaves, J. V. Ringwood, *"Assessing the validity of regular wave theory in a short physical wave flume using particle image velocimetry"*, under review in Experimental Thermal and Fluid Science, n.d.

1.3 Thesis layout

The remainder of this thesis is separated into two parts, comprising a total of 11 chapters, and is organised as follows:

- Part I provides the necessary background information to provide an understanding of the numerical modelling approaches used throughout this thesis. Furthermore, Part I delivers a comprehensive literature review which provides the interface between the background material of Part I and the main original work of Part II. In particular:
    - Chapter 2 presents the underlying mathematical description of the fluid dynamics within a high–fidelity, CFD–based NWT and details the governing equations of the dynamics of viscous, inviscid, as well as inviscid and irrotational flows. For viscous flows, a closer look is taken at the physical and mathematical description of the prevailing flow conditions.
    - Chapter 3 gives a brief overview of the mathematical description of ocean waves and the specific wave theories employed throughout this thesis. More specifically, the chapter treats the description of regular, irregular, and focuses waves, which are considered in Part II of this thesis.
    - Chapter 4 presents the numerical methods used for the solution of the governing equations within a CFD–based NWT. In particular, the chapter provides a brief overview of the finite–volume method, solution schemes for the discretised governing equations, and the treatment of the pressure–velocity coupling. In addition, the chapter elaborates on the requirements of a CFD–based NWT for WEC applications.
    - Chapter 5 reviews the existing literature of CFD–based NWTs for WEC applications. The reviewed literature is organised into different sections based on the specific WECs, considered in the reviewed studies, the application, and the included WEC sub–systems, as well as numerical aspects (problem discretisation, flow regimes, numerical wave generation and absorption, fluid–structure interaction), the model validation, and the employed CFD software. Ultimately, the chapter identifies shortcomings of existing CFD–based NWTs for WEC applications, which are partly filled by the contributions documented in Part II.
- Part II comprises the last seven chapters and documents the main contributions of this thesis. In particular:

- Chapter 6 treats the topic of numerical wave generation. First, advances of the impulse source wave maker[4], initially developed in [20], are presented together with a calibration procedure for the efficient generation of desired target wave trains. Subsequently, a rigorous assessment procedure for numerical wave makers is proposed and demonstrated by an illustrative example, considering widely used numerical wave makers within OpenFOAM.
- Chapter 7 presents comprehensive validation studies of the different NWT models, used in subsequent Chapters 8–11. Specifically, the validation studies treat four different devices: a 1/5th and 1/20th scale Wavestar device [21], as well as two different moored point absorber type WECs, based on the Blind Test Series 2 and 3, organised by the Collaborative Computational Project in Wave–Structure Interaction (CCP–WSI) [22, 23].
- Chapter 8 presents the evaluation of the overset grid method for control studies of WECs. The newly available overset grid method in OpenFOAM shows potential to improve the stability of CFD–based NWTs for the application of WEC experiments, specifically for control studies, featuring exaggerated WEC motion. This chapter provides an in–depth comparative study between the classical mesh morphing method and the overset grid method, based on a suite of test cases with increasing complexity, for single– and multi–phase problems.
- Chapter 9 investigates the flow field around WECs, in particular the turbulence modelling requirements within CFD–based NWTs, for WEC applications. Two different case studies are considered for the analysis: a heave plate forced into oscillating motion and two moored point absorber type WECs in operational conditions.
- Chapter 10 presents an analysis of scaling effects for WECs. The analysis is based upon the Wavestar device at three different scales, i.e. 1/20th, 1/5th, and 1/1. A suite of test cases with increasing complexity is considered, ranging from regular wave–only test cases to wave driven WEC motion in irregular waves under controlled conditions. By exploiting the capability of CFD–based NWTs to easily change the transport properties of the involved fluids, an analysis of the employed scaling laws (Reynolds and Froude) [24] is included in this chapter.

---

[4] Note that the term *wave maker* is taken to comprise both wave generation and absorption throughout this thesis (see Chapter 4).

- Chapter 11 moves towards holistic WEC modelling and presents an assessment of the evaluation framework for WEC controllers, investigating the effects of the *aggressiveness* of a controller on the required fidelity of the evaluation framework[5].
- Finally, Chapter 12 presents the thesis conclusions, drawn from the previous chapters and, in addition, gives an outlook on potential extensions of the presented contributions as pertinent future work.

---

[5] Note that an assessment of wave–to–wire modelling frameworks for WECs is omitted in this thesis for brevity; however, the interested reader is referred to [JPA] for a study of different wave–to–wire models of varying model fidelity.

Part I

Background

2

Fluid dynamics

Contents

For a better understanding of the underlying mathematical description of the fluid dynamics within a high–fidelity numerical wave tank, this chapter presents the governing equations of the dynamics of viscous (Section 2.1), inviscid (Section 2.2), as well as inviscid and irrotational flows (Section 2.3). For viscous flows, Section 2.4 pays special attention to the physical and mathematical description of the prevailing flow conditions (laminar or turbulent). Note that the numerical solution methods for the governing equation, introduced in this chapter, are detailed in Chapter 4.

In the literature, a large number of text books, such as [25–32], can be found, deriving the mathematical description of fluids flows. For the sake of brevity, this chapter will not give a complete recapitulation of the derivation, but rather aims to provide a concise overview of the governing equations. For more detailed insights, the interested reader is referred to the literature [25–32].

2.1 Viscous flow – Navier–Stokes equations

The governing equations which describe the dynamics of a fluid flow stem from the three conservation laws for mass, momentum, and energy. Under the assumption of iso-thermal fluids, which holds for all cases considered in this thesis and the majority of cases considered in the literature of hydrodynamic WEC models (see Chapter 5), only mass and momentum conservation are considered explicitly. For an arbitrary control mass of fluid, mass conservation expresses that the mass over time is invariant, while momentum conservation follows Newton's second law of motion. Formally, the conservation laws for mass and momentum are described in a general form as

$$\frac{\mathrm{d}m}{\mathrm{d}t} = 0 \qquad \text{and} \tag{2.1}$$

$$\frac{\mathrm{d}(m\mathbf{u})}{\mathrm{d}t} = \sum \mathbf{f}\,, \tag{2.2}$$

respectively. In Equation (2.1) and (2.2), $^{\mathrm{d}}/_{\mathrm{d}t}$ denotes the time derivative, m is the mass, t is time, $\mathbf{u}$ the velocity vector, and $\mathbf{f}$ are the acting forces.
This set of equations allows the description of various types of flows and fluid: Newtonian or non–Newtonian[1], laminar or turbulent (see Section 2.4), single–phase or multi–phase (see Section 4.3.1), compressible or incompressible (see Sections 2.1.1 and 2.1.2).

2.1.1 Compressible flow

It will be shown, in Chapter 4, that it is convenient for the numerical solution procedure, employed throughout this thesis, to describe the conservation laws for mass and momentum in a control volume form rather than in the above control mass form. Transforming Equations (2.1) and (2.2) from the control mass to the control volume form, by applying the control volume equation and, furthermore, exploiting the Gauss' divergence theorem, yields the continuity (2.3) and the momentum equation (2.4) in the common form – the Navier–Stokes equations[2]:

$$\frac{\partial \rho}{\partial t} + \nabla \cdot (\rho \mathbf{u}) = 0\,, \tag{2.3}$$

$$\frac{\partial (\rho \mathbf{u})}{\partial t} + \nabla \cdot (\rho \mathbf{u}\mathbf{u}) = \nabla \cdot \mathbf{T} + \rho \mathbf{f}_b\,. \tag{2.4}$$

In Equations (2.3) and (2.4), $\nabla \cdot \phi$ denotes the divergence of the generic fluid property $\phi \in \mathbb{R}^3$, defined as $\nabla \cdot \phi = \frac{\partial \phi_x}{\partial x} + \frac{\partial \phi_y}{\partial y} + \frac{\partial \phi_z}{\partial z} \in \mathbb{R}$. $\nabla \phi$ denotes the gradient of $\phi \in \mathbb{R}^3$, defined as $\nabla \phi = \left[\frac{\partial \phi}{\partial x}, \frac{\partial \phi}{\partial y}, \frac{\partial \phi}{\partial z}\right] \in \mathbb{R}^3$. ρ is the fluid density and $\mathbf{f}_b$ are

---

[1] By and large, fluids in engineering applications can be considered Newtonian, showing a proportionality between the viscous stresses and the rates of deformation of a fluid element [29, 30].

[2] Note that the energy equation is omitted here for brevity.

external body forces, such as gravitational forces. The stress tensor, $\mathbf{T}$, includes both normal as well as viscous stresses and follows:

$$\mathbf{T} = -\left(p + \frac{2}{3}\mu\nabla\cdot\mathbf{u}\right)\mathbf{I} + 2\mu\mathcal{D}\,. \tag{2.5}$$

In Equation (2.5), p is the pressure, μ describes the dynamic viscosity, $\mathbf{I}$ is the unit tensor, and $\mathcal{D} = {}^1\!/_2\left[\nabla\mathbf{u} + (\nabla\mathbf{u})^{\intercal}\right]$ is the rate of strain tensor. The interested reader is referred to [30, Chapter 2] for a detailed derivation of $\mathbf{T}$ and $\mathcal{D}$.

The compressibility of the fluid is formally expressed by the partial time derivative of ρ in the continuity equation (2.3). Generally, for hydrodynamic modelling, and in particular for WSI problems, the working fluid, i.e. (sea) water, can be considered incompressible. The literature review in Chapter 5 will highlight that only a few studies, considering oscillating water column devices, investigate the effects of compressibility for the air flow through the (idealised) PTO system. The modelling of oscillating water column devices is not subject of this thesis, thus, incompressible flow is considered throughout this thesis.

2.1.2 Incompressible flow

Assuming incompressibility, the partial derivative ${}^{\partial\rho}\!/_{\partial t}$ is zero, reducing the continuity equation (2.3) to[3]:

$$\nabla\cdot(\rho\mathbf{u}) = 0\,. \tag{2.6}$$

With that, the second term $(\frac{2}{3}\mu\nabla\cdot\mathbf{u})$ of the stress tensor $\mathbf{T}$ in Equation (2.5) is zero, reducing $\mathbf{T}$ to:

$$\mathbf{T} = -p\mathbf{I} + 2\mu\mathcal{D}\,. \tag{2.7}$$

Substituting Equation (2.7) into Equation (2.4) and rearranging yields the momentum equation for incompressible flows:

$$\frac{\partial(\rho\mathbf{u})}{\partial t} + \nabla\cdot(\rho\mathbf{u}\mathbf{u}) = -\nabla p + \rho\nabla\cdot(\nu\nabla\mathbf{u}) + \rho\mathbf{f}_b\,, \tag{2.8}$$

where $\nu = {}^{\mu}\!/_{\rho}$ is the kinematic viscosity. Depending on the particular conditions within the flow (laminar or turbulent), the observed flow behaviour requires explicit treatment within the governing equation for efficient numerical solution (see Section 2.4).

---

[3] Note that the density is retained in Equation (2.6) due to the single fluid approximation when accounting for the multi–phase problem, see Chapter 4.

2.2 Inviscid flow – Euler equations

Although high–fidelity hydrodynamic models are generally applied to solve WSI problems for which viscosity is non-negligible (e.g. exaggerated structural motion due to control action), it can be beneficial to investigate WSI under the assumption of inviscid fluids (e.g. for the assessment of viscous effects). Neglecting viscosity yields the Euler equations (2.6) and (2.9), for mass and momentum conservation, respectively.

$$\frac{\partial\left(\rho\mathbf{u}\right)}{\partial t} + \nabla\cdot\left(\rho\mathbf{u}\mathbf{u}\right) = -\nabla p + \rho\mathbf{f}_b\,. \tag{2.9}$$

Due to the present non–linearities in the conservation equations, no general analytical solutions[4] are available for the introduced governing equations for viscous (incompressible and compressible) and inviscid flows, which led to the development of numerical solution procedures (see Chapter 4).

2.3 Inviscid and irrotational flow – Laplace equation

While still preventing a general analytical solution of the governing equations, but significantly reducing the computational overhead during the numerical solution process, the fluid flow can be further simplified by assuming an inviscid *and* irrotational fluid. Under a set of assumptions (see Section 2.3.1), solutions for inviscid and irrotational flows deliver reasonable results for engineering problems. A physical interpretation of irrotationallity is visualised in Figure 2.1. Formally, irrotationality is expressed as $\nabla\times\mathbf{u} = 0$, where $\nabla\times$ defines the cross gradient.

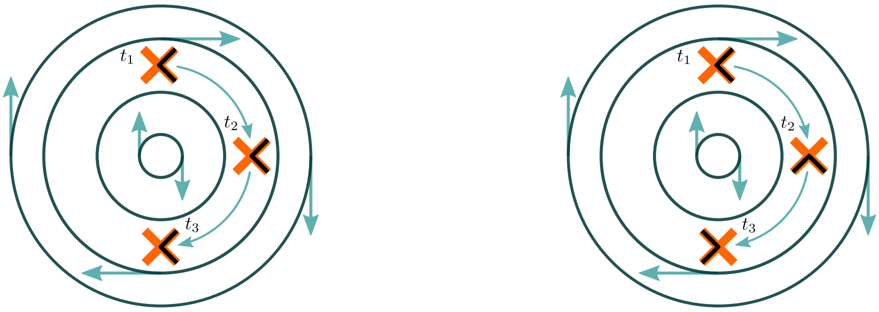

(a) Irrotational **(b)** Rotational

Figure 2.1: Visualisation of the physical interpretation of an (a) irrotational flow compared to a (b) rotational flow (adapted from [33]). In an irrotational flow with circular stream lines, the cross–shaped tracers (orange colour code) do not change their orientation. Conversely, in a rotational flow with circular stream lines, the cross–shaped tracers change their orientation.

---

[4] Examples of analytical solutions for specific fluid flow problems can, for example, be found in [28].

With the assumption of an irrotational fluid, the velocity can be defined through the velocity potential, Φ, following:

$$\mathbf{u} = \nabla\Phi \tag{2.10}$$

Substituting Equation (2.10) into the continuity equation (2.6) yields the Laplace equation:

$$\nabla^2\Phi = 0\,. \tag{2.11}$$

With the Laplace equation (2.11) and, furthermore, only considering gravitational forces in $\mathbf{f}_b$, the momentum equation (2.9) can be rearranged to

$$\nabla\left(\frac{\partial\Phi}{\partial t} + \frac{1}{2}(\nabla\Phi)^2 + \frac{p}{\rho} + gz\right) = 0\,, \tag{2.12}$$

where g is the gravitational acceleration. Integration of Equation (2.12) then delivers the Bernoulli equation:

$$\frac{\partial\Phi}{\partial t} + \frac{1}{2}(\nabla\Phi)^2 + \frac{p}{\rho} + gz = C\,, \tag{2.13}$$

where C denotes an integration constant.

2.3.1 Linear potential flow theory

For WSI problems, the Laplace and Bernoulli equations have found widespread application in the ocean and offshore engineering field in the form of linear potential flow theory [12, 35]. For the solution of the Bernoulli equation (2.13) for WSI problems, boundary conditions are defined. Namely the kinematic and dynamic (free surface) boundary conditions. The kinematic boundary condition can be split into a boundary condition for impermeable surfaces (e.g., the idealised flat sea bed) and the free surface. For impermeable surfaces, the boundary condition states that no fluid enters or leaves the surface, resulting in

$$\frac{\partial\Phi}{\partial z} = 0 \tag{2.14}$$

on the flat sea bed at $z = -d$, where d is the water depth. On the free surface, the kinematic boundary condition states that fluid particles stay on the free surface, such that

$$\frac{\partial\eta}{\partial t} + \frac{\partial\Phi}{\partial x}\frac{\partial\eta}{\partial x} + \frac{\partial\Phi}{\partial y}\frac{\partial\eta}{\partial y} - \frac{\partial\Phi}{\partial z} = 0 \tag{2.15}$$

on the free surface at $z = \eta$, where η is the free surface elevation.

The dynamic free surface conditions, finally, states that the pressure on the free surface is equal to the atmospheric pressure $p_{\text{atmospheric}}$. With C in Equation (2.13) defined as $p_{\text{atmospheric}}/\rho$, the dynamic free surface conditions is expressed as

$$\frac{\partial \Phi}{\partial t} + \frac{1}{2}\left[\left(\frac{\partial \Phi}{\partial x}\right)^2 + \left(\frac{\partial \Phi}{\partial y}\right)^2 + \left(\frac{\partial \Phi}{\partial z}\right)^2\right] + g\eta = 0\,, \tag{2.16}$$

Assuming small wave amplitudes (relative to the wave length) and small body motion (relative to the body dimensions), the kinematic and dynamic boundary conditions can be linearised (see Chapter 3), such that solutions for the velocity potential can be found numerically, e.g. through boundary element method (BEM) solvers [36]. For a detailed derivation of the linear potential flow theory for WSI problems, and the numerical solution procedure in frequency and time domain, the interested reader is referred to [34, 37].

2.4 Laminar and turbulent flow

As stated in Section 2.1, in viscous flows, the characteristics of the observed flow may show significant differences based on the prevailing conditions: laminar or turbulent. By way of example, Figure 2.2 depicts the (idealised) stream lines of a flow past a circle, with a free stream velocity, u_∞, for a (a) fully laminar flow and a (b) laminar flow with turbulent wake. As will be shown in the literature review in Chapter 5, and further discussed in Chapter 9, the definition (and modelling) of the flow conditions in the near flow field of WECs is still a source of uncertainty.

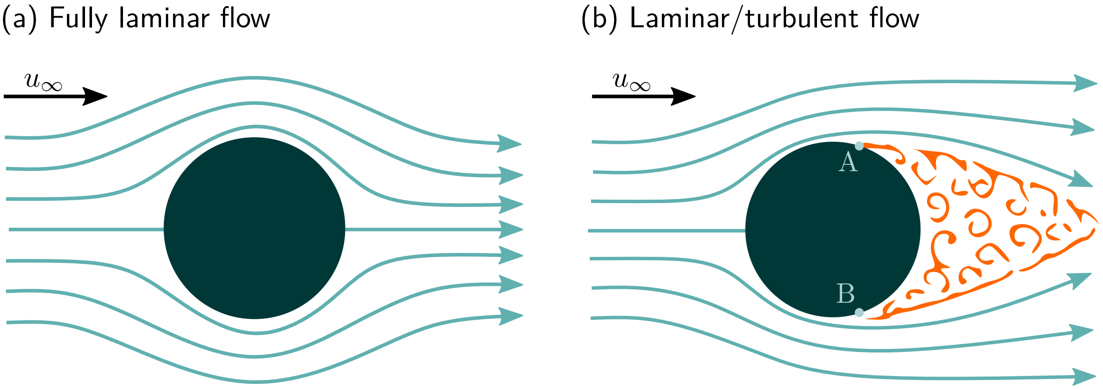
(a) Fully laminar flow

(b) Laminar/turbulent flow

Figure 2.2: Visualisation of a (a) fully laminar flow and (b) a laminar flow with turbulent wake past a circle with a free stream velocity u_∞. In (b), the flow features laminar flow conditions up to the point of separation (A and B), after which a turbulent wake develops (orange colour code) (adapted from [38]).

2.4.1 Laminar flow

In laminar flows, infinitesimal fluid layers move smoothly past each other and no mixing occurs between the layers. In such *orderly* flows, small perturbations in the flow are damped out and viscous forces are predominant over inertial forces. The ratio between inertial and viscous forces within the fluid flow can be expressed through the dimensionless Reynolds number, Re (see Equation (2.17)), which is commonly used to characterise the condition of a fluid flow (laminar or turbulent).

$$Re = \frac{u_\infty \cdot L}{\nu} \tag{2.17}$$

In Equation (2.17), L denotes a characteristic length scale, such as the diameter of the circle in Figure 2.2. Generally, for small Re (inertial forces $<$ viscous forces), the flow can be considered laminar. Increasing Re past a certain, critical Reynolds number, Re^*, e.g. by increasing the free stream velocity or reducing the kinematic viscosity, the flow transitions from laminar to turbulent. For a number of *standard* flows, Re^* has been determined through experimental studies and can be extracted from well known text books (e.g. [28]).

2.4.2 Turbulent flow

Once the flow is characterised by Re larger than Re^*, small perturbations in the flow are amplified and the flow turns turbulent. Turbulent flows can be characterised as random and, following Kundu *et al.* [32], feature:

- fluctuations of the field quantities,
- rapid diffusion due to mixing,
- three–dimensional (3D) turbulent structures due to vorticity, i.e. eddies,
- dissipation of energy and vorticity,
- non–linearities.

Figure 2.3 visualises the fluctuating nature of a flow quantity ϕ in a turbulent flow. Measuring ϕ at a specific location within the flow over time, the measurement can be decomposed into a mean value $\bar{\phi}$ and its fluctuation $\phi^{'}$, so that $\phi = \bar{\phi} + \phi^{'}$. This decomposition approach is commonly referred to as Reynolds decomposition.

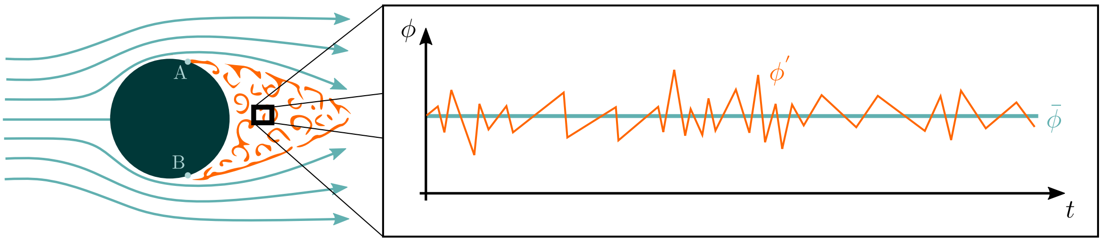

Figure 2.3: Visualisation of the field quantity ϕ in a turbulent flow and its decomposition into mean value $\bar{\phi}$ and the fluctuation $\phi^{'}$ (adapted from [30]).

Considering the velocity vector $\mathbf{u} = [u, v, w]$, where u, v, and w denote the velocity components for the three Cartesian coordinates x, y, and z, respectively, the Reynolds decomposition yields $u = \bar{u} + u^{'}$, $v = \bar{v} + v^{'}$, and $w = \bar{w} + w^{'}$. With the variance of the velocity fluctuations, denoted as $\overline{\overline{u^{'}}}$, $\overline{\overline{v^{'}}}$, and $\overline{\overline{w^{'}}}$, two quantities to characterise the turbulence of a flow can be defined: The kinetic turbulent energy, k_t (see Equation (2.18)), and the turbulence intensity, T_i (see Equation (2.19)).

$$k_t = \frac{1}{2}\left(\overline{\overline{u'^2}} + \overline{\overline{v'^2}} + \overline{\overline{w'^2}}\right) \tag{2.18}$$

$$T_i = \frac{\left({}^2\!/\!_3\, k_t\right)^{0.5}}{\bar{\mathbf{u}}_\infty} \tag{2.19}$$

Induced by the fluctuations within the flow, turbulent structures (eddies) develop, which cause the mixing of the fluid and introduce turbulent stresses, or Reynolds stresses, between fluid layers, leading to energy dissipation within the flow. Figure 2.4 visualises the (idealised) process of fluid mixing due to turbulent eddies. Considering a control volume within a shear flow (velocity gradient in the z direction), the turbulent eddies cause a momentum transfer into and out of the control volume which, in turn, leads to acceleration and declaration of fluid layers and, thus, to additional (Reynolds) stresses between the fluid layers. This physical behaviour helps in the development and interpretation of modified governing equations for the efficient solution of the fluid dynamics of turbulent flows.

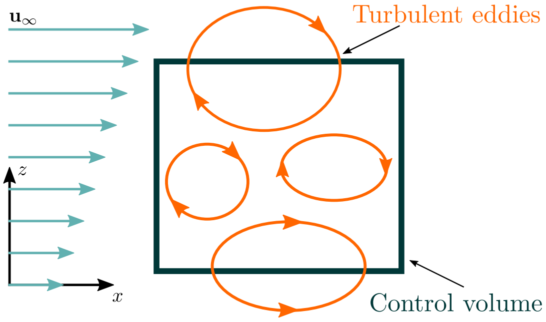

Figure 2.4: Fluid mixing of the fluid and Reynolds stresses due to turbulent eddies (adapted from [30]).

Direct numerical simulation – DNS

Generally, turbulent flows are readily described by the Navier–Stokes equations (2.3) and (2.4) (or (2.6) and (2.8) for incompressible flows) and solutions can be found through direct numerical simulation (DNS). Due to the occurring high frequency temporal fluctuations and the wide range of turbulent eddies sizes, DNS requires fine temporal and spatial discretisation sizes down to the Kolmogorov scale, at which viscous forces dominate the flow and the turbulent kinetic energy is dissipated. Such fine discretisation sizes are associated with immense computational cost, thus, render DNS infeasible for engineering purposes.

Large eddy simulation – LES

Lower fidelity solutions, with lighter computational requirements, are obtained by modelling, rather than resolving, the fine scale turbulent effects. To avoid discretisation down to the Kolmogorov length scale, large eddy simulation (LES) directly resolves only larger turbulent eddies [39]. The effects of smaller scale eddies are modelled, instead, using a sub–grid–scale (SGS) model. Prior to the solution of the governing equations, spatial filtering decomposes the velocities into resolved and residual components based on the SGS model. Unfiltered velocity components are directly resolved, whereas the system of equations for the residual turbulent stresses is closed by the underlying empirical turbulence model. A discussion of specific SGS models is presented in Chapter 4. Although LES come at a lower computational cost than DNS, LES is still associated with high (and usually unacceptable) computational demand.

Reynolds averaged Navier–Stokes – RANS

If turbulence has to be considered within the numerical model, but simulations should be performed at reasonable computational cost, turbulence models, based on the Reyonlds averaged Navier–Stokes (RANS) equations, can be employed. The RANS equations can be deduced by applying Reynolds decomposition to all relevant flow quantities, leading to the momentum equations (2.20) – (2.22), for the three Cartesian coordinates x, y, and z, respectively. Note that, for a better interpretation, the momentum equations are explicitly stated here for the three Cartesian coordinates x, y, and z, as opposed to the compact form in Equation (2.8).

$$\begin{aligned}\frac{\partial\,(\rho\bar{u})}{\partial\,t} + \nabla\cdot(\rho\bar{u}\,\mathbf{u}) = &-\frac{\partial\,p}{\partial\,x} + \rho\nabla\cdot(\nu\nabla\bar{u}) \\ &+ \left[\frac{\partial(-\rho\,\overline{\overline{u'^2}})}{\partial\,x} + \frac{\partial(-\rho\,\overline{\overline{u'\,v'}})}{\partial\,y} + \frac{\partial(-\rho\,\overline{\overline{u'\,w'}})}{\partial\,z}\right] + \mathbf{f}_b\end{aligned} \tag{2.20}$$

$$\begin{aligned}\frac{\partial\,(\rho\bar{v})}{\partial\,t} + \nabla\cdot(\rho\bar{v}\,\mathbf{u}) = &-\frac{\partial\,p}{\partial\,y} + \rho\nabla\cdot(\nu\nabla\bar{v}) \\ &+ \left[\frac{\partial(-\rho\,\overline{\overline{v'^2}})}{\partial\,y} + \frac{\partial(-\rho\,\overline{\overline{u'\,v'}})}{\partial\,x} + \frac{\partial(-\rho\,\overline{\overline{v'\,w'}})}{\partial\,z}\right] + \mathbf{f}_b\end{aligned} \tag{2.21}$$

$$\begin{aligned}\frac{\partial\,(\rho\bar{w})}{\partial\,t} + \nabla\cdot(\rho\bar{w}\,\mathbf{u}) = &-\frac{\partial\,p}{\partial\,z} + \rho\nabla\cdot(\nu\nabla\bar{w}) \\ &+ \left[\frac{\partial(-\rho\,\overline{\overline{w'^2}})}{\partial\,z} + \frac{\partial(-\rho\,\overline{\overline{u'\,w'}})}{\partial\,x} + \frac{\partial(-\rho\,\overline{\overline{v'\,w'}})}{\partial\,y}\right] + \mathbf{f}_b\end{aligned} \tag{2.22}$$

Special attention should be paid to additional terms including the variance of the velocity fluctuations, highlighted in blue. In the light of the momentum exchange within fluid layers, as explained above, these terms can be interpreted as the Reynolds stresses. The occurrence of additional terms in the RANS momentum equations requires additional equations to achieve closure of the system of equations. These additional equations can be provided in the form of turbulence models, which will be discussed in Chapter 4.

2.5 Concluding remarks

The dynamics of of an arbitrary, iso-thermal fluid flow obey the conservation laws for mass and momentum and are, consequently, described by the Navier-Stokes equations (2.3) and (2.4). Provided that no general analytical solution is available for the governing equations [40], numerical solutions are sought by discretising the problem in space and time to form a system of linear algebraic equations. Under certain assumption for the fluid flow (incompressible, inviscid, irrotational) the Navier-Stokes equations can be reduced, allowing a more efficient solution of the problem at the cost of reduced fidelity. The consequential fidelity/cost spectrum is depicted in Figure 2.5.

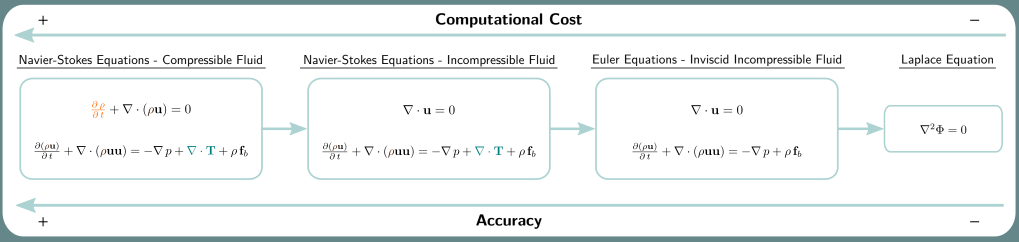

Figure 2.5: Relative accuracy and computational cost of different governing equations describing the dynamics of fluids under varying assumptions (adapted from [11]).

Throughout this thesis, iso-thermal, viscous and incompressible flows, governed by the RANS equations, are considered. A detailed description of the numerical methods for the solution of the RANS equations, together with a detailed discussion of the peculiarities and requirement of CFD–based numerical wave tanks is presented in Chapter 4.

3

Ocean Waves

Contents

Observing the surface of the ocean, the visible surface waves often appear random (see Figure 3.1) and an accurate mathematical description may seem impossible. However, over the centuries, theories for the descriptions of ocean waves have been proposed and a myriad of text books, such as [34, 12, 41–45], to highlight only a few, can be found, presenting the mathematical descriptions of surface waves. Since this thesis, at its core, treats the numerical modelling of waves and their interaction with WECs, this section will give a brief overview of the specific wave theories employed throughout this thesis (see Chapter 4 for the numerical implementation of the discussed wave theories). Initially, the simplest, but most unrealistic, description of ocean waves in the form of regular waves is considered in Section 3.1. Following on, a more realistic description, in the form of irregular waves, is detailed in Section 3.2. Finally, Section 3.3 introduces the mathematical description of focused waves, commonly used for modelling extreme events.

Figure 3.1: Photograph of ocean waves in the Black Sea, off the coast of Istanbul

3.1 Regular waves

Even though the observation of the ocean surface suggests that realistic ocean conditions can, if at all, only be described as a composition of various wave components with different amplitudes, periods, and directions (see Section 3.2), an insightful (and simple) description of ocean waves is delivered by Airy [43], describing waves in an incompressible, inviscid, and irrotational fluid (see Chapter 2) as regular, long crested, and linear, i.e. featuring a single frequency and amplitude, which is small compared to the wave length, as well as an invariant wave field in the lateral direction.

3.1.1 Free surface elevation

With the assumption of small wave amplitudes, the kinematic and dynamic free surface boundary conditions introduced in Section 2.3.1 can be linearised around the the still water level (SWL), resulting in

$$\frac{\partial \eta}{\partial t} = \frac{\partial \Phi}{\partial z}\,, \tag{3.1}$$

and

$$g\eta + \frac{\partial \Phi}{\partial t} = 0\,, \tag{3.2}$$

on $z = 0$, for the kinematic and dynamic boundary condition, respectively[1]. Combining Equations (3.1) and (3.2) leads to

$$\frac{\partial^2 \Phi}{\partial t^2} + g\frac{\partial \Phi}{\partial z} = 0\,, \tag{3.3}$$

---

[1] It should be noted here again that, throughout this thesis, waves are defined to travel in the x–direction and SWL lies at $z = 0$, with z pointing away from the sea floor, which is located at $z = -d$.

on $z = 0$. Following [46], a solution for Φ can be found as

$$\Phi = A\,\cosh(kz + kd)\,\sin(kx - \omega t)\,, \tag{3.4}$$

where A denotes the wave amplitude, $k = {}^{2\pi}/_{\lambda}$ is the wave number, with wave length λ, and $\omega = {}^{2\pi}/_{T}$ is the angular wave frequency, with wave period T. Substituting (3.4) in Equation (3.3) yields

$$0 = \omega^2 A \cosh(kz + kd)\sin(kx - \omega t)\,. \tag{3.5}$$

Reformulating Equation (3.5) then results in the linear dispersion relation

$$\frac{2\pi}{T} = \sqrt{\frac{2\pi}{\lambda} g \tanh\left(\frac{2\pi}{\lambda} d\right)}\,, \tag{3.6}$$

formally expressing the relationship between the space and time domain (see Figure 3.2); or, the relationship between the wave speed, $c = {}^{\lambda}/_{T} = {}^{\omega}/_{k}$, and the wave length.

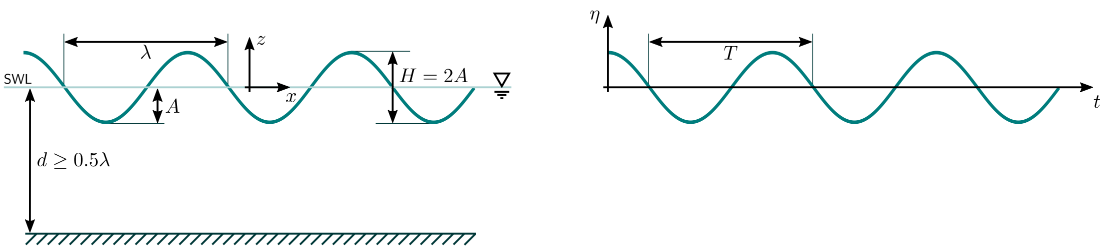

(a) Space domain

(b) Time domain

Figure 3.2: Definition of a linear, regular wave in the (a) space and (b) time domain. d denotes the water depth, SWL is the still water level. λ is the wave length, and T the wave period. A denotes the wave amplitude and $H = 2A$ is the wave height.

To find an expression for the free surface elevation in the time domain, the dynamic boundary condition in Equation (3.2) can again be considered together with the solution of the velocity potential in (3.4), yielding

$$\eta = \frac{A\omega}{g}\cosh(kd)\cos(kx - \omega t)\,. \tag{3.7}$$

Defining the wave height as the difference between the surface elevation at the crest ($kx - \omega t = 0$) and the wave trough ($kx - \omega t = \pi$) yields, after some reformulation (see [46]),

$$\eta^{(1)} = \frac{H}{2}\cos(kx - \omega t)\,, \tag{3.8}$$

and

$$\Phi^{(1)} = \frac{H}{2}\frac{g}{\omega}\frac{\cosh(kz + kd)}{\cosh(kd)}\sin(kx - \omega t)\,. \tag{3.9}$$

Equations (3.8) and (3.9) show the solution for the first order (as indicated by the supercript $^{(1)}$), linear, wave theory. However, one of the main motivations to use high–fidelity numerical models is desired to model higher order, non–linear, waves. To that end, first order wave theory can be extended to higher orders, resulting in Stokes' wave theory [47]. The higher order extension stems from the Taylor series expansion used to transform the boundary conditions from $z = \eta$ to $z = 0$. Formally, following [46], this is expressed as:

$$\left.\frac{\partial \Phi}{\partial x}\right|_{z=\eta} = \left.\frac{\partial \Phi}{\partial x}\right|_{z=0} + \eta \left.\frac{\partial^2 \Phi}{\partial x \partial z}\right|_{z=0} + \ldots \tag{3.10}$$

To derive the first order wave theory, the Taylor series expansion is formulated for the kinematic and dynamic boundary conditions but then truncated after the first term on the right hand side. Retaining higher order terms results, after some significant calculus, in solutions for, e.g., the second order surface elevation:

$$\eta^{(2)} = \eta^{(1)} + \frac{\pi H^2}{8\lambda} \frac{\cosh(kd)}{\sinh^3(kd)} \cdot [2 + \cosh(2kd)] \cos(2(kx - \omega t)) \,. \tag{3.11}$$

An example of the solution for fifth order Stokes waves has been derived in [48]. It should be noted here that other wave theories, such as the stream function wave theory [44, Chapter 3], are available.

By way of example, Figure 3.3 shows time traces of three different waves, described by the 1st (dashed, $T = 8$s, $H = 0.5$m, $d = 70$m), 2nd (dotted, $T = 8$s, $H = 1.5$m, $d = 70$m), and 5th order (solid, $T = 19$s, $H = 1.5$m, $d = 7$m) Stokes wave theory.

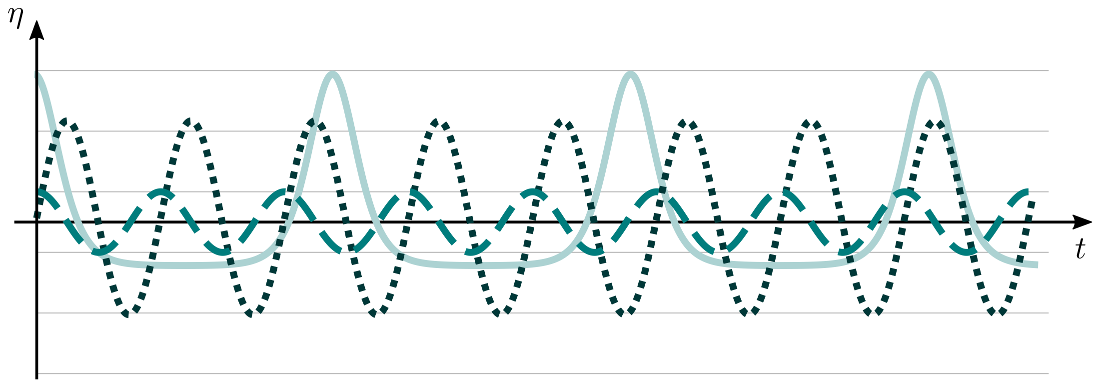

Figure 3.3: Time traces of a 1st (dashed, $T = 8$s, $H = 0.5$m, $d = 70$m, $H/\lambda = 0.005$), 2nd (dotted, $T = 8$s, $H = 1.5$m, $d = 70$m, $H/\lambda = 0.015$), and 5th order (solid, $T = 19$s, $H = 1.5$m, $d = 7$m, $H/\lambda = 0.010$) Stokes wave.

A convenient visualisation of the required order of the wave theory for an accurate description of a wave is provided by the Le Méhauté diagram [41], depicted in Figure 3.4.

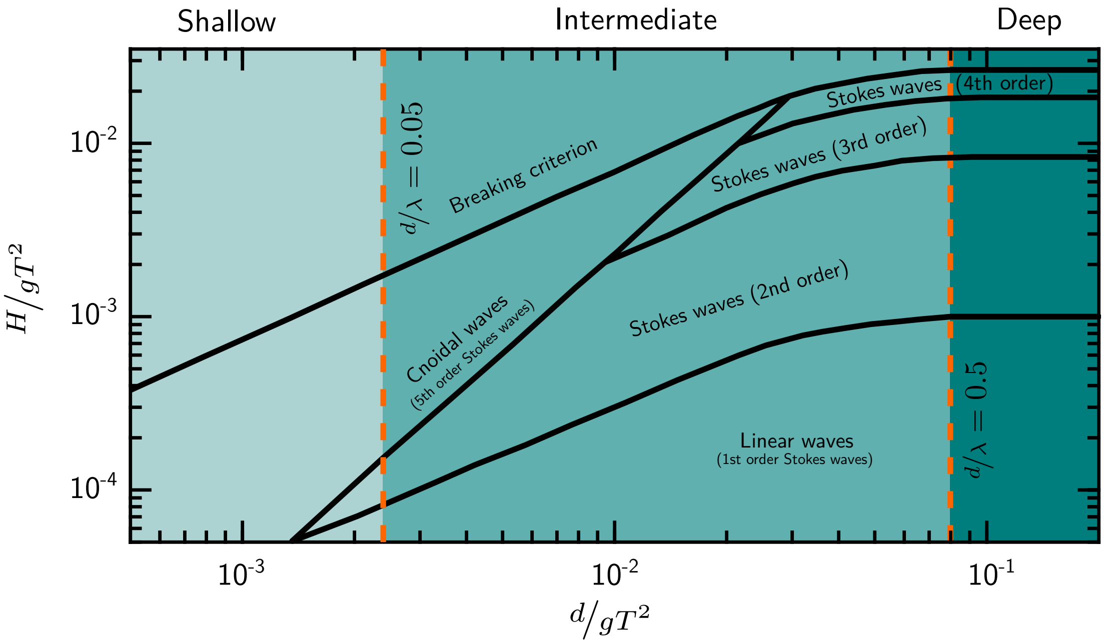

Figure 3.4: Le Méhauté diagram (adapted from [41])

Figure 3.4 includes the indicators for the shallow ($d/\lambda \leq 0.05$) and deep water conditions ($d/\lambda \geq 0.5$). Going back to the dispersion relation (3.6) and expressing it in terms of the wave speed

$$\frac{c}{\sqrt{gd}} = \sqrt{\frac{\tanh(2\pi d/\lambda)}{2\pi d/\lambda}}\,, \tag{3.12}$$

one can plot the dimensionless wave speed $c/\sqrt{gd}$ as a function of the dimensionless wave length λ/d (see Figure 3.5).

Investigating the extreme cases $\lambda/d = \infty$ (i.e., very shallow water), it can be observed that the dimensionless wave speed asymptotically approaches 1, indicating that the wave speed is independent of the wave length. Based on Figure 3.5 is can be stated that this 'shallow water limit' is reached for $\lambda/d \geq 20\,(= d/\lambda \leq 0.05)$. For the extreme case $\lambda/d = 0$ (i.e., very deep water), it can be shown that the wave speed is independent of the water depth. This 'deep water limit' is reached for $\lambda/d \leq 2\,(= d/\lambda \geq 0.5)$.

A quantification of the latter 'deep water limit' is possible when considering the $\cosh$ term in Equation (3.9). For $\lambda/d = 0 \rightarrow kd = \infty$

$$\frac{\cosh(kz + kd)}{\cosh(kd)} = \frac{e^{kz+kd}}{e^{kd}} = e^{kz} \tag{3.13}$$

holds. Then substituting $z = -\lambda/2$ results in

$$e^{-\pi} \approx 0.04\,, \tag{3.14}$$

showing that the influence of the wave induced disturbance reduces to 4% when moving down half the wave length in the water column.

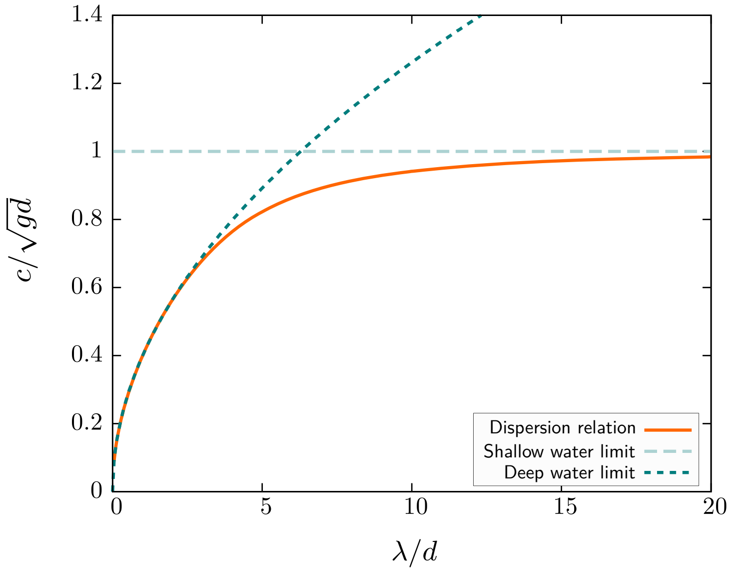

Figure 3.5: Dimensionless wave speed over dimensionless wave length (redrawn from [46])

3.1.2 Velocity profiles

In addition to the mathematical description of the free surface elevation, Stokes wave theory also delivers a description of the velocity profile in the water column underneath the wave. The availability of the velocity profile is important from a wave modelling point of view, since numerical wave generation (and absorption) methodologies, generally, prescribe the time varying surface elevation *and* velocity at the far field boundary of the domain (see Chapter 4 for a detailed discussion).

For first order linear waves, the horizontal, $u_\eta^{(1)} = \frac{\partial \Phi}{\partial x}$, and vertical velocities, $v_\eta^{(1)} = \frac{\partial \Phi}{\partial z}$, are derived from Equation (3.9), following:

$$u_\eta^{(1)} = \frac{H}{2}\frac{gk}{\omega}\frac{\cosh(kz+kd))}{\cosh(kd)}\cos(kx-\omega t) \qquad \text{and} \tag{3.15}$$

$$v_\eta^{(1)} = \frac{H}{2}\frac{gk}{\omega}\frac{\sinh(kz+kd))}{\cosh(kd)}\sin(kx-\omega t)\,, \tag{3.16}$$

respectively. Note that no lateral velocities are available from Stokes wave theory, since only long crested waves are considered. Extending the description of the wave velocities to, e.g., second order delivers:

$$u_\eta^{(2)} = u_\eta^{(1)} + \frac{3}{4}\frac{\pi H}{T}\left(\frac{\pi H}{\lambda}\right)\frac{\cosh[2k(z+d)]}{\sinh^4(kd)}\cos[2(kx-\omega t)] \qquad \text{and} \tag{3.17}$$

$$v_\eta^{(2)} = v_\eta^{(1)} + \frac{3}{4}\frac{\pi H}{T}\left(\frac{\pi H}{\lambda}\right)\frac{\sinh[2k(z+d)]}{\sinh^4(kd)}\sin[2(kx-\omega t)]\,, \tag{3.18}$$

for the horizontal and vertical velocities, respectively. By way of example, Figure 3.6 (a) shows the typical horizontal velocity profiles underneath a wave crest, wave trough, and during the zero crossing. It can be seen in Figure 3.6 (a) that the Stokes wave theory does not account for the no–slip condition (see Chapter 4) at the sea floor. For a single water particle, the horizontal and vertical velocity components result in an orbital motion trajectory. For deep water waves, the (theoretical) trajectory is circular with decaying size towards the sea floor. For intermediate and shallow water conditions, the (theoretical) trajectories are circular close to the free surface, but turn elliptical towards the sea floor. Figure 3.6 (b) shows a photograph of the water particle trajectories in the water column underneath a regular wave in a physical wave tank at intermediate water conditions. A clear warping of the trajectories in the dependency of the vertical location along the water column can be observed, highlighting the interaction between the sea floor and the surface wave.

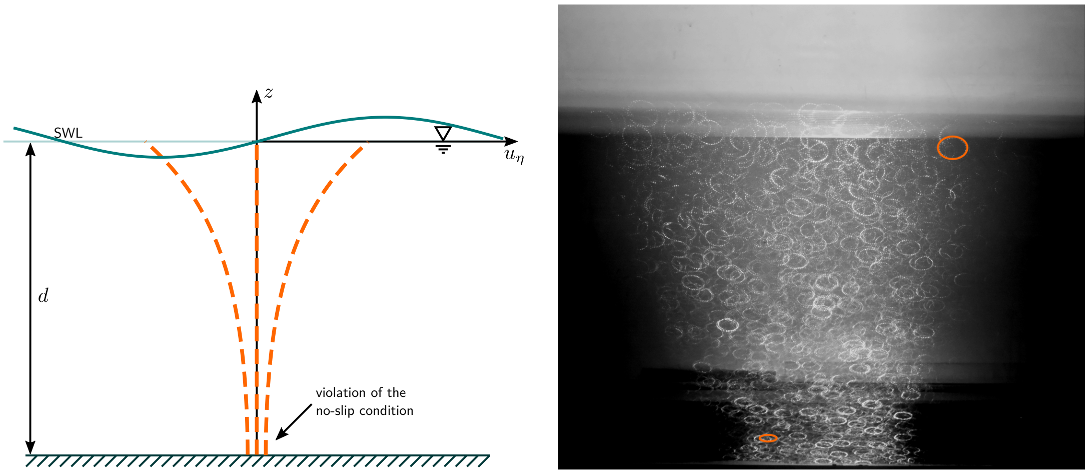

(a) Theoretical horizontal velocity profiles underneath a linear, regular surface wave

(b) Photograph of the orbital particle trajectory in a physical wave tank.

Figure 3.6: Regular wave (a) velocity profiles and (b) particle trajectories

3.2 Irregular waves

Moving towards a more realistic description of the ocean environment, surfaces waves can be described as a composition of individual, linear, regular waves with varying frequencies, amplitudes, and phases (φ): an irregular wave train (or sea state). Note that uni–directional waves with an invariant wave field in lateral direction are still assumed here. For an irregular wave, composed of n_η components, the surface elevation is expressed as:

$$\eta = \sum_{i=1}^{n_\eta} A_i \cos(k_i x - \omega_i t + \varphi_i)\,. \tag{3.19}$$

Figure 3.7 visualises the composition of an irregular wave as the summation of the n_η wave components at each time instant. Figure 3.7 also shows the frequency domain representation of the sea state by means of the wave spectrum, S_η, as a function of the angular frequency ω, which can be expressed as:

$$S_{\eta,i} = \frac{A_i^2}{2\Delta\omega}\,, \tag{3.20}$$

where $\Delta\omega$ is the uniform frequency step.

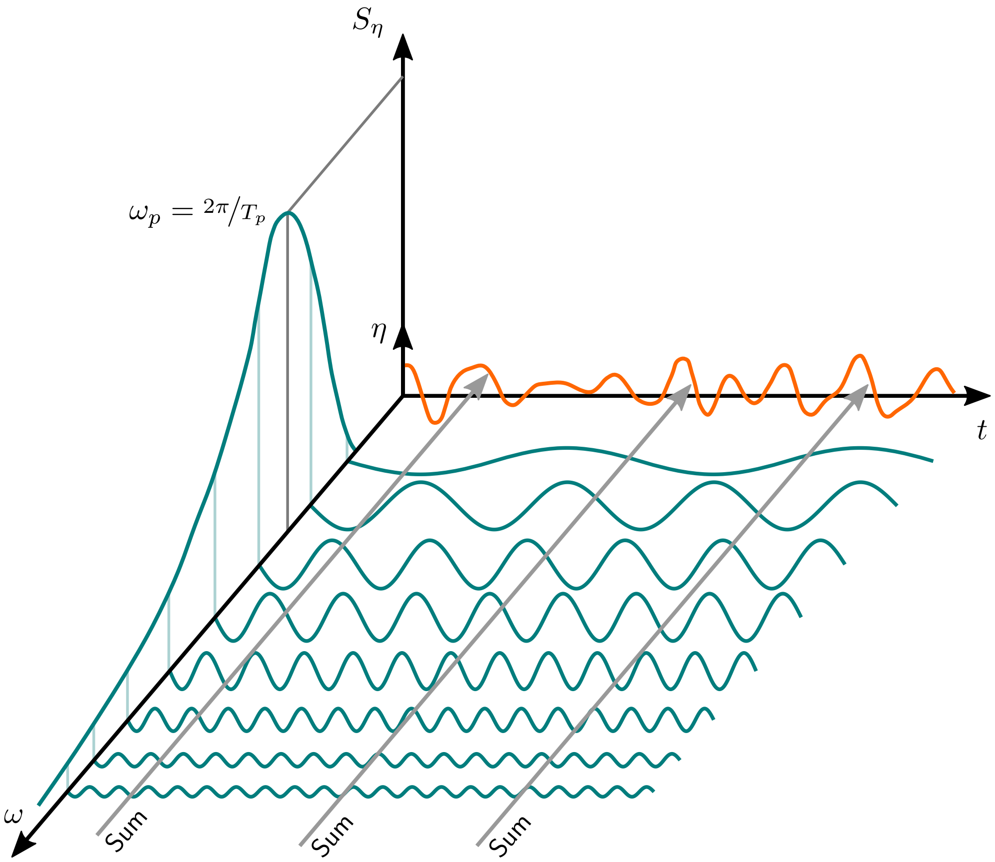

Figure 3.7: Composition of an irregular wave as the summation of the n_η wave components (adapted from [12]).

The most common formulations of the wave spectrum S_η are the Bretschneider spectrum for developing seas [49], the Joint North Sea Wave Project (JONSWAP) spectrum for wind-generated seas with fetch limitations [50], and the Pierson-Moskowitz spectrum for fully-developed seas [51]. By way of example, the formal expression of the JONSWAP spectrum is given in Equations (3.21)–(3.23).

$$S_\eta = 155\frac{H_s^2}{(0.834T_p)^4\omega^5}\exp\left(\frac{-944}{(0.834T_p)^4\omega^4}\right)3.3^Y\,, \qquad \text{with} \tag{3.21}$$

$$Y = \exp\left[-\left(\frac{0.191\omega\,0.834T_p - 1}{2^{0.5}\sigma_\eta}\right)^2\right] \qquad \text{and} \tag{3.22}$$

$$\sigma_\eta = \begin{cases} 0.07 & \text{for} \quad \omega \leq \frac{5.24}{0.834T_p}, \\ 0.09 & \text{for} \quad \omega > \frac{5.24}{0.834T_p}. \end{cases} \tag{3.23}$$

In Equations (3.21)–(3.23), T_p denotes the peak wave period (see Figure 3.7) and H_s is the significant wave height. Figure 3.8 shows the time traces of an irregular and regular wave with $H = H_s = 0.12$m and $T = T_p = 1.94$s, thereby visualising the correlation between T_p and H_s for an irregular wave with T and H for a regular wave.

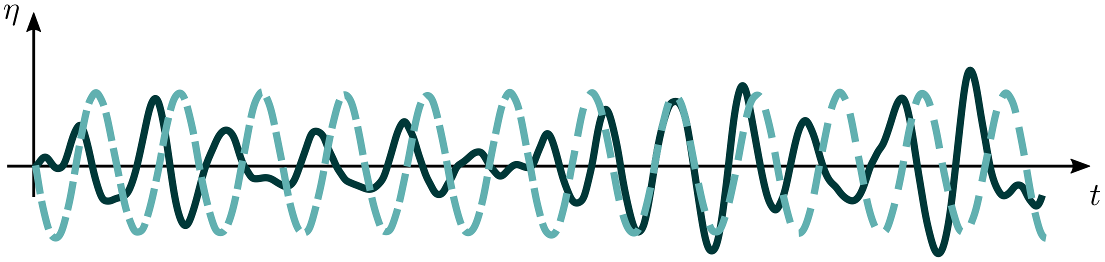

Figure 3.8: Time traces of an irregular (solid) and regular (dashed) wave train with $H = H_s = 0.12$m and $T = T_p = 1.94$s

3.3 Focused Waves

Efficient modelling of extreme events during WSI can be achieved by considering focused waves (see the literature review in Chapter 5 for example studies). All focused waves considered throughout this thesis (see Chapter 7) are based on the NewWave formulation as presented, e.g., in [52]. Generally, focused waves can be considered as a spatially and temporally compact form of a sea state for which the surface elevation is described as:

$$\eta = \sum_{i=1}^{n_\eta} a_i \cos(k_i(x - x_0) - \omega_i(t - t_0))\,, \qquad \text{where} \tag{3.24}$$

$$a_i = A_0\frac{S_\eta \Delta\omega}{\sum_{i=1}^{n_\eta} S_{\eta,i}\Delta\omega}\,, \qquad \text{with} \tag{3.25}$$

$$A_0 = \sqrt{2(0.25H_s)^2\ln(n_\eta)}\,. \tag{3.26}$$

In Equation (3.24), x_0 represents the spatial focal location and t_0 the temporal focal instant. A visualisation of the development of a focused wave in space and time is shown in Figure 3.9.

Form a numerical modelling point of view, focused waves are not only valuable to replicate extreme events. Given that a focused wave represents a *complete* spectrum in a confined space and time window, responses of WECs to the *complete* spectrum can be evaluated with short simulations (thus minimised computational cost) and with reduced pollution due to wave reflection (see Chapter 4).

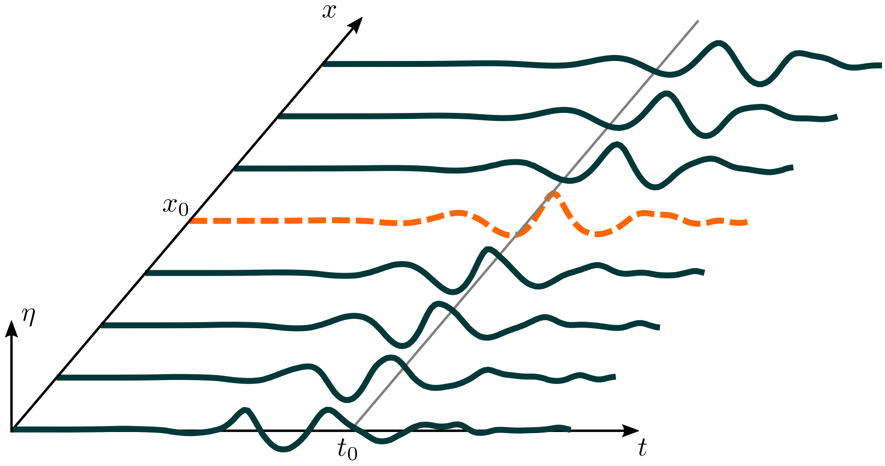

Figure 3.9: Free surface elevation time traces measured at different locations along a wave tank. At the spatial and temporal focal point x_0 and t_0, the phases of the wave components are aligned, resulting in the focused waves (orange colour code).

3.4 Concluding remarks

This chapter presents the mathematical description of ocean waves in the form of regular (Stokes) waves, irregular wave trains (or sea states), and focused waves. While regular waves are characterised by a single wave frequency and amplitude, irregular and focused waves are composed of a number of wave components. Generally, the analysis of WSI with regular waves can deliver valuable insights into the behaviour of a device regarding the behavioural dependency on the wave period and/or amplitude. WSI of devices exposed to irregular waves is commonly used for the power production assessment of WECs, since irregular waves replicate more realistic conditions, compared to regular waves. Finally, focused waves can be employed to analyse the WSI of WECs in extreme seas or to evaluate the WEC response to a *complete* spectrum in a confined space and time window. Throughout this thesis, the complete range from regular, irregular, to focused waves will be considered. In the next chapter, Chapter 4, the numerical generation of waves will be introduced and an assessment of different numerical wave generation (and absorption) methodologies is presented in Chapter 6.

4

CFD–based numerical wave tanks

Contents

Following the introduction of the governing equations of the fluid dynamics, and the mathematical description of ocean waves, in Chapters 2 and 3, respectively, this chapter presents the numerical methods used for the solution of the governing equations within a CFD–based NWT. Initially, Section 4.1 briefly discusses available high–fidelity CFD–based NWTs and delivers the definition of a CFD–based NWT within this thesis. Subsequently, Section 4.2 provides a brief overview of the numerical methods within the particular CFD–based NWT employed in this thesis, namely the finite–volume method, solution schemes for the discretised governing equations, the treatment of the pressure–velocity coupling, and the boundary conditions. Section 4.3 elaborates on the requirements (and their numerical treatment) of a CFD–based NWTs for WEC applications.

4.1 High–fidelity numerical wave tanks

Numerical simulation is an integral part of offshore and coastal engineering. High–fidelity, CFD–based NWTs have been demonstrated to deliver valuable insights into the flow field around marine structures [7–9]. The governing equations within high–fidelity, CFD–based, NWTs are discretised in time and space to form an algebraic set of equations. While the discretisation in time is relatively straightforward (see Section 4.2), for the spatial discretisation, one can differentiate between meshless (Lagrangian), mesh–based (Eulerian), and hybrid (Lagrangian–Eulerian) methods, as schematically depicted in Figure 4.1.

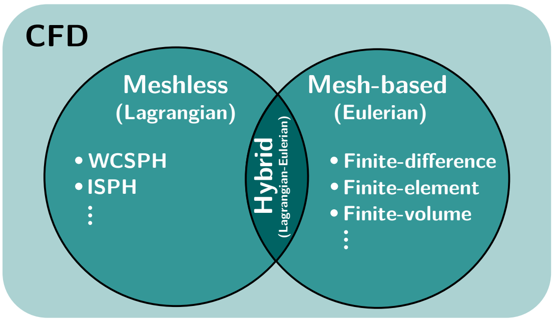

Figure 4.1: In this thesis, CFD is the overarching identifier for meshless (Lagrangian), mesh–based (Eulerian), and hybrid (Lagrangian–Eulerian) solution methods for the governing Navier–Stokes equations.

Smoothed particle hydrodynamic (SPH) solvers [53, 54] are amongst the most prominent representatives for meshless CFD methods[1], which can be differentiated by the treatment of fluid compressibility, i.e. incompressible SPH (ISPH) [57] or weakly compressible SPH (WCSPH) [58]. Generally, within the family of meshless methods, the governing equations are discretised using particles, leading to the definition of field variables, such as the pressure, at discrete locations. For a continuous representation within the solution domain, smoothing kernels are employed, enabling the defining of field variables at any desired location on the basis of the results for the neighbouring particles.

Within Eulerian, mesh–based, CFD methods, the governing equations are solved on a computational mesh and different methods have been developed for the specific discretisation of the governing equations: finite–difference (FD), finite–element (FE), and finite–volume (FV) [59].

In the FD method, finite differencing (see Section 4.2.2) is used to form the set of algebraic equations to represent the governing equations. The FE method employs shape functions (usually piecewise defined polynomials) to numerically treat the partial

---

[1] Other example of meshless Lagrangian methods can be found in [55] or [56].

differential equations. Within the FV method, the computational mesh is composed of control volumes (CVs) and the governing equations are evaluated at central nodes or vertices of the CVs. Different numerical schemes (see Section 4.2.2) are then used to approximate the governing equations.

Particle–in–cell (PIC) methods [60] are the consequential hybrid of Lagrangian and Eulerian methods and have only recently gained relevance in the field of WSI [61, 62] (see also Chapter 5). Within PIC methods, the advection terms are solved using the Lagrangian method, while the non–advection terms are solved using the Eulerian method. The coupling between the Lagrangian and Eulerian methods requires complex solution schemes to retain numerical accuracy and stability.

CFD–based NWTs employing Eulerian mesh–based methods, in particular the FV method, are well established within ocean and coastal engineering and have experienced increased attention in the field of marine renewable energy, and in particular wave energy (see Chapter 5), due to their flexibility, stability, and accuracy.

A major catalyst for the increasing use of CFD–based NWTs employing Eulerian, mesh–based, FV methods has been the availability of extensible open-source software, eliminating license costs and providing users with ready made, but editable, solvers and toolboxes for the solution of WSI problems. The OpenFOAM toolbox has gained increased popularity within the field of WEC R&D and, in fact, is found to be the most used mesh–based CFD software suite for WEC applications (see Chapter 5). In this thesis, OpenFOAM will be used for the setup of all CFD–based NWTs; thus, for brevity, CFD–based NWTs employing Eulerian mesh–based, cell–centred, FV methods will henceforth be simply referred to as CFD–based NWTs.

4.2 Numerical methods

The following section provides a brief summary of the numerical methods employed within the CFD–based NWTs in this thesis. The discussion follows [29, 30, 63], which the interested reader is referred to for more details on the numerical methods.

4.2.1 Finite–volume method

As stated in Section 4.1, within mesh–based NWTs, the governing equations of the fluid flow are discretised in time (timestep) and space (mesh) to form a system of linear algebraic equations. For the spatial discretisation, different methods have been developed (FD, FE, FV). The FV method allows for a direct physical interpretation where, in the absence of any source terms, the flux into and out of a CV has to be equal, to obey conservation laws. Consequently, the governing equations, i.e. conservation equations, of the fluid flow can be solved for each individual CV.

Formally, the fluxes can be expressed as a surface integral over the CV faces. For a simple, steady-state diffusion problem without source term, the transition from the control volume form to the surface integral form follows:

$$\nabla \cdot (\mu \nabla \phi) \approx \int_{\mathsf{CV}} \nabla \cdot (\mu \nabla \phi)\, \mathrm{d}V = \int_{A_{CV}} \mathbf{n} \cdot (\mu \nabla \phi)\, \mathrm{d}A_{CV} = 0\,, \tag{4.1}$$

where V is the volume of the CV, $\mathbf{n}$ denotes the normal vector of a given CV face, and A_{CV} is the area of the CV face.

For the further development of the FV method, Figures 4.2 (a)–(c) provides the necessary definition of the CV nodes and faces for one–, two–, and three–dimensional cases, respectively[2]. In Figures 4.2 (a)–(c), the central node of the CV, at which the field variables are stored (cell–centred approach), is denoted with P. The neighbouring cell centre nodes are denoted W and E (one–dimensional); N, S, E, W (two–dimensional); or N, S, E, W, T, and B (three–dimensional). The corresponding cell faces over which fluxes can enter or exit the CV are indicated with lower cases (n, s, e, w, t, b).

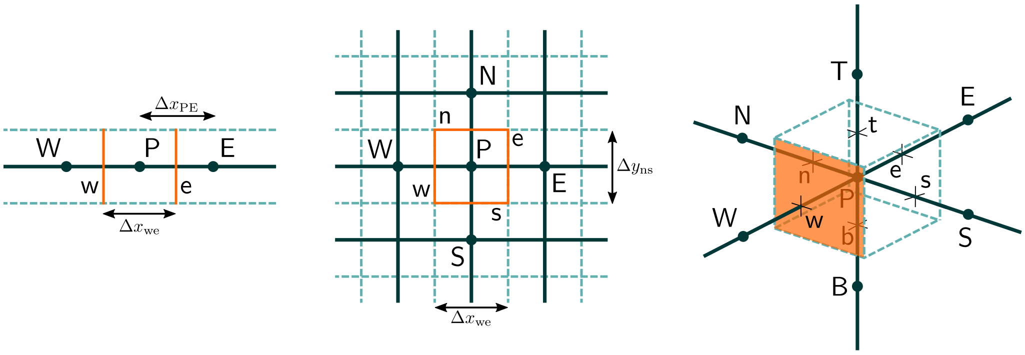

(a) one–dimensional (1D) **(b)** two–dimensional (2D) **(c)** three–dimensional (3D)

Figure 4.2: Definition of the CV nodes and faces in one (a), two (b), and three (c) dimensions. The orange colour code indicates the cell faces. The central node of CV is denoted with P. The neighbouring cell centre nodes are denoted W and E (one–dimensional); N, S, E, W (two–dimensional); or N, S, E, W, T, and B (three–dimensional). The corresponding cell faces are indicated with lower cases (n, s, e, w, t, b). In the three–dimensional case only one cell face is given colour, for clarity. (adapted from [30]).

Following the definitions for the CVs in Figure 4.2, the diffusion problem described by Equation (4.1) is reformulated following:

$$\left(\mu A_{CV} \frac{\mathrm{d}\phi}{\mathrm{d}x}\right)_e - \left(\mu A_{CV} \frac{\mathrm{d}\phi}{\mathrm{d}x}\right)_w = 0\,, \tag{4.2}$$

$$\left[\left(\mu A_{CV} \frac{\mathrm{d}\phi}{\mathrm{d}x}\right)_e - \left(\mu A_{CV} \frac{\mathrm{d}\phi}{\mathrm{d}x}\right)_w\right] + \left[\left(\mu A_{CV} \frac{\mathrm{d}\phi}{\mathrm{d}y}\right)_n - \left(\mu A_{CV} \frac{\mathrm{d}\phi}{\mathrm{d}y}\right)_s\right] = 0\,, \tag{4.3}$$

---

[2] Note that, for the sake of simplicity, only Cartesian grids are considered in this section.

$$\left[\left(\mu A_{CV}\frac{\mathsf{d}\phi}{\mathsf{d}x}\right)_e-\left(\mu A_{CV}\frac{\mathsf{d}\phi}{\mathsf{d}x}\right)_w\right]+\left[\left(\mu A_{CV}\frac{\mathsf{d}\phi}{\mathsf{d}y}\right)_n-\left(\mu A_{CV}\frac{\mathsf{d}\phi}{\mathsf{d}y}\right)_s\right]+$$
$$\left[\left(\mu A_{CV}\frac{\mathsf{d}\phi}{\mathsf{d}z}\right)_t-\left(\mu A_{CV}\frac{\mathsf{d}\phi}{\mathsf{d}z}\right)_b\right]=0\,, \qquad (4.4)$$

for the one–, two–, and three–dimensional case in (4.2), (4.3), and (4.4), respectively. The above equations highlight the physical interpretability of the FV method, where, in the absence of sources, entering and exiting fluxes have to cancel each other out. To form a set of algebraic equations, based on the surface integral form of the governing equations, the calculation of the fluxes over the CV faces requires the approximation of the values of ϕ, and its gradients, at the CV faces. For this approximation, from central nodes to cell faces, different numerical schemes have been developed and some of the most prominent ones are detailed in the following Section 4.2.2.

4.2.2 Solution schemes

To illustrate different solution schemes for the approximation of the values of ϕ and its gradients at the CV faces, the diffusive problem in Equation (4.1) is extended to include a convection term ($\nabla\cdot(\rho\mathbf{u}\phi)$):

$$\nabla\cdot(\rho\mathbf{u}\phi)-\nabla\cdot(\mu\nabla\phi)=\int_{A_{CV}}\mathbf{n}\cdot(\rho\mathbf{u}\phi)\,\mathsf{d}A_{CV}-\int_{A_{CV}}\mathbf{n}\cdot(\mu\nabla\phi)\,\mathsf{d}A_{CV}=0\,, \qquad (4.5)$$

Reduced to a one–dimensional problem, Equation (4.5) can be rewritten as:

$$\frac{\mathsf{d}}{\mathsf{d}x}(\rho u\phi)-\frac{\mathsf{d}}{\mathsf{d}\,x}\left(\mu\frac{\mathsf{d}\phi}{\mathsf{d}x}\right)=\int_{A_{CV}}\mathbf{n}\cdot(\rho u\phi)\,\mathsf{d}A_{CV}-\int_{A_{CV}}\mathbf{n}\cdot\left(\mu\frac{\mathsf{d}\phi}{\mathsf{d}x}\right)\,\mathsf{d}A_{CV}=0\,, \qquad (4.6)$$

which, according to the FV method, can further be expressed as:

$$\int_{A_{CV}}\mathbf{n}\cdot(\rho u\phi)\,\mathsf{d}A_{CV}-\int_{A_{CV}}\mathbf{n}\cdot\left(\mu\frac{\mathsf{d}\phi}{\mathsf{d}x}\right)\,\mathsf{d}A_{CV}=$$
$$[(\rho uA_{CV}\phi)_e-(\rho uA_{CV}\phi)_w]-\left[\left(\mu A_{CV}\frac{\mathsf{d}\phi}{\mathsf{d}x}\right)_e-\left(\mu A_{CV}\frac{\mathsf{d}\phi}{\mathsf{d}x}\right)_w\right]=0\,. \qquad (4.7)$$

It should be noted that, for the following development of the approximation schemes, complete knowledge of the velocity field $\mathbf{u}$ is assumed. Under realistic conditions, this knowledge can not be assumed and $\mathbf{u}$ is amongst the set of unknown variables. A closer look at the treatment of $\mathbf{u}$ in the solution process is taken in Section 4.2.3. Before elaborating on different approximation schemes, important properties of these schemes, ensuring accurate computation on computational meshes with finite numbers of CVs, are discussed. These properties are: (1) conservativeness; (2) boundedness; and (3) transportiveness, which are illustrated in Figure 4.3.

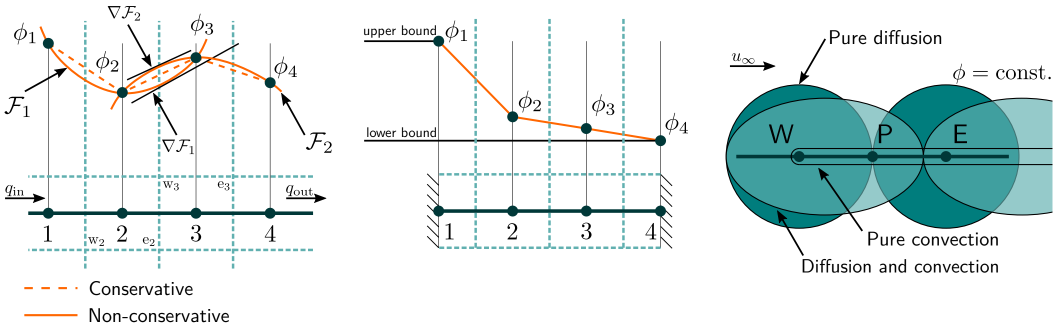

(a) Conservativeness: Differences in the expression of the fluxes across cell faces lead to conservation violations.

(b) Boundedness: Across a domain with a set of boundary conditions, these boundary conditions define the bounds of ϕ

(c) Transportiveness: For pure diffusion, ϕ_P is influenced by ϕ_W and ϕ_E. For pure convection, ϕ_P is solely influenced by ϕ_W

Figure 4.3: Illustration of the required properties of the approximation schemes to ensure accurate computation on computational meshes with finite numbers of CVs (adapted from [30]).

Conservativeness defines the consistency of the expression of the fluxes, q, across cell faces. To ensure conservation, the absolute flux across, for instance, face e of cell 2 (indicated as e_2 in Figure 4.3 (a)), has to be equal to the absolute flux across face w of cell 3 (indicated as w_3 in Figure 4.3 (a)). Or simply: in the absence of source terms, the overall sum of all fluxes between internal cell faces has to be zero. In Figure 4.3 (a), linear interpolation between the nodes (dashed line) ensures conservativeness, while the quadratic interpolation (solid line) leads to inconsistencies between fluxes, thus non-conservativeness.

Boundedness defines the existence of lower and upper bounds in a computational domain, in the absence of sources. Across a domain with a set of boundary conditions, these boundary conditions define the lower and upper bounds of ϕ (see Figure 4.3 (b)). Boundedness further implies a consistent increase/decrease in ϕ at a node, if ϕ at a neighbouring node is increased/decreased. By obeying boundedness, the approximation schemes avoids large, unrealistic, over– or under–shoot of the solution.

Transportiveness defines the capability of an approximation scheme to account for the direction of the flow. For pure diffusive problems (i.e. $u_\infty = 0$), ϕ is distributed equally in all directions, resulting in circular ϕ–contours (see Figure 4.3 (c)). Thus, ϕ_P is equally influenced by ϕ_W and ϕ_E. Adding convection, the flow is directed, and a stronger influence of the upstream node (ϕ_W in Figure 4.3 (c)), compared to the downstream node (ϕ_E in Figure 4.3 (c)), on ϕ_P can be observed. This directionality of the flow has to be captured within the approximation scheme.

Based on the three properties detailed above, the suitability and accuracy of the available approximation schemes can be assessed. The most prominently used approximation schemes are discussed in the following. Note that the set of discussed approximation schemes does not claim to be complete.

Central differencing

The simplest scheme to calculate ϕ and its gradients at the CV faces employs linear interpolation between nodal values and is referred to as central differencing (CD). For the diffusion terms in Equation (4.7) on a grid with uniform cell size, CD yields:

$$\left(\mu A_{CV}\frac{\mathrm{d}\phi}{\mathrm{d}x}\right)_e - \left(\mu A_{CV}\frac{\mathrm{d}\phi}{\mathrm{d}x}\right)_w = \frac{\mu_P+\mu_E}{2}A_{CV}\left(\frac{\phi_E-\phi_P}{\Delta x_{PE}}\right) - \frac{\mu_W+\mu_P}{2}A_{CV}\left(\frac{\phi_P-\phi_W}{\Delta x_{WP}}\right) . \quad (4.8)$$

Equivalently, for the convective term in Equation (4.7), CD yields:

$$(\rho u A_{CV}\phi)_e-(\rho u A_{CV}\phi)_w = \rho\frac{u_P+u_E}{2}A_{CV}\left(\frac{\phi_P+\phi_E}{2}\right) - \rho\frac{u_W+u_P}{2}A_{CV}\left(\frac{\phi_W+\phi_P}{2}\right) . \quad (4.9)$$

Regarding the properties of conservativeness, boundedness, and transportiveness, it can be stated that the CD scheme is inherently conservative, due to the consistent description of the fluxes through linear interpolation (see Figure 4.3 (a)). For the convective–diffusive problem in Equation (4.7), only conditional boundedness can be achieved, depending on the ratio between the diffusive and convective contribution. For convection dominated flows, the boundedness criteria is quickly violated while, for diffusion dominated flows, unconditional boundedness is achieved (see [30, Chapter 5] for a complete derivation of this condition). Transportiveness is inherently not recognised within the CD scheme.

Based on the specific properties of the CD scheme, it can be shown that, for the diffusive term, the CD scheme yields accurate results on grids with an acceptable cell size (see [30, Chapter 4] for according examples). Conversely, the convective term can be solved accurately with the CD scheme only on relatively fine grids (see [30, Chapter 5] for corresponding examples).

In addition to the properties of the CD scheme, the overall accuracy of the scheme can be determined by analysing the truncation error of its Taylor series expansion. It can be shown that the leading truncation error in the CD scheme is of 2^{nd} order. A summary of the properties and the accuracy of the CD scheme, and all following approximation schemes, is given in Table 4.1.

Upwind differencing

To overcome the conditional boundedness and, more importantly, the lack of transportiveness, the upwind difference (UD) scheme can be employed. To account for the direction of the flow, the UD scheme considers only the upwind node when determining the cell face values of ϕ. Thus, for a flow direction from the west to the east face (see Figure 4.2), $\phi_w = \phi_W$ and $\phi_e = \phi_P$. For a flow direction from the east to the west face, $\phi_w = \phi_P$ and $\phi_e = \phi_E$. Consequently, for the convective term in Equation (4.7), under the assumption of a flow from the west to the east face, the UD scheme yields:

$$(\rho u A_{CV} \phi)_e - (\rho u A_{CV} \phi)_w = \rho \frac{u_P + u_E}{2} A_{CV}\, \phi_P - \rho \frac{u_W + u_P}{2} A_{CV}\, \phi_W \,. \tag{4.10}$$

Regarding the properties of conservativeness, boundedness, and transportiveness, it can be stated that the UD scheme is inherently conservative, unconditionally bounded, and transportiveness is recognised. Regarding accuracy, it can be shown that the UD scheme is only 1^{st} order accurate, thereby leading to false diffusion, ultimately resulting in smeared solutions. The effect of the false diffusion can be partly mitigated by a fine grid resolution; however, at the cost of reduced efficiency.

To obtain solutions for the convection terms which hold the properties of unconditional conservativeness, boundedness, and transportiveness (as with the UD scheme), while retaining high solution accuracy (as with the CD scheme), more complex approximation schemes have been developed. Amongst such more complex schemes, total variation[3] diminishing (TVD) schemes are commonly applied.

Total variation diminishing

The general idea of TVD schemes is the addition of a second order extension, $\frac{1}{2}\psi(\varrho)(\phi_E - \phi_P)$, to the UD scheme to increase the overall accuracy. However, the extension has to be limited, formally achieved by the limiter function $\psi(\varrho)$, to result in a TVD scheme in order to suppress undesired oscillations within the solution. The value of ψ is a function of the ratio, ϱ, between the upwind– and downwind–side gradients. The general form of the TVD scheme for the convection term in Equation (4.7), under the assumption of a flow from the west to the east face, follows:

$$\begin{aligned}(\rho u A_{CV} \phi)_e - (\rho u A_{CV} \phi)_w &= \\ &\rho \frac{u_P + u_E}{2} A_{CV} \left[\phi_P + \frac{1}{2}\psi(\varrho_e)(\phi_E - \phi_P)\right] - \\ &\rho \frac{u_W + u_P}{2} A_{CV} \left[\phi_W + \frac{1}{2}\psi(\varrho_w)(\phi_P - \phi_W)\right] ,\end{aligned} \tag{4.11}$$

---

[3] The total variation is used as a measure for the oscillation within the solution whereby a diminished total variation expresses reduced oscillation, which is desired here.

with

$$\varrho_e = \frac{\phi_P - \phi_W}{\phi_E - \phi_P} \tag{4.12}$$

and

$$\varrho_w = \frac{\phi_W - \phi_{WW}}{\phi_P - \phi_W}\,, \tag{4.13}$$

where ϕ_{WW} is the central node upstream of the W node.

A considerable amount of research has been conducted regarding the definition of the limiter function $\psi(\varrho)$ to achieve 2^{nd} order accuracy, while experiencing little artificial diffusion, and oscillation free solutions. Intuitively, it can be seen that, if $\psi(\varrho) = 0$, the TVD turns into the UD scheme, with its known properties. For $\psi(\varrho) = {}^{3+\varrho}/_{4}$, the TVD scheme turns into the quadratic upstream interpolation for convective kinetics (QUICK) scheme [64]. In OpenFOAM, the van Leer limiter function ($\psi(\varrho) = {}^{\varrho+|\varrho|}/_{1+\varrho}$) [65–68] or the `limitedLinear` limiter function ($\psi(\varrho) = \max\left[\min({}^{2\varrho}/_{\iota}, 1), 0\right]$, where ι denotes a user defined scalar value) are frequently applied [69].

Table 4.1: Assessment of FV approximation schemes

Scheme	Conservativeness	Boundedness	Transportiveness	Accuracy
CD	✓	Conditional	✗	2^{nd} order
UD	✓	✓	✓	1^{st} order
TVD (van Leer)	✓	✓	✓	2^{nd} order
TVD (`limitedLinear`)	✓	✓	✓	2^{nd} order

Time derivatives

For the discussion of the CD, UD, and TVD schemes, for clarity, only steady state diffusion and convection problems are considered, neglecting the time derivative ${}^{\partial(\rho\mathbf{u})}/_{\partial t}$. However, WSI problems are inherently unsteady, thus requiring treatment of the time derivative. Formally, this treatment is expressed by an additional integration over a finite time step Δt:

$$\begin{aligned} &\frac{\partial}{\partial t}(\rho\phi) + \nabla\cdot(\rho\mathbf{u}\phi) - \nabla\cdot(\mu\nabla\phi) = \\ &\qquad \int_{\text{CV}}\left[\int_{t^0}^{t^1}\frac{\partial}{\partial t}(\rho\phi)\text{d}t\right]\text{d}V + \int_{t^0}^{t^1}\left[\int_{A_{CV}}\mathbf{n}\cdot(\rho\mathbf{u}\phi)\,\text{d}A_{CV}\right]\text{d}t - \\ &\qquad \int_{t^0}^{t^1}\left[\int_{A_{CV}}\mathbf{n}\cdot(\mu\nabla\phi)\,\text{d}A_{CV}\right]\text{d}t = 0\,, \end{aligned} \tag{4.14}$$

where t^0 is the current time and $t^1 = t^0 + \Delta t$.

For clarity, only the transient, 1D, diffusion problem is considered in the following:

$$\frac{\partial}{\partial t}(\rho\phi) - \nabla\cdot(\mu\nabla\phi) = \int_{\mathsf{CV}}\left[\int_{t^0}^{t^1}\frac{\partial}{\partial t}(\rho\phi)\,\mathrm{d}t\right]\mathrm{d}V - \int_{t^0}^{t^1}\left[\int_{A_{CV}}\mathbf{n}\cdot\left(\mu\frac{\mathrm{d}\phi}{\mathrm{d}x}\right)\mathrm{d}A_{CV}\right]\mathrm{d}t = 0\,. \tag{4.15}$$

Applying first–order differencing for the transient term, and CD for the diffusive term, yields:

$$\begin{aligned}&\int_{\mathsf{CV}}\left[\int_{t^0}^{t^1}\frac{\partial}{\partial t}(\rho\phi)\,\mathrm{d}t\right]\mathrm{d}V - \int_{t^0}^{t^1}\left[\int_{\mathsf{A}}\mathbf{n}\cdot\left(\mu\frac{\mathrm{d}\phi}{\mathrm{d}x}\right)\mathrm{d}A_{CV}\right]\mathrm{d}t = \\ &\rho\left(\phi_P^1-\phi_P^0\right)\Delta x A_{CV} - \int_{t^0}^{t^1}\left[\left(A_{CV}\mu_e\frac{\phi_E-\phi_P}{\Delta x}\right)-\left(A_{CV}\mu_w\frac{\phi_P-\phi_W}{\Delta x}\right)\right]\mathrm{d}t = 0\,,\end{aligned} \tag{4.16}$$

where the superscript ^{0} indicates values of ϕ at the current time and ^{1} values of ϕ at the future time. In accordance with Equation (4.8), $\mu_e = \frac{\mu_P+\mu_E}{2}$ and $\mu_w = \frac{\mu_W+\mu_P}{2}$. Depending on the 'time of evaluation' for ϕ_E, ϕ_P, and ϕ_W, different schemes for the approximation of the time integral of the diffusive term are available, including only current values (explicit), only future values (implicit, Euler), or a blending of current and future values (Crank–Nicolson). In a generalised form, the approximation of Equation (4.16) can be expressed as:

$$\begin{aligned}&\rho\left(\phi_P^1-\phi_P^0\right)\Delta x A_{CV} - \int_{t^0}^{t^1}\left[\left(A_{CV}\mu_e\frac{\phi_E-\phi_P}{\Delta x}\right)-\left(A_{CV}\mu_w\frac{\phi_P-\phi_W}{\Delta x}\right)\right]\mathrm{d}t = \\ &\rho\left(\frac{\phi_P^1-\phi_P^0}{\Delta t}\right)\Delta x - \Psi\left[\left(\mu_e\frac{\phi_E^1-\phi_P^1}{\Delta x}\right)-\left(\mu_w\frac{\phi_P^1-\phi_W^1}{\Delta x}\right)\right] - \\ &(1-\Psi)\left[\left(\mu_e\frac{\phi_E^0-\phi_P^0}{\Delta x}\right)-\left(\mu_w\frac{\phi_P^0-\phi_W^0}{\Delta x}\right)\right] = 0\,.\end{aligned} \tag{4.17}$$

Depending on the blending factor, $0 \leq \Psi \leq 1$, a specific scheme is chosen. For $\Psi = 0$, only past values of ϕ are considered, resulting in a fully explicit, 1^{st} order accurate, conditionally stable[4] scheme. For $0 < \Psi \leq 1$, both past and future values of ϕ are considered, resulting in an implicit scheme. For $\Psi = 1$ only future values of ϕ are considered, resulting in a fully implicit, 1^{st} order accurate, unconditionally stable scheme. For $\Psi = 1/2$, the Crank–Nicolson scheme is applied, featuring unconditional stability and 2^{nd} order accuracy.[5] Following the recommendation in [30], the implicit (Euler) scheme is used throughout this thesis for the treatment of time integration.

---

[4] Stable, in the context of time derivative schemes, refers to the occurrence of undesired oscillation of the solution.

[5] It should be noted here that the control over the blending factor Ψ is implemented in OpenFOAM via the coefficient $c_0 = \frac{1-\Psi}{\Psi}$, where $0.5 \leq \Psi \leq 1$ and $0 \leq c_0 \leq 1$ [70].

4.2.3 Pressure–velocity coupling

For the discussion of the discretisation schemes in Section 4.2.2, knowledge of the velocity field is assumed. Naturally, this is not the case for flow problems, and the determination of the velocity field is part of the solution procedure. The solution of *all* relevant flow quantities presents a challenge, since the governing equations are non–linear (e.g. by nature of the convection term $\nabla \cdot (\rho \mathbf{u}\mathbf{u})$) and coupled through the velocity field. Furthermore, for incompressible flows, no explicit equation for the pressure is available, which is of particular concern, since the pressure gradient is the main driver in engineering purpose flows.

For a solution of the complete flow field, the coupling between the pressure and velocity, through the continuity equation, can be leveraged: A correctly determined pressure field, applied in the momentum equation, must obey mass conservation, thereby satisfying the continuity equation.

Iterative solution algorithms have been developed to solve this pressure–velocity coupling, most prominently the semi-implicit method for pressure linked equations (SIMPLE) proposed in [71], the pressure implicit split operator (PISO) developed in [72], or the pressure implicit for pressure linked equations (PIMPLE) algorithm [73, 74].

SIMPLE

A visualisation of the SIMPLE algorithm (for steady problems) is depicted in Figure 4.4. The SIMPLE algorithm follows a guess–and–correct approach whereby, initially, a guessed pressure field, p^*, is employed. With p^*, the momentum equation can be solved (step (1)), resulting in a 'guessed' velocity, $\mathbf{u}^*$. To further proceed, it is assumed that the correct pressure field p can be decomposed, such that $p = p^* + p^{\mathsf{c}}$, where p^{c} is a correction value. Similarly, the velocity field can be decomposed as $\mathbf{u} = \mathbf{u}^* + \mathbf{u}^{\mathsf{c}}$. Substituting this relationship in the momentum equation, together with the continuity equation, a pressure correction equation can be obtained. The solution of the pressure correction equation yields p^{c} (step (2)), so that the correct value p, as well as $\mathbf{u}$, can be determined (step (3)). Finally, all remaining transport equations can be solved to obtain the complete solution for the flow field. Since SIMPLE is an iterative process, convergences is assessed after each iteration.

The stability of the SIMPLE algorithm is dependent on the initial guess p^* and too large values can result in divergence. Thus, under–relaxation can be applied, such that $p^{new} = p^* + \alpha_p p^{\mathsf{c}}$, where $0 \leq \alpha_p \leq 1$ is the relaxation factor.

Variations of the SIMPLE algorithm, aiming at higher efficiency, have been proposed in [75] (SIMPLE-revised) and [76] (SIMPLE-consistent). The interested reader is referred to [30, Chapter 6] for further details.

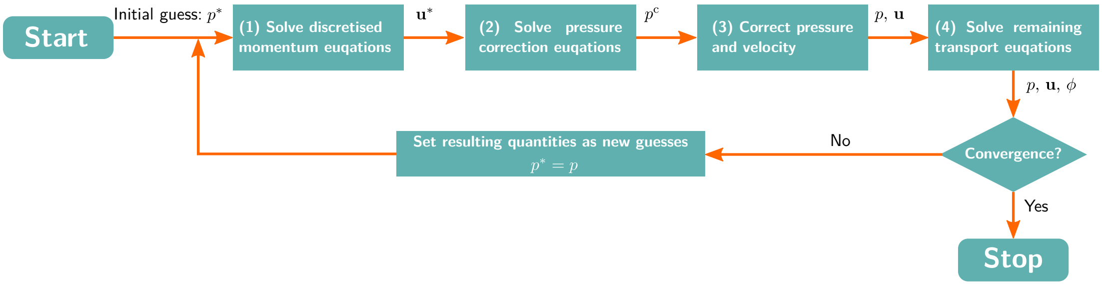

Figure 4.4: Visualisation of the pressure linked equations (SIMPLE) algorithm (adapted from [30]).

PISO

Figure 4.5 shows a visualisation of the PISO algorithm. PISO extends the SIMPLE algorithm by a second pressure correction step. In the predictor step (step (1)), the velocity field is computed based on the initial pressure (guess). Next, the first corrector step is executed, solving the pressure correction equation (step (2)) and correcting the pressure and velocity fields (step (3)). Finally, the second corrector step (steps (4) and (5)) is executed, after which all remaining transport equations can be solved (step (6)). Again, convergence is assessed after each iteration.
Generally, although adding an additional corrector step, the PISO algorithm is found to be computationally more efficient than the SIMPLE algorithm [72].

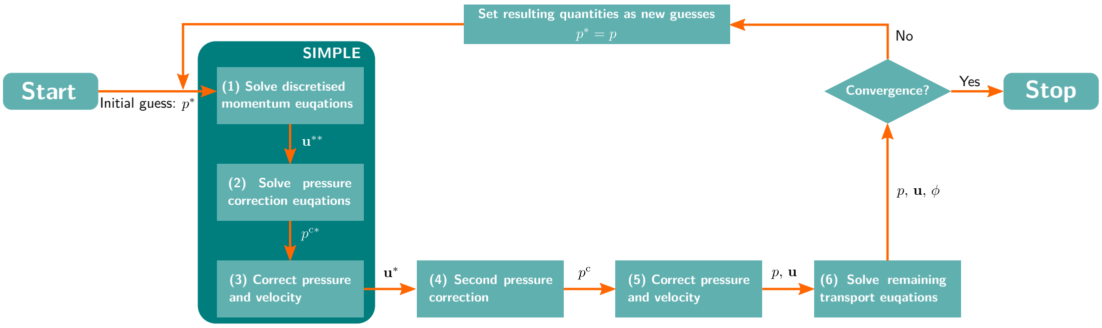

Figure 4.5: Visualisation of the pressure implicit split operator (PISO) algorithm (adapted from [30]).

While the SIMPLE and PISO algorithms described above, and depicted in Figures 4.4 and 4.5, deliver solutions for steady state problems, the algorithms can readily be embedded into a transient iteration loop, visualised in Figure 4.6.

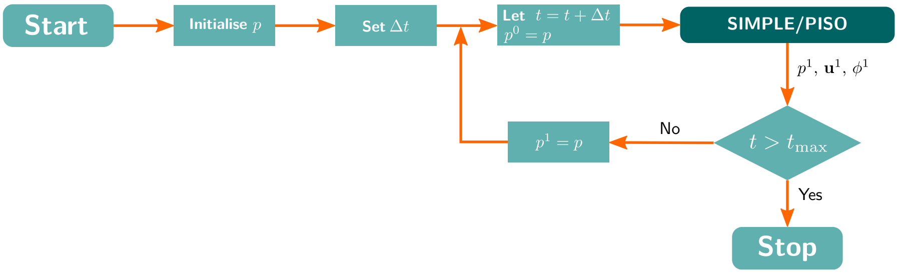

Figure 4.6: Adaption of the SIMPLE algorithm for transient problems (adapted from [30, 63]). The superscript ^{0} denotes quantities at the current time step, while ^{1} denotes quantities at the next time step.

PIMPLE

Within OpenFOAM, another pressure–velocity coupling algorithm, PIMPLE, is available. A visualisation of the algorithm is depicted in Figure 4.7. The user can set a specific number of inner loops, m_{max}, referring to the number of pressure corrections. Furthermore, the user can specify the number of outer loops, n_{max}, thereby restarting the algorithm after the pressure correction loop. If $n_{\text{max}} = 1$, PIMPLE operates in PISO 'mode'. For transient problems, the PIMPLE algorithm can be embedded in a time iteration, following the procedure depicted in Figure 4.6 [74].

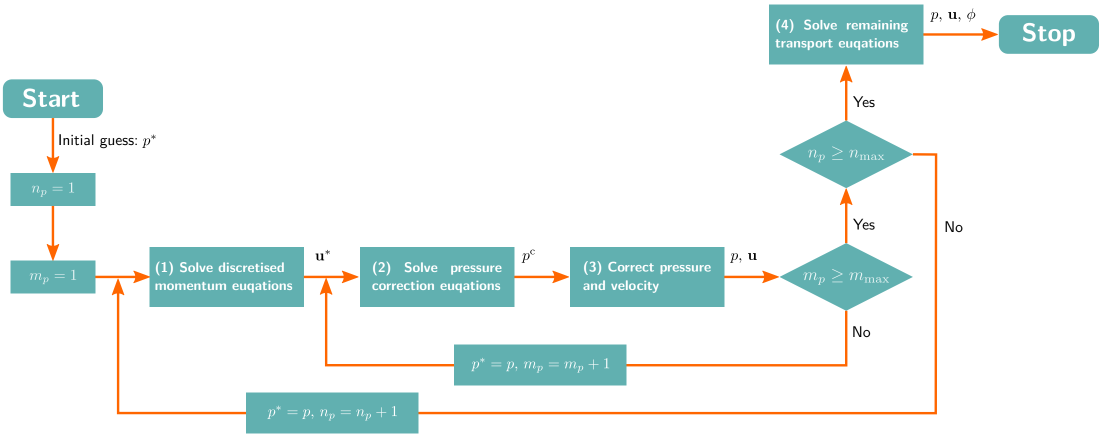

Figure 4.7: Visualisation of the PIMPLE algorithm (adapted from [74]). In the OpenFOAM framework, n_p is referred to as `nOuterCorrectors` and m_p is referred to as `nCorrectors`

4.2.4 Boundary conditions

The definition of a set of boundary conditions for the flow quantities is required at each boundary in a CFD–based NWT. Generally, two types of boundary conditions can be distinguished:

- Dirichlet boundary conditions: The value of a quantity is set at the boundary.
- Neumann boundary conditions: The gradient of a quantity in a specific direction is set at the boundary.

In the following, the most important boundary conditions for WSI problems are briefly discussed. First, general boundary conditions are discussed: fixed value, slip/no–slip, zero gradient, and symmetry. After that, OpenFOAM specific boundary conditions are introduced [77]: `inletOutlet`, `totalPressure`, `fixedFluxPressure`, and `pressureInletOutletVelocity`. Specific boundary conditions may be required for the generation and absorption of waves, which are discussed in Section 4.3.3.

Fixed value

The fixed value boundary conditions is the direct implementation of a Dirichlet boundary conditions and allows the specifications of specific values of a quantity at the boundary. At walls, the fixed value boundary conditions translates into the no–slip boundary conditions (see below).

Slip and no–slip

When considering stationary walls, the slip and no–slip (Dirichlet) boundary conditions define the velocity at the wall. While the slip condition allows velocities $\neq 0$, the no–slip condition[6] sets the velocity at the wall to 0 (see Figure 4.8). For moving walls, the velocity at the wall is equal to the velocity of the wall.
In OpenFOAM, the no–slip boundary condition for the velocity at the wall (i.e. fixed value of 0), is usually used in conjunction with the `fixedFluxPressure` detailed below.

Zero gradient

The zero gradient is a Neumann–type boundary condition and sets the normal gradient of a quantity to zero. This has the physical interpretation of the quantity spatially continuing beyond the boundary with a constant value.

---

[6] Note that the no–slip condition is physically correct for viscous fluids.

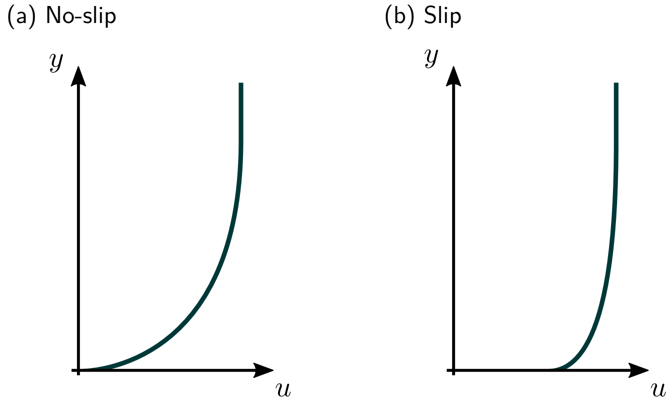

Figure 4.8: Idealised illustration of (a) the no–slip and (b) slip boundary condition.

Symmetry

If a flow problem features symmetry planes (see Part II for examples), the symmetry boundary condition can be applied. At the symmetry plane/boundary, the normal velocity and the normal gradients of all quantities are set to zero.

`fixedFluxPressure`

As stated in the discussion of the no–slip boundary condition, the `fixedFluxPressure` boundary condition is commonly used in conjunction with the fixed value boundary condition at the wall [77]. `fixedFluxPressure` adjusts the gradient depending on the prevailing body forces.

`inletOutlet`

Within OpenFOAM, the `inletOutlet` boundary condition is commonly used as the boundary condition for the volume fraction, α_{VF}, in multi–phase problems (see Section 4.3.1) at the atmospheric boundary of a CFD–based NWT. In the case of an outflow, a zero gradient condition is set for α_{VF}, while for the inflow case, α_{VF} is fixed to zero.

`totalPressure`

As for the `inletOutlet` boundary condition, the `totalPressure` boundary condition is commonly used as the condition for the pressure at the atmospheric boundary of the CFD–based NWT. In the case of an outflow, the pressure is set to a fixed value, while for the inflow case, the pressure is corrected depending on the prevailing velocity at the boundary.

`pressureInletOutletVelocity`

Finally, for the boundary condition of the velocity at the atmospheric boundary of a CFD–based NWT, the `pressureInletOutletVelocity` boundary condition is commonly applied. A zero gradient boundary condition is imposed on the velocity apart from the case of inflow, for which the tangential velocity is defined by a fixed value.

4.3 CFD–based NWT requirements

Following the introduction of the relevant numerical methods for the solution of the governing equations within a CFD–based NWT in Section 4.2, this section takes a closer look at the specific requirements of a CFD–based NWT for WEC applications and the corresponding numerical implementation.

Figure 4.9 schematically depicts the main requirements of a CFD–based NWT for WEC applications, which are discussed in the individual subsections below. Specifically, these requirements are:

- The capturing (and monitoring) of the multi–phase problem (see Section 4.3.1).
- The determination of a correct discretisation of the domain in space and time, with a focus on the spatial discretisation in the free surface interface region (see Section 4.3.2).
- The generation and absorption of waves (see Section 4.3.3).
- The accommodation of body motion, induced by hydrodynamic and external forces, through dynamic mesh motion methods (see Section 4.3.4).
- The modelling of turbulence (see Section 4.3.5).

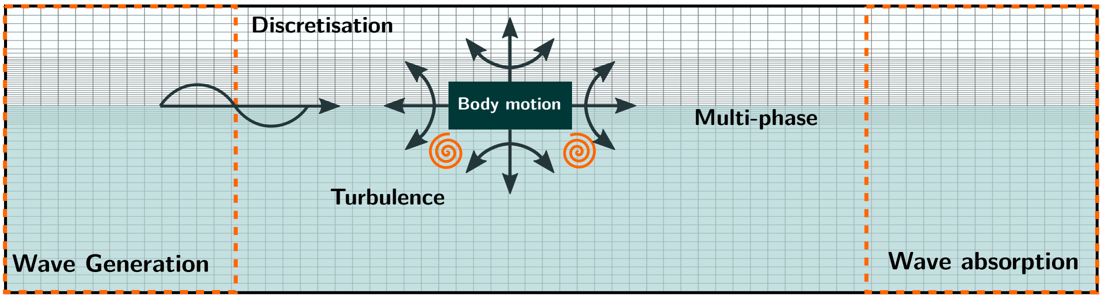

Figure 4.9: Visualisation of the requirement for a CFD–based NWT.

4.3.1 The Volume–of–fluid method

Compared to many other CFD applications, the modelling of WSI in CFD–based NWTs is complicated by virtue of the multi–phase problem, where both the water and air phase must be considered in the same CFD domain. In the FV method, the two phases are commonly captured by the volume–of–fluid (VOF) method proposed by Hirt and Nichols [78]. In the VOF method, the governing equations of the fluid mixture are developed for a single fluid and the multi–phase nature is introduced by the volume fraction, α_{VF}. α_{VF} is limited to fall within the range $0 \leq \alpha_{\mathsf{VF}} \leq 1$, where, in general WSI applications, $\alpha_{\mathsf{VF}} = 0$ represents the gaseous, i.e. air, phase and $\alpha_{\mathsf{VF}} = 1$ the liquid, i.e. water, phase. With α_{VF}, the properties of the fluid mixture (density and viscosity) can be expressed as:

$$\rho = \alpha_{\mathsf{VF}}\rho_{\mathsf{water}} + (1 - \alpha_{\mathsf{VF}})\rho_{\mathsf{air}}\,, \tag{4.18}$$

and

$$\mu = \alpha_{\mathsf{VF}}\mu_{\mathsf{water}} + (1 - \alpha_{\mathsf{VF}})\mu_{\mathsf{air}}\,. \tag{4.19}$$

The transport equation for α_{VF} follows:

$$\frac{\partial\, \alpha_{\mathsf{VF}}}{\partial\, t} + \nabla \cdot (\mathbf{u}\alpha_{\mathsf{VF}}) = 0\,. \tag{4.20}$$

By way of example, Figure 4.10 shows a screen shot of the α_{VF} field for a dam break case with an obstacle. At $t = 0$ a column of water collapses and the bulk of water runs against the obstacle. The colour code indicates the value of α_{VF}, where $\alpha_{\mathsf{VF}} = 1$ and $\alpha_{\mathsf{VF}} = 0$ are shown in blue and yellow, respectively.

Figure 4.10 furthermore includes the α_{VF} iso–lines for $\alpha_{\mathsf{VF}} = [0.05, 0.5, 0.95]$. Throughout this thesis, the common approach is employed whereby the location of the free surface interface is defined at $\alpha_{\mathsf{VF}} = 0.5$. It is straightforward that the distance between the $\alpha_{\mathsf{VF}} = [0.05, 0.5, 0.95]$ iso–lines indicates the sharpness of the interface and, thereby, the accuracy of the solution for fluid– and wave–structure interaction problems. Sharp water–air interfaces can be supported by a fine spatial discretisation in the interface region (see Section 4.3.2), but are also significantly driven by the numerical interface capturing method.

Available interface capturing methods are, for example: the high resolution interface capturing (HRIC) method proposed in [79], the compressive interface capturing scheme for arbitrary meshes (CICSAM) proposed in [80], or the interface compression method, implemented in OpenFOAM [81–83]. It should be noted that the choice of the interface capturing method is mostly defined by the applied CFD code. Thus, the interface compression method in OpenFOAM is employed throughout this thesis and detailed below.

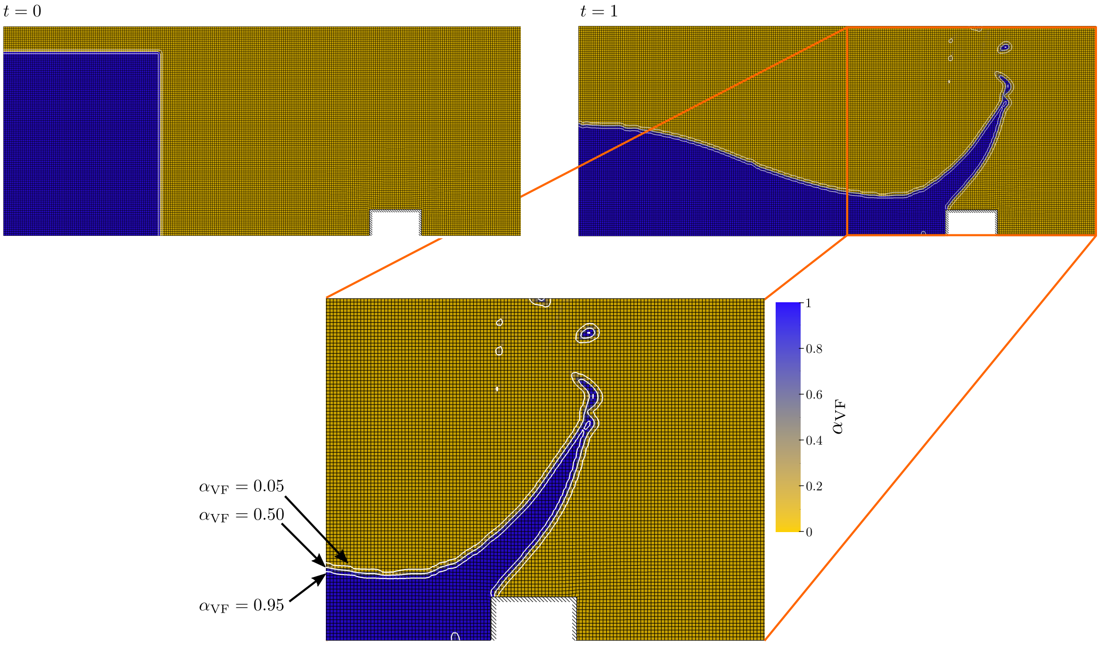

Figure 4.10: Visualisation of the volume–of–fluid method for dam dam break case with an obstacle. The white lines indicate the iso–lines of $\alpha_{\mathsf{VF}} = [0.05, 0.5, 0.95]$

To achieve a sharp phase interface and reduce numerical diffusion, thereby preventing smeared solutions, a compression term $(\nabla \cdot [\mathbf{u_r}\alpha_{\mathsf{VF}}(1-\alpha_{\mathsf{VF}})])$ is added into the transport equation (4.20), yielding:

$$\frac{\partial\,\alpha_{\mathsf{VF}}}{\partial\,t} + \nabla \cdot (\mathbf{u}\alpha_{\mathsf{VF}}) + \nabla \cdot [\mathbf{u_r}\alpha_{\mathsf{VF}}(1-\alpha_{\mathsf{VF}})] = 0\,, \tag{4.21}$$

where $\mathbf{u_r}$ is the compression velocity, representing the relative velocity between the liquid and the gaseous phase. $\mathbf{u_r}$ is determined as:

$$\mathbf{u_r} = \min\left[c_r|\mathbf{u}|, \max\left(|\mathbf{u}|\right)\right]\ , \tag{4.22}$$

where c_r is a user–defined factor to control the interface compression [84]. The compression term is only active in the area close to the phase interface, by virtue of the multiplier $\alpha_{\mathsf{VF}}(1-\alpha_{\mathsf{VF}})$, which is 0 if $\alpha_{\mathsf{VF}} = 1$ or 0. The discretisation of Equation (4.21) is performed with the multi–dimensional limiter for explicit solution (MULES) algorithm [85], ensuring boundedness and conservativeness. In a semi–implicit variant, MULES follows a predictor–corrector procedure with an implicit predictor step and explicit correction[7]. The performance of the interface compression method is assessed in [83].

Recently, novel techniques to increase interface sharpness [86] or mitigate well known problems, such as spurious, undesired, velocities in the gaseous phase [87], have been

---

[7] In OpenFOAM, the number of correction steps is defined by the number of MULES iterations `nLimiterIter`

developed. However, such novel numerical methods gain maturity only slowly and do not see widespread application yet. Throughout this thesis, the native OpenFOAM interface compression method is used.

4.3.2 Discretisation and convergence

As noted in Section 4.3.1, the spatial discretisation has an immediate effect on the sharpness of the phase interface. It is common practice for WSI problems to parametrise the discretisation in the phase–interface region by the wave height H and the wave length λ, resulting in the two measures:

- Cells per wave height (CPH), for the discretisation perpendicular to the wave propagation direction, i.e. z–direction.
- Cells per wave length (CPL), for the discretisation in the wave propagation direction, i.e. x–direction.

Generally, the values of CPH and CPL are linked by the cell aspect ratio which, ideally, is 1 [29]. The values of CPH and CPL and, thereby, the appropriate grid size, needs to be determined through convergence studies [88–90].

The spatial discretisation and the temporal discretisation are linked by the Courant–Friedrichs–Lewy (CFL) condition [91], following:

$$Co = \frac{u\Delta t}{\Delta x}\,, \tag{4.23}$$

where Co denotes the Courant number.

Generally, $Co \leq 1$ is desired throughout the flow domain and simulation duration. Consequently, information can not be 'passed on' further than one cell within one time step, thereby ensuring accuracy and stability of the solution process. The Courant number can be employed to control the time step size throughout the simulation. By specifying a maximum Courant number, Co_{max}, Δt is adjusted at every temporal iteration step, such that $Co \leq Co_{\mathsf{max}}$. If fixed time step sizes are employed, monitoring of the Courant number is advised to ensure $Co \leq 1$. Similarly to the spatial discretisation, the appropriate time step size has to be determined through convergence studies.

Convergence studies

To mitigate parasitic influence of the selected discretisation size on the solution accuracy and stability, convergence studies must be performed for both the temporal and spatial discretisation. Standard procedures can be followed to determine the convergence properties of a certain grid size or time step size. Following the convergence analysis described by Roache [88], Stern *et al.* [92], and Vukčević [93], a figure of merit can be evaluated with three different discretisation levels, i.e. fine, medium, and coarse. From the solution for the finest ($\mathcal{S}_f$), medium ($\mathcal{S}_m$), and coarsest ($\mathcal{S}_c$) discretisation size, the discrimination ratio, R_D, is determined as follows:

$$R_D = \frac{\mathcal{S}_f - \mathcal{S}_m}{\mathcal{S}_m - \mathcal{S}_c}\,. \tag{4.24}$$

R_D is used to differentiate between four different solution characteristics, listed in Table 4.2.

Table 4.2: Solution characteristics based on the discrimination ratio R_D.

Convergence	
(i) Monotone Convergence	$0 < R_D < 1$
(ii) Oscillatory Convergence	$R_D < 0$ and $\lvert R_D\rvert < 1$
Divergence	
(i) Monotone Divergence	$R_D > 1$
(ii) Oscillatory Divergence	$R_D < 0$ and $\lvert R_D\rvert > 1$

Neglecting any case in which divergence is encountered, the absolute grid uncertainty, $\mathcal{U}_a$, can be calculated for monotonic (see Equation (4.25)) and oscillatory (see Equation (4.26)) convergence.

$$\mathcal{U}_a = F_s \frac{|\mathcal{S}_f - \mathcal{S}_m|}{\mathcal{R}^{\mathcal{P}} - 1} \tag{4.25}$$

$$\mathcal{U}_a = F_s\, 0.5 \,|\max(\mathcal{S}_f, \mathcal{S}_m, \mathcal{S}_c) - \min(\mathcal{S}_f, \mathcal{S}_m, \mathcal{S}_c)| \tag{4.26}$$

In Equations (4.25) and (4.26), $\mathcal{R}$ is the refinement ratio between the fine, medium, and coarse discretisation levels (a value of 2 is used throughout this thesis), F_s is a safety factor (chosen to be 1.5 following [94]), and $\mathcal{P}$ is the order of accuracy from Richardson extrapolation [95]:

$$\mathcal{P} = \frac{\ln \left[{}^{(\mathcal{S}_f - \mathcal{S}_m)}\!/\!_{(\mathcal{S}_m - \mathcal{S}_c)} \right]}{\ln \mathcal{R}} \tag{4.27}$$

Finally, $\mathcal{U}_a$ can be normalised by $\mathcal{S}_f$ and, thus, represents the relative grid uncertainty, $\mathcal{U}$, (see Equation (4.28)).

$$\mathcal{U} = \frac{\mathcal{U}_a}{\mathcal{S}_f} \cdot 100\% \tag{4.28}$$

The convergence analysis detailed above is used throughout this thesis, and results for the relative grid uncertainty $\mathcal{U}$ are presented throughout Chapters 6–11.

4.3.3 Numerical wave generation and absorption

Efficient and accurate wave generation and absorption is of crucial importance for timely, high quality, numerical results. A variety of numerical algorithms, termed numerical wave makers, have been developed for the purpose of wave generation and absorption in CFD–based NWTs.

For wave generation, five different methods are well known: the relaxation zone method [96–100], the static and dynamic boundary method [101–103], the mass source method [104, 105], and the impulse source method [106–109]. For numerical wave absorption, six different methods are available, i.e. the relaxation zone method, the static boundary method, the dynamic boundary method, sponge layer or numerical beach implementations [110–112], geometrically sloped beaches [113–115], and the cell stretching method [116]. Schematics of the different methods are depicted in Figure 4.11.

Relaxation zone method

The relaxation zone method blends a target solution, ϕ_{target}, with the computed solution, ϕ_{computed}, for the values of the velocity field, $\phi = \mathbf{u}$, and fluid volume fraction, $\phi = \alpha_{\text{VF}}$, within defined relaxation zone regions (see Figure 4.11), via

$$\phi = \chi_R \phi_{\text{computed}} + (1 - \chi_R)\phi_{\text{target}} \, . \tag{4.29}$$

The weighting function, χ_R, is zero at the NWT boundary, unity at the interface with the simulation zone, and should vary smoothly along the relaxation zone to ensure a gradual transition in the blending of the target and computed solutions. For wave generation, analytical solutions are obtained from wave theory (see Chapter 3) for the fluid velocity and free surface elevation to obtain the target solutions, $\mathbf{u}_{\text{target}}$ and $\alpha_{\text{VF,target}}$. For wave absorption, $\mathbf{u}_{\text{target}}$ is zero, and $\alpha_{\text{VF,target}}$ defines the location of the SWL.

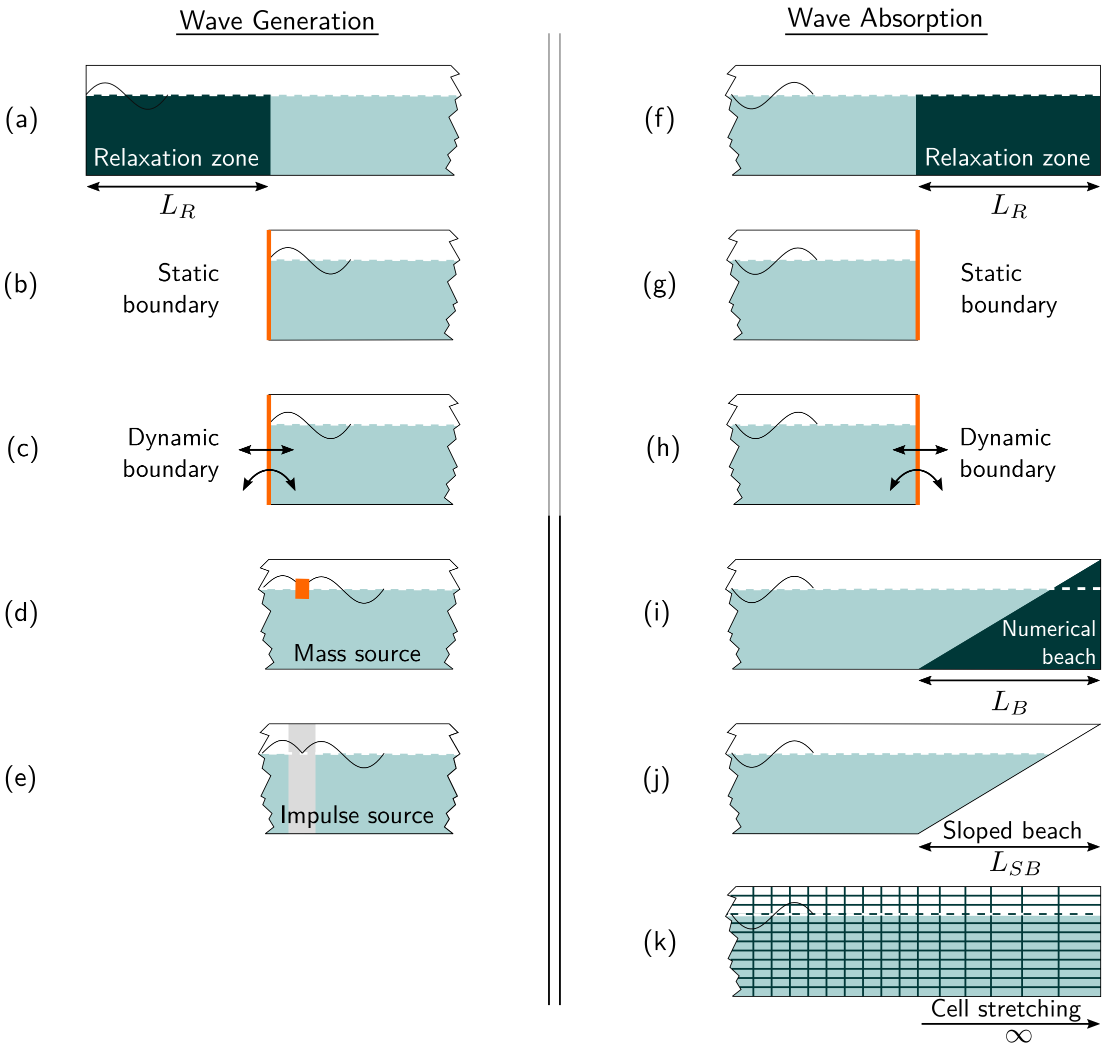

Figure 4.11: Schematic representation of available numerical wave maker methodologies for wave generation (a-e) and wave absorption (f-k): (a)/(f) relaxation zone method, (b)/(g) static boundary method, (c)/(h) dynamic boundary method, (d) mass source method, (e) impulse source method, (i) numerical beach, (j) geometrical sloped beach, (k) cell stretching.

Static boundary method

The static boundary method defines $\mathbf{u}$ and α_{VF} as Dirichlet boundary conditions at the generation/absorption boundaries of the CFD–based NWT. Compared to the relaxation zone method, the definition at the NWT boundary has the advantage of a reduced computational domain size (see Figure 4.11). At the wave generation boundary, the boundary conditions are obtained from wave theory. For the absorption boundary, the determination of the necessary boundary values may be based on shallow water theory (i.e. constant velocity profile along the water column) [117], where a correction velocity, $\mathbf{u}_c$, is applied at the boundary, cancelling the incident wave field. Most recently, an extension of the absorption methodology in [117] to arbitrary water depths has been proposed by Higuera [118].

Dynamic boundary method

The dynamic boundary method represents the numerical replication of a piston or flap-type wave maker in a physical wave tank. By mimicking the physical wave maker geometry and motion, using a moving wall and dynamic mesh motion (see Section 4.3.4) in the CFD–based NWT, the dynamic boundary method affords the same wavemaking capabilities as in a physical wave tank, whilst also incurring the same complexities and inaccuracies, such as evanescent waves near the wave maker and the requirements of control strategies for the wave maker motion. The time series of the wave maker displacement, or velocity, serves as the input to the wave maker. This input data may issue from analytical expressions (e.g. [119, 120]) or from real measurements of the wave maker motion in physical wave tank experiments. Similarly, the dynamic boundary method can be used for wave absorption. Here, the motion of the moving boundary is controlled by force feedback, analytical expressions, or physical measurements [121, 122].

Mass source method

The mass source method, proposed in [104], displaces the free surface with a fluid inflow and outflow. A source term, s_m, is defined which couples the free surface elevation η, the wave celerity c, and the surface area of the source, A_s:

$$s_m = \frac{2\,c\eta}{A_s} \tag{4.30}$$

The source term facilitates wave generation through a volume source term included in the incompressible[8] continuity equation (2.6), leading to the modified incompressible continuity equation:

$$\nabla \cdot \rho \mathbf{u} - s_m = 0\,. \tag{4.31}$$

Since the source term does not alter waves travelling through the source, wave absorption can only be achieved through the relaxation zone method, the static boundary method, the dynamic boundary method, or an additional beach, examples of which are described below.

---

[8] Note that the same procedure is followed for compressible flows.

Impulse source method

For the impulse source method, proposed in [107], a source term, $r_s \rho \mathbf{a}_{wm}$, is added to the momentum equation of the Navier–Stokes equations ((2.4) or (2.8)), yielding, for incompressible flows:

$$\frac{\partial (\rho \mathbf{u})}{\partial t} + \nabla \cdot (\rho \mathbf{u}\mathbf{u}) = -\nabla p + \rho \nabla \cdot (\nu \nabla \mathbf{u}) + \rho \mathbf{f}_b + r_s \rho \mathbf{a}_{wm} \,. \tag{4.32}$$

The location of the wave maker zone is defined by $r_s = 1$, with $r_s = 0$ everywhere else in the domain. $\mathbf{a}_{wm}$ is the acceleration input to the wave maker, which can be determined analytically for shallow water waves [107] or via an iterative calibration method for waves in any water depth. Again, wave absorption can only be achieved through the relaxation zone method, the static boundary method, the dynamic boundary method, or an additional beach. A more in–depth discussion of an impulse source wave maker is presented in Chapter 6.

Numerical beach

To absorb waves in the numerical domain, various methods, termed 'numerical beaches' or 'sponge layers', were developed. In the following, the implementation in [110] will be discussed. Introducing the additional dissipation term, $s_b \rho \mathbf{u}$, to the momentum equation of the Navier–Stokes equations ((2.4) or (2.8)), yields, for incompressible flows:

$$\frac{\partial (\rho \mathbf{u})}{\partial t} + \nabla \cdot (\rho \mathbf{u}\mathbf{u}) = -\nabla p + \rho \nabla \cdot (\nu \nabla \mathbf{u}) + \rho \mathbf{f}_b + s_b \rho \mathbf{u} \,. \tag{4.33}$$

In Equation (4.33), the variable field s_b is the damping factor and controls the strength of the dissipation, with a value of zero in the simulation zone and then gradually increasing towards the boundary over the length of the numerical beach, following a pre-defined analytical expression [110]. A more in–depth discussion of the above described implementation of a numerical beach, including the determination of optimal values of s_b, is presented in Chapter 6.

Sloped bathymetry

While the aforementioned wave absorption methods include additional terms in the governing equations to account for wave absorption or actively absorb waves through moving boundaries, for a sloped bathymetry only changes to the domain layout are required. Implementing a slope at the far field boundary of the CFD–based NWT dissipates the wave energy, replicating the effect of real beaches in the physical world.

Mesh stretching

Another wave absorption method, which does not require additional terms in the governing equations, or active absorption, is the cell stretching method. Here, the spatial discretisation in one direction is gradually enlarged towards the far field boundary and any wavelengths shorter than the cell size are filtered out. This requires relatively long domains in order to reach cell sizes which are able to absorb waves used in practical applications; however, due to the larger cell sizes, this does not dramatically increase the cell count. Cell stretching is often used to supplement active wave absorption methods and also reduce the number of required cells in a given absorption domain length.

4.3.4 Dynamic mesh motion

Modelling WSI of WECs in CFD–based NWTs requires three main components:

- The WEC structure has to be 'implemented' in the numerical grid through body representation methods.
- The forces, acting on the WEC structure, have to be determined and the according acceleration, velocity, and displacement need to be calculated. This is achieved by motion solvers.
- Based on the calculated dynamics of the WEC structure, the motion has to be explicitly accommodated in the CFD domain. This is achieved by dynamic mesh motion methods, in close conjunction with the body representation method.

Before elaborating on the body representation methods, the motion solver, and the different dynamic mesh motion methods, the DoFs of a WEC structure, used throughout this thesis, are defined in Figure 4.12. The translational motion in the x–, y–, and z–directions are referred to as surge, sway, and heave, respectively. The rotational motion around the x–, y–, and z–axis are referred to as roll, pitch, and yaw, respectively.

Body representation method

To accommodate a structure in the computational domain of a CFD–based NWT, different body representation methods are available [123–125]. The different body representation methods vary in terms of initial setup complexity, handling of dynamic mesh adaption, as well as computational accuracy and efficiency. In some cases, the body representation method is intrinsic to the CFD software and must be considered when choosing CFD software for a particular problem. A brief overview of the most prominent body representation methods is given below and examples of the different methods for WEC applications are given in Chapter 5.

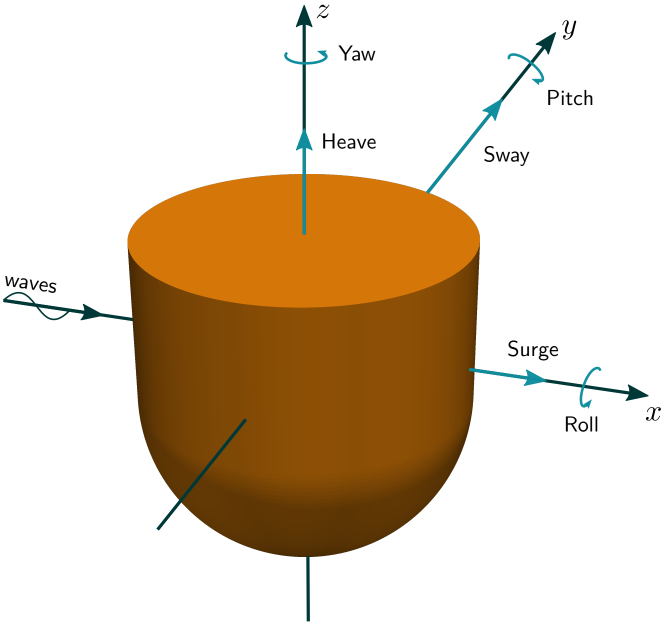

Figure 4.12: Definition of the degrees of freedom of a WEC, used throughout this thesis

Immersed boundary method: To avoid complex and time consuming grid generation to represent a body, as well as reducing numerical errors, the immersed boundary method can be used, where the body is cut out of the (Cartesian) background mesh, leaving partially cut cells, specially treated in the numerical method. Body motion is handled by simply repeating the cutting procedure with the new boundary positions. Causon *et al.* [124] propose the use of the Cartesian cut–cell method, a specific implementation of the immersed boundary method, for multi–phase flow calculations. In this approach, the mesh at the body boundary is adjusted after the cutting, resulting in a body fitted mesh.

Fast–fictitious–domain: In the fast–fictitious–domain body representation method, proposed in [126], the governing equations are solved throughout the entire computational domain; however, structures are represented as solid zones attributed with high values of viscosity. Thereby, the fast–fictitious–domain readily handles arbitrary, large amplitude, multi–DoF body motion.

Fractional area-volume obstacle representation (FAVOR): The FAVOR technique, implemented in the commercial CFD toolbox Flow-3D [127, 128], represents the body by using fractional cell volumes and areas, in a similar manner to the VOF method for tracking the free surface, thereby allowing the body to pass through a stationary mesh.

Body fitted meshes: Contrary to the previously introduced body representation methods, for body fitted meshes, the computational grid is directly adjusted to the present structure (see Figure 4.13). Depending on the CFD and/or meshing software, either (block-) structured or un–structured grids can be used. As stated in [124, 125], this method requires considerable effort to ensure sufficient mesh quality throughout the domain. In particular when (large amplitude) body motion needs to be accommodated, body fitted meshes can be pushed beyond the limits of numerical stability, depending on the dynamic mesh motion method, due to the distortion and skewing of the mesh.

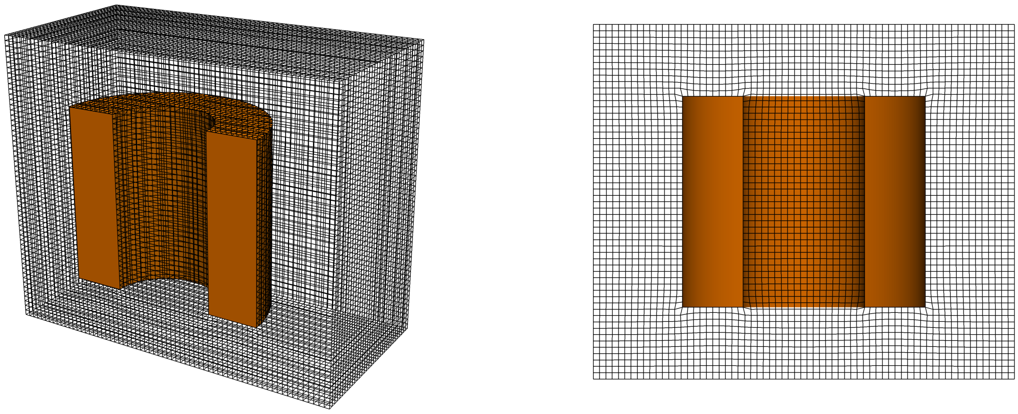
(a) 3D view
(b) Front view

Figure 4.13: Screen shot of the (a) 3D and (b) 2D (front) view of a body fitted mesh.

Motion solver

For a fixed structure, the WEC structure can simply be treated as solid boundary (wall) in the CFD domain (see Section 4.2.4). However, for a dynamical system, the WEC motion, due to interaction between the waves and the structure, must be calculated. This process is performed by the motion solver (see Figure 4.14). Within a time step or solver iteration, the motion solver performs the following steps:

(1) Update position
(2) Calculate forces
(3) Update acceleration
(4) Move object

The hydrodynamic forces on the body are composed of the pressure and shear forces from the fluid. The pressure force is obtained by integration of the calculated fluid pressure over the surface area of the body. Likewise, the shear force is obtained by integrating the shear, due to the fluid viscosity, and the relative WEC–fluid motion. Additional, external, forces may be applied to the WEC due to gravity, but also the PTO and/or mooring system. Based on the sum of the acting forces, the WEC motion is solved via Newton's 2^{nd} law of motion.

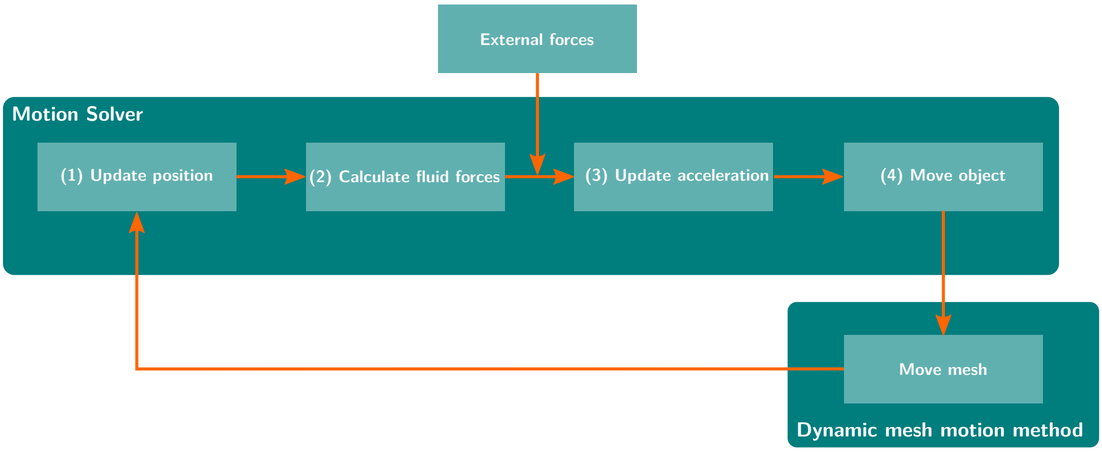

Figure 4.14: Schematic of a generic motion solver in the CFD solution process. The motion solver performs the sequential steps of updating the position, calculating force, updating the acceleration, and moving the object. The dynamic mesh motion method is then required to move the mesh according to the body dynamics. (adopted from [129]).

For calculation of the body dynamics, OpenFOAM follows a partitioned approach, whereby the motion solver and the fluid solver operate independently, but are (sequentially) coupled. A comprehensive review of the `sixDoFRigidBodyMotionSolver` used within OpenFOAM (and, thus, throughout this thesis) is given in [129, 84], highlighting stability issues and proposing potential improvements.

The `sixDoFRigidBodyMotionSolver` provides a set of restraint functions, facilitating the numerical implementation of, for example, PTOs or control systems. Furthermore, the motion solver provides a set of constraints, enabling constrained motion of the WEC in a limited number of DoFs.

Dynamic mesh motion methods

In order to accommodate the required mesh motion (for body fitted meshes), a number of dynamic mesh motion methods have been developed, such as: arbitrary mesh interfaces (AMIs), re–meshing methods, mesh morphing, or overset grid methods (see Chapter 5 for examples of the different implementations). Throughout this thesis, a focus is put on mesh morphing (because of its widespread application) and overset grid methods (because of its novelty within the OpenFOAM framework), which are detailed below. Note that the details provided in the following are specific for the implementation of the dynamic mesh motion method in OpenFOAM.

Mesh morphing: For body fitted meshes, if grid connectivity should be retained (meaning no topological changes), mesh morphing is the classical method to accommodate body motion in the computational domain. In the `sixDoFRigidBodyMotionSolver` in OpenFOAM, the spherical linear interpolation (SLERP) algorithm is implemented to calculated the mesh displacement based on the distance of a cell to the moving body, which gives control over the grid quality during mesh deformation [130]. As depicted in Figure 4.15, the displacement of a structure leads to a deformation of single CVs, while the total volume of all control volumes in the domain remains constant throughout the simulation. The user specifies an inner and outer distance, between which mesh deformation is allowed and prohibited elsewhere (see Figure 4.15). For large translational WEC displacements, moderate rotational WEC displacements, or multiple bodies moving in close proximity, the deformation of the original, good quality, mesh can lead to poor grid quality, such as large aspect ratios and/or highly skewed, non-orthogonal cells, resulting in numerical instability and, ultimately, causing the simulation to crash.

The reduction in mesh quality depends on the layout of the numerical domain, the choice of the inner and outer distances, and the amplitude of the body motion. If the amplitude of the WEC motion is (roughly) known *a priori*, the simulation can be set up such that the likelihood of numerical instability from mesh distortion is reduced. However, if the dynamics are not known *a priori*, time consuming preliminary studies must be performed. This weakness of the mesh morphing method, in handling large displacements, limits the range of allowable motion in WEC experiments. This is especially true for rotational DoFs, which commonly forces studies to constrain rotational modes of motion and consider WECs moving only in heave, for example. Certain sea states, or control settings, which result in large resonant WEC motions, can not be simulated, due to the numerical instability caused by the degradation in mesh quality. However, it is these sea states and conditions where the CFD–based NWT is required most, since the large resonant motions lead to non–linearities, not captured by lower fidelity simulation models (see Chapter 8).

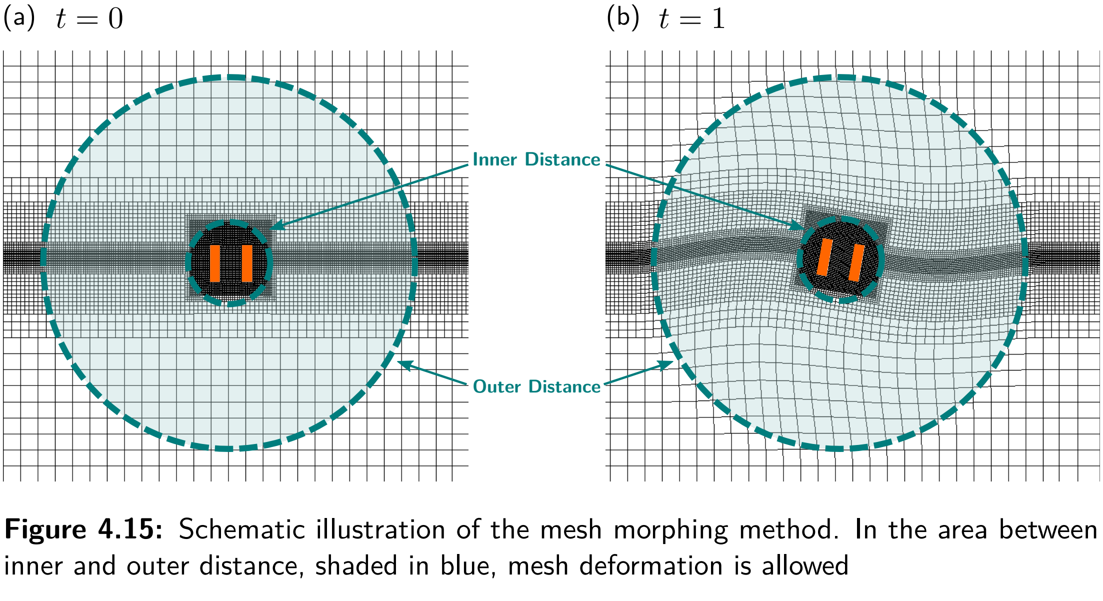

Figure 4.15: Schematic illustration of the mesh morphing method. In the area between inner and outer distance, shaded in blue, mesh deformation is allowed

Overset grids: In the overset grid method, (at least) two grids (background and body-fitted) are defined, which may arbitrarily overlay each other (see Figure 4.16). The different grids are internally static, thereby retaining their original structure and quality, but are allowed to move relative to each other. To pass information between the different grids, interpolation must be performed. The overset grid method can be split into the four sequential steps:

(1) Identification of hole cells
(2) Identification of fringe cells
(3) Identification of donor cells
(4) Interpolation between fringe and donor cells

Hole cells embrace cells in the background grid, lying inside the moving body. These cells are marked and blanked out during the solution process. This step is the main cause for the extensive computational cost of the overset grid method [131]. In the second step, cells adjacent to hole cells are identified as fringe cells. Likewise, cells at the outer boundary of the body-fitted grid are also identified as fringe cells. These cells are used as boundary cells in the solution procedure. Boundary values for fringe cells are determined through solution interpolation. In the third step, the interpolation partners on both grids, the donor cells, are identified. Finally, interpolation between fringe and donor cells is performed. For unsteady simulation, all steps have to be performed at every iteration. The quality of the numerical results is directly impacted by these four steps, and therefore depends on the employed interpolation scheme and the domain discretisation in the background and body–fitted grid.

The major advantage of the overset method is that large amplitude motion in multiple DoFs is possible, with the mesh structure and quality remaining constant throughout the simulation. The overset grid method has been used, for example, to simulate ship motion, with a moving rudder and a spinning propeller, using separate overset grids for the hull, rudder, and propeller [132].

The disadvantage of the overset grid method is the increase in computational time, due to steps (1)-(4) described above. In addition, interpolation of field variables (e.g. α_{VF}, p) between grids can lead to conservation and/or convergence issues and represents the biggest challenge of the overset grid method [29]. For a detailed analysis of interpolation strategies and their implications on the solution accuracy, the interested reader is referred to [133].

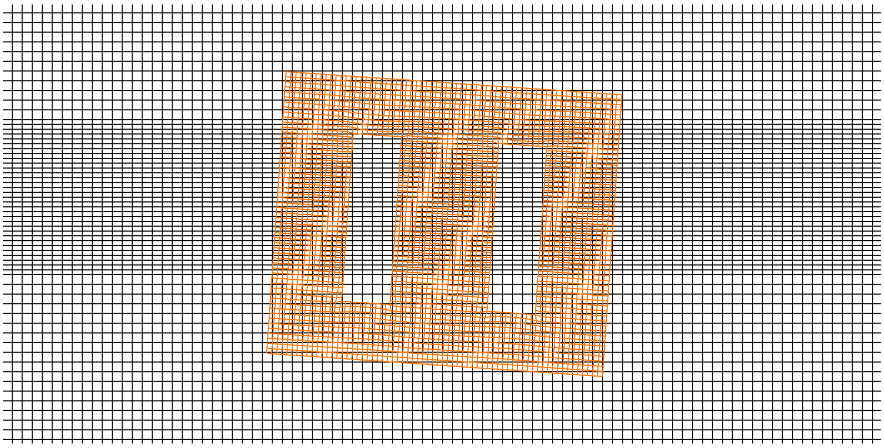

Figure 4.16: 2D illustration of an overset grid domain for the modelling of a cylindrical WEC with moon–pool. Background mesh in black; overset mesh in orange

4.3.5 Turbulence modelling

The basic concept and mathematical description of turbulent flows is presented in Chapter 2. It has been stated that, generally, all flows can be modelled by solving the Navier–Stokes equations (2.3) and (2.4) (or (2.6) and (2.8) for incompressible flows) using DNS; however at an exorbitant computational cost. To be able to sufficiently model the prevailing flow conditions, turbulence modelling can be applied within a CFD–based NWT. In the following, a close look is taken at the development and implementation of turbulence models in a CFD–based NWT. The description follows [39, 29, 30] and the interested reader is referred to these reference for more detailed information.

For the development of turbulence models, it is helpful to acknowledge the similarity between viscosity and the effects of turbulence, i.e. increased transport and dissipation. Thus, conceptually, turbulence models formulate additional equations, based on the concept of viscosity, to achieve closure of the system of governing equations.

Assuming some equivalence between fluid viscosity and turbulence effects, an eddy viscosity can be defined. To that end, one can recap Newton's law of viscosity (see Equation (4.34)), whereby viscous stresses, τ_v, are proportional to the rate of strain.

$$\tau_{v,ij} = \mu S_{ij} \, , \tag{4.34}$$

where S_{ij} denotes the rate of strain in suffix notation. i or $j = 1$ denotes the x–direction, i or $j = 2$ denotes the y–direction, and i or $j = 3$ denotes the z–direction. Following Reynolds decomposition, $S_{ij} = \bar{S}_{ij} + S'_{ij}$.

For turbulent flows, Equation (4.34) can be interpreted such that the turbulent stresses are proportional to the mean rate of strain $\bar{S}_{ij}$ – the so called Boussinesq hypothesis [134].

Large eddy simulation

As stated in Section 2.4.2, while temporal filtering, by means of the Reynolds decomposition, is employed in the RANS equations, LES is based on spatial filtering to distinguish between larger, resolved, and smaller, modelled, eddies. Thereby, lower fidelity solutions, with lighter computational requirements, compared to DNS, are obtained by modelling, rather than resolving, the fine scale turbulent effects.

Typically, for the filtering, a top hat (or box) filter is employed[9], with a cut–off width Δ, which indicates the size of the eddies that are resolved. In the FV framework, Δ is, generally, chosen not to be smaller than the grid size, but rather of the same order as the grid size. Thus, the cube root is commonly applied for the definition of the cut–off width: $\Delta = \sqrt[3]{\Delta x \, \Delta y \, \Delta z}$.

Applying the filter leads to the LES continuity and momentum equations in which similar terms to Reynolds stresses (see Equation (2.20)–(2.22)), the so called SGS stresses, appear. The SGS stresses can be interpreted as the result from momentum exchange between the resolved and unresolved turbulent eddies. Following suffix notation, the SGS stresses are then described as:

$$\tau_{ij} = -2\mu_{\mathsf{SGS}}\bar{S}_{\mathsf{rf},ij} + \frac{1}{3}\tau_{ii}\delta_{ij}\,, \tag{4.35}$$

where $\bar{S}_{\mathsf{rf},ij}$ is the local rate of strain of the resolved flow, μ_{SGS} is the SGS turbulent viscosity, and δ_{ij} is the Kronecker delta:

$$\delta_{ij} = \begin{cases} 1, & i = j\,, \\ 0, & i \neq j\,. \end{cases} \tag{4.36}$$

LES then requires the definition of SGS turbulence models, such as the Smagorinsky-Lilly SGS model [136], for the definition of the SGS turbulent viscosity μ_{SGS}.

In the Smagorinsky-Lilly SGS model, based on the Boussinesq eddy viscosity hypothesis and the assumption of an isotropic character of small turbulent eddies, the local SGS stresses proportional to the local rate of strain of the resolved flow, thereby delivering a description of the influence of the unresolved on the resolved flow. With that, the μ_{SGS} is defined as a function of the cut–off width Δ, following:

$$\mu_{\mathsf{SGS}} = \rho(C_{\mathsf{SGS}}\Delta)^2\sqrt{2\bar{S}_{\mathsf{rf},ij}\bar{S}_{\mathsf{rf},ij}}\,, \tag{4.37}$$

where C_{SGS} is a modelling constant (i.e. 0.17–0.21 [137, 138]).

Examples of the LES turbulence model and all following turbulence models in the WEC literature are given in Chapter 5.

---

[9] Note that other filters, such as a Gaussian filter or spectral cut–off, could be used instead [135].

RANS $k - \varepsilon$ model

If turbulence has to be considered within the CFD–based NWT, but simulations need to be performed at lower computational cost, compared to LES, RANS turbulence models can be employed. As stated in Section 2.4.2, the decomposition of the flow quantities in the Navier–Stokes equations into the (temporal) mean and fluctuating part, by means of Reynolds decomposition, results in additional terms representing Reynolds stresses (see Equations (2.20)–(2.22)). With the above stated equivalence between fluid viscosity and turbulence effects, the eddy viscosity is defined by turbulence models, allowing closure of the system of the governing equations.

The two-equation (standard) $k-\varepsilon$ turbulence model, developed by Launder *et al.* [139], introduces two new transport equations for the kinetic turbulent energy k_t (see Equation (2.18)) and the dissipation rate of turbulent kinetic energy, ε_t (see Equation (4.38)).

$$\varepsilon_t = 2\nu \overline{\overline{S'_{ij} S'_{ij}}} \tag{4.38}$$

The transport equations for k_t and ε_t, omitted here for brevity, feature terms for the diffusive transport of k_t and ε_t. The diffusive transport is connected to the eddy viscosity, which follows:

$$\mu_t = \rho\, C_\mu \frac{k_t^2}{\varepsilon_t}\,, \tag{4.39}$$

where C_μ is a model constant. The definition of μ_t can be derived from dimensional analysis and the definition of two turbulent scales for the velocity, Υ , and the length, ℓ, where

$$\Upsilon = k_t^{1/2}\,, \tag{4.40}$$

and

$$\ell = \frac{k_t^{3/2}}{\varepsilon_t}\,. \tag{4.41}$$

With the the eddy viscosity, the Reynolds stresses are computed based on the Boussinesq hypothesis, following:

$$\tau_{ij} = -2\mu_t \bar{S}_{ij} + \frac{2}{3}\rho\, k_t \delta_{ij}\,, \tag{4.42}$$

Note that the term $\frac{2}{3}\rho\, k_t \delta_{ij}$ is included to ensure physically correct results. A derivation of this term can be found in [30, Chapter 3].

The transport equations for k_t and ε_t include additional model constants, i.e. $C_{1\varepsilon}$, $C_{2\varepsilon}$, σ_k, and σ_ε, which are found by empirical data fitting. Standard values for the aforementioned constants, extracted from [30], are listed in Table 4.3.

Table 4.3: Suggested values for the adjustable constants in the k_t and ε_t transport equations of the standard $k-\varepsilon$ turbulence model [30]

C_μ	$C_{1\varepsilon}$	$C_{2\varepsilon}$	σ_k	σ_ε
0.09	1.44	1.92	1.00	1.30

Special care must be taken of the initial and boundary conditions for the standard $k-\varepsilon$ model and, in fact, any turbulence model. To define the initial conditions for k_t and ε_t, [30] provides the following definitions:

$$k_t = \frac{2}{3}(U_{\text{ref}} T_i)^2 \tag{4.43}$$

$$\varepsilon_t = C_\mu^{3/4} \frac{k^{3/2}}{\ell} \,, \tag{4.44}$$

where U_{ref} denotes a reference velocity and $\ell = 0.07L$, where L is the characteristic length scale of the flow (see Equation (2.17)).
A detailed discussion of the boundary conditions at the wall is presented at the end of this Section 4.3.5.

RANS realizable $k-\varepsilon$ model

Shih *et al.* [140, 141] highlight the potential lack of accuracy of the standard $k-\varepsilon$ turbulence model due to over–prediction of turbulent eddy viscosity and false turbulent length scales. To tackle this problem, the authors propose a new model for the ε_t transport equation and the eddy viscosity that is ‘physically realistic’. To that end, a non-constant variable C_μ^* is included in the eddy viscosity equation, thus following:

$$\mu_t = \rho\, C_\mu^* \frac{k_t^2}{\varepsilon_t} \,. \tag{4.45}$$

The definition of the new eddy viscosity influences the calibration of the model constants for the refined ε_t transport equation, i.e. $C_{1\varepsilon}$, C_2, σ_k, σ_ε. Suggested values are listed in Table 4.4.

Table 4.4: Suggested values for the adjustable constants in the k_t and ε_t transport equations of the realizable $k-\varepsilon$ turbulence model [142]

$C_{1\varepsilon}$	C_2	σ_k	σ_ε
1.44	1.9	1.00	1.2

RANS Re-Normalisation group $k - \varepsilon$ model

Another refined turbulence model base on the standard $k - \varepsilon$ model is proposed by Yakhot *et al.* [143] and applies the Re-Normalisation group (RNG) method. The RNG method allows the consideration of different turbulent length scales within a modified ε_t equation. This modification introduces two new model constants (η_0, β) and, moreover, allows the explicit, rather than empirical, determination of the unknown constants. Compared to the standard $k - \varepsilon$ model, the RNG $k - \varepsilon$ model achieves improved accuracy due to this explicit formulation of the involved model constants. Standard values for the involved model constants are listed in Table 4.5.

Table 4.5: Suggested values for the adjustable model constants of the RNG $k-\varepsilon$ turbulence model [144, 145]

C_μ	$C_{1\varepsilon}$	$C_{2\varepsilon}$	σ_k	σ_ε	η_0	β
0.0845	1.42	1.68	0.7194	0.7194	4.38	0.012

RANS $k - \omega$ model

In the standard $k - \varepsilon$ turbulence model, the turbulent length scale ℓ for the definition of the turbulent eddy viscosity is a function of the rate of dissipation of turbulent kinetic energy (see Equation (4.41)). Another definition for this turbulent length scale stems from the turbulent frequency, defined as:

$$\omega_t = \frac{\varepsilon_t}{k_t}\,, \tag{4.46}$$

leading to

$$\ell = \frac{\sqrt{k_t}}{\varepsilon_t}\,. \tag{4.47}$$

Consequently, the turbulent eddy viscosity is defined as:

$$\mu_t = \frac{\rho\, k_t}{\omega_t}\,. \tag{4.48}$$

This definition is used in the $k - \omega$ turbulence model developed by Wilcox [146–148]. Transport equations for k_t and ω_t can be formulated and, as for the transport equations in the standard $k - \varepsilon$ turbulence model, a set of adjustable constants must be defined for which standard values are listed in Table 4.6.

Due to the nature of the introduced turbulence frequency, benefits for the $k-\omega$ model are found in the treatment of near wall boundary layer flows, compared to the standard $k - \varepsilon$ turbulence model. However, accuracy issues may occur in the free stream, due to the sensitivity of the solution to the initial value of ω_t in the far wall region.

Table 4.6: Suggested values for the adjustable constants in the k and ω transport equations for the $k-\omega$ turbulence model [30]

σ_k	σ_ω	γ_1	β_1	β^*
2.0	2.0	0.553	0.075	0.09

RANS $k-\omega$ shear stress transport model

While the standard $k-\varepsilon$ model achieves accurate modelling of fully turbulent far wall regions, and accurate modelling of near wall boundary layers is achieved by the Wilcox $k-\omega$ model, the $k-\omega$ shear stress transport (SST) model, proposed by Menter [149–152], blends the standard $k-\varepsilon$ and $k-\omega$ models to achieve accurate modelling for both far wall and near wall regions. Introducing a blending function F_C ($F_C = 0$ at the wall; $F_C = 1$ in the far field), a smooth transition half way between the wall and the edge of the boundary layer is achieved. The model constants associated with the $k-\omega$ SST model are listed in Table 4.7.

Table 4.7: Suggested values for the adjustable constants in the k and ω transport equations for the $k-\omega$ SST model based upon [30]

σ_k	$\sigma_{\omega,1}$	$\sigma_{\omega,2}$	γ_2	β_2	β^*
1.0	2.0	1.17	0.44	0.083	0.09

Wall treatment

When employing turbulence models, care must be taken of the boundary conditions in the vicinity of solid walls. Due to the steep gradient of the velocity when moving towards the wall (see Figure 4.17 (a)), the flow characteristics in the near wall region are significantly different from the characteristics in the far wall region. The different characteristics can easily be understood when defining a Reynolds number, $Re(y)$, as a function of the distance to the wall y:

$$Re(y) = \frac{\bar{u}\, y}{\nu}\,. \tag{4.49}$$

Since the velocity $\bar{u}$ decreases, resulting in $\bar{u} = 0$ at the wall, $Re(y)$ also decreases. Recalling the definition of the Reynolds number as the ratio between inertial and viscous forces, four regions of the flow in the vicinity of the wall can be defined:

- Outer layer: Inertial forces largely overweight viscous forces ($Re(y) >> 1$)
- Log–law layer: Viscous force are smaller than internal forces, but are non–negligible

- Buffer layer: Viscous and inertial forces are approximately equal
- Viscous sublayer: Viscous forces outweigh inertial forces ($Re(y) \leq 1$)

Figure 4.17 (b) shows a schematic of the staggering of the different layers. While the flow in the outer layer does not require specific treatment, the log–law, buffer, and viscous (sub)layers deserve special attention. The location of the different layers can be defined by the dimensionless distance to the wall, y^+, following:

$$y^+ = \frac{y\, u_\tau \rho}{\mu}\,, \tag{4.50}$$

where u_τ denotes the friction velocity, following $u_\tau = \sqrt{\tau_w/\rho}$, with the wall shear stress, τ_w.

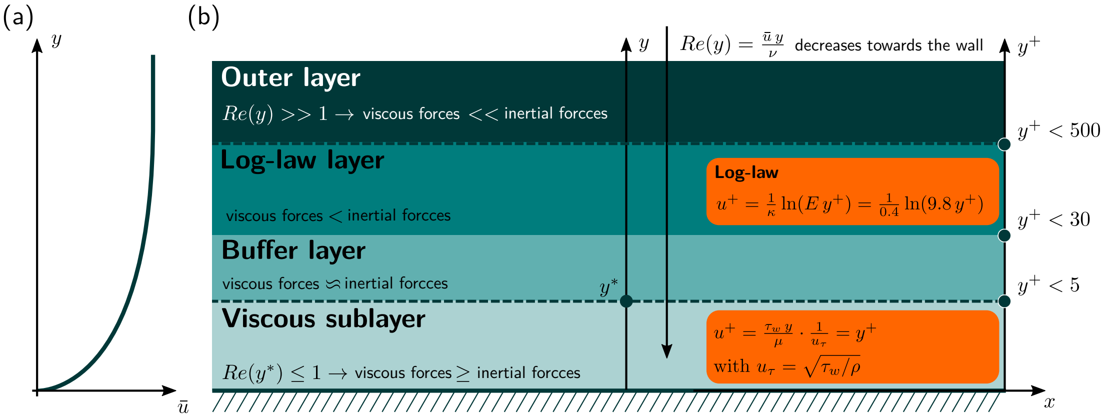

Figure 4.17: Schematic illustration of the velocity profile in the vicinity of a solid wall (a) and the staggering of the four relevant layers (b): Outer layer, log–law layer, buffer layer, and viscous sublayer. (Schematic not at scale).

In the viscous sublayer ($y^+ < 5$), viscous forces are dominant, implying that the velocity $\bar{u}$ is independent of the free stream properties and can be expressed as a function of the wall shear stress τ_w, the distance from the wall y, and the viscosity μ:

$$\bar{u} = \frac{\tau_w\, y}{\mu}\,. \tag{4.51}$$

Normalisation (based on dimensional considerations) with the friction velocity delivers a second well known, non–dimensional, quantity:

$$u^+ = \frac{\bar{u}}{u_\tau}\,. \tag{4.52}$$

Consequently, it can be shown that y^+ and u^+ are linearly dependent, i.e. $u^+ = y^+$. In the log–law layer ($30 < y^+ < 300$), viscous and inertial forces affect the flow and, following [153], the non–dimensional velocity can be expressed as:

$$u^+ = \frac{1}{\kappa} \ln\left(E\, y^+\right)\,, \tag{4.53}$$

where κ is the von Karman constant ($\kappa = 0.41$) and E is a model constant ($E = 9.8$). In the buffer layer ($5 < y^+ < 30$), a transition from the linear to the logarithmic relation between y^+ and u^+ takes place; however, no explicit formulations are available. In the context of turbulence modelling, the analytical expressions of the non–dimensional velocity in the viscous sub– and log–law layer are important, enabling the reduction of the required spatial discretisation at solid walls. For high Reynolds numbers, the viscous sublayer is very thin and can be neglected. Thereby, discretisation of this layer can also be avoided. As a result, and ensuring the location of the first cell at the wall to fall within $30 < y^+ < 300$, validity of the log–law (see Equation 4.53) can be assumed and wall functions can be defined for the turbulent quantities. At low Reynolds numbers, the viscous sublayer cannot be neglected and the log–law cannot be applied 'down to the wall'. Thus, wall functions for the turbulent quantities also loose validity, ultimately requiring discretisation of the viscous sublayer. For that, $y^+ \approx 1$ at the wall has to be ensured, requiring relatively small grid sizes.

Oscillating flows

Recalling that y^+ is a function of u^+ and, thereby, the flow velocity, it can readily be noticed that the validity of wall functions within oscillating flows, such as the flow around WECs, is challenged. The requirement on y^+ to fall within the range $30 < y^+ < 300$ is, with a single mesh, unlikely be fulfilled over a complete oscillation cycle, thereby adding uncertainty to the modelling of turbulence for oscillating body. The case of an oscillating flows highlights the discrepancy between the design case for a large number of turbulence models (aerodynamics) and the general applicability in other engineering fields.

4.4 Concluding remarks

This chapter provides the necessary background information on the numerical schemes and methods for the solution of the governing equations of fluid flows. Furthermore, this chapter includes a discussion on the specific requirements of a CFD–based NWT for WEC application and shows how the requirements are addressed numerically. The discussion highlights the complexity of a CFD–based NWT for WEC applications and indicates the wide range of aspects, ranging from the treatment of multi–phase flows and the representation and motion of WEC structure to the modelling of turbulence effects, which have to be covered accurately and efficiently when considering WEC modelling in a CFD-based NWT.

The following Chapter 5 will provide a comprehensive literature review with a focus on the requirements of CFD–based NWTs for WEC application, as identified in this chapter.

5

Review of CFD–based NWTs for wave energy applications

Contents

While Chapters 2–4 present the background information to provide an understanding of the numerical modelling approaches used throughout this thesis, this chapter delivers a comprehensive literature review of CFD–based NWTs for WEC applications and provides the interface between the background material of Part I and the main original work of Part II.

Since the fist review of numerical WSI modelling approaches for WEC applications was published by Evans [154] in the 1980's, several reviews of the numerical modelling approaches for WECs have been published over the last few years:

- Li and Yu [155] specifically focus on the modelling methods for point absorbers, reviewing analytical and boundary integral equation methods, viscous drag calculation for potential flow solutions and, finally, CFD–based methods.
- Folley *et al.* [156] focus on the hydrodynamic interactions of WECs in arrays, presenting the underlying principles, strengths, and weaknesses for a range of different models, covering potential flow, Boussinesq and mild-slope, spectral wave, and CFD models. Folley has also edited a book [37] on numerical modelling of WECs, covering the complete range of available numerical WEC modelling approaches.
- Coe and Neary [157] review modelling methods for WECs in extreme seas, highlighting the unique challenges of modelling survivability, covering semi-empirical, potential flow, CFD, and physical modelling.
- Focusing on oscillating water column (OWC) devices, Bouhrim and El Marjani [158] present modelling approaches for the flow behaviour inside an OWC chamber. The study ranges from 1D to fully 3D viscous unsteady CFD models.
- Day *et al.* [159] present a state–of–the–art review of hydrodynamic modelling approaches for various marine renewable energy technologies. The authors cover wave energy, tidal current, as well as offshore wind energy systems, and discuss the physical modelling of PTO systems, the numerical modelling of marine renewable energy technologies, and wind load modelling for wind turbines.
- Wolgamot and Fitzgerald [160] review the use of non–linear hydrodynamic models to analyse WEC behaviour and performance, covering partially and fully non–linear potential flow, CFD, and SPH models.
- Saincher and Banerjee [161] review the influence of wave breaking on the hydrodynamics of WECs, based on the three energy transfer processes due to turbulence, vortices, and the free surface interface. No specific focus is put on a particular modelling approach; however, the review suggests that only experimental and CFD–based models are able to capture the relevant hydrodynamics.

- Penable *et al.* [18] review the influence of non–linear dynamics on the entire conversion chain of a WEC (incoming wave trains, WSI, PTO systems, and mooring lines), with a focus on the different modelling approaches for non–linear WSI.
- Dias *et al.* [162] focus their review specifically on the *Oyster* oscillating wave surge converter (OWSC). Collating their own studies on various hydrodynamic aspects, such as viscous and non–linear effects, slamming loads, array interaction, etc., the authors conclude that CFD methods are valuable to investigate WSI on a "local level", by means of flow separation, turbulence, or wave impacts.
- Zullah and Lee [163] aim to review the available modelling approaches for the WSI of WECs with a focus on CFD–based methods. However, the review stays relatively broad, by including various examples of lower fidelity models.
- Most recently, Davidson and Costello [164] provide a comprehensive review of modelling approaches of intermediate fidelity, covering the area between linear potential flow theory and CFD–based NWTs.

From the published reviews of the available hydrodynamic modelling approaches for WEC applications, it is clear that no attempt has yet been undertaken to comprehensively review only CFD–based NWT approaches for WECs. To that end, this chapter presents a thorough review of high-fidelity numerical modelling of WECs using CFD–based NWTs. There are two main objectives of the present literature review:

(i) Collating the publications related to CFD–based NWTs for WEC applications, and
(ii) Identifying the current shortcomings of CFD–based NWTs for WEC applications.

The continual improvement and availability of high performance computing has led to the steady increase of WEC experiments in CFD–based NWTs in recent years, as shown in Figure 5.1 and Table 5.1. The data in Figure 5.1 is based on the literature collated within the present review. Table 5.1 acts to chronologically order the reference numbers. Note that, for completeness, Figure 5.1 and Table 5.1 include also the publications listed in Section 1.2, which are omitted throughout the remainder of this review. Only [JPI, JPK] are included in the later sections of this review, due to their specific importance for the completeness of this review.

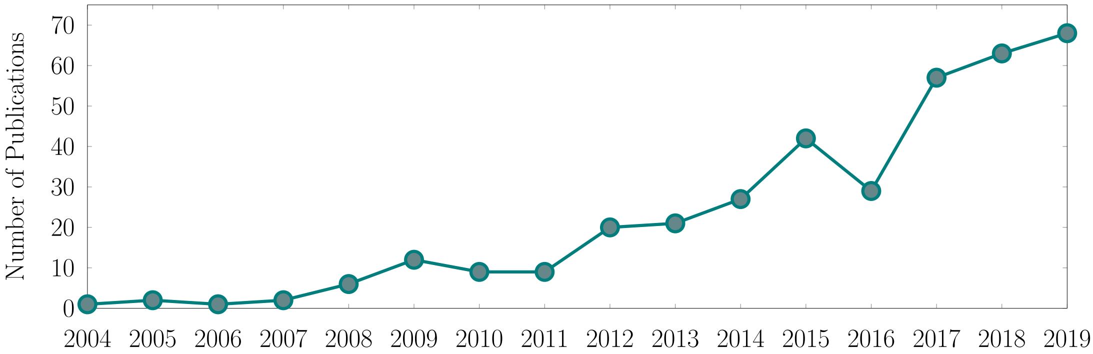

Figure 5.1: Number of publications using CFD–based NWT analysis of WECs

Table 5.1: Publications of CFD–based NWTs for WEC applications

Year	Publications	Year	Publications
2004	[165]	2011	[196–205]
2005	[166, 167]	2012	[113, 155, 206–223]
2006	[168]	2013	[20, 224–244]
2007	[169, 170]	2014	[111, 114, 123, 245–269]
2008	[171–176]	2015	[129, 115, 270–310]
2009	[177–186]	2016	[9, 311–345]
2010	[187–195]	2017	[CPA] [346–402]
2018	[CPB, CPC, JPA–JPC] [403–462]	2019	[CPD–CPG, JPD–JPF, SMC, SME] [62][74][84][463–519]
2020	[JPH, JPI, JPK] [520–531]		

The review begins by collating the published literature pertaining to the use of CFD for WEC applications, categorised by the different WEC device types. The various WEC operating principles and subsystems are discussed to highlight the wide variety of systems included in the CFD–based NWT simulations. The types of analysis applications the CFD–based NWTs are employed in are also explored:

- Section 5.1 presents the different device types and discusses the operating principles.
- Section 5.2 discusses the different analysis applications and WEC subsystems addressed by CFD–based NWTs.

The technical CFD aspects of the literature are then reviewed, delving into the general requirements of a CFD–based NWT for WEC applications, as discussed in Chapter 4:

- Section 5.3 focusses on the domain discretisation.
- Section 5.4 concerns wave generation and absorption methods.
- Section 5.5 investigates body representation and dynamic mesh motion methods.
- Section 5.6 discusses the modelling of different flow regimes.

The end of the review contains three disparate sections:

- Section 5.7 outlines validation strategies for the evaluation of the NWT accuracy.
- Section 5.8 details the available software packages.
- Finally, concluding remarks are presented in Section 5.9.

5.1 CFD analysis of WECs

This section collates the literature containing CFD analysis of WECs, categorised corresponding to the device type, the considered DoFs, and the number of devices considered (single device or an array), as detailed in Sections 5.1.1 – 5.1.3, respectively, and tabulated in Tables 5.2 – 5.5.

5.1.1 Device types

There are well over 1000 patented WEC devices [532] with inventors and researchers conceiving a myriad of techniques to convert the raw energy from the oscillating ocean surface into useful electricity. WECs can be broadly classified into several categories based on their operating principle. The European marine energy centre (EMEC) [533] defines the following groups of device types: point absorbers, terminators[1], attenuators, OWSC, OWCs, and pressure differential WECs. Schematics of the different device types are depicted in Figure 5.2.

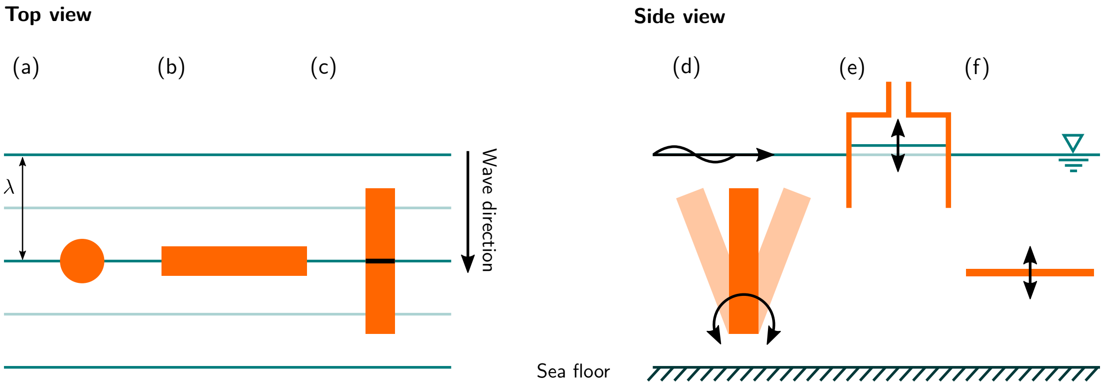

Figure 5.2: Schematic of different WEC types: (a) Point absorber; (b) Terminator; (c) Attenuator; (d) OWSC; (e) OWC; (f) Pressure differential.

A point absorber (Figure 5.2 (a)) is characterised by its small size relative to the wavelength, absorbing power from the wavefield analogously to antennas in electromagnetic wave fields. Terminators (Figure 5.2 (b)) are aligned perpendicular to the incident wave direction, being geometrically wide to intercept and stop as

---

[1] Note that overtopping devices are categorised as terminators in this thesis.

much of the incoming wave as possible. Attenuators (Figure 5.2 (c)) are aligned parallel to the incoming wave direction and utilise the phase difference along the length of the wave to convert energy through relative motion between WEC subsections. OWSCs (Figure 5.2 (d)) oscillating around a hinge point, extracting power from the surging wave motion. OWCs (Figure 5.2 (e)) operate by converting wave energy into pneumatic energy, whereby the oscillating water level inside a chamber force entrapped air through a turbine. Pressure differential devices (Figure 5.2 (f)) are located below the ocean surface and utilise the change in pressure, caused by passing waves, for energy conversion. The reviewed literature considering point absorber type devices is listed in Tables 5.2 and 5.3, while Table 5.4 contains the literature of OWSCs, terminators, attenuators, and pressure differential devices. Table 5.5 contains the literature considering OWCs.

An additional classification of the devices and, thus, the reviewed literature, regards whether generic or specific WECs are considered. While generic devices are mostly considered during fundamental academic research (e.g. [365]), specific devices are considered to support the design and commercialisation of that specific WEC (e.g. [304]). In Tables 5.2 – 5.5, generic devices are indicated with *gen*, while studies of specific devices are marked with *spec*. Furthermore, descriptions on the particular device are included in Tables 5.2 – 5.5.

5.1.2 Degrees of freedom

WEC motion within a CFD–based NWT presents a challenge, not only requiring the solution for the WEC dynamics, but also involving an adaptation of the CFD domain/mesh to the WEC motion (see Section 4.3.4). Hence, classifying the literature based on the considered WEC motion constraints, namely single DoF or multi DoF, is helpful to evaluate the required model complexity. On this note, OWCs deserve special attention, being often represented by a fixed structure, characterised with no structural DoF (e.g. [353–356]). An additional category of *fixed structures* can be included embracing e.g. horizontal or vertical cylinders, which are mostly considered for extreme load analysis. Relevant studies for the wave energy field are listed in Table 5.5. Tables 5.2 – 5.5 include the considered DoF(s) within the reviewed literature, where *Su*, *Sw*, *He*, *Ro*, *Pi* indicate surge, sway, heave, roll, and pitch.

Only a relatively small number of studies (e.g. [308, 230, 455, 521]) can be found considering all six DoFs, which can be reasoned by the aforementioned challenges regarding adaptation of the CFD domain/mesh. Also posing a challenge for the stable accommodation of device motion are multi–body systems. Again, only a relatively small number of studies (e.g. [204, 243, 292, 293, 311, 317, 363, 422, 419, 481, 502, 503, 523]) can be found in the literature. Studies considering six DoF device motion or multi–body systems are usually used in conjunction with advanced dynamic mesh motion methods (see Section 5.5)

5.1.3 Arrays

To contribute significant amounts of energy to the electrical grid, WECs can be deployed in large arrays or farms. Thus, understanding the hydrodynamic interaction between devices within the array is an important problem, which can be investigated using a CFD–based NWT. The reviewed literature will therefore also be categorised in a binary way, differentiating between studies considering individual devices or WEC arrays. Due to the challenges arising from the implementation of multiple bodies and their motion, as well as the increased computational burden when modelling WEC arrays, it can be anticipated that only a few studies tackle this problem using CFD–based NWTs [171, 351, 352, 348, 395, 483]. In Tables 5.2 – 5.5, if arrays of devices are considered, the number of devices is indicated as well. Worth highlighting, amongst the array simulations in CFD–based NWTs, is the study by Devolder *et al.* [453], simulating up to nine devices in a single CFD domain.

5.2 Analysis applications and WEC subsystems

Since CFD simulation is several orders of magnitude more computationally demanding compared with low– or mid–fidelity hydrodynamic models [229], the use of CFD–based NWTs for WEC applications must be well justified by the specific application to which they are employed. Section 5.2.1 details the different WEC analysis applications found within the CFD–based NWT literature. Furthermore, within the different application areas, the CFD–based NWTs may differ in terms of the WEC subsystems included in the simulations, i.e. the PTO, mooring, and control systems (see Figure 1.5). The interaction between subsystem models increases the model complexity and potentially the computational burden, while fidelity imbalances between the subsystem models may undermine the overall model fidelity, or give a computationally inefficient solution. A more detailed discussion of the different subsystems is given in Section 5.2.2.

Table 5.2: CFD–based NWT experiments considering generic point absorber devices. Su, Sw, He, Ro, Pi for surge, sway, heave, roll, pitch, respectively. The array superscript indicates the number of considered devices

Point Absorber	Type	DoF	Array	Description
[455]	gen	6–DoF	–	Cylindrical buoy
[192, 232, 261, 334, 361, 515]	gen	Su, He, Pi	–	Cylindrical buoy
[113, 129, 196, 277, 320, 330, 371, 376, 418, 508, 531]	gen	He	–	Cylindrical buoy
[171]	gen	He	$\bullet^{2}$	Cylindrical buoy
[380]	gen	He, Pi	–	Cylindrical spar
[367, 406, 464, 526]	gen	He	–	Cylindrical buoy with varying bottom shape
[62, 74, 299, 382, 446]	gen	Su, He, Pi	–	Spherical-bottomed cylinder
[351, 352, 453]	gen	He	$\bullet^{2,5,9}$	Spherical-bottomed cylinder
[442, 452]	gen	He	–	Spherical-bottomed cylinder
[454]	gen	6–DoF	–	Spherical-bottomed and truncated cylinder
[521]	gen	6–DoF	–	Spherical buoy
[254, 364]	gen	Su, He	–	Spherical buoy
[483]	gen	Su, He	$\bullet^{2}$	Spherical buoy
[84, 252, 298, 315, 319, 327–329, 336, 350, 364, 365, 404, 417]	gen	He	–	Spherical buoy
[372, 439, 514, 524]	gen	Su, He, Pi	–	submerged spherical buoy
[522, 523, 495]	gen	He	–	Box shaped buoy with varying bottom shape
[445]	gen	Sw, He, Ro, Pi	–	Box shaped buoy
[441, 493, 500, 521]	gen	Su, He, Pi	–	Box shaped buoy
[289, 283]	gen	He, Pi	–	Box shaped buoy
[437]	gen	Su, He	–	Box shaped buoy
[364]	gen	Ro	–	Box shaped buoy
[206, 273]	gen	Su	–	Box shaped buoy
[84, 129, 228, 281, 361, 443, 447, 484, 494]	gen	He	–	Box shaped buoy
[123, 186, 202, 484]	gen	He	–	Cone shaped buoy
[292]	gen	He	–	Multi–body buoy
[344]	gen	He, Pi	–	Elliptical buoy
[465–475]	gen	Su, He, Pi	–	Spherical-bottomed cylinder and truncated cylinder with moon–pool (CCP–WSI Blind Test Series 2&3)

5.2.1 Analysis applications

The following WEC analysis applications can be identified from the CFD–based NWT literature:

- Evaluation of viscous (drag) effects
- Performance analysis
- Device optimisation
- Code assessment
- (Extreme) Load estimation
- Device scaling
- System identification
- Control evaluation
- Conceptual design

Details and relevant example studies for the individual application cases are given in the following subsections. Table 5.6 gives a complete list of studies corresponding to the analysis application.

Table 5.3: CFD–based NWT experiments considering specific point absorber devices. Su, Sw, He, Ro, Pi for surge, sway, heave, roll, pitch, respectively.

Point Absorber	Type	DoF	Array	Description
[451]	spec	He, Pi	–	Coaxial symmetric articulated absorber
[507]	spec	He	–	Open caisson
[460, 504]	spec	He, Su, Pi	–	RM3 reference model
[519]	spec	He	–	RM3 reference model
[459]	spec	–	–	RM3 reference model
[505]	spec	He, Su, Pi	–	CENTIPOD
[314]	spec	–, He	–	SINN Power
[295]	spec	–	–	Stationary Blow-Jet
[175]	spec	–	–	Stationary Spiral-Reef
[318]	spec	Pi	–	Point–pivoted absorber
[180]	spec	Pi	–	SEAREV
[177–179]	spec	Pi	–	WRASPA
[202, 193]	spec	He, Su	–	Manchester Bobber
[123, 182, 188, 198, 202]	spec	He	–	Manchester Bobber
[293]	spec	He	–	WaveBob
[300, 501, 530]	spec	Su, He, Pi	–	CETO
[362, 424, 445]	spec	Su, He, Pi	–	CorPower
[272]	spec	Su, He, Pi	–	ISWEC
[349, 391–393]	spec	Su, He, Pi	–	Seabased
[308]	spec	6–DoF	–	Stewart-Gough Platform
[203]	spec	Su, Pi	–	Pelican
[245]	spec	Su, He	–	Bristol Cylinder
[205, 481]	spec	Su, He, Pi	–	OPT PowerBuoy
[204, 155, 243, 481]	spec	He	–	OPT PowerBuoy
[115, 299, 383]	spec	Pi	–	Wavestar
[502, 503]	spec	Su, He, Pi	–	TRITON
[373]	spec	He, Pi	–	TRITON

Viscous effects

A significant advantage of CFD–based NWTs is the inherent consideration of viscosity in the governing equations which separates CFD–based NWTs from low–/mid–fidelity models (see Chapter 2). Hence, one of the main applications of CFD–based NWTs is the analysis of viscous effects.

In [196, 206, 249, 273, 296, 300, 304, 365, 373, 456], CFD–based NWT simulations are used to identify the viscous drag coefficient in the Morrison equation (5.1) [15] or similar viscous correction terms.

$$F_{d,i} = \frac{1}{2}\rho C_{d,i}\mathbf{u}_i|\mathbf{u}_i|\,, \tag{5.1}$$

where the subscript $i = [1, 2, 3]$ indicates the x–, y–, or z–coordinate, respectively, $F_{d,i}$ denotes the drag force on the body, and C_d viscous drag coefficient.

The study in [365] discusses the challenges of a correct identification methodology for the viscous drag coefficient. The authors find relatively large variations in the values of the drag coefficient, stemming from five different drag identification tests; however, the authors conclude that even non–optimal drag coefficients (compared with no drag correction) can improve the accuracy of low–/mid–fidelity mathematical models. This

Table 5.4: CFD–based NWT experiments considering OWSCs, terminator, attenuator, and pressure differential devices. g or s for generic or specific, respectively; Su, Sw, He, Ro, Pi for surge, sway, heave, roll, pitch, respectively; The array superscript indicates the number of considered devices

OWSC	Type	DoF	Array	Description
[165, 167, 270, 275, 364, 377, 434, 435, 400, 488]	gen	P	–	Flap-type OWSC
[520]	gen	Pi	–	Top–hinged flap–type OWSC
[400]	gen	Pi	–	Cylinder-type OWSC
[333]	spec	Pi	–	WaveRoller
[20, 218, 219, 236, 241, 242, 249, 255, 268, 301, 309, 310, 325, 342, 343, 337, 387, 432, 482]	spec	Pi	–	Oyster OWSC
[311]	spec	Pi	–	modular Oyster OWSC
[348]	spec	Pi	$\bullet^2$	CCell
[402, 436]	spec	Pi	–	CCell
Terminator	Type	DOF	Array	Description
[173, 210, 264, 267, 403, 405, 440]	gen	–	–	Overtopper
[429]	gen	Pi	–	Rectangular barge
[395]	gen	He	$\bullet^2$	Vertical cylinder
[430]	gen	Pi	–	Vertical cylinder
[366]	spec	–	–	Rotating cylinder
[224, 246, 271]	spec	Ro	–	Single-Bucket Wave Turbine
[282]	spec	Pi	–	Seaspoon
[274, 307, 368]	spec	–	–	Seawave Slot-cone Generator
[374, 375, 448, 345, 489–491]	spec	–	–	OBREC
[429, 485, 496–499]	spec	Pi	–	Salter's Duck
[176, 185, 253]	spec	–	–	Wave Dragon
[346]	spec	He, Pi	–	WaveCat
[227]	spec	–	–	CycWEC rotating Hydrofoil
Attenuator	Type	DOF	Array	Description
[230]	gen	6–DoF	–	Rectangular Barge
[384]	gen	He, Pi	–	Rectangular Barge
[251, 254, 270, 316]	gen	Ro	–	Rectangular Barge
[431]	gen	He, Pi	–	Horizontal cylinder
[296]	gen	Su, He	–	Multi–body
[317]	gen	He, Pi	–	Twin–raft
[363]	gen	Pi	–	Twin–raft
[304, 456]	spec	Su, He	–	M4
[221]	spec	He	–	Vigor
[419]	spec	Su, He, Pi	–	Pelamis
Pressure Differential	Type	DOF	Array	Description
[264–266, 286, 480, 486, 492]	gen	–	–	Fixed horizontal plate WEC
[428]	gen	Su, He, Pi	–	submerged circular plate
[257, 331]	spec	–	–	Bombora

is illustrated by van Rij *et al.* [475], who tune C_d to achieve an agreement between mid–fidelity modelling results and CFD–based reference data.

Schubert *et al.* [439, 530] compare linear and 'pseudo' non–linear hydrodynamic models of a submerged buoy with results from a CFD–based NWT. In the study, the pseudo non–linear model uses gain scheduling for the drag coefficient and CFD results (based on [300]) serve as the reference during the comparative study.

Stansby *et al.* [304] and Gu *et al.* [456] investigate viscous drag coefficients, aiming at drag minimisation of the *M4* device. Flat and round bottomed float shapes were considered, highlighting a significant power output increase for the latter. Similarly,

Table 5.5: CFD–based NWT experiments considering OWC devices and relevant fixed structures. Su, Sw, He, Ro, Pi for surge, sway, heave, roll, pitch, respectively; The array superscript indicates the number of considered devices

OWC	Type	DOF	Array	Description
[114, 168, 172, 174, 183, 184, 187, 190, 194, 197, 201, 211, 213, 214, 223, 226, 239, 258, 269, 280, 290, 291, 294, 312, 322, 347, 394, 396–399, 401, 425, 449, 450, 457, 458, 506, 510, 529]	gen	–	–	fixed at the far field boundary
[199, 209, 220, 229, 237, 248, 256, 262, 264, 285, 288, 302, 321, 322, 353–356, 359, 369, 388–390, 420, 421, 423, 426, 458, 476, 477, 513, 516, 525, 527]	gen	–	–	fixed in the domain centre
[421, 511]	gen	–	–	fixed multi-chamber
[357, 358, 360]	gen	Su, He, Pi	–	Floating-moored OWC
[259, 378, 433, 531]	gen	He	–	Heaving OWC
[323, 386, 449, 450, 512, 528]	spec	–	–	U–OWC
[305, 339, 385]	spec	–	–	REWEC
[191, 195, 207, 217, 244, 260, 381, 427]	spec	–	–	Direct Drive Savonius Turbine (DTT)
[297]	spec	–	–	PICO
[438, 509]	spec	–	–	KRISO OWC
[231]	spec	Su, He, Pi	–	OWEL
[518]	spec	Su, He, Pi	–	Spar buoy OWC

Fixed structures	Type	DOF	Array	Description
[407–416, 463]	gen	–	–	FSPO[†]–like structure (CCP–WSI Blind Test Series 1)
[169]	gen	–	–	submerged horizontal cylinder
[315, 404]	gen	–	–	submerged sphere
[111, 123, 186, 189, 198, 202, 212, 222, 284, 330, 461]	gen	–	–	semi–submerged horizontal cylinder
[444]	gen	–	–	semi–submerged box
[284]	gen	–	–	semi–submerged cone
[235, 287, 299, 382]	gen	–	–	truncated vertical cylinder
[335, 341]	gen	–	–	submerged rigid plate
[487]	gen	–	–	porous sheet
[517]	spec	–	–	CALM buoy

[†] FSPO: Floating storage production and offloading unit

Chen *et al.* [406] investigate viscous effects for a cylindrical point absorber with varying bottom shapes based on free decay tests, finding that conical shapes, generally, reduce viscous effects. In [418], the authors highlight the importance of viscosity during power production assessment by performing simulations using linear and non–linear state space models of a flat–bottomed cylindrical buoy.

In a study on a generic moored point absorber, Palm *et al.* [232] investigate the effect of viscosity on the mooring loads by employing both RANS and Euler simulations. The differences between viscous and inviscid simulations are found to be dependent on the treated DoF. The authors of [232] extend their study in [455], analysing viscous effects in combination with scale effects (see below). The authors conclude that Euler and RANS simulation should be employed to distinguish viscous drag and induced drag.

Studying wave–induced roll motion of a rectangular barge, Chen *et al.* [251, 270, 316] find significant differences between laminar CFD–based NWT simulation and potential flow theory. The same authors extend their study to the hydrodynamic performance of an OWSC, comparing RANS simulation and results from potential flow theory to analyse the effect of viscosity [270, 275]. In all studies, the authors find that results based on potential flow theory are overestimated, compared with the CFD–based equivalent, due to the absence of viscous drag from potential flow.

To determine the significance of viscous losses during operation of an OWSC, Wei *et al.* [241, 309] investigate the wave field around the absorber structure and study the effect of viscosity when including PTO damping. From (qualitative) wave field analysis, it is concluded that vortex shedding is a short lived phenomenon of half a wave cycle. Furthermore, the authors provide a thorough discussion of the importance of including/excluding viscous effects based on the two dimensionless measures: Keulegan–Carpenter number (see Equation (5.2)) and a diffraction parameter (see Equation (5.3)).

$$KC = {}^{2\pi A}/_{L} \tag{5.2}$$

$$Kl = {}^{2\pi L}/_{\lambda} \tag{5.3}$$

Based on the discussion in [309], Chen *et al.* [349] perform a similar comparative study on a multi–DoF point absorber in viscous and inviscid fluids. Again, using KC and Kl, regular and irregular sea states can be identified for which the significance of viscous effects can be ascertained. However, a comparison of hydrodynamic forces and other data, such as WEC displacement, reveals overall negligible influence of viscous effects.

In a feasibility study on the application of CFD–based NWTs during WEC design iterations, Eskilsson *et al.* [253] compare viscous and inviscid simulations of the full scale overtopping *Wave Dragon* device, where the main driver for the consideration of the inviscid simulations is the reduced cell count due to the unnecessary resolution of the boundary layer. For regular waves, the differences in the overtopping discharges are small between the obtained results; however, the authors highlight potential inaccuracies of the inviscid simulations due to underestimated viscous dissipation.

Performance analysis

CFD–based NWT experiments can be utilised to assess WEC performance, calculating important metrics such as absorbed power and device efficiency. Analysis of performance requires simulation over relatively long time frames (of the order of hundreds of seconds) and the inclusion of subsystem models (PTO, control, and/or the mooring system). From the reviewed literature, it can be observed that the modelling fidelity of WEC subsystems varies significantly and that no study includes a complete, non–linear, wave-to-wire model.

The performance of stationary OWC devices has been assessed in many studies (see Table 5.5), owing to the relative simplicity of modelling this type of WEC in a CFD–based NWT. The PTO system of an OWC is, generally, represented in the NWT as a simple pressure outlet (i.e. orifice) and analysis of the OWC geometry, or PTO characteristics, is performed. An example of a comprehensive performance analysis can be found in the series of studies by Elhanafi *et al.* [321, 353–356, 359, 420, 421, 511], where, after validating the OWC model, effects of front lip submergence, PTO orifice shape and size, the number of OWC chambers, as well as model scaling and air compressibility, on the OWC performance are investigated.

A slightly more sophisticated OWC PTO representation is delivered by modelling porous media inside the OWC duct (see for example [258, 280, 290, 291, 312]). Monino *et al.* [398] develop an actuator disc model for the OWC PTO system, tuned against experimental turbine data. The model is subsequently applied in [399] for analysis of the influence of realistic bottom topography on the device performance.

Investigating the power output of a cylindrical point absorber, Agamloh *et al.* [171], in a pioneering study, implement a linear damper PTO system. The study considers both a single device and an array-like arrangement of two devices, revealing that a phase shift between the in–line bodies leads to differing power output of the two WECs.

Investigating the *Bristol cylinder*, Anbarsooz *et al.* [245] calculate the device efficiency for a linear spring–damper PTO system. The authors find that the efficiency decreases for increased wave heights and the maximum efficiency shifts towards higher frequencies. Also, optimal spring and damping coefficients are evaluated, showing discrepancies compared with linear potential flow theory.

Ghasemi *et al.* [364] simulate a point absorber including a mooring and PTO system, both represented through a linear spring–damper system. Power absorption and efficiency are determined for varying PTO damping values. Yu and Li [204, 243], as well as Xu *et al.* [481], consider a simplified multi–body model of the *OPT PowerBuoy*, including a spring–damper PTO system, and evaluate the absorbed power for varying PTO coefficients. Chen *et al.* [349] analyse the *Seabased* point absorber where the inclusion of the mooring characteristics and stroke-length control of the linear damper PTO system allows a more realistic power assessment. More recently, Meng *et al.* [524], analyse the performance of a point absorber with asymmetric mass distribution. The study includes results from linear potential flow theory and the authors find that surface piercing of the structure has a significant effect on performance prediction by the linear model. Compared to a generic point absorber, the authors also highlight the significant increase in power due to asymmetric mass distribution.

CFD–based NWT experiments have also been applied for the performance assessment of more unconventional WEC devices; for example, Caskey *et al.* [227] analyse the *CycWEC* by the means of pressure and force coefficients for its hydrofoils.

Generally, it can be seen that wave–to–wire models, including CFD–based NWT models for the hydrodynamic part and non–linear sub–system models, have not yet reached a level of sophistication at which comprehensive performance analysis can be performed. This can mainly be reasoned by the time consuming verification and validation processes, as well as the lack of high–fidelity subsystem models (e.g. non–linear PTO models).

Device optimisation

For WEC optimisation studies, a large number of simulations, with varying parameters (device shape and dimensions, PTO setting, wave conditions, etc.), are necessary. Thus, fast-computing low–/mid–fidelity numerical models are preferable. However, if hydrodynamic non–linearities are prevalent in the systems under investigation, non–linear models must be employed.

CFD–based NWTs have been utilised for the optimisation of OWCs (e.g. [209, 226, 285, 347]). To reduce the number of required simulations, Bouali and Larbi [226, 347] propose sequential optimisation. Optimising PTO orifice and OWC chamber size, front wall thickness and immersion depth, a total of 168 simulations are performed, showing, for given wave conditions, that optimal OWC characteristics can be determined. However, the studies only consider a fixed OWC structure in 2D, so it is yet to be determined if the method can deliver meaningful results, at acceptable computational cost, for more complex and dynamic structures in 3D.

Schmitt *et al.* [236] perform shape optimisation on the *Oyster* OWSC device, considering five discrete flap geometries. The authors note that, although CFD–based NWT optimisation studies can only be used to limited extents, such studies can guide the design of subsequent physical wave tank experiments. The same authors also perform an optimisation study on the PTO damping coefficient [337], revealing that optimal damping values do not scale linearly with wave height; therefore, simulations based on potential flow theory will provide suboptimal results.

More recently, Zhang *et al.* [522, 523] perform a comprehensive performance assessment and device optimisation study on a heaving buoy WEC. The authors analyse the floater bottom shape, width, distance between fixed reference body and the floater, floater draft, and overall system conception. To quantify the performance, the authors consider numerous performance metrics and find satisfying performance for a triangle shaped buoy, with similar performance metrics compared to the structurally more complex *Berkeley Wedge*.

Code assessment

Code assessment, by means of proof of concept and validation, holds, by far, the biggest share of published CFD–based NWT applications. Therefore, only a number of relevant examples are discussed here and the complete list of publications including code assessment is given in Table 5.6. In addition, a discussion of the applied methodologies for validation is given in Section 5.7.

Aiming at modelling the *Bombora* WEC, King *et al.* [257, 331] include a fluid–structure interaction (FSI) methodology for the device's flexible membrane. Comparing coupled and uncoupled FSI models, the authors find that more efficient, uncoupled, models may already deliver meaningful results.

Iturrioz *et al.* [229] use CFD–based NWT results as an accuracy benchmark to assess a novel time-domain model for OWCs, which uses CFD data for calibration by the means of the viscous and turbulent losses, as well as discharge coefficients. It is concluded that the more efficient time-domain model should be used for initial analysis, whereas CFD–based NWTs should be applied for specific non–linear analysis problems.

Based on the *CETO* device, Tran *et al.* [501] conduct a code–to–code comparison of CFD–based results, to results based on WECSim [534], where the NWTs include models of a PTO system subject to failure. The two numerical models are also included in a code–to–experiment comparison, where overall better agreement of the device dynamics to the experimental data is found for the CFD–based model.

Ding *et al.* [514] perform a comparison between NWTs based on CFD, weak scatterer potential flow theory, body exact potential flow theory, and linear potential flow theory for a submerged heaving point absorber WEC. The authors note that a spherical device is considered to avoid non–linearties due to vortices. For small wave amplitudes, good agreement of the response amplitude operator (RAO) is found between the models. For larger waves, inducing surface piercing and wave breaking, more significant differences can be observed between the models.

Other examples of code–to–code comparison studies can be found in [123, 187, 239, 463] and [JPI, JPK]. In particular the studies by Ransely *et al.* [463] [JPI, JPK] , documenting the results of CCP–WSI Blind Test Series 1–3, should be highlighted here. Delivering comprehensive code–to–code comparison of a variety of different modelling approaches, together with dedicated experimental validation data, the studies present a unique analysis of different NWTs for WSI analysis. A more detailed discussion of the code comparison is presented in Section 5.8.

Focusing on the numerical methods in CFD–based NWTs, [61, 62, 169, 192, 254, 297, 400, 447, 526] present different, novel, numerical approaches to solve the governing equations within a CFD–based NWT. For these studies, the authentic modelling of WECs is the driver for the development and/or delivers case studies for code verification and validation.

Load estimation

As specified by numerous authors (e.g. [74, 186, 299, 330]), the use of CFD for the analysis of WECs is well justified when considering extreme loading and extreme sea states, driven by non–linear free surface deformation. Extreme conditions push low– and mid–fidelity models beyond their limits so that (extreme) load estimation of WECs can be stated as another major field of application for CFD–based NWTs. In the reviewed literature, different types of extreme load cases are considered which can be differentiated by the wave condition, the WEC device, or the modelling approach.
Extreme load estimation on fixed structures has been performed in [186, 202, 235, 111, 123, 274, 270, 330, 382, 407–416, 463]. Furthermore, mobile structures, such as flap-type WECs [218, 20, 255, 268, 310, 325, 342] or point absorbers [186, 193, 198, 123, 300, 349, 382, 383, 391–393], are considered for (extreme) load analysis. The analysed sea states cover regular waves [186, 202, 218, 20, 255, 268, 123, 310, 342, 325], irregular waves [274, 349], tsunamis [391–393], and (focused) wave groups [186, 188, 198, 202, 234, 235, 240, 111, 123, 270, 300, 407–416, 463].
The work in [234, 235, 382, 383], summarised in the dissertation of Ransley [299], provides a comprehensive study on CFD–based assessment of extreme loads on WECs, considering cases ranging from wave–only, waves incident on fixed structures, to wave–induced motion of WECs, concluding that CFD is well suited for extreme load analysis.
More recently, a series of studies [384, 460, 502–505] was published to determine design loads on WECs. Coe *et al.* [502] perform a comprehensive design load study where low–/mid–fidelity hydrodynamical models are employed to determine irregular sea states, relevant for design load analysis. Based on the results, a representative regular wave train and a focused wave are defined, which can be modelled in a CFD–based NWT, at acceptable computational cost. The authors find that focused waves predict larger loads compared to the equivalent regular wave train. Furthermore, the authors find under–predicted maximum loads from the CFD–based model, compared with the low–/mid–fidelity model, which is attributed to modelling inaccuracies of the mooring model in the CFD–based model (linear springs), compared with the mooring implementation in the low–/mid–fidelity model (OrcaFlex [535]). van Rij *et al.* [460, 504] extend the previous study by including one–way coupled FSI, by means of FE analysis of structural loads, in the analysis of the *RM3* and *CENTIPOD* devices.

Device scaling

Scaled model tests are commonly used to evaluate and optimise the performance of WECs. From small scale model tests, researchers and developers extrapolate the full scale performance of devices by applying well-known scaling laws, i.e. Froude and

Reynolds scaling [24], to scale dimensions of the structure and wave characteristics. Although the applied scaling laws are well established, errors are inherently induced due to the discrepancy between Froude and Reynolds scaling within physical wave tanks, induced by the difficulty to correctly scale physical fluid viscosity [536]. To overcome this issue during physical testing, full scale testing can be considered. However, full scale trials require extensive capital expenditure and pose difficulties regarding the control and monitoring of the test conditions. To get a better understanding of hydrodynamic scaling effects, CFD–based NWTs are powerful tools, allowing the analysis of WECs at different scales at virtually no additional cost.

In the literature, a number of studies can be found investigating the effect of different scales during model testing. Wei *et al.* [241, 309] investigate scaling effects on the *Oyster* OWSC, for the cases of undamped, damped, and fixed flaps in regular waves. Negligible differences in WEC motion are found for scales between 1/1 and 1/100th. Deviations between the scales are only observed when analysing the vorticity; however, the overall effect of these deviations is mitigated by scale independent effects.

Also considering the *Oyster* device, Schmitt and Elsässer [387] investigate the application of Froude scaling by changing the viscosity of the fluid in a CFD–based NWT, while retaining the dimensions of the structure and the tank across the scales. Comparing angular displacement and power output, small deviations of $\leq 5\%$ are found. The authors also point out the importance of the correct wall treatment and requirements on meshes, at different scales, for the particular device.

Mundon *et al.* [373] perform drag identification tests of the reaction body of a two-body point absorber WEC. In the study, four different scales, between 1/75th – 1/36th, are considered and multiple DoFs are analysed. The authors find good agreement between numerical and experimental results for high Keulegan–Carpenter (see Equation (5.2)) and low Reynolds numbers (see Equation (2.17)) and, furthermore, confirm validity of the scaling laws in such test conditions. For lower KC numbers, the agreement between CFD and experiments diminishes and the application of scaling laws fails, leading to overestimation of the drag coefficients.

Investigating OWCs, Elhanafi *et al.* [355] study the influence of model scale and air compressibility on the WEC efficiency. With the assumption of incompressible air, scaling effects are negligible; however, analysis at full scale, including compressible air, shows a considerable reduction in efficiency.

Palm *et al.* [455] assess the effects of scale, viscous forces, and drag (viscous and induced) on a moored point absorber WEC. Simulations at full scale, as well as 1/16th model scale, are performed. Using RANS, Euler, and linear radiation–diffraction (ANSYS AQWA [537]) simulation types, the authors are able to break down the effect of the non–linear mooring response, Froude-Krylov, and viscous forces, as well as the induced drag, non–linear added mass, and radiation forces on the device dynamics. Concluding, the authors suggest the use of experimental tank tests, together with RANS and Euler simulations, to gain a complete understanding of scale–dependent and scale–independent effects.

Dai *et al.* [516] investigate the hydrodynamic scaling effects on a fixed OWC–type WEC, using experimental and numerical data. Two different scales, with a scaling ratio of 1:3, are considered in the experimental and numerical tests. Good agreement between experimental and numerical data, with an error of the order of 3%, is found when excluding the PTO. Between the scales, an error of the order of 10% is observed in both the numerical and experimental studies. When including the PTO, the disparity between the physical and numerical wave tank, as well as across the scales, is exacerbated. Ultimately, the authors conclude that the CFD-based NWT is able to reproduce the scaling effects observed in the physical wave tank.

Most recently, Zabala *et al.* [518] propose a methodology that employs experimental wave tank tests to validate a CFD–based NWT which will deliver calibration data for a potential flow solver with a drag correction term. The methodology comprises small–scale experimental and CFD–based NWT tests (for validation purposes), as well as full–scale CFD–based NWT tests (for calibration purposes). The authors state that an underlying assumption of this methodology is that a validated small–scale NWT setup is also valid at full–scale. The OWC spar buoy WEC, for which experimental data is available at 1/16th and 1/120th scale, is used by the authors to prove the proposed concept. For the 1/16th scale model, the body motion and free surface elevation are compared against experimental data, but only in a qualitative manner. Declaring the 1/16th scale numerical model as validated, the authors perform a numerical heave decay test at 1/120th scale. The qualitative comparison to the experimental data shows good agreement. Ultimately, the CFD–based numerical wave tank model is used for the calibration of a potential flow model which, in turn, is used for power assessment of the full–scale spar buoy WEC.

System identification

System identification (SID) techniques [538] allow the determination of low–/mid–fidelity hydrodynamic WEC models from recorded data of the WEC force and motion variables. The SID procedure comprises four steps [319]:

(1) Choice of a parametric structure for the model
(2) Synthesis of a suitable input signal to the system
(3) Recording of the resulting output signal from the system
(4) Determination of the optimal model parameters through an identification algorithm using the input/output data

To obtain the input/output data, the dynamic behaviour of the WEC can be simulated in a CFD–based NWT. Although CFD–based NWT experiments can be computationally costly, the simulation has to be run only once to produce the data. With the parametric model, identified from the CFD data, a similar level of fidelity (under equivalent conditions) can be achieved as with the CFD simulation, but with a fraction of the computation time.

Davidson *et al.* [228, 277] identify state-space models for a heaving point absorber using signals generated from a free decay experiment in a CFD–based NWT. Similarly, Armesto *et al.* [248] employ SID to determine a state-space model of an OWC. More recently, the studies in [252, 284, 298, 329] employ SID for the determination of discrete time models for heaving point absorbers. Ringwood *et al.* [336] detail the identification of hydrodynamic models for WECs using CFD–based NWT experiments.

Control evaluation

To push WECs towards commercial viability, allowing the conversion of energy at a competitive LCoE, EMCSs for WECs are under development [539]. Since the objective of WEC device control is to drive the system towards resonance with the incoming wave field, the operational space of the WEC is enhanced and power conversion is increased (see Figure 1.4).

During the design and evaluation of EMCSs, control engineers rely on numerical modelling, typically based on linear hydrodynamic models, either stemming from linear potential flow theory, or data-driven SID techniques (see [540] for further detail on dynamical models considered in the WEC control literature). Such linear models generally assume small wave amplitudes (relative to the wave length) and body motion (relative to the body dimensions). In classical feedback control applications, the mathematical models, used for control design, are often linearised around a desired operational point, corresponding to the desired operating point of the process under analysis. The controller is subsequently synthesised to drive the system towards this set point and, thus, in the neighbourhood of this operational point, the linearising assumption is inherently obeyed.

However, the large amplitude motion, induced by reactive WEC control action, may result in viscous drag, flow separation, vortex shedding, and other non-linear hydrodynamic effects [541]. Thus, in contrast to the aforementioned classical feedback control applications, energy-maximising operating conditions and objectives do not comply with the linearising assumptions in the control design model, rendering CFD–based NWTs particularly valuable for the realistic evaluation of EMCSs for WEC applications.

Giorgi and Ringwood [327] describe the implementation of latching control for a generic, heaving, spherical WEC in a CFD–based NWT which is used to evaluate optimal latching control parameters under regular wave excitation. The authors compare CFD–based results of the converted energy to results from a linear model, where the latter is based on BEM–based potential flow solutions. The presented results highlight differences in the optimal control parameters and, in addition, an over–prediction in converted energy by the BEM–based linear model.

A more complex, adaptive, EMCS, based on a receding-horizon pseudospectral optimal control (RHPC) formulation, is implemented and evaluated in a CFD–based NWT by Davidson *et al.* [350, 417]. Online SID techniques are employed in the control algorithm to identify and update the linear control model during the simulation, creating a best fitting linear control model representative of the non-linear conditions in the CFD–based NWT. A direct comparison between the non–linear, CFD–based NWT and the linear modelling framework is only undertaken for the parameter adaption of the adaptive RHPC. The comparison shows unsurprising larger changes of the controller parameters within the CFD–based modelling framework, which the authors attribute to e.g. viscous damping, present in the CFD–based NWT.

Conceptual design

During early stage R&D of WECs, fast-computing low– to mid–fidelity numerical models are generally used. Fast computation allows for numerous iterations during the conceptual design process. However, the validity of fast-computing models may reach their limit under certain circumstances, such as consideration of complex geometries or system dynamics; therefore, high-fidelity CFD–based NWT models must be employed. For example, Akimoto *et al.* [224, 246, 271] use a CFD–based NWT to prove the device concept for a novel single bucket wave turbine.

5.2.2 WEC subsystems

In addition to the wave–absorbing structure of the WEC, a device can be further decomposed into subsystems, including the PTO, mooring, and control system (see Figure 1.5). Depending on the device and analysis application, certain subsystems must be included or may be omitted in the CFD–based NWT simulation. The

Table 5.6: Applications of CFD–based NWTs

Application	Literature
Viscous effects	[196, 203, 206, 232, 233, 241, 249, 251, 253, 261, 273, 270, 275, 281, 296, 300, 304, 309, 316–318, 328, 335, 349, 365, 367, 373, 406, 418, 428–430, 460, 464, 454–456, 481, 485]
Performance analysis	[20, 114, 168, 171–174, 183, 190, 191, 195, 201, 204, 207–211, 213, 217, 219, 223, 226, 227, 231, 236, 241, 243–247, 258–260, 264–266, 269, 270, 280, 271, 275, 281, 282, 285, 288, 290, 291, 289, 309, 312, 317, 321, 322, 363, 337, 347, 353–356, 359, 368–370, 394–397, 399, 403, 420, 421, 425–427, 430, 431, 433–436, 438, 440, 449, 451, 400, 402, 457, 477, 480–482, 493, 494, 501, 506–508, 511, 513, 516, 524, 526–528]
Device optimisation	[115, 175, 208, 209, 226, 236, 264–266, 285, 311, 285, 337, 347, 356, 484, 486, 490–492, 495, 510, 522, 523]
Code assessment	[9, 20, 84, 111, 113, 114, 123, 129, 155, 165, 167, 169, 172–174, 176–183, 185–187, 189–192, 195, 197–201, 203–205, 207, 210, 212–214, 216–222, 224, 227–229, 231–233, 237, 239, 240, 242–245, 251, 252, 254, 256–262, 265, 266, 268, 272, 270, 276, 277, 280, 281, 283, 284, 288–293, 295, 297, 298, 301–303, 305, 306, 308, 311, 312, 315, 316, 319–322, 324, 325, 327–331, 333, 334, 336, 343, 346, 348, 350, 352, 351, 353, 354, 369, 378, 372, 374–376, 380, 381, 395, 398, 401, 403, 404, 419, 423, 424, 432, 437, 439, 441–446, 450, 451, 453, 454, 457, 458, 461, 407–416, 422, 460, 463, 465–475, 477–479, 481–485, 487–490, 495, 521, 496–501, 505, 508, 509, 512–517, 519, 520, 522–525, 529–531]
Load estimation	[111, 115, 123, 155, 186, 189, 198, 205, 218, 234, 235, 240, 255, 268, 270, 274, 280, 292, 294, 295, 300, 307, 310, 311, 314, 315, 325, 330, 341, 342, 344, 349, 376, 382, 383, 391–393, 404, 405, 432, 452, 460, 407–416, 463, 476, 481, 483, 502–505]
Scaling	[241, 309, 355, 373, 387, 400, 454, 455, 516, 518]
System identification	[228, 248, 252, 277, 284, 298, 319, 329, 336, 339, 418]
Control evaluation	[277, 327, 319, 350, 417]
Conceptual design	[224, 246, 247, 271, 366]

PTO system is inherently required to assess the power output of a WEC, hence has been historically the first subsystem included into CFD–based NWTs. In contrast, only recently, mooring (e.g. [231, 232, 261, 308, 455]) and control systems (e.g. [327, 328, 349, 362, 424]) have been implemented and considered in CFD–based NWT WEC experiments. Generally, the implementation of high-fidelity models for the WEC subsystems are desired to justify the enhanced cost for CFD simulations. Otherwise, the accuracy of the high–fidelity hydrodynamic model may be undermined by the inclusion of lower fidelity WEC subsystem models.

Power take–off

A range of different levels of model fidelity are implemented for the representation of the PTO subsystem within a CFD–based NWT. The simplest implementation is found for OWC devices, for which the PTOs can be modelled as orifices or porous media in the OWC duct. For other WEC types, linear (spring) damper systems are typically employed for the PTO representation (e.g. [171, 219, 232, 20, 241, 245, 270, 275, 300, 309, 328, 333, 349, 439, 481, 522, 523]).

A higher–fidelity PTO model is implemented by Hodge *et al.* [436], who include a model of a hydraulic PTO system (accumulators, motor, and values), implemented as a restraint function, in the CFD–based NWT for the modelling of the *CCell* device. The authors perform a successful verification study on the developed PTO model by means of a code–to–code comparison with an established commercial solver (Simscape Fluids [542]). However, the authors omit important information on the PTO system component efficiencies. Comparing the generated power predicted with a linear damper, coulomb damper, and the hydraulic PTO, the authors find differences of up to 88%. Especially for studies on the power production performance of WECs, the implementation of non–linear PTO systems is of crucial importance in order to justify the use of CFD–based NWTs. Employing a costly high-fidelity CFD solution is often unjustified, if only unrealistic, linear, PTO systems are considered.

Mooring

The mooring system provides station keeping (passive mooring) or directly influences the system dynamics (active mooring) and/or the power extraction method (reactive mooring) of the WEC. A comprehensive review of mathematical mooring models for WECs is given in [543]. From the reviewed literature, it can be seen that only a limited number of authors include mooring analysis in their CFD–based NWT. A simple mooring representation can be found in [364], where the motion of a spherical point absorber is constrained to heave and surge through springs with fixed anchoring points. Similarly, Luo *et al.* [259] or Mohapatra *et al.* [433] implement massless springs in the model of a floating OWC, constraining the body motion to heave only. Ransley *et al.* [382], as well as the participants of the CCP–WSI Blind Test Series 2 and 3 [465–475], implement a linear spring as a mooring representation. Body motion is allowed in the three DoFs: surge, heave, and pitch.

Verduzco-Zapata and Ocampo-Torres [308] model 6–DoF WEC motion, where the mooring and PTO system are represented as a rope system. However, details of the mathematical implementation of the mooring system are omitted. In [349], the mooring line is included in the mathematical model of the PTO system (with stroke length control) of the *Seabased* device. Non-linearities of the mooring line (e.g. snap loads) are not taken into account.

More detailed mooring analyses are performed in [205, 231] for the *OPT Power buoy* and *OWEL* device, respectively. Yu *et al.* [205] design a mooring system using OrcaFlex and, subsequently, compare results from OrcaFlex with CFD–based NWT results, highlighting the accuracy of OrcaFlex only under linear wave excitation. Nicholls-Lee *et al.* [231] present a one–way coupling between OrcaFlex and a CFD–based NWT, where the mooring loads are coupled to the CFD solver as a function of the device dynamics.

A more sophisticated representation of a mooring line is given in [232, 261, 334], which utilises a high–order non–linear FE solver, so that non–linear mooring forces and snap loads can be captured. In a follow up study [454], the authors highlight the importance of a mooring system for the correct analysis of parametric device motion. Lee *et al.* [437] and Jiang *et al.* [515] independently present the coupling of OpenFOAM with the lumped–mass mooring model MoorDyn [544]. Both authors, again independently, validate the implementation of the mooring model using the same experimental data set as in [334].

Martin *et al.* [441, 521] develop their own lumped mass mooring model for the open source CFD toolbox REEF3D [545]. The authors successfully validate the implementation against different tests cases and highlight the model's ability to not only capture slack type, but also tension leg type, mooring arrangements.

Recently, Zhao *et al.* [483] implemented a mooring model based on the finite segment approach, where the mooring chain is divided into discrete cylinder segements. The models are coupled via the device motion (from the fluid solver) and the mooring tension (from the mooring model).

Control

In addition to the EMCSs implemented in [327, 328, 350, 417] and discussed in Section 5.2.1, stroke length control and *passive* control can be found in [349] and [362, 424], respectively. Chen *et al.* [349] include the stroke control system, i.e. end stops, within the mathematical PTO model by the means of end stop spring forces. In [362, 424, 445], passive control is realised by replicating a pressurized pneumatic cylinder, i.e. air spring, of the *CorPower* device in the numerical model.

Hybrid simulation

Through the coupling of CFD–based NWTs with other numerical solvers, hybrid simulation can be performed. In [257, 331, 115, 384, 504, 505], structural solvers are coupled with the CFD solver, using fluid forces as input only (one–way), or additionally feeding structural displacements back to the CFD solver (two–way). Connecting CFD solvers to a numerical toolbox, such as Matlab, PTO systems [349], sophisticated control algorithms [350, 417], or mooring models [232, 261] can be included in the CFD–based NWT.

The authors in [180, 200, 324, 325, 343] propose the coupling of potential flow theory based hydrodynamic models with high–fidelity CFD-based NWTs. The wave field in the far–field domain is modelled via the low–/mid–fidelity model, while the WSI and the flow field in the vicinity of the WEC is modelled with the viscous, non–linear

CFD model. Such coupled models can significantly reduce the computational cost ($\sim 40\%$ [343]), compared to 'pure' CFD–based models.

For OpenFOAM, a (one–way) coupling between the fully non–linear potential flow solver OceanWave3D [13] and the wave generation toolbox waves2Foam [97] is proposed in [546] and applied in [500] for the modelling of a box–shaped buoy in three DoFs. Another coupling between OpenFOAM and a FE method–based fully non–linear potential flow solver is prosed in [547] and employed to generate results for a contribution to the CCP–WSI Blind Test Series 1 [414], 2 [473], and 3 [471, 472]. Also considering OpenFOAM, Higuera *et al.* [412] propose a coupling with a Lagrangian 2D solver for the generation of the incident wave field using a dynamic boundary wave generation method. The coupling is achieved via the wave generation toolbox olaFlow [102].

Yang *et al.* [422] propose a two–way coupling of two CFD solvers (STAR-CCM+ [548] and FINE/Marine [549]) for modelling of the *Wave Glider*. While STAR-CCM+ is used for modelling of the flow around the hydrofoils, FINE/Marine is used for the modelling of the wave–induced floater motion.

Considering turbulence modelling, Zhan *et al.* [531] propose a domain decomposition based on laminar and turbulent (realizable $k - \varepsilon$) flow regimes (see also Section 5.6).

Gatin *et al.* [411] employ the spectral wave explicit Navier–Stokes equations (SWENSE) decomposition method [550] together with implicit relaxation zones [98]. In the SWENSE method, the wave field is decomposed into the incident wave field, solved with potential flow theory, and the perturbed wave field, for which the complete Navier–Stokes equations are solved.

Musiedlak *et al.* [74, 446] present a 'hot–start' methodology for WSI simulation, enabling temporal problem decomposition, where WaveDyn software [551] is used for the linear solution and OpenFOAM for the non–linear solution.

Table 5.7: WEC subsystems included in CFD–based NWTs

Subsystem	Literature
PTO	[20, 114, 171–174, 183, 187, 190, 195, 197, 199, 201, 204, 205, 208–210, 213, 214, 217, 219, 220, 223, 224, 226, 228, 229, 232, 239, 236, 237, 241, 243–247, 252, 254, 256–260, 262, 264–266, 269–272, 275, 277, 284, 285, 288–292, 298, 300–303, 308, 309, 312, 317–319, 321, 322, 328, 329, 331, 333, 336, 337, 347–349, 352, 351, 353, 354, 356, 363, 367, 378, 380, 381, 392–395, 397, 401, 418, 464, 420, 421, 425–427, 430, 432–436, 438, 439, 442, 447, 449–451, 455, 400, 457, 458, 476, 477, 480–482, 484, 488, 494–497, 501–503, 507–513, 516, 520, 522–528, 530, 531]
Mooring	[231–235, 254, 259, 261, 272, 308, 349, 362, 364, 376, 382, 392, 393, 398, 399, 424, 433, 441, 454, 455, 460, 465–475, 483, 501–506, 515, 521, 524]
Control	[327, 328, 349, 350, 362, 424, 445, 417]
Hybrid simulations	[74, 115, 180, 200, 205, 231, 232, 257, 261, 324, 325, 331, 343, 349, 350, 384, 411, 412, 417, 422, 414, 446, 471–473, 500, 501, 504, 505, 531]

5.3 Problem discretisation

Problem discretisation, in terms of the computational mesh (spatial) and the time step (temporal), is one of the key parameters to be selected by the user to ensure efficient and accurate simulation. In the field of naval architecture and ship hydrodynamics, effort has been undertaken to provide guidelines for the mesh and time step sizes [552–554]. However, in the reviewed literature, only a limited number of studies (e.g. [315, 358, 404, 420, 421, 493, 511, 524]) are found to refer to general CFD engineering guidelines. This may be reasoned by the conceptual difference between these *classical* offshore engineering applications and WECs (e.g. large resonant motions, small device sizes). Instead of general engineering guidelines, [502–505] use discretisation recommendation for wave modelling provided by the STAR-CCM+ software package.

5.3.1 Convergence

As stated in Chapter 4, appropriate problem discretisation must be determined via convergence studies. Various methods are found in the reviewed literature to declare the discretisation to be *converged*.

Very few studies employ established convergence measures. Evolving from the enhanced use of CFD engineering in the field of aerodynamics, Roache [88] proposes the use of the grid convergence index (GCI) in order to produce comparable and coherent convergence results. For the proposed method, three different discretisation sizes are used to determine the GCI, which can prove converged solutions. In the reviewed literature, the GCI is used by [123, 330, 501].

Jiang *et al.* [515] perform rigorous convergence analysis based on the procedure in [555], allowing simultaneous convergence analysis of both spatial and temporal discretisation. Eskilsson *et al.* [361, 362] apply a methodology, based upon [556, 557] to ensure and quantify the uncertainty of CFD–based NWT experiments. The authors use an established four grid method, based upon Richardson interpolation, and compare results to simpler convergence tests based on relative difference between quantities from different meshes. It is pointed out that more sophisticated approaches to identify grid convergence are needed and should be favoured over simpler, quantitative or qualitative (i.e. visual inspection), methods.

Omitting a standardised convergence procedures, three different levels of fidelity for the assessment of convergence can be observed in the reviewed literature:

(i) Providing no information and simply defining the discretisation as converged.

(ii) Qualitative assessment by visual inspection of graphs.

(iii) Quantitative assessment via the relative change of a certain quantity (or the deviation to reference data) between the discretisation levels.

Categories (i) and (ii) are the most common but least accurate procedures. For category (iii), some examples are found in the literature. In [181, 243, 265, 381, 394] a quantified convergence assessment is presented, reporting differences between tested meshes of 0.5% to 12%. Wu *et al.* [415] compare CFD–based results to results obtained with the linear hydrodynamic solver ANSYS AQWA to determine convergence. Evaluating the error between the results for two different meshes, the authors chose the finer discretisation, which leads to overall smaller errors. Brown *et al.* [407] use the error between numerical and experimental surface elevation data of a focused wave to determine sufficient grid sizes, ultimately achieving an error $< 2\%$. A similar approach is used by the same authors in [465, 466]. Xu *et al.* [477] consider the quadratic loss coefficient for an OWC and find $< 3\%$ difference between the finest and medium mesh. Schubert *et al.* [530] perform the convergence study on wave height and, for 10CPH, find numerical results with 3% deviation to the nominal wave height.

5.3.2 Discretisation quantities

For the application of CFD–based NWTs for WEC analysis, wave propagation must be resolved with the highest possible accuracy, at reasonable computational cost. Hence, in the reviewed literature, convergence studies mainly focus on the discretisation around the free surface. Table 5.8 lists the publications which include convergence studies for spatial domain discretisation. Spatial discretisation is categorised by the value of CPH. It can be stated that, in the vicinity of the free surface interface, structured grids with a spatial discretisation of the order of 10CPH and 100CPL are most widely applied in the literature.

It should be noted here that, when WSI is considered (especially in turbulent conditions), the discretisation around a body is of importance as well. Only in [203, 243, 261, 315, 245, 254, 268, 330, 342, 347, 364, 404], is the discretisation around the WEC structure included in the convergence analysis.

Avoiding static grid sizes, Eskilsson *et al.* [445] investigate an adaptive mesh refinement method based on wave propagation and wave–induced body motion test cases. The authors find equivalent solutions for the static discretisation and adaptive mesh refinement while significantly reducing the computational burden. Limitations regarding dynamic load balancing and the application with overset grids are also highlighted.

Regarding temporal discretisation, Table 5.9 lists the publications which include temporal convergence studies. Temporal discretisation is categorised by the use of fixed or variable time steps, where the latter is controlled by the CFL condition and the maximum Courant number Co_{max} (see Section 4.3.2). It should be noted that convergence studies are performed less often when variable time stepping is used, compared to studies with fixed time steps. This, however, does not suggest that fixed time step sizes are generally used more often in CFD–based NWTs for WEC applications.

Table 5.8: Spatial discretisation determined through convergence studies used in the reviewed literature

CPH	Literature
$0 \leq CPH \leq 10$	[168, 181, 113, 227, 265, 266, 111, 251, 316, 290, 291, 320, 351, 352, 330, 333, 334, 369, 394, 382, 383, 367, 418, 434, 435, 453, 455, 464, 521, 407, 487, 488, 493, 495] [270, chap.5], [270, chap.6]
$10 < CPH \leq 20$	[172–174, 183, 181, 190, 198, 201, 213, 243, 259, 268, 292, 315, 314, 321, 322, 353–360, 378, 374, 375, 404, 420, 421, 432, 433, 455, 465, 466, 485, 501, 508, 511, 516, 522–524, 526, 530] [270, chap.4]
$CPH > 20$	[181, 275, 283, 314, 346, 454, 477, 487, 494, 502–505] [270, chap. 7]

Table 5.9: Temporal discretisation used in the reviewed literature

Time step	Literature
Fixed	[165, 167, 172–174, 183, 190, 201, 213, 199, 203, 113, 216, 225, 245, 259, 283, 315, 317, 321, 322, 353–360, 335, 381, 420, 421, 432, 440, 482, 483, 485, 492, 508, 522, 523]
Variable (CFL condition)	[111, 314, 320, 347, 351, 352, 378, 372, 373, 382, 383, 394, 453, 514, 516] [270, chap.5]

5.4 Numerical wave generation and absorption

CFD–based NWT WEC experiments rely on accurate wave generation and absorption at the NWT boundaries. The different methodologies for numerical wave generation and absorption are introduced in Section 4.3.3. This sections reviews the literature of CFD–based NWTs for WEC applications with a focus on the employed wave generation (Section 5.4.1) and wave absorption methods (Section 5.4.2). Table 5.10 lists the reviewed literature, categorised based on the employed numerical wave makers.

5.4.1 Wave generation

As stated in Section 4.3.3, for wave generation, five different methods are well known: the relaxation zone method, the static and dynamic boundary methods, the mass source method, and the impulse source method.

Relaxation zone method

Table 5.10 indicates that the relaxation zone method is the second most widely used wave generation method within the review literature. The method requires an appropriate choice of the relaxation zone length. For the analysis of a fixed OWC device, Vyzikas *et al.* [394] employ the relaxation zone method and find biased results in terms of the device efficiency caused by re-reflection of waves from the relaxation zone. To avoid such re-reflection, the relaxation zone length can be increased, at additional computation cost. As a guideline for the choice of the relaxation zone length L_R, a length of $L_R = 1 - 2\lambda$ can be extracted from the reviewed literature. For the simulation of extreme waves, a number of studies apply NewWave theory (see Section 3.3) to generate focused waves with the relaxation zone method [234, 235, 240, 300, 330, 382, 407]. A detailed description of the representation, implementation, and validation of the generation of focused waves, with the relaxation zone framework, can be found in [299, Chapter 4]

Poguluri *et al.* [496, 497] perform a comparative study between the relaxation zone method and the static boundary method (without active absorption). However, since the wave absorption methods are also varied for the two wave generation methods, no direct comparison is possible.

Li *et al.* [517] perform a comprehensive comparison between the impulse source method, the relaxation zone method, and the SWENSE model. For the study, the authors investigate the WSI of the *CALM* buoy, comparing surface elevation and excitation force data. The authors conclude that all considered methods can achieve good agreement with the experimental reference data, as long as the discretisation size is chosen correctly. The SWENSE model is the most efficient amongst the tested models, with a reduction in cell count (compared to the relaxation zone method) of up to $\sim 25\%$. The relaxation zone method is also included in the analysis of different numerical wave makers for the open-source CFD toolbox REEF3D in [462]. The authors find that the relaxation zone method delivers better quality waves, compared with the static boundary method, particularly for short and steep waves. However, the relaxation zone is less computational efficient, compared to the static boundary method.

Static boundary method

The static boundary method is the most prominently used wave generation method in the reviewed literature (see Table 5.10). Some relevant examples are discussed in the following.

Wei and Dias [310] employ the static boundary method in a circular NWT for the study of wave impacts on an OWSC. The use of a circular domain is justified by the reduction of the overall domain size and, hence, computational cost. Finnegan and Goggins [283] present a comprehensive study on irregular wave generation using the static boundary method, in which the authors adopt the CFD–based NWT used previously for dynamic boundary wave generation [113]. Good quantitative agreement is found between the analytical approximation and CFD results.

Chen *et al.* [317] induces waves *and* current in the CFD–based NWT using the static boundary method; however, no validation of the methodology is given. Zhao *et al.* [483] employ the static boundary method to generate 'real world' tsunami waves, based on field measurements. Good agreement of the numerical data with the real world reference is achieved. In addition, the authors include a comparison of the forces and motion of a moored, floating, cylinder when subject to a realistic tsunami wave or an equivalent solitary wave. The realistic tsunami wave induces larger force and motion of the structure, compared to the equivalent solitary wave.

Dynamic boundary method

The dynamic boundary method is the third most popular wave generation method in the reviewed literature (see Table 5.10). Studying slamming events on an OWSC, Wei *et al.* [268, 342] justify the use of the dynamic boundary method with the aim of reproducing the setup of the physical experiments as closely as possible. Results show satisfactory agreement between numerical and experimental results of the free surface elevation and the device dynamics.

Simonetti *et al.* [302] perform a comparison study between the relaxation zone method and a piston type wave generation method, simulating regular 2^{nd} order Stokes waves (see Section 3.1). Results from numerical simulation are validated against experimental data, revealing similar deviations for a piston type dynamic boundary and the relaxation zone method. However, a run time comparison (6h for dynamic boundaries versus 2h for the relaxation method) drive the decision towards using the relaxation zone method for the remainder of the study.

Finnegan and Goggins [113] develop a dynamic boundary flap-type wave maker for a comprehensive study on the generation of regular waves. Results indicate that the wave maker, hinged at the tank floor, does not compare well with wave maker theory in deep water; however, compared with linear wave theory, better agreement is achieved.

While the above mentioned references rely on mesh distortion and remeshing of the domain (see Section 4.3.4), Anbarsooz *et al.* [225] propose a dynamic boundary wave generator employing the fast–fictitious–domain method for the modelling of both piston– and flap–type wave makers. Using the Cartesian cut–cell method, Abadie *et al.* [311] and Chen *et al.* [526] include the (piston–type) dynamic boundary method in their CFD–based NWT.

Mottahedi *et al.* [432] include a wet–back, flap–type, wave maker in their NWT. To avoid reflection in the gap between the tank boundary and the back of the wave maker flap, a numerical beach is added. Motivated by the use of a CFD–based NWT for WEC design, the authors in [478, 479] successfully perform a validation study of a dynamic boundary wave maker, feeding experimental data of the paddle motion to the NWT.

Mass source method

As indicated in Table 5.10, only a few authors are found to employed the mass source method for numerical wave generation. In an early work, Alves and Sarmento [168] use the mass source method in a study on OWC devices, considering 2^{nd} and 3^{rd} order Stokes waves (see Section 3.1). Although no quantitative evaluation of the numerical wave maker method is provided, surface elevation plots reveal inaccuracies in wave height.

Victor *et al.* [176, 185] apply the mass source method to generate regular waves in intermediate water depths. Lopez *et al.* [214, 114] aim to generate regular and irregular waves in intermediate water depths. None of the above studies [176, 185, 214, 114] provide information on the quality or efficiency of the mass source method.

More recently, Zhang *et al.* [484] implement the mass source method in ANSYS Fluent [558] and find good performance; however, only a qualitative assessment of the procedure based on the simulation of regular waves is included in the study.

Impulse source method

The impulse source method is used in the series of publications analysing the *Oyster* OWSC [20, 236, 249, 255, 301, 337, 387]. The same authors also include the impulse source method in a high–level review of different numerical wave makers presented in [110]. Li *et al.* [517] include the impulse source method in a comparative study on wave modelling method and find that the impulse source method, compared to the relaxation zone and the SWENSE method, can deliver results of the same accuracy if the domain discretisation is chosen appropriately. Furthermore, the authors highlight that the wave absorption method, used in conjunction with the impulse source wave maker, is not efficient.

5.4.2 Wave absorption

Wave reflection from NWT tank walls or structures within the NWT must be eliminated, or at least significantly mitigated to replicate open ocean conditions. As stated in Section 4.3.3, for numerical wave absorption, six different methods are available, i.e. the relaxation zone method, the static boundary method, the dynamic boundary method, numerical beach implementations, geometrically sloped beaches, and the cell stretching method. In the reviewed literature, no study is found using exclusively the cell stretching method for wave absorption. Thus, no dedicated subsection is introduced for this method.

Relaxation zone method

Wei and Dias [310], as well as Mishra *et al.* [293], employ the relaxation method in circular NWTs. As stated in [310], the implementation of a circular domain significantly reduces its size. In [293], radiation tests on the *WaveBob* are performed and the cylindrical shape of the device suggests the use of a circular domain to most efficiently avoid wave reflection from the boundaries.

Palm *et al.* [454] use the relaxation zone method in a rectangular NWT to investigate parametric device motion and highlight the importance of efficient wave absorption for correct modelling of parametric motion. Zhang *et al.* [522] perform a comparison between a numerical beach and the relaxation zone method. From visual inspection, the authors find better absorption performance for the relaxation zone method, which is then used in a follow up study in [523]. Quantifying the wave absorption, a reflection coefficient of 0.05 is calculated when using relaxation zone lengths between 2–4λ in [476, 477]. However, no exact formulation for the calculation of the reflection coefficient is provided.

Uniquely, for the wave absorption at the inlet boundary, Dai *et al.* [516] use a static boundary method in conjunction with a relaxation zone method based on the Euler overlay method [559]. However, no further analysis of the particular method is provided.

Generally, if the relaxation zone method for wave absorption is employed in a rectangular NWT, a length of $1-4\lambda$ can be extracted from the reviewed literature as guideline for the choice of the relaxation zone length L_R.

Static boundary method

In the reviewed literature, significantly fewer study can be found to employ the static boundary method for wave absorption, compared to wave generation. Specifically [229, 256, 129, 288, 320, 325, 351, 352, 453] use the proposed method by Higuera *et al.* [102].

In [182, 198], the in–house CFD code AMAZON-SC 3D allows the definition of a non-reflective boundary. Unfortunately, further information on characteristics or the implementation of this boundary are not given. Using the Sommerfeld radiation condition [560], Verduzco-Zapata *et al.* [308, 486] prescribe fluid velocities at the far field boundary to absorb the incident waves.

Only Feichtner, *et al.* [487] provide a qualitative analysis of the absorption capabilities of the employed static boundary method by means of the reflection coefficient, following [561]. The authors find a "sufficiently small" reflection coefficient of 6.1%.

Dynamic boundary method

In the reviewed literature, Armesto *et al.* [248] and the consecutive studies by Liu *et al.* [172–174, 183, 190, 201, 210, 213] employ the dynamic boundary method for wave absorption. In [248], no evidence for issues related to wave absorption can be found. However, surface elevation data outside of the tested OWC chamber are not shown, so that no conclusions on the absorption quality can be drawn.

In [172–174, 183, 190, 201, 210, 213], the dynamic boundary method for wave absorption is implemented based upon the Sommerfeld radiation condition. Giving a relation between free surface elevation and the horizontal velocity component, the moving wall at the absorption boundary can be driven accordingly. Again, no evaluation of accuracy and efficiency is provided.

Numerical beach

In the consecutive studies by Chen *et al.* [111, 251, 270, 316], as well as in [219, 20, 249, 255, 337, 387], a numerical beach is implemented in the CFD–based NWT for wave absorption. Authors provide quantified absorption efficiency in terms of the reflection coefficient, showing reflection coefficients of the order of 2%.

In a validation study of a 2D numerical wave flume in [478, 479], authors use a dedicated model to replicate the porosity of a physical pebble–mound beach using a numerical beach formulation. However, the authors do not present a reflection analysis and only use short time trace snippets which are relatively free of reflection. Thus, the effectiveness of the numerical beach can not be judged.

Generally, to achieve low reflection coefficients (i.e. high absorption efficiency), authors in the reviewed literature use beach lengths of the order of $1 - 5\,\lambda$, which is similar to the relaxation zone length.

Geometrically sloped beach

Lopez *et al.* [114] include a geometric beach upstream of a mass source wave maker. Chen *et al.* [115] and Scarpetta *et al.* [305] employ a geometric beach for the study of the *REWEC1* submerged OWC and a *Wavestar*–like point absorber, respectively. Investigating different slopes for geometric beaches, ranging from 1:3 to 1:6, Finnegan and Goggins [113] recommend a 1:5 slope for optimal wave absorption. In contrast, Prasad *et al.* [427] test a 1:3 and 1:5 slope, suggesting a 1:3 slope for optimal absorption; however, quantitative analysis is omitted. Based on the recommendation in [113], Mohapatra *et al.* [433] implement a 1:5 sloped beach in their CFD–based NWT. van Rij *et al.* [475] simulate the entire physical wave tank in the COAST Laboratory at the University of Plymouth, including the sloped beach, for their contribution to the CCP–WSI Blind Test Series 2.

Table 5.10: Numerical wave generation and absorption methods used in the reviewed literature

Method	Generation	Absorption
Relaxation	[212, 292, 219, 232, 261, 234, 235, 240, 246, 262, 271, 276, 275, 280, 253, 281, 290, 291, 295, 294, 300, 302, 327, 328, 330, 333–335, 361, 362, 382, 383, 391–393, 388–390, 394, 395, 400, 423, 424, 426, 430, 436, 443–446, 454, 455, 460–462, 411, 407, 465, 466, 476, 477, 489, 522, 523, 493, 496, 497, 500, 498, 499, 501, 504, 508, 513, 517, 518]	[212, 292, 232, 261, 234, 235, 240, 246, 271, 262, 276, 281, 293, 295, 300, 302, 310, 327, 328, 330, 333–335, 343, 361, 362, 371, 382, 383, 391–393, 388–390, 395, 423, 424, 426, 430, 436, 437, 443–447, 454, 455, 400, 461, 462, 411, 410, 407, 465, 466, 474, 469, 476, 477, 489, 522, 523, 493, 496, 497, 500, 498, 499, 501, 508, 513, 516–518, 526]
Static Boundary	[166, 178, 179, 181, 182, 198, 186, 123, 202, 189, 155, 204, 205, 243, 202, 222, 285, 264–266, 220, 237, 223, 224, 226, 347, 229, 256, 239, 187, 251, 111, 316, 258, 258, 269, 273, 274, 115, 129, 283, 288, 308, 310, 312, 314, 315, 317, 325, 321, 322, 343, 341, 344, 346, 349, 351–360, 369, 378, 372, 401, 403–405, 420, 421, 425, 433–435, 438, 440, 452, 453, 457, 458, 462, 416, 413, 408, 412, 409, 467–470, 475, 480–483, 485–488, 490–492, 495, 496, 502–505, 507, 509–511, 514, 516, 520, 524, 525, 527, 530, 531]	[182, 198, 229, 256, 273, 129, 288, 308, 320, 325, 351, 352, 372, 392, 405, 428, 452, 453, 462, 408, 412, 409, 486, 487, 490, 491, 507, 509, 514, 519, 524, 530, 531]
Dynamic Boundary	[165, 167, 171–174, 183, 190, 201, 213, 210, 181, 192, 199, 203, 113, 216, 225, 245, 242, 241, 309, 244, 195, 191, 217, 260, 207, 248, 254, 364, 268, 342, 305, 302, 311, 368, 380, 381, 396, 398, 399, 419, 427, 432, 447, 449–451, 410, 478, 479, 494, 506, 512, 526, 528, 529]	[248, 172–174, 183, 190, 201, 210, 213, 474]
Mass Source	[114, 168, 176, 185, 214, 484]	
Impulse Source	[20, 236, 249, 255, 301, 337, 387, 517]	
Numerical Beach		[168, 176, 185, 189, 155, 202, 222, 204, 205, 243, 219, 20, 249, 255, 225, 245, 251, 111, 270, 314, 316, 254, 364, 259, 268, 342, 309, 311, 317, 321, 322, 341, 344, 346, 349, 378, 353–360, 367–369, 380, 384, 392, 418–421, 429, 432, 434, 435, 464, 521, 456, 460, 416, 413, 470, 478, 479, 481, 482, 484–486, 488, 492, 494–496, 502–505, 510, 511, 516, 517]
Geometrically sloped beach		[113–115, 427, 433, 475]

5.5 Dynamic mesh motion

The commonly used body representation methods and dynamic mesh motion methods are introduced in Section 4.3.4. This section reviews the published literature of CFD–based NWTs for WEC applications focussing on the body representation methods

(Section 5.5.1), the different types of body motion (Section 5.5.2), and the dynamic mesh motion methods (Section 5.5.3).

5.5.1 Body representation methods

In the following, examples of the different body representation methods within the reviewed literature are discussed and tabulated in Table 5.11. Note that, for clarity, only body fitted methods *not* used in conjunction with mesh morphing are included in Table 5.11.

Cartesian cut–cell

In the reviewed literature, the pioneering studies [165, 167] on rotating vanes employ the Cartesian cut–cell method. Furthermore, the cut cell method is used in [182, 188, 198] for the analysis of floating bodies in extreme waves. Westphalen *et al.* [186, 222, 123] include the Cartesian cut–cell method in the code comparison studies.

In [194, 223, 290, 291], the Cartesian cut–cell method is employed for the analysis of fixed OWCs, while Nematbakhsh *et al.* [296] implement the generic multi–body WEC of the OMAE hydrodynamic modelling competition [562] with the Cartesian cut–cell method.

Simulating a modular flap–type OWSC, Abadie and Dias [311] employ the Cartesian cut–cell method implemented in an in–house code. Also employing an in–house code, Xie *et al.* [408] model the static FSPO–like structure of the CCP–WSI Blind Test Series 1 with the Cartesian cut–cell method. For the contribution to the CCP–WSI Blind Test Series 1 and 2, Chen *et al.* [410, 474] employ the PIC code and the Cartesian cut–cell method. The same authors also present a study on a heave constrained box–shaped buoy in [447, 526].

The relatively limited number of studies considering the Cartesian cut–cell method can be reasoned by the limited accessibility of CFD software implementing this body representation method, e.g. the in-house code AMAZON-SC 3D or the commercial software Flow-3D [563].

Fast–fictitious–domain

An even smaller number of studies, compared with the Cartesian cut–cell method, employ the fast–fictitious–domain method: [215, 225, 245, 254, 364, 400, 432]. This particular method is only available in in–house codes, hindering the widespread application. The study by Mottahedi *et al.* [432] should be highlighted here, which includes a comparison between the fast–fictitious–domain method and experimental and numerical (based on re–meshing) reference data from [342]. Overall agreement between the simulated results and the reference data is found, highlighting the capabilities of the fast–fictitious–domain method.

Fractional area-volume obstacle representation

The FAVOR method is proprietary to the commercial CFD software Flow-3D. Thus, only authors with access to the Flow-3D software employ this body representation method (see Table 5.11).

Body fitted meshes

By far the most widely applied body representation method uses body fitted meshes. This body representation method is used in conjunction with AMIs , re–meshing methods, mesh morphing, or overset grid methods. A more detailed discussion of dynamic mesh motion methods for body fitted meshes is presented in Section 5.5.3.

Table 5.11: Body representation methods used in the reviewed literature (excluding, for clarity, body fitted methods used in conjunction with mesh morphing)

Body representation method	References
Cartesian cut–cell	[165, 167, 169, 182, 186, 188, 194, 198, 222, 223, 123, 272, 290, 291, 296, 311, 441, 521, 410, 447, 474, 526]
Fast–fictitious–domain	[215, 225, 245, 254, 364, 400, 432]
FAVOR	[175–179, 185, 273, 308, 380, 397, 401, 425, 434, 435, 486, 525]
Body fitted meshes	[172–174, 183, 190, 201, 210, 213, 231, 241, 242, 268, 309, 342, 349, 204, 205, 243, 292, 317, 218, 219, 224, 227, 231, 20, 236, 246, 249, 255, 271, 301, 325, 333, 337, 387, 304, 315, 318, 344, 396, 404, 406, 422, 429, 430, 433, 442, 454, 456, 460, 409, 467, 468, 475, 481, 484, 485, 495–499, 520, 522, 523, 501–505, 507, 518, 519, 531]

5.5.2 Body motion

The body motion can be categorised based on the number of DoFs considered in a particular study (see Table 5.2 – 5.5). Another categorisation of the reviewed literature is possible by considering the type of motion:

- **Prescribed motion:** Involves driving the body motion along a predefined trajectory, irrespective of the hydrodynamic forces acting upon it. Prescribed motion tests are generally useful for SID purposes [336], where the force on the body is the input and the resulting device state (displacement, velocity) is the output. These tests can be used to identify the hydrostatic restoring force as a function of body position [252, 284], or the radiation and/or viscous forces on the body [206, 227, 293, 300, 365, 373].
- **Solved motion:** Involves the calculation of the body's trajectory from the forces acting upon it via Newton's 2^{nd} law of motion. If required, the motion can be constrained to specific DoFs by the motion solver.

For solved motion, the motion may result from an initial displacement from equilibrium (free decay test), or due to excitation from incident waves or external forces:

- **Free decay tests** are a simple example of body motion, whereby the body is initially displaced from its equilibrium position (either non–zero position or velocity) and the resulting motion is simulated as the body oscillates back to its rest position. Free decay experiments are used for the analysis of viscous drag effects [178, 192, 204, 243, 245, 249, 261, 304, 316, 364, 456], the identification of the WEC state dynamics [228, 248, 277], or the identification of the WEC resonant period [298, 319].
- **Wave–induced motion** is obviously a crucial element of a CFD–based NWTs for WEC applications. The variations in the free surface elevation and the resulting pressure on the body, due to incident waves, results in excitation forces on the body, from which body motion is calculated within the motion solver. Examples of wave induced motion can be found in the majority of the reviewed literature.
- **External forces** from the WEC subsystems (e.g. mooring or PTO system) may be incorporated into the motion solver. Examples can be found in the literature discussed in Section 5.2.2, e.g. [232, 257, 261, 327, 331, 349, 350, 417]. Input forces have also been used for SID purposes, identifying models between input forces and body motion [298, 329]. A discussion of the input force characteristics for efficient model identification is given in [319].

5.5.3 Dynamic mesh motion methods

Focussing on body fitted meshes, commonly applied dynamic mesh motion methods are mesh morphing, re–meshing, AMIs, and overset grids (see Section 4.3.4). Table 5.12 lists the corresponding literature for the different methods.

Mesh morphing

Mesh morphing is the most prominent dynamic mesh motion method, but requires careful model setup in order to retain a good quality mesh throughout the simulation. Due to the relatively large number of studies using mesh morphing, only a few relevant examples are discussed below.

From the limited number of publications considering multi–body WECs (see Section 5.1.2), the studies in [204, 243, 481], [292], and [317] employ the mesh morphing method for the simulation of the *OPT Power Buoy*, a generic multi–body WEC, and a twin–raft attenuator, respectively.

Chen *et al.* [275, 316] models a flap–type OWSC using the mesh morphing method. The device tilts with angles between 10° and -15° and the results do not indicate any problems related to the dynamic mesh motion method.

Bridgwater Court *et al.* [348] perform simulations of the *CCell*, flap–type OWSC and highlight difficulties of modelling the device in an array configuration, resulting in numerical instability when a device tilts more than 30°.

van Rij *et al.* [460] state that the use of mesh morphing morphing for free decay tests during drag identification is preferred over the overset grid method to avoid interpolation errors. Subsequently, for the simulation of the design load cases, the overset grid method is used.

Musiedlak *et al.* [446, 74] propose a novel 'hot–start' methodology (see Section 5.2.2), for which the authors developed a new `deformDYMMesh` toolbox within OpenFOAM, allowing the placement of the device within the domain depending on the results from the lower fidelity hydrodynamic model.

For the modelling of parametric excitation, Palm *et al.* [454] adapt the native morphing methodology within OpenFOAM for good mesh quality during the simulation of large parametric WEC motion.

Re–meshing

If mesh connectivity is not fixed, re–meshing can be applied. Compared with mesh morphing, re–meshing allows larger body displacements, but significantly increases the computational burden and potentially introduces numerical errors to the solution. Good re–meshing examples can be found in the consecutive studies [241, 242, 268, 309, 342] modelling an OWSC, as well as [172–174, 183, 190, 201, 213, 210], where the re–meshing method is used for the implementation of a dynamic boundary wave generation method.

Arbitrary mesh interfaces

AMIs provide sliding interfaces between mesh blocks, allowing large displacements, without distorting or re–meshing the computational domain. Problems, however, can occur during interpolation of the solution across the mesh interfaces. Prominent examples can be found in the consecutive studies on the *Oyster* OWSC [218, 249, 255, 219, 20, 236, 301, 337], where AMIs are employed to cater for the large rotational angles of a flap. More recently, Devolder *et al.* [320, 351, 352, 452, 453, 84] use AMIs to simulate a single device and an array of heaving WECs, where vertical cylindrical mesh blocks, surrounding the WECs, slide vertically past each other.

Uniquely, Nicholls-Lee *et al.* [231] extend the AMI method, including mesh morphing and re–meshing, to model the floating *OWEL* OWC, where pitching motion is captured through rotation of a horizontal cylindrical mesh block surrounding the body, and translational motion is accounted for by mesh morphing and re–meshing.

Overset grids

To date, only a relatively small number of studies have employed the overset grid method for CFD–based numerical wave tank WEC experiments (see Table 5.12). The limited use of the overset grid method in the wave energy field can be attributed to the fact that, until recently, the overset grid method was only available in commercial CFD software packages. The majority of WEC–related studies, which employed the overset grid method, were implemented in the commercial CFD solver STAR-CCM+. The first study was conducted by Stansby *et al.* [304], investigating drag effects on the performance of the *M4* WEC for different floater shapes. Forced oscillation tests are performed in a CFD–based numerical wave tank to determine the drag coefficient term. The same setup is later used in [456].

Similarly, Coiro *et al.* [318] perform CFD–based numerical wave tank experiments, employing the overset grid method, to evaluate the influence of viscous effects on the performance of a point–pivoted WEC. The authors indicate "worrying" mismatch, compared with physical wave tank data, for some system characteristics, such as the natural frequency of the WEC. No further investigation of the cause of the mismatch is provided.

Elhanafi *et al.* [357, 358, 360] investigate the performance and survivability of a moored floating OWC device. Numerical results for the device motion, generated power, and mooring line tension are compared with physical wave tank data. Bharath *et al.* [404] perform numerical simulation of diffraction and radiation experiments for a spherical WEC operating in the heave and surge DoFs. Numerical results from CFD simulations are compared with lower fidelity numerical models, as well as physical wave tank data. Coe *et al.* [502, 503] perform a design load analysis of the two–body *TRITON* WEC, employing the overset grid method to account for the relative motion of the two bodies. Regular and focused waves are modelled to analyse design load conditions, showing that focused waves result in larger loads, compared with equivalent monochromatic waves. Also performing a design load analysis, van Rij *et al.* [504, 505] consider the *RM3* WEC. The authors evaluate structural loads on the device at three different levels of computational fidelity: low–, mid–, and high–fidelity. For the high–fidelity simulations, the CFD solver is coupled with a finite element solver, for which good agreement between experimental and numerical results is found. The authors conclude that the numerical model can deliver reliable design load data.

More recently, the availability of the overset grid method in CFD software has been improved via the code release of the overset grid method for the open-source

CFD toolbox OpenFOAM v1706 [564] and later, making it freely available to a wider user community.

Chen *et al.* [519] show a number of different hydrodynamic free-surface problems, modelled using the overset grid method implemented in OpenFOAM. A free decay test of a locked self-reacting floating point absorber is modelled. A qualitative and quantitative analysis is presented for radiated waves and heave decay, respectively. For heave decay, sufficient agreement with the available experimental data is found. The same authors use the overset grid method for their contribution to the CCP–WSI Blind Test Series 1–3 [409, 468, 467].

Table 5.12: Dynamic mesh motion methods for body fitted meshes used in the reviewed literature

Dynamic mesh motion	References
Morphing	[9, 129, 171, 203–205, 228, 232, 233, 243, 251, 252, 261, 275, 277, 278, 281, 283, 289, 292, 298, 300, 316, 317, 319, 326–329, 334, 336, 338, 348, 350, 361, 362, 365, 371–373, 376, 382–384, 391–393, 424, 433, 437, 446, 417, 454, 455, 439, 481, 493, 494, 508, 514, 515, 524, 530]
Re–meshing	[172–174, 183, 190, 201, 210, 213, 231, 241, 242, 259, 268, 309, 314, 342, 343, 349, 378, 396, 433, 484, 507, 531]
AMI	[218, 219, 224, 227, 231, 20, 236, 246, 249, 255, 271, 293, 301, 325, 333, 337, 387, 430, 485, 498, 499]
Overset grids	[304, 315, 318, 346, 357, 358, 360, 404, 406, 422, 429, 442, 456, 460, 467, 468, 475, 495–497, 501–505, 518, 520, 522, 523]

5.6 Flow regime

The relevant flow types, i.e viscous and inviscid, for WEC analysis, are introduced in Chapter 2 and the differences between laminar and turbulent flow are highlighted. The numerical modelling of turbulent flows is then discussed in Chapter 4. Consequently, the following section categorises the reviewed literature based on the considered flow regime (Section 5.6.1 and 5.6.2/5.6.3) and the exclusion (Section 5.6.2) or inclusion (Section 5.6.3) of turbulence modelling. To summarise the findings of this section, Table 5.13 lists the different modelling techniques for the different flow regimes and the related studies in the literature. Note that Table 5.13 only includes studies which provide specific information on the flow regime and laminar/turbulent flow conditions.

5.6.1 Inviscid flow

The pioneering studies [165, 167], on rotating vanes in a CFD–based NWT, use the AMAZON-SC 3D code, solving the Euler equations. AMAZON-SC 3D is also included in a comparative study of different CFD techniques by Westphalen *et al.* [123]. The comparison with viscous flow solvers reveals similar results for cases considering interaction of waves with fixed structures and forced oscillation tests. Investigating the heave response of a structure to extreme waves, similar results between viscous and inviscid flow solvers are found; however, neither results agree with experimental findings. Palm *et al.* [261] employ the Euler equations in a study of a moored point absorber to specifically investigate the influence of viscosity. A comparison between turbulent viscous and inviscid flow simulations show discrepancies in the device dynamics for certain DoFs. In two follow up studies, the authors employ Euler equations to study the influence of viscous effects on parametric excitation [454] or scale effects [455].

5.6.2 Viscous flow – laminar

To evaluate the validity of laminar flow assumptions, two dimensionless quantities, the Reynolds number Re (see Equation (2.17)) and the Keulegan-Carpenter number KC (see Equation (5.2)) can be employed [565].

In the study on a submerged cylindrical WEC, Anbarsooz *et al.* [245] assume laminar flow conditions based on $Re < 1 \cdot 10^4$ and $KC < 1.0$. For the simulation of a heaving WEC including latching control, Giorgi *et al.* [327, 328] find $Re \approx 2 \cdot 10^4$ and, hence, assume laminar flow. Devolder *et al.* [320] justify the laminar flow assumption for a single floating point absorber with "low" KC numbers and find underpinning agreement of the numerical results with experimental data.

In [111, 275, 316], insignificant effects due to turbulence are assumed for the tested horizontal fixed cylinder, rolling barge, and flap–type WEC. In fact, negative effects associated with the empirical nature of turbulence models are identified. In addition, the reduced computational cost for laminar flow simulations is highlighted.

In a study on extreme waves and WSI of a vertical cylinder, Hu *et al.* [330] consider laminar flow conditions, stating that no wave breaking occurs and, hence, insignificant effects due to turbulence are expected. Furthermore, the Re is kept "low" ($Re = 975$) throughout the study, justifying the assumption of laminar flow. Rajagopalan and Nihous [335], studying force coefficients on horizontal and vertical plates, assume laminar flow justified by $5000 \leq Re \leq 10000$.

In a wave–only study, Ransley *et al.* [235] expect no influence from turbulence due to the absence of a solid structure in the flow. The validity of laminar flow in wave–only studies is also indicated in [20] and [270]. Comparing results of surface elevation, Chen [270] finds negligible turbulent effects when comparing laminar results with the $k-\omega$ turbulence model for a single sea state only. Also studying wave–only cases, Finnegan and Goggins [113, 283] compared results under laminar assumption with results gained using turbulence models ($k-\varepsilon$, $k-\omega$ SST), finding no significant difference.

A comparison between laminar and turbulent (model with the RNG $k-\varepsilon$ turbulence model) flow is undertaken in [333] for 2D and 3D tests on a flap–type WEC. The authors concluded that, for the 3D tests, turbulence flow assumptions are appropriate, while, for the 2D case, laminar flow can be assumed.

Comparing results of the WSI between a focused wave and a fixed FSPO–type structure from turbulent ($k-\omega$ SST) and laminar simulations, Brown *et al.* [407] find negligible difference in the time traces of the wave run–up and pressure on the structure.

These studies highlight the validity of laminar flow assumptions for a variety of WEC application cases. However, an assessment and justification of the accuracy of laminar flow conditions on a case by case basis is suggested, either driven by hydrodynamic boundary conditions (Re or KC), presence of WSI, or the mere reduction of computational cost.

5.6.3 Viscous flow – turbulent

As stated in Section 4.3.5, to be able to efficiently model prevailing turbulent flow conditions, turbulence modelling can be applied within a CFD–based NWT.

Large eddy simulation

For WEC applications, LES is employed in the consecutive studies on OWCs in [262, 302, 388–390]. In [302], a comparative study between the $k-\omega$ SST model and LES is presented, finding better agreement between experimental reference data and numerical results for LES, compared with the $k-\omega$ SST model. Deviations of the order of 10% are found for the free surface elevation, the pressure inside the OWC chamber, and the velocity in the duct. However, the computational cost increases by 15% for LES compared with the $k-\omega$ SST model.

Zhang *et al.* [522] perform a comparison between LES and the $k-\varepsilon$ and $k-\omega$ SST turbulence model, as well as laminar simulations, for wave–only cases. Significant wave damping is found for simulations with the $k-\varepsilon$ and $k-\omega$ turbulence models, which is avoided with LES or laminar simulation. Extending simulations to wave–induced motion of a heaving point absorber, the authors find a dependency of the accuracy, when compared to numerical and experimental reference data, of LES and laminar simulations on the width of the devices. In a follow up study [523], the same authors only consider laminar flow conditions.

Uniquely, Rafiee and Valizadeh [428] employ the delayed detached eddy simulations [566], where regions of flow separation are modelled with LES and boundary layers are modelled with RANS models. A reasoning for the particular choice of turbulence mode is, however, omitted.

RANS – $k-\varepsilon$ model

With reasonable computational cost and accuracy in practical applications, the most common method to account for turbulent effects in WEC applications are turbulence models based on the RANS equations.

The $k-\varepsilon$ model is mainly applied for the simulation of OWCs (e.g. [168, 172, 174, 183, 187, 190, 201, 213, 214, 226, 229, 244, 248, 256, 114, 258, 259, 269, 312, 347, 394]). The application of the CFD–based NWT in these different studies range from performance analysis [269, 394, 312, 168] and (structural) optimisation [226, 347] to SID [248]. However, none of the studies disclose a reasoning for the choice of the turbulence model.

Studying drag effects on the *M4* WEC, Stansby *et al.* [304, 456] compare the standard $k-\varepsilon$, $k-\omega$ SST, and the adopted $k-\varepsilon$ V2F [567] models with experimental data and laminar flow simulation. From the results of free decay test, it is concluded that the $k-\omega$ SST and the $k-\varepsilon$ V2F model give similar results. Ultimately, in [304], the authors select the $k-\varepsilon$ V2F model for subsequent studies, while in [456] the $k-\omega$ SST is used for the remainder of the study.

In the study of viscous effects for an OWSC, Wei *et al.* [309] present comparative results considering the standard $k-\varepsilon$, the RNG $k-\varepsilon$, the realizable $k-\epsilon$, and the $k-\omega$ SST turbulence model. Finding negligible differences between the results, the reduced computational costs for the standard $k-\varepsilon$ model lead to its implementation in the remainder of [309].

RANS – Realizable $k-\varepsilon$ model

The realizable $k-\varepsilon$ turbulence model is only employed in [293, 309, 322, 378, 508, 531]. Mishra *et al.* [293] test the ability of CFD to simulate a small scale model of the multi–body *WaveBob* WEC, featuring a moon–pool between its two bodies. A justification of the employed turbulence model is not given.

Also employing the realizable $k-\varepsilon$ turbulence model without justification, O'Connell *et al.* [378] develop a CFD–based NWT model of a heaving OWC device including a non–linear PTO, based on an analytical expression for the pressure drop across the turbine. Luan *et al.* [508] employ the realizable $k-\varepsilon$ turbulence model for the simulation of a generic cylindrical point absorber. Again, no justification for the particular turbulence model is provided.

Wei *et al.* [309] include the realizable $k-\varepsilon$ turbulence model in the comparative study of various turbulence models, finding negligible differences between the different models. Zhan *et al.* [531] propose a domain decomposition methodology, allowing a spatial decomposition of the NWT into regions assuming laminar and turbulent flow conditions.

In the 'turbulent' region, the realizable $k - \varepsilon$ turbulence model is employed. The proposed methodology is motivated by the increased wave damping due to turbulence modelling. Comparing results between pure turbulent and the novel laminar/turbulent simulations for a wave–only case, significant improvement regarding wave damping is achieved. However, no comparison is included considering WSI. Furthermore, no justification for the particular choice of turbulence model is provided.

RANS – RNG $k - \varepsilon$ model

The RNG $k - \varepsilon$ turbulence model is employed for a number of WECs, such as overtopping [274, 405], point absorber [178, 273, 261, 455], or OWSC devices [333]. Applications range from extreme load estimation [274] and model validation [178, 179, 261, 333] to the assessment of viscous drag effects [273].
Loh *et al.* [333] compare results of laminar flow simulations and the RNG $k - \varepsilon$ turbulence model, finding slightly better agreement with the experimental reference data (OWSC velocity, displacement, torque, and surface elevation) for the case of turbulent simulation. In a study on the WSI of a floating point absorber, Li and Yu [155] compare the RNG $k-\varepsilon$ and the standard $k-\varepsilon$ turbulence model to experimental results, finding that the RNG $k-\varepsilon$ turbulence model yields better agreement for the force data. Bhinder *et al.* [178] provide a justification for the applied turbulence model by stating that the RNG $k - \varepsilon$ turbulence model is the "preferred" model within the employed CFD software Flow-3D. Similarly, Kuo *et al.* [397] employ the RNG $k - \varepsilon$ turbulence model, stating that the particular turbulence model "is more popularly adopted than the $k - \varepsilon$ model because the RNG model can provide more accurate results in low strength turbulence and shear fluid regions" in Flow-3D.

RANS – $k - \omega$ model

The $k-\omega$ turbulence model is, for instance, applied in [246, 290, 291, 335, 385, 423]; however, none of the studies provides a reason for the selection of the turbulence model. Only Scarpetta *et al.* [385] provide a rather qualitative comparison between turbulent and laminar simulations, concluding that the necessity of modelling turbulent effects has to be assessed on a case by case basis.
Nguyen *et al.* [488] perform an assessment of different RANS turbulence models based on a bottom hinged OWSC. The authors include the standard $k - \varepsilon$, the RNG $k - \varepsilon$, and the standard $k-\omega$ turbulence model, as well as laminar simulations. Experimental data are included as a reference in the study. Comparing the *capture factor* and the rotational angle of the flap, the authors conclude that the standard $k - \omega$ turbulence model delivers the best agreement with the experimental data and, thus, is used for

subsequent simulations. However, the authors also identify good agreement between the laminar simulations and the experimental data. Given the close agreement of all numerical results and the fact that no measurement uncertainty is provided for the experimental data, the authors' conclusion is somewhat undermined.

RANS – $k-\omega$ SST model

Amongst the RANS turbulence models, the $k-\omega$ SST turbulence model can be identified as the second most applied turbulence model in the reviewed literature (see Table 5.13). In addition to the aforementioned comparative study in [309], the $k-\omega$ SST model is also compared against LES in [302], for the case of an OWC, where better agreement with experimental reference data is found with LES.

Studying the 2D flow field around a fixed OWC, Elhanafi *et al.* [322] compare the $k-\varepsilon$, the realisable $k-\varepsilon$, and the $k-\omega$ SST turbulence models. No difference is found between the two $k-\varepsilon$ models; however, differences between the $k-\varepsilon$ model and the $k-\omega$ SST model are observed, revealing more realistic results, compared with experimental reference data, for the $k-\omega$ SST model.

In a study on the design loads of a WEC device, van Rij *et al.* [504] justify the use of the $k-\omega$ SST turbulence model by identifying it as a "good compromise of computational stability, cost, and accuracy between the simpler RANS turbulence models and the more complex LES".

Devolder *et al.* [352, 452, 453] employ their proposed buoyancy modified $k-\omega$ SST model [568, 569] for the simulation of point absorber devices. The modified turbulence model tackles the problem of excessive wave damping by including the density in the transport equations and adding a buoyancy terms in the turbulent kinetic energy equation.

Wall treatment

As stated in Section 4.3.5, the modelling of turbulent flow in the vicinity of stationary walls, in particular for oscillating flows, is challenging [387]. For the successful application of wall functions, the dimensionless distance of the first cell to the wall is constrained to $30 < y^+ < 300$. If wall functions should be avoided, $y^+ \approx 1$ is required. In the following, the available literature is reviewed on the basis of the wall treatment, in terms of y^+ and wall functions.

In one of the early applications of CFD–based NWT for WECs, Alves and Sarmento [168] verify the spatial discretisation around the tested OWC structures, finding $y^+ < 300$, thereby assuming appropriate discretisation for the use of wall functions.

Table 5.13: Flow regimes and turbulence models used in the reviewed literature

Model	Literature
Euler	[165, 167, 176, 198, 216, 123, 281, 261, 341, 419, 454, 455]
Laminar	[176, 215, 222, 235, 240, 245, 111, 270, 275, 261, 315, 316, 320, 327, 328, 330, 333, 335, 344, 351, 380, 385, 398, 399, 403, 432, 434, 435, 442–444, 456, 461, 416, 413, 411, 410, 407, 465, 466, 474, 470, 472, 473, 480, 487, 487, 492–495, 506, 513, 522, 523]
LES	[262, 302, 388–390, 408, 428, 469, 522, 486, 489]
$k-\varepsilon$	[168, 172–174, 183, 187, 189–191, 195, 201, 203, 207, 113, 210, 213, 214, 217, 226, 232, 239, 244, 248, 114, 258–260, 268, 269, 283, 292, 304, 309, 312, 318, 346, 347, 363, 368, 381, 394, 401, 429, 430, 438, 456–458, 478, 479, 496–499, 507, 509, 518, 525, 527, 529]
Realizable $k-\varepsilon$	[293, 309, 322, 378, 508, 531]
RNG $k-\varepsilon$	[155, 166, 178, 179, 273, 274, 253, 281, 261, 309, 333, 334, 361, 391–393, 405, 425, 437, 454, 455, 484, 485, 491]
$k-\omega$	[246, 290, 291, 335, 385, 423, 441, 521, 449, 415, 476, 477, 483, 502, 503, 512, 516, 528]
$k-\omega$ SST	[204, 205, 227, 236, 243, 249, 115, 288, 289, 301, 302, 314, 317, 321, 322, 337, 349, 353–360, 362, 372, 373, 384, 395, 404, 420–422, 424, 426, 445, 452, 456, 460, 409, 475, 481, 494, 501, 504, 505, 510, 511, 513–515, 517]

Mishra *et al.* [293] avoid the use of wall functions at the WEC walls and find $y^+ \approx 2-3$ for "most of the simulations". No further discussion on the accuracy of the wall boundary conditions is provided.

Elhanafi *et al.* [322] test different values of y^+ (i.e. $y^+ \approx 1$ and > 30) when modelling a stationary OWC, with the $k-\varepsilon$ and the realizable $k-\varepsilon$ turbulence model, in conjunction with an "all y^+ wall treatment" within STAR-CCM+. The authors find no difference between the different discretisation sizes. Ultimately, the authors use $y^+ \approx 1$ with the $k-\omega$ turbulence SST model. The "all y^+ wall treatment" of STAR-CCM+ is also employed in [243, 460, 475, 501–505, 508]. Where [460, 475, 504, 505] state an average y^+ of < 10. [502, 503] achieve $y^+ \approx 150$.

Similar to Coe *et al.* [502, 503], a number of authors (e.g. [261, 281, 422, 428, 455, 362, 424]) provide approximations of the achieved y^+ values (all of the order of $1 \cdot 10^1$), but do not specify how these values are calculated for the considered oscillating flow. Other authors provide lower bounds [292, 518], upper bounds [361, 496, 497], or ranges [243, 334, 429, 494, 522] of y^+.

Zhang *et al.* [522] should be highlighted here, providing an analysis of the influence of the y^+ value on the heave motion of the *Berkeley Wedge* by means of a convergence study. Holding the overall thickness of the prism layer in the vicinity of the body constant but changing the number of layers and, thereby, the y^+ value, the authors find significant difference when using $1.4 \leq y^+ \leq 3.5$, compared to $0 \leq y^+ \leq 0.8$. Turbulence is modelled using LES. Palm *et al.* [261] hold the first layer thickness in the vicinity of the investigated point absorber constant during their mesh convergence study, thereby retaining a theoretically predicted $y^+ = 30$. Turbulence is modelled using the RNG $k-\varepsilon$ turbulence model.

5.7 Model validation

It is well-known, in all branches of engineering, that the application of CFD relies heavily on both verification and validation [88, 89]. Verification of CFD simulations covers the quantification of spatial and temporal discretisation errors, whereas general coding errors and bugs are assumed to be solved during code development.

5.7.1 Validation strategies

From the reviewed literature, four validation strategies can be identified. Comparison of CFD results to:

- Analytical results (e.g. [522])
- Potential flow theory simulations (e.g. [277])
- Third–party CFD simulations (e.g. [123])
- Experimental data (e.g. [463])

Reviewing the available literature regarding the employed validation strategies and methods, it can been observed that the comparison between numerical and experimental data is a well–established strategy. Some relevant examples are presented in the following. Palm *et al.* [334] identify the influence of physical model inaccuracies on the CFD–based NWT model validation for a novel mooring model. The authors mention that, for instance, the cylindrical buoy used in the physical experiments did not have perfectly sharp bottom corners as in the CFD–based NWT model. Also, an offset in the static tension in the mooring lines can be observed between the physical and CFD–based NWT models. Prasad *et al.* [381] detail measurement uncertainties caused by the instrumentation, ranging from $\pm 1\% \sim 2\%$. Similar ranges of measurement uncertainty are found in [355, 359].

Hu *et al.* [330] and Ransley *et al.* [382] perform comprehensive validation studies for extreme wave conditions, considering both wave–only and WSI cases. Hu *et al.* [330] finds maximum differences of 15% in the measured forces compared with experimental results.

Schmitt *et al.* [301] provide a quantitative comparison between experimental and simulation results for the *Oyster* OSWC. The authors highlight the complexity and potential inaccuracies of the particular experimental setup, identifying perturbations in the exciting waves, due to e.g. reflections, as a significant contribution to the observed differences between the numerical and experimental data.

Providing high resolution data sets and flow field visualisation, CFD enables the comparison of the experimental and numerical flow field visualisations. As some of the few, Schmitt [20] and Wei *et al.* [309] undertake such a comparison for OWSCs. Employing particle image velocimetry (PIV), Schmitt [20] highlights the complexity and potential inaccuracies of the experimental setup. Hence, comparison between numerical and physical results in a quantitative manner are hard to conduct. Looking at vortex shedding, Wei *et al.* [309] find agreement between physical and numerical results. Elhanafi *et al.* [322] use PIV in order to investigate the 2D flow field around a fixed offshore OWC. Satisfactory agreement between PIV and CFD are found for both velocity and vorticity. Similarly, Tsai *et al.* [425] include a qualitative comparison of flow field inside an OWC chamber using experimental data from a particle tracing method. Also considering an OWC, Deng *et al.* [513] present an extensive validation study, including a variety of different measures in the comparison between numerical and experimental data.

Dai *et al.* [516] validate a numerical model of a fixed OWC against physical wave tank tests to analyse scale effects. For the experimental measurement uncertainty, the authors follow the recommendations in [570]. Comparing the RAOs and the captured power, between experimental and numerical results, discrepancies of up to 15% are observed when including measurement uncertainty.

Xu *et al.* [481] perform experimental and numerical analysis of a two–body, floating point absorber type WEC in operational and survival conditions. For both conditions, independent experimental test campaigns in different test facilities, and at different scales, were performed. For the survivability test cases, discrepancies for the surge and pitch RAOs are attributed to a mismatch in the model geometries and the centre of mass (CoM). Quantification of the model's geometrical discrepancies is, however, omitted.

Palma *et al.* [490] compare numerical and experimental reflection coefficients for the *OBREC* device and declare differences of up to 66% as "slight". Better agreement is found for the device discharge, suggesting that the deviations in the reflection coefficient do not propagate through to the device discharge. The same authors [489], uniquely, use open ocean field data (e.g., pressure data) for validation purposes.

Wu *et al.* [485] discuss the influence of the differences between the desired and resulting wave height at the device location, due to e.g. numerical dissipation, on the validation results. The authors state that the influence is negligible and the observed similarity of the trend of the experimental and numerical results is already sufficient. The authors also mention the influence of friction in the experimental tests, influencing the validation results.

Generally, from validation studies, in which quantification of the accuracy is given, it can be stated that results with $< 10\%$ difference to the reference data are considered to be effectively validated. However, this number only serves as a guideline and the exact desired accuracy must be defined by the user for the specific problem at hand. Furthermore, if available, users are advised to take measurement uncertainties from experimental setups into account when evaluating the validity of the CFD solution.

5.8 CFD software

To set up a CFD–based NWT, numerous toolboxes and software packages are available. Figure 5.3 shows the CFD software used within CFD–based NWTs for WEC applications and their relative popularity in the reviewed literature.

Ranging from commercial and open source software to in-house developments, the different packages can readily be differentiated by availability and accessibility. Commercial tools usually provide *easy to use* graphical user interfaces (GUIs) and specific numerical tools, e.g. for the body representation. Also, some commercial software suites, e.g. ANSYS, provide multi-physics solvers, allowing fully coupled structural analysis with two–way FSI. However, the considerable license fees and, to some extend, the restricted access to the source code (which makes code tailoring difficult/impossible), possibly hinders the usage of commercial software for WEC applications. Commercial CFD tools include ANSYS Fluent and CFX [571], FLOW-3D, and STAR-CCM+.

Avoiding license purchase and enabling source code editing, open source CFD software has gained popularity and is backed by large support communities, forums, work groups, etc. Drawbacks here are the lack of user–friendly GUIs, often resulting in considerable learning times required to use the software. Furthermore, developments of new (advanced) numerical tools are left to the user or the community, potentially slowing down advancements and their spread. On the other hand, unlimited access to the source code caters for tailored code development and the application of open source software to an almost limitless range of applications.

Finally, in-house codes are also employed for the setup of CFD–based NWTs. Either being driven by a specific (physical) problem or the desire to include advanced numerical tools, in-house codes are highly efficient. Their nature, however, makes them unavailable for a large community. Examples of such codes can be found in [169, 182, 192, 254].

Being able to choose between numerous CFD software suites raises the question of which one to select. As discussed throughout the preceding sections, decision drivers can be identified when looking at the requirements on the CFD software, such as the available turbulence models, numerical wave generation and absorption, or body representation methods. Additional decision drivers may include project time frame, budget, and user experience.

Within the reviewed literature, some studies can be identified which perform comparative analyses of different CFD software. Based on the analysis of extreme wave loading, Westphalen *et al.* [186, 123] consider STAR-CCM+, ANSYS CFX, the in-house Cartesian cut-cell solver AMAZON-SC 3D, and an SPH solver. Testing wave–only, fixed structure, and dynamic body cases, the authors generally find matching

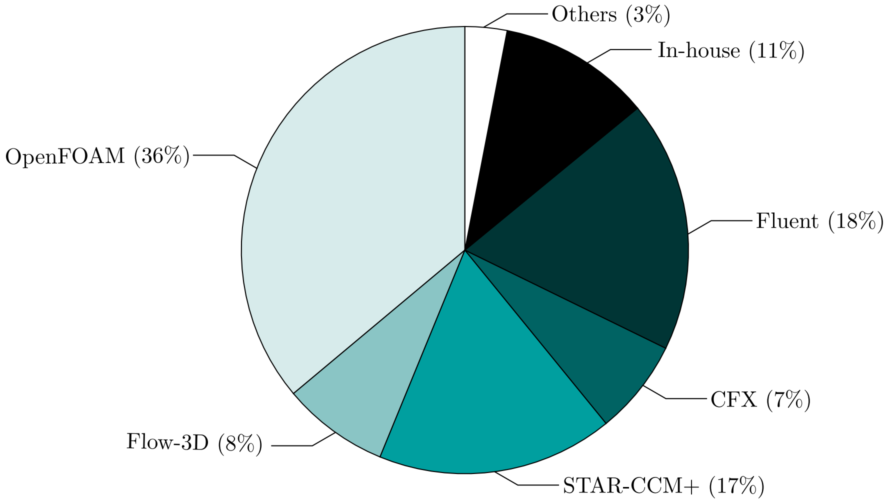

Figure 5.3: CFD software used for CFD–based NWT WEC applications and their relative popularity in the reviewed literature

results for the different software platforms. The meshless nature of the SPH solver is stated as being beneficial for extensive body motion. Unfortunately, simulations were not run on a dedicated machine, so that the CPU run times for the different solvers can not be compared.

Studying the hydrodynamic and aerodynamic behaviour of OWCs, Teixeira *et al.* [239] compare the commercial solver ANSYS Fluent with the in-house FE method solver Fluinco. Overall good agreement between the codes is found; only for the sloshing inside the OWC chamber are significant differences between the codes observed.

Based on the analysis of body dynamics and loads in tsunami waves, Sjökvist *et al.* [392, 393] presents a comparison of OpenFOAM with ANSYS Fluent. Lower computational cost, but also lower accuracy, is reported for Fluent for the particular test case.

More recently, Barbosa *et al.* [403] compare ANSYS Fluent and OpenFOAM in their study of a generic overtopping device. The authors find 15% difference in mass flow and identify numerical diffusion as a problem within OpenFOAM. However, the authors furthermore state that the observed similarity of the trend of the results (similar magnitudes and periodicity) is “most important”.

Most recently, the CCP–WSI Blind Test Series 1–3, documented in [463] and [JPI, JPK], aim at delivering comprehensive code–to–code and code–to–experiment comparison of different modelling approaches and dedicated experimental validation data.

For the CCP–WSI Blind Test, high quality experiments in a physical wave tank are performed, and relevant measurements (e.g. free surface elevation, pressure data, or device motion) are recorded. Participants of the blind test competition are given information on the physical setup (tank dimensions, measurement location, body mass, etc.), in order to replicate the experiment with their CFD–based NWT. The results of the simulation are then submitted for a blind comparison to the reference data. This procedure prevents *tuning* of numerical models to fit known experimental tank test results, thereby undermining the confidence and generalisation ability of the numerical models. In all three Blind Test Series, structures are exposed to a range of focused wave groups. While for Blind Test Series 1, a fixed FSPO–type structure was considered, two mobile WEC–type structures (see Chapter 7) were considered for Blind Test Series 2 and 3.

Results[2] were submitted from commercial software [411, 415, 475], open source solvers [407, 409, 412, 465–468], and in–house codes [410, 414, 408, 416, 413, 469–474]. From Blind Test Series 1, the organisers conclude that codes agree well with the experimental reference data so that a fidelity threshold, potentially as a function of the wave steepness, could not be identified [463]. From Blind Test Series 2 and 3, the organisers find a dependency of the code accuracy on the DoF. While heave is predicted well across the different models, differences can be observed for surge and pitch. Furthermore, it can be observed that the prediction quality of the WEC motion depends "strongly" on the accurate reproduction of the incident wave, which is most pronounced for the heave DoF [JPI, JPK].

5.9 Concluding remarks

This chapter concludes the first part of this thesis and presents a comprehensive review of the available literature concerned with CFD–based NWTs for WEC applications. Thereby, this chapter provides the interface between the background material of Part I and the main original work of Part II.

The review documents the effort of the numerical modelling community in the field of ocean wave energy to enhance the capabilities of CFD–based NWTs for WEC experiments. Starting with the pioneering work by Qian *et al.* [165], increasing model fidelity and capability can be observed. However, the reviewed literature also reveals model shortcomings and inconsistent fidelity for different WEC subsystems, which impede the development of a holistic high–fidelity CFD–based NWT WEC model:

- **Wave generation & absorption:** A variety of numerical wave makers is available; however, due to a lack of a comprehensive comparison, the choice of a particular numerical wave maker for a given problem is mostly driven by the availability within the employed CFD software. It is desirable to formulate guidelines for the selection of numerical wave makers based on a quantitative comparison in terms of accuracy and computational efficiency (see Chapter 6).

---

[2] Note that here only the CFD–based contributions are considered, linear or weakly/fully non–linear potential flow solutions are omitted

- **Validation:** In the reviewed literature, a considerable number of studies only provide qualitative descriptions of the achieved accuracy in a semantic way. However, if possible, quantification of the validation should be provided (see Chapter 7). From the reviewed literature, it can be concluded that deviations of order $< 10\%$ between numerical results and experimental reference data allow the numerical model to be effectively considered as validated.
- **Advanced mesh motion:** Regarding dynamical systems, the literature reveals a focus on single DoF devices with small device motion, which is driven (amongst others) by the difficulty in accommodating body motion within a CFD–based NWT. In the physical world, single DoF systems can rarely be found and enhanced device motion is essential for commensurate increases in power generation. Advanced mesh motion methods, such as the overset grid method, are thus desirable to model realistic WEC operation. Recent progress in the implementation of the overset grid method in OpenFOAM enhances the model capabilities of open source codes (and, thereby, a large group of user) to model realistic WEC operation. However, an assessment of the novel implementation of the overset grid method in OpenFOAM is yet missing (see Chapter 8).
- **Turbulence:** Reviewing the existing literature of CFD-based NWTs for WEC experiments, a general uncertainty regarding the accuracy and necessity of turbulence modelling (and the required wall treatment) during the simulation of WECs can be noticed. To get a better understanding of the modelling requirement for, and capabilities of, industry standard turbulence models, a thorough analysis of the available turbulence models for WEC modelling in realistic conditions is desired (see Chapter 9).
- **Device scaling:** From the reviewed literature, it can be observed that there is a lack of validated CFD-based NWT models of the same device across different scales. Thus, there is a need to investigate the scale effects on the performance of a resonating WEC system, in operational conditions, based on validated numerical models. Furthermore, since CFD-based NWTs provide the capability of by-passing the well known discrepancy between Froude and Reynolds scaling, by allowing the alteration of the transport properties of the involved fluid, scaling effects can be analysed via cases considering Froude scaling only, as well as Froude and Reynolds scaling, which can give valuable insight to the hydrodynamic scaling errors in physical wave tanks (see Chapter 10).
- **Holistic WEC modelling:** To conduct a comprehensive analysis of WEC performance, high–fidelity model representation of WEC subsystems is required to justify the computational cost for a CFD–based NWT. In this respect, shortcomings can be identified for the PTO, control, or mooring sub–systems. Currently, more progress towards a truly holistic high–fidelity CFD–based NWT is desired (see Chapter 11).

Part II

Contributions

6

Numerical wave makers

Contents

The methodologies for the wave generation and absorption within CFD–based NWTs, termed ‘numerical wave makers’ throughout this thesis, are introduced in Chapter 4 and a review of the different methodologies in CFD–based NWTs for WEC applications is presented in Chapter 5. From the literature review, it is concluded that a thorough methodology, using quantitative metrics, is missing for the assessment of numerical wave makers. Section 6.2 presents such a suite of assessment methodologies and metrics and illustrates their applicability based on well–known numerical wave makers in the OpenFOAM framework. Before treating the assessment of numerical wave makers, Section 6.1 presents advances in the impulse source wave maker, initially developed in [20]. The impulse source wave maker is included in the assessment in Section 6.2 and subsequently used during some of the validation studies presented in Chapter 7.

6.1 Impulse source wave maker

The difficulty in utilising an impulse source for wave generation in a CFD–based NWT lies in calculating the required source term to obtain a desired target wave train. Since the free surface is not a variable in the governing equations of a CFD–based NWT, there is no expression directly relating the impulse source term to the resulting generated wave trains. However, for depth–integrated equations, the free surface appears as a variable, which Wei *et al.* [106] utilise to derive a transfer function between the source term and the surface wave characteristics, generating regular and irregular waves in Boussinesq–type wave models. Following this approach, of manipulating the impulse term in the Navier–Stokes equation, shallow water waves have successfully been generated in CFD–based NWTs in [107, 108]. Despite those promising early applications, impulse source–type wave makers have not seen widespread application (see Chapter 5).

In theory, limitations due to the Boussinesq simplification might be overcome by employing stream functions or other higher–order wave theories. In practice, evaluating higher–order wave theories at multiple spatial positions (across all faces of the patch or all cells in the wave maker zone) can be computationally expensive. Furthermore, in many practical CFD applications, an accurate wave trace description is required at some distance away from the wave maker, typically in the middle of the domain.

Here, an alternative, more generalised, method to determine the required source function is proposed. The method stems from standard calibration procedures utilised for physical wave generators in real wave tanks, which iteratively tune the input signal applied to the paddles/pistons, to minimise the error between the measured and desired wave series. Unlike previous methods to determine the source term, which are restricted to shallow water waves, the calibration method is applicable from deep to shallow water conditions, able to generate realistic wave series at a desired location in the CFD–based NWT, without explicitly employing any wave theory. In addition, while dissipation can attenuate a theoretically correct wave height at the source region as it travels to the target location (see Section 6.2), the proposed method overcomes this problem since it is designed to obtain the desired wave signal at the target location.

Iterative calibration methods will, of course, increase the computational burden when compared to a directly analytically derived analytically source term. However, by performing the calibration runs in a 2D domain, the computational overhead is significantly reduced compared to 3D simulations, for realistic test cases. Applying a calibrated 2D result to a corresponding 3D domain is efficient and is also the recommended approach in [105]. It should be noted that a calibration of the source term in 2D domains is, however, only sufficient for long crested waves, with an invariant wave field in the lateral direction.

It will be demonstrated that, by utilising the calibration method, the source term can consist of a purely horizontal impulse component that varies in time. The time evolution of the magnitude and direction of this simple impulse source term can be calibrated using a standard spectral analysis method, which is commonly used in physical wave tanks. The remaining parameters of the impulse source that need to be chosen are the geometric size and shape of the source function inside the CFD–based NWT domain. An investigation of the effect of these geometric parameters will be presented, to offer guidance on the selection of those values.

6.1.1 Implementation

The basic implementation of the impulse source wave maker in the governing equations is discussed in Section 4.3.3. In the following sections and chapters, the impulse source wave generation method is always used in conjunction with the numerical beach implementation proposed in [110][1]. Thus, the momentum equations (4.32) and (4.33) are combined, yielding:

$$\frac{\partial(\rho\mathbf{u})}{\partial t} + \nabla\cdot(\rho\mathbf{u}\mathbf{u}) = -\nabla p + \rho\nabla\cdot(\nu\nabla\mathbf{u}) + \rho\mathbf{f}_b + r_s\rho\mathbf{a}_{wm} + s_b\rho\mathbf{u} \qquad (6.1)$$

To recall:

- $r_s\rho\mathbf{a}_{wm}$ is the source term used for wave generation, where r_s is a scalar variable that defines the geometric extent of the source region and $\mathbf{a}_{wm}$ is the acceleration input at each cell centre within $r_s = 1$. r_s is dimensionless, while $\mathbf{a}_{wm}$ is given in the units of $\mathrm{m\,s^{-2}}$.
- $s_b\rho\mathbf{u}$ describes a dissipation term used to implement a numerical beach, where the variable field s_b controls the strength of the dissipation, equalling zero in the central regions of the domain where the desired wave field is required and then gradually increasing towards the boundary over the length of the numerical beach L_B. s_b is given in units of $\mathrm{s^{-1}}$.

The values for the parameter fields r_s and s_b are set during pre–processing and their definition is crucial for the correct functioning of the method:

- r_s is set to one in the region where the wave maker is acting and zero everywhere else in the numerical domain. Therefore, the size of the source region and its position within the domain must also be selected. To offer guidance on the selection of the source region size and position, the case study presented in Sections 6.1.3 and 6.1.4 investigates the effect of the geometric parameters on the wave maker performance.

---

[1] This combination of methods is henceforth referred to as impulse source wave maker.

- s_b is initialised using an analytic expression relating the value of s_b to the geometric coordinates of the NWT. The simplest expression would be a step function, where the values of s_b are constant inside the beach and zero everywhere else in the domain. However, such a sharp increase in the dissipation will cause numerical reflections. Instead, the value of s_b is increased gradually from the start to the end of the numerical beach. Throughout this thesis, Equation (6.2), inspired by [572], is used to define the gradual increase of s_b towards the domain boundaries.

$$s_b = -2s_{b,\text{Max}} \left(\frac{(L_B - x_b)}{L_B} \right)^3 + 3s_{b,\text{Max}} \left(\frac{(L_B - x_b)}{L_B} \right)^2 , \tag{6.2}$$

where x_b is the position within the numerical beach, equalling zero at the start and increasing to L_B at the NWT wall, and $s_{b,\text{Max}}$ denotes the maximum value of s_b. Guidance on the selection of the parameters L_B and $s_{b,\text{Max}}$ is given in Section 6.1.4. Given that the impulse source generates waves in both the positive and negative x–direction, a numerical beach is not only implemented towards the far field boundary of the CFD–based NWT but also 'behind' the source region. A typical domain layout is depicted in Figure 6.1.

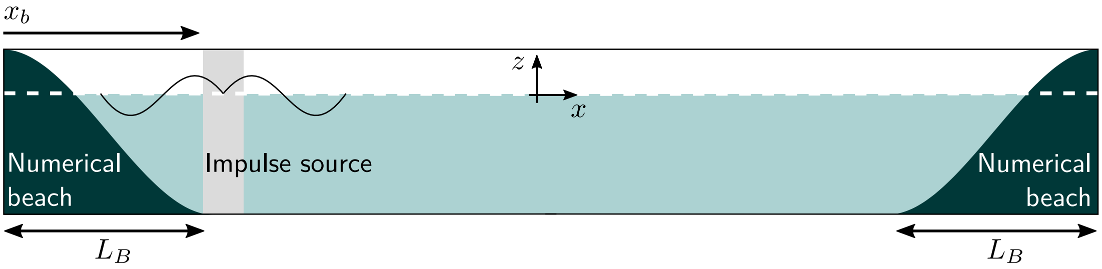

Figure 6.1: Schematic of a typical domain layout for the use of the impulse source wave maker including the source region ($r_s = 1$, grey colour code) and the numerical beaches. The shape of the numerical beach reflects the gradual increase of s_b based on Equation (6.2).

6.1.2 Calibration procedure

The acceleration input $\mathbf{a}_{wm}(t)$[2] is calibrated using linear calibration method, based on a standard spectral analysis method, adapted from [573], to produce a target wave series at a desired position within the CFD–based NWT. The calibration method comprises the following steps (for a graphical representation see Figure 6.2):

---

[2] Note that the dependence on t and f are specifically indicated in this section to highlight the difference between time and frequency domain.

1. Define a target wave time series, $\eta_t(t)$
2. Perform the fast Fourier transform (FFT) on $\eta_t(t)$ to obtain the amplitudes, $\mathcal{A}_{\eta_t}(f_j)$, and phases, $\Lambda_{\eta_t}(f_j)$, for each frequency component, f_j
3. Define an initial time series for $\mathbf{a}_{wm,1}(t)$
4. Run the OpenFOAM simulation for calibration iteration i, using $\mathbf{a}_{wm,i}(t)$ and extract the resulting surface elevation, $\eta_{r,i}(t)$, at the location of interest
5. Perform the FFT on $\eta_{r,i}(t)$ to obtain the amplitudes, $\mathcal{A}_{\eta_{r,i}}(f_j)$, and phases, $\Lambda_{\eta_{r,i}}(f_j)$, for each frequency component f_j of $\eta_{r,i}(t)$
6. Perform the FFT on $\mathbf{a}_{wm,i}(t)$ to obtain the amplitudes, $\mathcal{A}_{\mathbf{a}_{wm,i}}(f_j)$, and phases, $\Lambda_{\mathbf{a}_{wm,i}}(f_j)$, for each frequency component f_j of $\mathbf{a}_{wm,i}(t)$
7. Correct the amplitude components of $\mathbf{a}_{wm,i}(t)$ by scaling with the ratio of the $\eta_t(t)$ and $\eta_{r,i}(t)$ amplitude components:
$$\mathcal{A}_{\mathbf{a}_{wm,i+1}}(f_j) = \frac{\mathcal{A}_{\eta_t}(f_j)}{\mathcal{A}_{\eta_{r,i}}(f_j)}\mathcal{A}_{\mathbf{a}_{wm,i}}(f_j)$$
8. Correct the phase components of $\mathbf{a}_{wm,i}(t)$ by summing the phase with the difference between the $\eta_t(t)$ and $\eta_{r,i}(t)$ phase components:
$$\Lambda_{\mathbf{a}_{wm,i+1}}(f_j) = \Lambda_{\mathbf{a}_{wm,i}}(f_j) + \left[\Lambda_{\eta_t}(f_j) - \Lambda_{\eta_{r,i}}(f_j)\right]$$
9. Construct $\mathbf{a}_{wm,i+1}(t)$ using the inverse Fourier transform of the corrected amplitude $\mathcal{A}_{\mathbf{a}_{wm,i+1}}(f_j)$ and phase $\Lambda_{\mathbf{a}_{wm,i+1}}(f_j)$ components
10. Repeat Steps 4 – 9, either for a maximum number of iterations or until a threshold for a pre–defined error metric, between $\eta_t(t)$ and $\eta_{r,i}(t)$, is reached

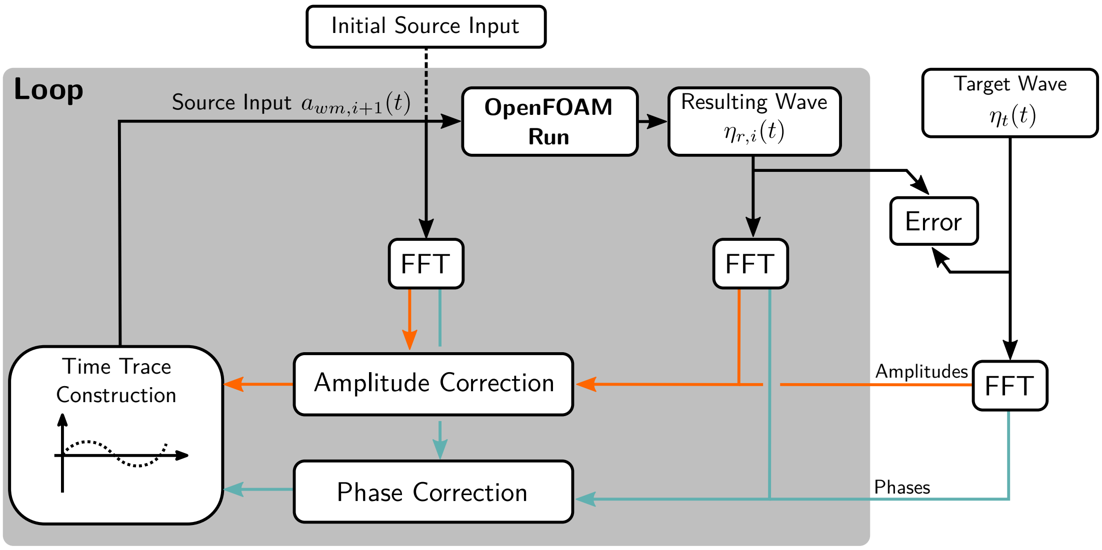

Figure 6.2: Schematic of the calibration method.

Regular waves

For regular waves, the phase of the wave is generally not of interest, allowing simplification of the calibration, where the amplitude of $\mathbf{a}_{wm,i}(t)$ is simply tuned to create the regular waves of a desired height. The period of the surface wave is directly proportional to the oscillation period of $\mathbf{a}_{wm,i}(t)$. The following calibration method is used for regular waves:

1. Define the source term, for instance, as:

   $$\mathbf{a}_{wm,i}(t) = A_{\mathbf{a}_{wm},i} \sin(\omega_{wm}\, t)\,,$$

   where ω_{wm} is equal to the angular wave frequency ω.
2. Initialise the amplitude $A_{\mathbf{a}_{wm},i}$ with an arbitrary value
3. Run the OpenFOAM simulation for calibration iteration i, using $\mathbf{a}_{wm,i}(t)$ and extract the surface elevation at the location of interest
4. Determine the mean wave height, $\bar{H}_{r,i}$, of the resulting wave in a pre–defined temporal interrogation window
5. Correct $A_{\mathbf{a}_{wm},i}$ based on the ratio of the target wave height, H_t, and $\bar{H}_{r,i}$ following:

   $$A_{\mathbf{a}_{wm},i+1} = ({}^{H_t}/_{\bar{H}_{r,i}}) A_{\mathbf{a}_{wm},i}$$
6. Repeat steps 3 – 5, either for a maximum number of iterations or until a threshold for a pre–defined error metric, between the target and the resulting wave, is reached.

It should be noted that the linear calibration methods used for the calibration of irregular and regular waves has an inherent limitation in its applicability to highly non–linear waves and, thus, also cannot capture effects such as bound harmonics. It should, however, also be noted that this is a limitation of the calibration method, not of the impulse source wave maker. Implementing non–linear calibration methods, more accurate results could potentially be achieved for non–linear waves.

6.1.3 Illustrative examples

In the following, illustrative examples are presented with two main objectives: firstly, to demonstrate the capabilities of the impulse wave maker and the self–calibration procedure in producing wave trains in deep, intermediate, or shallow water conditions at a specified location in a CFD–based NWT. The second objective is to provide guidance on the selection of the geometric parameters of the source region by investigating the effect that the size and position of the source region has on the resulting waves. It might be expected that a very wide source region will decrease accuracy, whereas a very short source region will require very large velocity components to create a target wave. For the shallow water impulse wave maker presented in [107], a source width of about a quarter to half a wave length is recommended. In shallow water, the entire water column, from the sea floor up to the water surface, performs an oscillating motion whereas, in deep water, only part of the water column is affected, and the wave motion does not extend to the sea floor. It is thus an interesting question how to choose the width and height of the source region to achieve optimal results. Furthermore, the influence of the user–define parameters of the numerical beach (i.e. L_B and $s_{b,\mathsf{Max}}$) on the absorption capabilities are investigated.

Target waves

To demonstrate the ability of the impulse source wave maker, unidirectional multi–frequency focused wave groups are generated at a specified location in the CFD–based NWT. The focused wave groups are a realisation of the NewWave formulation as presented in Section 3.3. Three different focused wave groups for deep, intermediate, and shallow water conditions are considered. The wave characteristics for the different waves are listed in Table 6.1.

While, for the deep and intermediate water case, the wavelength is kept constant, the water depth is equal for the deep and shallow water case. It should be noted that the choice of the parameters for the shallow water case requires care to avoid breaking waves. Time traces for the free surface elevation η[3] and plots of the spectral density function, SDF, are shown in Figure 6.3 for all three focused wave groups.

To illustrate the generation of regular waves, three regular waves in deep, intermediate, and shallow water conditions are considered. The wave characteristics follow the definition in Table 6.1 such that the target wave height is set to $H_t = 2A_0$ and the wave period is $T = T_p$.

---

[3] For the remainder of this section, the dependence on t and f is omitted for clarity

Table 6.1: Wave characteristics for the focused wave groups: water depth d, peak amplitude A_0, peak period T_p, peak wave length λ_p, peak–to–trough height, H_{PT}

	d [m]	A_0 [m]	T_p [s]	λ_p [m]	d/λ_p [–]	H_{PT} [m]
Deep water	0.74	0.020	0.975	1.48	0.50	0.038
Intermediate water	0.25	0.020	1.100	1.48	0.17	0.038
Shallow water	0.74	0.015	6.000	15.9	0.05	0.027

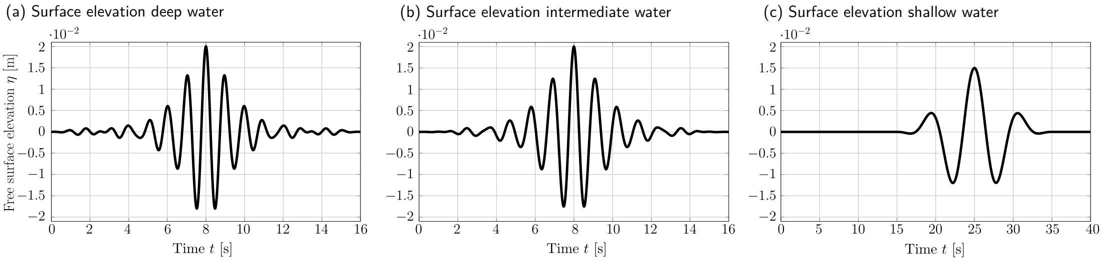
(a) Surface elevation deep water (b) Surface elevation intermediate water (c) Surface elevation shallow water

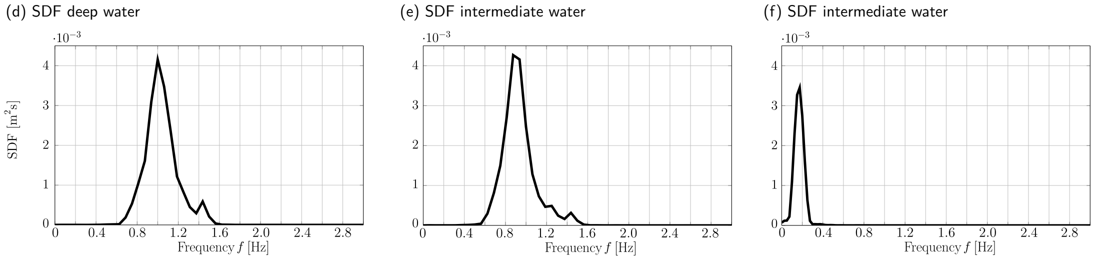
(d) SDF deep water (e) SDF intermediate water (f) SDF intermediate water

Figure 6.3: Target focused wave groups considered in the illustrative examples: free surface elevation η (a, b, c) and SDF (d, e, f) for the deep, intermediate, and shallow water case, respectively.

Numerical wave tank

The setup of the 2D NWT follows the generic setup depicted in Figure 6.1. An impulse source region of width w_s and height h_s, with its centroid position at a water depth of $d/2$, is located two wave lengths up–wave of the location of interest, at which the free surface elevation is measured[4]. To investigate the influence of the size of the source region, 90 (30 for each water condition) complete calibration runs with a maximum number of nine iterations are performed with varying source region layouts. The width of the source region w_s is parametrised by the peak wave length of the focused wave group λ_p. Five different widths are considered, i.e. $0.125\lambda_p$, $0.25\lambda_p$, $0.5\lambda_p$, $0.75\lambda_p$, $1\lambda_p$. The height of the source region h_s is parametrised by the water depth d. Six different heights are considered, i.e. $0.125d$, $0.25d$, $0.5d$, $0.75d$, $1d$, $1.25d$.

Two numerical beaches are located towards the left– and right–hand side of the source region. The left–hand side beach starts at a distance of 1.5λ away from the source centre. The right–hand side beach starts at a distance of 3.0λ away from the

---

[4] Note that the term 'measured' refers to numerically measured for the remainder of this chapter

source centre. The optimal lengths of the numerical beaches are determined for the deep, intermediate, and shallow water case individually as discussed in Section 6.1.4. Section 6.1.4 also includes the convergence studies, performed to determine sufficient spatial and temporal discretisation sizes.

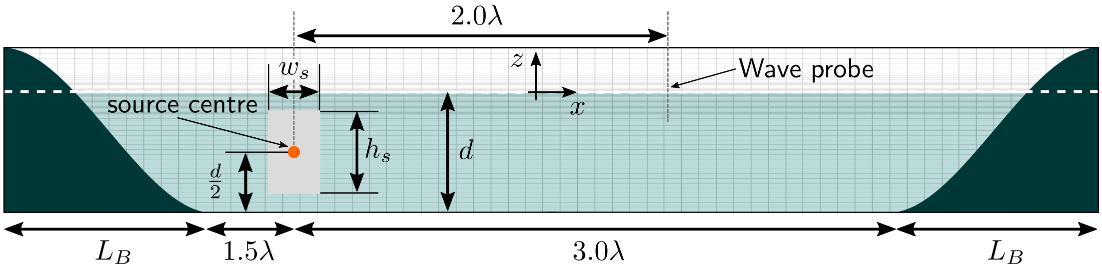

Figure 6.4: Schematic (not at scale) of the domain layout used for the illustrative examples with all relevant dimensions. The left– and right–hand side boundaries, as well as the bottom boundary, are defined as no–slip walls. The top boundary is defined as atmospheric outlet. The optimal length of the numerical beaches is determined for the deep, intermediate, and shallow water case individually.

6.1.4 Results and discussion

In this section, the results of the illustrative example are presented and discussed. Initially, preliminary results of the convergence study and the optimisation of the numerical beach settings are presented. Subsequently, example results are shown to highlight the performance of the calibration procedure. Next, the influence of the source region geometry on the quality of the three focused wave groups is examined. Finally, the capability of the impulse source wave maker to generate regular waves is illustrated.

Preliminaries

The spatial and temporal discretisation sizes are determined through convergence studies, following the procedure outlined in Section 4.3.2. For the spatial discretisation, the grid size in the z-direction (see Figure 6.4) is parametrised by the wave height defined, here, as $H = 2A_0$. It should be noted that, for simplicity, the grid sizes are kept constant between the deep, intermediate, and shallow water cases. Thus, the smallest A_0 of the three cases is considered for the parametrisation of the grid size to ensure convergence for all three test cases. The grid size in the x-direction is defined through the grid aspect ratio of 4. Three different grid sizes, i.e. 5, 10, and 20 CPH, are considered and the peak–to–trough wave height measured at the location of interest (see Figure 6.4) is used as the input to the convergence study. The results of the convergence study for the deep, intermediated, and shallow water case are listed in Tables 6.2, 6.3, and 6.4, respectively.

Tables 6.2 – 6.4 also include the results for the temporal convergence study. For the illustrative examples in this section, variable time stepping, based on the CFL condition and a maximum Courant number Co_{max}, is employed. Three different values of Co_{max}, i.e. 0.1, 0.2, and 0.4, are considered.

Table 6.2: Spatial and temporal convergence: Deep water case.

Spatial

Co$_{\mathsf{max}}$	Δz =5CPH	Δz =10CPH	Δz =20CPH	Convergence type	$\mathcal{U}$
0.2	$3.55 \cdot 10^{-3}$m	$3.72 \cdot 10^{-3}$m	$3.80 \cdot 10^{-3}$m	Monotone	4.00%

Temporal

Δz	Co$_{\mathsf{max}} = 0.4$	Co$_{\mathsf{max}} = 0.2$	Co$_{\mathsf{max}} = 0.1$	Convergence type	$\mathcal{U}$
10CPH	$3.68 \cdot 10^{-3}$m	$3.72 \cdot 10^{-3}$m	$3.73 \cdot 10^{-3}$m	Monotone	0.68%

Table 6.3: Spatial and temporal convergence: Intermediate water case.

Spatial

Co$_{\mathsf{max}}$	Δz =5CPH	Δz =10CPH	Δz =20CPH	Convergence type	$\mathcal{U}$
0.2	$3.74 \cdot 10^{-3}$m	$3.91 \cdot 10^{-3}$m	$3.98 \cdot 10^{-3}$m	Monotone	2.13%

Temporal

Δz	Co$_{\mathsf{max}} = 0.4$	Co$_{\mathsf{max}} = 0.2$	Co$_{\mathsf{max}} = 0.1$	Convergence type	$\mathcal{U}$
10CPH	$3.88 \cdot 10^{-3}$m	$3.91 \cdot 10^{-3}$m	$3.93 \cdot 10^{-3}$m	Monotone	1.70%

Table 6.4: Spatial and temporal convergence: Shallow water case.

Spatial

Co$_{\mathsf{max}}$	Δz =5CPH	Δz =10CPH	Δz =20CPH	Convergence type	$\mathcal{U}$
0.2	$2.94 \cdot 10^{-3}$m	$2.95 \cdot 10^{-3}$m	$2.96 \cdot 10^{-3}$m	Monotone	0.18%

Temporal

Δz	Co$_{\mathsf{max}} = 0.4$	Co$_{\mathsf{max}} = 0.2$	Co$_{\mathsf{max}} = 0.1$	Convergence type	$\mathcal{U}$
10CPH	$2.94 \cdot 10^{-3}$m	$2.95 \cdot 10^{-3}$m	$2.95 \cdot 10^{-3}$m	Monotone	1.12%

Based on the results of the convergence study shown in Tables 6.2 – 6.4, a grid size of 10CPH and a maximum Courant number Co_{max} of 0.2 delivers converged solutions with acceptable grid uncertainties $\mathcal{U}$ for the deep, intermediate, and shallow water cases. These discretisation sizes are used for all subsequent simulations in this section. To determined the optimal, i.e. most efficient, settings for the numerical beaches for the deep, intermediate, and shallow water focused wave group cases, the reflection coefficient, R, is considered. Following Mansard and Funke [561], R is calculated following

$$R = \frac{\hat{S}_{\eta\,\mathsf{R}}}{\hat{S}_{\eta\,\mathsf{I}}} \cdot 100\% \,, \tag{6.3}$$

where $\hat{S}_{\eta\,\mathsf{I}}$ is the peak value of the spectral density of the incident wave at a frequency f_p. $\hat{S}_{\eta\,\mathsf{R}}$ is the spectral density of the reflected wave at f_p. To separate the incident and reflected wave field, a three point method is proposed in [561], where the free surface elevation time traces are measured at three different wave probes that are spaced at specific relative distances from each other. Based on the guidelines provided in [561], the distance between wave probe 1 (WP1) and wave probe 2 (WP2) is set to $\lambda_p/10$, and the distance between WP1 and wave probe 3 (WP3) is set to $\lambda_p/4$. Table 6.5 lists the reflection coefficients determined for the deep, intermediate, and shallow water focused wave group cases in NWT domains with varying beach length L_B and maximum damping factors $s_{b,\mathsf{Max}}$. The results in Table 6.5 indicate a varying reflection coefficient, i.e. numerical beach efficiencies, depending on the beach length and the maximum damping factor. While decreasing values of $s_{b,\mathsf{Max}}$ generally lead to larger reflection coefficients, longer beach lengths result in decreased reflection coefficients. The results clearly highlight the flexibility of the employed numerical beach implementation allowing, for instance, the tuning of the beach properties to a specific experimental test facility, for accurate validation studies. For the subsequent simulations in this section, a beach length of 1λ, 2λ, and 3λ is used for the shallow, deep, and intermediate water cases, respectively. Those lengths, together with $s_{b,\mathsf{Max}} \geq 6$, result in reflection coefficients of $R \leq 1.5\%$ for all test cases which, compared to reflection coefficients achieved in experimental test facilities, can be considered low [573, 574].

Calibration procedure

To illustrate the capabilities of the employed calibration procedure, the normalised root–mean square error (nRMSE) between the target and the resulting wave train (see Equation (6.4)) is monitored over a number of calibration iterations, where:

$$\mathsf{nRMSE} = \sqrt{\frac{\sum_{i=1}^{n}\left[\digamma(i) - \hat{\digamma}(i)\right]^2}{n}}\,\frac{100\%}{\mathcal{N}} \,, \tag{6.4}$$

Table 6.5: Reflection coefficients for different lengths and damping coefficients of the numerical beach.

Deep water conditions				
Maximum damping factor $s_{b,\mathsf{Max}}$ [s^{-1}]	1.5	3	6	12
Numerical beach length $L_B = 1\lambda$	28.52%	17.39%	4.81%	3.42%
Numerical beach length $L_B = 2\lambda$	1.29%	0.37%	0.69%	0.51%
Intermediate water conditions				
Maximum damping factor $s_{b,\mathsf{Max}}$ [s^{-1}]	1.5	3	6	12
Numerical beach length $L_B = 1\lambda$	53.53%	48.46%	37.64%	14.43%
Numerical beach length $L_B = 2\lambda$	22.66%	14.68%	6.36%	1.22%
Numerical beach length $L_B = 3\lambda$	1.58%	0.67%	0.16%	0.30%
Shallow water conditions				
Maximum damping factor $s_{b,\mathsf{Max}}$ [s^{-1}]	1.5	3	6	12
Numerical beach length $L_B = 1\lambda$	3.28%	2.52%	1.03%	1.44%

where $\mathcal{F} = \eta_r$ and $\hat{\mathcal{F}} = \eta_t$. n defines the signal length via the number of samples and normalisation is achieved by $\mathcal{N}$, defined as the peak–to–trough height H_{PT} of η_t. Furthermore, the time traces of the target free surface elevation and the resulting free surface elevation can be inspected.

By way of example, Figure 6.5 shows the values of the nRMSE over nine calibration iterations[5] for the deep water case and an impulse source size of $w_s = 0.25\lambda$ and $h_s = 0.5d$. Note that the evolution is non–monotonic, which is explained by Figure 6.6, showing the corresponding surface elevation time traces for a selection of the calibration iterations shown in Figure 6.5.

The first iteration is initialised with a random input of small amplitude, and the resulting surface elevation is almost zero (Figure 6.6 (a)), resulting in a relatively large nRMSE. Progressing in the calibration procedure, iteration 3 yields the largest nRMSE. Figure 6.6 (b) highlights that the peak frequency is already captured in the resulting wave train; however, the wave amplitude, specifically towards the tail of the signal, is over–estimated. After this maximum nRMSE, the error decreases monotonically for iterations 4, 5, and 6. At iteration 6, the nRMSE has decreased by approximately one order of magnitude compared to iteration 3. This is highlighted in the free surface elevation time trace in Figure 6.6 (c). Deviations can mostly be observed between $0s \leq t \leq 5s$ and $11s \leq t \leq 16s$. Progressing further in the calibration procedure, only marginal changes in the nRMSE can be observed,

---

[5] Each calibration iteration requires a runtime of the order of $1000\,$s.

highlighted in the free surface elevation time trace in Figure 6.6 (d). Compared to iteration 6, slightly better agreement between the target and the resulting free surface elevation is achieved at the tail of the wave train.

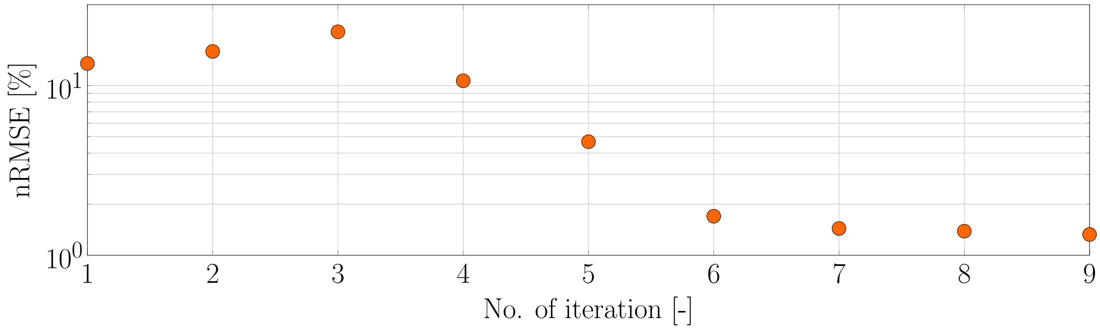

Figure 6.5: Evolution of the nRMSE over nine calibration iterations.

(a) Iteration 1

(b) Iteration 3

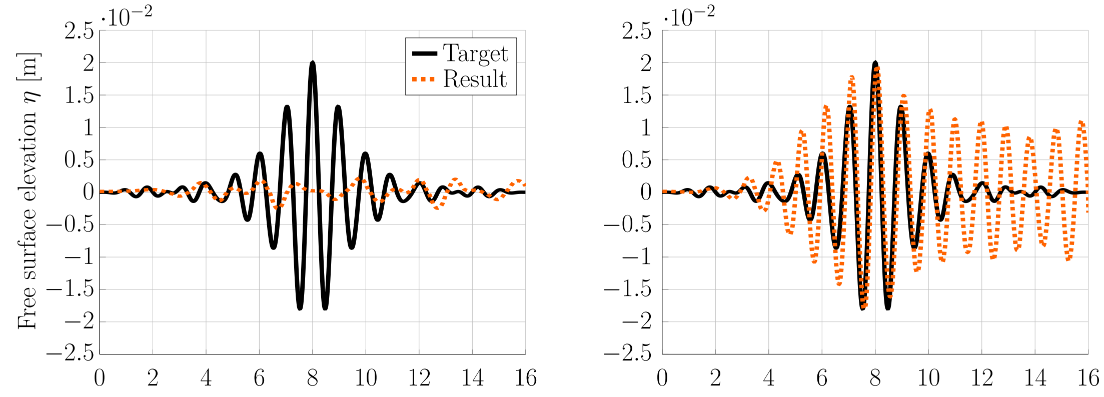

(c) Iteration 6

(d) Iteration 9

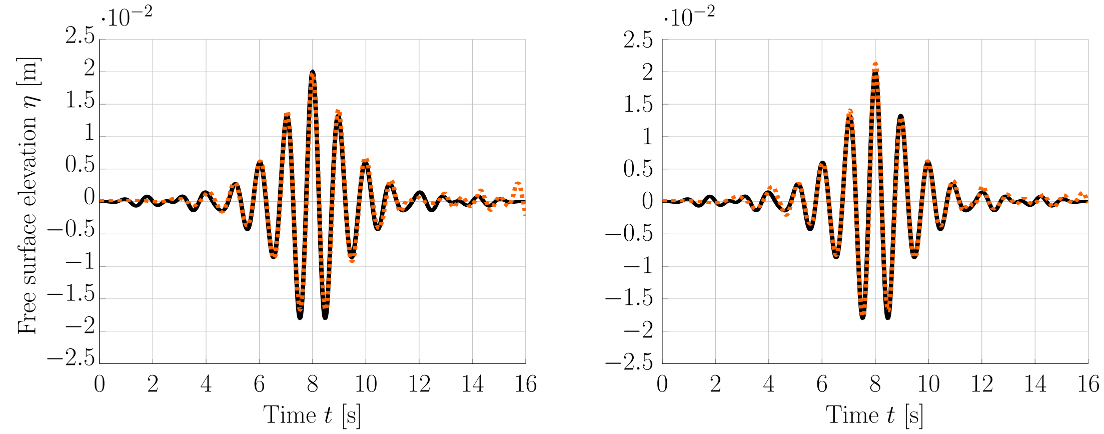

Figure 6.6: Target and resulting free surface elevation for (a) iteration 1, (b) iteration 3, (c) iteration 6, (d) iteration 9.

Focused waves groups

Figures 6.7 (a)–(c) show the results of the minimum nRMSE (see Equation (6.4)) within one calibration run for the different source layouts in deep, intermediate, and shallow water conditions. The simulated data points are marked with black dots and the surfaces in between are interpolated. The top row of Figures 6.7 (a)–(c) shows a 3D view and the bottom row of Figures 6.7 (a)–(c) shows a 2D plane view.

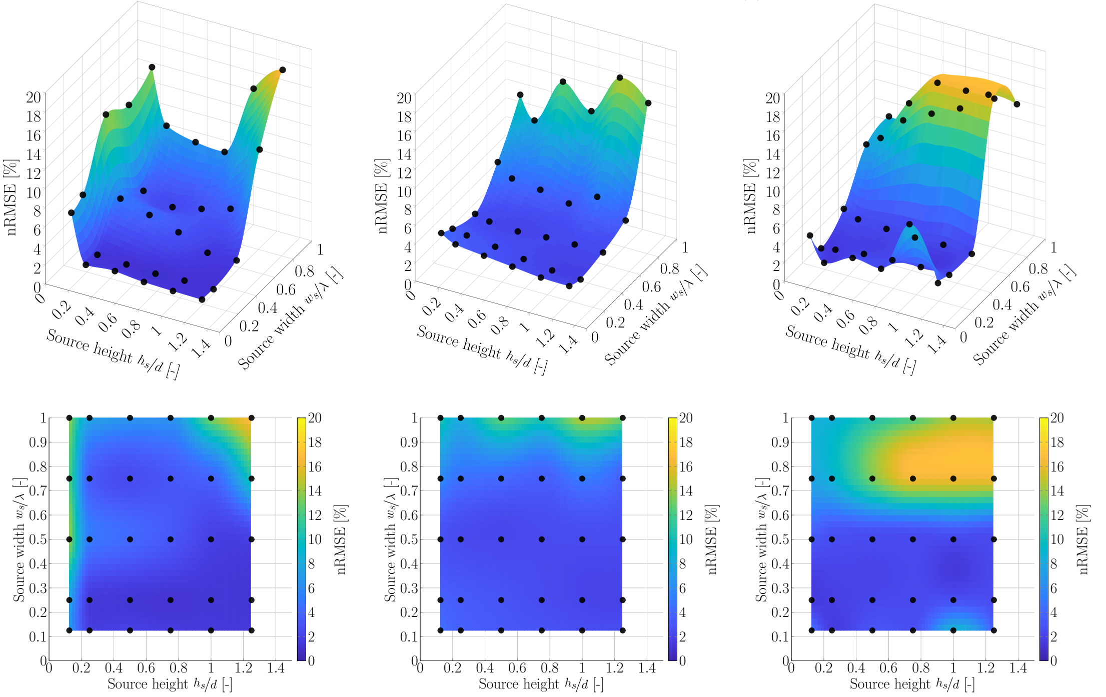
(a) Deep water (b) Intermediate water (c) Shallow water

Figure 6.7: nRMSE values over the source geometry parameter space for the (a) deep, (b) intermediate and (c) shallow water case. 3D view in the top row and 2D plane view in the bottom row. The interpolation points are marked in black.

Some trends can be observed in Figures 6.7 (a)–(c). The nRMSE shows a significant dependency on the source width, with decreasing error values for decreasing source widths. Moving from $w_s = 1\lambda$ to $w_s = 0.5\lambda$, a significant drop in the nRMSE from $\sim 20\%$ to $\sim 5\%$ can be observed. Decreasing the source width even further, the nRMSE only shows relativity small variations.

Analysing the influence of the source height, overall smaller variations for the tested values are observed, in particular for source widths $< 0.5\lambda$. For $w_s < 0.5\lambda$, in deep and intermediate water conditions, larger source heights generally result in smaller values of the nRMSE. For the deep water case, with $h_s \geq 0.25d$ and $w_s \leq 0.25\lambda$, a plateau in the nRMSE can be observed. For the intermediate water case, this plateau spans all source heights for $w_s \leq 0.5\lambda$. The shallow water case shows slightly more scattered values of the nRMSE for $w_s < 0.5\lambda$. Two distinct peaks can be observed for $w_s = 0.125\lambda$ & $h_s = 0.125d$ and $w_s = 0.125\lambda$ & $h_s = 1d$. The latter peak is of particular interest, since it is expected that, due to the shallow water condition, a source region spanning the complete width of the water column should deliver accurate results. The minimum values of the nRMSE are found for $w_s = 0.25\lambda$ & $h_s = 0.75d$, $w_s = 0.25\lambda$ & $h_s = 1.25d$, and $w_s = 0.25\lambda$ & $h_s = 0.125d$ for the deep (nRMSE$= 1.3\%$), intermediate (nRMSE$= 2.0\%$), and shallow water case (nRMSE$= 1.5\%$), respectively. The corresponding free surface elevation time traces are shown in Figures 6.8 (a)–(c). Formulating guidelines for the setup of the impulse source wave maker, source regions of a width of $w_s = 0.25\lambda$ and heights of $h_s \geq 0.75d$ are suggested for deep and intermediate water conditions. For shallow water conditions, source regions of a width of $w_s = 0.25\lambda$ and heights of $h_s \leq 0.5d$ are suggested. Generally, it can be stated that sufficient agreement between the target and resulting focused wave groups (nRMSE$\leq 5.0\%$) can be achieved over a wide range of parameters.

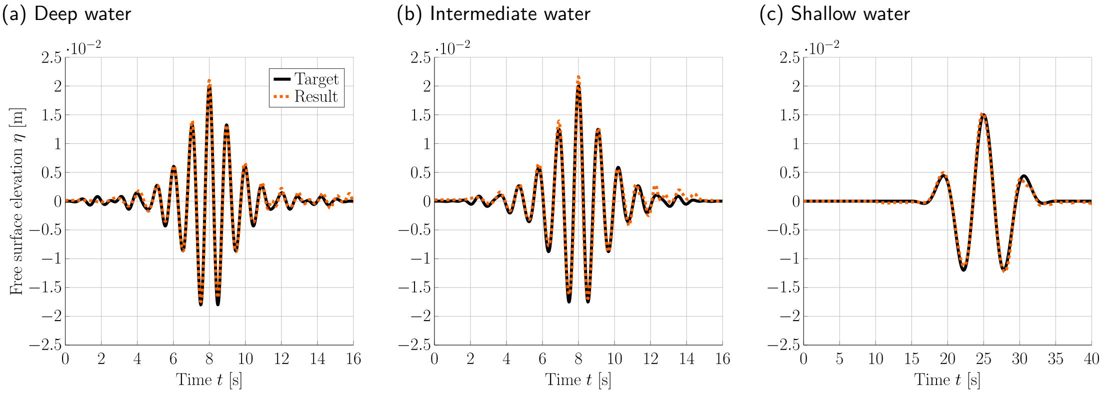
(a) Deep water (b) Intermediate water (c) Shallow water

Figure 6.8: Free surface elevation time traces with the minimum nRMSE between the target and resulting free surface elevation from the parametric study on the source region layout for (a) deep, (b) intermediate, and (c) shallow water conditions.

Regular waves

The source region layout found during the analysis of the three focussed wave groups is used to illustrate the capabilities of the impulse source wave maker to generate regular waves. Applying the calibration method for regular waves outlined in Section 6.1.2, the surface elevation and the relative error, $\epsilon_{\bar{H}_{r,i},H_t}$ following Equation (6.5), can be monitored over several calibration iterations.

$$\epsilon_{\bar{H}_{r,i},H_t} = \frac{\bar{H}_{r,i} - H_t}{H_t} \cdot 100\% \,, \tag{6.5}$$

where $\bar{H}_{r,i}$ is determined through phase averaging (see Section 6.2.1).

Figures 6.9 (a)–(c) shows the phase averaged free surface elevation over four calibration iterations for the deep, intermediate, and shallow water case, respectively[6]. The corresponding relative errors between the resulting and the target wave height are listed in Table 6.6.

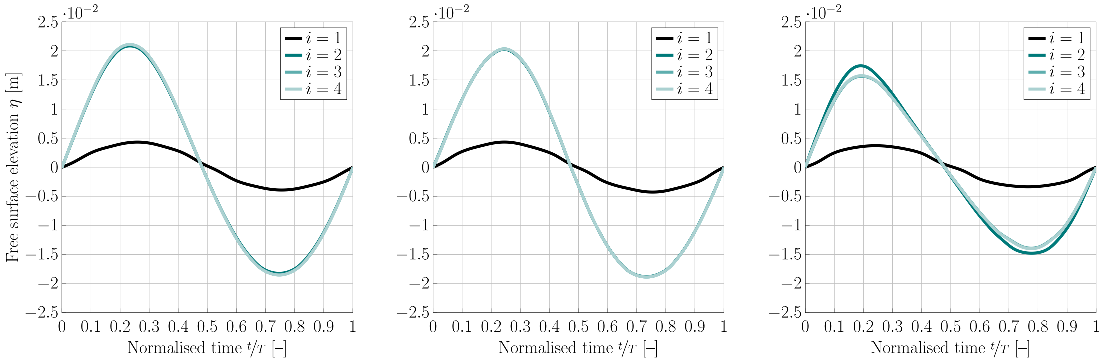
(a) Deep water

(b) Intermediate water

(c) Shallow water

Figure 6.9: Phase averaged resulting free surface elevation for the (a) deep, (b) intermediate, and (c) shallow water regular wave case over four calibration iterations. The corresponding relative errors between the resulting and the target wave height are listed in Table 6.6.

Table 6.6: Error $\epsilon_{\bar{H}_{r,i},H_t}$ between the target and resulting wave height for the deep, intermediate, and shallow water regular waves cases.

No. of iteration	1	2	3	4
Deep water	-79.2%	-1.6%	-0.4%	-0.3%
Intermediate water	-78.3%	-1.6%	-1.2%	-1.2%
Shallow water	-76.3%	8.1%	-0.7%	-0.1%

From the results in Figure 6.9 and Table 6.6, it can readily be observed that a significant improvement of the resulting wave height with respect to the target wave height is achieved, with a drop in $\epsilon_{\bar{H}_{r,i},H_t}$ of approximately one order of magnitude after just one calibration iteration. In calibration iterations 3 and 4, fine tuning of the acceleration input to the impulse source is performed with marginal changes in the surface elevation, leading to small changes in $\epsilon_{\bar{H}_{r,i},H_t}$. For the deep and shallow water cases minimum errors of $|\epsilon_{\bar{H}_{r,i},H_t}| \leq 0.4\%$ are achieved, while the intermediate water case shows a slightly larger minimum error of -1.2%. In all cases, the resulting wave height is underestimated with respect to the target wave height.

---

[6] Also for the regular wave case each calibration iteration requires a runtime of the order of $1000\,\mathrm{s}$.

6.2 Assessment of numerical wave makers

After the closer look at the impulse source wave maker in Section 6.1, the remainder of this chapter is focussed on the general assessment of numerical wave makers. A variety of numerical wave makers have been developed for the purpose of wave generation and absorption in CFD–based NWTs (see Section 4.3.3). Therefore, to select the most appropriate numerical wave maker for a given problem, knowledge of the relative strengths and weaknesses for each numerical wave maker is important. The decision matrix for the selection of a numerical wave maker may comprise criteria such as:

- Performance of the numerical wave maker, measured by the accuracy of the generated wave field, the efficiency of wave absorption, and the computational cost
- Availability of the numerical wave maker methods in a specific CFD toolbox
- Prior user experience

While the availability and user experience are subjective decision drivers, the performance of a numerical wave maker can be objectively and quantitatively assessed. This section proposes an assessment framework based on three key parameters: accuracy, computational requirement, and available features.

- *Accuracy*: CFD–based NWTs are utilised when high accuracy is required; otherwise, lower fidelity NWTs with less computational cost can be used. Since the accuracy of the numerical wave maker limits the overall accuracy of the entire CFD–absed NWT, it is the most important metric to quantify when assessing different numerical wave makers. To that end, several test cases and evaluation metrics are introduced in Section 6.2.1.
- *Computational requirements*: The various numerical wave makers place differing amounts of additional computational burden on the CFD–based NWT, which affect the overall runtime of the simulation. When selecting a numerical wave maker, those with lower computational requirements (and comparable accuracies) are obviously preferable. Therefore, quantifying the relative computational requirements of the numerical wave makers is a key part of any assessment. The computational requirements can be quantified by the run time, t_{run}, normalised by the simulated time, t_s, and the normalised run time per cell. For a fair comparison, any influence from parallelisation schemes should be avoided and simulations should be performed on a single core of a dedicated server. Furthermore, solver settings and numerical solution schemes should be consistent, to avoid bias.

- *Available features*: Unlike the previous two quantitative performance parameters, the available features of a numerical wave maker are more qualitative, considering factors such as the range of implemented wave theories, application to deep and shallow water conditions, coupling to external wave propagation models (see Section 5.2.2), and required calibration methods. The assessment of the available features is presented in a binary fashion.

The generalised assessment metrics presented in the remainder of this section are designed to:

- Gain an understanding of the general accuracy of numerical wave makers
- Draw attention to features and pitfalls, specific to certain numerical wave makers
- Aid in the choice of 'the best' numerical wave maker method for a given application
- Provide guidance on the setup of the different numerical wave makers

Due to the large number of different numerical wave maker implementations, the metrics are delivered in a general form, so that readers can apply these metrics to their specific numerical wave maker for evaluation. An illustrative example is shown at the end of this chapter to demonstrate the general applicability of the proposed assessment methodologies and metrics. The example comprises several different numerical wave makers (implemented in OpenFOAM) for which the accuracy and computational cost are assessed over a range of different wave conditions. The available features are, as mentioned previously, assessed in a binary fashion.

6.2.1 Assessment metrics

This section describes the proposed test cases and metrics for the quantitative assessment of a numerical wave maker. First, the error produced by the numerical wave maker must be isolated from the other error sources in the CFD–based NWT setup. It its well known that CFD–based NWTs incur some level of general modelling inaccuracy, stemming from the numerical solution process, such as:

- Uncertainty due to spatial and temporal discretisation
- Artificial numerical wave damping
- Sensitivity to solver settings and solution schemes
- Numerical wave probes, used to monitor the free surface elevation

Next, the accuracy of the wave generation and absorption should be assessed independently, spanning a range of wave conditions.

General modelling inaccuracies – Discretisation

To isolate the general modelling inaccuracies from those produced by the numerical wave maker, a simple wave propagation test case, without numerical wave makers, as proposed in [575], is considered. In this test case, a free surface wave is initiated[7] in a domain of length $n \cdot \lambda$, with $n = 1, 2, \ldots$, and cyclic boundary conditions, so that the wave continuously propagates through the domain (see Figure 6.10). During the course of the simulation, characteristic measures, such as wave height or velocity profiles, can be monitored for a number of wave cycles. Laminar flow conditions are assumed and the viscosity of the two fluids, i.e. air and water, is set to zero, effectively reducing the problem to inviscid flow. This removes any dissipation due to viscous effects and allows for an assessment of pure numerical dissipation of energy.

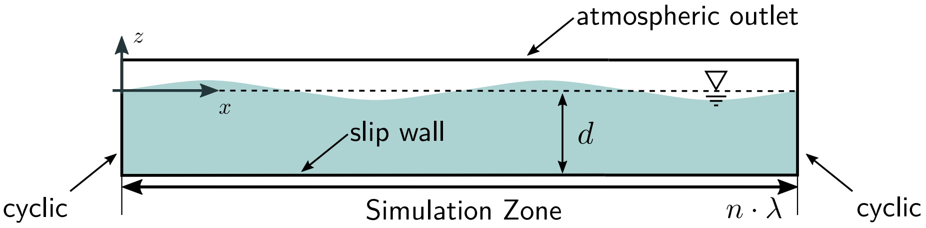

Figure 6.10: Generalised domain layout of length $n \cdot \lambda$ and cyclic boundary conditions at the left– and right–hand side boundaries for the wave propagation test case.

As discussed in Section 4.3.2, the solution of the flow quantities in CFD–based NWTs is dependent on the domain discretisation in space and time. To remove any parasitic influence of the discretisation level on the solution, convergence studies must be performed. The convergence study follows the procedure detailed in Section 4.3.2 and the relative grid uncertainty $\mathcal{U}$ is henceforth referred to as metric #1 for the remainder of this chapter.

The input quantity to the convergence study is the measured mean phase averaged wave height, $\bar{H}_{\mathsf{m}}(x_n)$[8], which can be calculated using the following procedure:

(m1.i) Throughout the complete run of the simulation, record the free surface elevation data, $\eta(x_n, t)$, at a specific location x_n.

(m1.ii) Split the $\eta(x_n, t)$ time trace into individual periods, $\eta_i(x_n, t^*)$, where $t^* \in [0, T]$ and i is the number of periods, using a zero crossing analysis.

---

[7] The free surface wave is initiated by simply setting the velocity and α_{VF} field, based on wave theory along the NWT.

[8] Throughout the remainder of this section, the dependency on x and t is specifically declared when not clear from the context.

(m1.iii) Using several periods, $j \in [i_1, i_1 + j]$, calculate the wave height, $H_{\mathsf{m}\,j}(x_n)$, following

$$H_{\mathsf{m}\,j}(x_n) = |\min[\eta_j(x, t^*)]| + \max[\eta_j(x_n, t^*)] \tag{6.6}$$

(m1.iv) Calculate the mean phase averaged wave height $\bar{H}_{\mathsf{m}}(x_n)$ following

$$\bar{H}_{\mathsf{m}}(x_n) = \frac{1}{j}\sum_{i=i_1}^{i_1+j} H_{\mathsf{m}\,j}(x_n) \tag{6.7}$$

General modelling inaccuracies – Solvers and schemes

The accuracy of the VOF method can be dependent on solver settings and solution schemes (see Section 4.2.2) applied in the numerical framework [69, 575]. These factors are very specific to the CFD solver and should be chosen based on best practice and user experience. However, it is desirable to carry out sensitivity studies to ensure satisfying results. The solver settings and solution schemes largely influence the underlying numerical model, but not necessarily the numerical wave maker. Thus, the generic wave propagation test case can be considered to analyse the sensitivity of the CFD–based NWT results to the solver settings and solution schemes.

To quantify the influence of the solver settings and solution schemes, the relative deviation of the measured wave height H^*_{m} to the initialised wave height, H_{init}, is considered, following

$$\epsilon_{H^*_{\mathsf{m}}} = \frac{H^*_{\mathsf{m}} - H_{\mathsf{init}}}{H_{\mathsf{init}}} \cdot 100\% \,. \tag{6.8}$$

In particular, H^*_{m} is the wave height of the same wave, monitored at a specific location, each time it passes the wave probe. ϵ_{H_m} is henceforth referred to as metric #2 for the remainder of this chapter.

General modelling inaccuracies – Numerical wave damping

VOF methods can suffer from interface smearing, leading to numerical wave damping and, subsequently, inaccuracies in the measured wave height (see Section 4.3.1). Thus, the numerical damping of free surface waves should be assessed as part of the quantification of the general model inaccuracies. Numerical wave damping can be assessed using the generic wave propagation test and metric #2 (see Equation (6.8)).

General modelling inaccuracies – Numerical wave probes

Various types of numerical wave probes are available which utilise different techniques to measure the free surface elevation. These techniques all incur some level of inherent inaccuracy while tracking the free surface interface. Although the tracking of the surface elevation in the CFD–based NWT is a pure post–processing step, independent of the solution of the governing equation, it is important to first quantify the achievable accuracy of the numerical wave probes used in the assessment of the numerical wave maker. However, the accuracy of a numerical wave probe can only be determined by comparing the results measured with different wave probes.

Wave generation – Regular waves

For a regular wave, the accuracy of the wave generation is evaluated by comparing two different measures against wave theory: (1) the generated wave height; and (2) the fluid velocity profile beneath a wave crest/trough (see Section 3.1.2). The generalised domain layout utilised for the assessment is depicted in Figure 6.11. A simulation zone is specified with a length of $n \cdot \lambda$, with $n = 1, 2, \ldots$. The up–wave extension (UExt) of the domain may vary, depending on the specific numerical wave maker due to, e.g., the relaxation zone or the numerical beach length. To focus purely on wave generation, the down–wave extension (DExt) of the domain should be pseudo-infinite, which eliminates the possibility of reflected waves from the far field boundary and the need to implement a wave absorption method.

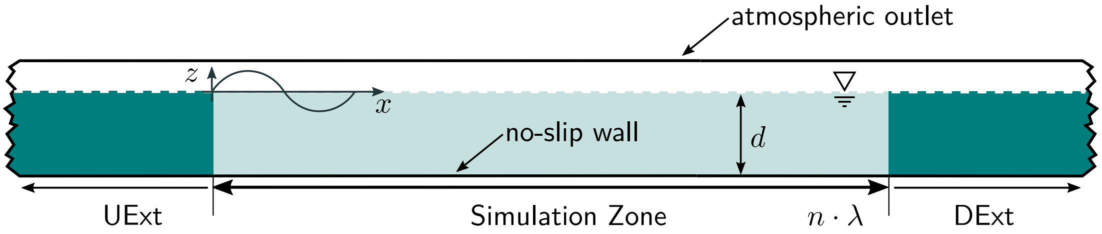

Figure 6.11: Generalised domain layout for the assessment of wave generation accuracy: A simulation zone of $n \cdot \lambda$ length is used. Depending on the specific test case and numerical wave maker, the length of the up–wave (UExt) and down–wave (DExt) extension may vary.

The evaluation metric for the generated wave height is the error, $\epsilon_{\bar{H}_\mathrm{m}}(x_n)$, of the measured mean phase averaged wave height $\bar{H}_\mathrm{m}(x_n)$ and the desired theoretical wave height, H_Theory. To evaluate wave dissipation over the length of the simulation zone, the error $\epsilon_{\bar{H}_\mathrm{m}}(x_n)$ is evaluated at different locations x_n along the simulation zone. The values for $\epsilon_{\bar{H}_\mathrm{m}}(x_n)$ are obtained using the following procedure:

(m3.i) Calculate $\bar{H}_\mathrm{m}(x_n)$ based on steps (m1.i)–(m1.iv). Note that the first period, i_1, should be chosen large enough to ensure that any wave periods in the transient part of the signal $\eta(x_n, t)$ are excluded.

(m3.ii) Calculate the the upper ($\bar{H}^+_{\mathsf{m}}(x_n)$) and lower bounds ($\bar{H}^-_{\mathsf{m}}(x_n)$) of $\bar{H}_{\mathsf{m}}(x_n)$:

$$\bar{H}^{\pm}_{\mathsf{m}}(x_n) = \bar{H}_{\mathsf{m}}(x_n) \pm \sigma_{H_{\mathsf{m}}}(x_n)\,, \tag{6.9}$$

where $\sigma_{H_{\mathsf{m}}}(x_n)$ is the standard deviation of $H_{\mathsf{m}}(x_n)$

(m3.iii) Calculate the relative error $\epsilon_{\bar{H}_{\mathsf{m}}}(x_n)$, following

$$\epsilon_{\bar{H}_{\mathsf{m}}}(x_n) = \frac{\bar{H}^{\pm}_{\mathsf{m}}(x_n) - H_{\mathsf{Theory}}}{H_{\mathsf{Theory}}} \cdot 100\% \tag{6.10}$$

$\epsilon_{\bar{H}_{\mathsf{m}}}(x_n)$ is henceforth referred to as metric #3 for the remainder of this chapter.

The wave induced fluid velocity beneath the free surface should decrease exponentially with depth, following the theoretical profile (see Section 3.1.2). Beneath a wave crest or trough, the fluid velocity should also be purely horizontal with a zero vertical component. Therefore, the wave generation accuracy is assessed by comparing the measured horizontal fluid velocity $u_\eta(x_n, z_m)$ against the theoretical equivalent $u_{\eta\,\mathsf{Theory}}(x_n, z_m)$ at specific points in space x_n and $z_m \in [-d, 0]$. Note that, for the wave crest and trough, the accuracy must not be assessed at $z_m = -d$, since wave theories, generally, do not take the no–slip condition at the tank floor into account. To quantify the accuracy of the velocity profile generated by the wave maker, the error, $\epsilon_{\bar{u}_\eta}(x_n, z_m)$, between measured and theoretical horizontal velocity, is calculated, using the following procedure:

(m4.i) Throughout the course of the simulation, extract the numerical horizontal velocity profile $u_\eta(t, x_n, z_m)$.

(m4.ii) Select a number of time instances $j \in [i_1, i_1 + j]$ so that the surface elevation $\eta(x_n, t)$ at $t = t_j$ and locations x_n corresponds to either a wave crest or a wave through. Again, care should be taken when choosing the time instances j, so that t_{i_1} is large enough to exclude any transient part of the wave signal.

(m4.iii) At each specific combination of horizontal, x_n, and vertical, z_m, locations, calculate the mean horizontal velocity profile, $\bar{u}_\eta(x_n, z_m)$ (see Equation (6.11)).

$$\bar{u}_\eta(x_n, z_m) = \frac{1}{j}\sum_{i=i_1}^{i_1+j} u_\eta(t_i, x_n, z_m) \tag{6.11}$$

(m4.iv) Calculate the error $\epsilon_{\bar{u}_\eta}(x_n, z_m)$ along the water column between theoretical and measured horizontal velocity at the specific location x_n for the wave crest and trough, following:

$$\epsilon_{\bar{u}_\eta}(x_n, z_m) = \frac{\bar{u}^{\pm}_\eta(x_n, z_m) - u_{\eta\,\mathsf{Theory}}(x_n, z_m)}{u_{\eta\,\mathsf{Theory}}(x_n, z_m)} \cdot 100\%\,, \tag{6.12}$$

with

$$\bar{u}^{\pm}_\eta(x_n, z_m) = \bar{u}_\eta(x_n, z_m) \pm \sigma_{u_\eta}(x_n, z_m) \tag{6.13}$$

$\epsilon_{\bar{u}_\eta}(x_n, z_m)$ is henceforth referred to as metric #4 for the remainder of this chapter.

Wave generation – Irregular waves

Synthesised irregular waves deliver a realistic representation of the physical ocean environment by building up a wave spectrum through superposition of a finite number of waves (see Section 3.2). To evaluate the wave generation accuracy for irregular waves, the nRMSE (see Equation (6.4)) between the theoretical (input) wave spectrum[9], $S_{\eta,\text{Theory}}$, and the measured average (output) wave spectrum, $\bar{S}_{\eta,\text{m}}$, at specific locations x_n, along the simulation zone, is considered. The spectral density distribution is calculated at a specific location by performing a FFT on the measured free surface elevation data $\eta(x_n, t)$. The initial part of $\eta(x_n, t)$ should be excluded from the FFT calculation, since most numerical wave makers induce waves into a CFD–based NWT with initially calm water. Thus, there is a subsequent ramp up time for the irregular waves to be fully developed. This ramp-up time differs for each location x_n along the CFD–based NWT and the $\eta(x_n, t)$ time trace (snippet) should hence be chosen such that it covers a fully developed sea state. Since synthesised irregular wave are a superposition of a finite number of waves with distinct frequencies, the wave length and celerity of the shortest (slowest travelling) wave in the irregular wave can easily be determined from the known frequency components. Depending on the distance between the evaluation location and the wave generation boundary, the travel time of this shortest wave can be determined and provides an estimate of the time required for a fully developed irregular waves to reach a specific location in the CFD–based NWT. Furthermore, the statistical nature of an irregular wave requires long simulation times to accurately evaluate $S_{\eta,\text{m}}$ from the FFT [576]. For the CFD–based NWT simulation, this would require extremely long domains to avoid wave reflection from the far field boundary. Alternatively, several shorter simulations, with varying random phases, can be run and the results are averaged to yield a good approximation of the statistical properties of the irregular wave. Following recommendations given in [576], four sets of $50T_p$–long time traces with differing random phases yield statistically converged solutions. Averaging of the measured wave spectrum $S_{\eta,\text{m}}$ of the different sets yields $\bar{S}_{\eta,\text{m}}$. Consequently, in Equation (6.4), $\mathcal{F} = \bar{S}_{\eta,\text{m}}$, $\hat{\mathcal{F}} = S_{\eta,\text{Theory}}$, and $\mathcal{N} = \max(S_{\eta,\text{Theory}})$. The nRMSE is henceforth referred to as metric #5 for the remainder of this chapter.

---

[9] Note that the theoretical input wave spectrum refers to the spectrum used within the numerical wave maker to describe the desire irregular wave.

Wave absorption – Standing wave

The quality of waves generated in the CFD–based NWT can be affected by the wave maker's ability to handle waves travelling towards the wave generation boundary. The presence of walls and fixed (or floating) bodies in the CFD–based NWT can cause waves to be reflected/radiated back towards the wave generator. Thus, the numerical wave maker must be able to absorb these reflected/radiated waves, in addition to generating the desired wave field.

To assess the wave absorption ability of the numerical wave maker at the wave generator, a standing wave test case is proposed. Generating a regular wave in the CFD–based NWT with a fully reflective wall opposite the wave generator (see Figure 6.12) leads to the build–up of a standing wave. If no re–reflection occurs from the wave generation boundary, the mean height of the measured standing wave, $\bar{H}_{\text{msw}}(x_n)$ (determined via phase averaging, see (m1.i)–(m1.iv)), should be twice the theoretical wave height H_{Theory}, or slightly less, due to wave dissipation. The metric for evaluating the absorption ability of the wave generator is the relative deviation between $\bar{H}_{\text{msw}}(x_n)$ and H_{Theory}, following

$$\epsilon_{\bar{H}_{\text{msw}}}(x_n) = \frac{\bar{H}^{\pm}_{\text{msw}}(x_n) - 2H_{\text{Theory}}}{2H_{\text{Theory}}} \cdot 100\% \,. \tag{6.14}$$

Any deviation $|\epsilon_{\bar{H}_{\text{msw}}}(x_n)| > 0\%$ indicates re–reflection occurring from the wave generation boundary. $\epsilon_{\bar{H}_{\text{msw}}}(x_n)$ is henceforth referred to as metric #6 in the remainder of this chapter.

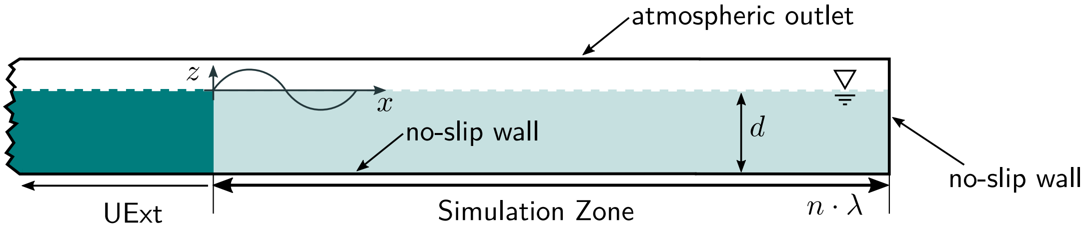

Figure 6.12: Generalised domain layout for the assessment of wave absorption at the wave generator with a fully reflective wall at the down–wave domain boundary. Depending on the numerical wave maker, the length of the up–wave extension may vary.

Wave absorption – Regular and irregular waves

The capability of absorbing waves travelling from the generation boundary towards the far field boundary is crucial for an efficient CFD–based NWT. The far field boundary must absorb the incoming waves to prevent undesired reflections back into the simulation zone, contaminating the generated wave field. Wave reflection, quantified by the reflection coefficient R (see Equation (6.3)), should ideally be eliminated ($R = 0\%$), or at least minimised ($R << 10\%$), by the numerical wave maker at the far field boundary. The domain layout for the analysis of the reflection coefficient is depicted in Figure 6.13, including the distances between the three wave probe locations, following [561].

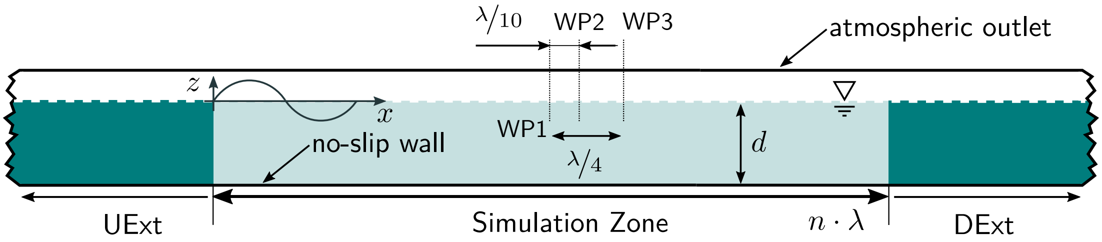

Figure 6.13: Generalised domain layout for the assessment of wave absorption efficiency: A simulation zone of $n \cdot \lambda$ length is used. Depending on the specific test case and numerical wave maker, the length of the up–wave and down–wave extension may vary. Three wave probes are placed in the CFD–based NWT with a specific distance between each other to comply with the requirements for the reflection analysis.

6.2.2 Overview of Evaluation Metrics

To summarise the above proposed assessment metrics and methodologies, Table 6.7 lists the different metrics, their application, the quantity, and its unit.

Table 6.7: Overview of the evaluation metrics.

Metric #	Application	Quantity	Unit	Equation #
1	Discretisation uncertainty	$\mathcal{U}$	[%]	(4.28)
2	Sensitivity to solution schemes, solver setting, and numerical wave damping	$\epsilon_{H^*_\mathsf{m}}$	[%]	(6.8)
3	Wave generation of regular waves (wave height)	$\epsilon_{\bar{H}_\mathsf{m}}(x_n)$	[%]	(6.10)
4	Wave generation of regular waves (velocity profiles)	$\epsilon_{\bar{u}_\eta}(x_n, z_m)$	[%]	(6.12)
5	Wave generation of irregular waves	nRMSE	[%]	(6.4)
6	Wave absorption at generation boundary	$\epsilon_{\bar{H}_\mathsf{msw}}(x_n)$	[%]	(6.14)
7	Wave absorption at the far field boundary	R	[%]	(6.3)

6.2.3 Illustrative example

Given the vast number of available CFD solvers and numerical wave maker implementations, as well as the virtually infinite number of wave conditions, it is impossible to assess all potential combinations in a single study. The assessment metrics and methodologies have hence been presented in a general form, to be straightforwardly applied by interested readers to their specific wave maker implementation and setup at hand. However, an illustrative example is presented in the following, to show the applicability of the metrics and methodologies proposed in Section 6.2.1. While results for the illustrative example are shown in Section 6.2.4, this section introduces the considered test cases, wave conditions, and the numerical framework.

Test cases

Wave propagation test cases are considered for the quantification of general modelling inaccuracies, i.e. discretisation uncertainty, sensitivity to solution schemes and solver setting, and numerical wave damping. Regular waves (in deep and shallow water conditions), as well as an irregular wave train in deep water, are used to assess the performance of the numerical wave makers in terms of wave generation and wave absorption (at the generation boundary and the far field boundary). The complete test matrix is shown in Table 6.8.

Table 6.8: Test matrix for the illustrative example.

	Wave propagation test	**Regular waves**		**Irregular waves**
	Deep water	Deep water	Shallow water	Deep water
Discretisation uncertainty	●	–	–	–
Schemes and solver settings	●	–	–	–
Numerical wave damping	●	–	–	–
Wave generation	–	●	●	●
Wave absorption at the wave generation boundary	–	●	–	–
Wave absorption at the far field boundary	–	●	●	●

Input waves

Three types of unidirectional, long crested waves are considered to assess the numerical wave makers: Regular waves in both deep and shallow water, and an irregular wave train in deep water. The characteristics of these input waves are listed in Table 6.9. The peak period T_p, the significant wave height H_s, and the water depth d of the irregular wave, represent realistic open–ocean conditions at sites such as BIMEP in the Bay of Biscay [18]. The period T and the wave height H for the deep water regular wave are derived from the irregular wave. The shallow water regular wave is then derived from the deep water regular wave, such that the wave height was kept constant, which simplified the setup of the numerical domain. Theoretical time traces of the free surface elevation for the deep and shallow water regular waves are plotted in Figures 6.14 (a) and (b), respectively. The locations of the deep and shallow water regular wave in the Le Méhauté diagram [41] are shown in Figure 6.14 (c). The SDF of the irregular wave train is shown in Figure 6.14 (d).

Table 6.9: Sea states characteristics.

	T (T_p) [s]	H (H_s) [m]	d [m]	λ (λ_p) [m]	d/λ [–]	Wave Theory
Regular waves						
Deep Water	8	1.5	70	100	0.70	2nd order Stokes
Shallow Water	19	1.5	7	163	0.04	Cnoidal wave theory
Irregular wave						
Deep Water	8	1.5	70	100	0.70	JONSWAP

(a) 2nd order Stokes wave

(b) Cnoidal wave

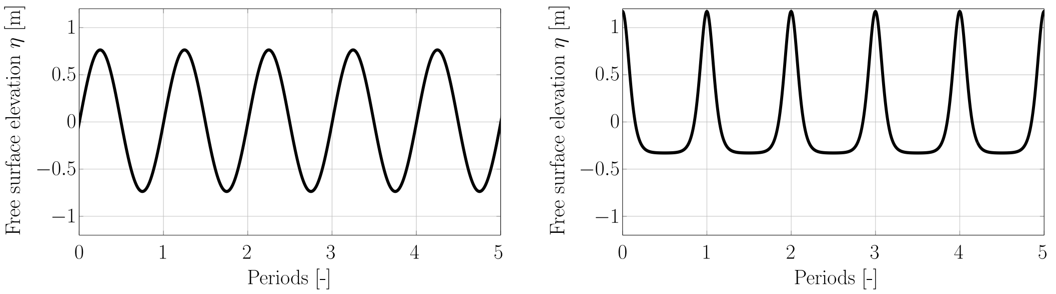

(c) Location in the wave theory diagram

(d) SDF of the irregular wave

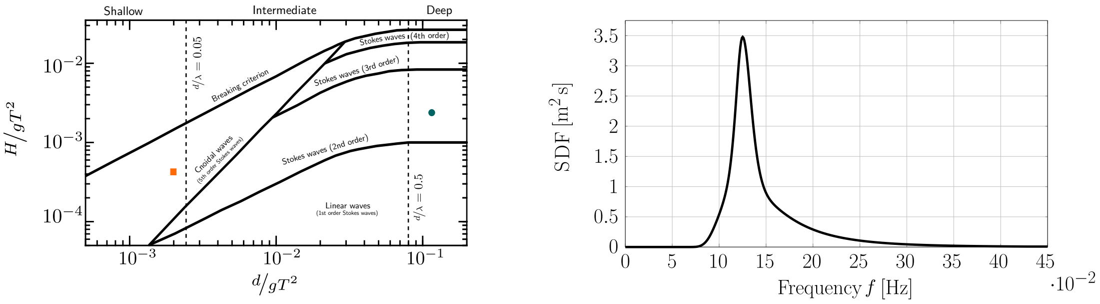

Figure 6.14: Theoretical time traces for the (a) deep water regular wave, (b) shallow water regular wave, (c) the location in the Le Méhauté diagram, and (c) the spectral density function for the irregular wave train.

Numerical wave tanks

In the illustrative example, all numerical simulations are performed using the open source CFD software OpenFOAM, specifically version 6.0 of the OpenFOAM Foundation fork [577]. All simulations are run on a Dell PowerEdge machine with 48 GB RAM and Intel Xeon(R) E5-2440 processors with 2.4 GHz[10]. The specific numerical wave makers are:

---

[10] Note that, for the comparison of the computational requirements, simulations are run on a single core of the dedicated machine.

- A relaxation zone method as implemented in the *waves2Foam* toolbox [578] (as of September 2018), henceforth referred to 'RZM'
- A static boundary method as implemented in the *olaFLOW* toolbox [579] (as of September 2018), henceforth referred to 'SBM (ola)'
- A static boundary method as implemented in OpenFOAM 6.0 [577] (as of September 2018), henceforth referred to 'SBM (OF)'
- A dynamic boundary method as implemented in the *olaFLOW* toolbox [579] (as of September 2018), henceforth referred to 'DBM'
- An impulse source wave maker as detailed in Section 6.1, henceforth referred to 'ISM'

For all test cases, a 2D numerical domain is considered, due to the consideration of purely uni-directional waves. The simulation zone is set to a length of 2λ, while the up– and down–wave extensions may vary depending on the specific numerical wave maker. In the OpenFOAM framework, different numerical wave probes are available. Three different probe types are selected in this illustrative example:

- Wave probes using the integral approach, implemented as an in–house wave probe, henceforth referred to as 'ihWP'. The in–house wave probe evaluates surface elevation in the following way:
  - The user specifies the vector of the wave probe position $\mathbf{x}_{\mathsf{WP}} = [x_{\mathsf{WP}}\, y_{\mathsf{WP}}\, z_{\mathsf{WP}}]$ and the resolution r_{WP}
  - A search vector $\mathbf{v}_s$ is defined as $\mathbf{v}_s = \left[0\, 0\, \frac{|z_{\mathsf{Max}} - z_{\mathsf{WP}}|}{r_{\mathsf{WP}}}\right]$, where z_{Max} is the maximum value in the z–direction of the domain bounding box
  - Starting from the probe position $\mathbf{x}_{\mathsf{WP}}$, the method then iterates in the z–direction, summing the values of α_{VF}, following

    $$\alpha_{\mathsf{VF},S} = \sum_{i=1}^{r_{\mathsf{WP}}} \alpha_{\mathsf{VF}}(\mathbf{x}_{\mathsf{Eval},i})$$

    where $\mathbf{x}_{\mathsf{Eval},i} = \mathbf{x}_{\mathsf{Eval},i-1} + \mathbf{v}_s$, with $\mathbf{x}_{\mathsf{Eval},0} = \mathbf{x}_{\mathsf{WP}}$
  - The surface elevation location $\mathbf{x}_\eta = [x_{\mathsf{WP}}\, y_{\mathsf{WP}}\, z_\eta]$ is then evaluated as:

    $$z_\eta = z_{\mathsf{WP}} + \frac{\alpha_{\mathsf{VF},S}}{r_{\mathsf{WP}}} \cdot (|z_{Max} - z_{\mathsf{WP}}|)$$

  For all simulations performed in the illustrative example, the resolution r_{WP} was set to 500.
- Wave probes using the integral approach, as implemented in OpenFOAM 6.0 [580], henceforth referred to as 'OFWP'. The OFWP differs from the ihWP such that the user has no control over the resolution. Furthermore, while in the ihWP the wave probe position z_{WP} should be placed underneath the free surface interface, the OFWP always iterates over the whole domain bounding box.

- Wave probes sampling the iso–surface $\alpha_{\mathsf{VF}} = 0.5$, henceforth referred to as 'isoWP'

Results of the different wave probes for the various test cases are presented throughout the illustrative example. Note that this selection does not cover all available wave probes in the OpenFOAM toolbox. Alternative wave probes are for example implemented in the *waves2Foam* toolbox.

6.2.4 Results and discussion

This section presents the results and discussion of the illustrative example. First, the general modelling inaccuracies are analysed. Then, wave generation and wave absorption capabilities are assessed for the different wave conditions.

General modelling inaccuracies – Discretisation

The assessment of the general modelling inaccuracies utilises the generic wave propagation in a CFD–based NWT with cyclic boundaries test case, depicted in Figure 6.10. Waves, characteristic of the deep water regular wave in Table 6.9, are initialised in the tank at $t = 0$.
Three uniform grids with incrementally decreasing cell sizes, i.e. 5, 10, and 20 CPH, are considered for the grid convergence study. Considering cell aspect ratios of 1, this results in cell sizes of 333, 666 and 1332 CPL, respectively. Temporally, the problem is discretised using fixed time steps with a time step size of 400 time steps Δt per wave period T, i.e. $T/\Delta t = 400$, for the spatial convergence study.
Simulations in the cyclic domain are performed for a simulated time of $t_{\mathsf{s}} = 3T$. As stated in Section 4.3.2, the grid convergence methodology proposed by [88], [92], and [93] takes a single measure for each grid size as input. Therefore, the mean phase averaged wave height (see Equation (6.7)) was determined at a location $x = \lambda$ (i.e. the centre of the numerical domain). The resulting wave heights for each grid size and from different wave probes, as well as the convergence characteristics and the relative grid uncertainty $\mathcal{U}$, are listed in Table 6.10.

Table 6.10: Spatial convergence.

	$\Delta z = 5$CPH	$\Delta z = 10$CPH	$\Delta z = 20$CPH	Convergence type	$\mathcal{U}$
ihWP	1.483m	1.493m	1.494m	Monotone	$< 0.01\%$
OFWP	1.486m	1.494m	1.496m	Monotone	0.02%
isoWP	1.491m	1.493m	1.497m	–	–

Table 6.10 shows that the spatial discretisation converges for a vertical resolution of 10CPH, with a resulting relative grid uncertainty of the order of 0.01%. It should be pointed out that the ihWP and OFWP indicate monotonic convergence, while the isoWP indicates divergence. This inconsistency, however, is due to the relatively small differences in mean phase–averaged wave height found with the isoWP wave probe. Generally, the difference in mean phase–averaged wave height between the three considered wave probes, for a grid resolution of 10CPH, is $< 0.1\%$ of the target wave height.

In addition to the free surface elevation, the velocity profile along the water column is an important, but often neglected, quantity for free surface waves and is thus considered in the convergence study. The definition of a single measure, to be used in the convergence study, is not straightforward for the velocity profile. Hence, visual inspection of the profile was used.

Figures 6.15 (a) and (b) shows the velocity profile measured at $x_n = \lambda$, i.e. the centre of the domain, at a single time instance, representing a wave crest and trough, respectively. The close ups of the velocities in the vicinity of the free surface and the bottom wall clearly show that a cell size of 10CPH does not yet deliver converged results in terms of the velocity profile. This suggests that a cell size of 20CPH should be considered throughout the presented illustrative examples. Note that no further discretisation size, i.e. 40CPH, is considered in this convergence study since this would lead to an excessive cell count, unsuitable for engineering purposes. Furthermore, a discretisation size of 10CPH – 20CPH is consistent with the findings from the reviewed literature in Chapter 5.

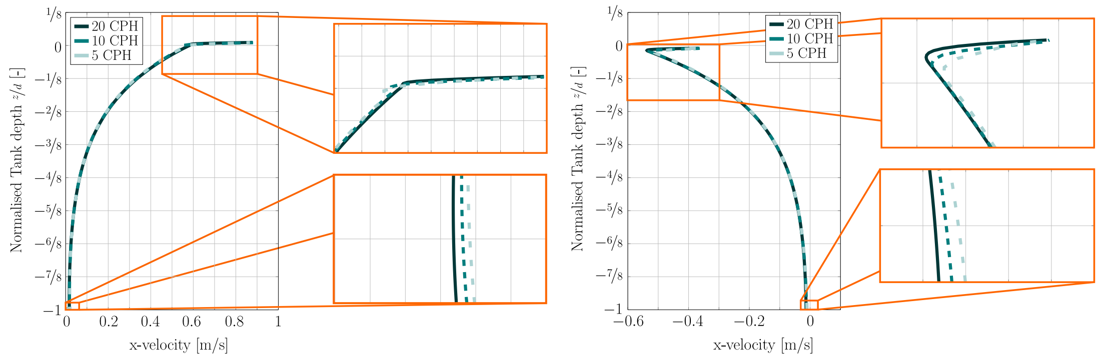

(a) Wave crest

(b) Wave trough

Figure 6.15: Velocity profiles extracted along the tank depth for the (a) wave crest and (b) wave trough for three different discretisation sizes.

After defining the required spatial discretisation, a convergence study on the temporal discretisation is performed along the same lines as the spatial discretisation. Using a uniform mesh with 20CPH and 1332CPL, the temporal discretisation was varied between $T/\Delta t = 200$, 400, and 800. The results for the phase averaged wave height, alongside the convergence characteristic and the relative grid uncertainty, are listed in Table 6.11 for the three different wave probes. The results consistently show monotonic convergence and relative grid uncertainty of the order of 0.05%. Furthermore, inspection of the velocity profiles at the crest and trough time instances, for the different temporal discretisation sizes, shows virtually no difference. For brevity, the profiles are not plotted here.

Table 6.11: Temporal convergence.

	$T/\Delta t = 200$	$T/\Delta t = 400$	$T/\Delta t = 800$	Convergence type	$\mathcal{U}$
ihWP	1.482m	1.494m	1.496m	Monotone	0.06%
OFWP	1.484m	1.496m	1.498m	Monotone	0.06%
isoWP	1.488m	1.497m	1.498m	Monotone	0.04%

Although the temporal convergence is determined based on the wave propagation test case, the numerical wave makers may also show some dependency on the time step size. Thus, the dependency of the numerical wave maker performance on the time step size is assessed throughout the following sections.

In the spatial convergence studies, a uniform grid with cubic cells was used. For engineering applications, such a discretisation is not desirable, due to the high cell count. It is rather desired to reduce the required cell count by using different refinement levels and/or mesh grading within the numerical wave tank. Five additional mesh layouts are considered to test the influence of non–uniform meshes on the resulting surface elevation and velocity profile. Figure 6.16 schematically depicts the mesh layouts for the uniform mesh and mesh layouts #1–#5. Layouts #1–#4 only feature different mesh refinement levels, while layout #5, the final mesh layout (see Figure 6.17), also includes grading in the vertical z–direction.

Table 6.12 shows the relative deviation, $\mathrm{d}\bar{H}_{\#i}$, following Equation (6.15), where $\bar{H}_{\mathrm{m},\#i}$ is the mean measured phase averaged wave height for mesh layout #1–#5, and $\bar{H}_{\mathrm{uf}}$ is the phase averaged wave height from the uniform mesh.

$$\mathrm{d}\bar{H}_{\#i} = \frac{\bar{H}_{\mathrm{m},\#i} - \bar{H}_{\mathrm{uf}}}{\bar{H}_{\mathrm{uf}}} \cdot 100\% \tag{6.15}$$

In addition, the runtime, as well as the relative cell count, C_r, for each mesh layout, following Equation (6.16), is listed in Table 6.12.

$$C_r = \frac{\text{cell count}_{\text{Mesh }\#\text{i}}}{\text{cell count}_{\text{Uniform}}} \tag{6.16}$$

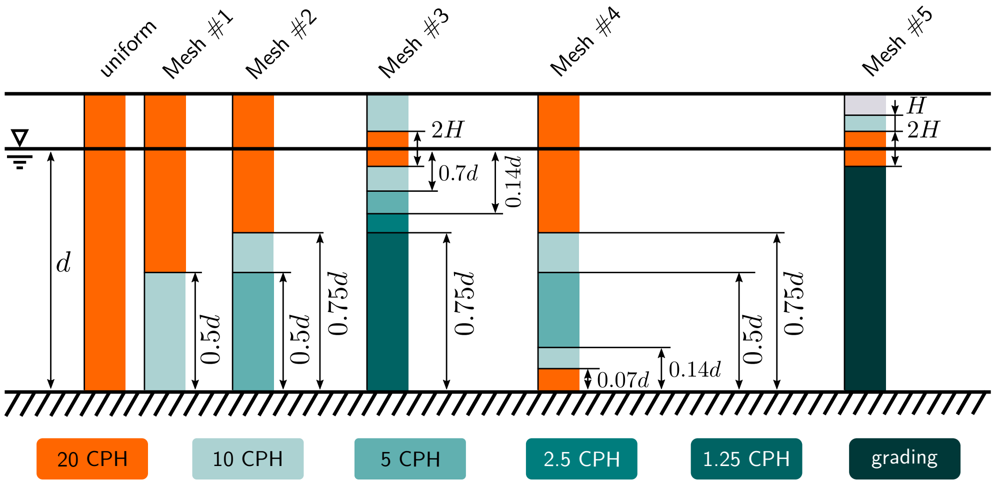

Figure 6.16: Examples of different meshes using varying refinement layers along the water column: Different colours mark different mesh sizes, parametrised by the wave height (Schematic not at scale).

Table 6.12: Relative deviation d$\bar{H}_{\#i}$ of the phase average wave height for different mesh layouts.

		Uniform	Mesh #1	Mesh #2	Mesh #3	Mesh #4	Mesh #5
C_r	[-]	1	0.66	0.46	0.77	0.11	0.04
runtime	[s]	~ 100k	~ 63k	~ 56k	~ 11k	~ 61k	~ 5k
ihWP	[%]	0.0	< -0.1	0.1	0.2	0.2	-0.1
OFWP	[%]	0.0	< -0.1	0.1	0.1	< 0.1	< 0.1
isoWP	[%]	0.0	< -0.1	< 0.1	0.1	0.1	0.0

The relative deviation in wave height shows relatively small scatter over the range of mesh layouts and wave probes with a maximum values of 0.2%.

Inspection of the velocity profiles along the water column at wave crest and trough time instances (see Figure 6.18 (a)/(c) and (b)/(d), respectively), reveals only relatively small deviations close to the free surface. However, close to the bottom wall, larger differences are visible. Interestingly, even meshes with similar cell sizes, in the vicinity of the bottom wall, compared to the uniform mesh (i.e., mesh layout #4 and mesh layout #5), show relatively large differences in the velocity close to the wall.

This makes a clear definition of *the correct* spatial discretisation difficult, if uniform meshes with large cell counts are to be avoided. As a trade–off, mesh layout #5 is chosen, delivering results in 'the middle' of the solution spectrum (see Figure 6.18 (a)/(c) and (b)/(d)) at a relatively low cell count ($C_r = 0.04$).

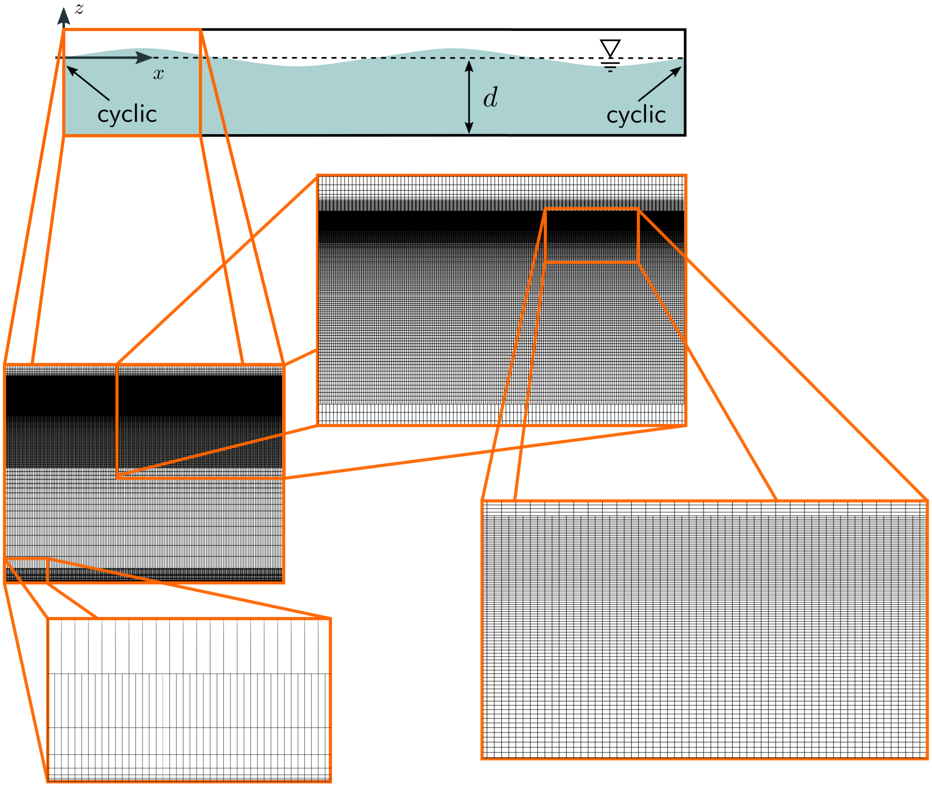

Figure 6.17: Screenshot of the final spatial discretisation of the CNWT with mesh layout #5.

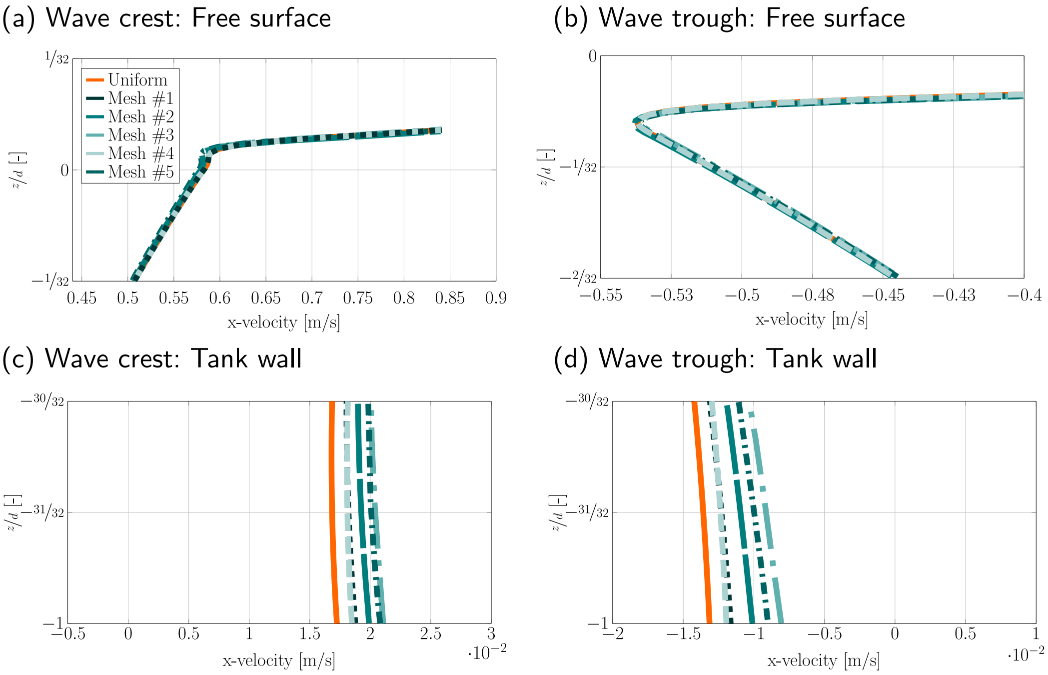
(a) Wave crest: Free surface

(b) Wave trough: Free surface

(c) Wave crest: Tank wall

(d) Wave trough: Tank wall

Figure 6.18: Velocity profiles extracted along the tank depth for the wave crest (a)/(c) and the wave trough (b)/(c) for different meshes using varying refinement layers along the water column according to Figure 6.16.

General modelling inaccuracies – Solvers and schemes

In the OpenFOAM toolbox, users have the option to select specific solution schemes and solver settings for their simulations (see Chapter 4). Based on appropriate tutorial cases, different solution schemes and solver settings are tested to determine the sensitivity to these settings. Initially, a number of cases with different discretisation schemes for the time derivatives and divergences are tested. The test matrix is listed in Table 6.13. For brevity, the considered divergence schemes are limited to divergence related to the water volume fraction α_{VF}, i.e. $\nabla \cdot \mathbf{u}\alpha_{\mathsf{VF}}$ and $\nabla \cdot [\mathbf{u_r}\alpha_{\mathsf{VF}}(1-\alpha_{\mathsf{VF}})]$. The solver settings are kept constant throughout these test cases, and refer to test case #1 in Table 6.14. The sensitivity of the simulation results to solver settings and solution schemes is evaluated and quantified using metric #2 (see Equation (6.8)), i.e. the relative deviation between the measured wave height H^*_{m} and the initialised wave height H_{init}. The results are shown in Figure 6.19 (a). Furthermore, the normalised run time t_{run}/t_s, as a quantification of the computational cost, is listed in Table 6.13.

Table 6.13: Test matrix for the sensitivity analysis to numerical solution schemes.

Case #	Time derivative schemes	Divergence schemes		t_{run}/t_s
		$\nabla \cdot \mathbf{u}\alpha_{\mathsf{VF}}$	$\nabla \cdot [\mathbf{u_r}\alpha_{\mathsf{VF}}(1-\alpha_{\mathsf{VF}})]$	
1	Euler	TVD (`MUSCL` [1])	`interfaceCompression`	255
2	Crank–Nicolson ($\Psi = 0.9$)	TVD (`MUSCL` [1])	`interfaceCompression`	252
3	Crank–Nicolson ($\Psi = 0.5$)	TVD (`MUSCL` [1])	`interfaceCompression`	242
4	Crank–Nicolson ($\Psi = 0.1$)	TVD (`MUSCL` [1])	`interfaceCompression`	241
5	Euler	TVD (`vanLeer`)	`interfaceCompression`	242
6	Euler	TVD (`MUSCL` [1])	Central differencing	257
7	Euler	TVD (`vanLeer`)	Central differencing	258

[1] Monotone upstream-centred schemes for conservation laws [68].

In Figure 6.19 (a), some deviations, compared to the initial wave height, can be observed when employing the Crank–Nicolson scheme for time derivatives, while all simulations using the Euler scheme show virtually no difference relative to each other and relatively small deviations from the target wave height. In terms of run time, only considering cases with Euler time schemes (i.e. cases #1, #5, #6, and #7), case #5, with the TVD (`vanLeer`) and the `interfaceCompression` schemes for the divergence, is the computationally most efficient setup, with a normalised run time of $t_{\mathsf{run}}/t_s = 242$. To test the sensitivity of the wave propagation to the solver settings, a number of test cases with varying solver settings are considered. Due to the vast number of tunable settings, the test cases are limited to different settings for the PIMPLE algorithm[11]

---

[11] Note that the PIMPLE algorithm operates in the PISO mode throughout this illustrative example.

(see Section 4.2.3) and the solution of the water volume fraction α_{VF}. The test matrix is shown in Table 6.14. The influence of the solver settings is quantified using metric #2 and results for $\epsilon_{H^*_{\mathsf{m}}}$ are shown in Figure 6.19 (b). The normalised run times for the considered cases are listed in Table 6.14.

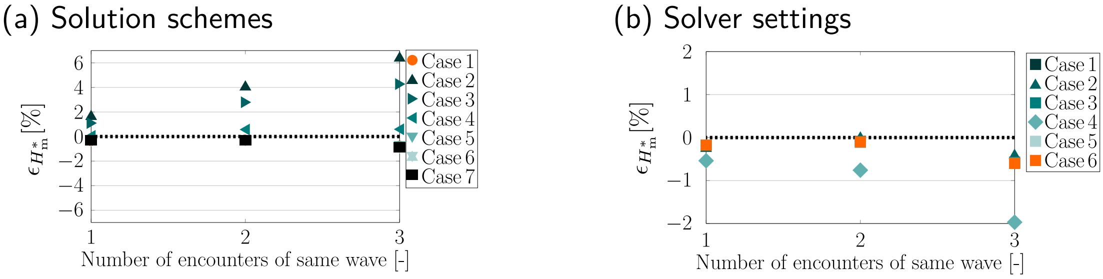
(a) Solution schemes
(b) Solver settings

Figure 6.19: Relative deviation of measured wave height to target wave height over consecutive wave periods. Results are extracted using a single wave probe, i.e. OFWP.

Table 6.14: Test matrix for the sensitivity analysis to numerical solver settings.

Case #	# of `nCorrectors`	c_r (`cAlpha`)	Semi–implicit MULES	# of MULES iterations	t_{run}/t_s
1	3	1	yes	3	255
2	3	0	yes	3	255
3	3	0.5	yes	3	260
4	1	1	yes	3	228
5	3	1	yes	1	248
6	3	1	no	–	240

From the results plotted in Figure 6.19 (b), it can be seen that the reduction of the number of `nCorrectors` has a relatively large influence on the simulation results, specifically for the last considered wave period. Excluding this combination of settings (case #4), it can be seen that all results fall within a relatively narrow error band of $\pm 0.5\%$. Together with the normalised run times, listed in Table 6.14, case #6 delivers accurate results for the least computational cost. However, it is found that some numerical wave makers show numerical instability when omitting the semi-implicit MULES scheme. Hence, for all further test cases shown in the remainder of this section, solver settings according to test case #1 in Table 6.14, and solutions schemes according to case #5 in Table 6.13, are employed.

General modelling inaccuracies – Numerical wave damping

To evaluate numerical damping in the CFD–based NWT, the simulations in the cyclical NWT (see Figure 6.10) are run for $t_{\mathsf{s}} = 10T$. The free surface elevation is measured at location $x_n = \lambda$ (i.e. the centre of the domain). The relative error $\epsilon_{H_\mathrm{m}^*}$ (metric #2) calculated from data extracted with the three available wave probes is shown in Figure 6.20.

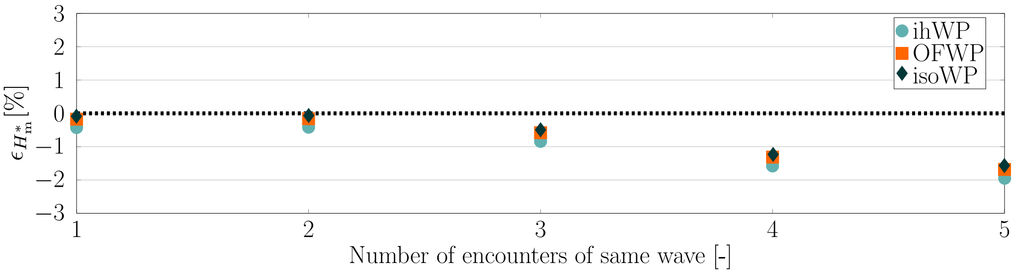

Figure 6.20: Relative deviation of measured wave height to target wave height over consecutive wave periods for the three different wave probes.

As expected, the wave is damped (decreasing wave height) while travelling through the tank, with a maximum degradation of 2% after five wave cycles. These results should be taken into account when evaluating and comparing the wave height at different locations in a larger, i.e. longer, domain. Furthermore, the results plotted in Figure 6.20 indicate very small differences in the sampled free surface elevation for the different wave probes. For each data point in the plot, marginal differences of the order of $< 0.25\%$ can be observed, which is consistent with the findings from the temporal and spatial convergence study.

Wave generation – Regular deep water waves

In this section, results for the assessment of wave generation of deep water regular waves are presented, studying the effect of the temporal problem discretisation, wave damping along the CFD–based NWT, and the velocity profiles along the water column. For the optimum setup of the RZM and ISM wave maker, preliminary calibration studies had to be performed which are omitted here for brevity and can be found in [JPD]. The temporal convergence study has been performed based on the wave propagation test. However, since the numerical wave makers used in this illustrative example can show dependency on the temporal discretisation, different time step sizes are again tested for the considered wave makers. To investigate the time step dependency of the numerical wave makers, metric #3 is applied and the error $\epsilon_{\bar{H}_\mathrm{m}}(x_n)$ is monitored for the five numerical wave makers, using four different time step sizes, i.e., $^T/_{\Delta t} = 200$, 400, 800, and 1600. Free surface elevation data is extracted at a single location, i.e. at the centre of the domain $x_n = \lambda$. By way of example, Figure 6.21 (a) shows the free surface elevation time traces for the five numerical wave makers for a single time step size ($^T/_{\Delta t} = 800$), with the interrogation window for the zero crossing analysis highlighted in grey. For the SBM (ola) wave maker, Figure 6.21 (b) shows the error $\epsilon_{\bar{H}_\mathrm{m}}(x_n)$, plotted over the four different time steps. For clarity, only a single numerical wave maker is considered in Figure 6.21 (b). Furthermore, Figure 6.21 (b) only shows results from the OFWP wave probe. Results for all wave makers and all wave probes are listed in Table 6.15. Note that Table 6.15 shows some voids for the DBM wave maker, for time step $^T/_{\Delta t} = 200$ stemming from numerical instabilities.

(a) Free surface elevation

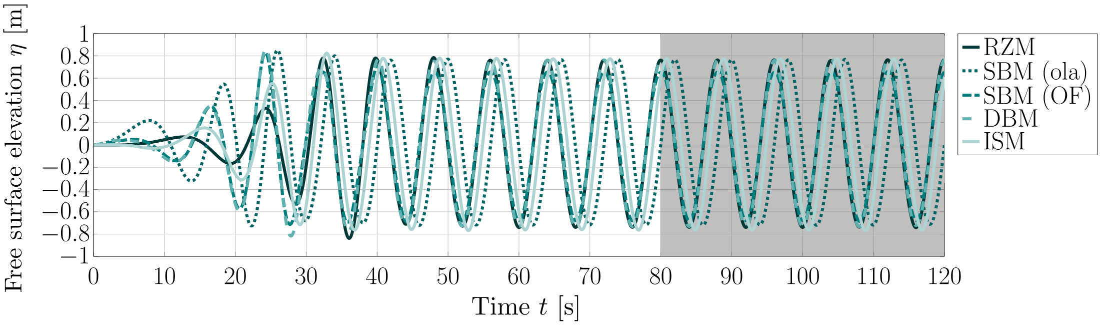

(b) Metric #2 for SBM (ola)

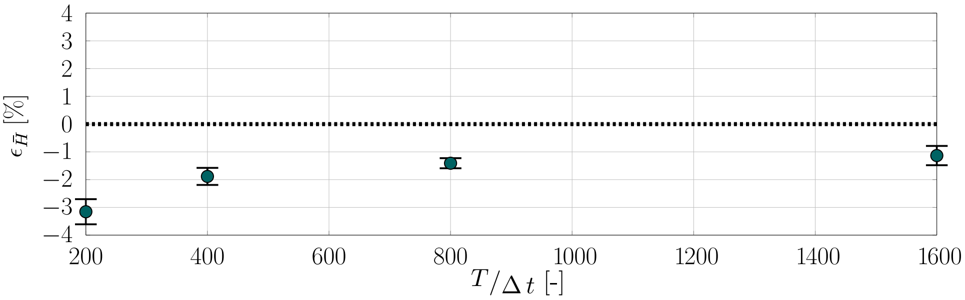

Figure 6.21: (a) Example plots of the free surface elevation time traces for different numerical wave makers and (b) the time step sensitivity on the error $\epsilon_{\bar{H}_\mathrm{m}}(x_n)$ for the SBM (ola) wave maker. For clarity, results are only shown for the OFWP wave probe.

A clear dependency of the error $\epsilon_{\bar{H}_\mathrm{m}}(x_n)$ on the time step size can be observed in Figure 6.21 (b) as well as in Table 6.15. Generally, converged solutions can be found for time steps $^T/_{\Delta t} \geq 800$. The results listed in Table 6.15 also show the dependency of the results on the different numerical wave probes. In Figure 6.20, a first comparison of different numerical wave probes is shown, indicating a deviation of the order of $< 0.25\%$. These findings can be confirmed from the results in Table 6.15. It can be observed that the OFWP and isoWP consistently show comparable results while, in comparison, the ihWP generally over–predicts the error, but only to a relatively small extend ($\sim 0.1\%$). Only for the SBM (OF) wave maker relatively large discrepancies be found between the ihWP and the OFWP/isoWP wave probes. The error for this numerical wave maker is overall relatively large ($\sim -10\%$) compared to the other wave makers, so that the differences between the wave probes can be considered insignificant. Overall, it can be concluded that the numerical wave probes employed here perform with similar precision.

Table 6.15: Error $\epsilon_{\bar{H}_\mathrm{m}}(x_n)$ between target and resulting wave height for different time step sizes numerical wave makers and wave probes.

[%]	$^T/_{\Delta t} = 200$			$^T/_{\Delta t} = 400$		
	ihWP	OFWP	isoWP	ihWP	OFWP	isoWP
RZM	-3.4 ± 0.4	-3.0 ± 0.3	-3.0 ± 0.3	-1.6 ± 0.4	-1.3 ± 0.3	-1.3 ± 0.4
SBM (ola)	-3.4 ± 0.4	-3.2 ± 0.4	-3.0 ± 0.5	-2.1 ± 0.3	-1.9 ± 0.3	-1.8 ± 0.3
SBM (OF)	-12.9 ± 0.5	-11.9 ± 0.5	-12.0 ± 0.5	-11.4 ± 0.3	-10.3 ± 0.3	-10.3 ± 0.3
DBM	–	–	–	-2.7 ± 0.1	-2.4 ± 0.1	-2.4 ± 0.1
ISM	-1.4 ± 0.7	-1.2 ± 0.6	-1.2 ± 0.5	0.1 ± 0.5	0.3 ± 0.5	0.4 ± 0.4

	$^T/_{\Delta t} = 800$			$^T/_{\Delta t} = 1600$		
	ihWP	OFWP	isoWP	ihWP	OFWP	isoWP
RZM	-0.1 ± 0.4	0.2 ± 0.2	0.2 ± 0.3	-0.1 ± 0.1	0.1 ± 0.1	0.1 ± 0.2
SBM (ola)	-1.6 ± 0.2	-1.4 ± 0.2	-1.4 ± 0.2	-1.4 ± 0.3	-1.1 ± 0.4	-1.1 ± 0.4
SBM (OF)	-11.6 ± 0.4	-10.5 ± 0.3	-10.5 ± 0.3	-12.0 ± 0.4	-10.9 ± 0.3	-10.9 ± 0.4
DBM	-1.2 ± 0.2	-0.9 ± 0.2	-0.9 ± 0.2	-0.8 ± 0.5	-0.5 ± 0.5	-0.6 ± 0.5
ISM	0.8 ± 0.1	0.9 ± 0.1	0.9 ± 0.2	1.0 ± 0.1	$1.1 \pm < 0.1$	1.0 ± 0.2

Metric #3 is also used to evaluate the consistency of the wave field along the length of the CFD–based NWT. Figure 6.22 shows $\epsilon_{\bar{H}_\mathrm{m}}(x_n)$ at different (normalised) locations $^x/_\lambda$ (where $^x/_\lambda = 0$ is the wave generation boundary), ranging from $^x/_\lambda = 0.25$ to $^x/_\lambda = 1.75$. Free surface elevation data for the evaluation of metric #3 is extracted with the OFWP wave probe in the interrogation window $t = 80 - 120$s. For comparative purposes, all results are listed in Table 6.16.

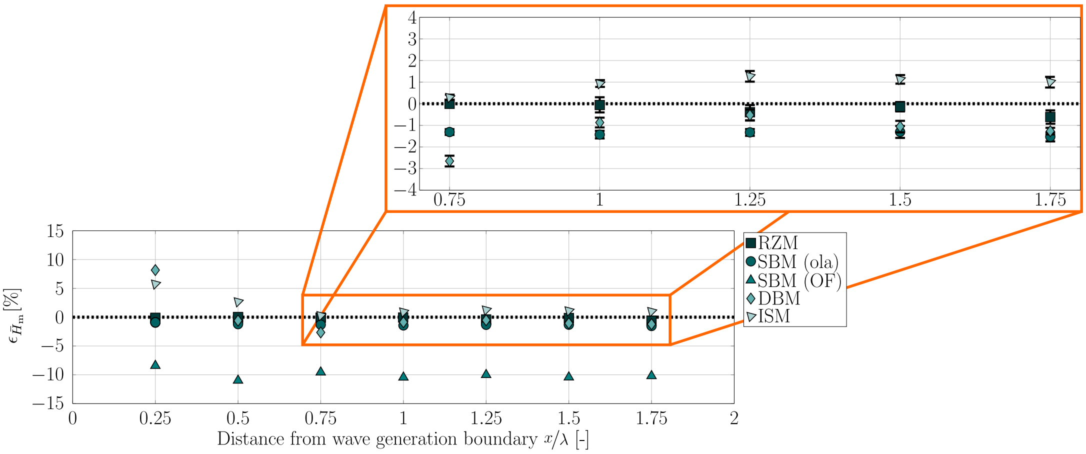

Figure 6.22: Error $\epsilon_{\bar{H}_\mathrm{m}}(x_n)$ between target and resulting wave height for the five different numerical wave makers at different locations along the CFD–based NWT. Note that, for clarity, the standard deviation is only included in the zoom box. Metric #3 is evaluated based on the surface elevation data monitored with the OFWP wave probe.

Considering each numerical wave maker independently, the results in Figure 6.22 and Table 6.16 indicate overall consistent wave fields for all wave makers for $^x/_\lambda \geq 1$. Only the DBM and the ISM wave makers show relatively large deviations for $^x/_\lambda < 1$

Table 6.16: Error $\epsilon_{\bar{H}_\mathrm{m}}(x_n)$ between target and resulting wave height for the five different numerical wave makers at different locations along the CFD–based NWT.

[%]	$x/\lambda = 0.25$	$x/\lambda = 0.5$	$x/\lambda = 0.75$	$x/\lambda = 1$	$x/\lambda = 1.25$	$x/\lambda = 1.5$	$x/\lambda = 1.75$
RZM	-0.1 ± 0.1	$< 0.1 \pm 0.2$	-0.3 ± 0.1	0.2 ± 0.2	-0.4 ± 0.3	-0.1 ± 0.2	-0.6 ± 0.3
SBM (ola)	-0.9 ± 0.1	-1.2 ± 0.2	-1.3 ± 0.1	-1.4 ± 0.2	-1.3 ± 0.2	-1.3 ± 0.3	-1.5 ± 0.2
SBM (OF)	-8.4 ± 0.2	-11.0 ± 0.3	-9.6 ± 0.2	-10.5 ± 0.3	-10.0 ± 0.3	-10.4 ± 0.3	-10.2 ± -0.4
DBM	8.2 ± 0.4	-0.6 ± 0.2	-2.7 ± 0.2	-0.9 ± 0.2	-0.5 ± 0.3	-1.1 ± 0.2	-1.3 ± 0.1
ISM	5.8 ± 0.2	2.7 ± 0.1	0.3 ± 0.1	0.9 ± 0.2	1.3 ± 0.2	1.1 ± 0.2	1.0 ± 0.3

and $x/\lambda < 0.75$, respectively. These larger deviations indicate the occurrence of evanescent waves induced by the motion of the body of water at the DBM or in the ISM wave maker. To ensure good quality results, this should be taken into account when positioning a structure or WEC device in a CFD–based NWT.

Although consistent errors along the CFD–based NWT can be found for the SBM (OF) wave maker, the magnitude of the errors is relatively large ($\sim -10\%$), indicating an under–prediction of the generated wave. The RZM wave maker consistently generates the smallest errors along the length of the tank ($\sim 0.5\%$). The ISM, SBM (ola), and DBM wave makers deliver similar results ($\sim \pm 1\%$). While the ISM wave maker over–estimates the wave height, the SBM (ola) and DBM wave makers under–estimate the wave height. The standard deviation for all numerical wave makers, at all positions along the NWT, is relatively small, indicating not only a spatially consistent, but also a temporally consistent, wave field. Considering the general modelling inaccuracy, all numerical wave makers (except SBM (OF)) perform well for the deep water regular wave.

Finally, the velocity profiles of the horizontal velocity component are considered for the assessment of the wave generation accuracy of the numerical wave makers. The accuracy of the velocity profiles is evaluated using metric #4 (see Equation (6.12)). Results for the error $\epsilon_{\bar{u}_\eta}(x_n, z_m)$ at the wave crest and trough are shown in Figure 6.23. For the wave crest, overall consistent results along the water column can be observed for the different numerical wave makers. The error $\epsilon_{\bar{u}_\eta}(x_n, z_m)$ falls within a band of $< \pm 0.25\%$ and negligible standard deviations can be observed. The RZM and DBM wave makers show slightly increasing errors towards the floor of the CFD–based NWT. The velocities for the SBM (OF) wave maker show relatively large deviations, compared to the other wave makers, over the full water column, under–predicting the velocity profile. However, given the relatively small magnitude of the error ($< 0.25\%$), these errors fall within the range of numerical uncertainty. It should be noted that the results for the SBM (OF) wave maker indicate a decoupling of the accuracy of surface elevation and velocity profile. While the surface elevation shows large errors along the CFD–based NWT, the velocity profile does not seem to be affected by this inaccuracy. This finding is underpinned by the results for the wave trough.

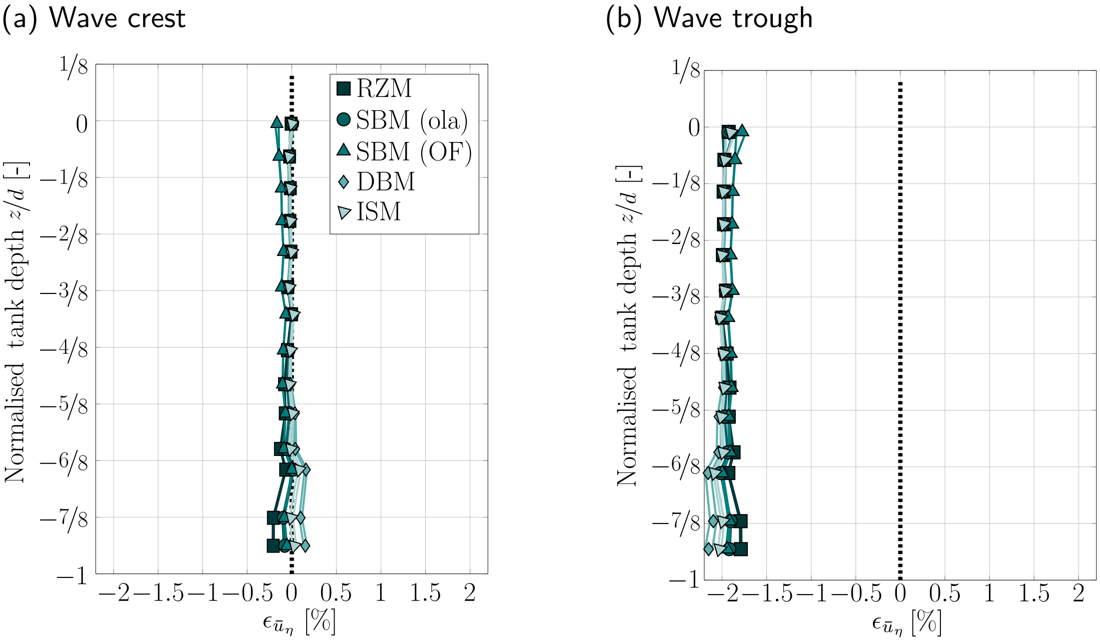

Figure 6.23: Error $\epsilon_{\bar{u}_\eta}(x_n, z_m)$ between the velocity profiles of the horizontal velocity component along the water depth for (a) wave crests and (b) wave troughs. The standard deviation is included by means of the continuous lines connecting the markers.

For the velocity profile underneath the wave trough, generally, a larger error, compared to the wave crest, of the order of -2% can be observed. This error is, again, consistent along the water column for all numerical wave makers, with small divergence towards the bottom wall of the domain. While the RZM, SBM (ola), DBM, and ISM wave makers show very similar errors within a range of tank depths $-^6/_8 \leq {}^z/_d \leq 0$, the SBM (OF) wave maker shows slightly smaller errors. However, again, the magnitude of the difference between the SBM (OF) wave maker and the other numerical wave makers is relatively small and falls within the range of numerical uncertainty.

Wave generation – Regular shallow water waves

For the shallow water regular waves, solely metric #3 is evaluated. Furthermore, only the RZM and SBM (ola) wave makers are able to generate the desired wave field for the Cnoidal wave, considered in the illustrative example. The SBM (OF), the ISM, and the DBM wave makers fail to generate this specific shallow water wave. By way of example, Figure 6.24 shows the free surface elevation time trace, extracted with the OFWP wave probe at the centre of the domain, for a single time step ${}^T/_{\Delta t} = 800$. The interrogation window used to evaluate metric #3 is shaded. As for the deep water regular wave, the time step dependency of the error is analysed for four different time steps (i.e. ${}^T/_{\Delta t} = 400,\ 800,\ 1600,\ 3200$) and all wave probes are considered (see Table 6.17). A qualitative inspection of Figure 6.24 reveals high frequency noise in the free surface elevation time trace of the SBM (ola) wave maker. This noise appears to a smaller

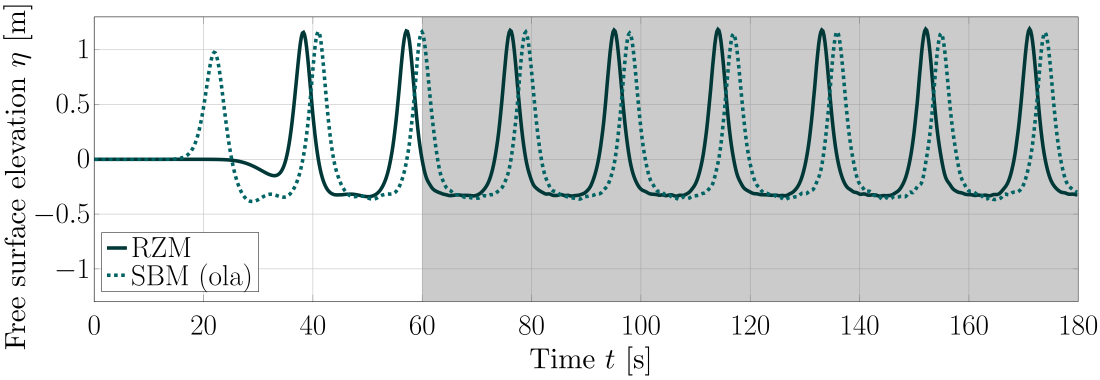

Figure 6.24: Plot of the free surface elevation time traces at the centre of the CFD–based NWT for the RZM and SBM (ola) wave makers. The interrogation window used for the zero up-crossing is shaded. For clarity, results are only shown for the OFWP wave probe.

Table 6.17: Error $\epsilon_{\bar{H}_\mathrm{m}}(x_n)$ between target and resulting wave height for different time step sizes numerical wave makers and wave probes.

[%]	$T/\Delta t = 400$			$T/\Delta t = 800$		
	ihWP	OFWP	isoWP	ihWP	OFWP	isoWP
RZM	0.2 ± 1.5	-0.6 ± 1.6	-0.6 ± 1.5	1.1 ± 0.3	0.3 ± 0.4	0.4 ± 0.5
SBM (ola)	2.2 ± 1.4	1.4 ± 1.3	1.5 ± 1.4	2.1 ± 0.5	1.4 ± 0.4	1.4 ± 0.5
	$T/\Delta t = 1600$			$T/\Delta t = 3200$		
	ihWP	OFWP	isoWP	ihWP	OFWP	isoWP
RZM	1.9 ± 0.3	1.2 ± 0.3	1.3 ± 0.4	1.9 ± 0.3	1.2 ± 0.3	1.2 ± 0.4
SBM (ola)	2.4 ± 0.3	1.7 ± 0.3	1.8 ± 0.4	1.7 ± 0.5	0.9 ± 0.5	1.0 ± 0.6

extent in the time trace for the RZM wave maker. In terms of the wave probes, the results for the shallow water wave, generally, follow the results from the deep water wave, showing consistent errors for the OFWP and isoWP wave probe. Using the ihWP wave probe for the extraction of free surface elevation data results in larger errors, compared to the OFWP and isoWP wave probe. In terms of time step size, larger scatter, compared to the case of the deep water wave, can be observed. However, overall, a similar error magnitude of the order of $\sim 1\%$ is achieved, indicating a modest over–prediction of the wave height. For the subsequent simulations, a time step size of $T/dt = 1600$ was used.

To analyse the consistency of the wave field along the CFD–based NWT, the error $\epsilon_{\bar{H}_\mathrm{m}}(x_n)$ is evaluated at different (normalised) locations x/λ in the tank, ranging from $x/\lambda = 0.25$ to $x/\lambda = 1.75$ (see Figure 6.25). Free surface elevation data for the evaluation of metric #3 is extracted with the OFWP wave probe in the interrogation window $t = 60$–180 s. For comparative purposes, all results are listed in Table 6.18. In Figure 6.25 and Table 6.18, an error of the order of 1% can be observed, indicating overall over–estimation of the wave height for the RZM and SBM (ola) wave makers.

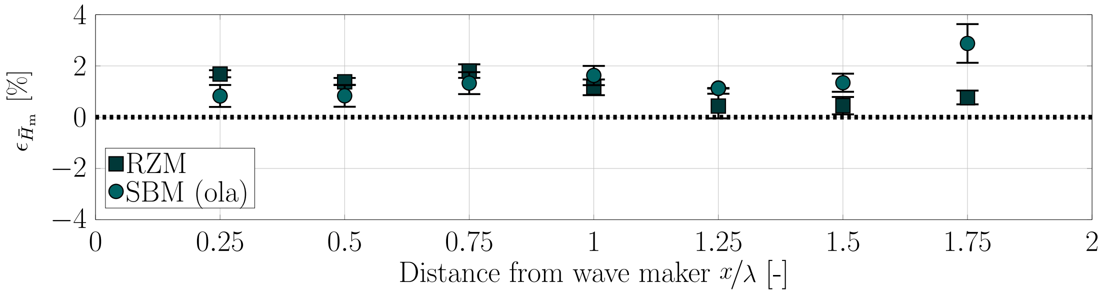

Figure 6.25: The error $\epsilon_{\bar{H}_\mathrm{m}}(x_n)$ between target and resulting wave height along the CFD–based NWT for the RZM and SBM (ola) wave maker. For clarity, results are only shown for the OFWP.

Table 6.18: Error $\epsilon_{\bar{H}_\mathrm{m}}(x_n)$ between target and resulting wave height for the five different numerical wave makers at different locations along the CFD–based NWT.

[%]	$x/\lambda = 0.25$	$x/\lambda = 0.5$	$x/\lambda = 0.75$	$x/\lambda = 1$	$x/\lambda = 1.25$	$x/\lambda = 1.5$	$x/\lambda = 1.75$
RZM	1.7 ± 0.1	1.4 ± 0.1	1.8 ± 0.2	1.2 ± 0.3	0.4 ± 0.5	0.4 ± 0.4	0.8 ± 0.2
SBM (ola)	0.8 ± 0.4	0.9 ± 0.3	1.3 ± 0.2	1.7 ± 0.3	1.5 ± 0.5	1.3 ± 0.7	2.3 ± 0.9

Compared to the deep water regular wave, the RZM wave maker shows larger errors for the shallow water wave, while the SBM (ola) wave maker shows similar performance. For both numerical wave makers the wave height is over–estimated for the shallow water regular wave case while, for the deep water regular wave, the wave height is underestimated. The standard deviation for both numerical wave makers shows a similar magnitude as for the deep and shallow water cases, indicating little temporal scatter. An outlier in the error can be found for the SBM (ola) wave maker at the furthest location from the wave generation boundary, at $x/\lambda = 1.75$, where both the error and standard deviation show relatively large magnitudes.

Wave generation – Irregular deep water wave train

Finally, an irregular wave train is considered for the assessment of the wave generation capabilities of the numerical wave makers. Only the RZM and SBM (ola) wave makers are considered for this particular test case. For the SBM (OF) wave maker, the implementation of the required wave theory is missing. The DBM wave maker uses pre-processed time traces for the wave maker paddle motion for which no pre-processing tool is readily provided for irregular waves. Since the ISM wave maker requires the calibration of each irregular wave train and given the requirement of either a single long time series or, as considered here, four sets of $50T_p$–long time traces to achieve statistically converged solutions, the setup of the ISM wave maker is time consuming. Thus, the ISM wave maker is excluded in this illustrative example.

Metric #5 is applied and the wave spectra are determined from the free surface elevation time traces which are, for brevity, only extracted with the OFWP. Furthermore, results are only shown for a single time step, i.e. $T/\Delta t = 800$, chosen based on the previously presented results. As mentioned in the description of the methodology for metric #5 (see Section 6.2.1), the results are averaged over four simulations of length $t_s = 400\text{s}\,(= 50T_p)$ each, to obtain statistically converged results. The different distances between the wave generation boundary and the evaluation locations is taken into account, as described in Section 6.2.1.

Figures 6.26 (a) and (b) show the SDF plot obtained from time traces measured at different locations λ/x along the numerical domain for the RZM and SBM (ola) wave maker, respectively. Figure 6.26 (c) shows the corresponding nRMSE (metric #5) distribution over the domain length.

A qualitative analysis of Figures 6.26 (a) and (b) reveals that the RZM wave maker does not capture the peak as well as the SBM (ola) wave maker. In contrast, a better match between lower and higher frequency components is achieved by the RZM wave maker, compared to the SBM (ola) wave maker. These qualitative results are reflected in the results of the quantitative analysis shown in Figure 6.26 (c). Overall, consistent results of the nRMSE over the length of the CFD–based NWT can be observed, where deviations of the order of $\pm 0.5\%$ in the nRMSE between the location appear for both numerical wave makers. The results of the RZM wave maker show consistently larger nRMSEs ($\sim 6\%$), compared to the SBM (ola) wave maker ($\sim 5\%$). Considering the corresponding results for the regular wave, this difference between the wave makers is consistent with previous findings. However, it is interesting that both numerical wave makers deliver nRMSEs of a similar order of magnitude, although considerable differences between the SDFs in Figures 6.26 (a) and (b) can be observed. The peak mismatch in the RZM wave maker is compensated by the relatively good match in the lower and higher frequency components. In contrast, the mismatch in the lower and higher frequency components of the SBM (ola) wave maker is compensated by the relatively good match in the peak.

Wave absorption – Standing wave

Metric #6 is employed to evaluate the wave absorption quality at the wave generation boundary. For a qualitative comparison, time traces of the free surface elevation, extracted at the centre location of the domain, which are used for the evaluation of metric #6, are shown in Figure 6.27 in the normalised form η/H_{Theory}.

Differences in absorption at the wave generation boundary can be observed from the qualitative inspection of the free surface elevation time traces for the different numerical wave makers. While the RZM, SBM (ola), and the ISM wave makers show similar free

(a) SDF RZM

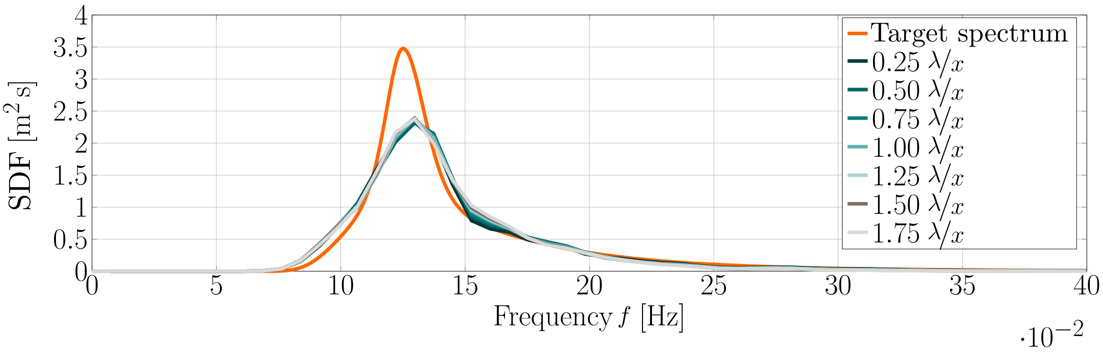

(a) SDF SBM (ola)

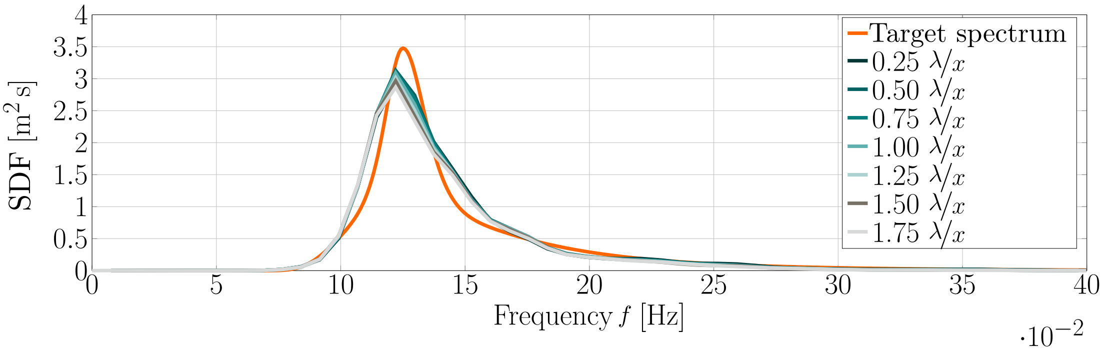

(c) Metric #5

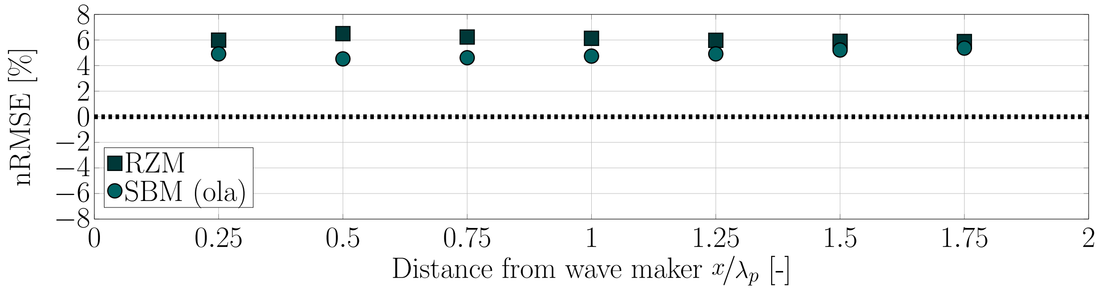

Figure 6.26: Results for the wave generation test case for the irregular wave train generated with the RZM and SBM (ola) numerical wave maker.

surface elevation traces, with wave heights of $\sim 2H_{\text{Theory}}$ (indicated by the orange lines in Figure 6.27), the SBM (OF) and the DBM show increasing surface elevations over the course of the simulation. This indicates re–reflections from the wave generation boundary, which is an indicator of poor wave absorption at the generation boundary. The qualitative results are underpinned by the quantitative values of the error $\epsilon_{\bar{H}_{\text{msw}}}$, listed in Table 6.19. The RZM and ISM wave makers show errors of $-2.7\% \pm 2.1\%$ and $-1.4\% \pm 1.5\%$, respectively. This indicates under–estimation of the expected wave height of the standing wave of $H_{\text{msw}} = 2H_{\text{Theory}}$. The SBM (ola) wave maker shows an error of $5.5\% \pm 2.8\%$, indicating an over–estimation of the expected wave height H_{msw}. To draw conclusions from these results, the achieved accuracy of the wave generation test case has to be taken into consideration. The RZM wave maker

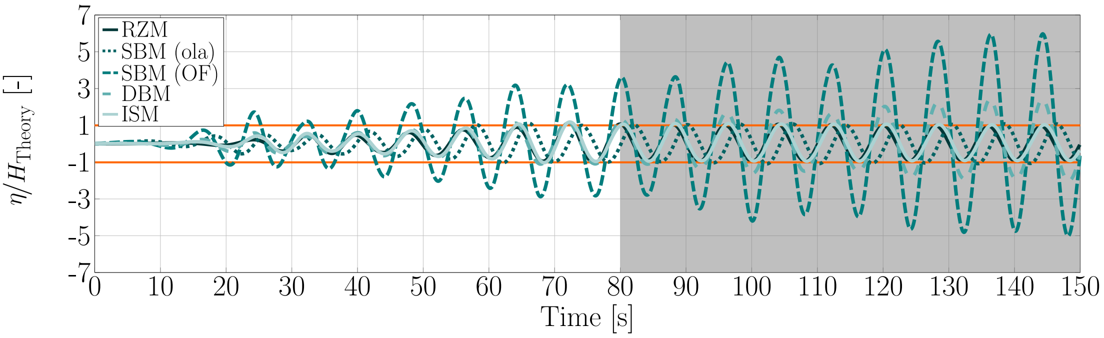

Figure 6.27: Free surface elevation time traces extracted at the centre location of the CFD–based NWT extracted with the OFWP for the RZM, SBM (ola), SBM (OF), DBM, and ISM wave maker. The interrogation window for the evaluation of metric #6 is highlighted in grey. The orange lines indicate the bounds of the free surface elevation in the case of perfect wave absorption at the generation boundary.

shows relatively small errors for the wave generation test case. Hence, the error found for the standing wave test case actually indicates under–estimation of the standing wave height which, in turn, indicates too much wave damping at the wave generation boundary. The error for the ISM wave maker, in the standing wave case, suggests better performance of the ISM than the RZM wave maker. However, as shown in the pure wave generation case, the incoming wave from the ISM wave maker is already larger than H_{Theory} (see Table 6.16). Thus, the relative performance of the ISM and RZM wave makers is similar. For the SBM (ola) wave maker, the error for the pure wave generation test is found to be $-1.4\% \pm 0.2\%$, under–estimating the wave height. For wave absorption at the generation boundary, this means that the performance is even worse than indicated by the error listed in Table 6.19.

For the SBM (OF) wave maker relatively large errors of $361.7\% \pm 50.4\%$ can be observed, which is already indicated by the free surface elevation time trace (see Figure 6.27 (c)). This suggests that no absorption at the wave generation boundary is implemented in the SBM (OF). Similarly, the DBM wave maker shows a relatively large error of $80.5\% \pm 23.5\%$, compared to the RZM, SBM (ola), and ISM wave makers. Since the DBM wave maker uses pre–computed time series as an input for the wave paddle movement, no feedback from reflected waves is considered in the wave maker motion, leading to the large error.

Table 6.19: Error $\epsilon_{\bar{H}_{\text{msw}}}$ for the evaluation of the absorption quality at the wave generation boundary.

[%]	RZM	SBM (ola)	SBM (OF)	DBM	ISM
$\epsilon_{\bar{H}_{\text{msw}}}$	-2.7 ± 2.1	5.5 ± 2.8	361.7 ± 50.4	80.5 ± 23.5	-1.4 ± 1.5

Wave absorption – Regular deep water waves

The wave absorption capabilities of the numerical wave makers are assessed for the deep water regular wave. The wave absorption test cases are furthermore used for the assessment of the computational requirements of the different numerical wave makers. For assessment of the absorption capabilities, the reflection coefficient R (metric #6, Equation (6.3)), as well as the wave height error $\epsilon_{\bar{H}_\mathsf{m}}(x_n)$ (metric #3, Equation (6.10)), is considered. To evaluate R, free surface elevation data is extracted at $x_\mathsf{WP1} = \lambda$, $x_\mathsf{WP2} = \lambda + \lambda/10$, and $x_\mathsf{WP3} = \lambda + \lambda/4$, using the OFWP wave probe. Only results for a single time step, $T/\Delta t = 800$, are evaluated. To calculate $\epsilon_{\bar{H}_\mathsf{m}}(x_n)$, free surface elevation data at various locations along the CFD–based NWT are considered. The interrogation window was chosen to be the same as for pure wave generation assessment. For an optimal setup of the RZM and ISM wave maker, some preliminary calibration studies need to be performed. For brevity, these calibration studies are omitted here. The interested reader is refer to [JPD] for the results of the preliminary calibration studies. It should furthermore be noted here that wave generation for the SBM (ola) and DBM wave makers, in this specific test case, is the same, i.e. SBM (ola), and only the wave absorption method is different.

The results for R are listed in Table 6.20. Furthermore, Table 6.20 includes the normalised run time t_run/t_s and the normalised run time per cell $(t_\mathsf{run}/t_s)/\mathsf{cell\ count}$. While t_run/t_s can provide an estimate of the absolute time required for a specific simulation to run, $(t_\mathsf{run}/t_s)/\mathsf{cell\ count}$ decouples the run time from the number of cells required to build up the numerical domain and, thus, can be consulted to compare the computational requirements of the underlying numerical method. The error $\epsilon_{\bar{H}_\mathsf{m}}(x_n)$, over normalised positions x/λ in the CFD–based NWT, is plotted in Figure 6.28.

Table 6.20: Reflection coefficient, normalised run time, and normalised run time per cell for the deep water regular wave.

	R [%]	t_run/t_s [−]	$\frac{t_\mathsf{run}/t_s}{\mathsf{cell\ count}}$ [−]
RZM	5.1	291	$8.7 \cdot 10^{-4}$
SBM (ola)	26.2	77	$6.9 \cdot 10^{-4}$
SBM (OF)	1.6	152	$6.8 \cdot 10^{-4}$
ISM	2.0	202	$7.3 \cdot 10^{-4}$
DBM	25.6	188	$16.9 \cdot 10^{-4}$

The reflection coefficients listed in Table 6.20 show relatively large differences, depending on the employed numerical wave maker. The largest R values, of the order of 25%, can be observed for the SBM (ola) and DBM wave makers. This can be explained by the underlying wave theory, implemented for wave absorption. In the SBM

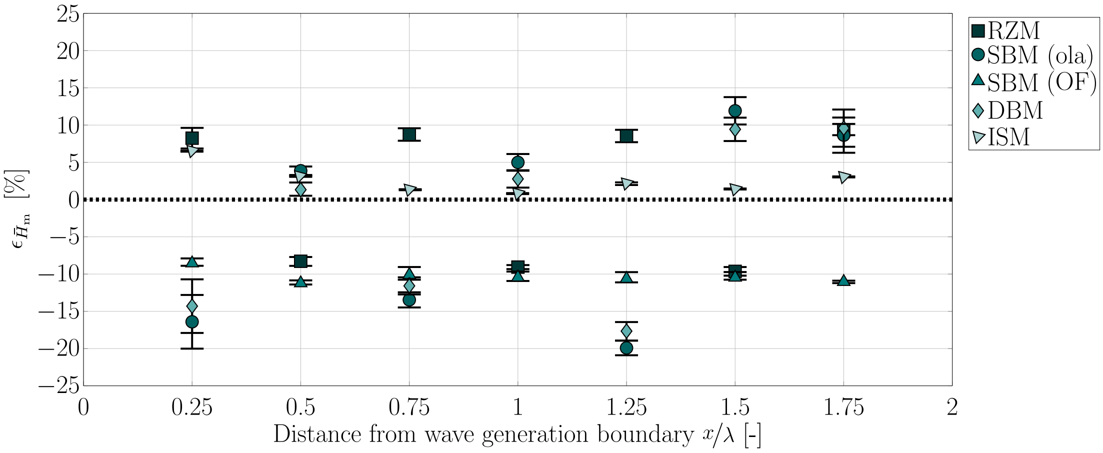

Figure 6.28: $\epsilon_{\bar{H}_\mathrm{m}}(x_n)$ for the deep water regular wave at different locations along the CFD–based NWT

(ola) wave maker, the correction velocity, calculated to cancel out the incoming waves, is based upon shallow water theory. For the DBM wave maker, only a piston–type wave paddle is implemented in the wave maker toolbox. These piston–type wave absorbers (and generators) are generally used for the absorption (and generation) of shallow water waves. Hence, both SBM (ola) and DBM wave makers show poor wave absorption at the far field boundary for the deep water regular wave.

The findings for R are supported by the wave height error plotted in Figure 6.28. From the plot in Figure 6.28, a clear scatter of the wave height can be observed for the SBM (ola) and DBM wave makers. This scatter is believed to stem from the build–up of a standing wave in the CFD–based NWT. Comparing the SBM (ola) and DBM wave makers, the spatial scatter of $\epsilon_{\bar{H}_\mathrm{m}}(x_n)$ is, as expected, very similar, since both absorption methods show similar R values. In terms of error margin, relatively large maximum errors of up to -20% are observable while, for the pure wave generation test case, relatively small errors of the order of -1% are achieved.

The RZM, SBM (OF), and ISM wave makers show relatively small reflection coefficients of 5.1%, 1.6%, and 2.0%, respectively. Although the reflection coefficient for the RZM wave maker shows a value approximately five times smaller than the SBM (ola) and DBM wave makers, the error plotted in Figure 6.28 still shows a relatively large magnitude of the order of $\pm 10\%$. Compared to the error of the order of $\pm 0.1\%$ in the pure wave generation test, this is a considerable increase. For the RZM wave maker, a regular spatial scatter can be observed, likely caused by a standing wave build–up in the numerical domain. It should be noted that the absorption efficiency of the RZM wave maker can be controlled by the user through the choice of the relaxation zone length L_R (see Figure 4.11). Better absorption performance can thus be ‘bought’ for a higher cell count.

With the ISM wave maker, a reflection coefficient of 2% is achieved. However, this accuracy can be influenced by the user, as shown in Section 6.1.4. Effective wave absorption results in comparable errors of the wave height, over the length of the CFD–based NWT, compared to the pure wave generation test (see Figure 6.28).
The smallest reflection coefficient R of 1.6% can be found for the SBM (OF) wave maker. This is underpinned by the results shown in Figure 6.28. Although the error amplitude is relatively large ($\sim -10\%$), the relative difference to the error found for the wave generation test case is marginal. Note that the settings for the numerical beach implemented in the SBM (OF) wave maker are also user defined, giving control over the absorption efficiency, dependent on the available computational resources. Good guidelines for the setup of the numerical beach are provided in the source code, avoiding potentially laborious, manual, calibration.
Comparing $^{t_\text{run}}/_{t_s}$, it can readily be seen that the SBM (ola) wave maker requires the least computational resources to simulate one second of wave propagation ($^{t_\text{run}}/_{t_s} = 77$), while the RZM wave maker requires the most resources ($^{t_\text{run}}/_{t_s} = 291$). This is expected, since the RZM wave maker requires relaxation zones at the upstream and downstream boundaries, while the CFD–based NWT in the case of the SBM (ola) wave maker only comprises the simulation zone. This is also the case for the DBM wave maker; however, this wave maker requires more than twice as much computational resource as the SBM (ola) wave maker ($^{t_\text{run}}/_{t_s} = 188$). This increase can be explained by the additional computations needed to account for the dynamic mesh motion, which can easily be seen when comparing $^{(t_\text{run}/t_s)}/_{\text{cell count}}$. For this quantity, the DBM wave maker shows, by far, the largest value, indicating the additional costs for the underlying numerical method. In contrast, the SBM (ola), SBM (OF), and ISM wave makers show comparable results of the order of $\sim 7 \cdot 10^{-4}$. The RZM wave maker shows a slightly larger value of $8.7 \cdot 10^{-4}$, associated with the relaxation procedure.

Wave absorption – Regular shallow water waves

After assessing the wave absorption capabilities of the numerical wave makers for the deep water regular wave, the shallow water regular wave is considered. Again, the wave absorption test cases are used for the assessment of the computational requirements of the different numerical wave makers. For the assessment, metric #6 (see Equation (6.3)) and metric #3 (see Equation (6.10)) are considered. To evaluate R, free surface elevation data were extracted at $x_\text{WP1} = \lambda$, $x_\text{WP2} = \lambda + {}^{\lambda}/_{10}$, and $x_\text{WP3} = \lambda + {}^{\lambda}/_{4}$, using the OFWP. Only results for a single time step, $^{T}/_{\Delta t} = 1600$, are used. The interrogation window is chosen to be the same as for the pure wave generation case. For the RZM wave maker, the relaxation zone length L_R is chosen to be 2λ. Since only the RZM and SBM (ola) wave maker are able to generate the desired shallow water wave, the SBM (OF) and ISM wave maker are omitted in the following. Note that the wave generation method for the SBM (ola) and DBM wave makers are the same for this test case, so that results can also be shown for the DBM wave maker. The results for R are listed in Table 6.21 and the error $\epsilon_{\bar{H}_\mathrm{m}}(x_n)$, over normalised positions x/λ in the numerical domain, is plotted in Figure 6.29. Furthermore, Table 6.21 includes the normalised run time t_run/t_s and the normalised run time per cell $(t_\mathrm{run}/t_s)/\text{cell count}$.

Table 6.21: Reflection coefficient, normalised run time, and normalised run time per cell for the shallow water regular wave.

	R [%]	t_run/t_s [−]	$\frac{t_\mathrm{run}/t_s}{\text{cell count}}$ [−]
RZM	3.8	148	$6.8 \cdot 10^{-4}$
SBM (ola)	3.7	63	$8.8 \cdot 10^{-4}$
DBM	3.2	123	$17.2 \cdot 10^{-4}$

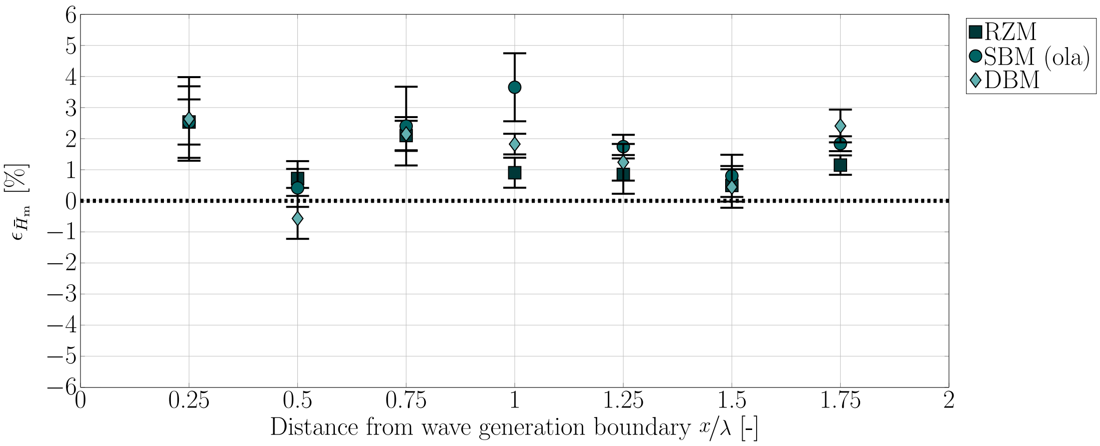

Figure 6.29: $\epsilon_{\bar{H}_\mathrm{m}}(x_n)$ for the shallow water regular wave at different locations along the CFD–based NWT

In terms of the reflection coefficient R, Table 6.21 shows consistent result for the three numerical wave makers ($R \approx 3\%$). Compared to the deep water case, the SBM (ola) and DBM wave maker show a significant decrease of R of almost one order of magnitude. As mentioned previously, the correction velocity imposed at the far field boundary in the SBM (ola) wave maker is based on shallow water theory and, thus, fits the wave considered in this test case. Similarly, the moving wall, used for wave absorption in the DBM wave maker, is implemented as a piston–type absorber and, thus, suits the absorption of shallow water waves.

In Figure 6.29, a maximum error $\epsilon_{\bar{H}_\mathrm{m}}(x_n)$ of $\sim 5\%$ can be observed, indicating an increase compared to the wave generation test case (see Figure 6.25). Furthermore, a larger spatial and temporal scatter of the wave height error can be observed, which can be related to the non–zero reflection coefficient. Overall, similar errors can be seen for the three different numerical wave makers, which is, in the light of the similar reflection coefficients and the similar performance during the wave generation of the shallow water wave, expected.

Regarding the computational requirements, similar results for t_{run}/t_s and $(t_{\text{run}}/t_s)/\text{cell count}$ are achieved for the shallow water case as for the deep water case. The lowest t_{run}/t_s can be found for the SBM (ola) wave maker ($t_{\text{run}}/t_s = 63$), while the RZM wave maker shows the highest $t_{\text{run}}/t_s = 148$. For $(t_{\text{run}}/t_s)/\text{cell count}$, all numerical wave makers show similar performance as for the deep water case. However, for the shallow water wave, the RZM wave maker outperforms the SBM (ola) wave maker, while the opposite is the case for the deep water. This suggests a dependency of the computational requirements on the considered wave theory.

Wave absorption – Irregular deep water waves

Finally, the wave absorption capabilities and computational requirements of the numerical wave makers are assessed for the irregular wave train. For brevity, only the reflection coefficient R is considered for the assessment of wave absorption. To evaluate R, free surface elevation data were extracted at $x_{\text{WP1}} = \lambda$, $x_{\text{WP2}} = \lambda + \lambda/10$, using the OFWP wave probe. Again, results are only shown for a single time step, $T/\Delta t = 800$. The results for the reflection coefficient and run times (t_{run}/t_s and $(t_{\text{run}}/t_s)/\text{cell count}$) are listed in Table 6.22. Since only the RZM and SBM (ola) wave makers are employed during the pure wave generation test case of the irregular wave train, these two wave makers are considered for the wave absorption test case. Since the wave generation method for the SBM (ola) and the DBM wave maker are the same for the wave absorption cases, and only wave absorption is implemented as a moving wall boundary in the DBM, results for the absorption assessment are also available for the DBM wave maker.

The reflection characteristics for the RZM, SBM (ola), and the DBM wave makers follow the results achieved for the deep water regular wave case (see Table 6.20). The smallest reflection coefficient can be found for the RZM wave maker (7.2%), while the SBM (ola) and DBM wave makers show similar performance (25.3% and 23.6%, respectively). Since the peak period and significant wave height of the irregular wave train fall in the deep water regime, these results are expected. The differences between the results for the irregular wave train and deep water regular wave cases can be explained with the additional wave components in the irregular wave train, leading to better (for the SBM (ola) and DBM wave maker), or slightly poorer (RZM wave maker), performance.

Table 6.22: Reflection coefficients, normalised run time, and normalised run time per cell for the irregular wave absorption test case.

	R [%]	t_run/t_s [−]	$\frac{t_\text{run}/t_s}{\text{cell count}}$ [−]
RZM	7.2	2238	$67.1 \cdot 10^{-4}$
SBM (ola)	25.3	105	$9.4 \cdot 10^{-4}$
DBM	23.6	235	$21.1 \cdot 10^{-4}$

Regarding the computational requirements, the SBM (ola) and DBM wave maker show results comparable to the regular wave cases. An increase in t_run/t_s and $(t_\text{run}/t_s)/\text{cell count}$ can be observed, compared to the regular wave case, which is expected since the numerical wave maker has to handle the generation (and absorption) of different wave frequency and amplitude components. Striking results are found for the RZM wave maker. The normalised run time t_run/t_s, and subsequently $(t_\text{run}/t_s)/\text{cell count}$, increases dramatically, compared to the regular wave case, by a factor of almost 10. In contrast, the SBM (ola) and DBM wave maker only show an increase by a factor of 1.3.

Available features

As mentioned in Section 6.2, the available features of the different numerical wave makers can be assessed in a binary fashion. To that end, different important features are first identified:

- Implemented wave theories
- Ability to model wave current interaction
- Requirement for (user) calibration
- Required user inputs
- Ability to be coupled to external wave propagation models

The results of the binary assessment of these features is listed in Table 6.23. Note that the list of the above mentioned features does not claim completeness and, dependent on the application of the numerical wave maker, different features may be important. A discussion of the features of the different numerical wave makers is in the following.

- The RZM wave maker provides an easy to use environment to generate waves for a broad range of sea states and wave theories. In particular for irregular waves, only key parameters have to be provided by the user and are subsequently used in the available pre-processing tool to generate the wave components. The definition of the relaxation zone lengths enables a user–defined trade-off between accuracy and computational expense. Finally, the RZM wave maker can easily be incorporated into the domain decomposition method, as shown in [546], and the coupling with the non-linear potential flow solver OceanWave3D is readily implemented in the toolbox.

Table 6.23: Assessment of important numerical wave maker features.

		RZM	SBM (ola)	SBM (OF)	ISM	DBM
Implemented wave theories	Stokes 1st	•	•	•	–	•
	Stokes 2nd	•	•	•	–	•
	Stokes 3rd	–	•	–	–	•
	Stokes 5th	•	•	•	–	–
	Cnoidal	•	•	–	–	–
	Stream–function	•	•	–	–	–
	Solitary	•	–	•	–	–
	Irregular	JONSWAP Pierson-Moskowitz	•	–	•	If paddle motion data is available
	Wave–current interaction	•	•	•	•[†]	–
Calibration required	Generation	•	–	–	•	–
	Absorption	•	–	•	•	–
User input	Regular waves	Ramp time, water depth, wave theory, H, T, k, ω, wave direction	H, T, wave direction, φ, wave theory	λ, A, φ, ramp time	η time trace	H, T, water depth, wave direction, paddle motion time trace
	Irregular waves	Wave spectrum, number of frequencies, ramp time, H_s, T_p, γ, water depth, wave direction	Components of: T, H, φ, wave direction	–	η time trace	Paddle motion time trace
	Coupling to external wave propagation models	•	–	–	–	–

[†] see [SMA]

- The SBM (ola) wave maker implements a broad range of sea states and wave theories. A downside of the SBM (ola) wave maker is found in the definition of irregular waves. The toolbox does not provide a pre–processing tool to generate the necessary components of wave amplitude, frequency, phase, and direction. Users are required to resort to external tools. Compared to the RZM wave maker, no calibration of the wave generation or absorption boundary is required, making the setup of the CFD–based NWT comparatively easy.
- The SBM (OF) wave maker provides a limited number of wave theories and, furthermore, the definition of irregular waves is not straightforward. Since the SBM (OF) wave maker is a rather recent development, general improvements can be expected. For the SBM (OF) wave maker, calibration of the numerical beach is required. However, good guidelines are provided for the tuning of the damping coefficient as a function of the wave length and the wave celerity, making the definition of the numerical beach comparatively easy.
- For the DBM wave maker, technically, no wave theory has to be implemented directly. The waves are generated through the motion of the up–wave wall as either a piston– or flap–type wave paddle. The input for the paddle motion is derived from wave maker theory or *real* time domain signals of paddle motion. Hence, the range of waves which can be generated is dependent on the available sources for the paddle motion input. In the implementation considered in

the illustrative example, pre–processing tools for flap– and piston–type wave generators are provided. However, no pre–processing script for the definition of the paddle motion time traces for irregular waves is provided. This is a considerable drawback in the flexibility of this numerical wave maker. However, if physical data for wave maker motion is available, the DBM wave maker is able to directly mimic the physical domain.

- As for the DBM wave maker, no wave theory has to be implemented directly for the ISM wave maker. If a time trace of a given wave is provided, the ISM wave maker is able to calibrate the impulse source input accordingly. This calibration of a wave field at a specific location in the CFD–based NWT allows for high–fidelity reproduction of experimental wave tank tests. While this feature can be seen as a strength, the required calibration also adds additional computational cost when considering long or multiple wave time traces. The linear calibration method used as a standard has furthermore shown to be limited in its applicability to highly non–linear waves.The definition of the numerical beach length and damping factor provides the possibility of defining the trade-off between accuracy and computational expense, but requires calibration of the tunable properties.

6.3 Concluding remarks

This chapter treats the topic of numerical wave generation. First, advances of the impulse source wave maker, initially developed in [20], are presented together with a calibration procedure. From Section 6.1, the following conclusions can be drawn:

- The simple formulation of the source term facilitates a straightforward implementation in the flow solver and can easily be extended to other solvers in the OpenFOAM framework [SMF].
- The calibration procedure ensures that the target wave is created at the desired position in space and time in the CFD–based NWT. Furthermore, reflection analysis demonstrates the ability of the numerical beach to achieve arbitrarily low reflection.
- Even when starting from a poor initial impulse source input specification, the calibration method has been shown to converge to an accurate solution within a small number iterations.
- Parameter sensitivity studies on the size of the impulse source region show that correct results can be achieved over a wide range of parameters. An impulse source region width of a quarter of a wave length, with varying requirements on the source height, is suitable for deep, intermediate, and shallow water wave generation.

A rigorous assessment procedure for numerical wave makers is also proposed and demonstrated by a suite of test cases, applied to widely used numerical wave makers within OpenFOAM. From Section 6.2, the following conclusions can be drawn:

- The illustrative example highlights the complexity of a general and fair comparison of different numerical wave makers. The proposed metrics and methodologies prove to be applicable to a variety of wave makers and wave conditions. Readers are advised to apply the proposed metrics to their specific problem to get an understanding of the achievable accuracy and errors of particular numerical wave makers.
- The results of the illustrative example highlight the potential trade–off between accuracy, computational requirements, and available features. Therefore, the selection of an appropriate numerical wave maker depends on the specific application the CFD–based NWT is being employed.
- Amongst the tested numerical wave makers, the RZM wave maker shows overall good performance over the range of tested cases and provides good flexibility in terms of accuracy control, via the definition of the relaxation zone lengths; however, the RZM wave maker comes at a relatively high computational cost.
- A computationally efficient, flexible, and relatively accurate numerical wave maker could be composed by combining the SBM (ola) for wave generation and a numerical beach as implemented in the SBM (OF) or the ISM wave makers for wave absorption.

7

Model validation

Contents

From the introduction (Chapter 1) and the review of CFD–based NWTs for wave energy applications (Chapter 5), it is clear that numerical modelling of WSI is an integral part of the development of WECs, complementing physical wave tank tests. To ensure high–fidelity of the generated data, CFD–based NWTs rely on both verification and validation [89]. Verification embraces the quantification of spatial and temporal discretisation errors using convergence studies. Validation covers the comparison of numerical results to reference data. In general, four different validation strategies can be identified, in which CFD results are compared to: analytical results, low– to mid–fidelity numerical data, third–party CFD–based NWT data, or, most prominently, experimental data. Examples of these different strategies can be found in Chapter 5. Also using experimental reference data, this chapter presents comprehensive validation studies of the different NWT models, used in the subsequent Chapters 8–11. Specifically, the validation studies treat four different devices: a 1/5th and 1/20th scale Wavestar device, as well as two different taut–moored point absorber type WECs, based on the CCP–WSI Blind Test Series 2 and 3.

In general, validation studies should consider test cases, where, for instance, the PTO and control systems are acting on the WEC. In such cases, the WEC experiences realistic operational conditions and, when controlled for energy maximisation, will typically experience increased non-linear hydrodynamic behaviour. Section 7.1 presents the validation of a numerical 1/5th scale model of the Wavestar WEC. The employed reference data set is particularly useful, since pressure data on the device hull is recorded; the 1/5th scale is larger than most physical experiments, representing more realistic hydrodynamic effects compared to an actual full-scale device [387]; in addition the hydraulic PTO system operates in different conditions: undamped, damped, and reactively control.

Subsequently, Section 7.2 presents the validation of a 1/20th scale Wavestar WEC against experimental reference data. Based on the reviewed literature in Chapter 5, an existing lack of validated CFD-based NWTs models of the same device across different scales can be observed. Such model validation across different scales is desired to investigate the hydrodynamic scale effects on the performance of a resonating WEC system, particularly in operational conditions. Thus, together with the validation study in Section 7.1, the validated 1/20th scale Wavestar model forms the basis for the analysis of hydrodynamic scale effects in Chapter 10.

Validating a CFD–based NWTs model against experimental data risks the danger of drawing false conclusions if not all crucial system parameters are available with high precision and/or the system under investigation is too complex. Thus, when using experimental data as the reference, an incremental validation procedure is recommended, considering different test cases of increasing complexity, to identify error propagation between the cases and ensure the fidelity of the CFD–based NWT. Such an incremental approach is followed in both Section 7.1 and 7.2.

In addition to knowledge of the measurement uncertainty, the sensitivity of the body dynamics to such uncertainties is crucial. Specifically, the inertial properties, as well as the location of the centre of mass, which are challenging to measure accurately, can have a significant influence on the system dynamics. To that end, based on two point absorber type WECs, Section 7.3 presents a sensitivity analysis of the agreement between experimental and numerical data sets to the *quality* of the incident, focused wave, as well as the inertial properties and the location of the centre of mass.

7.1 Wavestar – 1/5th scale

The Wavestar WEC consists of several hemispherical hulls, each with a single operational DoF, rotating around a hinge on a fixed structure, which is rigidly connected to the hull. On the full scale device, the hydraulic PTO system consists of a cylinder, pumping fluid through a generator, with a rated power of 500kW for a device with 20 floaters [581]. In the following, only a single float is considered. The experimental validation data set stems from tests performed on a 1/5th scale model of the Wavestar WEC (see Figure 7.1 (a)), reported by Jakobsen [582] and Jakobsen *et al.* [583]. Ransley et al. [383] used this data set for the validation of a CFD–based NWT model, for a fixed WEC and undamped, freely moving, WEC cases. The study in this section extends [383] by considering cases in which the hydraulic PTO system is actively engaged. In addition to the requirement of modelling the effect of the PTO system on the WEC, including the controlled PTO also challenges the CFD–based NWT model by introducing increased non–linear hydrodynamic effects compared to the free floating case [327]. Here, the effects of the PTO system are implemented using a representative spring–damper model (see Section 7.1.3).

7.1.1 Physical wave tank

The experimental test campaign was conducted in the ocean wave basin of the COAST laboratory at Plymouth University (see Figure 7.2), detailed in [582] and [583]. A schematic of the experimental test setup, including relevant dimensions, is depicted in Figure 7.1 (b). System properties (mass, inertia, etc.) are listed in Table 7.1. The experimental data comprises:

- WEC motion: measured via the displacement of the hydraulic PTO cylinder (see Figure 7.1 (b)).
- PTO force: measured at the connection of the hydraulic PTO cylinder with the arm, using a 1–DoF load cell (see Figure 7.1 (b)).
- Pressure on the WEC hull: measured at 29 locations on the hull, using pressure gauges. Note that only four of the 29 pressure gauges are considered for the validation of the numerical model. (see Figure 7.1 (c) for the pressure gauge numbering)
- Free surface elevation: measured at 16 locations in the tank, using wave probes. Note that only six of the 16 wave probes are considered for the validation of the numerical model (see Figure 7.2 for the wave probe numbering).

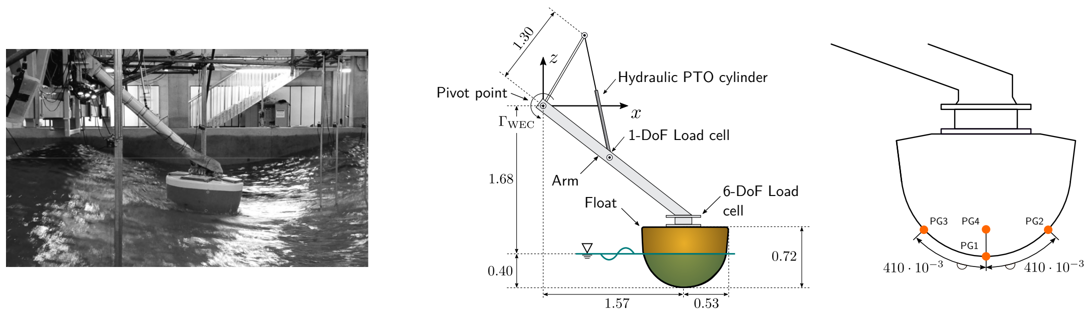
(a) Physical device (b) Device schematic (c) Pressure gauges

Figure 7.1: (a) Photograph of the physical device (adopted from [582]) and schematics (not at scale, all dimensions in [m]) of (b) the device and (c) the pressure gauge positions.

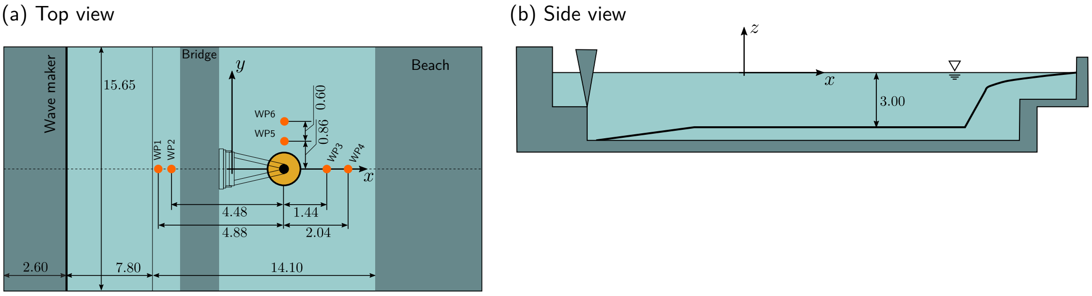
(a) Top view (b) Side view

Figure 7.2: Schematic (not at scale, all dimensions in [m]) of the physical wave tank including the wave probe positions.

Table 7.1: Physical properties of the 1/5th scale Wavestar model

Property	Value	Unit
Mass (float & arm)	220	[kg]
Inertia (float & arm)	124	[kg m^2]
Submergence (in equilibrium)	0.40	[m]
Water depth d	3.00	[m]
CoM of the floating system in equilibrium relative to the hinge position:		
x	1.40	[m]
y	0.00	[m]
z	-1.33	[m]

7.1.2 Test cases

For validation of the CFD–based NWT, the following four test cases, with incrementally increasing complexity, are considered: Initially, to ensure an accurate representation of the incident waves in the numerical domain, wave–only test cases are considered. Next, to introduce WSI but still keep the complexity of the model relatively low, wave excitation force tests are considered. Progressively increasing the complexity of the test cases, forced oscillation tests are studied, before considering wave–induced motion tests.

Waves–only

For the wave–only test cases, the device is lifted out of the water and the waves propagate through the tank undisturbed. The characteristics of the waves, i.e. wave ID, wave height H, wave period T, wave frequency f, wave length λ, and the wave steepness $^H/_\lambda$, are listed in Table 7.2. During the wave–only tests, the free surface elevation is measured with six resistive wave probes, WP1–WP6 (see Figure 7.2 (a)).

Table 7.2: Characteristics of the regular waves

Wave ID	H	T	f	λ	$^H/_\lambda$
RW1$_{1/5\text{th}}$	0.10m	1.4s	0.71Hz	3.06m	0.03
RW2$_{1/5\text{th}}$	0.15m	1.4s	0.71Hz	3.06m	0.05
RW3$_{1/5\text{th}}$	0.25m	1.4s	0.71Hz	3.06m	0.08
RW4$_{1/5\text{th}}$	0.25m	2.8s	0.36Hz	11.4m	0.02

Wave excitation

During the wave excitation force tests, the WEC is locked in its equilibrium position, while being exposed to waves RW1$_{1/5\text{th}}$–RW4$_{1/5\text{th}}$. During these tests, the free surface elevation, as well as the pressure on the hull, is measured using the wave probes and the pressure gauges, respectively.

Forced oscillation

The forced oscillation tests provide an initial validation of the WEC motion induced by a PTO force. These tests are conducted in a tank with no input waves and the WEC motion is driven by a sinusoidal PTO force. Three cases are considered, with increasing PTO force amplitude, A_{PTO}, and constant frequency, f_{PTO}, as listed in Table 7.3.

Table 7.3: Forced oscillation test cases

Test ID	f_{PTO}	T_{PTO}	A_{PTO}
FO300	0.35Hz	2.86s	300N
FO400	0.35Hz	2.86s	400N
FO600	0.35Hz	2.86s	600N

Wave–induced WEC motion

Finally, the full system is tested, with the WEC free to move, while subjected to incoming waves ($\mathsf{RW1}_{1/5\mathsf{th}}$–$\mathsf{RW4}_{1/5\mathsf{th}}$) and PTO forces. Resistive feedback control is employed, and different rotational PTO damping factors, D_{exp}, are considered in the physical experiments, i.e. $D_{\mathsf{exp}} = 0$, 50, 100, and 200N m s which, in theory, lead to a PTO torque, τ_{PTO}, following Equation (7.1), where the rotational spring stiffness K_{exp} is 0. In the experimental setup, the PTO torque is transformed into a linear PTO force, F_{PTO}, applied through the hydraulic cylinder (see Figure 7.1 (b)).

$$\tau_{\mathsf{PTO}} = D_{\mathsf{exp}} \cdot \omega_{\mathsf{WEC}} + K_{\mathsf{exp}} \cdot \Gamma_{\mathsf{WEC}} \tag{7.1}$$

In Equation (7.1), ω_{WEC} is the angular velocity of the WEC, and Γ_{WEC} is the corresponding rotation angle around the pivot point (see Figure 7.1 (b)).

7.1.3 Numerical wave tank

The CFD–based NWT is implemented in OpenFOAM version 4.1 of the OpenFOAM Foundation fork [584]. In the following, details on the numerical wave generation and absorption, the computational domain, and the assumed flow conditions, as well as the dynamic mesh motion method, the PTO representation, and the solver settings and solution schemes are provided.

Numerical wave generation and absorption

It is highlighted, in Chapters 4, 5, and 6, that various methodologies are available and used in OpenFOAM to implement wave generation and absorption. Here, the relaxation zone method, implemented in the *waves2Foam* toolbox [97], is employed. Generally, this method requires larger domain sizes, thus longer computing times, compared to a static boundary numerical wave maker (see Chapter 6). However, for the desired regular waves, preliminary studies revealed better accuracy for the *waves2Foam* wave maker, compared to the static boundary numerical wave maker, as implemented in the *olaFOAM* toolbox [102].

To closely replicate the experimental conditions, no wave absorption is implemented at the domain boundary in the y–direction (see Figure 7.4). Calibration studies are performed to determine the required wave generation relaxation zone length, $L_{R,g}$, and wave absorption relaxation zone length, $L_{R,a}$, for efficient wave generation and absorption, leading to $L_{R,g} = 1\lambda_{\mathsf{RW1}_{1/5\mathsf{th}}-\mathsf{RW4}_{1/5\mathsf{th}}}$ and $L_{R,a} = 3\lambda_{\mathsf{RW1}_{1/5\mathsf{th}}-\mathsf{RW4}_{1/5\mathsf{th}}}$. Screen shots of the weighting function in relaxation zone method χ_R (see Equation (4.29)) are shown in Figures 7.3 (a) and (b) for the regular waves $\mathsf{RW1}_{1/5\mathsf{th}}$–$\mathsf{RW3}_{1/5\mathsf{th}}$ and $\mathsf{RW4}_{1/5\mathsf{th}}$, respectively.

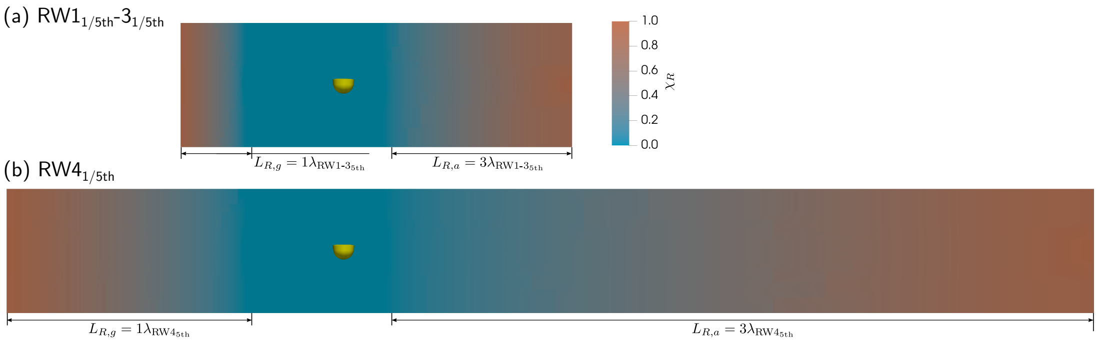

Figure 7.3: Side view of the computational domain: Screen shot of the weighting function in relaxation zone method χ_R.

Computational domain

Figures 7.4 (a) and (b) show the top and side view of the numerical domain, including all relevant dimensions, respectively. To reduce the overall cell count, the symmetry of the problem is exploited and only half of the physical wave tank is modelled numerically. A symmetry boundary condition is employed in the x-z plane, following the convention in this thesis, where x points in the wave propagation direction, and z away from the tank floor. All other relevant boundary conditions are indicated in the Figures 7.4 (a) and (b).

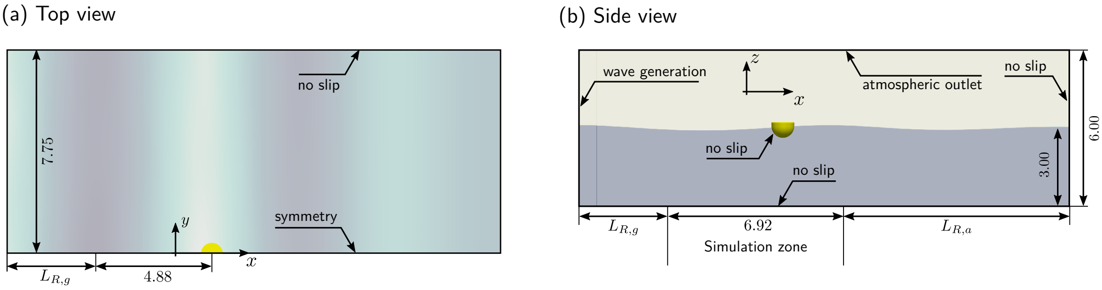

Figure 7.4: Schematic of the numerical wave tank (all dimensions in [m]): (a) top view and (b) side view.

The choice of the spatial and temporal discretisation sizes is inspired by the discretisation size commonly used in the reviewed literature (see Chapter 5) as well as the findings from the assessment of numerical wave makers (see Chapter 6). For the spatial discretisation, the grid size in the z–direction is parametrised by the wave height. It should be noted that, for simplicity, the grid sizes are kept constant between the four different waves RW$1_{1/5\text{th}}$–RW$4_{1/5\text{th}}$. Thus, the smallest wave height $H = 0.10$m (RW$1_{1/5\text{th}}$) of the four regular waves is considered for the parametrisation of the grid size, thereby ensuring convergence for the larger waves RW$2_{1/5\text{th}}$–RW$4_{1/5\text{th}}$. The grid size in the x-direction is defined through a grid aspect ratio of 4. Three different grid sizes, i.e. 5, 10, and 20CPH, are considered and the wave height, extracted at wave probe WP1, is used as the input to the convergence study. Similarly, for the temporal convergence study, three different fixed time step sizes, i.e. $\Delta t = 0.002$s, 0.001s, and 0.0005s, are considered. The results of the spatial and temporal convergence study are listed in Table 7.4.

Table 7.4: Spatial and temporal convergence: $\text{RW1}_{1/5\text{th}}$.

Spatial					
Δt	Δz =5CPH	Δz =10CPH	Δz =20CPH	Convergence type	$\mathcal{U}$
0.001s	0.096m	0.101m	0.102m	Monotone	0.37%
Temporal					
Δz	$\Delta t = 0.002$s	$\Delta t = 0.001$s	$\Delta t = 0.0005$s	Convergence type	$\mathcal{U}$
10CPH	0.097m	0.101m	0.102m	Monotone	0.49%

Based on the results of the spatial convergence study, the interface region in the simulation zone (see Figure 7.4 (b)), and the region around the body, are discretised with cells of a (vertical) size of $10\text{CPH}_{\text{RW1}_{1/5\text{th}}}$. Based on the results of the temporal convergence study, a fixed time step size of 0.001s is used. By way of example, a screen shot of the discretisation in the x-z plane is shown in Figure 7.5.

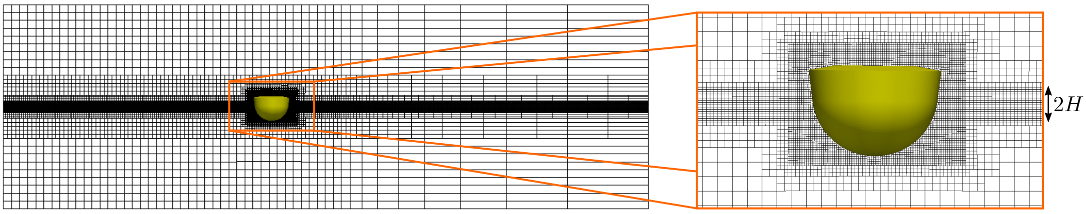

Figure 7.5: Screen shot of the computational mesh in the x-z plane.

Flow conditions

This study follows the previous work by Ransely *et al.* [383], where laminar flow conditions are assumed. Thus, here, laminar flow conditions are assumed as well.

Dynamic mesh motion method

The body motion, induced by the incident wave or external force, is solved via Newton's 2^{nd} law of motion, within the `sixDoFRigidBodyMotionSolver` in the OpenFOAM framework (see Chapter 4). The resulting body motion is accommodated in the numerical domain through mesh morphing by means of the SLERP algorithm.

The `sixDoFRigidBodyMotionSolver` motion solver provides a set of motion constraints. For this study, the WEC motion is constrained to move in the pitch DoF only. For the comparison with experimental data, the cylinder displacement, $x_c(t)$[1], is calculated using geometrical transformations from the numerically monitored, translational, displacement of a reference point on the WEC (orange dot in Figure 7.6). During post–processing, $x_c(t)$ is calculated following:

$$\gamma_{\text{1/5th}}(t) = \beta_{\text{1/5th}}(t) - \theta_{\text{1/5th}} \tag{7.2}$$

$$\alpha'_{\text{1/5th}}(t) = \alpha_{\text{1/5th}} + \gamma_{\text{1/5th}}(t) \tag{7.3}$$

$$x_c(t) = \sqrt{-[\cos(\alpha'_{\text{1/5th}}(t)) \cdot 2 \cdot a_{\text{1/5th}} \cdot b_{\text{1/5th}}] - a^2_{\text{1/5th}} - b^2_{\text{1/5th}}} \quad . \tag{7.4}$$

All relevant angles and distances are depicted in Figure 7.6. $\beta_{\text{1/5th}}(t)$ and, subsequently, $\gamma_{\text{1/5th}}(t)$ and $x_c(t)$ are calculated from the x and z displacement of the reference point.

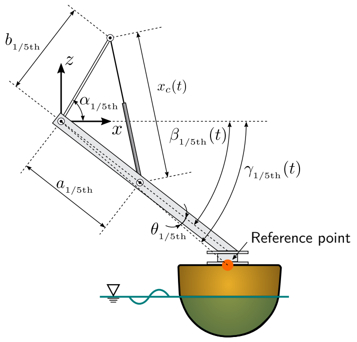

Figure 7.6: Relevant angles and distances for the calculation of the PTO cylinder displacement $x_c(t)$. The orange dot represents the reference point, tracked throughout the simulation. From the x and z displacement of the reference point, $\beta_{\text{1/5th}}(t)$ is calculated.

PTO representation

A model of the actual physical PTO system is implemented in the CFD–based NWT, whereby the PTO force acts on the arm at the position of the 1–DoF load cell (see Figure 7.1 (b)). The PTO force is modelled as a linear spring–damper system, which is defined in the `sixDoFRigidBodyMotion` solver via an anchor point, fixed throughout the simulation, and a reference point, moving with the body (located at position of the 1–DoF load cell). The spring and damper forces are then calculated at each time step, by multiplying user–defined spring, K_{num}, and damping, D_{num},

---

[1] For clarity, time dependent variables are denoted with (t) in this subsection.

coefficients by the relative anchor–reference point displacement x_c and velocity $\dot{x}_c$, respectively (see Equation (7.5)).

$$F_{\mathsf{PTO}} = D_{\mathsf{num}} \cdot \dot{x}_c + K_{\mathsf{num}} \cdot x_c \tag{7.5}$$

For the numerical forced oscillation tests, the PTO excitation force is fed to the numerical model through a modified restraint function in the `sixDoFRigidBodyMotion` solver.

Solver settings and solution schemes

All relevant solver settings and solution schemes (following Chapter 6) are listed in Table 7.5.

Table 7.5: Relevant solver settings and solution schemes.

Time derivative schemes	Euler
Divergence schemes ($\nabla \cdot \mathbf{u}\alpha_{\mathsf{VF}}$)	TVD (`vanLeer`)
Divergence schemes ($\nabla \cdot [\mathbf{u_r}\alpha_{\mathsf{VF}}(1-\alpha_{\mathsf{VF}})]$)	`interfaceCompression`
# of `nOuterCorrectors`	1
# of `nCorrectors`	2
c_r (`cAlpha`)	1
Semi–implicit MULES	yes
# of MULES iterations	3

7.1.4 Results and discussion

This section presents the numerical results for the four different test cases introduced in Section 7.1.2, including a comparison with the experimental data.

Waves–only

The generation and propagation of waves in the CFD–based NWT are validated first, comparing the numerical wave field to the wave field measured in the physical wave tank. Free surface elevation data is compared at four wave probes: WP1, WP2, WP3, and WP6, where WP1, WP2, and WP3 are aligned with the WEC centre in the direction of wave propagation and WP6 is inline with the WEC, perpendicular to the wave propagation direction (see Figure 7.2 (a)). Phase averaged free surface elevation time traces, from a zero crossing analysis (see Section 6.2.1 for details on the phase averaging procedure) are investigated, considering ten consecutive wave periods.

Initially, the temporal scatter of the free surface elevation is analysed by calculating the standard deviation, $\sigma_{\eta_{1/5\mathsf{th}}}$, for the ten consecutive wave periods, at each wave probe. By way of example, Figure 7.7 shows the experimental, phase averaged, free surface elevation $\eta_{1/5\text{th}} \pm \sigma_{\eta_{1/5\text{th}}}$ for wave RW$1_{1/5\text{th}}$. The results of the experimental and numerical $\sigma_{\eta_{1/5\text{th}}}$ are listed in Table 7.6 and reveal that the standard deviation is relatively small (of the order of $1 \cdot 10^{-3}$m) in both the physical and numerical domain, thereby indicating negligible temporal scatter between consecutive wave periods.

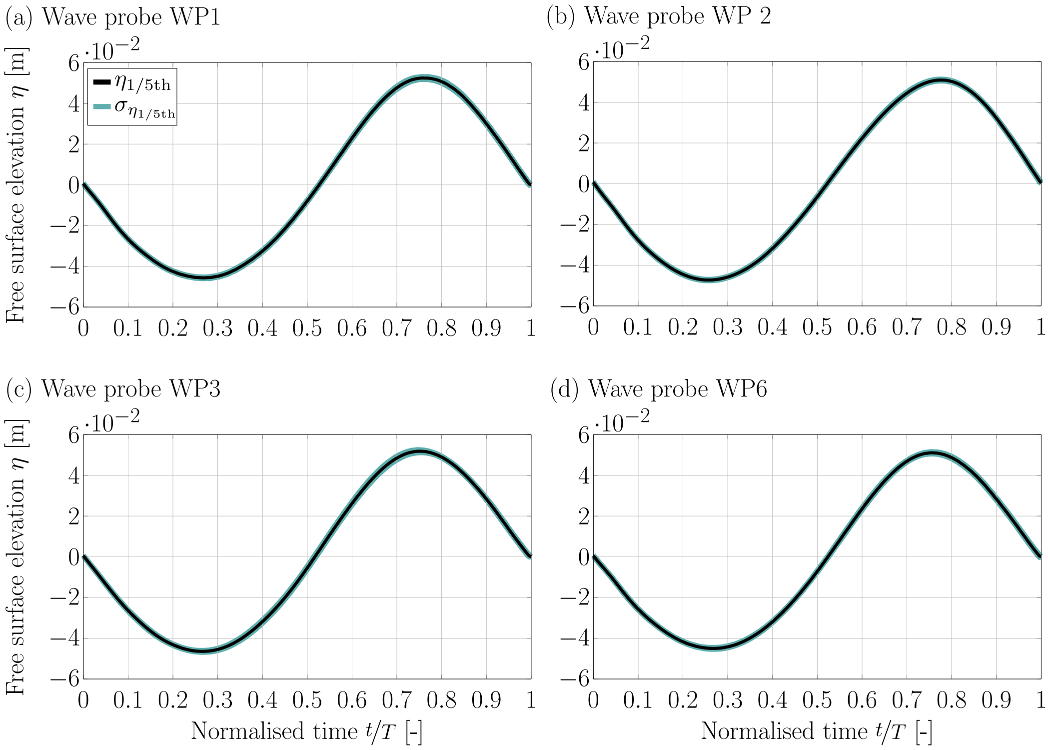

Figure 7.7: Phase averaged free surface elevation $\eta_{1/5\text{th}} \pm \sigma_{\eta_{1/5\text{th}}}$ for wave RW$1_{1/5\text{th}}$, measured in the physical wave tank.

Next, the spatial scatter of the free surface elevation is analysed by comparing the three down–wave wave probes (WP2, 3, and 6) to wave probe WP1, which is the wave probe located closest to the wave maker. The comparison is quantified using the nRMSE (see Equation (6.4)), where $\mathcal{F}$ is the phase averaged free surface elevation at wave probe WP1, $\hat{\mathcal{F}}$ is the phase averaged free surface elevation at wave probes WP2, 3, or 6, and $\mathcal{N}$ is the wave height at wave probe WP1. Ideally, the phase averaged free surface elevation at the different wave probes should match, resulting in a nRMSE of zero. However, due to effects such as (numerical) wave dissipation or reflections from the tank walls, some scatter between the free surface elevation, monitored at the different wave probes, may be observed. The results are listed in Table 7.7 showing that the numerical free surface elevation exhibits very little spatial scatter, suggesting relatively low numerical dissipation or reflections in the CFD–based NWT. In the physical wave tank, larger spatial scatter can be observed, especially for sea states RW$3_{1/5\text{th}}$ and RW$4_{1/5\text{th}}$, which may stem from reflections from the end wall in the physical domain.

Table 7.6: Standard deviation $\sigma_{\eta_{1/5\text{th}}}$ for ten consecutive wave periods.

Experimental				
WP #	1	2	3	6
$\text{RW1}_{1/5\text{th}}$	0.006m	0.004m	0.006m	0.005m
$\text{RW2}_{1/5\text{th}}$	0.001m	0.001m	0.001m	0.001m
$\text{RW3}_{1/5\text{th}}$	0.002m	0.002m	0.002m	0.002m
$\text{RW4}_{1/5\text{th}}$	0.006m	0.006m	0.006m	0.006m
Numerical				
WP #	1	2	3	6
$\text{RW1}_{1/5\text{th}}$	0.001m	0.001m	0.002m	0.003m
$\text{RW2}_{1/5\text{th}}$	$<$ 0.001m	$<$ 0.001m	0.001m	$<$ 0.001m
$\text{RW3}_{1/5\text{th}}$	0.001m	$<$ 0.001m	0.002m	0.001m
$\text{RW4}_{1/5\text{th}}$	$<$ 0.001m	$<$ 0.001m	0.001m	$<$ 0.001m

Table 7.7: nRMSE of the phase averaged free surface elevation in the numerical and experimental wave tank.

Experimental				
WP #	1	2	3	6
$\text{RW1}_{1/5\text{th}}$	–	1.62%	1.63%	1.05%
$\text{RW2}_{1/5\text{th}}$	–	1.38%	2.17%	1.73%
$\text{RW3}_{1/5\text{th}}$	–	2.70%	1.60%	3.27%
$\text{RW4}_{1/5\text{th}}$	–	1.87%	5.00%	5.80%

Numerical				
WP #	1	2	3	6
$\text{RW1}_{1/5\text{th}}$	–	0.73%	0.98%	0.48%
$\text{RW2}_{1/5\text{th}}$	–	1.92%	1.83%	1.81%
$\text{RW3}_{1/5\text{th}}$	–	0.80%	0.75%	2.19%
$\text{RW4}_{1/5\text{th}}$	–	0.19%	0.28%	0.25%

Finally, the numerical free surface elevation data is directly compared against the experimental data. For a qualitative comparison, Figures 7.9–7.11 plot the numerical and experimental mean phase averaged free surface elevation at each wave probe for the four different regular waves. For a quantitative comparison, the nRMSE is calculated following Equation (6.4), where $\mathcal{F}$ refers to the experimental data, and $\hat{\mathcal{F}}$ is the numerical data, and $\mathcal{N}$ is the experimental wave height. Results of the nRMSE are listed in Table 7.8.

Table 7.8: nRMSE between numerical and experimental free surface elevation for the wave–only cases

WP #	1	2	3	6
$\text{RW1}_{1/5\text{th}}$	1.28%	1.56%	1.83%	2.11%
$\text{RW2}_{1/5\text{th}}$	1.53%	1.73%	1.21%	1.68%
$\text{RW3}_{1/5\text{th}}$	5.81%	3.90%	3.75%	4.13%
$\text{RW4}_{1/5\text{th}}$	6.22%	5.12%	5.88%	5.69%

Overall good agreement between the numerical and experimental results is observed, with values of the nRMSE$\leq 6\%$. Particularly good agreement is found for the regular waves with small wave heights, i.e. RW$1_{1/5\text{th}}$ and RW$2_{1/5\text{th}}$, with nRMSEs $\leq 2\%$. Increasing the wave height leads to larger deviations, i.e. nRMSEs $4-5\%$ for RW$3_{1/5\text{th}}$ and $5-6\%$ for RW$4_{1/5\text{th}}$. For RW$3_{1/5\text{th}}$, the main contribution to the deviation can be found at the wave crests. Similarly, for RW$4_{1/5\text{th}}$, at wave probes WP1 and WP2, large deviations can be seen at the crests. At wave probes WP3 and WP6, deviations occur in both the crests and troughs.

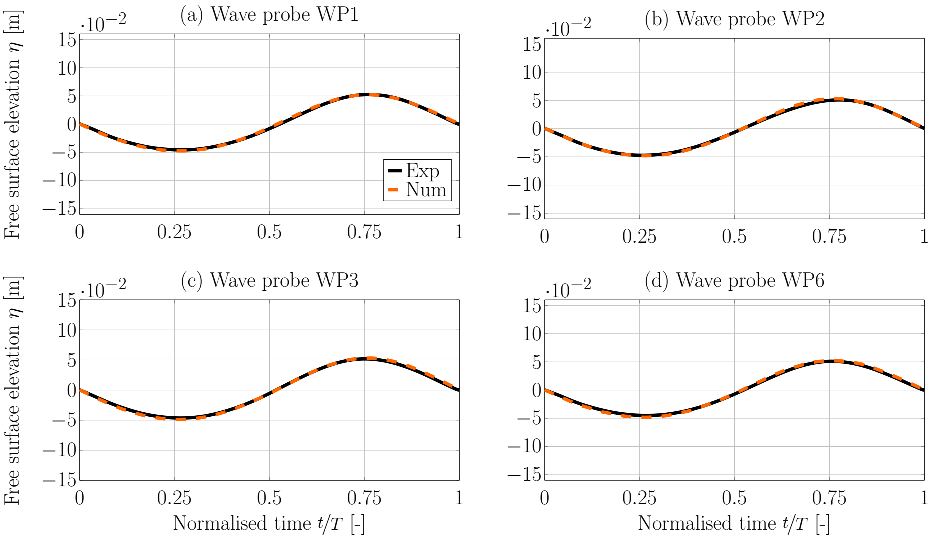

Figure 7.8: Numerical and experimental, phase averaged, free surface elevation for the regular wave RW$1_{1/5\text{th}}$ at wave probes (a) WP1, (b) WP2, (c) WP3, and (d) WP6

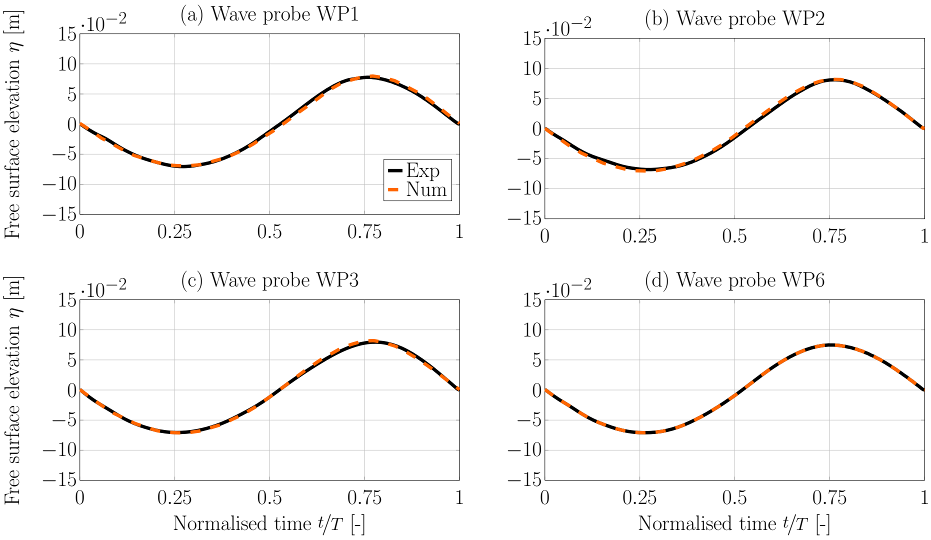

Figure 7.9: Numerical and experimental, phase averaged, free surface elevation for the regular wave RW$2_{1/5\text{th}}$ at wave probes (a) WP1, (b) WP2, (c) WP3, and (d) WP6

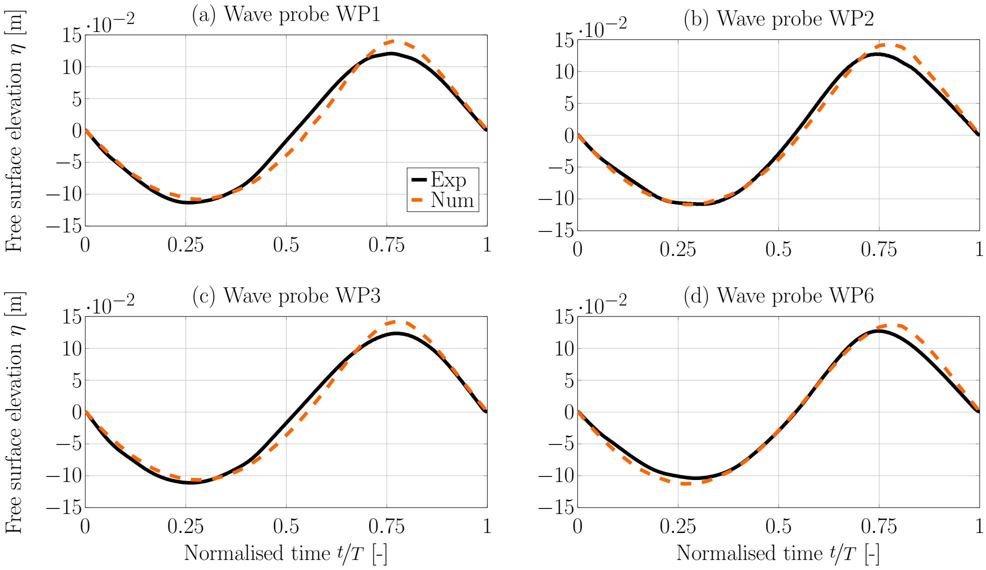

Figure 7.10: Numerical and experimental, phase averaged, free surface elevation for the regular wave RW3$_{1/5\text{th}}$ at wave probes (a) WP1, (b) WP2, (c) WP3, and (d) WP6

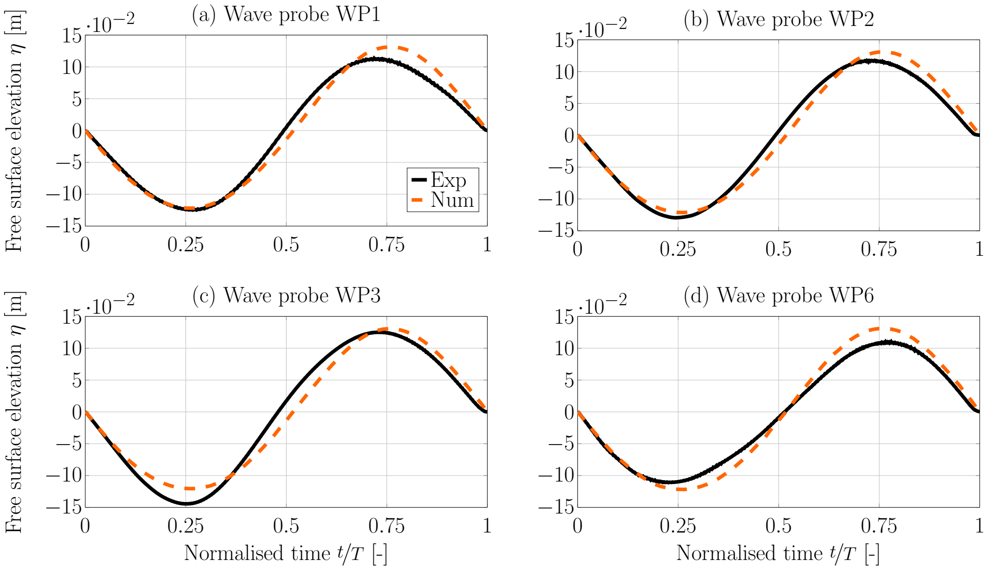

Figure 7.11: Numerical and experimental, phase averaged, free surface elevation for the regular wave RW4$_{1/5\text{th}}$ at wave probes (a) WP1, (b) WP2, (c) WP3, and (d) WP6

Wave excitation

The wave excitation test case provides an initial validation of the WSI, comparing the diffracted wave field, using wave probe data, and the fluid pressure on the WEC hull, using pressure gauge data. The free surface elevation data is compared for five wave probes: WP1, WP3, WP4, WP5, and WP6. Where WP1, WP3, and WP4 are aligned with the centre of the WEC in the wave propagation direction and WP5 and WP6 are inline with the WEC, perpendicular to the wave propagation direction (see Figure 7.2 (a)). Pressure data is compared for four pressure gauges: PG1, PG2, PG3, and PG4, where PG1 is located at the centre bottom, PG2 on the down–wave side, PG3 on the centre side, and PG4 on the up–wave side (see Figure 7.1 (c)).

For a qualitative comparison, time traces for the free surface elevation and pressure, for wave $RW2_{1/5th}$ and $RW4_{1/5th}$ are shown in Figures 7.12 – 7.15. Note that, for the wave excitation test case, the time traces are directly compared, rather than phase averaged results, to show transient behaviour in the data, as the diffracted and incident wave fields interact with each other. Note also that, for waves $RW1_{1/5th}$ and $RW3_{1/5th}$, no experimental free surface elevation data is available. For a quantitative comparison, the nRMSE between the numerical and experimental data is evaluated and listed in Table 7.9.

(a) Wave probe WP1

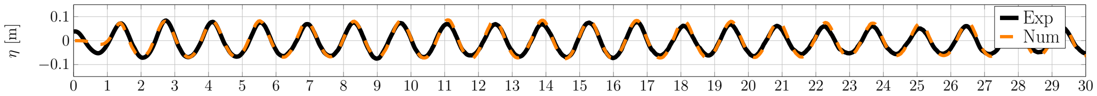

(b) Wave probe WP3

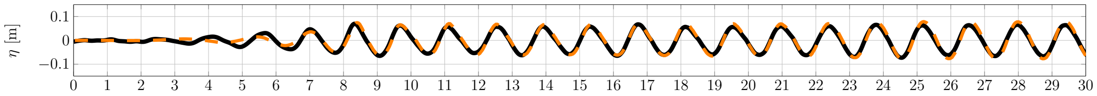

(c) Wave probe WP4

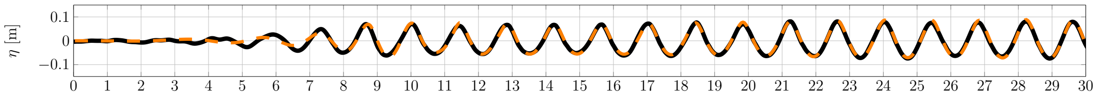

(d) Wave probe WP5

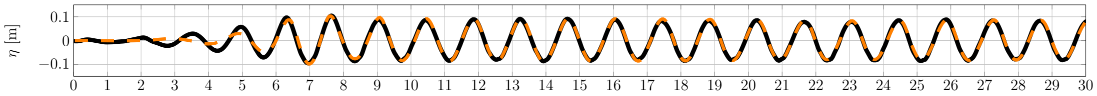

(e) Wave probe WP6

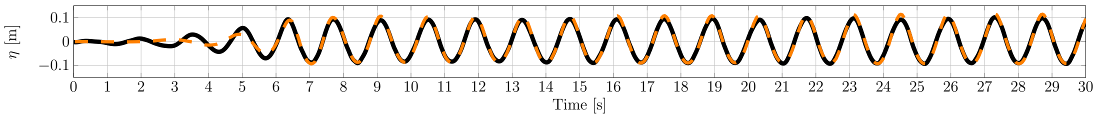

Figure 7.12: Experimental and numerical free surface elevation data for wave $RW2_{1/5th}$

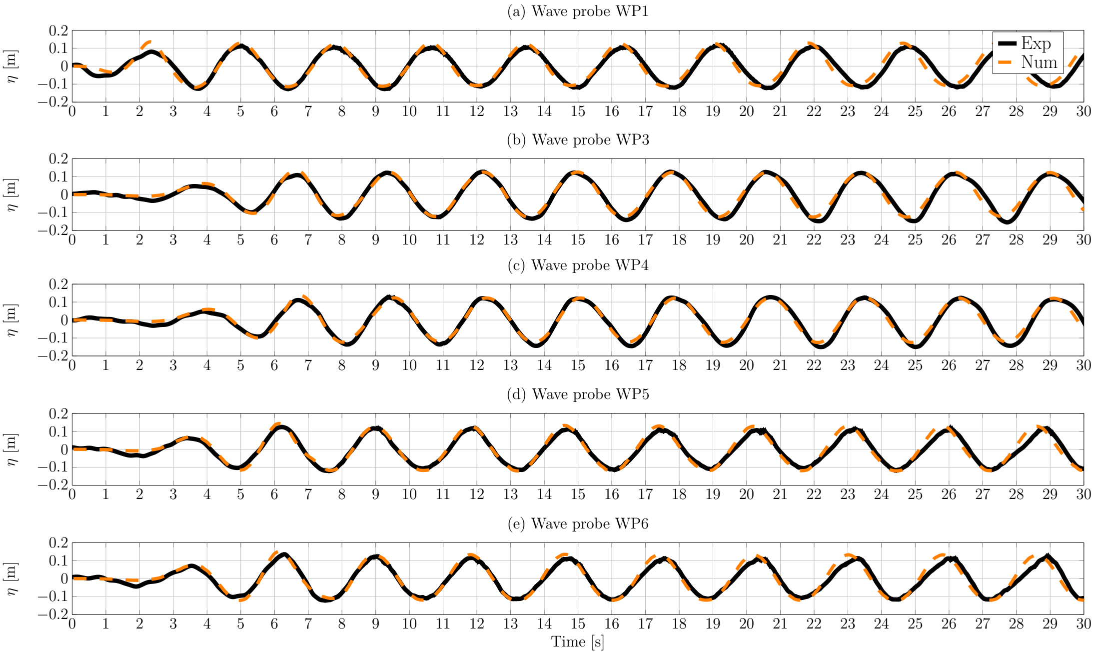

Figure 7.13: Experimental and numerical free surface elevation data for wave RW4$_{1/5\text{th}}$

Comparing the free surface elevations for the different waves, good qualitative and quantitative agreement can be observed. Similar to the wave–only cases, RW2$_{1/5\text{th}}$ shows better agreement (nRMSE$\leq 7\%$) than RW4$_{1/5\text{th}}$ (nRMSE$\leq 11\%$). However, for both waves, marginally larger deviations, compared to the wave–only cases, can be seen. For wave RW2$_{1/5\text{th}}$, the larger deviation can potentially be attributed to the influence of reflections of the diffracted wave field from the tank side wall. Figure 7.16 depicts the wave field in the CFD–based NWT for wave RW2$_{1/5\text{th}}$ at a simulation time of 10s, showing diffracted waves travelling away from the WEC towards the tank wall. Similarly, Figure 7.17 shows the wave field in the CFD–based NWT for wave RW4$_{1/5\text{th}}$. Here, the effect of wave diffraction appears to be minimal. For wave RW4$_{1/5\text{th}}$, the mechanical constraints on the body motion could results in larger deviations. When attempting to hold the WEC fixed in the physical wave tank, the wave force was transmitted to the supporting gantry which began to shake significantly and large vibrations could be observed in both the WEC and the wave probes (which are all attached to the gantry). The parasitic dynamics of the supporting restraints in the physical wave tank are not modelled in the CFD–based NWT, where a perfectly stationary body and wave probes are assumed.

The pressure data for the different waves RW1$_{1/5\text{th}}$ – RW4$_{1/5\text{th}}$ show very similar qualitative and quantitative results, compared to the free surface elevation data. The deviation for all pressure gauges for the different waves lies in the range of $5\% \leq$ nRMSE $\leq 10\%$.

(a) Pressure gauge 1

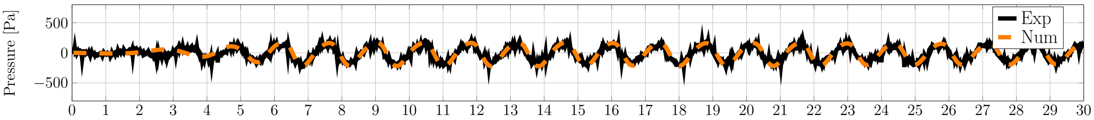

(b) Pressure gauge PG2

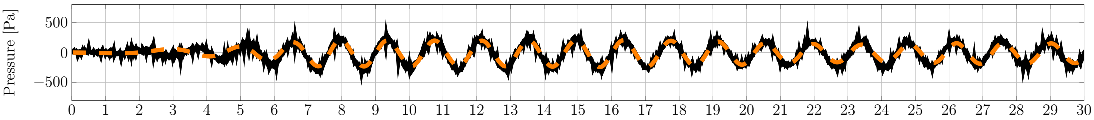

(c) Pressure gauge PG3

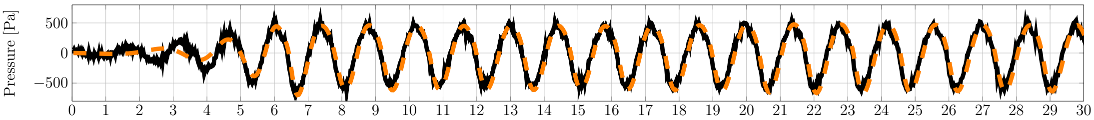

(d) Pressure gauge PG4

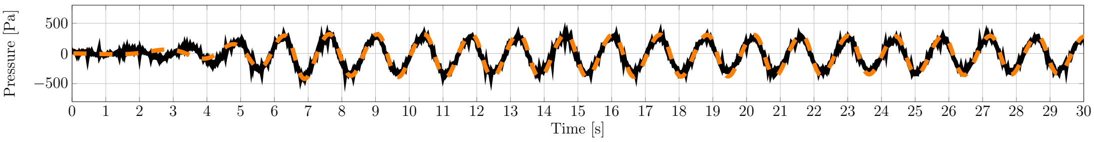

Figure 7.14: Experimental and numerical pressure data for wave $\mathrm{RW2}_{1/5\mathrm{th}}$

(a) Pressure gauge 1

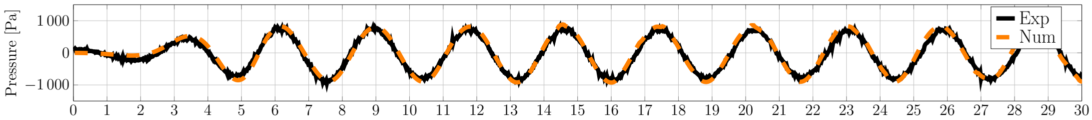

(b) Pressure gauge PG2

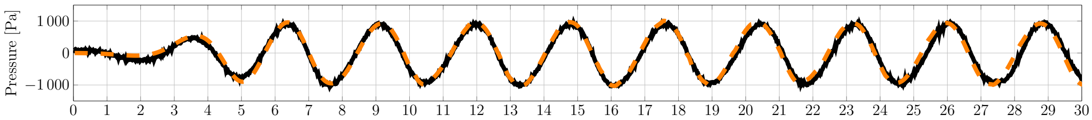

(c) Pressure gauge PG3

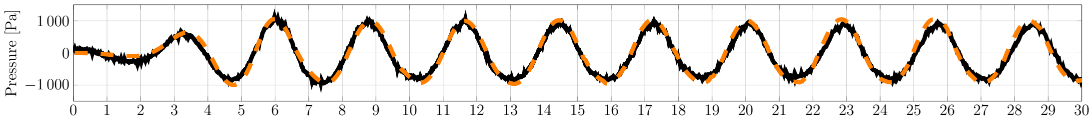

(d) Pressure gauge PG4

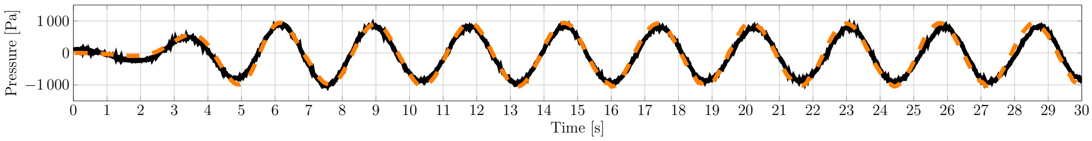

Figure 7.15: Experimental and numerical pressure data for wave $\mathrm{RW4}_{1/5\mathrm{th}}$

Table 7.9: nRMSE between numerical and experimental free surface elevation and pressure data for the wave excitation test cases

Free surface elevation					
WP #	1	3	4	5	6
$\text{RW1}_{1/5\text{th}}$	–	–	–	–	–
$\text{RW2}_{1/5\text{th}}$	6.61%	6.89%	5.05%	4.91%	5.31%
$\text{RW3}_{1/5\text{th}}$	–	–	–	–	–
$\text{RW4}_{1/5\text{th}}$	11.10%	6.69%	5.98%	7.87%	9.22%

Pressure				
PG #	1	2	3	4
$\text{RW1}_{1/5\text{th}}$	8.13%	8.98%	5.20%	6.95%
$\text{RW2}_{1/5\text{th}}$	10.21%	8.09%	8.72%	7.31%
$\text{RW3}_{1/5\text{th}}$	9.95%	10.10%	5.81%	9.12%
$\text{RW4}_{1/5\text{th}}$	8.22%	8.78%	8.12%	8.98%

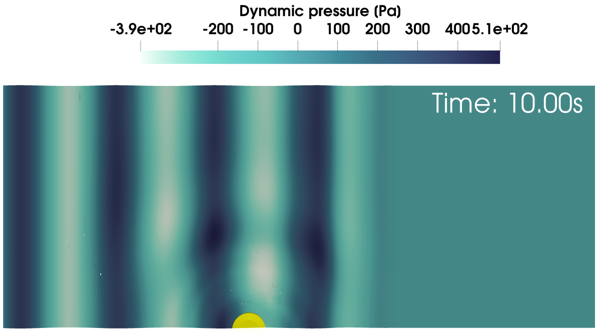

Figure 7.16: Screen shot of the dynamic pressure field across the domain for sea state $\text{RW2}_{1/5\text{th}}$.

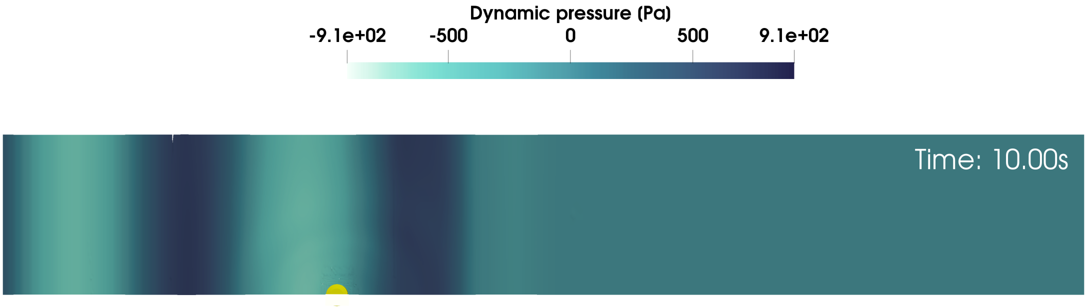

Figure 7.17: Screen shot of the dynamic pressure field across the domain for sea state $\text{RW4}_{1/5\text{th}}$.

Forced oscillation

The forced oscillation tests provide a first validation of the WEC response to the PTO force, by analysing the PTO cylinder displacement and the pressure on the WEC hull (at pressure gauges PG1, PG2, PG3, and PG4). The free surface elevation data is omitted from the comparison, due to the high signal–to–noise ratio in the experimental data. The time series of the PTO force, measured with the 1–DoF load cell in the experiments, is used as the input for the CFD–based NWT simulations.

The nRMSE values for the cylinder displacement and the pressure data are listed in Table 7.10. Figures 7.18 (a)–(c) show time traces for the cylinder displacement for case FO300, FO400, and FO600, respectively. By way of example, Figure 7.19 shows pressure data, measured at PG1, PG2, PG3, and PG4, for test case FO300.

From the qualitative comparison of the cylinder displacement in Figure 7.18 (a), sufficient agreement between the numerical and experimental data set can be observed. The phases of the experimental and numerical signals match, while some over– and under–prediction of the peak and trough values is found. Quantitatively, the cylinder displacement shows nRMSE values $< 10.5\%$ across the considered cases. The pressure data shows nRMSE$< 8\%$ across all pressure gauges and test cases. The trend in the nRMSE for the three cases FO300, FO400, and FO600 correlates with the results from the cylinder displacement data, with FO400 showing the smallest and FO300 the largest nRMSE for the cylinder displacement and the pressure data. This is expected since, for wave forced oscillation tests, the pressure is directly related to the body motion.

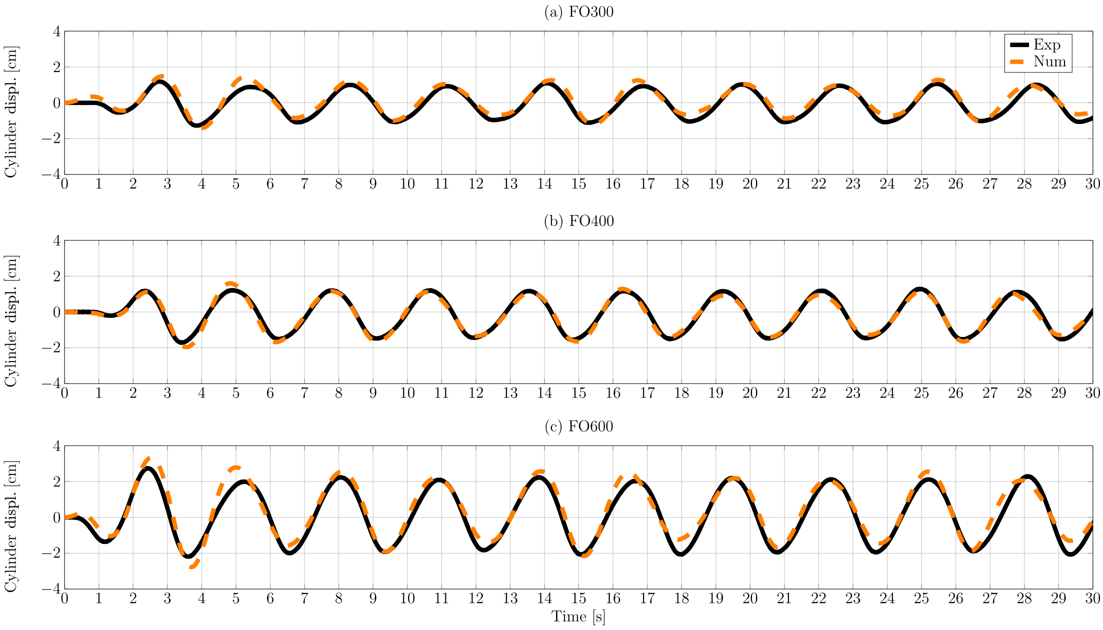

Figure 7.18: Numerical and experimental cylinder displacement during the forced oscillation tests (a) FO300, (b) FO400, and (c) FO600.

Wave–induced WEC motion

WSI, with WEC motion induced by the incident waves *and* PTO forces, is finally considered for validation in this test case. Experimental and numerical results are compared for the PTO cylinder displacement and velocity, the PTO force (measured with the 1–DoF load cell), the free surface elevation (measured with wave probes WP1, WP3, and WP5), and the pressure on the WEC hull (measured with pressure

(a) Pressure gauge PG1

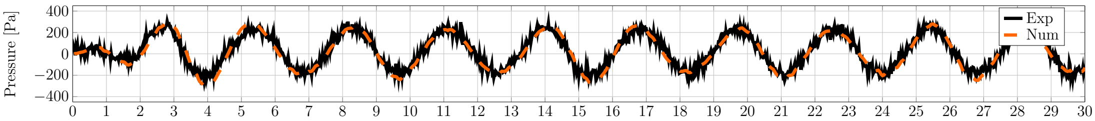

(b) Pressure gauge PG2

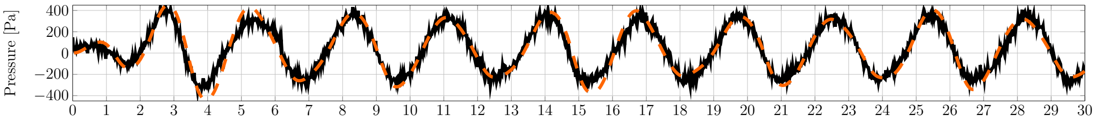

(c) Pressure gauge PG3

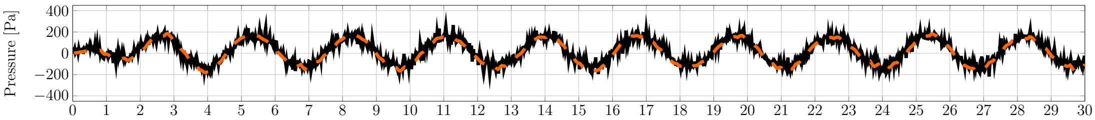

(d) Pressure gauge PG4

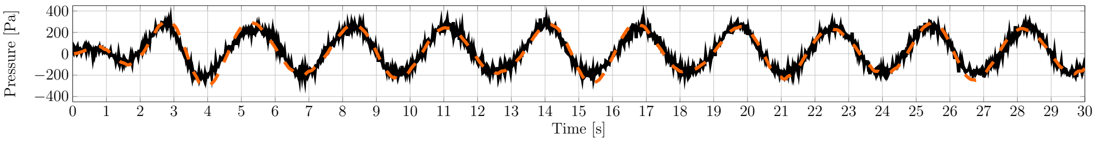

Figure 7.19: Experimental and numerical pressure data for the forced oscillation test FO300

Table 7.10: nRMSE between numerical and experimental cylinder displacement and pressure data for forced oscillation test cases

	Cylinder displ.	**Pressure**			
	x_c	PG1	PG2	PG3	PG4
FO300	10.45%	7.76%	7.66%	7.21%	7.38%
FO400	5.43%	5.33%	5.72%	5.90%	6.06%
FO600	8.62%	7.30%	7.85%	5.95%	7.75%

gauges PG1, PG2, PG3, and PG4). As in the previous sections, the quantitative comparison is achieved using the nRMSE, and qualitative comparison is achieved through the inspection of plotted time traces.

Before the numerical simulations can be run, the user–defined damping coefficient D_{num} and spring stiffness K_{num} of the linear spring–damper PTO system in the CFD–based NWT are calibrated to represent its physical equivalent. Since resistive feedback control is employed in the physical WEC model, only damping and no reactive force, i.e. $K_{\text{num}} = 0$, should be applied in the numerical model by the PTO (see Equation (7.1)). However, calculating an equivalent linear damping coefficient, using Equation (7.1) and an appropriate geometric transformation, did not lead to expected results from the numerical simulations, when compared with the physical data.

Inspection of the zero damping case, $D_{\text{exp}} = 0$, reveals that a PTO force is still being applied. Further inspection reveals that the time average of the power flow to the WEC from the PTO force is non–zero, meaning that the PTO is applying reactive power, i.e. $K_{\text{num}} \neq 0$. This *residual* reactive power may stem from delays of the controller and hardware between target and actual force, in the physical tank. Furthermore, it is well known that physical WEC models experience friction in the mechanical parts. This friction, generally, is a non–measurable quantity, which makes its replication in the numerical setup a challenging task.

To correctly replicate the experimental setup in the CFD–based NWT, calibration of the PTO coefficients D_{num} and K_{num} is required. Here, a linear least squares approach is applied to the experimental data, assuming that the PTO force follows the simple relation shown in Equation (7.5). F_{PTO}, x_c, and $\dot{x}_c$ are the measured PTO force, cylinder displacement, and velocity in the experiments, respectively. A least–squares regression, as shown in Equations (7.6)–(7.8), can be constructed, where ξ_j contains the damping and stiffness coefficients, while Ξ_j contains velocity and position data.

$$F_{\text{PTO}}(\xi) = \sum_{j=1}^{2} \xi_j \Xi_j(t) \tag{7.6}$$

$$X_{ij} = \Xi_j(t_i) \tag{7.7}$$

$$\hat{\xi} = \left(X^T X\right)^{-1} X^T F_{\text{PTO}} \tag{7.8}$$

The resulting, estimated, K_{num} and D_{num} values from the least squares fit for the different values of D_{exp}, for waves $\text{RW1}_{1/5\text{th}}$–$\text{RW3}_{1/5\text{th}}$, are plotted in Figure 7.20, showing consistent estimates for K_{num} and D_{num} between the different regular waves. In addition, a clear linear trend in the increase of K_{num} and D_{num} with the increase of D_{exp} can be seen. Linear regression is used again to create a line of best fit through the K_{num} and D_{num} values (also plotted in Figure 7.20), yielding the following relationships:

$$K_{\text{num}} = 184 D_{\text{exp}} - 4700 \tag{7.9}$$

$$D_{\text{num}} = 70 D_{\text{exp}} \tag{7.10}$$

Equations (7.9) and (7.10) are used to calculate the user–defined linear spring–damper coefficients for the numerical simulations, which are listed in Table 7.11. It should be noted that the necessary integration of a non–zero spring stiffness highlights the importance of PTO dynamics. Real hydraulic systems may have their own spring and/or inertia effects that can lead to effective provision of reactive power. Therefore, it is important to adequately define these using available data, or implement a high-fidelity PTO system.

(a) Damping coefficient

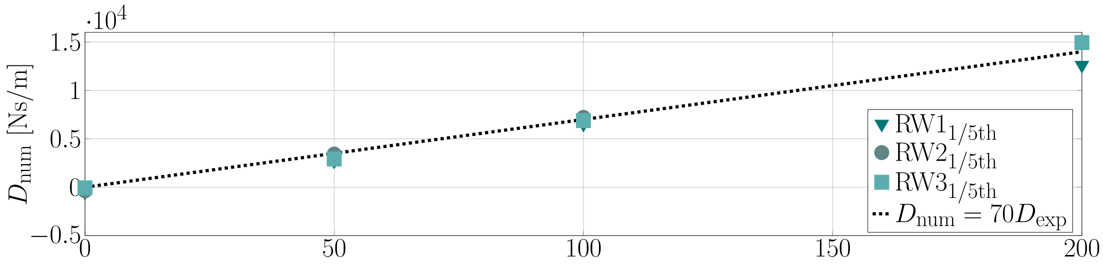

(b) Spring stiffness

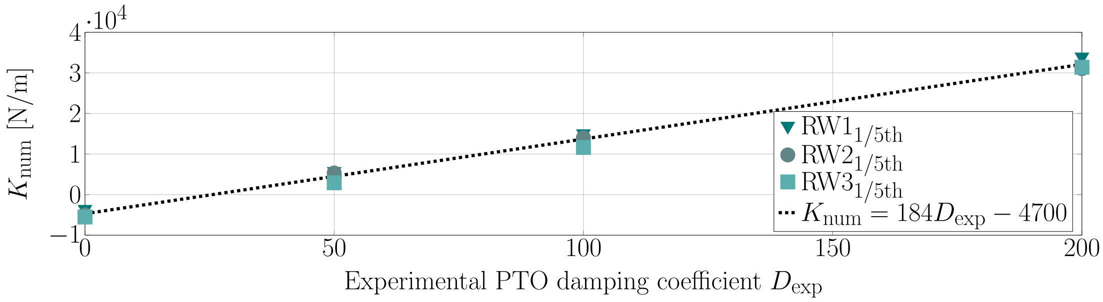

Figure 7.20: Numerical spring stiffness and damping coefficient determined through linear least squares regression

Table 7.11: Numerical damping coefficient and spring stiffness determine through linear least squares regression

D_{exp} [N m s]	D_{num} [N s m^{-1}]	K_{num} [N m^{-1}]
0	0	−4700
50	3500	4500
100	7000	13700
200	14000	32100

$\mathrm{RW1}_{1/5\mathrm{th}}$

For the case of highest experimental damping, $D_{\mathsf{exp}} = 200$N m s, the nRMSE for the PTO data (position, velocity, force), as well as the pressure and free surface elevation, are listed in Table 7.12. The corresponding time traces for the PTO, pressure, and free surface elevation are plotted in Figures 7.21 to 7.23, respectively.

For the PTO data, good agreement can be observed, with nRMSEs of $\sim 8\%$ for the position and velocity, and $\sim 12\%$ for the PTO force. In Figure 7.21, it can be seen that the magnitude for position, velocity, and force is over–predicted by the NWT, while phase is captured well. The experimental force signal shows second order effects in the troughs, which are not captured in the numerical model. However, due to the small force amplitude, it is not clear if these effects stem from noise in the recorded data, or reflect actual PTO characteristics.

Table 7.12: nRMSE between numerical and experimental data for regular wave $\mathrm{RW1}_{1/5\mathrm{th}}$

PTO data				
D_{exp} [N m s]	200	100	50	0
Displacement	8.19%	5.02%	5.78%	11.14%
Velocity	8.20%	4.72%	5.53%	11.20%
Force	12.41%	6.73%	9.36%	28.88%

Free surface elevation				
D_{exp} [N m s]	200	100	50	0
WP1	8.18%	6.63%	6.86%	5.78%
WP3	12.14%	8.30%	8.75%	7.43%
WP5	6.45%	6.97%	9.80%	11.67%

Pressure				
D_{exp} [N m s]	200	100	50	0
PG1	12.67%	7.08%	8.37%	12.22%
PG2	13.28%	9.47%	10.81%	10.60%
PG3	6.27%	10.30%	8.25%	14.74%
PG4	9.75%	14.32%	12.83%	12.62%

(a) Cylinder displacement

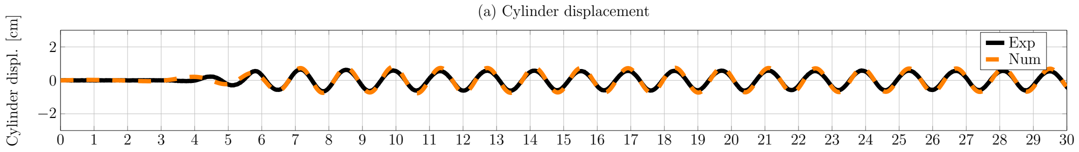

(b) Cylinder velocity

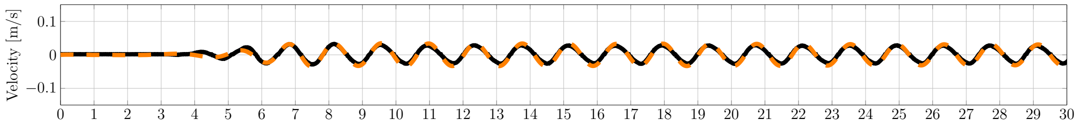

(c) PTO force

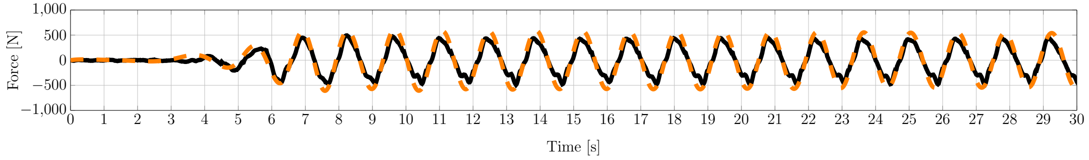

Figure 7.21: Numerical and experimental PTO data for sea state $\mathrm{RW1}_{1/5\mathrm{th}}$ with experimental damping $D_{\mathrm{exp}} = 200\mathrm{N\,m\,s}$

Inspection of the pressure time series, plotted in Figure 7.22, also reveal good agreement. The largest nRMSE, 13%, is found at PG1 and can be attributed to the low signal–to–noise ratio in the experimental data. The smallest nRMSE, 6%, occurs at PG3 which faces the wave generation boundary. For PG2 (nRMSE$=13\%$) and PG4 (nRMSE$= 10\%$) a small phase lag results in a larger nRMSE.

The free surface elevation time series, measured at wave probe WP1, WP3, and WP5, are plotted in Figure 7.23, and the nRMSE values are listed in Table 7.12. Again, good qualitative and quantitative (nRMSE$\leq 12\%$) agreement is found. The deviation in free surface elevation is found to be larger than for the wave–only cases (nRMSE$\leq 2\%$), which could be attributed to the interaction between radiated and diffracted waves. The largest deviation can be found at wave probe WP3, in the wake of the body, where a phase lag causes the mismatch. This lag coincides with the phase lag of the pressure data, recorded at pressure gauge PG2, which is also located at the down–wave side of the hull.

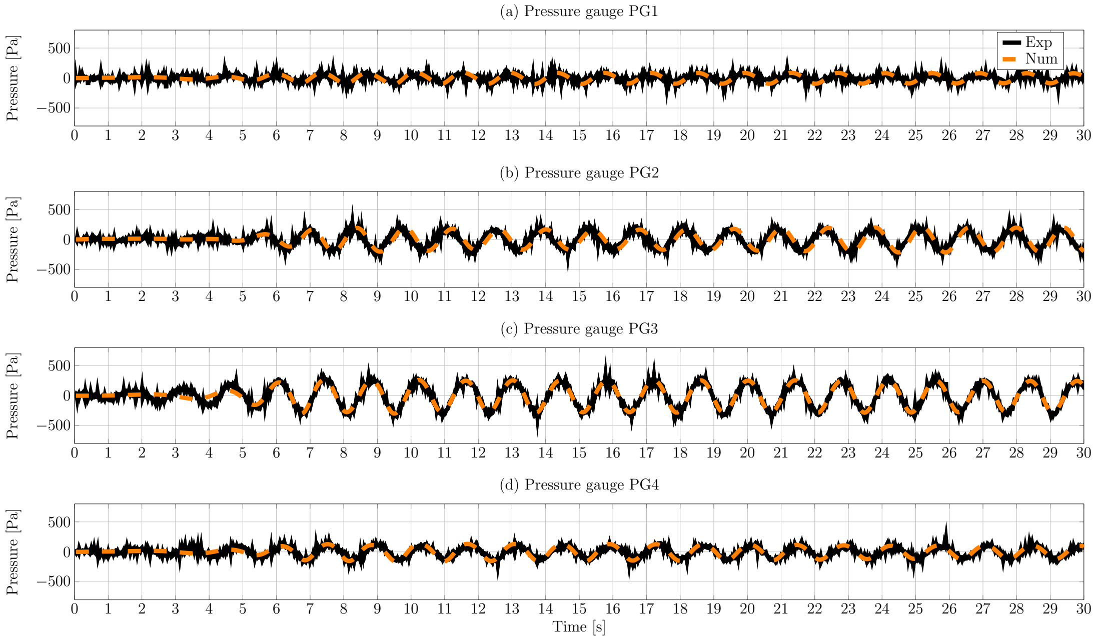

Figure 7.22: Numerical and experimental pressure data for sea state RW1$_{1/5\text{th}}$ with experimental damping $D_{\text{exp}} = 200\text{N m s}$

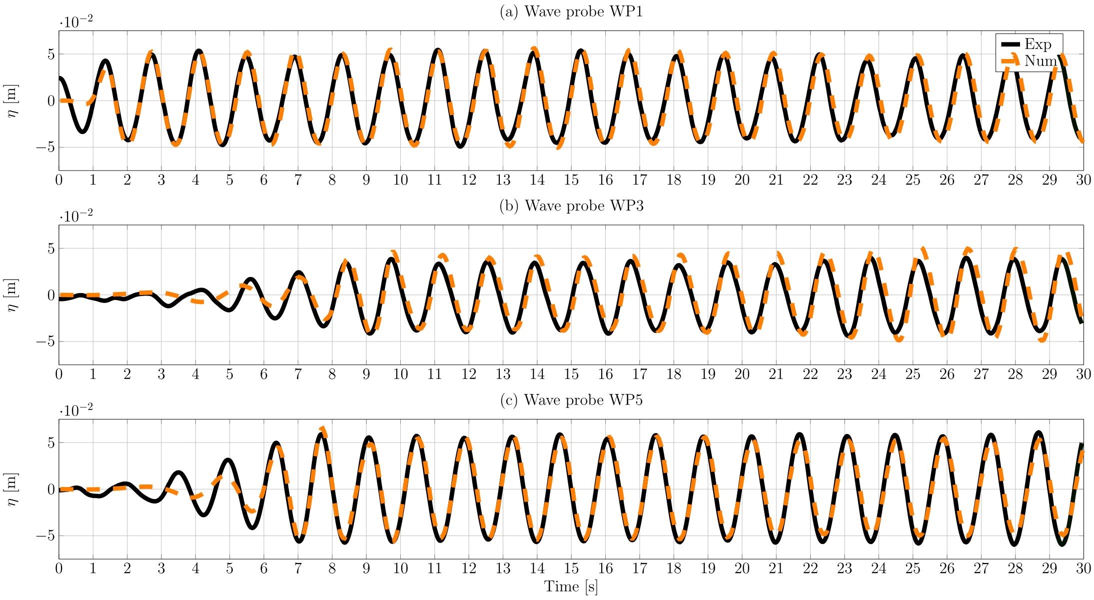

Figure 7.23: Numerical and experimental free surface elevation data for sea state RW1$_{1/5\text{th}}$ with experimental damping $D_{\text{exp}} = 200\text{N m s}$

In a similar fashion, results for the cases $D_{\text{exp}} = 100$, 50, and $0\,\text{N}\,\text{m}\,\text{s}$ are analysed. PTO data is plotted in Figures 7.24, 7.27, and 7.28, while pressure data is plotted in Figures 7.25, 7.27, and 7.29. Since the free surface elevation data show consistent behaviour for all different damping values, these plots are omitted for brevity.

For a PTO damping of $D_{\text{exp}} = 100\,\text{N}\,\text{m}\,\text{s}$ good quantitative and qualitative agreement for PTO data (nRMSE$\leq 7\%$), free surface elevation (nRMSE$\leq 8\%$), and pressure (nRMSE$\leq 14\%$) can be found. Specifically the PTO position and velocity is captured well, with a nRMSE of 5%.

(a) Cylinder displacement

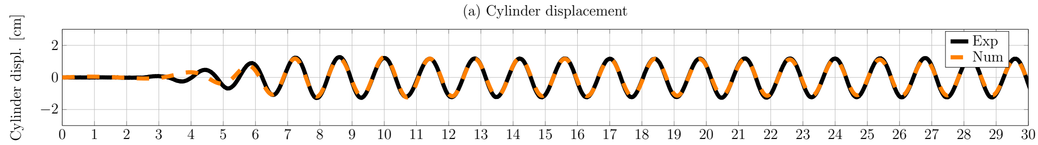

(b) Cylinder velocity

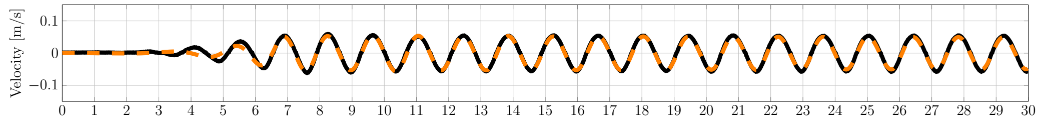

(c) PTO force

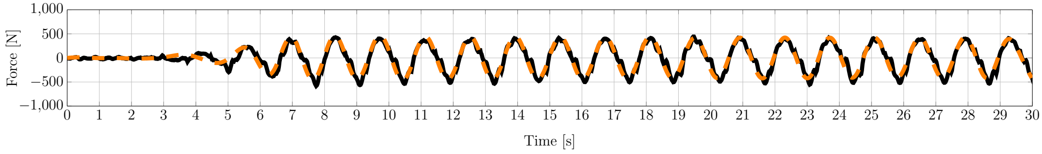

Figure 7.24: Numerical and experimental PTO data for sea state $\text{RW1}_{1/5\text{th}}$ with experimental damping $D_{\text{exp}} = 100\text{N}\,\text{m}\,\text{s}$

(a) Pressure gauge PG1

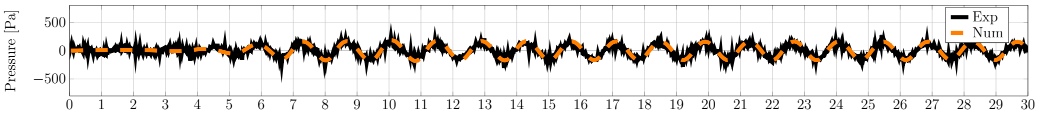

(b) Pressure gauge PG2

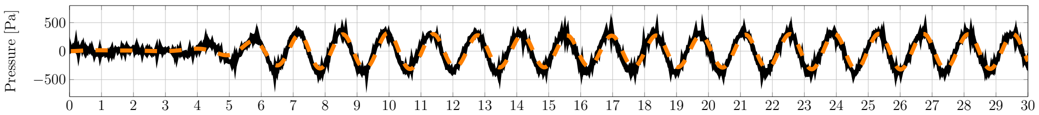

(c) Pressure gauge PG3

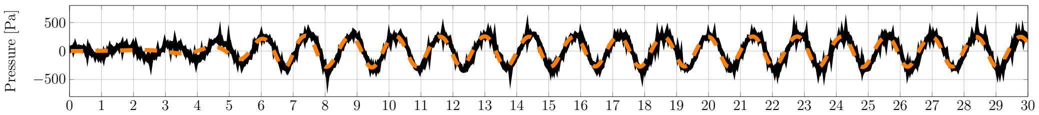

(d) Pressure gauge PG4

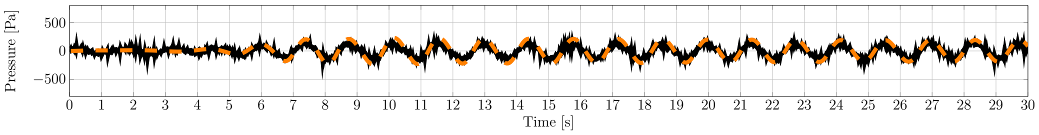

Figure 7.25: Numerical and experimental pressure data for sea state $\text{RW1}_{1/5\text{th}}$ with experimental damping $D_{\text{exp}} = 100\text{N}\,\text{m}\,\text{s}$

For $D_{\text{exp}} = 50\,\text{N m s}$, the position and velocity data show similar agreement to the $D_{\text{exp}} = 100\,\text{N m s}$ case (nRMSE$\approx 6\%$). The plotted time traces show under–estimation of the motion amplitude in the numerical simulation. The force magnitude is captured well, resulting in a nRMSE of $\sim 9\%$. Good agreement in phase can be observed for all PTO data. The pressure signals for $D_{\text{exp}} = 50\,\text{N m s}$ show a fit comparable the previous cases (nRMSE$\leq 13\%$), with the same deviation characteristics.

(a) Cylinder displacement

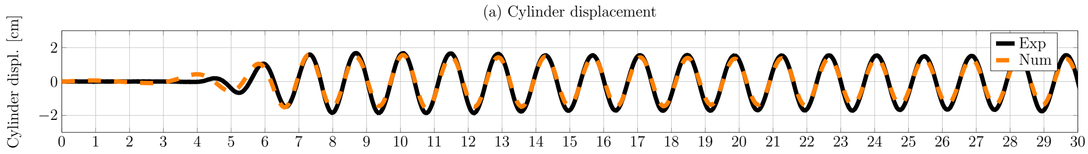

(b) Cylinder velocity

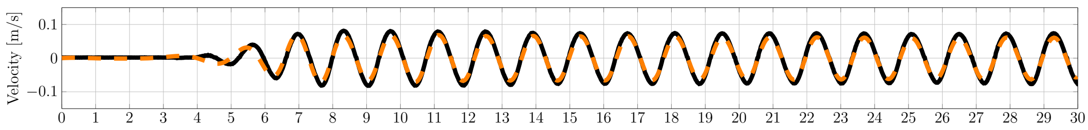

(c) PTO force

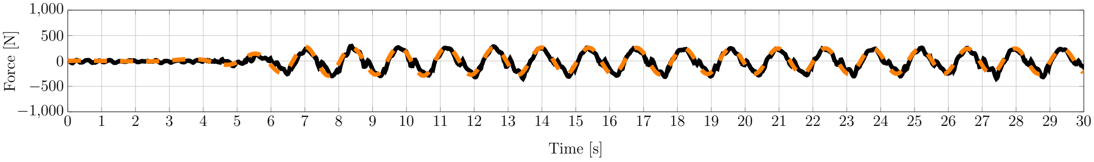

Figure 7.26: Numerical and experimental PTO data for sea state RW1$_{1/5\text{th}}$ with experimental damping $D_{\text{exp}} = 50\text{N m s}$

(a) Pressure gauge PG1

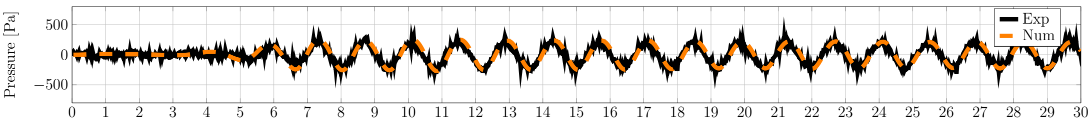

(b) Pressure gauge PG2

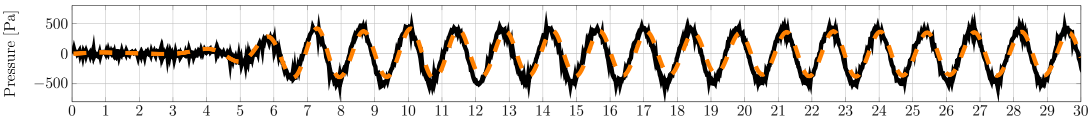

(c) Pressure gauge PG3

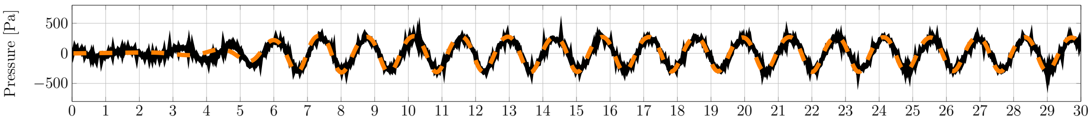

(d) Pressure gauge PG4

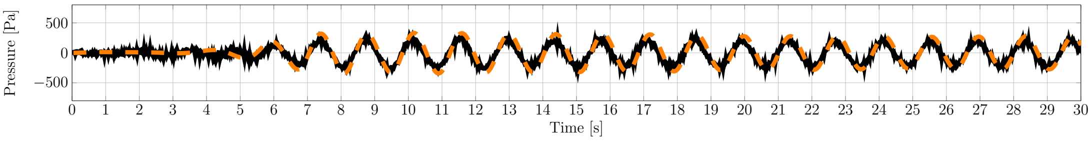

Figure 7.27: Numerical and experimental pressure data for sea state RW1$_{1/5\text{th}}$ with experimental damping $D_{\text{exp}} = 50\text{N m s}$

For the case of $D_{\text{exp}} = 0\,\text{N m s}$, the agreement between experimental and numerical PTO and pressure data decreases significantly (nRMSE$\leq 28\%$). Overall, the PTO position and velocity is under–predicted in the numerical model, resulting in a nRMSE of $\sim 11\%$ (see Figure 7.28). The PTO force shows the most severe deviation. While the force amplitude is captured reasonably well, a significant phase lag can be observed in the troughs. In addition, the experimental data shows a low signal–to–noise ratio, contribution to the relatively large nRMSE value. However, since the force amplitude is very small (approx. ± 200N), other background dynamics in the PTO system (or possibly gantry vibrations), with a high frequency oscillation, cause a non–negligible force, corrupting the signal and making the comparison difficult. The mismatch in body motion is also reflected in the measured pressure at PG1 (nRMSE$\approx 12\%$), PG2 (nRMSE$\approx 11\%$), and PG4 (nRMSE$\approx 13\%$) (see Figure 7.29). At these three probes, a similar pattern, as in the position/velocity data, can be observed. Interestingly, the pressure data at PG3 (nRMSE$\approx 15\%$), facing the wave generator, seems less affected by the previously described mismatch in motion amplitude, and shows relatively good agreement for the pressure magnitude. However, a phase lag causes the relatively large nRMSE.

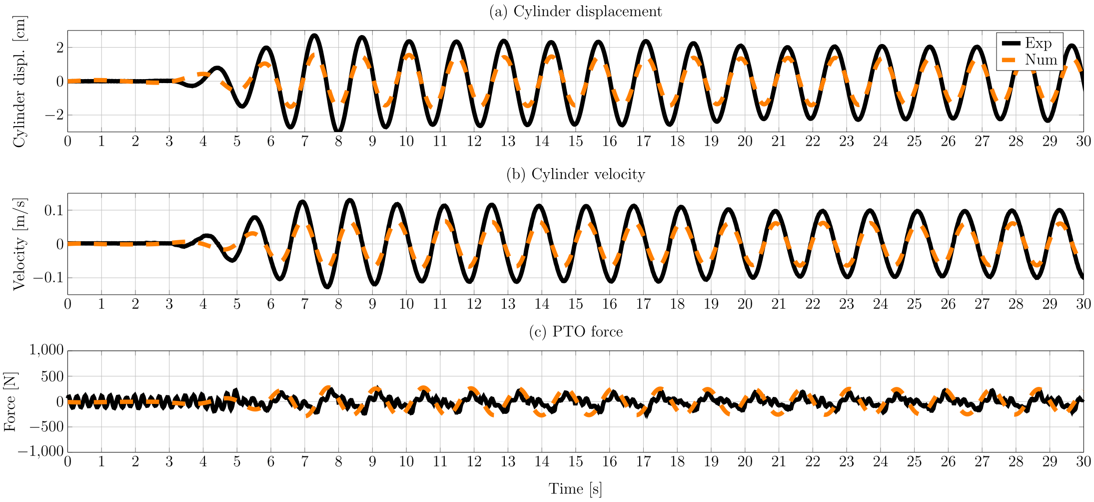

Figure 7.28: Numerical and experimental PTO data for sea state RW1$_{1/5\text{th}}$ with experimental damping $D_{\text{exp}} = 0\text{N m s}$

RW2$_{1/5\text{th}}$

For wave RW2$_{1/5\text{th}}$, the wave height is increased from 0.1m to 0.15m, compared to RW1$_{1/5\text{th}}$. The nRMSE for the PTO signals (displacement, velocity, force), the pressure, and free surface elevation data are listed in Table 7.13. For brevity, time traces of the PTO data and pressure are only plotted for cases $D_{\text{exp}} = 200\,\text{N m s}$ and

(a) Pressure gauge PG1

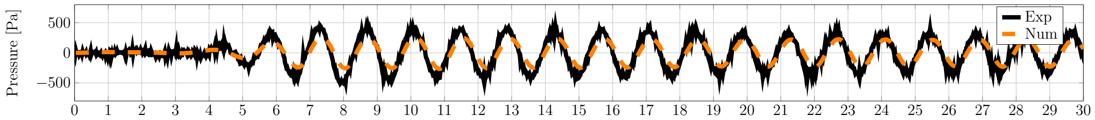

(b) Pressure gauge PG2

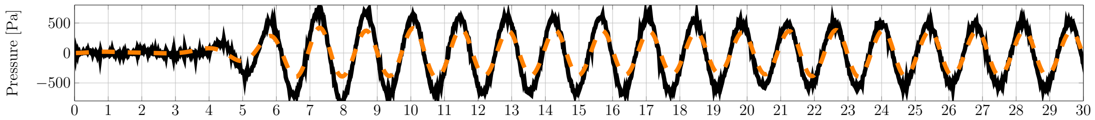

(c) Pressure gauge PG3

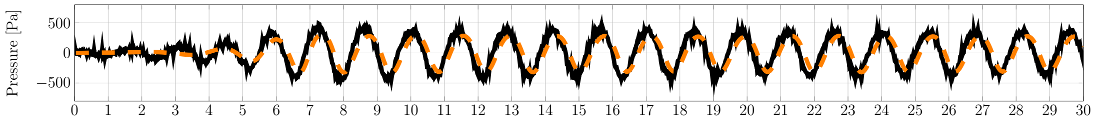

(d) Pressure gauge PG4

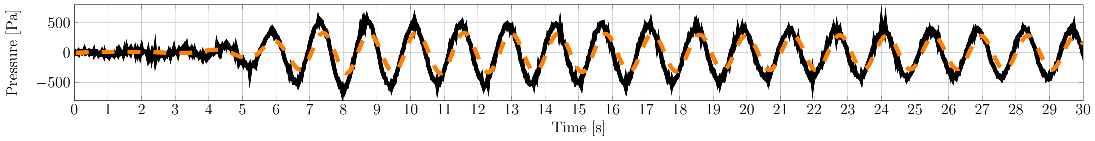

Figure 7.29: Numerical and experimental pressure data for sea state $\mathrm{RW1}_{1/5\mathrm{th}}$ with experimental damping $D_{\mathrm{exp}} = 0\,\mathrm{N\,m\,s}$

$D_{\mathrm{exp}} = 0\,\mathrm{N\,m\,s}$ (see Figures 7.30 to 7.33). Since the free surface elevation data shows consistently good agreement with nRMSE$\leq 11\%$, for brevity, plots are omitted here. Starting again with the highest damping, $D_{\mathrm{exp}} = 200\,\mathrm{N\,m\,s}$, the PTO data show good agreement, with a maximum nRMSE of $\sim 10\%$, for the cylinder displacement, velocity, and PTO force. Excellent agreement in phase is achieved, while the amplitudes for the displacement (nRMSE$=10\%$) and the velocity (nRMSE$=9\%$) are over–predicted. For the PTO force, taking into account noise in the experimental data, the amplitude is well captured in the numerical model (nRMSE$=9\%$). Inspection of the pressure time series, plotted in Figure 7.31, supports the good fit of the cylinder displacement,

Table 7.13: nRMSE between numerical and experimental data for regular wave $\mathrm{RW2}_{1/5\mathrm{th}}$

PTO data

D_{exp} [N m s]	200	100	50	0
Displacement	9.94%	7.87%	6.23%	9.14%
Velocity	8.71%	7.12%	5.96%	8.31%
Force	9.12%	7.76%	7.34%	13.76%

Free surface elevation

D_{exp} [N m s]	200	100	50	0
WP1	6.16%	5.85%	8.11%	7.19%
WP3	5.97%	7.32%	10.42%	8.59%
WP5	10.04%	8.69%	6.76%	10.29%

Pressure

D_{exp} [N m s]	200	100	50	0
PG1	11.86%	17.68%	17.35%	9.94%
PG2	18.68%	23.02%	20.58%	11.06%
PG3	7.12%	6.86%	10.12%	8.24%
PG4	11.08%	22.16%	18.91%	10.21%

velocity, and PTO force data. In particular at PG3, good agreement, with a nRMSE of 7%, is achieved. The larger deviation at PG1 (nRMSE=12%) can be attributed to the high noise level in the experimental data. For PG2 (nRMSE=19%) a phase lag causes the large nRMSE. At PG4 (nRMSE= 11%), again, satisfying results can be observed. For the free surface elevation data, good qualitative and quantitative (nRMSE$\leq$ 10%) agreement is found. As for RW1$_{1/5\mathrm{th}}$, the deviation is again found to be larger than for the wave–only cases (nRMSE$\leq$ 2%), which could be attributed to the influence of the radiated and diffracted waves by the WEC, which is highlighted by the good agreement farthest away form the device (WP1 and WP3) and increased deviations in the vicinity of the body (WP5).

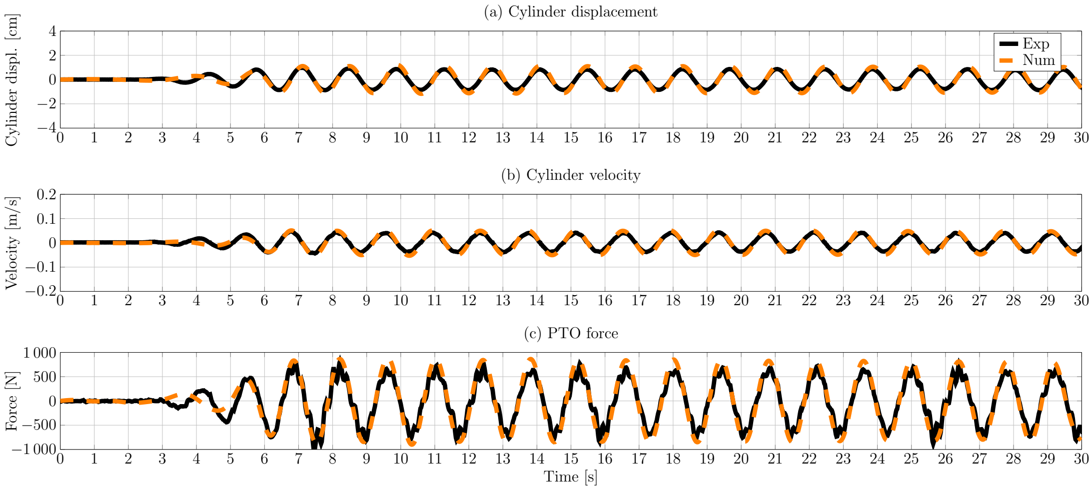

Figure 7.30: Numerical and experimental PTO data for wave RW2$_{1/5\mathrm{th}}$ with experimental damping $D_{\mathrm{exp}} = 200$N m s

For a PTO damping of $D_{\mathrm{exp}} = 100$ N m s similarly good quantitative and qualitative agreement for cylinder displacement (nRMSE=8%), velocity (nRMSE=7%), and PTO force (nRMSE=8%) can be found. Larger deviation can be observed for the pressure measured at PG1 (nRMSE=18%), PG2 (nRMSE=23%), and PG4 (nRMSE=22%). At PG1, over–prediction of the pressure leads to the increased nRMSE. However, considering the signal–to–noise ratio, the deviations lie within an acceptable range. At PG2, a phase lag between experimental and numerical results leads to increased quantitative deviation. The magnitude, however, compares well. At PG3 an over–prediction of the pressure leads to the increased nRMSE. The phase is captured reasonably well.

For $D_{\mathrm{exp}} = 50$ N m s, relatively small errors can be observed for the PTO data, with a minimum nRMSE of $\sim$ 6%. For the pressure data, similarly large deviations as for $D_{\mathrm{exp}} = 100$ N m s occur at PG1 (nRMSE=17%), PG2 (nRMSE=21%), and PG4

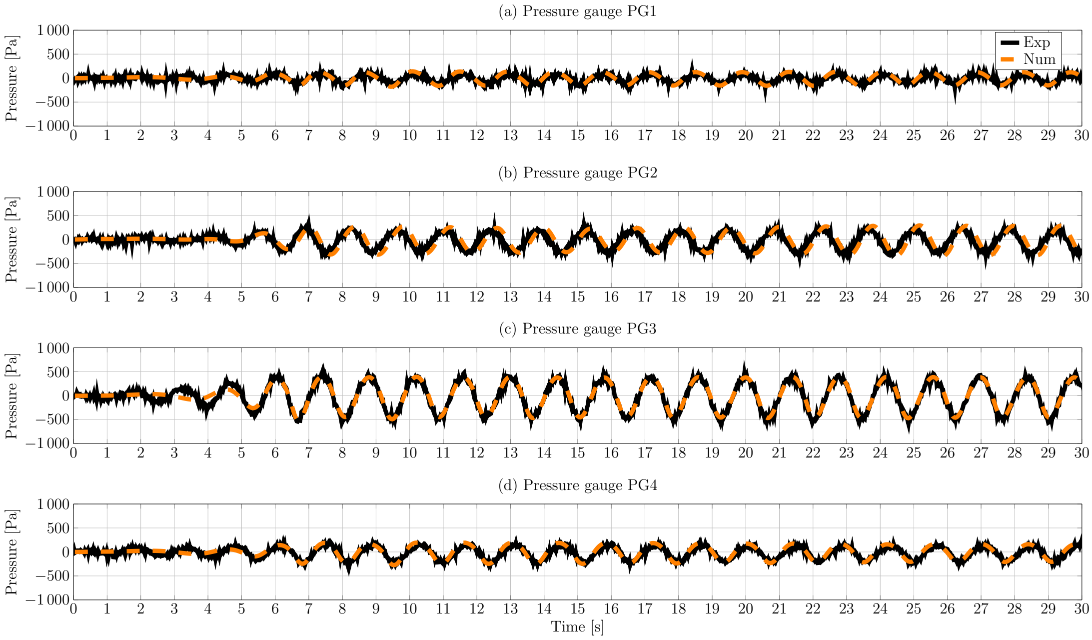

Figure 7.31: Numerical and experimental pressure data for wave RW2$_{1/5\text{th}}$ with experimental damping $D_{\text{exp}} = 200\text{N m s}$

(nRMSE=19%). These stem from a phase lag, while pressure magnitudes compare well for all pressure probes.

For the case of $D_{\text{exp}} = 0\,\text{N m s}$, the agreement between experimental and numerical PTO and pressure data show comparable errors as for $D_{\text{exp}} = 200\,\text{N m s}$. Overall, the cylinder displacement (nRMSE=9%) and velocity (nRMSE=8%) is under–predicted in the numerical model (see Figure 7.32). Furthermore, the body motion does not reach a steady state. Since the zero damping case is associated with significant WEC motion, it can be assumed that larger radiated waves are being generated and reflect from the non-absorbing side walls, which influences the body motion. The deviation in body motion is also reflected in the measured pressure at PG1 (nRMSE=10%), PG2 (nRMSE=11%), and PG4 (nRMSE=10%) (see Figure 7.33). At these probes, a similar pattern, as seen in the displacement/velocity data, can be observed. Interestingly, the pressure data at PG3, facing the wave generator, seems relatively unaffected by the described mismatch in body motion, still showing relatively good agreement between the numerical and experimental data. Lastly, comparing the PTO force, it can be stated that the force amplitude and phase in the numerical model and the experimental data show good agreement. However, the low signal–to–noise ratio in the experimental data leads to a relatively large nRMSE of 14%. Compared to regular wave RW1$_{1/5\text{th}}$, the use of a negative spring stiffness in the numerical model is able to reasonably replicate the experimental system dynamics, for the case of $D_{\text{exp}} = 0\,\text{N m s}$. This may be reasoned with the larger oscillation amplitude, mitigating unrepresented effects of the other background dynamics in the PTO and other system components.

(a) Cylinder displacement

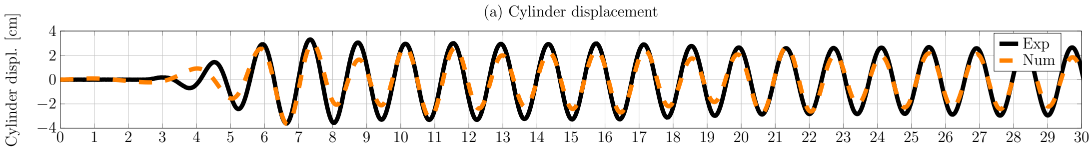

(b) Cylinder velocity

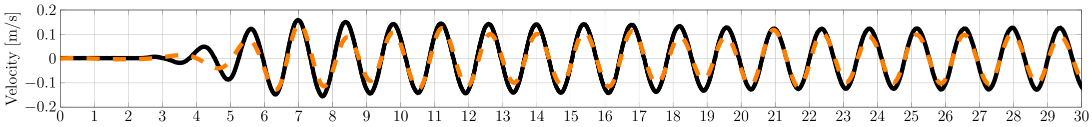

(c) PTO force

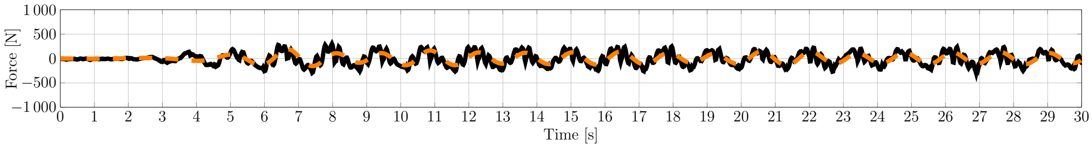

Figure 7.32: Numerical and experimental PTO data for wave RW2$_{1/5\text{th}}$ with experimental damping $D_{\text{exp}} = 0$N m s

(a) Pressure gauge PG1

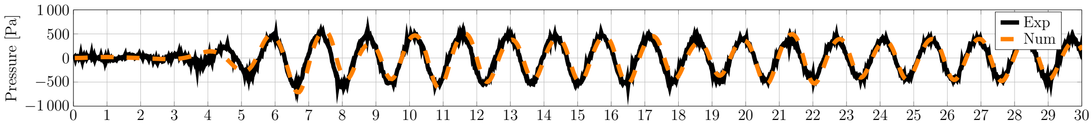

(b) Pressure gauge PG2

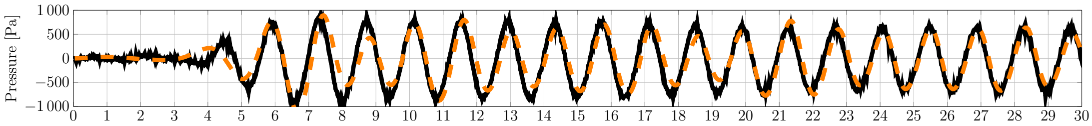

(c) Pressure gauge PG3

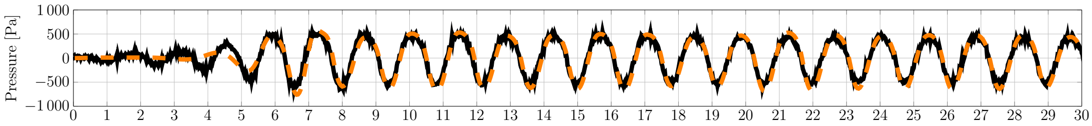

(d) Pressure gauge PG4

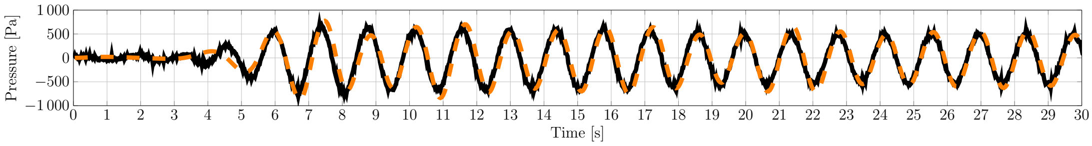

Figure 7.33: Numerical and experimental pressure data for wave RW2$_{1/5\text{th}}$ with experimental damping $D_{\text{exp}} = 0$N m s

RW3$_{1/5\text{th}}$

Considering an even larger wave height, i.e. 0.25m, the agreement between experimental and numerical results for the different PTO damping settings show accuracies of the same order of magnitude, compared to the previous waves RW1$_{1/5\text{th}}$ and RW2$_{1/5\text{th}}$. The results of the quantitative comparison are listed in Table 7.14 and Figures 7.34 to 7.37 show a selection of time traces for a qualitative comparison.

Table 7.14: nRMSE between numerical and experimental data for regular wave RW3$_{1/5\text{th}}$

PTO data				
D_{exp} [N m s]	200	100	50	0
Displacement	10.23%	11.02%	12.31%	11.87%
Velocity	10.42%	11.14%	10.75%	12.06%
Force	9.58%	10.69%	11.69%	12.86%

Free surface elevation				
D_{exp} [N m s]	200	100	50	0
WP1	14.20%	14.35%	16.33%	18.43%
WP3	10.35%	11.79%	9.84%	13.25%
WP5	21.18%	22.04%	17.89%	17.11%

Pressure				
D_{exp} [N m s]	200	100	50	0
PG1	14.21%	16.59%	14.22%	9.14%
PG2	14.16%	11.28%	17.09%	9.36%
PG3	7.96%	11.10%	10.12%	8.26%
PG4	17.36%	25.99%	20.66%	7.84%

From the quantitative and qualitative comparison of the free surface elevation for all damping values, a mismatch in the wave period is obvious, leading to significant differences in the phase after approx. 19s simulated time (see Figure 7.36). This phase divergence in the free surface elevation, consequently, leads to a mismatch in phase for the PTO and pressure data, resulting in relatively large nRMSE values, up to 13% for the PTO force and 26% for the pressure. Furthermore, for all cases, an increasing mismatch in wave amplitude in the vicinity of the body (i.e. WP5) can be observed (see Figure 7.36). This however, is not reflected in the PTO and pressure data (for cases $D_{exp} = 200 - 50$ N m s), where relatively good agreement in the displacement, velocity, force, and pressure amplitudes is achieved. Only the pressure data at pressure gauge PG4 shows consistently poor agreement due to over–prediction of the pressure amplitude.

For $D_{exp} = 0$, the results show very similar behaviour, as for RW2$_{1/5\text{th}}$. Again, an overall under–prediction of displacement, velocity, and force can be seen in the numerical model. Also, no steady state is reached. For the pressure, the fluctuation is reflected at PG1, PG2, and PG4, while, again, a good fit at PG3 is achieved. Here, the experimental data show a characteristic plateau at the pressure peaks. This is well captured in the numerical model.

RW4$_{1/5\text{th}}$

Finally, regular wave RW4$_{1/5\text{th}}$ is considered for validation. While, for the previous test cases, the wave period is constant at 1.4s, the wave period for RW4$_{1/5\text{th}}$ is 2.8s. The availability of experimental data for RW4$_{1/5\text{th}}$ only allows comparison at a single PTO damping setting, i.e. $D_{exp} = 200$ N m s, which, based on the least squares regression from sea states RW1$_{1/5\text{th}}$–RW3$_{1/5\text{th}}$, results in a numerical damping coefficient and spring stiffness of $D_{\text{num}} = 14000\,\text{N}\,\text{s}\,\text{m}^{-1}$ and $K_{\text{num}} = 32100\,\text{N}\,\text{m}^{-1}$, respectively.

(a) Cylinder displacement

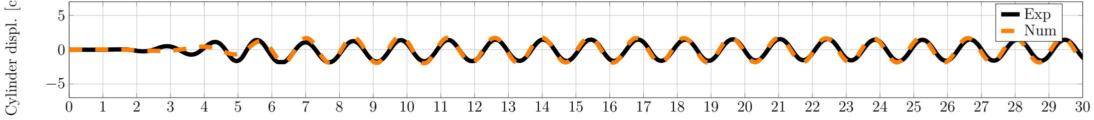

(b) Cylinder velocity

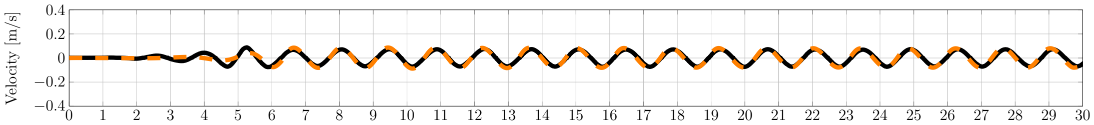

(c) PTO force

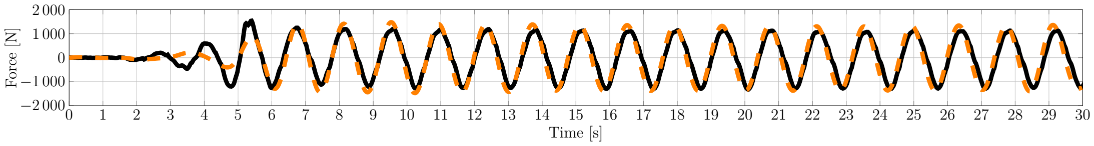

Figure 7.34: Numerical and experimental PTO data for wave RW3$_{1/5\text{th}}$ with experimental damping $D_{\text{exp}} = 200$N m s

(a) Pressure gauge PG1

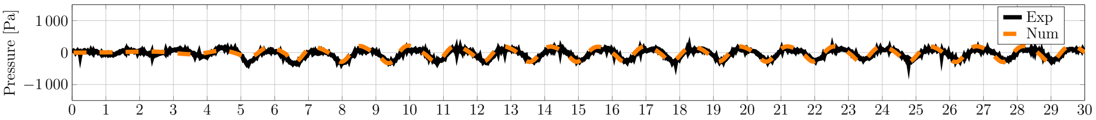

(b) Pressure gauge PG2

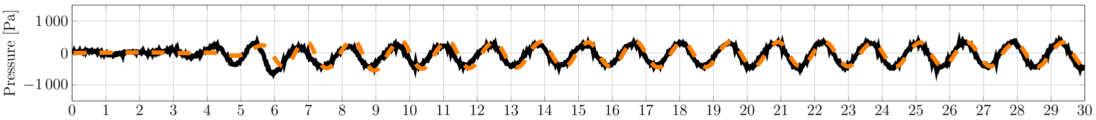

(c) Pressure gauge PG3

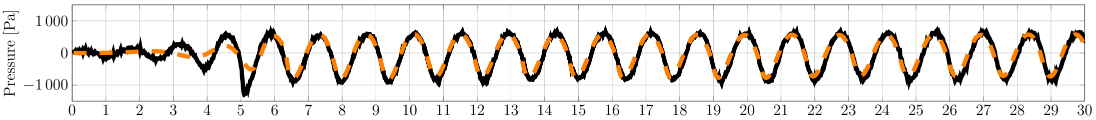

(d) Pressure gauge PG4

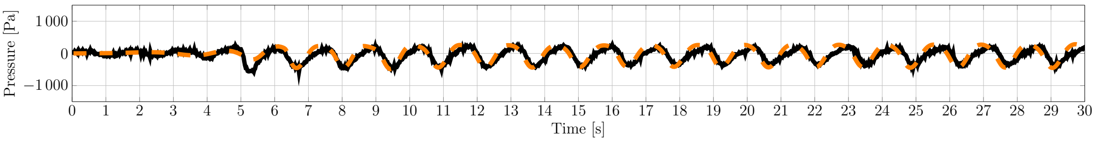

Figure 7.35: Numerical and experimental pressure data for wave RW3$_{1/5\text{th}}$ with experimental damping $D_{\text{exp}} = 200$N m s

Quantitative results are listed in Table 7.15. For a qualitative comparison, PTO, pressure, and free surface elevation data is plotted in Figure 7.38–7.40, respectively. Overall, similar results, as for the previous test cases, are found. For the free surface elevation, all nRMSE values fall below 13%, which is expected with respect to the results found for the wave–only case. The PTO cylinder displacement and velocity show relatively small deviations with nRMSE values of 6%. The force signal reveals a relatively small over–prediction of the PTO force in the numerical model. However, a phase lag between the numerical and experimental force signal can be observed,

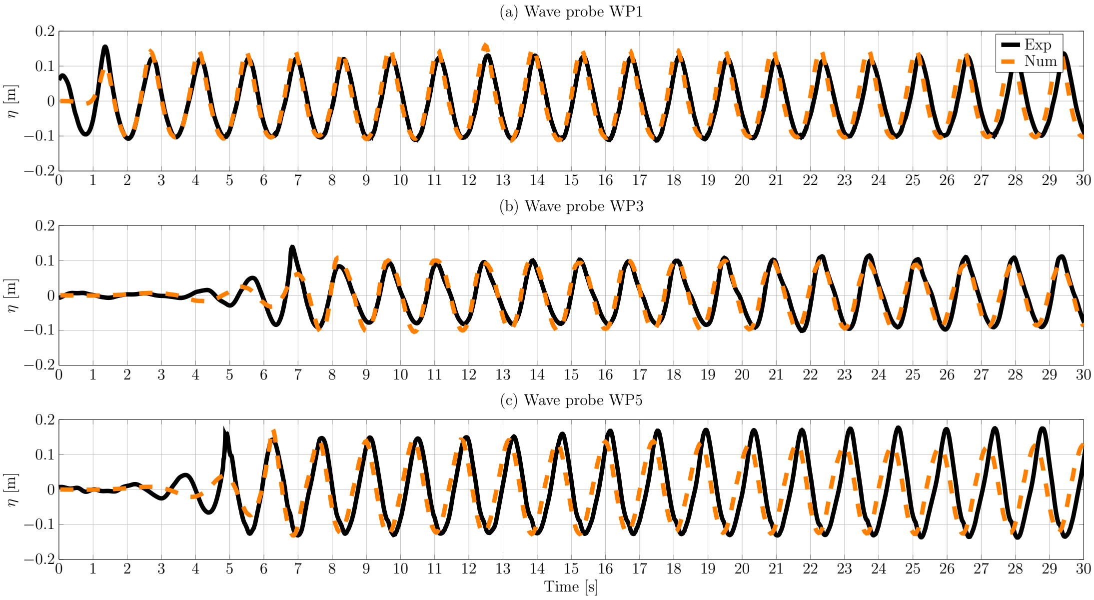

Figure 7.36: Numerical and experimental free surface elevation data for wave RW3$_{1/5\text{th}}$ with experimental damping $D_{\text{exp}} = 200\text{N m s}$

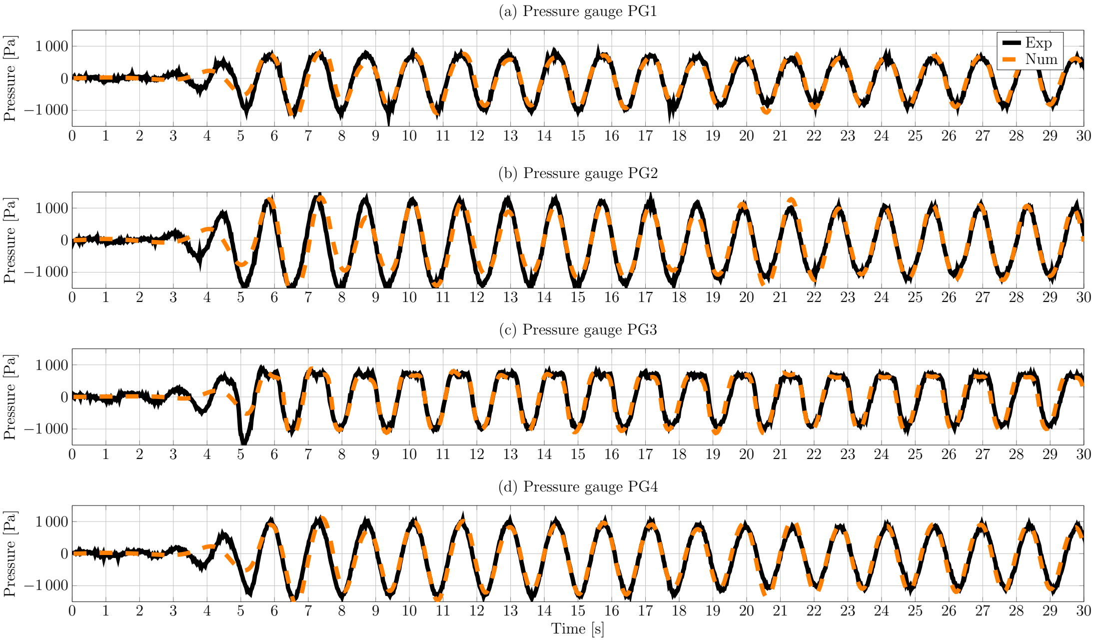

Figure 7.37: Numerical and experimental pressure data for wave RW3$_{1/5\text{th}}$ with experimental damping $D_{\text{exp}} = 0\text{N m s}$

leading to a nRMSE of 18%. This suggests that the employed combination of spring stiffness and damping coefficient does not accurately represent the physical system, which, in turn, suggests that the estimated coefficients D_{num} and K_{num}, to replicate the physical PTO system, are frequency dependent, implying non–linearity of the physical PTO system.

The phase deviation, found in the PTO force signal, also appears in the pressure data at all pressure gauges. Both force and pressure show a phase difference of approx. 0.3s. This highlights the assumption that the characteristics of the physical system are frequency dependent and currently not accurately represented in the numerical model. However, for the purpose of this study, the agreement between numerical and experimental results is acceptable.

Table 7.15: nRMSE between numerical and experimental data for regular wave RW4$_{1/5\text{th}}$

PTO data		**Free surface elevation**		**Pressure**	
D_{exp} [N m s]	200	D_{exp} [N m s]	200	D_{exp} [N m s]	200
Displacement	6.36%	WP1	13.10%	PG1	18.14%
Velocity	6.10%	WP3	8.96%	PG2	26.89%
Force	17.89%	WP5	12.07%	PG3	18.25%
				PG4	18.86%

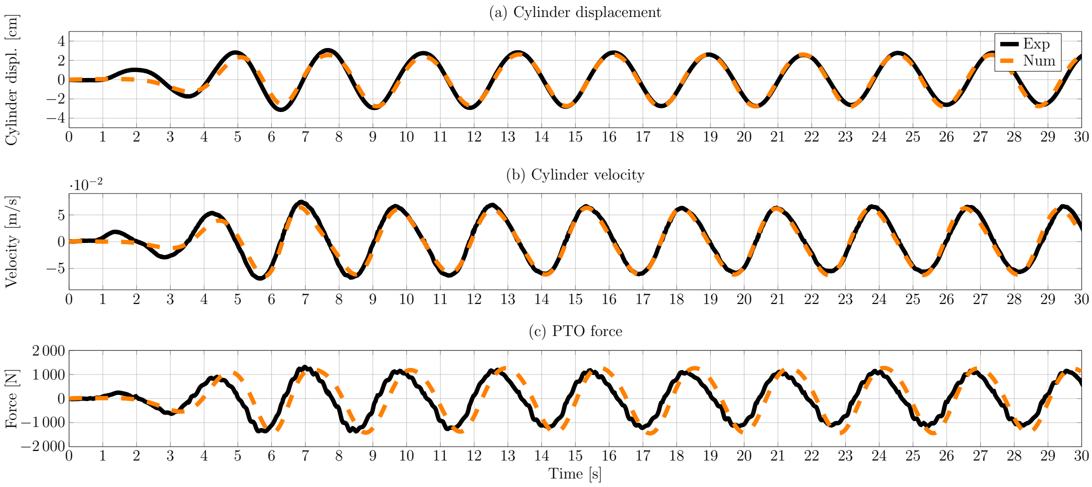

Figure 7.38: Numerical and experimental PTO data for sea state RW4$_{1/5\text{th}}$ with experimental damping $D_{\text{exp}} = 200$N m s

This section documents the validation of a 1/5th scale numerical model of the Wavestar WEC against experimental data under various test conditions. The dynamics of the experimental setup are captured with satisfying accuracy by introducing a linear spring–damper system in the CFD–based NWT, where coefficients are determined through linear least squares regression. Comparing the free surface elevation, as well as PTO data and the pressure on the hull, relatively consistent agreement between the numerical and experimental data is found across the range of test cases. Given the required assumptions and simplification in the CFD–based NWT, the presented model of the Wavestar WEC is considered to be, in a general sense, validated.

(a) Pressure gauge PG1

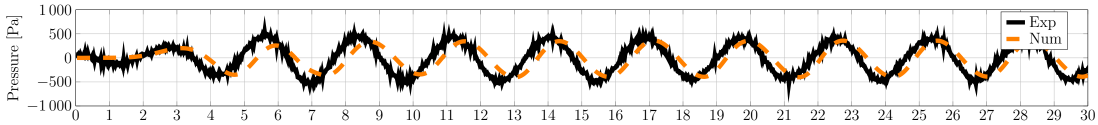

(b) Pressure gauge PG2

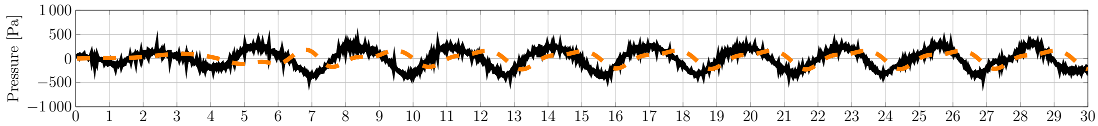

(c) Pressure gauge PG3

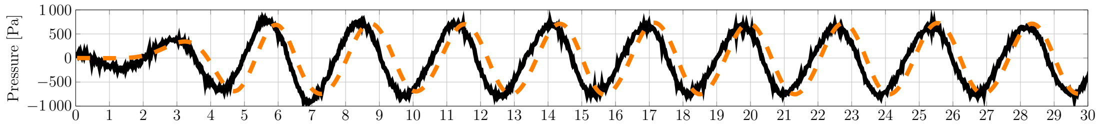

(d) Pressure gauge PG4

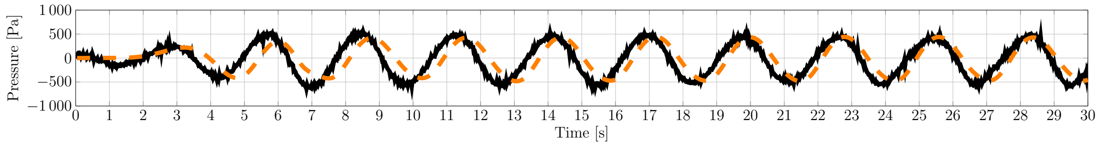

Figure 7.39: Numerical and experimental pressure data for sea state $\text{RW4}_{1/5\text{th}}$ with experimental damping $D_{\text{exp}} = 200\text{N m s}$

(a) Wave probe WP1

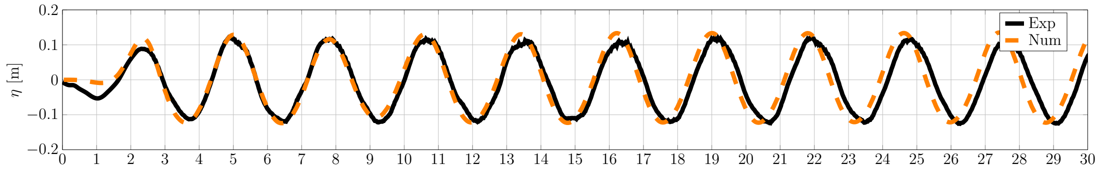

(b) Wave probe WP3

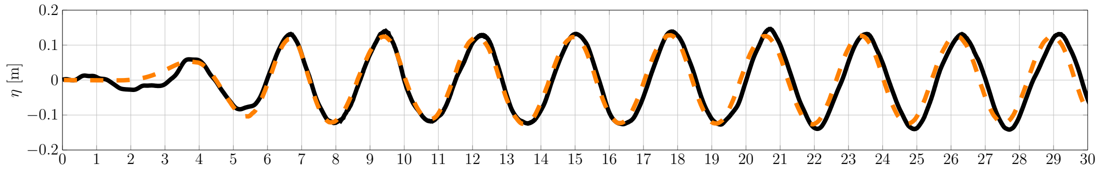

(c) Wave probe WP5

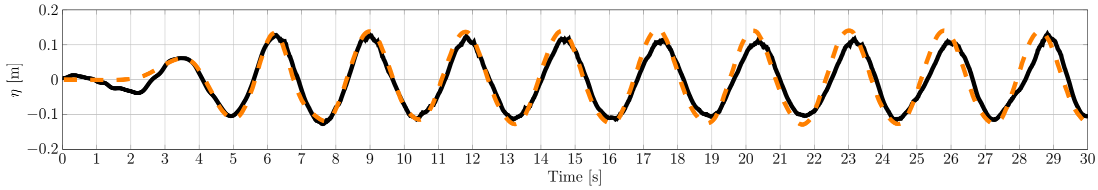

Figure 7.40: Numerical and experimental η data for sea state $\text{RW4}_{1/5\text{th}}$ with experimental damping $D_{\text{exp}} = 200\text{N m s}$

7.2 Wavestar – 1/20th scale

Recently, a set of experimental tank tests of a 1/20th scale Wavestar model were conducted at Aalborg University, as part of the international WEC control competition (WECCCOMP) [585]. This section documents the validation of a CFD-based NWT model of the 1/20th scale Wavestar model against the experimental data acquired during the test campaign. As in the previous Section 7.1, the present validation study follows an incremental procedure in which, first, wave–only cases will be validated, followed by wave excitation force, free decay, forced oscillation, and wave–induced motion cases. This allows an accurate assessment of potential misfits between experimental and numerical results. Together with the validation study in Section 7.1, the validated 1/20th scale Wavestar model forms the basis for the analysis of hydrodynamic scale effects in Chapter 10.

7.2.1 Physical wave tank

The experimental data, used within this validation study, was acquired during physical wave tank tests in the wave basin at Aalborg University. A schematic of the wave basin, including all relevant dimensions, is shown in Figure 7.41 (a). Throughout the test campaign, free surface elevation data is measured with four resistive wave probes (WP1–WP4), whose locations are indicated in Figure 7.41 (a).

For this validation study, a 1/20th scale model of a single float of the full scale device is considered with an electrical, direct drive actuator PTO, inspired by the case study for the WECCCOMP. In the wave basin, the device and the supporting structure are mounted on a gantry. Forces on the structure are measured with an S-type load cell, connecting the linear actuator with the arm and floating structure. The (translational) floater position is measured as the elongation of the linear actuator via an optical laser position sensor.

A schematic and a photograph of the device are shown in Figure 7.41 (b) and (c), respectively. The structural properties are listed in Table 7.16. Note that the mass and inertial properties, as well as the location of the centre of mass are taken from [586] and were not explicitly measured during the test campaign.

7.2.2 Test cases

During the physical test campaign, a number of different test cases were considered including, amongst others, wave–induced motion of a controlled device [SMD]; however, for the validation of the CFD–based NWT, only the following five test cases, with incrementally increasing complexity, are considered:

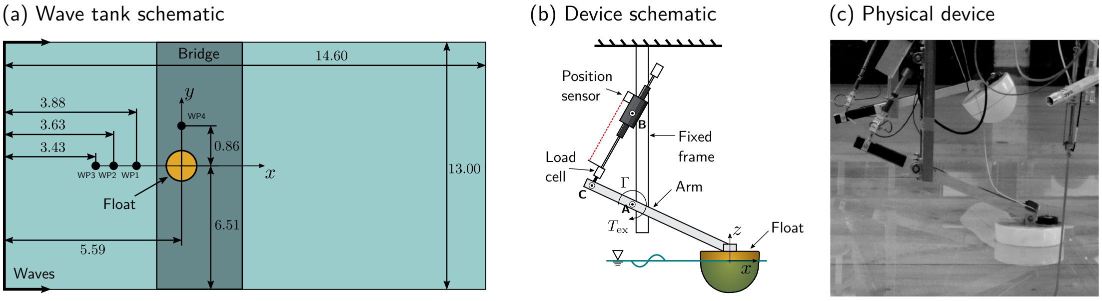

(a) Wave tank schematic (b) Device schematic (c) Physical device

Figure 7.41: Schematic (not at scale) (a) of the physical wave tank including the wave probe positions (all dimensions in [m]) and (b) the device. (c) shows a photograph of the physical device.

Table 7.16: Physical properties of the 1/20th scale Wavestar model. All measurements taken from [586] are highlighted in orange.

Property	Value	Unit
Mass (float & arm)	4.23	[kg]
Inertia (float & arm)	0.95	[kg m^2]
Floater diameter (at SWL)	0.25	[m]
Submergence (in equilibrium)	0.10	[m]
Water depth d	0.90	[m]
Hinge **A**:		
x	-0.45	[m]
y	0.00	[m]
z	0.23	[m]
Hinge **B**:		
x	-0.45	[m]
y	0.00	[m]
z	0.64	[m]
Hinge **C**:		
x	-0.64	[m]
y	0.00	[m]
z	0.30	[m]
Centre of mass:		
x	-0.05	[m]
y	0.00	[m]
z	0.11	[m]

(1) wave–only test cases, to ensure an accurate representation of the incident waves; (2) wave excitation force tests, to introduce wave–structure interaction, but still keep the complexity of the model relatively low; (3) free decay tests, to get a preliminary understanding of the ability of the numerical model to capture the system dynamics; (4) forced oscillation tests; (5) wave–induced motion tests.

Waves–only

For the wave–only test cases, the device is lifted out of the water and the waves propagate through the tank undisturbed. The characteristics of the waves, i.e. wave ID, target wave height[2], H_{tar}, wave period T, wave frequency f, wave length λ, and the wave steepness H_{tar}/λ, are listed in Table 7.17. During the wave–only tests, the free surface elevation is measured with four resistive wave probes, WP1–WP4 (see Figure 7.41).

Table 7.17: Characteristics of the regular waves

Wave ID	H_{tar}	T	f	λ	H_{tar}/λ
$\text{RW1}_{1/20\text{th}}$	0.021m	0.99s	1.01Hz	1.56m	0.0135
$\text{RW2}_{1/20\text{th}}$	0.063m	1.41s	0.71Hz	2.93m	0.0215
$\text{RW3}_{1/20\text{th}}$	0.115m	1.84s	0.54Hz	4.50m	0.0256

Wave excitation

During the wave excitation force tests, the WEC is locked in its equilibrium position, while being exposed to waves $\text{RW1}_{1/20\text{th}}$–$\text{RW3}_{1/20\text{th}}$. During these tests, the free surface elevation, as well as the wave excitation force, are measured using resistive wave probes and a load cell (see Figure 7.41 (b)), respectively.

Free decay

For the free decay tests, the body is manually lifted out of its equilibrium position and then released to oscillate freely around the equilibrium position. Three consecutive experimental runs are considered. Translational position data of the WEC is recorded throughout the tests using the optical position sensor (see Figure 7.41 (b)) and transformed into rotational displacement about hinge **A** through geometric transformation.

Forced oscillation

During the forced oscillation tests, the WEC is driven into motion by applying a defined input force through the linear actuator. Two different types of excitation can be distinguished:

---

[2] The target wave height denotes the wave height specified within the physical wave maker controller.

Single–frequency excitation

For the single–frequency excitation cases, a simple sinusoidal force signal is used to drive the system. Four different cases, with varying frequency and force amplitude, are considered. The excitation frequency correlates with the wave frequency ($^1/_T$) of waves $\text{RW1}_{1/20\text{th}}$–$\text{RW3}_{1/20\text{th}}$.

Multi–frequency excitation

The multi–frequency excitation experiments are initially performed for system identification purposes and are realised through up-chirp force signals [336, 319]. The input force is defined as a linear frequency sweep in the range of [0.7, 30] $^{\text{rad}}/_{\text{s}}$, with a fixed amplitude of 10N. Note that, due to unavailability of the experimental force signal in the post-processing stage, the torque about the centre of rotation, i.e. hinge **A**, is considered for the multi–frequency excitation experiments.

7.2.3 Wave–induced WEC motion

Finally, for the wave–induced WEC motion tests, the (uncontrolled) WEC is exposed to the incident waves $\text{RW1}_{1/20\text{th}}$–$\text{RW3}_{1/20\text{th}}$ and the motion, as well as the free surface elevation are monitored.

7.2.4 Numerical wave tank

The CFD–based NWT is implemented using the open-source CFD toolbox OpenFOAM version 4.1 of the OpenFOAM Foundation fork [584]. The setup of the CFD–based NWT in this section builds upon the validation study in Section 7.1. The same solver settings and solution schemes (see Table 7.5), flow conditions, as well as the dynamic mesh motion method, PTO representation, and boundary conditions as for the 1/5th scale model are used for the 1/20th scale numerical model. The problem discretisation is also informed by the results shown in Section 7.1 and adjusted to the wave characteristics considered throughout this section. Only the numerical wave generation and absorption methodology differs significantly from the numerical model presented in Section 7.1, allowing more efficient simulation.

Numerical wave generation and absorption

To ensure sufficient quality of the free surface elevation in Section 7.1, the relaxation zone method [97] is employed. It is well known that this methodology increases the computational overhead by introducing additional cells in the computational domain to accommodate the relaxation zones. The combination of a static boundary method for wave generation [102], and a numerical beach for wave absorption [110], in this study can deliver good free surface elevation fidelity with minimal wave reflection and low cell counts.

To determine the optimal beach length L_B and maximum damping factor $s_{b,\text{Max}}$ a preliminary parametric study is performed. Generally, the numerical beach settings are dependent on the wave height and wave length (see Chapter 6), where longer wave lengths require longer beach lengths for efficient wave absorption. Thus, the longest (and largest) wave RW3$_{1/20\text{th}}$ is used for the parametric study. Table 7.18 includes the reflection coefficient R, determined based on [561], for different combinations of L_B and $s_{b,\text{Max}}$. Even with a beach length of $L_B = 1\lambda_{\text{RW3}_{1/20\text{th}}}$, and a maximum damping factor of 2.5s^{-1}, a reflection coefficient of 1.7% is achieved, which can be considered small [574]. No significant differences can be observed regarding the reflection coefficient for the different beach lengths with a maximum damping factor of 2.5s^{-1}. Thus, to keep the overall cell count low, the shortest beach length is chosen for all subsequent simulations. A screen shot of the s_b field is shown in Figure 7.42.

Table 7.18: Reflection coefficients R for different combinations of L_B and $s_{b,\text{Max}}$. For reference, the run time is added in parenthesis for each individual case.

$s_{b,\text{Max}}$	$L_B = 1\lambda_{\text{RW3}_{1/20\text{th}}}$	$L_B = 1.5\lambda_{\text{RW3}_{1/20\text{th}}}$	$L_B = 2\lambda_{\text{RW3}_{1/20\text{th}}}$
2.5s^{-1}	1.77% (3087s)	1.50% (2567s)	1.68% (2294s)
5s^{-1}	1.77% (1990s)	1.50% (3613s)	1.68% (2006s)

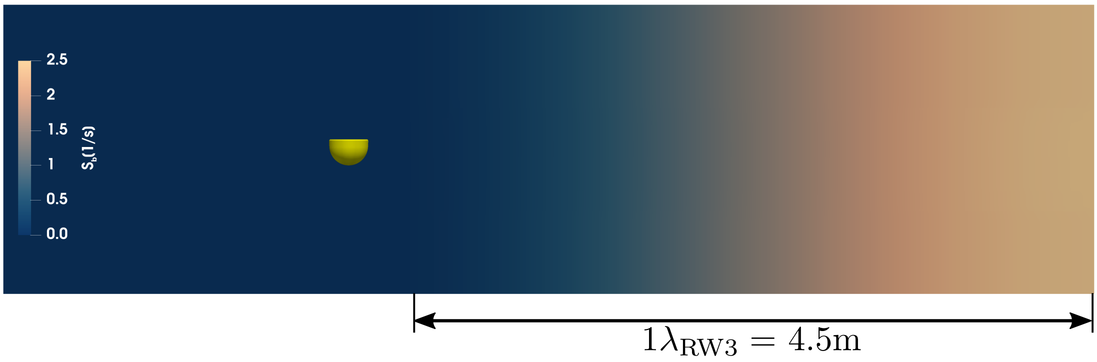

Figure 7.42: Side view of the computational domain: Screen shot of the s_b field.

Computational domain

The same computational domain is used for all the different test cases considered during the validation of the 1/20th scale model. Figures 7.43 (a) and (b) show the side and top view of the numerical domain, including all relevant dimensions, respectively. To reduce the overall cell count, the symmetry of the problem is exploited and only half of the physical wave tank is modelled numerically. A symmetry boundary condition is employed in the xz–plane. Furthermore, the width of the CFD–based NWT is reduced and the distance between the wave generation boundary and the device location is shortened, compared to the physical wave tank.

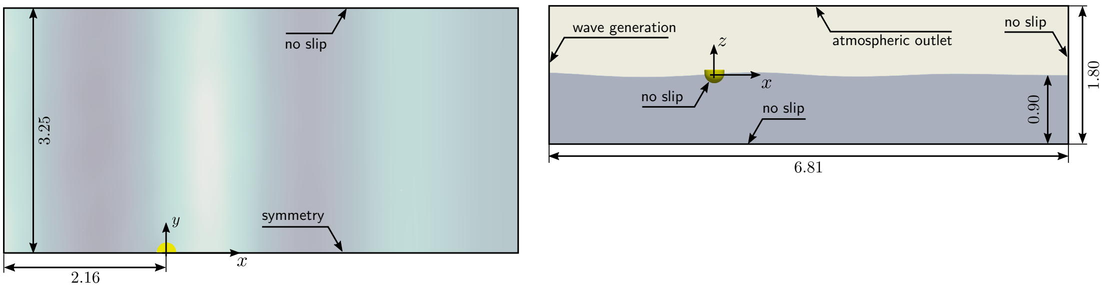
(a) Top view
(b) Side view

Figure 7.43: Schematic of the numerical wave tank (all dimensions in [m]): (a) top view and (b) side view.

The choice of the spatial and temporal discretisation sizes follows the choice in Section 7.1. Spatially, the interface region in the simulation zone (see Figure 7.44) and region around the body are discretised with cells of a (vertical) size of 10 cells per wave height of $\text{RW1}_{1/20\text{th}}$ ($\text{CPH}_{\text{RW1}_{1/20\text{th}}}$) and a maximum aspect ratio of 4 in the horizontal and lateral direction, resulting in 186 cells per $\lambda_{\text{RW1}_{1/20\text{th}}}$. For the temporal discretisation, a fixed time step size of $\Delta t = 0.001$s is used.

To determine an appropriate discretisation, three different cell and time step sizes are tested, where the former is parametrised by the wave height. The cell sizes (in the interface region) are: 5, 10, and 20CPH. The time step sizes are $\Delta t = 0.002$, 0.001, and 0.0005s. The phase averaged wave height at the intended device location ([x,y,z]=[0,0,0]) is used as the input to the convergence study. The results of the (numerically) measured wave height, together with the convergence type and the discretisation uncertainty is listed in Table 7.19. For completeness, temporal convergence studies are also performed for wave $\text{RW2}_{1/20\text{th}}$ and $\text{RW3}_{1/20\text{th}}$, for which results are listed in Table 7.20 and 7.21, respectively. A screen shot of the discretisation in the xz–plane is shown in Figure 7.44.

Table 7.19: Results of the spatial and temporal convergence study for RW$1_{1/20\text{th}}$

Δz	Δt [s] 2×10^{-3}	Δt [s] 1×10^{-3}	Δt [s] 0.5×10^{-3}	Conv. Type	$\mathcal{U}$
5CPH$_{\text{RW1}_{1/20\text{th}}}$	0.022m	0.022m	0.022m	Monotone	0.7%
10CPH$_{\text{RW1}_{1/20\text{th}}}$	0.022m	0.023m	0.023m	Monotone	0.2%
20CPH$_{\text{RW1}_{1/20\text{th}}}$	0.023m	0.023m	0.023m	–	–
Conv. Type	Monotone	Monotone	Monotone		
$\mathcal{U}$	1.2%	0.3%	0.7%		

Table 7.20: Results of the spatial and temporal convergence study for RW$2_{1/20\text{th}}$

Δz	Δt [s] 2×10^{-3}	Δt [s] 1×10^{-3}	Δt [s] 0.5×10^{-3}	Conv. Type	$\mathcal{U}$
10CPH$_{\text{RW1}_{1/20\text{th}}}$	0.059m	0.061m	0.061m	Monotone	0.8%

Table 7.21: Results of the spatial and temporal convergence study for RW$3_{1/20\text{th}}$

Δz	Δt [s] 2×10^{-3}	Δt [s] 1×10^{-3}	Δt [s] 0.5×10^{-3}	Conv. Type	$\mathcal{U}$
10CPH$_{\text{RW1}_{1/20\text{th}}}$	0.099m	0.100m	0.100m	Monotone	1.1%

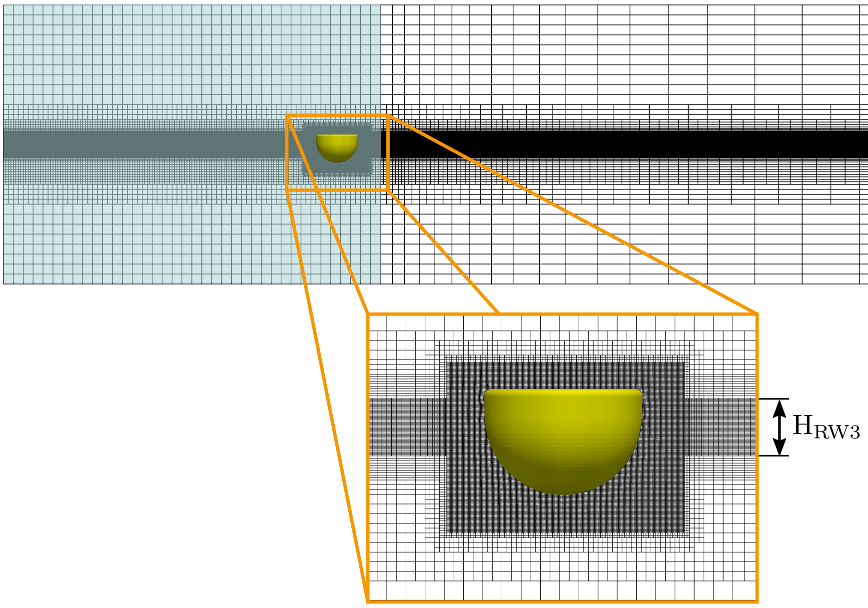

Figure 7.44: Screen shot of the computational mesh in the xz–plane. The simulation zone, in which the damping factor $s_b = 0$, is highlighted in blue.

7.2.5 Results and discussion

This section presents the numerical results for the five different test cases introduced in Section 7.2.2, including a comparison with the experimental data.

Waves–only

For the wave–only test case, the long crested plane waves, considered in the present section, allow simulation in a two–dimensional domain, since such waves are invariant in the lateral direction. Figures 7.45 (a)–(c) show the experimental phase averaged time traces of the free surface elevation, measured at wave probes WP1–WP4 (see Figure 7.41 (a)), for waves RW1$_{1/20\text{th}}$–RW3$_{1/20\text{th}}$, respectively. The results of the measured wave height, H_{exp}, and the relative standard deviation, $\sigma_{H_{\text{exp}}}$, normalised by H_{exp}, are listed in Table 7.22.

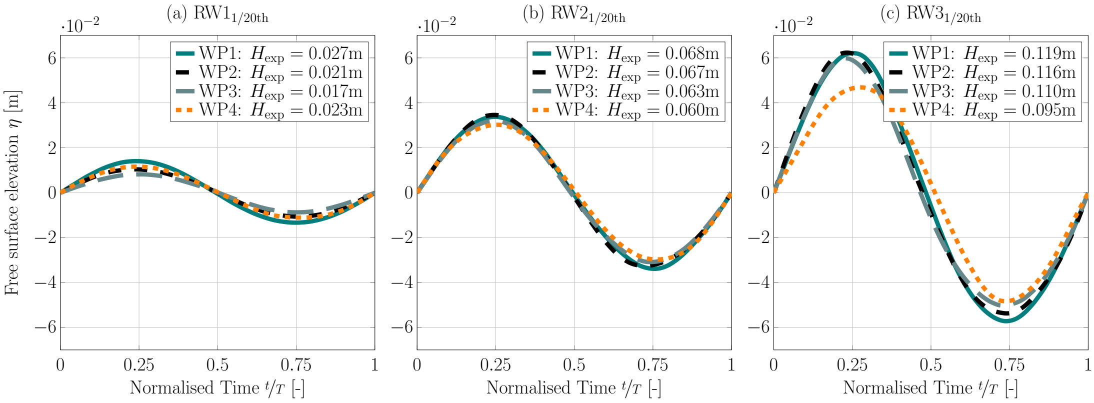

Figure 7.45: Phase averaged free surface elevation, measured at wave probes WP1–WP4 (see Figure 7.41), for waves (a) RW1$_{1/20\text{th}}$, (b) RW2$_{1/20\text{th}}$, and (c) RW3$_{1/20\text{th}}$.

The results in Table 7.22 show that $\sigma_{H_{\text{exp}}}$ is consistent between all wave probes and waves with values of the order of $\sim 0.5\%$, indicating relatively small deviations between consecutive wave periods, considered during the phase averaging. More inconsistencies can be observed for the wave heights between the different wave probes, as indicated in Figures 7.45 (a)–(c). Specifically for wave RW3$_{1/20\text{th}}$, significant discrepancies between the measured free surface elevation at wave probes WP1–WP3 ($H_{\text{exp}} \approx 0.110$m) and WP4 ($H_{\text{exp}} = 0.095$m) are found. Based on the increased spread between the wave probes with increased wave height and period, it can be assumed that the observed behaviour stems from the influence of wave reflections due to the absorption characteristics of the physical wave tank.

Table 7.22: Wave height H_{exp} and the relative standard deviation $\sigma_{H_{\text{exp}}}$, normalised by H_{exp}, from the experimental data for waves RW$1_{1/20\text{th}}$–RW$3_{1/20\text{th}}$.

RW$1_{1/20\text{th}}$	WP1	WP2	WP3	WP4
H_{exp} [m]	0.027	0.021	0.017	0.023
$\sigma_{H_{\text{exp}}}$ [%]	0.56	0.68	0.76	0.53
RW$2_{1/20\text{th}}$				
H [m]	0.068	0.067	0.063	0.060
$\bar{\sigma}$ [%]	0.66	0.58	0.48	0.31
RW$3_{1/20\text{th}}$				
H [m]	0.119	0.116	0.110	0.095
$\bar{\sigma}$ [%]	0.70	0.59	0.72	0.48

The discrepancy between the different wave probes for the individual waves poses a challenge for the selection of the 'correct' wave characteristic in the CFD–based NWT. Figures 7.46–7.48 show the comparison between the phase averaged experimental and numerical free surface elevation, measured at wave probes WP1–WP4, for waves RW$1_{1/20\text{th}}$–RW$3_{1/20\text{th}}$, respectively. For the individual waves, Table 7.23 lists the nRMSE (see Equation (6.4)), where $\mathcal{F}$ is the experimental free surface elevation, $\hat{\mathcal{F}}$ is the numerical free surface elevation, and $\mathcal{N}$ is the target wave height H_{tar}, listed in Table 7.17.

Table 7.23: nRMSE between the experimental and numerical free surface elevation, for waves RW$1_{1/20\text{th}}$–RW$3_{1/20\text{th}}$.

RW$1_{1/20\text{th}}$	WP1	WP2	WP3	WP4
nRMSE [%]	8.31	3.86	10.70	2.27
RW$2_{1/20\text{th}}$				
nRMSE [%]	4.66	4.78	2.82	2.42
RW$3_{1/20\text{th}}$				
nRMSE [%]	2.87	3.75	5.00	9.26

Generally, a relatively good match in phase can be observed for all waves at all wave probes in Figures 7.46–7.48. Furthermore, Figures 7.46–7.48 reveal a consistent wave field within the CFD–based NWT for all waves, with negligible differences in wave height and phase between the wave probes. The consistency in the wave field can be expected due to the excellent absorption capabilities achieved with the numerical beach, with a reflection coefficient below 2%. The difference in consistency of the experimental and numerical wave field leads to varying agreement between the experimental and numerical data (see Table 7.23), with a maximum deviation of 10.70% (RW$1_{1/20\text{th}}$ at wave probe WP3). This varying agreement has to be taken into account for any further comparison between the experimental and numerical data.

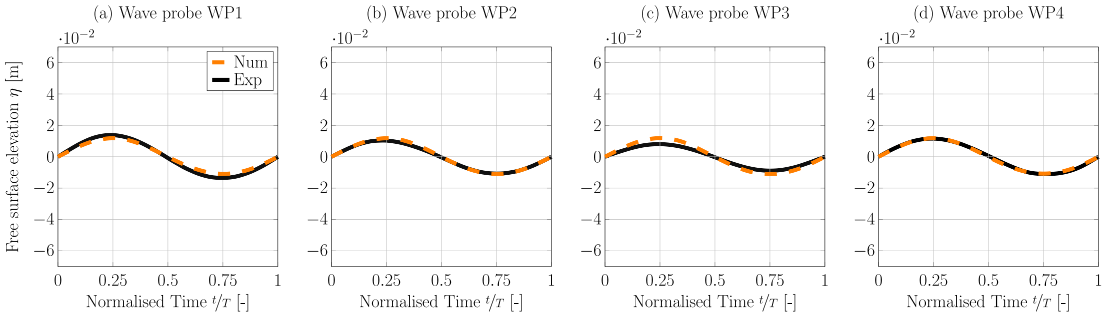

Figure 7.46: Experimental and numerical phase averaged free surface elevation, measured at wave probes WP1–WP4 (a)–(d), for wave RW$1_{1/20\text{th}}$.

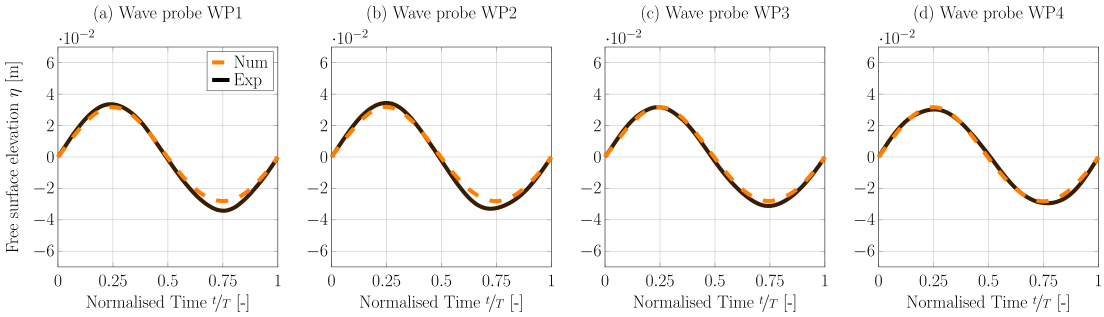

Figure 7.47: Experimental and numerical phase averaged free surface elevation, measured at wave probes WP1–WP4 (a)–(d), for wave RW$2_{1/20\text{th}}$.

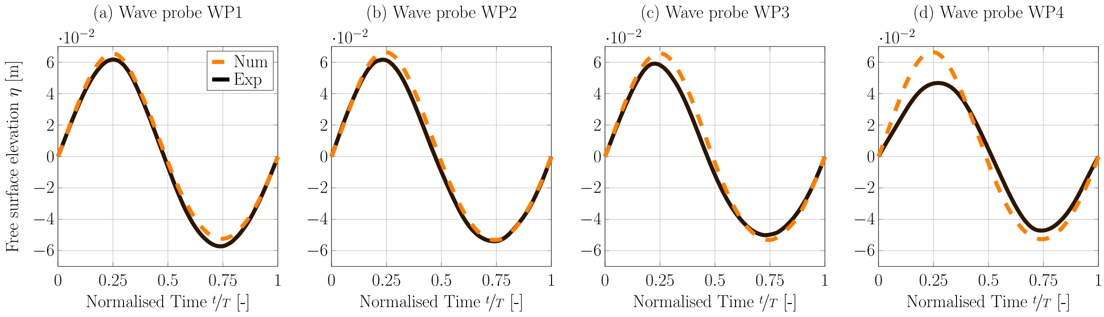

Figure 7.48: Experimental and numerical phase averaged free surface elevation, measured at wave probes WP1–WP4 (a)–(d), for wave RW$3_{1/20\text{th}}$.

Wave excitation

As stated in Section 7.2.2, the wave excitation force is measured with a load cell, connecting the linear actuator and the floater. From a post–processing point of view, it is simpler, in the CFD–based NWT, to extract the wave excitation torque, $T_{\text{ex,num}}$, instead of the linear force (see Figure 7.41 (b)). Thus, from geometric considerations, the experimental wave excitation torque, $T_{\text{ex,exp}}$, is selected as the comparison variable in the following.

Figures 7.49–7.51 show the results of the phase averaged wave excitation torque $T_{\text{ex,exp}}$ and $T_{\text{ex,num}}$, as well as the free surface elevation, measured at wave probes WP1–WP4. For a quantitative comparison, Table 7.24 lists the nRMSE between the experimental and numerical data. Note that the experimental excitation torque magnitude is used for the normalisation of the wave excitation torque RMSE.

Table 7.24: nRMSD between the experimental and numerical free surface elevation and excitation torque for waves RW1$_{1/20\text{th}}$–RW3*$_{1/20\text{th}}$.

RW1$_{1/20\text{th}}$	WP1	WP2	WP3	WP4	T_{ex}
nRMSD [%]	8.49	3.83	8.42	3.04	2.70
RW2$_{1/20\text{th}}$					
nRMSD [%]	5.56	4.45	2.82	1.93	9.32
RW3$_{1/20\text{th}}$ ($H = 0.115$m)					
nRMSD [%]	3.17	3.77	3.42	9.76	12.48
RW3*$_{1/20\text{th}}$ ($H = 0.090$m)					
nRMSD [%]	12.14	10.97	7.70	5.34	4.31

For the free surface elevation, overall, similar agreement between the experimental and numerical data can be observed, compared to the wave–only cases. A notable deviation in agreement between different wave probes for the individual waves is visible, which is consistent with the wave–only cases. Regarding the agreement between the experimental and numerical excitation torque, an expected close correlation between the agreement of the free surface elevation at wave probe WP4 (e.g. 3.04% for RW1$_{1/20\text{th}}$ and 9.76% for RW3$_{1/20\text{th}}$) and the agreement of T_{ex} (2.7% for RW1$_{1/20\text{th}}$ and 12.48% for RW3$_{1/20\text{th}}$) can be observed. Based on the observed correlation between the free surface elevation at wave probe WP4 and T_{ex}, together with the relatively large deviation between the numerical and experimental free surface elevation, measured at wave probe WP4 for RW3$_{1/20\text{th}}$, an additional simulation has been run, reducing the numerical target wave height to the measured wave height at wave probe WP4, i.e. 0.09m. This case is henceforth referred to as RW3*$_{1/20\text{th}}$ and results are shown in Figure 7.52. The acquired data follow the previously observed trend, with a nRMSE of 5.24% at wave probe WP4 and 4.31% for T_{ex}.

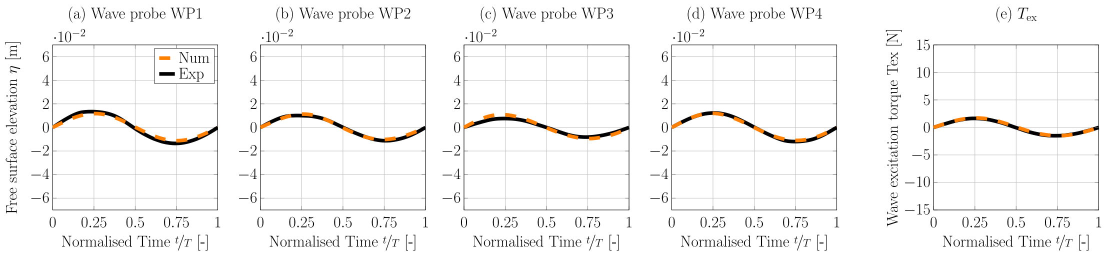

Figure 7.49: Experimental and numerical phase averaged free surface elevation, measured at wave probes WP1–WP4 (a)–(d), and wave excitation torque (e) for wave RW1$_{1/20\text{th}}$.

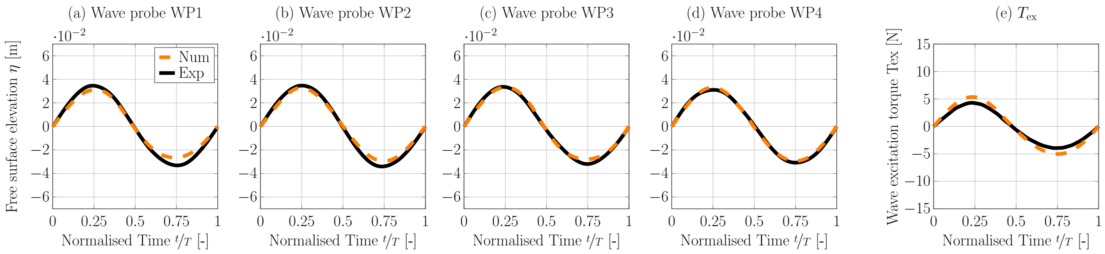

Figure 7.50: Experimental and numerical phase averaged free surface elevation, measured at wave probes WP1–WP4 (a)–(d), and wave excitation torque (e) for wave RW2$_{1/20\text{th}}$.

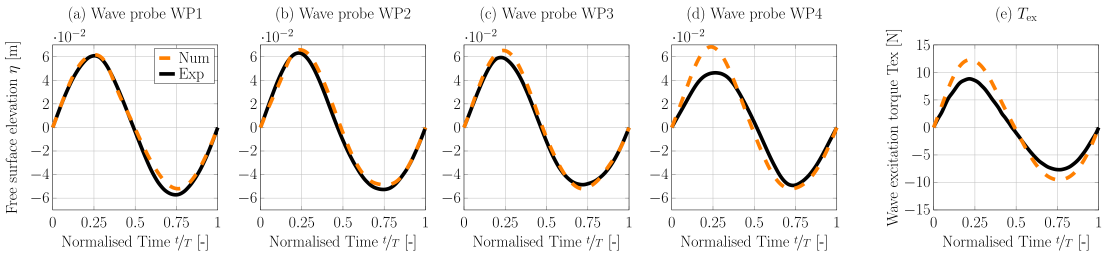

Figure 7.51: Experimental and numerical phase averaged free surface elevation, measured at wave probes WP1–WP4 (a)–(d), and wave excitation torque (e) for wave RW3$_{1/20\text{th}}$.

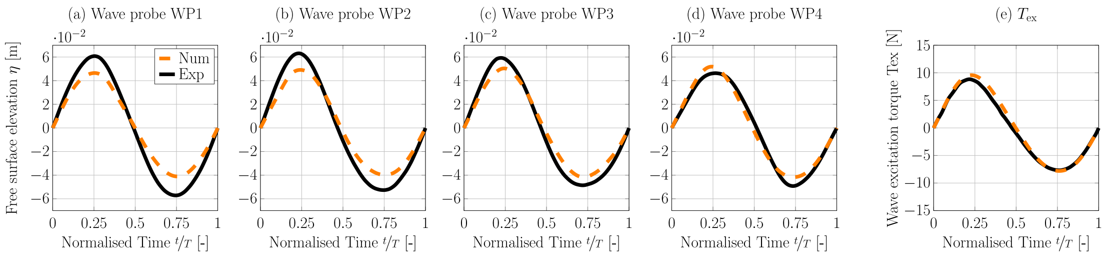

Figure 7.52: Experimental and numerical phase averaged free surface elevation, measured at wave probes WP1–WP4 (a)–(d), and wave excitation torque (e) for wave RW3*$_{1/20\text{th}}$.

Only the results for RW2$_{1/20\text{th}}$ do not quite follow the observed correlation between the agreement of the free surface elevation and T_{ex}. A relatively small nRMSE of

1.93% for the surface elevation at wave probe WP4 is achieved, but a relatively large nRMSE of 9.32% is achieved for T_{ex}. The larger nRMSE for T_{ex} is induced by overall smaller T_{ex} amplitudes in the experimental data, compared to the numerical data. To rule out inconsistencies in the NWT, as a cause for the larger deviation, the wave field at a specific time instance is examined and screen shots of the dynamic pressure field are shown in Figures 7.53 (a)–(c), for waves $\text{RW1}_{1/20\text{th}}$, $\text{RW2}_{1/20\text{th}}$, and $\text{RW3*}_{1/20\text{th}}$, respectively. For $\text{RW2}_{1/20\text{th}}$, as for the other two regular waves, no apparent inconsistencies in the wave field are visible. At this stage, with the available data, no clear cause for the observed differences between the numerical and experimental T_{ex} data can be found.

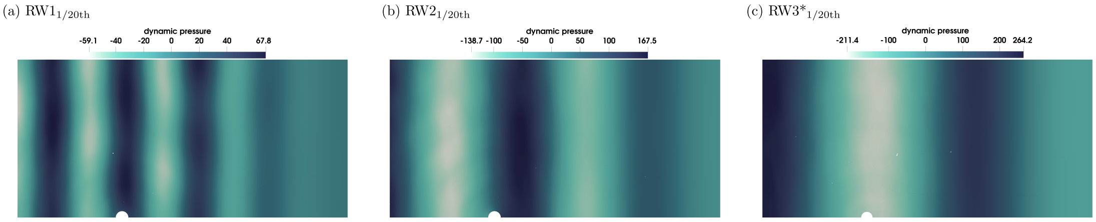
(a) $\text{RW1}_{1/20\text{th}}$ (b) $\text{RW2}_{1/20\text{th}}$ (c) $\text{RW3*}_{1/20\text{th}}$

Figure 7.53: Screen shot of the dynamic pressure for waves (a) $\text{RW1}_{1/20\text{th}}$, (b) $\text{RW2}_{1/20\text{th}}$, and (c) $\text{RW3*}_{1/20\text{th}}$.

Free decay

For the free decay test, experimental data from three different runs are available. Figure 7.54 shows the time trace of the normalised, rotational floater position, Γ (see Figure 7.41 (b)), for the three different experimental runs and their mean value (orange colour code in Figure 7.54). From the experimental time trace, a natural period of ~ 0.8s can be extracted for the WEC system. Figure 7.54 also includes time traces of the normalised floater position from numerical simulation. Specifically, results for four different values for the inertia of the system are plotted, i.e. 0.946, 0.600, 0.434, and 0.200kg m^2. As stated in Section 7.2.1, initially, the inertia has been extracted from [586] and lumped using the parallel–axis theorem, resulting in 0.946kg m^2. It can be seen, in Figure 7.54, that this value leads to over-prediction of the amplitude, as well as the period of the oscillation. Based on this result, two trial runs with a reduced inertia (0.3 and 0.2kg m^2) have been performed, resulting in an over– and under–prediction of the natural period of the system, respectively. Assuming, a quadratic relation between the value of the inertia and the natural period of the system, an inertia of 0.434kg m^2 is estimated to deliver a natural period matching the experimental results, which can be confirmed from Figure 7.54. Note that the amplitude of the oscillation is still over–predicted in the numerical simulation; however, this is expected since no mechanical friction, likely to effect the experimental results, is modelled numerically. An inertia value of 0.434kg m^2 is considered for all subsequent simulations.

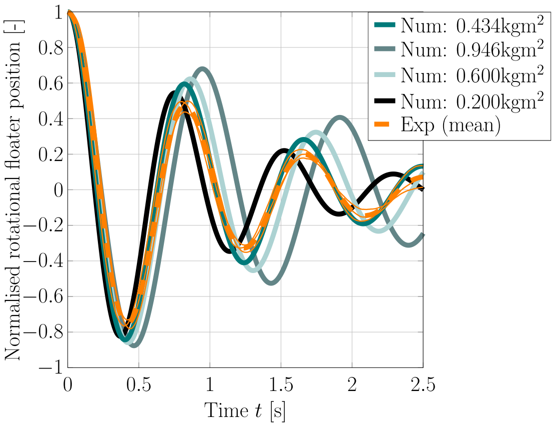

Figure 7.54: Time trace of the normalised floater position during the free decay test.

Forced oscillation

As stated in Section 7.2.2, two different types of excitations are considered for the forced oscillation test: single- and multi-frequency excitation.

Single–frequency excitation

Figures 7.55 (a) and (b) show the experimental and numerical time traces of the single–frequency (0.54Hz) input force (5N amplitude) and the resulting translational, floater position, respectively. It should be noted that, for the single–frequency cases, single–sided windowing is applied to the experimentally measured input force before feeding the force signal to the motion solver, to minimise the chance of numerical instability. From Figure 7.55 (a), it can be seen that the force in the numerical simulation matches the experimental force after the initial windowing time. This is expected, since the measured, experimental, input force values are the input applied to the numerical simulation, and the time trace is included here merely as a cross check for the numerical setup. From the floater position data, plotted in Figure 7.55 (b), it can be seen that excellent agreement in phase is achieved between the experimental and numerical data. Relatively small difference in the motion amplitude can be observed at the peaks (e.g. $t \approx 11.5$s) and troughs (e.g. $t \approx 14.1$s). Consistent behaviour is found in Figures 7.56 (a) and (b), showing time traces of the single–frequency excitation with a frequency of 0.54Hz and 10N force amplitude, as well as in Figures 7.57 (a) and (b), with a frequency of 0.71Hz and 5N force amplitude. Again, excellent agreement between the experimental and numerical data is achieved in the phase of the floater position, while some differences can be observed at the peaks and troughs.

For both excitation force frequencies, it can be observed that, although a force signal with constant peak and trough amplitudes is applied during the experiments, the floater position shows visible inconsistency between consecutive peaks and troughs (e.g. between 11 and 14s in Figure 7.57 (b)). This behaviour is not visible in the numerical data. Analysing the measured free surface elevation (at wave probe WP4) for the experimental runs, negligible free surface perturbations can be measured (of the order of $\leq 1 \cdot 10^{-3}$m), indicating that artefacts of the mechanical systems are the likely cause of the inconsistency in the experimental floater position signal. With the available experimental data, it is challenging to determine the exact cause of the observed behaviour.

Figures 7.58 (a) and (b) show the experimental and numerical time traces of the single–frequency excitation force (with a frequency of 1.01Hz and an amplitude of 5N) and the resulting floater position, respectively. It can readily be seen that the excitation close to the resonance frequency of the device (~ 1.25Hz) leads to considerably larger floater motion, compared to the excitation at 0.54 or 0.71Hz. Consequently, the larger floater motion leads to larger free surface perturbation, potentially influencing the system through wave reflection within the physical wave tank. Potential wave reflection together with the artefacts of the mechanical system, suggested by the previous results, lead to relatively large differences between consecutive periods in the experimental data and, thus, to relatively large differences between the experimental and numerical results.

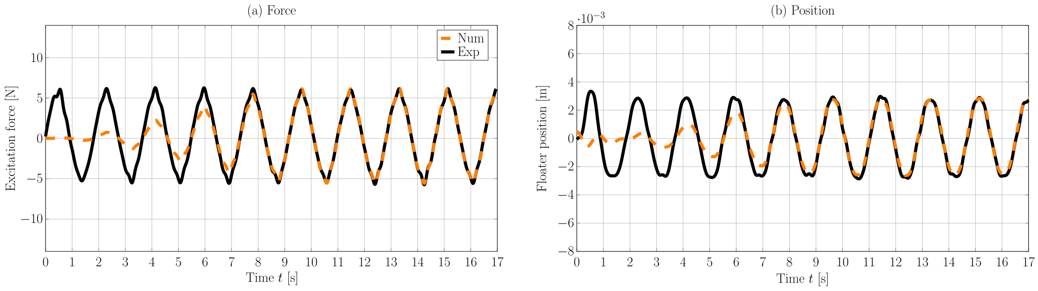

Figure 7.55: Time trace of the experimental and numerical single–frequency (0.54Hz) (a) excitation force (5N amplitude) and (b) the floater position.

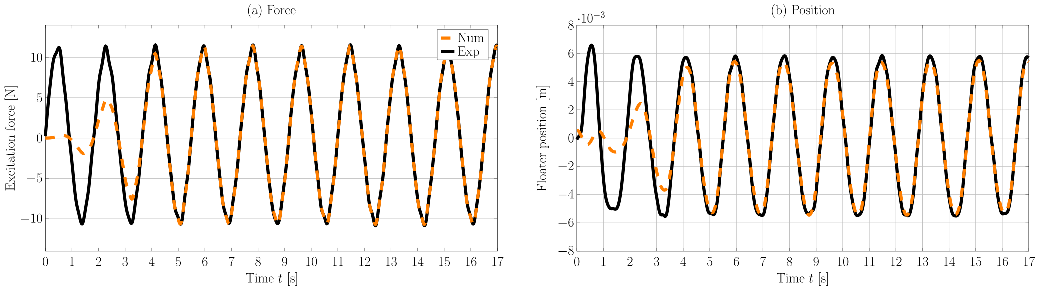

Figure 7.56: Time trace of the experimental and numerical single–frequency (0.54Hz) (a) excitation force (10N amplitude) and (b) the floater position.

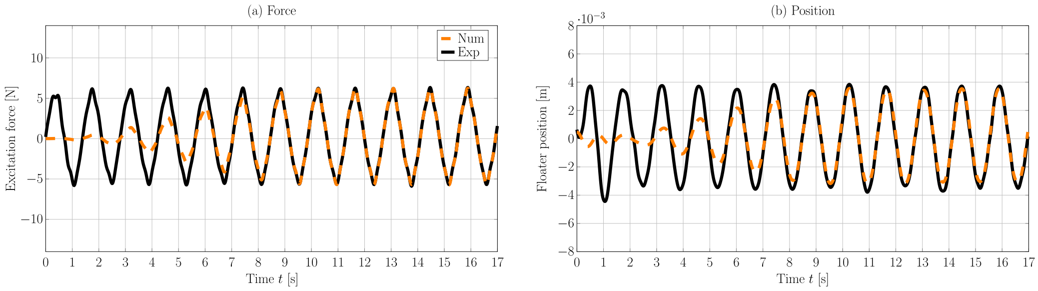

Figure 7.57: Time trace of the experimental and numerical single–frequency (0.71Hz) (a) excitation force (5N amplitude) and (b) the floater position.

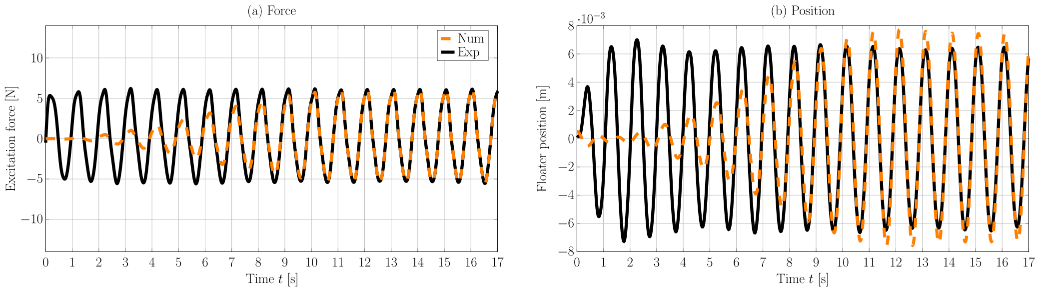

Figure 7.58: Time trace of the experimental and numerical single–frequency (1.01Hz) (a) excitation force (5N amplitude) and (b) the floater position.

Multi–frequency excitation

The results for the multi–frequency excitation test case are plotted in Figures 7.59 (a) and (b), showing the excitation torque and the translational floater position, respectively. It should be noted that, in contrast to the single–frequency case, no single sided windowing is applied to the excitation torque, since the T_{ex} follows a relatively smooth trajectory. As shown in Figure 7.59 (a), the numerical and experimental torque input virtually overlay each other. Comparing the experimental and numerical floater position data, a nRMSE of 6.3% can be computed. It is notable that the phase comparability shows a frequency dependency, manifesting itself as a mismatch in phase between $20\text{s} \leq t \leq 25\text{s}$. Similarly, a frequency dependency in the agreement between the amplitudes is visible, most notably between $20\text{s} \leq t \leq 22\text{s}$ and $24.5\text{s} \leq t \leq 27\text{s}$. Inspecting the free surface perturbation in the CFD–based NWT at $t = 25\text{s}$ (see Figure 7.60 (a)), the differences between the numerical and experimental floater position between $24.5\text{s} \leq t \leq 27\text{s}$ can be attributed to the influence of reflected waves from the domain boundaries and the different reflection behaviour in the physical and numerical wave tanks. However, inspecting the free surface perturbation at $t = 21\text{s}$ (see Figure 7.60 (b)), significantly smaller free surface perturbations can be observed in the CFD–based NWT. This suggests that the differences in the floater position amplitude between $20\text{s} \leq t \leq 22\text{s}$ may stem from mechanical features of the physical system, which are not captured in the CFD–based NWT, rather than different reflection behaviour in the physical and numerical wave tanks.

(a) Force

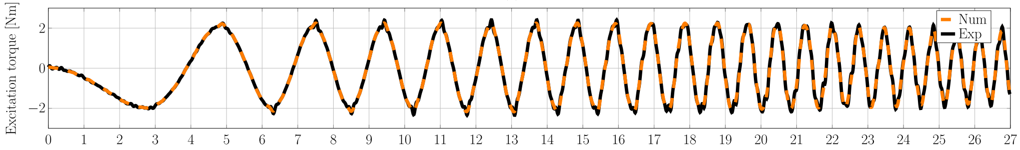

(b) Position

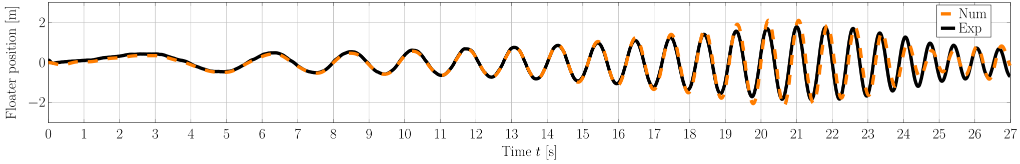

Figure 7.59: Time trace of the experimental and numerical multi–frequency excitation torque (a) and the floater position (b).

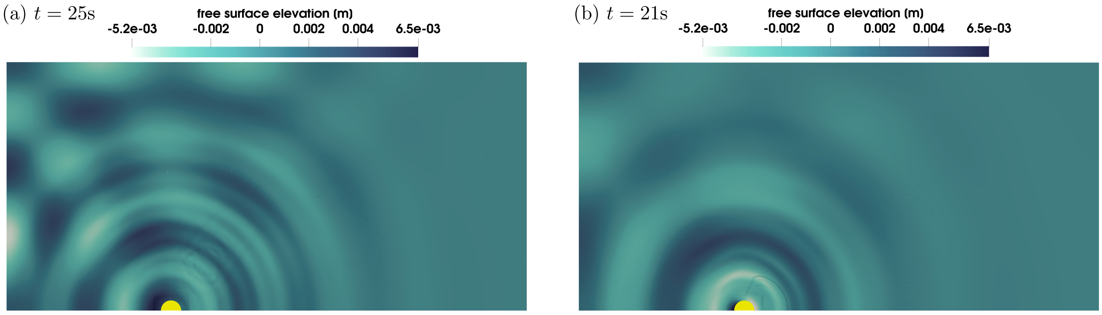
(a) $t = 25$s

(b) $t = 21$s

Figure 7.60: Screen shots of the free surface at (a) $t = 25$s and (b) $t = 21$s.

Wave–induced WEC motion

Finally, cases of wave induced WEC motion are considered for validation of the numerical 1/20th scale Wavestar model. Figures 7.61–7.63 show the phase averaged experimental and numerical free surface elevation, measured at wave probes WP1–WP4, as well as the phase averaged floater position. The values of the nRMSE are listed in Table 7.25. The experimental wave height and the experimental peak to trough magnitude of the floater position is used for normalisation of the RMSE for the free surface elevation and the floater position, respectively.

For the wave–induced WEC motion test cases, the overall achieved nRMSE is consistent with the previous test cases. From a qualitative analysis of Figures 7.61 – 7.63, a correlation between the agreement of the experimental and numerical data for the floater position and the free surface elevation at wave probe WP4 can be observed. Good agreement is, for instance, found for the free surface elevation at wave probe WP4 for wave $\text{RW1}_{1/20\text{th}}$ and also for the floater position. For wave $\text{RW3}_{1/20\text{th}}$, the free surface elevation at wave probe WP4 shows significant over–prediction at the wave crest and, correspondingly, the peak floater position is over–predicted in the numerical model. While overestimation at the peaks of the floater position correlates with overestimation of the free surface elevation peaks, it is curious that underestimation of the numerical free surface elevation troughs for waves RW2$_{1/20\text{th}}$ and RW3$_{1/20\text{th}}$ results in the observed overestimation of the numerical floater position.

From the quantitative analysis of the floater position, a maximum nRMSE of $\sim 6\%$ is found for wave RW2$_{1/20\text{th}}$. The minimum nRMSE of $\sim 0.3\%$ is found for wave RW1$_{1/20\text{th}}$. Overall, despite the observed deviations, the agreement between the experimental and numerical floater position data is acceptable.

Table 7.25: nRMSE between the experimental and numerical free surface elevation and floater position for waves RW1$_{1/20\text{th}}$–RW3*$_{1/20\text{th}}$.

RW1$_{1/20\text{th}}$	WP1	WP2	WP3	WP4	Floater position
nRMSE [%]	8.91	4.42	10.99	2.56	0.32
RW2$_{1/20\text{th}}$					
nRMSE [%]	4.45	4.56	3.73	2.28	6.06
RW3*$_{1/20\text{th}}$					
nRMSE [%]	9.95	9.75	8.56	3.89	5.54

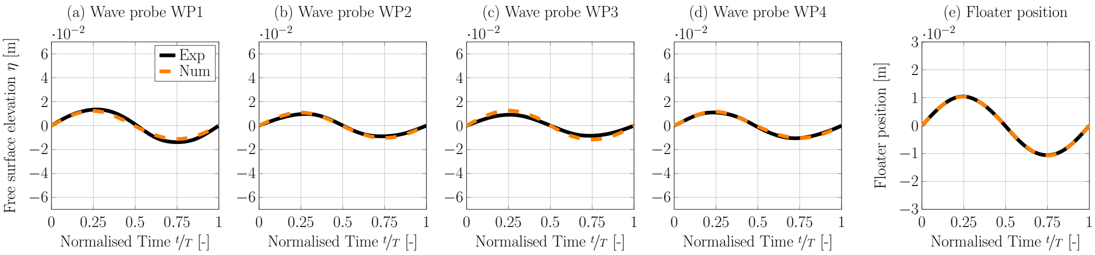

Figure 7.61: Experimental and numerical phase averaged free surface elevation, measured at wave probes WP1–WP4 (a)–(d), and floater position (e) for wave RW1$_{1/20\text{th}}$.

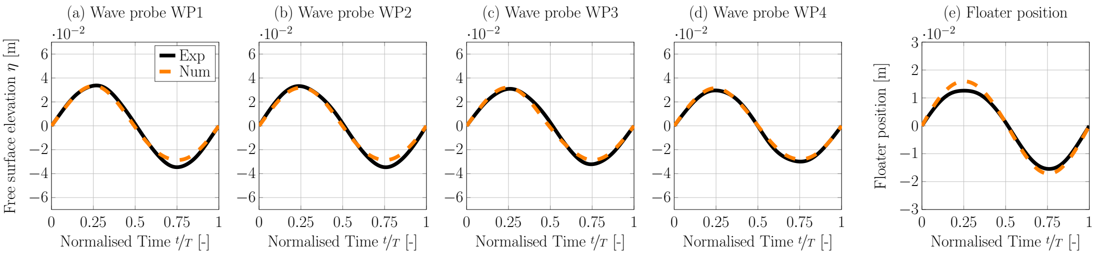

Figure 7.62: Experimental and numerical phase averaged free surface elevation, measured at wave probes WP1–WP4 (a)–(d), and floater position (e) for wave RW2$_{1/20\text{th}}$.

This section documents the validation of a 1/20th scale numerical model of the Wavestar WEC against experimental data under various test conditions. The free

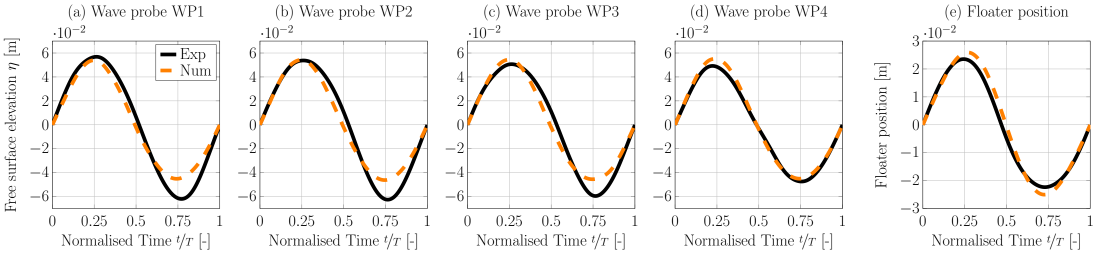

Figure 7.63: Experimental and numerical phase averaged free surface elevation, measured at wave probes WP1–WP4 (a)–(d), and floater position (e) for wave RW3*$_{1/20\text{th}}$.

surface elevation, measured in the physical wave tank, can be replicated numerically with acceptable agreement, considering the pollution of the physical data by wave reflection. Considering also the negligence of any mechanical friction in the CFD–based NWT model, the presented numerical model of the Wavestar WEC can be regarded as validated.

7.3 Moored point absorbers

As shown in the previous Sections 7.1 and 7.2, using experimental data allows for a direct comparison against measured physical reality. However, experimental reference data from physical wave tank tests may suffer from scaling effects, measurement uncertainty, and peculiarities of the test facility. Therefore, validating a CFD–based NWT model against experimental data risks the danger of drawing false conclusions when experimental inaccuracies and wave tank artefacts are not taken into account. In addition to the knowledge of the measurement uncertainty, the sensitivity of the body dynamics to model uncertainties of, e.g., inertial properties, as well as the location of the centre of mass, is important. To that end, this section presents a sensitivity analysis, for the simulated dynamics of two point–absorber type WECs, concerning the accuracy of the incident wave and crucial system parameters, such as inertial properties and the location of the CoM. The case study, used for the sensitivity analysis, is based on the CCP–WSI Blind Test Series 2 & 3. Throughout this study, the numerical results are compared to the recently disclosed experimental data.

7.3.1 Physical wave tank

For the CCP-WSI Blind Test Series 2 & 3, physical wave tank tests were conducted in the ocean basin of the COAST laboratory at the University of Plymouth. A schematic of the physical wave tank, including the locations of the wave probes, is depicted in Figure 7.64. For the validation and sensitivity study, two different WEC structures are considered, W1 and W2, resembling moored point absorber type devices. Both structures have axisymmetric, cylindrical, geometries. All relevant physical properties are shown in Figure 7.65. The mooring of the structures is implemented with a linear spring, with a stiffness of $67\,\mathrm{N\,m^{-1}}$, connecting the device with the tank floor.

In the following, measurement uncertainties for the inertial properties, as well as the exact location of the CoM, are assumed to have significant influence on the overall device dynamics. To analyse the sensitivity of the body dynamics and, thereby, the agreement between the numerical and experimental data set, to the uncertainty in the inertia and the location of the CoM, simulations are performed in which an uncertainty of $\pm 10\%$ is added to the inertia Ixx, Iyy, and Izz, and the vertical location of the CoM. The considered values are listed in Table 7.26. Note that the nominal case with $\pm 0\%$ is used in the subsequent chapters of this thesis.

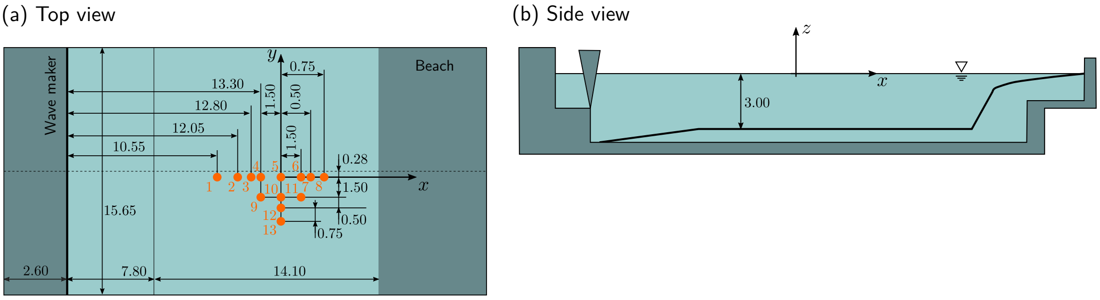
(a) Top view
(b) Side view

Figure 7.64: Schematic (not at scale, all dimensions in [m]) of the physical wave tank including the wave probe positions.

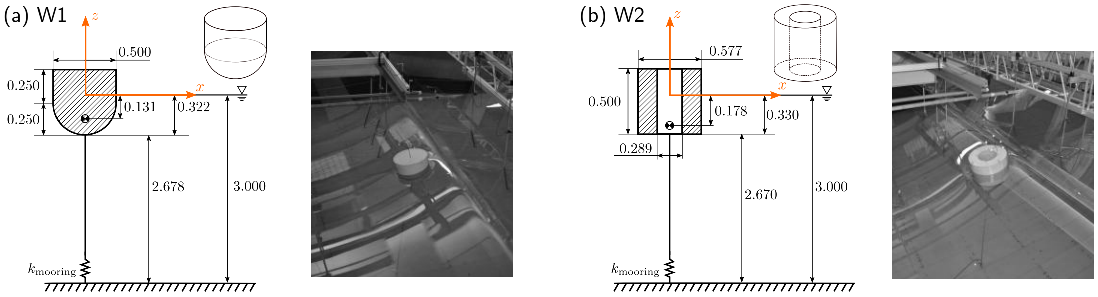
(a) W1
(b) W2

Figure 7.65: Schematic (not at scale, all dimensions in [m]) and photograph of (a) WEC structure 1 and (b) WEC structure 2. (Photographs are adapted from [22]).

7.3.2 Test cases

In this section, wave–only and wave–induced WEC motion test cases are considered. For both test cases, three different focused wave groups (focused location at the location of wave probe WP5, see Figure 7.64) of varying steepness are considered.

Table 7.26: Inertial properties and the vertical location of the CoM for the sensitivity analysis

W1		Inertia [kg m^2]			CoM [m]
		Ixx	Iyy	Izz	
$+10\%$	Inertia	1.782	1.782	1.257	-0.131
-10%	Inertia	1.458	1.458	1.029	-0.131
$\pm0\%$	Inertia CoM	1.620	1.620	1.143	-0.131
$+10\%$	CoM	1.620	1.620	1.143	-0.118
-10%	CoM	1.620	1.620	1.143	-0.144

W2		Inertia [kg m^2]			CoM [m]
		Ixx	Iyy	Izz	
$+10\%$	Inertia	3.916	3.916	3.628	-0.178
-10%	Inertia	3.204	3.204	2.968	-0.178
$\pm0\%$	Inertia CoM	3.560	3.560	3.298	-0.178
$+10\%$	CoM	3.560	3.560	3.298	-0.160
-10%	CoM	3.560	3.560	3.298	-0.196

Waves–only

For the wave–only test cases, the WEC structures are removed from the wave tank and the waves propagate through the tank undisturbed. The characteristics of the three different focused waves, 1BT2 – 3BT2, are listed in Table 7.27. While the peak wave amplitude A_0 and the water depth d are kept constant, the peak period T_p, varies between 2.67s (1BT2) and 2.38s (3BT2), resulting in wave steepnesses between 0.13 and 0.19, respectively.

The experimentally measured free surface elevation for each wave, at wave probe WP5, is plotted in Figure 7.66. Note that the free surface elevation is plotted against relative time, t_r, so that all peaks are artificially aligned at $t_r = 1$.

Table 7.27: Wave characteristics for the focused wave groups: water depth d, peak amplitude A_0, peak period T_p, peak wave length λ_p, steepness kA_0

Wave ID	d [m]	A_0 [m]	T_p [s]	λ_p [m]	$^d/_{\lambda_p}$ [–]	kA_0 [–]
1BT2	3.00	0.25	2.67	11.35	0.26	0.14
2BT2	3.00	0.25	2.50	9.41	0.32	0.17
3BT2	3.00	0.25	2.38	7.99	0.38	0.20

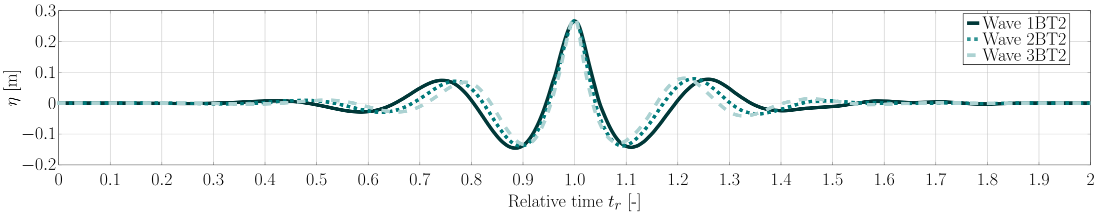

Figure 7.66: Free surface elevation time traces of the considered focused waves (1BT2–3BT2) at the focal location. The time traces are artificially aligned to match the peaks at $t_r = 1$.

Wave–induced WEC motion

For the wave–induced WEC motion cases, wave probe WP5 is removed from the wave tank and the considered WEC structure, W1 or W2, is place at the location of wave probe WP5. The device is free to move in all six degrees of freedom and the device motion is measured using a motion capture system.

7.3.3 Numerical wave tank

The CFD–based NWT is implemented in OpenFOAM version 4.1 of the OpenFOAM Foundation fork [584]. In the following, details on the numerical wave generation and absorption, the computational domain, and the assumed flow conditions, as well as the dynamic mesh motion method and solver settings and solution schemes are provided.

Numerical wave generation and absorption

For the numerical wave generation and absorption, the impulse source wave maker as detailed in Section 6.1 is used for this study. Section 6.1 discusses the influence of the source geometry on the achieved accuracy of the resulting wave, as well as the influence of the settings of the numerical beach on the absorption efficiency. For the present case, the source geometry is defined based on the findings in Section 6.1, i.e. source width $w_s = 0.1\lambda$ and source height $h_s = 1.1d$.

Preliminary studies are performed to identify efficient beach settings for the considered focused wave groups. Based on the findings in Chapter 6, the beach length was set to $L_B = \lambda_{\text{1BT2}}$, i.e. the longest wave length, and different $s_{b,\text{Max}}$ values are tested. The reflection coefficient R (see Equation (6.3)) is determined using the three point method, proposed in [561]. The results, for varying $s_{b,\text{Max}}$, are listed in Table 7.28, from which $s_{b,\text{Max}} = 3\text{s}^{-1}$ is chosen for all subsequent simulations. Screen shots domain showing the source region and the field variable s_b are shown in Figures 7.67 (a) and (b), respectively.

Table 7.28: Reflection coefficients for different values of $s_{b,\text{Max}}$

$s_{b,\text{Max}}$	[s^{-1}]	3	4	5	6
1BT2		1.9%	2.7%	3.3%	7.0%
2BT2		0.5%	0.6%	0.9%	1.0%
3BT2		3.4%	3.6%	3.8%	4.3%

Initially, to generate the desired target wave at a specific location within the CFD–based NWT, the calibration procedure, detailed in Section 6.1, is used to determine the required impulse source input $\mathbf{a}_{wm}$. To recall, the calibration method comprises the following steps (for a graphical representation, see Figure 7.68 (a)):

(a) Source region

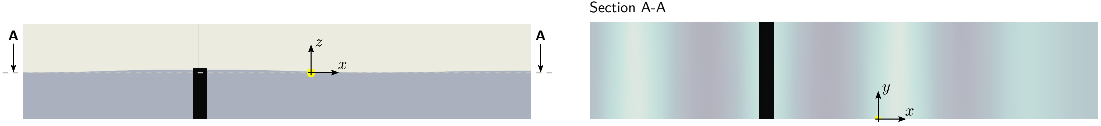

(b) Damping factor

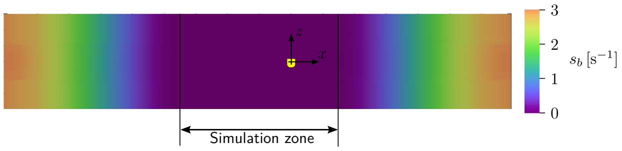

Figure 7.67: Screen shots of the CFD–based NWT showing (a) the impulse source region (black colour code). The WEC structure (yellow colour code) is located at $(x, y, z) = (0, 0, 0)$; (b) the gradually increasing damping factor s_b of the numerical beach. The simulation zone, i.e. $s_b = 0$, is indicated by the vertical lines.

1. Definition of $\eta_t(t)$
2. FFT on $\eta_t(t)$ to obtain $\mathcal{A}_{\eta_t}(f_j)$ and $\Lambda_{\eta_t}(f_j)$
3. Definition of initial time series for $\mathbf{a}_{wm,1}(t)$
4. Run iteration i, using $\mathbf{a}_{wm,i}(t)$ and extract $\eta_{r,i}(t)$
5. FFT on $\eta_{r,i}(t)$ to obtain $\mathcal{A}_{\eta_{r,i}}(f_j)$ and $\Lambda_{\eta_{r,i}}(f_j)$
6. FFT on $\mathbf{a}_{wm,i}(t)$ to obtain $\mathcal{A}_{\mathbf{a}_{wm,i}}(f_j)$ and $\Lambda_{\mathbf{a}_{wm,i}}(f_j)$
7. Correction of amplitude and phase components of $\mathbf{a}_{wm,i}(t)$
8. Inverse Fourier transform to construct $\mathbf{a}_{wm,i+1}(t)$
9. Repeat Steps 4 – 8

In the present study, the initial calibration method has been updated, to achieve better agreement between the target and the resulting waves. The improved agreement between target and resulting waves is presented and discussed in Section 7.3.4. The calibration method now comprises the following steps (for a graphical representation, see Figure 7.68 (b)):

1. Define a target wave time series $\eta_t(t)$
2. Extend $\eta_t(t)$ using zero padding for increased frequency resolution
3. Compute the frequency domain equivalent of $\eta_t(t)$, $\hat{\eta}_t(j\omega) = \mathscr{F}\{\eta_t(t)\}$
4. Define an initial time series for $\mathbf{a}_{wm,1}(t)$
5. Extend $\mathbf{a}_{wm,1}(t)$ using zero padding for increased frequency resolution
6. Compute the frequency domain equivalent of $\mathbf{a}_{wm,1}(t)$, $\hat{\mathbf{a}}_{wm,1}(j\omega) = \mathscr{F}\{\mathbf{a}_{wm,1}(t)\}$
7. Run the OpenFOAM simulation for calibration iteration i, using $\mathbf{a}_{wm,i}(t)$ and extraction of the resulting surface elevation $\eta_{r,i}(t)$ at the specific location
8. Compute the frequency domain equivalent of $\eta_{r,i}(t)$, $\hat{\eta}_{r,i}(j\omega) = \mathscr{F}\{\eta_{r,i}(t)\}$

9. Compute the transfer function $\underline{H}_{\mathbf{a},\eta,i}(j\omega)$ from $\mathbf{a}_{wm,i}(j\omega)$ to $\eta_{r,i}(j\omega)$
10. Compute the frequency domain equivalent of the new source input $\mathbf{a}_{wm,i+i}(j\omega)$ with $\underline{H}^{-1}_{\mathbf{a},\eta,i}(j\omega)$
11. Construct $\mathbf{a}_{wm,i+1}(t)$, using the inverse Fourier transform on $\mathbf{a}_{wm,i+i}(j\omega)$
12. Filter $\mathbf{a}_{wm,i+1}(t)$, using a cut–off frequency
13. Repeat Steps 7 - 13, either for a maximum number of iterations, or until a threshold for the error metric between the $\eta_t(t)$ and $\eta_{r,i}(t)$ is reached.

(a) Initial calibration method

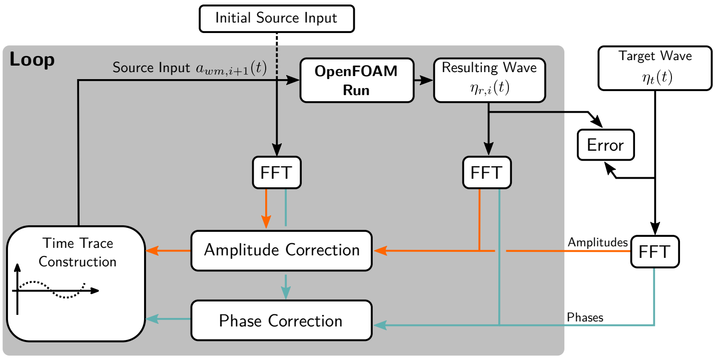

(b) Updated calibration method

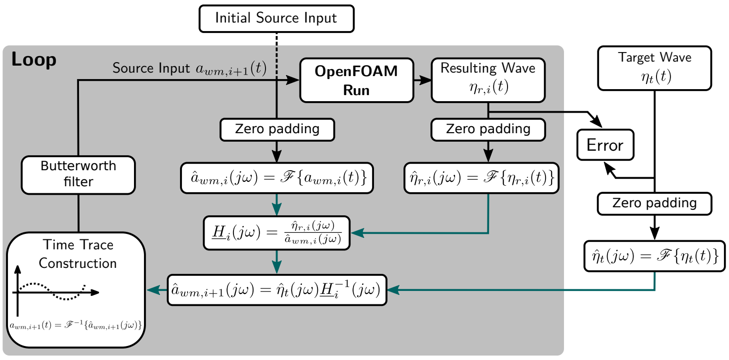

Figure 7.68: (a) Initial and (b) updated calibration method for the impulse source input.

Computational domain

Figures 7.69 (a) and (b) show the top and side view of the numerical domain, including all relevant dimensions, respectively. As for the numerical wave tanks in Section 7.1 and 7.2, the symmetry of the problem is exploited and only half of the physical wave tank is modelled numerically to reduce the overall cell count. All other relevant boundary conditions are indicated in the Figures 7.69 (a) and (b).

Convergence studies on the spatial and temporal problem discretisation have been performed, using three different discretisation levels. The peak values of the heave,

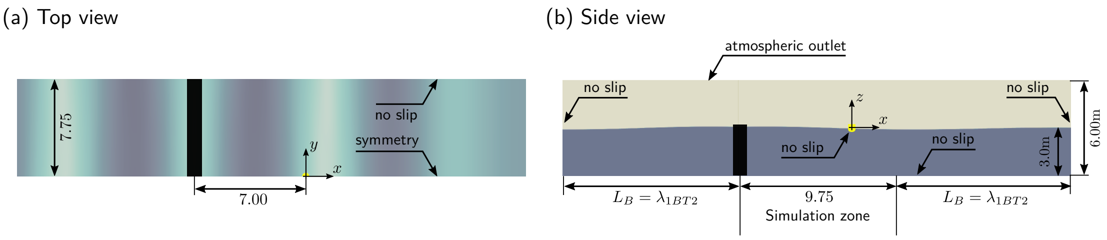
(a) Top view

(b) Side view

Figure 7.69: Schematic of the numerical wave tank including all relevant dimensions in [m]: (a) top view and (b) side view.

surge, and pitch displacement is used as input the convergence study. Table 7.29 shows the results for the convergence studies, based on the WSI simulations for wave 1BT2, including the convergence type and the discretisation uncertainty $\mathcal{U}$. Based on the results, a fixed time step size of 0.002s is used. The minimum cell size in the interface region and around the WEC structure is 10 cells per wave height ($= 2A_0$) of wave 1BT2. The maximum aspect ratio in the interface region is 2. Three refinement levels are used to reach the cell size in the interface region. A screen shot of the mesh layout is shown in Figure 7.70.

Table 7.29: Results of the spatial and temporal convergence study based on the WSI simulations for wave 1BT2

Spatial			
Δz	Max. heave [m]	Max. surge [m]	Max. pitch [°]
5CPHs	0.226	0.466	0.293
10CPHs	0.236	0.353	0.333
20CPHs	0.238	0.341	0.332
Convergence Type	Monotone	Monotone	Oscillatory
$\mathcal{U}$	0.6%	0.6%	< 0.1%
Temporal			
Δt	Max. heave [m]	Max. surge [m]	Max. pitch [°]
0.004s	0.239	0.338	0.338
0.002s	0.238	0.341	0.332
0.001s	0.238	0.342	0.329
Convergence Type	Monotone	Monotone	Monotone
$\mathcal{U}$	0.8%	0.6%	1.9%

Flow conditions

To evaluate if turbulence modelling is required for the specific test cases, preliminary simulations are performed. For the three different input waves and the two WEC structures, simulations with and without turbulence modelling are run, and results are

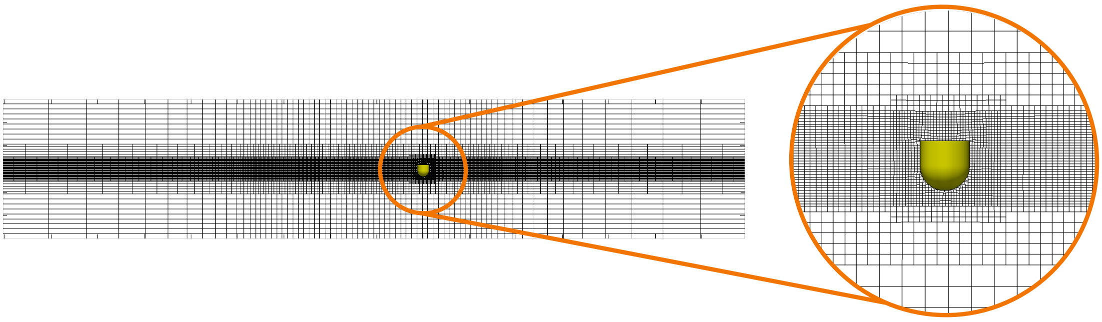

Figure 7.70: Screen shot of the computational mesh in the xz–plane.

compared. For turbulence modelling, a standard k-ω SST turbulence model [150] is chosen, based on the review in Chapter 5. Standard wall functions for the turbulent kinetic energy k_t, the turbulence frequency ω_t, and the eddy viscosity μ_t are used. To ensure the wall function validity, y^+ values should be inspected (see Chapter 4). For illustrative purposes, Figures 7.71 (a)–(f) show the distribution of y^+ on the wall of W2, for wave 3BT2, at three different time instances: immediately before the focused wave crest (9s), at the focused wave crest (10s), and immediately after the focused wave crest (11s). It can be seen that, dependent on the instantaneous velocities, y^+ changes. The time-variance of y^+ and, thus, the time-varying validity of wall functions, must be considered when analysing simulations of oscillating flows which include turbulence modelling.

Table 7.30 lists the relative deviation[3] of the peak values of the heave, surge, and pitch motion, as well as the mooring force, between the simulation results with and without turbulence modelling, for W2 in all three waves. The results indicate that including turbulence modelling mainly affects the surge and pitch motion, with maximum differences of -2.7% and 3.9%, respectively. Although the inclusion of turbulence modelling is observed to produce some differences in the results, laminar conditions are assumed for all subsequent simulations in this section. This is justified by the uncertain validity of the applied wall functions, together with the increased run times. A more detailed analysis of the capabilities and the necessity of including and modelling turbulence for WEC applications is shown in Chapter 9.

Dynamic mesh motion method

The body motion, induced by the incident wave or external force, is solved via Newton's 2nd law of motion, within the `sixDoFRigidBodyMotionSolver` in the OpenFOAM framework. The resulting body motion is accommodated in the numerical domain through mesh morphing by means of the SLERP algorithm. For this study, the

---

[3] The relative deviation is defined as: $(\text{Turbulent}-\text{Laminar}/\text{Laminar}) \cdot 100\%$

(a) Front view (b) Bottom view

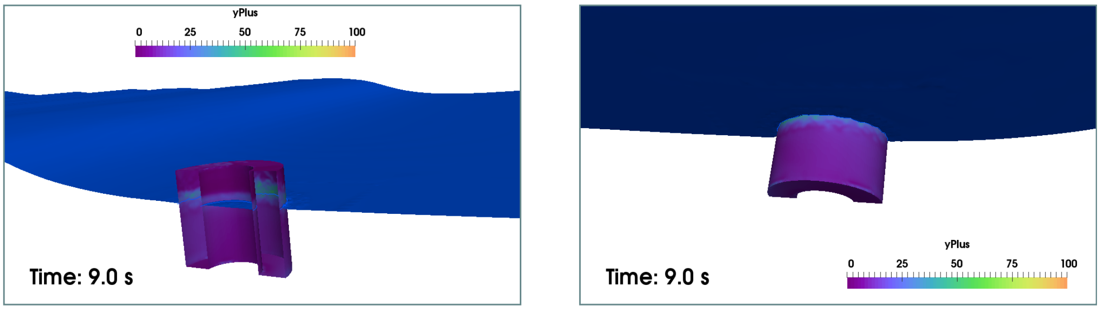

(e) Front view (d) Bottom view

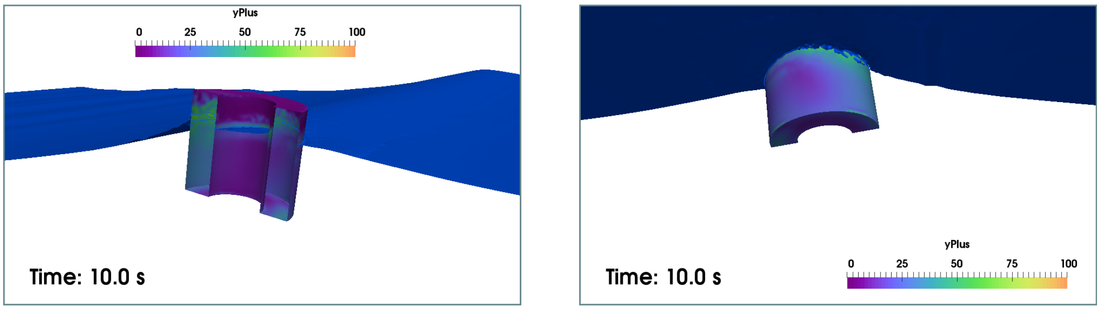

(e) Front view (f) Bottom view

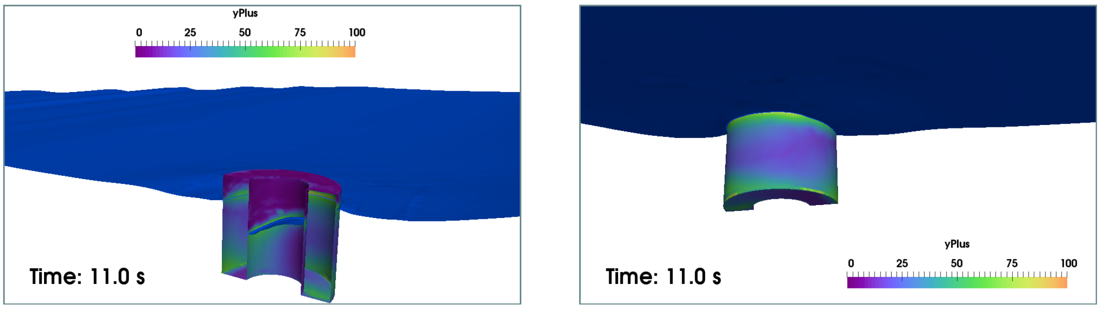

Figure 7.71: Screen–shots, showing the y^+ values on geometry W2, at different time instances, immediately before (9s), at (10s), and immediately after the focused wave crest (11s)

Table 7.30: Relative deviation, induced by including turbulence modelling, at the peaks of the heave, surge and pitch motion, as well as mooring force for WEC structure W2

	1BT2	2BT2	3BT2
Max. heave	$< -0.1\%$	$< 0.1\%$	0.1%
Max. surge	-2.0%	-1.7%	-2.7%
Max. pitch	1.2%	2.7%	3.9%
Max. mooring force	-0.2%	-0.1%	-0.2%

motion of the device is constrained via the `sixDoFRigidBodyMotionSolver` motion constraints to the three DoFs: heave, surge, and pitch. As stated in Section 7.3.2, in the physical wave tank, no motion constraints are applied. Thus, any asymmetric effects which may occur in the physical wave tank can not be captured in the CFD–based NWT. However, since only long crested focused wave groups are considered, minimal asymmetric effects are expected.

Mooring representation

The device mooring is modelled as a linear spring system, which is defined in the `sixDoFRigidBodyMotion` solver via an anchor point, fixed throughout the simulation, and a reference point, moving with the body. The stiffness of the spring, k_{mooring} (see Figure 7.65), is set to match the physical spring stiffness, i.e. $67\text{N}\,\text{m}^{-1}$.

Solver settings and solution schemes

All relevant solver settings and solution schemes (following Chapter 6) are listed in Table 7.31.

Table 7.31: Relevant solver settings and solution schemes.

Time derivative schemes	Euler
Divergence schemes ($\nabla \cdot \mathbf{u}\alpha_{\text{VF}}$)	TVD (`vanLeer`)
Divergence schemes ($\nabla \cdot [\mathbf{u_r}\alpha_{\text{VF}}(1-\alpha_{\text{VF}})]$)	`interfaceCompression`
# of `nOuterCorrectors`	2
# of `nCorrectors`	2
c_r (`cAlpha`)	1
Semi–implicit MULES	yes
# of MULES iterations	3

7.3.4 Results and discussion

In the following, the numerical results are presented and compared to the experimental data from CCP-WSI Blind Test Series 2. Quantification of the agreement between the data sets is achieved via the nRMSE (see Equation (6.4)), where $\mathcal{F}$ refers to the experimental data, and $\hat{\mathcal{F}}$ is the numerical data, and $\mathcal{N}$ is the standard deviation of the particular experimental data set, σ_{exp}. The normalisation factor is chosen based on [JPK].

7.3.5 Waves–only

Before considering wave–induced motion simulations, wave–only tests are simulated. Figure 7.72 shows the time traces of the target waves, together with the numerical results, stemming from the initial and the updated calibration method. Qualitatively, comparing the initial (see Figure 7.68 (a)) and the updated calibration method (see Figure 7.68 (b)), significant improvement in the numerical results can be observed

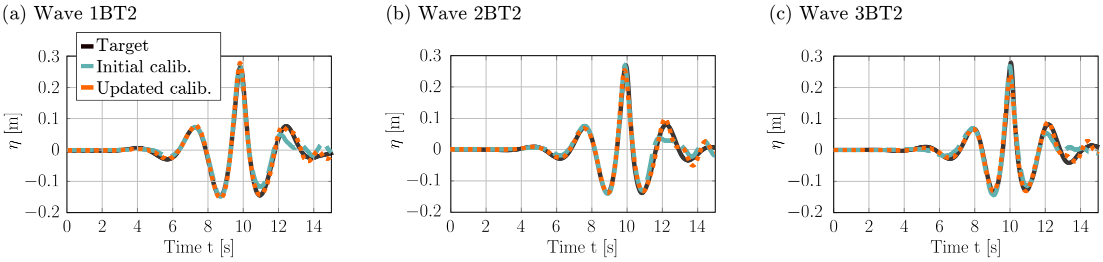

Figure 7.72: Target and resulting surface elevation for waves (a) 1BT2, (b) 2BT2, and (c) 3BT2.

in Figure 7.72, for the peak–succeeding troughs and the tail of the focused wave, induced by the updated calibration method. For a quantitative comparison, Table 7.32 lists the nRMSE values, for waves 1BT2–3BT2, achieved using the initial and the updated calibration method. The largest drop (14 percentage points) in the nRMSE can be identified for wave 3BT2. It is worth noting that the quality of the resulting wave (with the updated calibration method), quantified by the nRMSE, does not show a dependency on the wave steepness.

Table 7.32: nRMSE for the waves–only tests

Wave	Initial calibration method	Updated calibration method
1BT2	22.44%	10.89%
2BT2	23.29%	16.78%
3BT2	26.22%	12.66%

Any calibration procedure, whether initial or updated, runs the risk of producing a well–captured wave at the specific location considered in the calibration, without correctly capturing the wave propagation. To that end, Figures 7.73–7.75 show the time traces of the surface elevation measured at wave probes WP1, WP3, WP5, and WP8 (see Figure 7.64), for waves 1BT2–3BT2, generated with the initial and the updated calibration methods.

The agreement between the experimental and numerical surface elevation follows the trend identified from Figure 7.72. The peak–preceding part of the time trace is well captured for the waves at all wave probes, using either the initial or the updated calibration method. More significant differences between the initial and the updated calibration method can be observed towards the end of the time traces. Especially at wave probe WP1, high frequency components are induced by the initial calibration method, while a closer match between the updated calibration method and the experimental data is achieved. Overall, wave propagation in the physical wave tank is consistently well captured in the NWT.

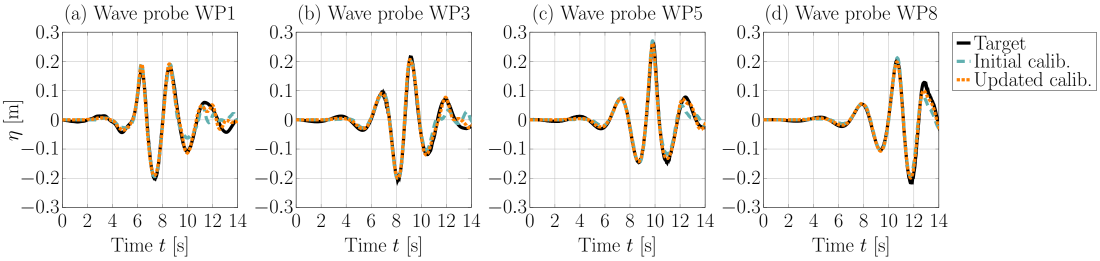

Figure 7.73: Experimental and numerical surface elevation time traces for wave 1BT2, measured at wave probes WP1, WP3, WP5, and WP8 (see Figure 7.64).

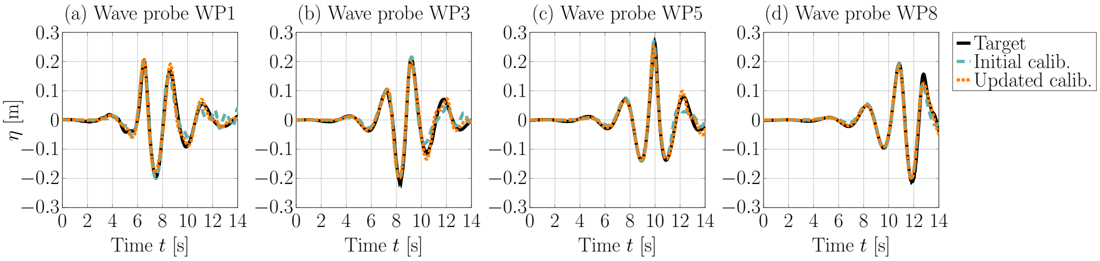

Figure 7.74: Experimental and numerical surface elevation time traces for wave 2BT2, measured at wave probes WP1, WP3, WP5, and WP8 (see Figure 7.64).

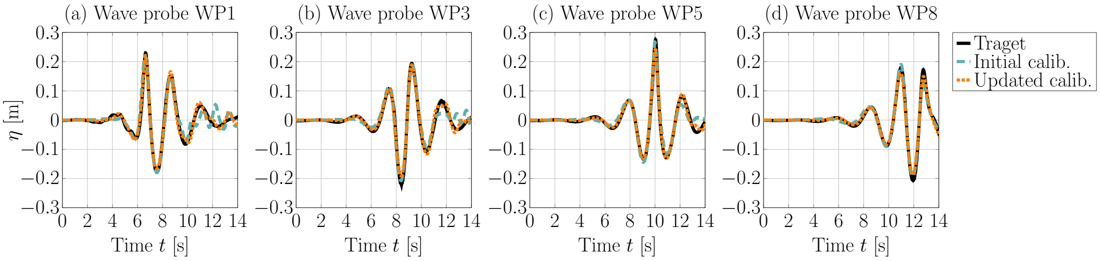

Figure 7.75: Experimental and numerical surface elevation time traces for wave 3BT2, measured at wave probes WP1, WP3, WP5, and WP8 (see Figure 7.64).

Wave–induced WEC motion

The sensitivity of the body dynamics to inaccuracies in the surface elevation, inertial properties, and the vertical CoM location is analysed in this section, by means of a comparison between experimental reference data and the numerical results.

W1

For WEC structure W1, the time traces of the heave, surge, and pitch motion, as well as the mooring force and surface elevation for waves 1BT2–3BT2, are shown in Figure 7.76. Specifically, two cases are shown: results with the waves generated using the initial and the updated calibration method[4]. A qualitative comparison

---

[4] Note, in the following, the results with the wave generated from the initial calibration method represent the results submitted to the Blind Test Series 2. A comparison between the different submissions to the Blind Test Series 2, including numerical results, as well as hardware and simulation times, is presented in [JPK]

between the different time traces reveals an overall good agreement between the experimental data set and both numerical data sets. The largest deviations can be observed towards the end of the signals, after the main crest and, specifically, for the surge and pitch DoFs. No significant qualitative difference in agreement can be observed between the three different waves.

Comparing the two numerical data sets from the initial and the updated calibration method, it can be observed that the improved agreement between the experimental and numerical surface elevation, after updating the calibration method, manifests itself by an improved agreement of the body motion. Specifically for heave motion and mooring force, better agreement is achieved towards the end of the signal, thereby following the trend of the surface elevation. For completeness, Figure 7.77 shows the spectral density function for heave, surge, and pitch motion, as well as mooring force and surface elevation for waves 1BT2–3BT2. The plots for the heave motion, mooring force, and surface elevation most clearly indicate the improvement in the agreement between the experimental and numerical data after updating the calibration method. Considering the time traces, the overall largest deviations are observed for the surge and pitch motion. The spectral density function reveals a mismatch, in the peak period of the pitch motion, between the numerical and experimental data, specifically for waves 2BT2 and 3BT2.

For a quantitative comparison, Figure 7.78 (a), (b), and (c) show the nRMSE for surface elevation, heave, surge, and pitch motion, as well as the mooring force, for waves 1BT2–3BT2, respectively. The bar graphs show that the improved agreement between the experimental and numerical results, for the surface elevation, induced by updated calibration method, has a positive influence on the heave motion (maximum drop of the nRMSE from 27% to 15% for wave 3BT2) and the mooring force (maximum drop from 26% to 14% for wave 3BT2). Regarding the sensitivity to changed inertial properties or CoM locations, the heave motion and mooring force show, as somewhat expected, negligible dependency on the changed properties. At this point, it should be noted that the sensitivity analysis to the physical WEC properties is carried out considering the updated calibration method.

Compared to the heave motion and the mooring force, the surge motion generally shows larger errors of the order of 30–40%. The time traces in Figure 7.76 indicate that the increased error mainly stems from the deviation at the tail of the signal. Interestingly, the surge motion also shows a stronger dependency on the agreement with the experimental results on the change of the physical properties. Together with the strong dependency of the nRMSE values on the physical properties for the pitch motion, a coupling between these two DoFs is indicated, potentially induced by the mooring line. Furthermore, it is striking that, for waves 1BT2 and 2BT2, the

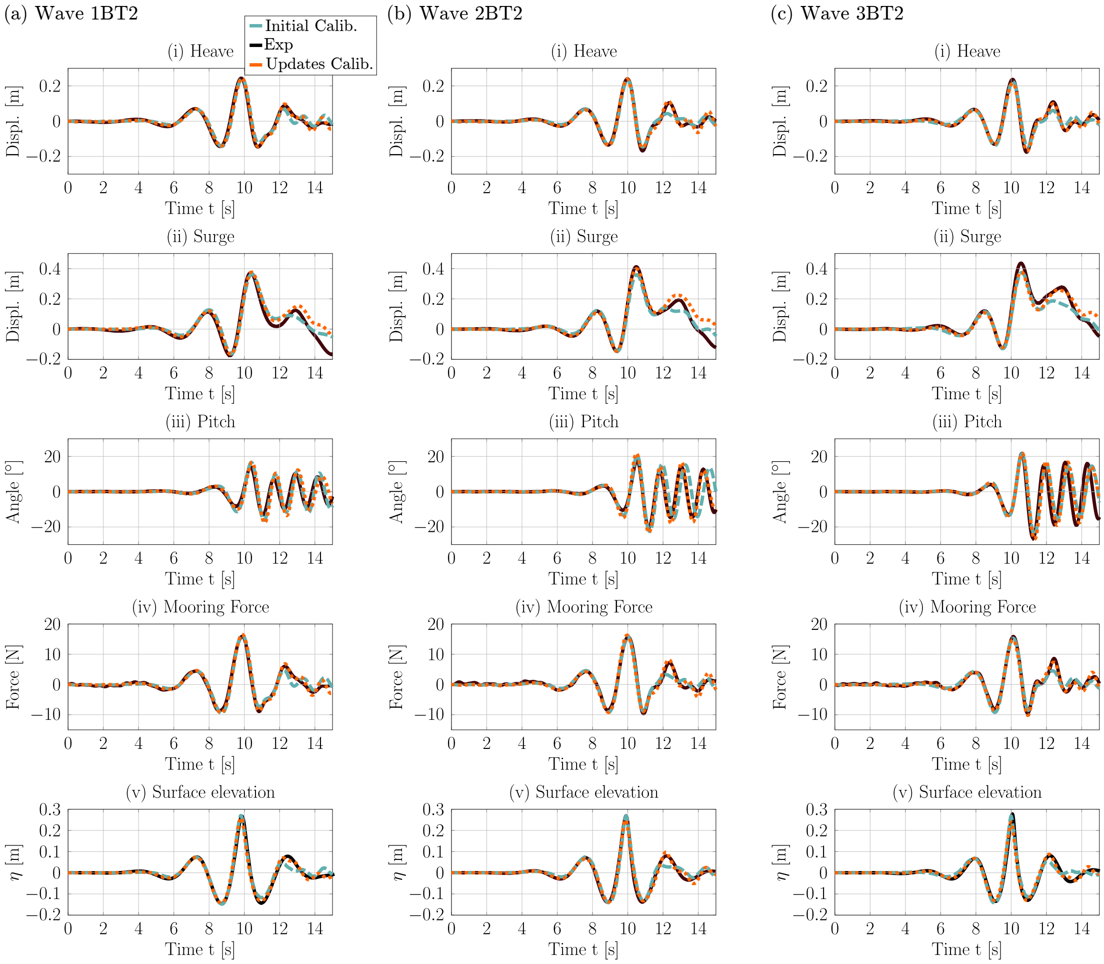

Figure 7.76: Time traces of the heave, surge, and pitch motion, as well as the mooring force and surface elevation for W1.

error between the experimental and numerical results with the improved incident wave increases, compared to the initial submission. Only for wave 3BT2, the error in the surge motion decrease when improving the agreement of the surface elevation, thereby following the trend of the heave motion and mooring force.

As expected, the greatest sensitivity to variations in different physical properties can be observed for pitch motion ($20\% \leq$nRMSE$\leq 138\%$). For waves 1BT2 and 3BT2, similar trends can be observed. The smallest errors are achieved either with a decreased inertia (30% for 1BT2 and 22% for 3BT2) or by lowering the CoM (36% for 1BT2 and 20% for 3BT2). Using the same inertial properties and location of the CoM, as provided by Blind Test Series 2 organisers, and only improving the fidelity of the surface elevation leads to an increase in the error for the pitch motion ($+24\%$ for wave 1BT2; $+3\%$ for wave 3BT2). The time traces in Figure 7.76 (a) indicate that the increased error for wave 1BT2 mainly stems from a divergence in the phase after approx. 12s. Interestingly, between $12\text{s} \leq t \leq 15$s, significantly better agreement

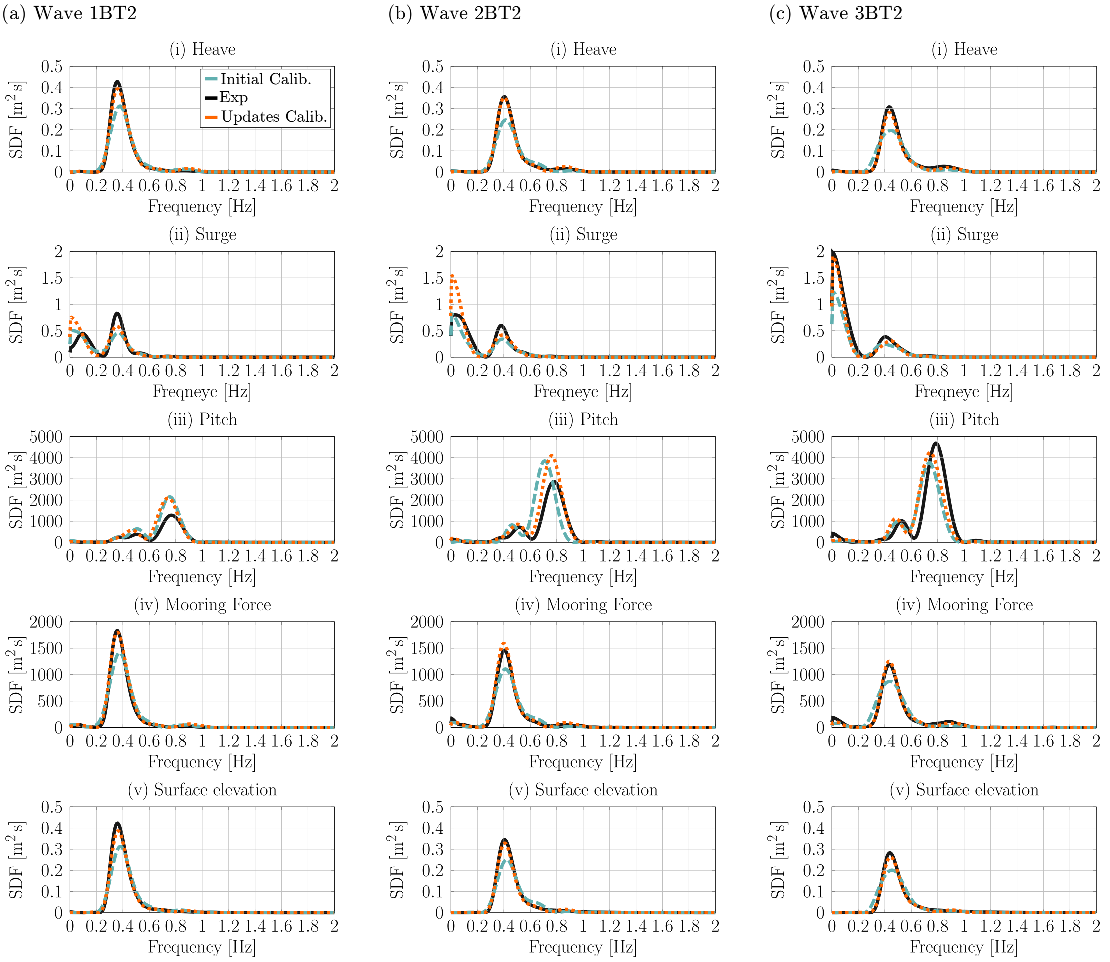

Figure 7.77: SDF of the heave, surge, and pitch motion, as well as the mooring force and surface elevation for W1.

between the experimental and numerical surface elevation can be observed for the surface elevation from the updated calibration method.

For wave 2BT2, the pitch motion does not follow the previously observed trend, showing the smallest error of the different test cases for the initial inertial properties, as well as location of the CoM, and the improved surface elevation (28%). The time trace in Figure 7.76 (b) indicates better agreement in phase between the experimental and the numerical data, with improved surface elevation, compared to the initial submission, while very similar agreement in amplitude between the two data sets can be observed for the three different waves. This highlights the sensitivity of the nRMSE to phase shifts and, furthermore, the importance of investigating both time traces and nRMSE to get a complete view of the agreement between experimental and numerical data. Nonetheless, no explanation was found for the cause of the observed phase shift for the pitch motion.

(a) W1 1BT2

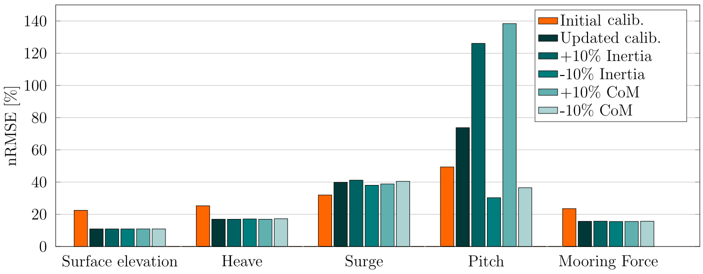

(b) W1 2BT2

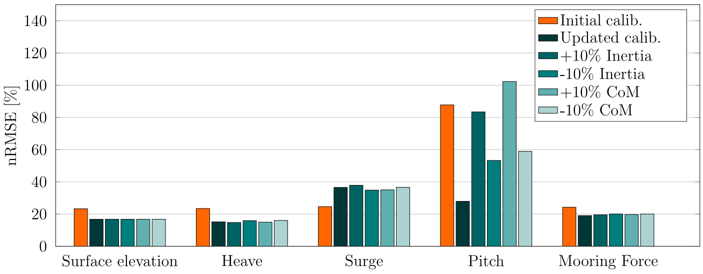

(c) W1 3BT2

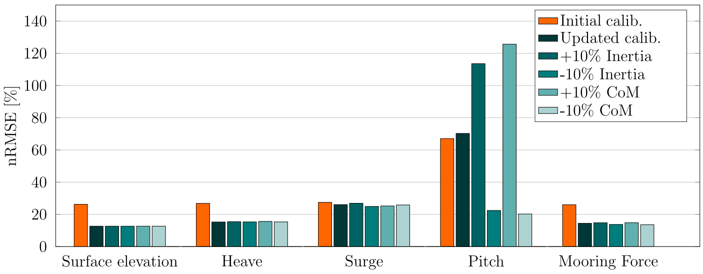

Figure 7.78: nRMSE between the experimental and numerical data for WEC structure W1 exposed to waves 1BT2–3BT2 for the different test cases considered in the sensitivity analysis.

W2

For WEC structure W2, Figure 7.79 shows the time traces of the heave, surge, and pitch motion, as well as the mooring force and surface elevation for waves 1BT2–3BT2, for the cases of the initial and the updated calibration method. The corresponding spectral density functions are shown in Figure 7.80.

Generally, similar trends as for W1 can be observed. Notably, relatively large differences between the experimental and both numerical data sets can be observed for the pitch motion. While, as for all motion data and the mooring force, the main peak and the preceding trough is well captured, significant differences in the phase and amplitude become visible towards the end of the pitch motion time traces. This is highlighted in the plots of the SDF, as well as the values of the nRMSE.

Comparing the nRMSE values (see Figure 7.81) from the initial calibration to the cases with the improved surface elevation and the nominal inertial properties and location

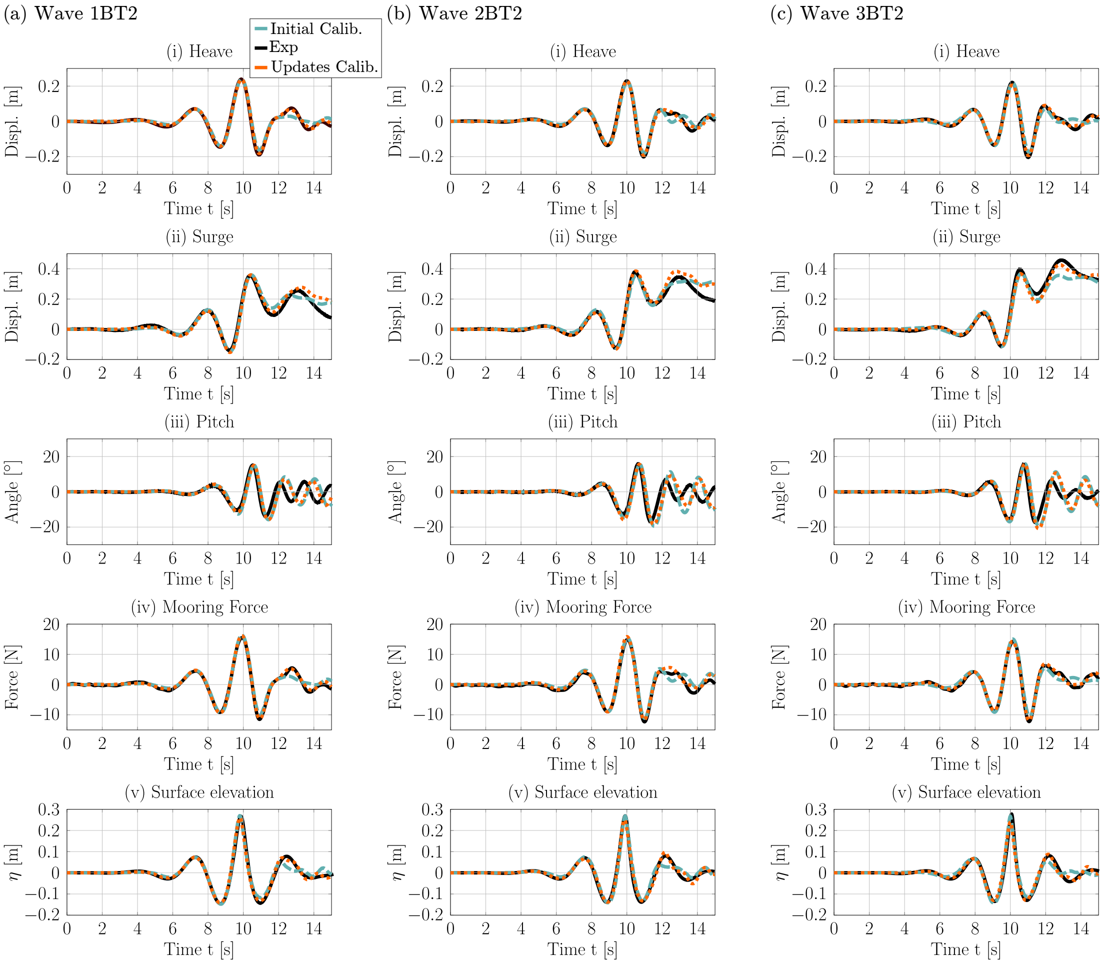

Figure 7.79: Time traces of the heave, surge, and pitch motion, as well as the mooring force and surface elevation for W2.

of the CoM, a consistent drop in the error can be observed for all waves (up to 13 percentage points for wave 1BT2). Compared to structure W1, the nRMSE values for the pitch motion are consistently higher for structure W2, for both the initial and updated surface elevation. However, by lowering the vertical position of the CoM, the error in pitch motion can be significantly reduced (down to 13%), thereby falling into the same range as for structure W1. Generally, an overall consistent trend can be observed for the pitch motion for all waves, whereby an increased inertia or a raised CoM significantly increases the observed nRMSE (up to 131% for wave 2BT2).

Regarding the nRMSE for the heave motion, as well as the mooring force, similar error values, following the same trends, are achieved for structures W2 as for W1. With an improved surface elevation, the error in the heave motion and mooring force is decreased and negligible scatter between the cases $\pm 10\%$ inertia or $\pm 10\%$ CoM can be observed, indicating an overall strong coupling between the surface elevation, heave motion, and mooring force. For the surge motion, more significant scatter between the cases can be observed. In contrast to structure W1, significant drops

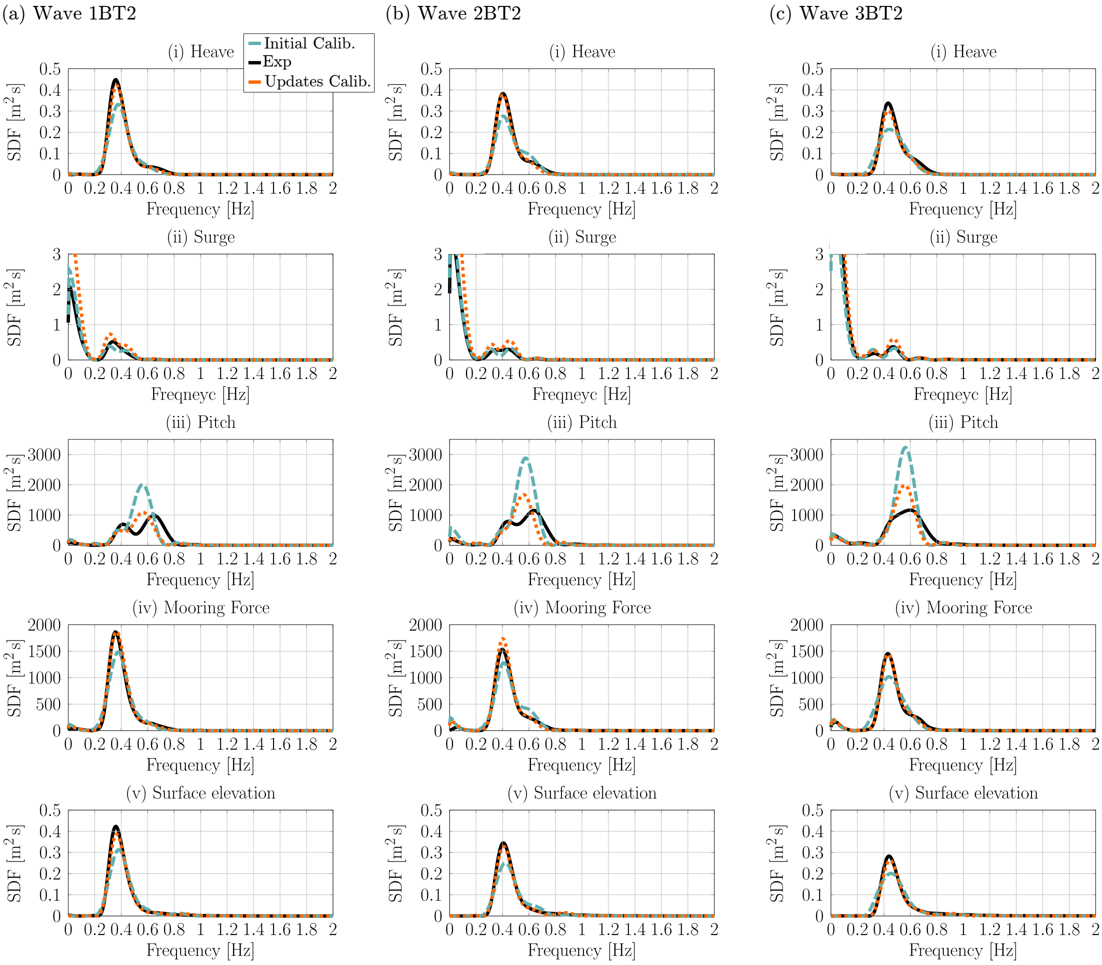

Figure 7.80: SDF of the heave, surge, and pitch motion, as well as the mooring force and surface elevation for W2.

in the error can be observed for W2 when lowering the vertical location of the CoM (minimum nRMSE $= 10\%$ for wave 2BT2).

Overall, the results for structure W2 indicate more consistent sensitivity of the modelled body dynamics to the physical device properties, resulting in the overall best agreement (nRMSE$\leq 21\%$) between the experimental and numerical results for the cases of a lower CoM.

(a) W2 1BT2

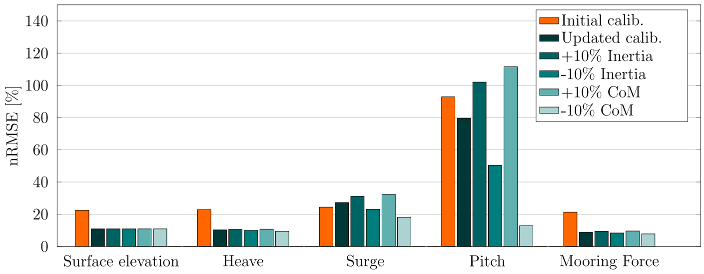

(b) W2 2BT2

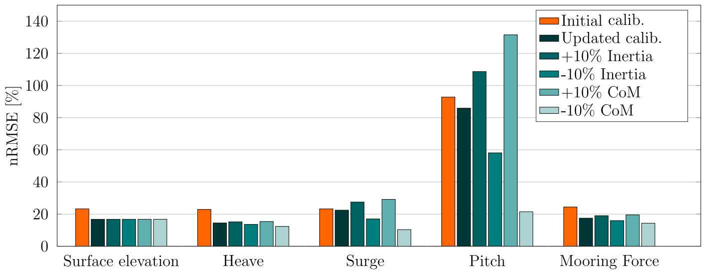

(c) W2 3BT2

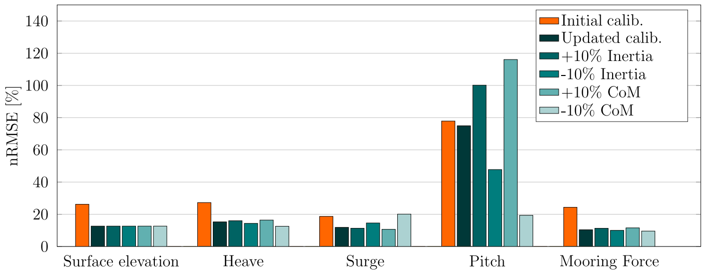

Figure 7.81: nRMSE between the experimental and numerical data for WEC structure W2 exposed to waves 1BT2–3BT2 for the different test cases considered in the sensitivity analysis.

In summary, the results presented in this section allow the two numerical models of WEC structures W1 and W2 to be declared validated. Regarding the sensitivity of the body motion, and thereby the agreement with the experimental reference data, it is shown that the quality of the surface elevation of the incident focused wave group has a significant influence on the body motion for both WEC structures, manifested in a strong coupling between the surface elevation, heave motion, and mooring force. Furthermore, coupling can be observed between the surge and pitch motion. Generally, the pitch motion shows strong sensitivity to the quality of the surface elevation and, most significantly, to changes in system parameters. In the contrary, the heave motion and mooring force are generally unaffected by the changed system parameters.

7.4 Concluding remarks

This chapter presents the successful validation of four different devices: a 1/5th and 1/20th scale Wavestar device, as well as two different moored point absorber type WECs. The validated CFD–based NWT models presented in this chapter will be applied for the analyses in the subsequent Chapters 8–11. The presented studies show that the validation of complex physical systems is a challenging task and requires exact knowledge of all system characteristics. This detailed knowledge is difficult to acquire but is required for the formulation of assumptions for the numerical model. This may influence the achievable order of accuracy for validation studies.

8

Evaluation of the overset grid method

Contents

For the economic operation of WECs, EMCSs are included in the device design, introducing hydrodynamic non–linearities and large structural motions (see Chapter 1). In such operational conditions, the fidelity of a CFD–based NWT is well suited for the evaluation of EMCSs (see Chapter 11). However, using the well known mesh morphing method (see Chapter 4), large amplitude WEC oscillations may deteriorate the quality of the spatial discretisation and push the NWT beyond the limits of numerical stability. To overcome this issue, advanced mesh motion methods, such as overset grids, have been developed.

Although the overset grid method shows particular potential for handling large amplitude, multi–DoF, WEC motion, limited application can be found in the WEC literature (see Chapter 5). The limited use of the overset grid method in the wave energy field can be attributed to:

(1) The significantly higher computational cost [587]
(2) The potential for numerical errors in the VOF framework, such as violation of mass conservation [29, 133]
(3) The limited availability of the overset grid method in commonly used CFD software (see Chapter 5).

Only recently the limitation in (3) has been removed through the code release of the overset method for OpenFOAM, making it available to a wide user community. In [CPB], the performance of the overset implementation in OpenFOAM version v1706 is assessed, comparing free decay experiments of the 1/5th scale Wavestar WEC (see Chapter 7). Major drawbacks, in terms of accuracy of the solution, computational overhead, and parallelisation of the solution process are revealed, rendering the particular implementation of the overset grid method infeasible. Subsequent to the publication of [CPB], improvements to the overset grid method have been implemented and released in OpenFOAM v1712 and v1812, namely, improved parallel computation through better performance of the momentum predictor and revised decomposition tolerances in v1712 [588], as well as a revised pressure–velocity coupling in v1812 [589]. In addition to the native implementation of the overset grid method in OpenFOAM, another overset grid implementation, *opera*, has recently been developed at the *Institute Of High Performance Computing*, Singapore, which works as an additional toolbox in the OpenFOAM environment [133].

This chapter presents an evaluation of the implementation of the overset grid method in OpenFOAM based on multi–phase (Section 8.1) and single–phase (Section 8.2) problems.

8.1 Multi–phase problems

In this section, the overset grid method in OpenFOAM is first evaluated based on a multi–phase problem by means of various, WEC related, test cases. Next to static equilibrium, free decay, and wave excitation force tests, a WEC under controlled and uncontrolled conditions is exposed to an irregular wave train, representing realistic operational conditions. This section purports to:

1. Highlight the importance of advanced mesh motion methods, in particular overset grids, for the analysis of WECs in CFD–based NWTs, under controlled conditions.
2. Investigate the performance, under the criteria of accuracy and computational overhead, of the overset grid method in OpenFOAM by comparing results against results using the conventional mesh morphing method.

8.1.1 Case study

This section presents the case study used to assess the performance of the overset grid method. First, the considered WEC device is described. Subsequently, the input waves, used for the different WSI simulations, are detailed.

WEC device

The considered device is based on WEC structure W2, considered for the CCP–WSI Blind Test Series 2 & 3, and validated in Chapter 7. For information on the device properties (dimensions, mass, inertia) see Section 7.3.

Input waves

In the case studies, both a regular wave and an irregular, JONSWAP, wave train are considered, with a (significant) wave height of $H\,(H_s) = 0.12$m and (peak) period of $T\,(T_p) = 1.94$s. The wave characteristics are chosen based on the scatter diagram of the AMETS test site in Bellmullet, Co. Mayo, off the West Coast of Ireland. Compared to other test sites (e.g. BIMEP, SEMREV), AMETS is characterised by relatively large wave heights [18, 590]. A full scale irregular sea state with a significant wave height $H_s = 3.5$m, and a peak period $T_p = 10.6$s shows the highest occurrence [591].
For the CCP–WSI Blind Test Series 2 & 3, the WEC device was tested in a physical wave tank with 3m water depth. Thus, Froude scaling [24] with a scaling factor of 1/30th is applied, to retain the deep water conditions of the AMETS site. This results in the scaled H_s of 0.12m, and a T_p of 1.94s.
Time traces of the recorded free surface elevation, measured in the CFD–based NWT at the intended WEC location, during a preliminary wave-only simulation, as well as the according spectral density distribution, are shown in Figures 8.1 (a) and (b), respectively, for the regular wave, and for the irregular wave train in Figures 8.2 (a) and (b), respectively.

8.1.2 Test cases

For the evaluation of the overset grid method, five different test cases, of increasing complexity, are considered, detailed in the following.

Static equilibrium

To test the numerical stability of the solver, a simple test case of a floating WEC, initialised at its equilibrium position, without external excitation (e.g. input waves), is simulated for a duration of 10s. The simulated body position and the resulting hydrodynamic forces are compared between the mesh morphing and overset grid methods.

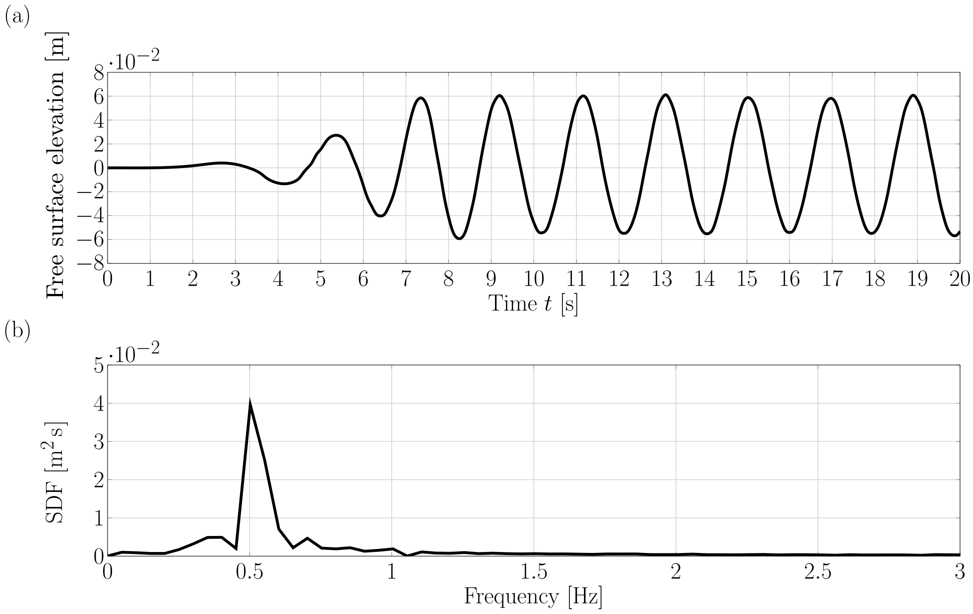

Figure 8.1: Surface elevation time trace and the corresponding spectral density distribution of the regular, 2^{nd} order, Stokes wave

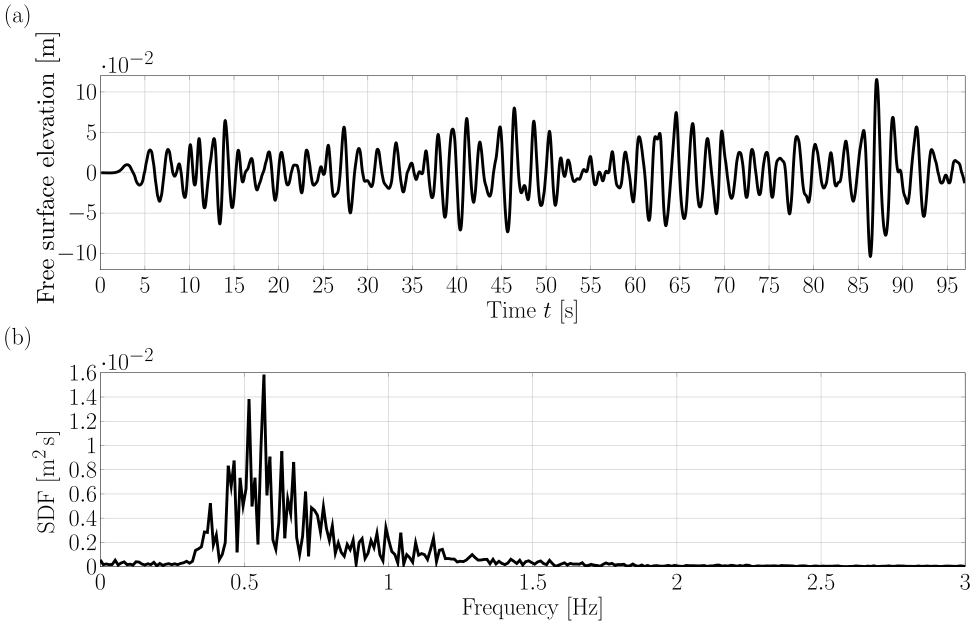

Figure 8.2: Surface elevation time trace and the corresponding spectral density distribution of the irregular wave train

Free decay

In a subsequent test case, the WEC is initialised away from its equilibrium position, in the form of an initial heave displacement of 0.05m. No input waves are considered for the test case, so that an oscillatory, decaying, motion around the device's equilibrium position is expected. Again, the simulated body motions and the resulting hydrodynamic forces are compared between the mesh morphing and overset grid methods.

Wave excitation

To introduce WSI in the evaluation of the overset grid method, wave excitation force experiments are considered. Regular waves are created by a numerical wave maker, propagate through the domain, and interact with the WEC device, which is held fixed at its equilibrium position. For the evaluation of the overset grid method, the excitation forces on the body are post-processed and compared with results from the mesh morphing method. Holding the body fixed in this test eliminates any dynamic mesh motion from the experiment; therefore, any difference between the two sets of results indicates interpolation errors in the overset grid method between the background and overset mesh.

Wave–induced motion – Uncontrolled WEC

As a first test of wave–induced WEC motion, regular waves are created by a numerical wave maker, similar to the wave excitation force test, propagate through the domain, and interact with the WEC device. However, in this test case, the uncontrolled WEC device is now allowed to move in three DoF, i.e. heave, surge, and pitch. The simulated body motions and the hydrodynamic forces are compared between the mesh morphing and overset grid methods.

Wave–induced motion – Controlled WEC

Finally, the performance of the overset grid method is assessed for a WEC in operational conditions. A PTO system is implemented in the CFD–based NWT as a linear spring–damper system. The implementation of the PTO allows the WEC to be controlled using a reactive output–feedback controller.

The energy maximising optimal controller, considered in this study, is synthesised in an output–feedback form[1], using both heave displacement and velocity of the device as measurable variables. An optimal control law f_u written in a parametric form

$$f_{\mathrm{u}} = k_u z + b_u \dot{z}, \tag{8.1}$$

with $\mathscr{H} = [k_{\mathrm{u}}\ b_{\mathrm{u}}]$, is applied to the WEC, realised by means of the PTO system, where z and $\dot{z}$ represent the heave displacement and velocity of the device in global coordinates, respectively. The optimal gain $\mathscr{H}$ is either computed analytically (for regular waves), or following exhaustive search procedures, explicitly using a dynamical model of the WEC system, for irregular waves (see also Chapter 11 for more insights on the WEC controller).

---

[1] The reader is referred to [592, Chapter 2] for further detail on the fundamentals behind feedback control techniques.

To assess the influence of the controller on the device dynamics, and, ultimately, on the dynamic mesh motion method, simulations of a controlled and uncontrolled WEC are performed and compared using the mesh morphing and overset grid methods. For these test cases, the simulated body motions are monitored and compared.

8.1.3 Numerical wave tanks

The CFD–based NWT is implemented in OpenFOAM version v1812 of the ESI fork [593]. The numerical wave tanks uesd in this section, implementing the mesh morphing and overset grid method, are inspired by the validated model, presented in Section 7.3. However, some adjustments are implemented and detailed in the following.

Numerical wave generation and absorption

While the impulse source wave maker (see Chapter 6) is used for the validation study in Section 7.3 to create the desired focused wave group, the IHFOAM [102] toolbox is employed in this section for wave generation and absorption. IHFOAM is readily implemented in OpenFOAM v1812, and can be classified as a static boundary method (see Chapter 4). Waves are generated at the up–wave boundary of the CFD–based NWT, by prescribing the target water level, through the water volume fraction, and the fluid velocity. For an irregular wave train, the wave amplitudes and phases for each frequency component of the wave act as inputs to the wave maker. For wave absorption, a correction velocity, based on shallow water theory, is imposed at the down–wave domain boundary, to cancel out the incoming wave. In contrast to the impulse source wave maker, the IHFOAM toolbox avoids calibration of the wave maker to a desired target wave, which is not required here, given that no exact reference waves are specified.

Computational domain

Figures 8.3 (a) and (b) show the top and side view of the numerical domain, respectively, including all relevant dimensions. The domain layout closely follows the domains in Chapter 7, where the symmetry of the problem is exploited and only half of the wave tank is modelled by means of a symmetry boundary condition is employed in the x-z plane. All other relevant boundary conditions are indicated in Figures 8.3 (a) and (b). To determine the converged spatial and temporal discretisation size, convergence studies are performed on the basis of the regular wave described in Section 8.1.1. As usual, for the spatial discretisation, the smallest cell size in the z-direction, around the free surface interface, is parametrised by the wave height. Three different cell sizes, i.e. 5, 10, and 20CPH are tested. In the interface region, the mesh features a horizontal to

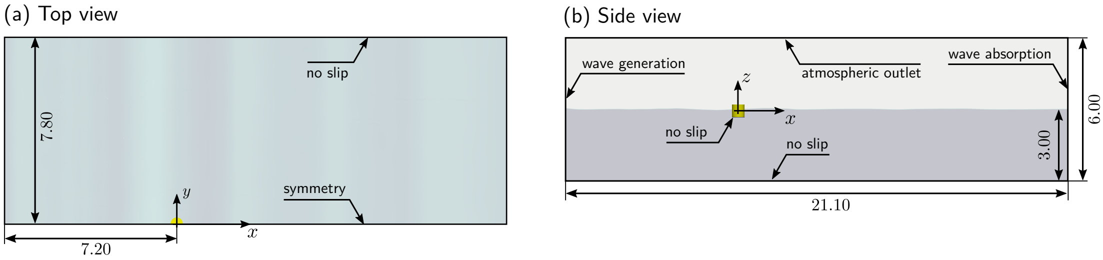

Figure 8.3: Schematic of the numerical wave tank (all dimensions in [m]): (a) top view and (b) side view.

vertical aspect ratio of 2. Towards the down–wave boundary of the CFD–based NWT, cell stretching is applied to enhance wave absorption and reduce the overall cell count. For the convergence studies, the phase averaged wave height is extracted from the simulations. Table 8.1 shows the result of the spatial convergence study. With a fixed time step of $\Delta t = 0.002$s, oscillatory convergence can be found for a cell size of $\Delta z = 10$CPH. The relative grid uncertainty $\mathcal{U}$ is 1.32%. To ensure converged solutions for the body motion, a spatial convergence study is also performed for the grid size around the body using the mesh morphing method. Three different grid sizes, equivalent to 5, 10, and 20CPH, are considered and the root–mean square (RMS) values of the heave motion are used as metric for the convergence study. The results are listed in Table 8.1. Monotonic convergence can be found for a cell size in the interface region of $\Delta z = 10$CPH with a relative grid uncertainty $\mathcal{U} = 0.26\%$. Generally, it is desirable to use uniform meshes in the interface region to prevent spurious velocities in the interface region, induced by cell nodes hitting cell faces. A screen shot of the spatial discretisation of the CFD–based NWT is shown in Figure 8.4. For the temporal convergence study, the cell size in the interface region Δz is fixed to 10CPH. Three different (fixed) time step sizes, i.e. $\Delta t = 0.004$s, 0.002s, and 0.001s, are considered. Again, the phase averaged wave height is used as a metric for the convergence study. Table 8.1 shows the results of the temporal convergence study. With a cell size in the interface region of $\Delta z = 10$CPH, monotonic convergence can be found for a time step size of $\Delta t = 0.002$s. The relative grid uncertainty $\mathcal{U}$ is 1.74%.

Dynamic mesh motion methods

In this study, the device motion is constrained, only allowing translational motion in surge and heave, as well as rotational motion in pitch. Since only unidirectional, long crested, waves are considered in this study, the sway, roll, and yaw DoFs are negligible. For the simulations considering the mesh morphing method, the standard OpenFOAM implementation, by means of the SLERP algorithm, is considered. The inner distance (see Chapter 4) for the mesh morphing method is set to 0.05m, while the outer distance

Table 8.1: Results of the spatial convergence study

Spatial: Wave height					
Δt	$\Delta z = 5$CPH	$\Delta z = 10$CPH	$\Delta z = 20$CPH	Convergence Type	$\mathcal{U}$
0.002s	0.111m	0.113m	0.112m	Oscillatory	1.32%
Spatial: Heave motion RMS					
Δt	$\Delta z = 5$CPH	$\Delta z = 10$CPH	$\Delta z = 20$CPH	Convergence Type	$\mathcal{U}$
0.002s	$3.33 \cdot 10^{-2}$m	$3.36 \cdot 10^{-2}$m	$3.37 \cdot 10^{-2}$m	Monotone	0.26%
Temporal: Wave height					
Δz	$\Delta t = 0.004$s	$\Delta t = 0.002$s	$\Delta t = 0.001$s	Convergence Type	$\mathcal{U}$
10CPH	0.108m	0.113m	0.115m	Monotone	1.74%

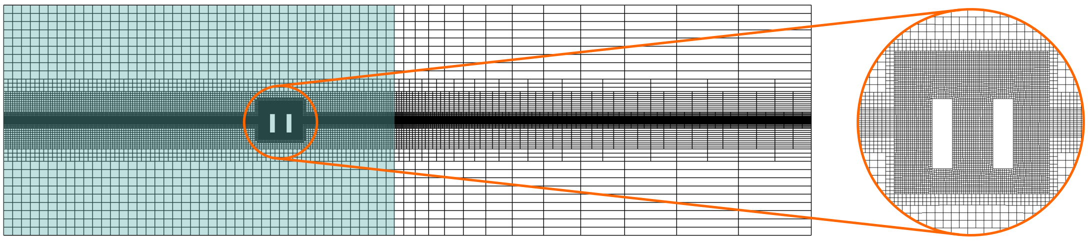

Figure 8.4: Screen shot of the computational mesh in the x-z plane for the mesh morphing method. The mesh region without cell stretching is highlighted in light blue.

is set to 1.5m, i.e. approx. 3 device diameters. Note that the outer distance is chosen based on the optimal distance between controlled WECs as indicated by [594, 595]. For the simulations considering the overset grid method, the domain comprises a background (light blue colour code in Figure 8.5) and an overset grid (petrol colour code in Figure 8.5). The dimensions, as well as the spatial discretisation of the background grid are the same as for the mesh morphing CFD–based NWT, and the symmetry boundary condition is also applied in the x-z plane. The overset grid region spans $1.6R_{\text{WEC}} \times 0.9R_{\text{WEC}} \times 1.6R_{\text{WEC}}$ in the x, y, and z directions, where R_{WEC} is the device radius (see Figure 7.65). The discretisation in the overset mesh has been chosen to reflect a similar discretisation around the WEC device, as in the mesh morphing CFD–based NWT. The device is located in the centre of the overset mesh. For this study, the in-house overset grid toolbox *opera*, developed at the *Institute Of High Performance Computing*, Singapore, is employed. Compared to the native overset grid method in OpenFOAM v1812, three main differences can be identified in *opera*:

1. The donor search algorithm uses a dual–level parallelism approach, for increased computational efficiency.

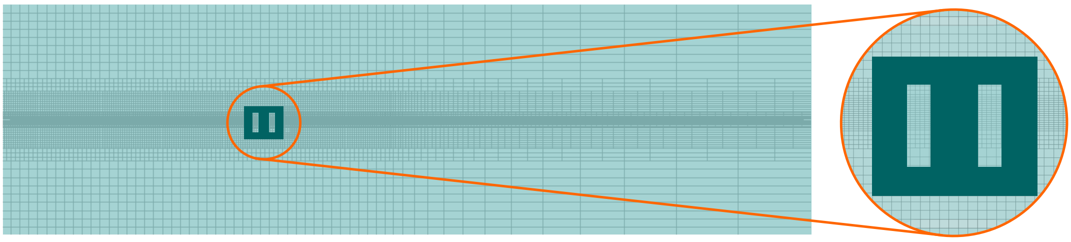

Figure 8.5: Screen shot of the CFD–based numerical wave tank for the overset grid method in the x-z plane. The background mesh is marked in light blue, the overset region is marked in petrol.

2. The interpolation layers on the overset grid are two–layered, avoiding the need for the interpolation of gradients.
3. The inverse distance interpolation algorithm has been improved.

For a more detailed description of the *opera* algorithm, and some performance assessment studies, the interested reader is referred to [133].

A comparison between the overset grid implementation in *opera* and the native overset grid implementation in OpenFOAM v1812 is undertaken in a preliminary study. As shown in Figure 8.6, qualitatively, good agreement is found between the two overset grid implementations, particularly for heave displacement. However, the implementation of the overset method in *opera* is observed to be more computationally efficient than the implementation in OpenFOAM v1812, delivering 1.42 times faster computation, in terms of run time for the particular case study, driving the decision to use *opera* for the subsequent simulations.

Flow conditions

In the following, turbulence modelling is only considered for the simulations of the last assessment test case: wave–induced motion of the controlled WEC. Under controlled conditions, it is assumed that turbulence effects are more likely of importance, compared to uncontrolled cases. For all other test cases, laminar flow conditions are assumed, to reduce the computational overhead for the comparative study between the mesh morphing and overset grid methods.

To account for turbulence, a RANS turbulence model, specifically the standard k-ω SST turbulence model, with industry standard wall functions (see Chapter 4), is employed. The choice of the turbulence model is based on the literature review presented Chapter 5.

(a) Surge displacement

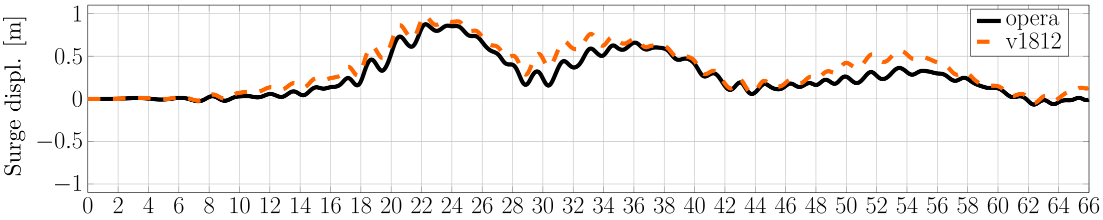

(b) Heave displacement

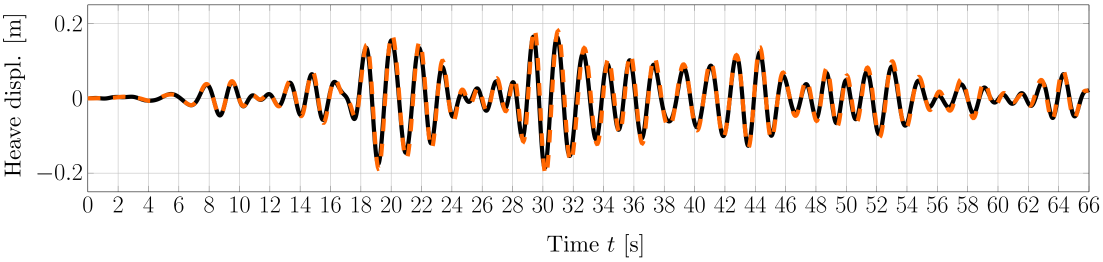

Figure 8.6: Heave and surge displacements of WEC structure W2, exposed to an irregular wave train, from simulations performed with *opera* and the native overset grid implementation in OpenFOAM v1812.

PTO representation

A PTO system is implemented in the CFD–based NWT as a linear spring–damper system within the `sixDoFRigidBodyMotion` solver. The PTO force follows Equation (8.1), where k_u and b_u are defined as $-1279\,\mathrm{N\,m^{-1}}$ and $35\,\mathrm{N\,s\,m^{-1}}$, respectively. Note that, even though the WEC structure is allowed to move in three DoFs, the PTO system only considers the heave displacement and velocity. The PTO force is applied along the axis of the mooring line.

Mooring representation

As in Section 7.3, the device mooring is modelled as a linear spring system, which is defined in the `sixDoFRigidBodyMotion` solver. The stiffness of the spring, k_{mooring}, is set to match the physical spring stiffness, i.e. $67\,\mathrm{N\,m^{-1}}$.

Solver settings and solution schemes

The solver setting and solution schemes have been adapted from the validation case in Section 7.3 and the relevant settings can be found in Table 7.31.

8.1.4 Results and discussion

This section presents and discusses the results of the assessment of the overset grid method based on the five different test cases, introduced in Section 8.1.2.

Static equilibrium

First, results for the static equilibrium test are presented in Figure 8.7, where Figures 8.7 (a), (b), and (c) show the device displacement in the surge, heave, and pitch DoF, respectively. Figures 8.7 (d), (e), and (f) show the hydrodynamic forces and moments in the surge, heave, and pitch DoF, respectively. For all subfigures (and all subsequent plots in this section, unless stated differently), the black solid line shows the results from *opera*, while the dashed orange line refers to the results with mesh morphing.

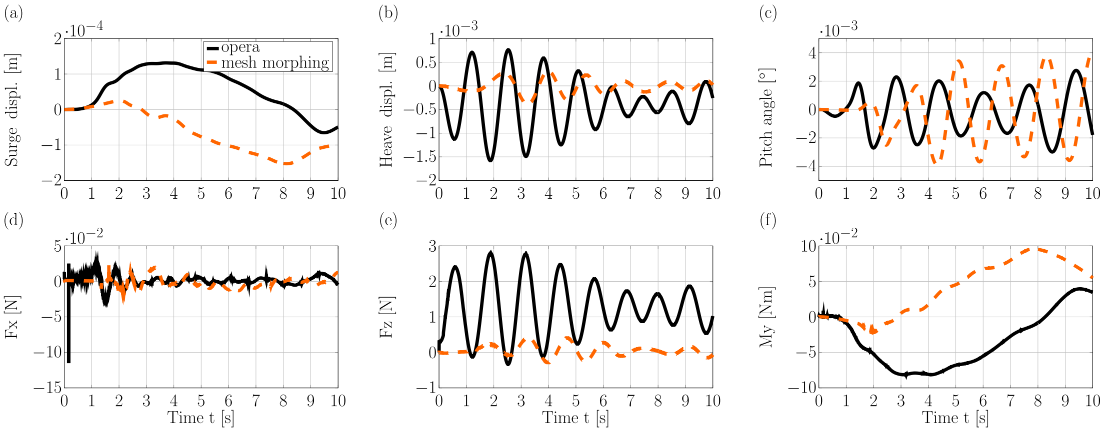

Figure 8.7: Heave, surge, and pitch displacements and loads during the free floating body test

A clear mismatch between *opera* and mesh morphing can be observed for all plotted quantities in Figure 8.7. Overall, relatively small amplitudes of device displacement are seen. The device displacement in the surge DoF shows an order of magnitude of 10^{-4} m, an order of magnitude of 10^{-3} m in the heave DoF, and an order of magnitude of $10^{-3}\,^{\circ}$ in the pitch DoF. Similarly, the order of magnitude of the hydrodynamic forces is relatively small (10^{-2} N in the surge DoF, 1 N in the heave DoF, and 10^{-2} N m in the pitch DoF). The plot of the heave displacement indicates an offset for the equilibrium position of the device simulated with *opera*. While the body oscillates around 0m in the heave DoF for mesh morphing, the equilibrium position for *opera* is at approximately $-0.25 \cdot 10^{-3}$m, which is reflected in the non–zero mean force ($\bar{F}_z \approx 1.25$N). This small offset can be induced by a mismatch in the body volume, between the mesh morphing and opera setup, induced by slight differences in the mesh. Following $V_d = {}^{\bar{F}_z}/_{\rho g}$, the volume defect can be estimated as $V_d = 1.8 \cdot 10^{-4}$m^3, which is 0.2% of the total device volume.

Comparing the different motion and force data, recorded during the static equilibrium test, to the WSI simulations, the observed WEC motion and forces on the WEC body are at least one or two orders of magnitude smaller. This indicates that, although qualitatively relatively large deviations can be observed between mesh morphing and *opera* for the static equilibrium test, these deviations are assumed to have a negligible influence for WSI simulations.

Since the difference between the two data sets for mesh morphing and *opera*, for this test case, is relatively obvious from a qualitative comparison, no quantitative comparison is subsequently presented here.

Regarding the computational expense of the overset grid method, the relative runtimes, $\hat{t}_{\text{run}}$, is introduced as

$$\hat{t}_{\text{run}} = \frac{t_{\text{run,o}}}{t_{\text{run,MM}}}\,, \tag{8.2}$$

where $t_{\text{r,MM}}$ denotes the runtime for the mesh morphing method and $t_{\text{r,o}}$ denotes the runtime of the overset grids method.

For the static equilibrium test case, $\hat{t}_{\text{run}} = 1.5$, indicating longer run times for the overset grid method. For comparative purposes, Table 8.2 lists the relative runtime for the first four considered test cases.

Free decay

Figures 8.8 (a) and (b) show the time traces of the displacement and hydrodynamic forces in the heave DoF, respectively, during the free decay test. A qualitative assessment of the results shows a closer match between the results from *opera* and mesh morphing, compared to the results of the static equilibrium test. The results suggest that the larger order of magnitude of the device motion and hydrodynamic force blurs the deviations observed for the static equilibrium test.

Generally, slightly larger motion and force amplitudes can be observed for the results from *opera*, compared to mesh morphing. Noteworthy are the spikes which can be observed in the force signal from *opera*; however, these spikes in the fluid force do not propagate to the motion of the device and seem to be smoothed out by the motion solver. At the time of writing, it was not possible to identify the cause of the observed spikes and further analysis of similar test cases with different initial conditions should be performed in the future.

For a quantitative assessment, the root-mean squared deviation (nRMSD) is considered, following

$$\text{nRMSD} = \sqrt{\frac{\sum_{i=1}^{n}\left[\varpi(i) - \hat{\varpi}(i)\right]^2}{n}\frac{100\%}{\mathcal{N}}}\,, \tag{8.3}$$

where n indicates the number of samples of the signal, ϖ is the result from mesh morphing, and $\hat{\varpi}$ is the result from *opera*. $\mathcal{N}$ is the normalisation factor. For the case of the heave free decay test, the initial displacement, i.e. 0.05m, is considered for the

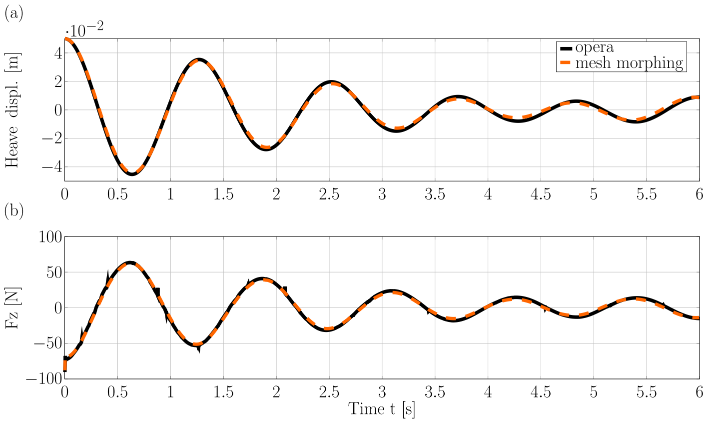

Figure 8.8: Heave displacement and forces during heave free decay test

normalisation of the RMSD of the heave displacement. For the heave force, $\mathcal{N}$ is chosen to be the analytical hydrostatic force in the equilibrium position, i.e. $\mathcal{N} = 634.14$N. nRMSD values of 2.7% and 0.2% are calculated for the heave displacement and heave forces, respectively. In terms of relative runtime, *opera* shows an increase in runtime, compared to mesh morphing, of a similar order of magnitude as for the static equilibrium test, i.e. $\hat{t}_{\text{run}} = 2$.

Wave excitation

Figures 8.9 (a), (b), and (c) show the wave excitation forces and moments in the surge, heave, and pitch DoF, respectively, from *opera* and mesh morphing. A qualitative inspection of the time traces from *opera* and mesh morphing show good agreement between the two dynamic mesh motion methods, similar to the heave free decay test. For a quantitative comparison, the nRMSD is considered, following Equation (8.3), where the RMSD is normalised by the maximum force/moment magnitude. For the forces and moments in the surge, heave, and pitch DoFs, relatively small nRMSD values of 0.6% can be calculated, revealing also quantitatively good agreement between overset grids and mesh morphing. Since the device is fixed during the wave excitation force tests and, thus, no mesh motion is allowed, any deviations are assumed to stem from interpolation in the overset grid method. From the relatively small nRMSD, it can be concluded that the interpolation errors are generally minimal.
Regarding the computational overhead, *opera* also shows an increased runtime, compared to mesh morphing, i.e. $\hat{t}_{\text{run}} = 1.9$, for this test.

Wave induced motion – Uncontrolled WEC

Figures 8.10 (a), (b), and (c) show the WEC displacement in the surge, heave, and pitch DoFs, respectively. Figures 8.10 (d), (e), and (f) show the hydrodynamic forces and moments acting on the WEC device in the surge, heave, and pitch DoFs, respectively.

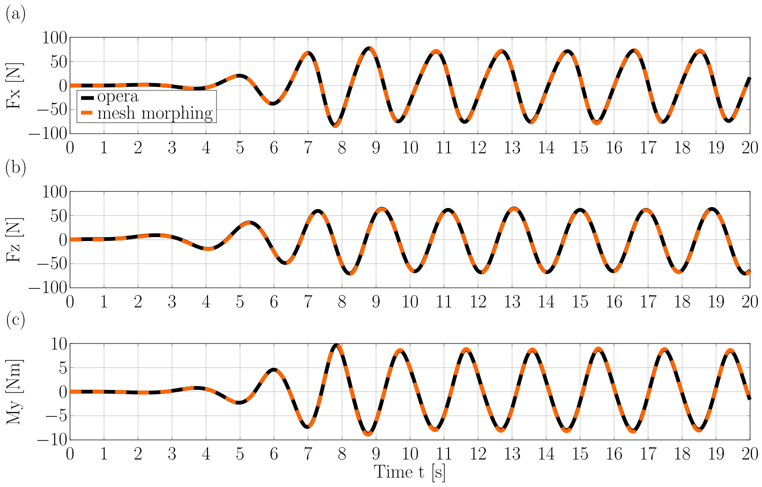

Figure 8.9: Forces and moments on the fixed WEC, exposed to regular waves

Similar to the free decay and wave excitation force test cases, relatively good qualitative agreement between *opera* and mesh morphing can be observed. For the quantitative assessment, the nRMSD, following Equation (8.3) is evaluated, where the RMSD is normalised by the maximum displacement or force/moment magnitude. nRMSD values of 3.9%, 0.4%, and 0.4% are calculated for the displacement in the surge, heave, and pitch DoFs, respectively. For the hydrodynamic forces in the surge and heave DoFs, and the moment in the pitch DoF, nRMSD values of 0.5%, 1.1%, and 4.5% are calculated, respectively.

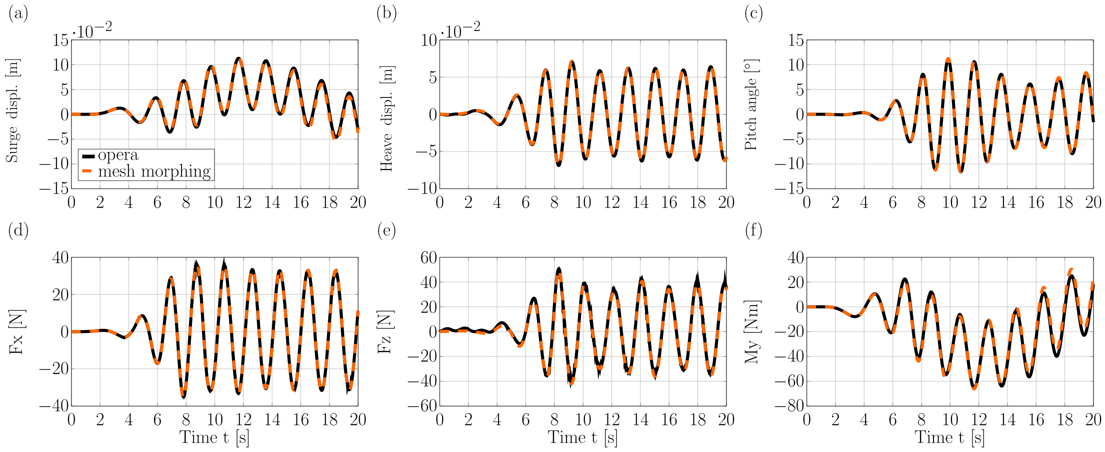

Figure 8.10: Heave, surge, and pitch displacements and loads of the moving WEC, exposed to regular waves

Comparing the nRMSD values of the hydrodynamic forces for the case of the wave induced motion test and the wave excitation force tests, larger deviations between mesh morphing and *opera* can be observed, specifically in the pitch DoF. The larger deviations could be attributed to either/both the required interpolation in the overset grid algorithm or the influence of the mesh deformation in the mesh morphing, i.e. skewed cells with larger aspect ratios. For dynamic WSI simulations, compared to the static body in the wave excitation force test, the interpolation between the grids is more challenging, due to the varying interpolation partners, caused by the larger relative motion between the grids.

Regarding the relative runtime, *opera* shows an increase in runtime, consistent with the previously presented test cases, at $\hat{t}_{\text{run}} = 2$.

Table 8.2: Runtime comparison between mesh morphing and *opera*

Test case	$\hat{t}_{\text{run}}$	$t_{\text{run,o}}$
Static equilibrium	1.5	77379s
Free decay	2.0	149026s
Wave excitation force	1.9	170080s
Wave–induced motion – Uncontrolled WEC	2.0	439630s

Wave induced motion – Controlled WEC

This section evaluates the performance of the overset grid method for a WEC in operational conditions, by considering an irregular wave train and contrasting the motion of a controlled and an uncontrolled WEC. Furthermore, this test case highlights the importance of advanced mesh motion methods for the analysis of controlled WECs. Considering mesh morphing, Figures 8.11 (a) - (c) show the surge, heave, and pitch displacement of the uncontrolled (solid) and controlled (dashed) WEC device, respectively. For the case of the uncontrolled WEC, it can be observed that the WEC surges in the wave propagation direction, and oscillates back due to the mooring forces, with a maximum displacement of 0.25m (from its equilibrium position). In heave, a maximum displacement amplitude of approx. 0.1m is measured at $t = 88$s, while a maximum pitch angle of approx. $20°$ can be measured at $t = 41$s. For the case of the controlled device, a clear increase in device motion, most significantly in surge motion, can be observed. Results for the controlled WEC, modelled with mesh morphing, are only available up to 50.2s, at which point the simulation crashes.

Figure 8.11 shows screen shots of the CFD–based numerical wave tank, for uncontrolled and controlled WEC cases, taken at four different time instances, representing: equal motion for the controlled and uncontrolled case ($t = 23$s), larger heave displacement in the controlled case, with similar surge and pitch motion ($t = 35$s), larger pitch and surge displacement in the controlled case, with similar heave motion ($t = 46$s), and the last time instance for the controlled device before the simulation crashes ($t = 50.2$s). At $t = 50.2$s, the mesh, down wave of the controlled WEC, is highly skewed, causing numerical instabilities due to the high cell non-orthogonality, as indicated by the `checkMesh` toolbox, implemented in OpenFOAM [596]. Overall, the results highlight the importance of using advanced mesh motion methods for WEC control studies.

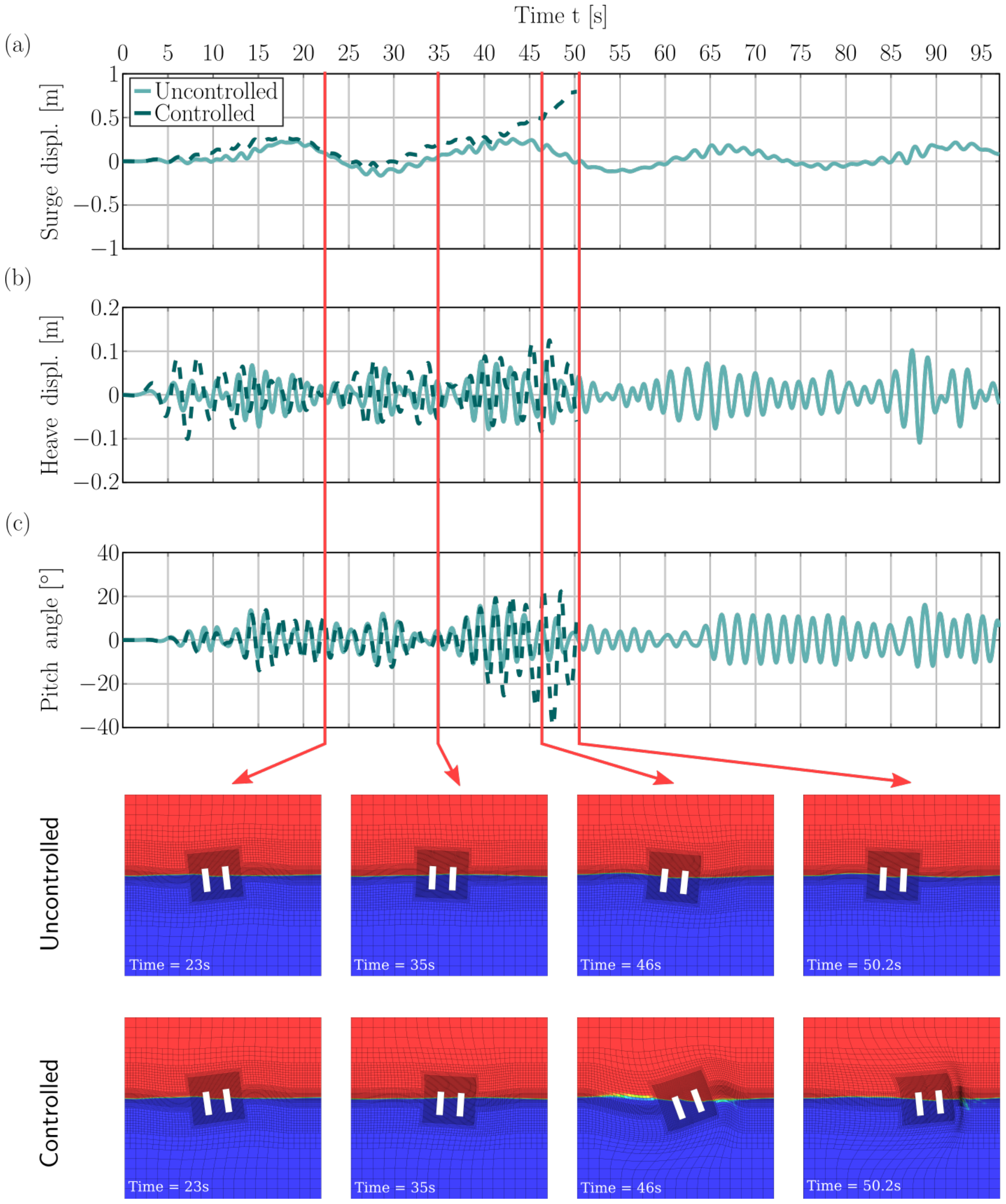

Figure 8.11: Heave, surge, and pitch displacements of the uncontrolled and controlled WEC device, modelled with mesh morphing. In addition, the mesh deformation in the CFD–based NWT is shown. After 50.2s, the simulation of the controlled WEC aborts, due to poor mesh quality.

For the overset grid method, Figures 8.12 (a) - (c) show the surge, heave, and pitch displacement of the uncontrolled (solid) and controlled (dashed) WEC device, respectively. Again, the enhanced device motion under controlled conditions is visible. The WEC surges in the wave propagation direction with a maximum displacement of 1m from its equilibrium position (at $t \approx 50$s). In heave, the maximum amplitude is ~ 0.12m (at $t = 64$s), while a maximum pitch angle of $-40°$ is measured at $t = 48$s.

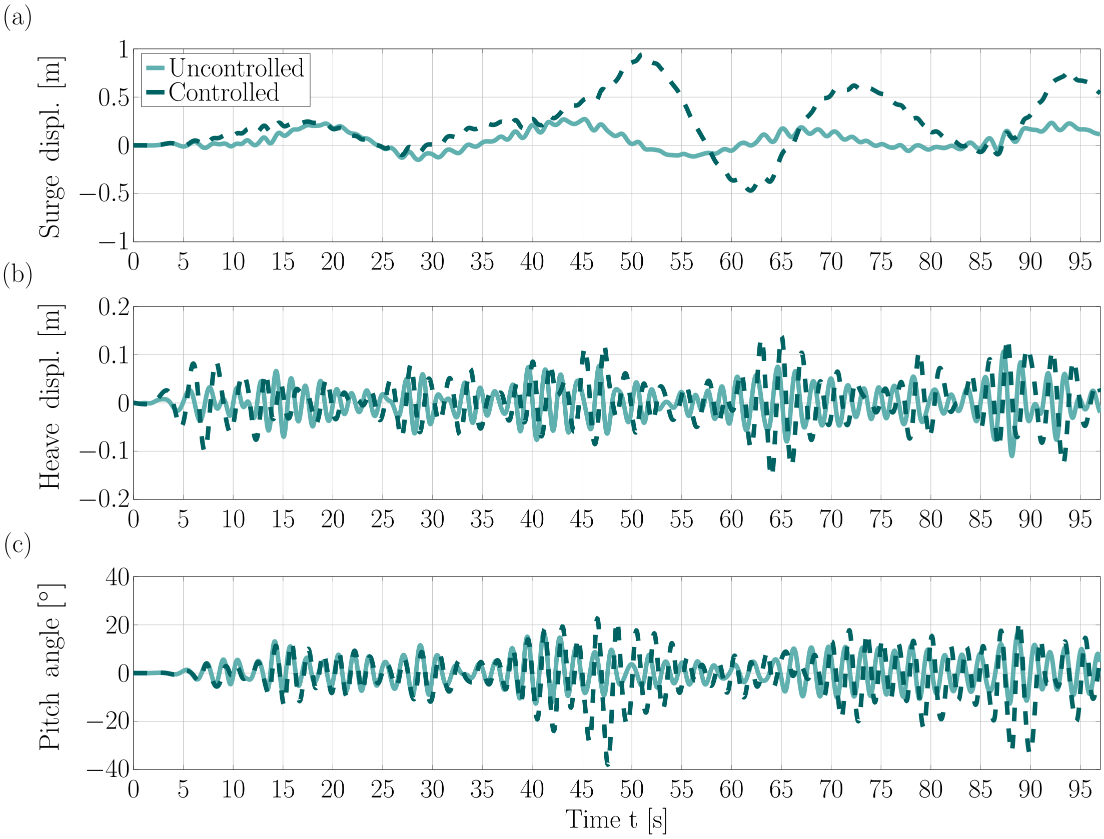

Figure 8.12: Heave, surge and pitch displacements of the uncontrolled and controlled WEC device, modelled with *opera*, exposed the irregular wave train.

For a better comparison between the results from mesh morphing and overset grids, Figures 8.13 (a) - (c) show the surge, heave, and pitch displacement of the uncontrolled WEC, modelled with the mesh morphing (orange dashed) and *opera* (solid black). For the case of the uncontrolled WEC, the device follows the same trajectory, when modelling with *opera* or mesh morphing, which is consistent with the findings for the previous test cases.

For the controlled WEC case (see Figures 8.14 (a) - (c)), the trajectories for the surge, heave, and pitch displacement also show similar results when modelled with *opera* or mesh morphing; however, modelling the controlled WEC with *opera* allows simulation of the complete wave train, avoiding any limitations induced by poor mesh quality.

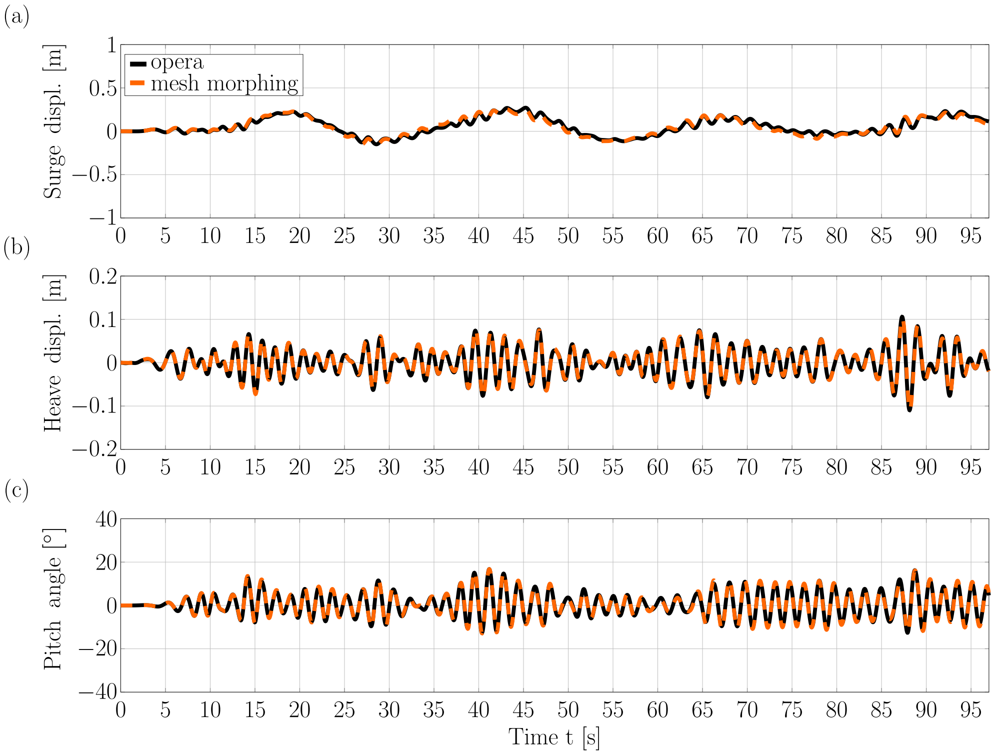

Figure 8.13: Heave, surge, and pitch displacements of the uncontrolled WEC device, modelled with *opera* and mesh morphing, exposed to the irregular wave train.

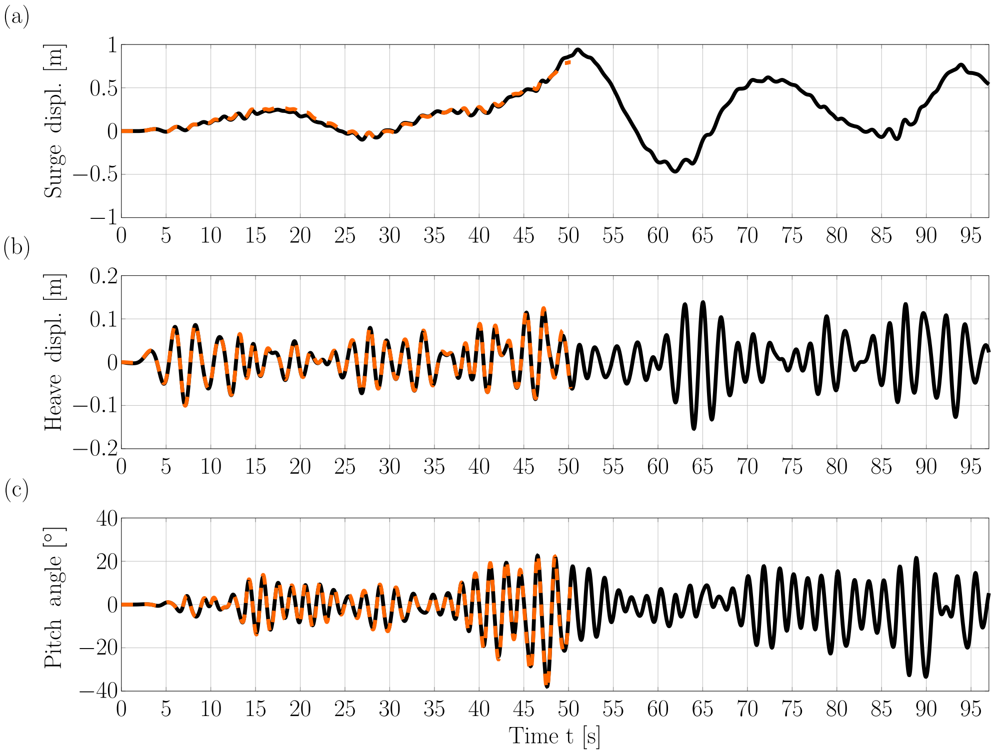

Figure 8.14: Heave, surge, and pitch displacements of the controlled WEC device, modelled with *opera* and mesh morphing, exposed to the irregular wave train.

This section presents the modelling of a WEC device, using two different dynamic mesh motion methods. In summary, the presented results indicate that the accuracy of the overset grid method, implemented in OpenFOAM through the *opera* toolbox, is equivalent to the mesh morphing method.

Comparing the results for the uncontrolled and controlled WEC device, when considering mesh morphing, highlights the importance of advanced mesh motion methods, especially for modelling WECs under controlled conditions. In such cases, the overset grids prove to be a particularly feasible alternative to the mesh morphing method, by avoiding the potential deterioration of the mesh quality due to large WEC motion. However, the drawback of the overset grid method is an approximate two-fold increase in runtime.

8.2 Single–phase problems

The overset grid method's accuracy of the solution for multi–phase flows has been proven in the previous section. To ensure accuracy of the employed overset grid method for single–phase flows in Chapter 9, simulation of the vortex shedding behind a cylinder is considered in the following. Simulations with the native overset grid implementation in OpenFOAM v1812 are compared against results with a stationary grid (i.e. no mesh motion), as well as reference data from the literature.

8.2.1 Test case

In particular, this section considers the vortex shedding behind a fixed or oscillating cylinder, based on the test cases presented in [597]. The observed flow phenomena are well understood and, thereby, act as good benchmark test cases. For the evaluation, a qualitative comparison of the stream lines and vorticity contours will be performed, for which the results, presented in [597], serve as a reference. The results for the stationary and oscillating cylinder are presented independently in Section 8.2.3.

8.2.2 Numerical framework

The incompressible Navier–Stokes equations are solved with OpenFOAM's transient solver for incompressible flow of Newtonian fluids with overset grids, `overPimpleDyMFoam`, implemented in OpenFOAM version v1812 of the ESI fork [593].
Figure 8.15 shows the domain layout for the present numerical model. For the cases using the overset grid method, the orange border indicates the location and size of the overset grid region. A fixed free stream velocity of $0.4385\mathrm{m\,s^{-1}}$ in the x-direction is specified at the left hand side (inlet) boundary of the domain. With a kinematic

viscosity of $\nu = 8.77 \cdot 10^{-4}\,\mathrm{m^2\,s^{-1}}$ and a cylinder diameter $D = 1$m, the Reynolds number of the problem is 500, as indicated in [597].
Horizontally, the cylinder is placed in the centre of the domain, $20D$ downstream of the inlet boundary. Vertically, the cylinder is placed in the centre of the domain, with a distance of $10D$ to the top and bottom, no slip, wall boundaries. All simulations are performed in a 2D domain. Laminar flow conditions are assumed throughout this case study. For the spatial discretisation, a first layer thickness of $5 \cdot 10^{-5}D$ is chosen. The cells sizes are then incrementally increased towards the domain boundaries, with a maximum cubical cell size $0.15D$. A screenshot of the spatial discretisation is shown in Figure 8.16. Variable time stepping with a maximum Courant number of 0.2 is chosen for the temporal discretisation.

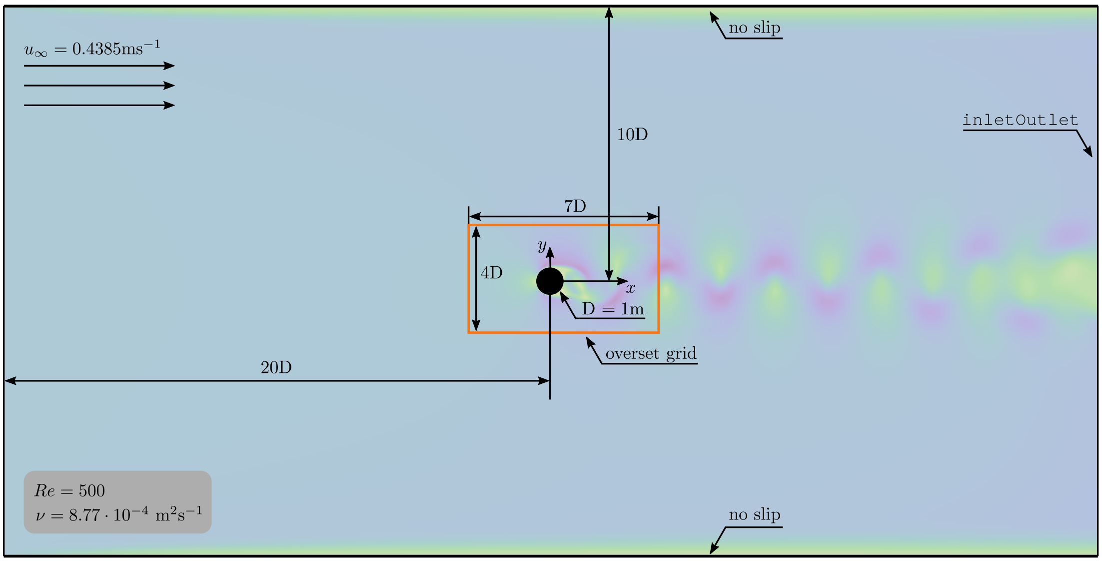

Figure 8.15: Domain layout for the present model. For the cases using the overset grid method, the orange border indicates the location and size of the overset grid.

8.2.3 Results and discussion

This section presents the results for the stationary and oscillating cylinder.

Stationary cylinder

First, results of the present numerical model with a stationary grid are compared against numerical reference data [597]. Figures 8.17 (a)–(j) show the vorticity contour plots for the case of a fixed cylinder, where black contours indicate positive vorticity, while grey contours indicate negative vorticity. Data[2] is extracted for half a period

---

[2] Note that all reference data has been digitalised from the original paper using image processing software.

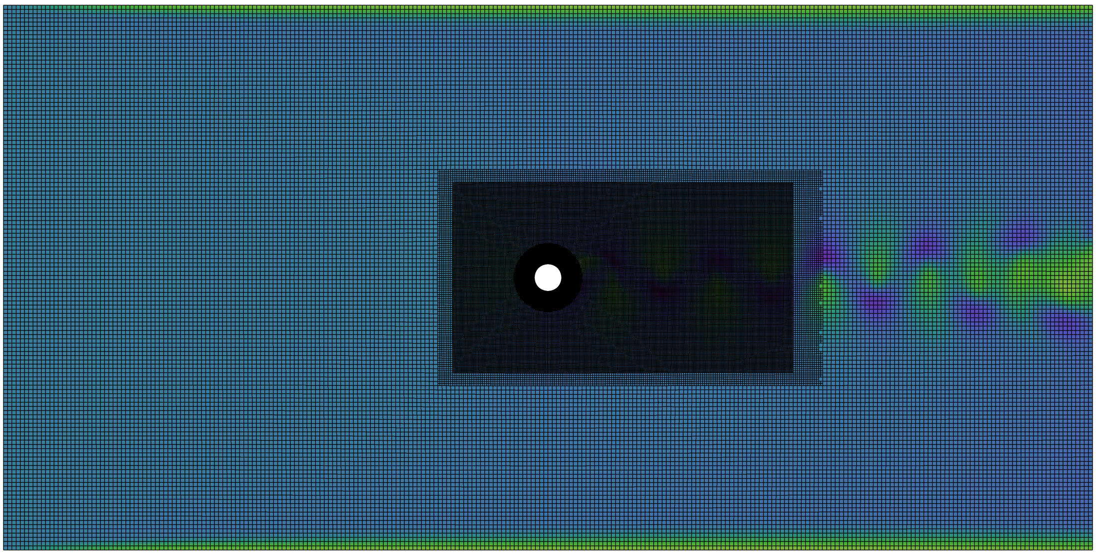

Figure 8.16: Spatial domain discretisation. A first layer thickness of $5 \cdot 10^{-5}D$ is chosen. The cells sizes are incrementally increased towards the boundary boundaries, with a maximum cubical cell size $0.15D$

of the vortex oscillation, based on a zero lift force at time instances, corresponding to Figures 8.17 (a)/(b) and (i)/(j).

The qualitative comparison of the image pairs shows a satisfying agreement between the reference and the present model. The separation point at the cylinder tip, as well as the shapes of the vortex structures in the wake, shows consistent agreement for the six different time instances.

Similarly good, qualitative, agreement can be observed for the plots of the stream lines, shown in Figures 8.18 (a)–(j). Here, the time instances of the data extraction coincide with the time instances of the evaluation of the vorticity contours. Again, sufficient agreement of the overall flow structure between the present model and the reference can be found. It should be noted that, for the results of the present model, the white spots in the wake of the cylinder are post–processing artefacts, stemming from the seeding and resolution properties. Achieving the same seeding and resolution properties as used for the generation of the reference data is, with the provided information in [597], impossible.

Based on the qualitative validation of the present numerical model with a stationary mesh, a comparison between the model setup with a stationary mesh and the native overset grid implementation in OpenFOAM v1812 is conducted, for the case of the fixed cylinder. This allows the identification of numerical errors induced by the overset grid method (i.e. interpolation errors).

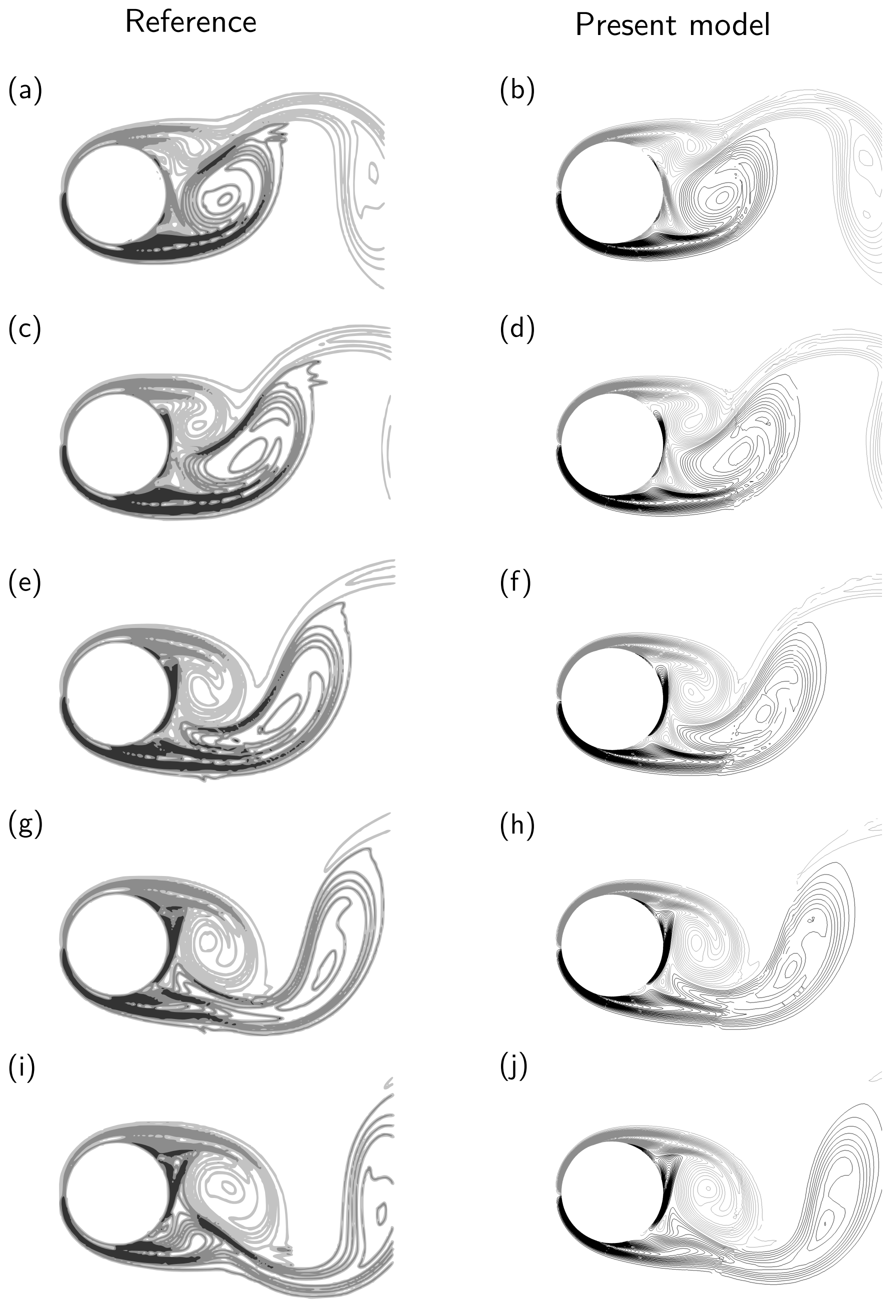

Figure 8.17: Comparison between the reference and present model: Vorticity contour plots for a fixed cylinder. Black contours indicate positive vorticity, grey contours indicate negative vorticity. The numerical simulation of the present model is performed using a stationary mesh.

For a qualitative comparison, Figures 8.19 (a)–(j) shows the field data of the velocity magnitude for half a period of the vortex oscillation, based on a zero lift force at time instances corresponding to Figures 8.19 (a)/(b) and (i)/(j). From visual inspection, virtually no differences can be observed between the two cases, at any of the highlighted time instances.

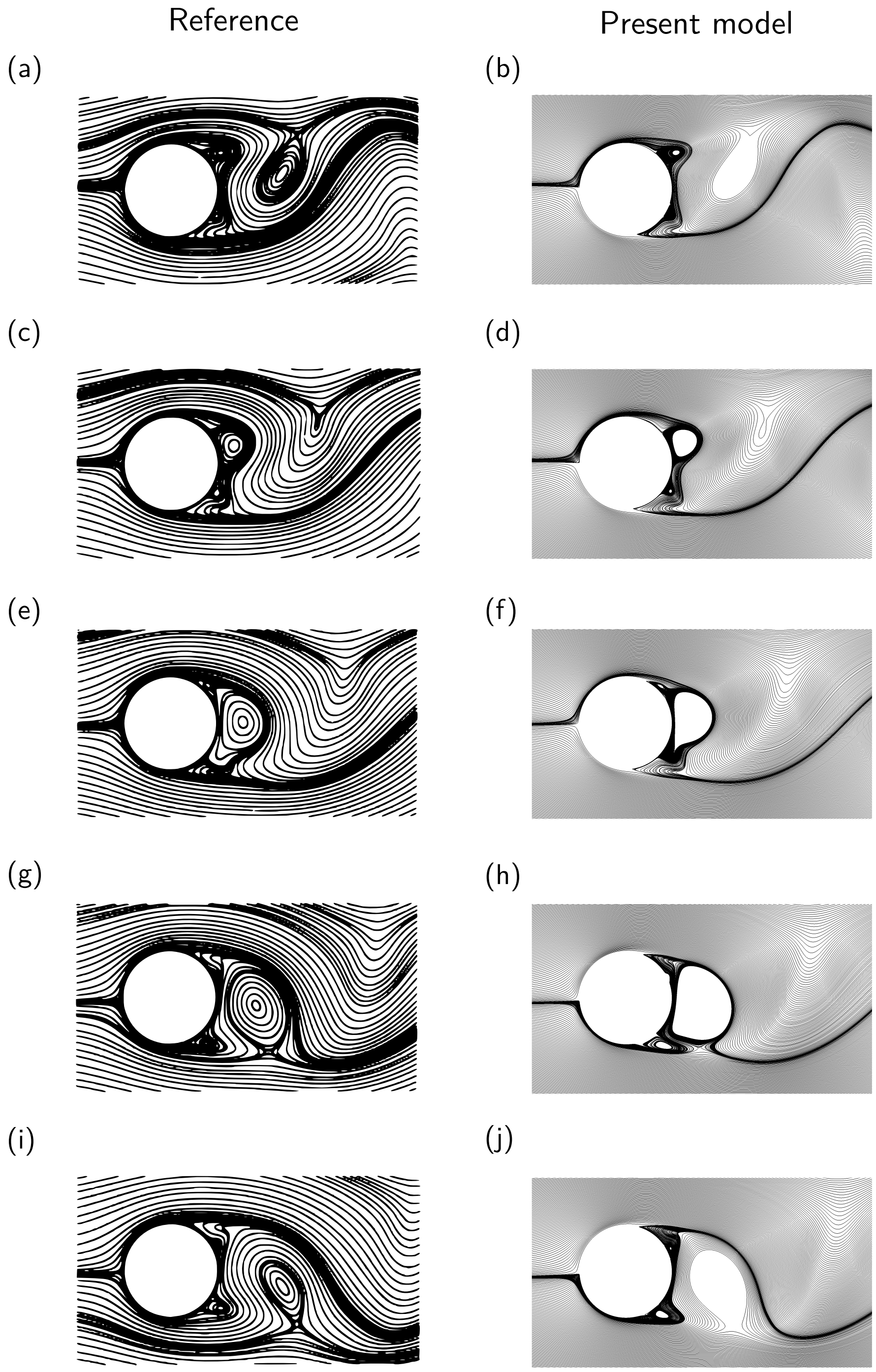

Figure 8.18: Comparison between the reference and present model: Stream lines for a fixed cylinder. The numerical simulations are performed using a stationary mesh.

To confirm this finding, the phase averaged lift force is analysed in Figure 8.20 for the model setup with a stationary mesh and overset grids. As for the velocity magnitude, virtually no difference between the two data sets can be observed. It should be noted here that an analysis of the shedding frequency reveals a mismatch of 1.5% between the stationary mesh and overset grids. Overall, based on the presented results, the present numerical setup, using either the stationary mesh or overset grids, shows

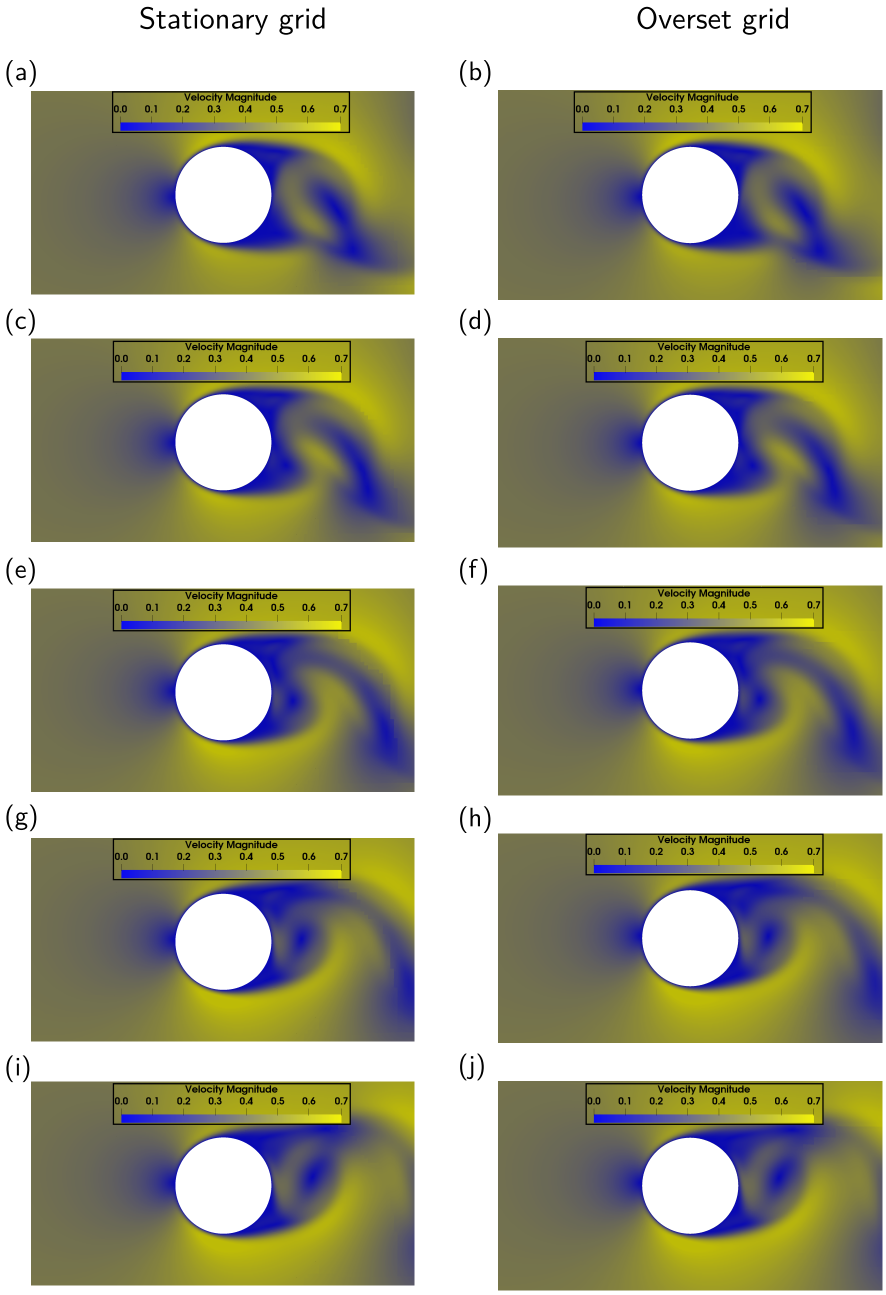

Figure 8.19: Velocity magnitude for the simulation of a fixed cylinder using the stationary mesh and overset grids.

satisfying accuracy with respect to the reference data and insignificant differences can be observed between the two present numerical models.

Oscillating cylinder

In a second step, the capability of the present numerical setup to capture the flow phenomena of an oscillating cylinder in a free stream flow are analysed. For this case, the cylinder is forced into vertical motion and oscillates with an amplitude of $0.25D$

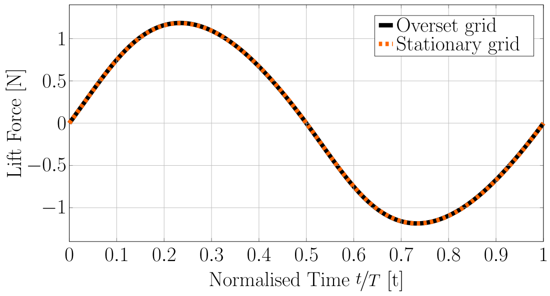

Figure 8.20: Phase average lift force for the stationary and overset grid setup.

at a frequency of 0.875 times the shedding frequency ($= 1$Hz).

Figures 8.21 (a)–(j) shows the vorticity contour plots for the case of a fixed cylinder, where, again, black contours indicate positive vorticity, while grey contours indicate negative vorticity. Data are extracted for half a period of the vortex oscillation, based on a zero lift force at time instance corresponding to Figures 8.21 (a)/(b) and (i)/(j). As for the case of a fixed cylinder, a satisfying, qualitative, agreement is achieved between the reference and present model, where the separation point at the cylinder tip, as well as the shapes of the vorticity structures in the wake are captured consistently well for the six different time instances.

8.3 Concluding remarks

This chapter presents the evaluation of the overset grid method for multi– and single–phase problems.

For the multi–phase problem, the performance of the overset grid method is evaluated by comparing the hydrodynamic forces and body motions of a moored point absorber WEC, simulated with the overset grid and the mesh morphing methods. From the results, it can be concluded that the accuracy of the overset grid method is equivalent to the mesh morphing method, but is better able to handle the large amplitude WEC motions during controlled motion. However, the drawback of the overset grid method is an approximate two-fold increase in run-time. To avoid unnecessary computational cost, CFD engineers are, thus, advised to push the limits of numerical stability of the mesh morphing methods (by, e.g., extending the outer distance), before resorting to the overset gird method.

For the single–phase problem, the performance of the overset grid method is evaluated qualitatively only. As for the multi–phase problem, the overset grid method proves to deliver accurate results.

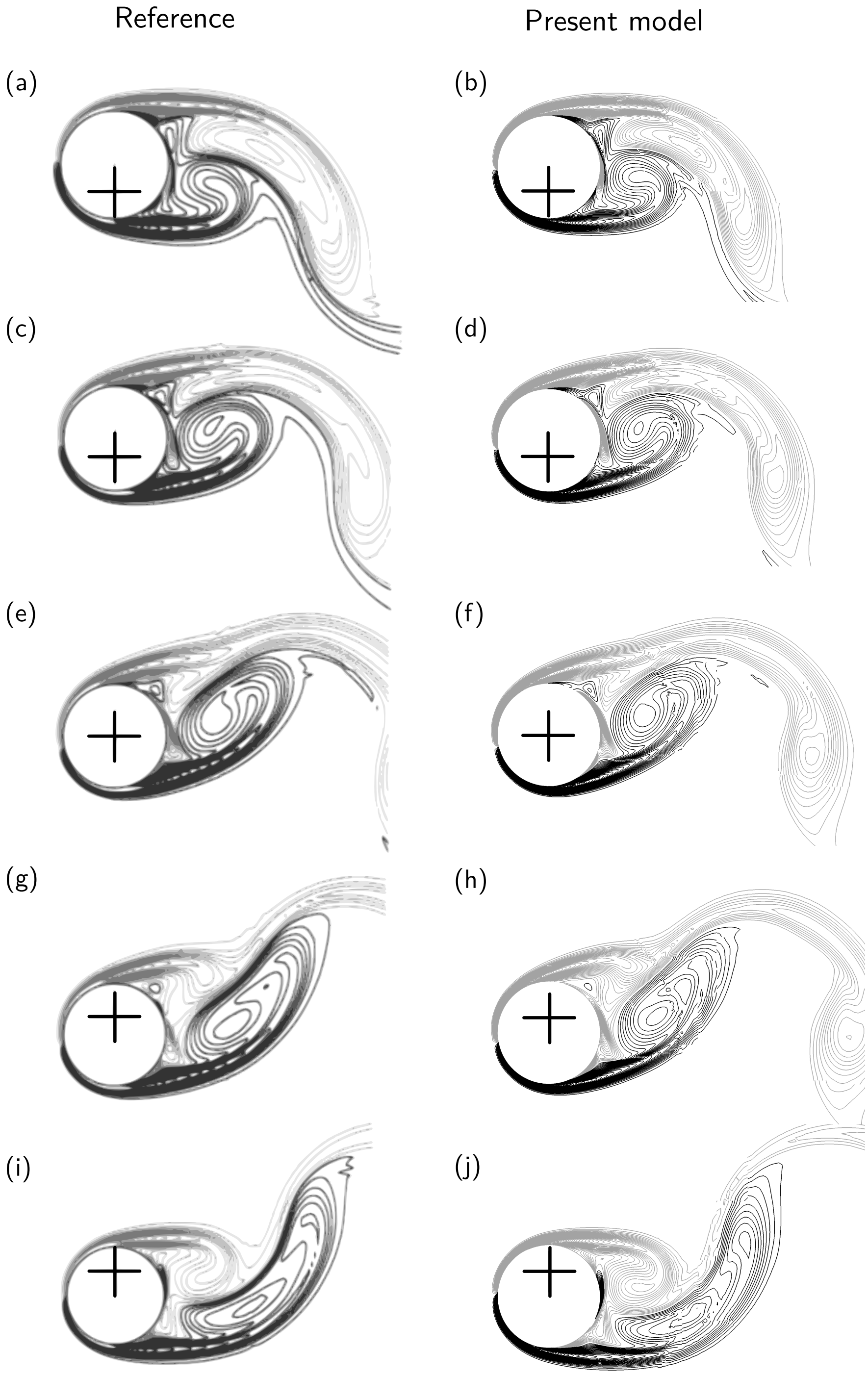

Figure 8.21: Comparison between the reference and present model: Vorticity contour plots for a moving cylinder. Black contours indicate positive vorticity, gray contours indicate negative vorticity. The cross indicates the centre of the cylinder at rest. The simulation with the present model is performed using overset meshes.

9

Flow field around WECs

Contents

Form the reviewed literature in Chapter 5, it can be observed that different flow conditions and different turbulence models are applied during numerical WEC experiments. However, no single turbulence model can be identified as 'industry standard' for WEC modelling, let alone the use of appropriate wall treatment (see Section 5.6.3). The complexity of the flow field around a WEC, together with the strong dependency of turbulent effects on the shape, operational conditions, and external forces hampers the formulation of general guidelines [37, Chapter 6]. The conceptionally different flow characteristics (i.e. oscillating, free surface flows), compared to the *design cases* of most turbulence models (i.e. continuous single–phase flow), can be identified as one of the major reasons for potential lack of accuracy of turbulence models.

This chapter aims to investigate the flow field around WECs and, thereby, the analysis of the necessity to include turbulence effects, by means of turbulence models, within

CFD–based NWTs for WEC applications. To that end, two different case studies are investigated. First, in Section 9.1, a numerical model for a heave plate in WEC applications is developed and numerical results are compared against experimental reference data, presented by Rusch *et al.* [598]. Subsequently, in Section 9.2, the influence of turbulence models and, in addition, the influence of the initial turbulence intensity (see Section 2.4.2) is investigated based on the two WEC structures W1 and W2, validated in Chapter 7.

9.1 Heave plate

Heave plates are slender structures, adding additional added mass to, e.g., spar platforms, thereby damping the response of the structure to wave excitation. In the wave energy field, heave plates are, for example, implemented as reaction body of multi–body WECs, such as the TRITON WEC [373, 502, 503].

Motivated by the oil and gas industry, as well as offshore wind problems, some studies can be found in the literature specifically focussing on the numerical modelling of the flow field around heave plates. Holmes *et al.* [599] employ CFD simulation to predict the hydrodynamic loads on heave plates for spar platforms. Although applying LES, the authors expect an inaccurate solution of the viscous drag effects, due to the size of the spatial discretisation. However, the authors argue that, for thin plates, viscous drag effects can be assumed small, compared to the total drag, and are, thus, negligible. Furthermore, the authors discuss the use of the employed turbulence model, stating that LES is likely to predict the large eddies well, compared to RANS models; however, viscous traction at the wall may be inaccurate. Unfortunately, no detailed information on the treatment of the wall, i.e the wall function, is provided. Ultimately, the authors conclude that the CFD model provides a “good” estimate of the loads on the heave plate and declare the CFD model to be an “efficient and effective supplement” to lower fidelity models.

Shen *et al.* [600] conduct a study on the hydrodynamic characteristics of a heave plate structure, with different form edges, of a spar platform. For numerical simulation, the authors solve the RANS equation together with a standard $k-\varepsilon$ turbulence model. Information on the wall treatment, as well as the grid convergence, is omitted.

Phan *et al.* [601] present a study on the finite amplitude vibrations of a rectangular cantilever beam, immersed in a viscous fluid, aiming to define a non–linear hydrodynamic function as a correction term for lower–fidelity models. For the simulation, laminar flow conditions are assumed.

Garrido-Mendoza *et al.* [602] compute the (2D) flow features and hydrodynamic coefficients around heave plates oscillating near a seabed. Due to the large Reynolds number of the problem, turbulent effect are predicted to be significant; however, given the size of the vortical structures and the known location of flow separation, laminar conditions are assumed for the simulation. Furthermore, regarding the treatment of the wall, the authors argue that, since the largest contribution to the hydrodynamic force is related to normal stresses, an accurate resolution of the boundary layers can be omitted. Comparing the numerical results of the added mass to analytical and numerical reference data, good agreement is found.

Lopez-Pavon and Souto-Iglesias [603] investigate the hydrodynamic coefficients and pressure loads on heave plates for semi-submersible floating offshore wind turbines. The authors conduct experimental and numerical analyses, where, for the latter, multi–phase RANS simulations are employed. The authors use a SST turbulence model; however, minimal information is provided on the numerical setup.

Similarly, Zhang and Ishihara [604] perform a parametric study of the geometric characteristics relating to the hydrodynamic coefficients (added mass and drag) of a multi–heave plate structure, employing experimental and LES data. Specifically, a LES model with the standard Smagorinsky-Lilly model for the SGS stresses, is employed. Since the structure is surface piercing, the VOF method is used for surface capturing. Regarding the wall treatment, the authors employ the standard wall function, available in ANSYS Fluent [605]. The grid refinement study was carried out, comparing numerical against experimental data; however, no exact measure of the spatial discretisation is provided. The authors conclude that the hydrodynamic coefficients, predicted by LES, show good agreement with the experimental data.

Most recently, the same authors [606] investigate distributed hydrodynamic forces on a circular heave plate using the VOF method in conjunction with LES turbulence modelling. Numerical results are validated against experimental data and the effects of geometric parameters and the Keulegan–Carpenter number on the radially distributed hydrodynamic coefficients are investigated. The choice of LES (standard Smagorinsky–Lilly) is reasoned with the overestimation of the drag coefficient by RANS–based models, as stated in [603].

While the previously mentioned studies concern the numerical investigation of heave plates for offshore oil and gas or wind energy problems, Rusch *et al.* [598] recently performed a set of physical flow visualisation experiments concerning the flow field around a heave plate for WEC applications, where the heave plate acts as a reaction body of a multi–body WEC. Generally, the flow around heave plates (for WEC or other applications) features some characteristics, valid for a wide range of WECs, which are of particular interest when trying to analysis the effect of turbulence. These characteristics are the oscillatory, rather than continuous, flow around the structure and the possibility of shape–induced viscous effects due to sharp corners.

Considering the case study in [598], this section presents the numerical analysis of the (heave) forces and flow field around a heave plate for WEC applications. The approach in [601, 602] is followed here, where simulations are performed with the assumption of laminar flow conditions. By comparing the numerical results to the experimental reference data, the study aims to analyse the capabilities of laminar flow conditions to capture the flow characteristics around WEC–like structures.

9.1.1 Case study

The experimental study on the flow around a heave plate, as outlined in [598], is considered as a case study herein. Experimental data of forced oscillation tests are available from dye visualisation technique and force measurements.

The experiments were carried out in the flow visualisation tank at the University of Washington, schematically depicted in Figure 9.1 (a). The tank dimensions are 1.3m × 1.3m × 1.5m (length x width x height), and it is filled with water to a volume of approximately 1300l. The hexagonal conic heave plate (see Figure 9.1 (b)) is excited with a linear actuator, supported by the enclosing frame, allowing a maximum stroke length of 0.4m. The heave plate, with a diameter, D_{HP}, of 0.27m, is attached to the driving rod of the actuator through a submersible, 6–DoF, load cell. The raw force data are phase averaged and filtered (low–pass filter with a 7Hz cut–off frequency) for the analysis. During the experiments, the linear actuator drives the plate in purely sinusoidal motion, with a fixed period, T_{HP}, and amplitude, A_{HP}. For the study presented here, two cases with different KC numbers are considered. The characteristics, including the case ID, oscillation period and amplitude, as well as the KC number, are listed in Table 9.1.

Table 9.1: Test matrix for the experimental and numerical case study

Case ID	Period T_{HP} [s]	Amplitude A_{HP} [m]	KC [-]
#1	1	0.020	0.47
#2	1	0.063	1.47

During the experiments, dye is used to visualise the flow structures, which is ejected at the inside edge of the heave plate's rim. The dye is manually ejected from the edge of the plate into the flow via a syringe. Note that, with this setup, the flow speed of the dye could not be captured and, thus, could not be replicated in the numerical setup. A digital single–lens reflex (DSLR) camera, recording at 60 frames per second, was positioned approximately 2m away from one side of the tank.

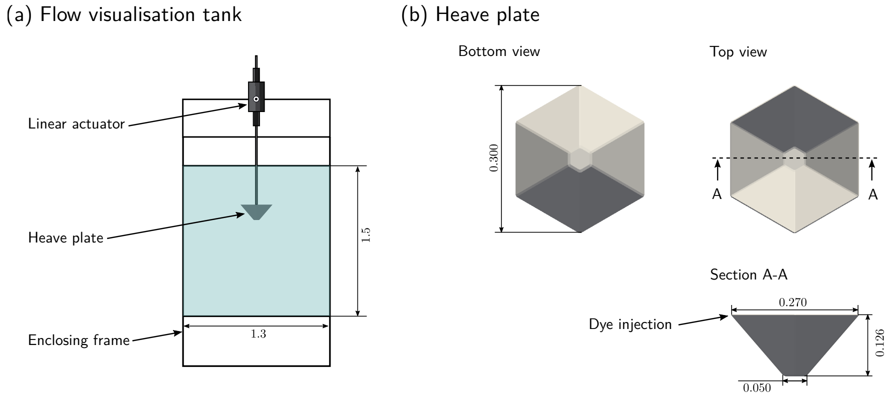

Figure 9.1: Schematic (not at scale) of (a) the flow visualisation tank and (b) the heave plate. All dimensions in [m].

9.1.2 Numerical framework

In the numerical model, only single–phase flow is assumed, neglecting any free surface effects. The incompressible Navier–Stokes equations are solved with OpenFOAM's transient solver for incompressible flow of Newtonian fluids with overset grids, `overPimpleDyMFoam`, implemented in OpenFOAM version v1812 of the ESI fork [593].

Dynamic mesh motion methods

For the simulation, the native implementation of the overset grid method in OpenFOAM v1812, whose performance is assessed in Chapter 8, is employed here. For the forced oscillation tests, the motion of the heave plate is forced to follow a given sinusoidal displacement profile, based on the period and amplitude given in Table 9.1.

Computational domain

Figures 9.2 (a) and (b) show a schematic of the computational domain including all relevant boundary conditions and dimensions (in [m]). To reduce the computational overhead, only one half of the heave plate is modelled numerically and a symmetry boundary condition is implemented.

Figure 9.3 shows the general layout of the (a) background grid and (b) the overset grid. The background grid is uniformly composed of cubical cells of edge size Δx. The cubical cells of the overset grid feature the same edge size as the background mesh; however, two refinement levels are employed in the vicinity of the heave plate. To determine the required cell sizes, convergence studies for the spatial and temporal problem discretisation are conducted, based on case #1 in Table 9.1. Simulations in a 2D domain, are performed with three different grid sizes ($\Delta x = 5.00 \cdot 10^{-3}$m, $2.50 \cdot 10^{-3}$m, $1.25 \cdot 10^{-3}$m). For the spatial convergence study, adjustable time stepping with a maximum Courant number of 0.225 is used. The convergence characteristics are determined based on the RMS of the vertical (z) force[1] on the heave plate, $\mathrm{RMS}_{\mathrm{fz}}$. For the temporal convergence study, three different maximum Courant numbers are tested, i.e. $Co_{\mathrm{max}} = 0.45$, 0.225, and 0.1125. The spatial discretisation with $\Delta x = 2.50 \cdot 10^{-3}$m is used. Again, the $\mathrm{RMS}_{\mathrm{fz}}$ is used as input to the convergence study. The results of the convergence study are listed in Table 9.2. Ultimately, the medium grid size (i.e. $\Delta x = 2.50 \cdot 10^{-3}$m) and the medium Co_{max} (i.e. $Co_{\mathrm{max}} = 0.225$) are used for the subsequent simulations.

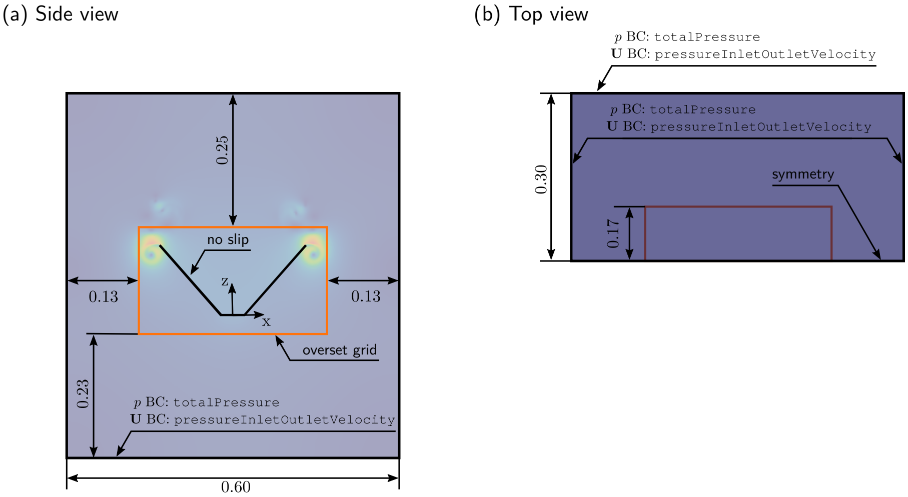
(a) Side view

(b) Top view

Figure 9.2: Domain layout (all dimensions in [m]): The orange square highlights the location of the overset grid. A no-slip boundary condition is applied at the heave plate wall. `pressureInletOutletVelocity` and `totalPressure` boundary conditions are applied at the x, y, and z boundaries of the domain. A symmetry boundary condition is applied at the front boundary.

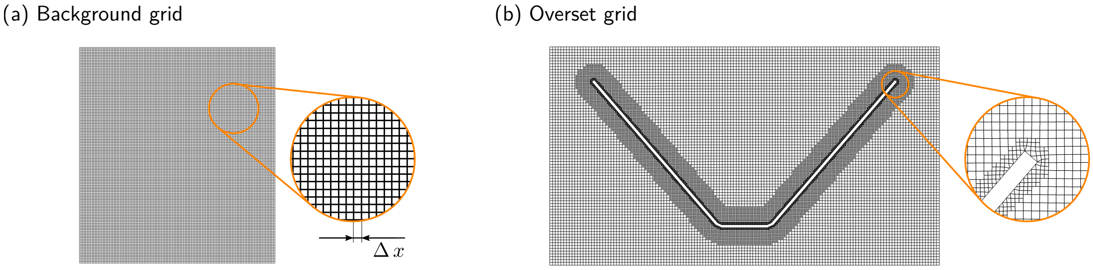
(a) Background grid

(b) Overset grid

Figure 9.3: Grid layout of (a) the background grid and (b) the overset grid

Flow conditions

As stated previously, for this study, the approach in [601, 602] is followed here, where simulations are performed assuming laminar flow conditions. An analysis, including turbulence modelling, is part of pertinent future work (see Chapter 12).

---

[1] The force is determined as the integral of the pressure over the heave plate surface.

Table 9.2: Results of the spatial and temporal convergence study

Spatial					
Co_{max}	$\Delta x = 5.00 \cdot 10^{-3}$m	$\Delta x = 2.50 \cdot 10^{-3}$m	$\Delta x = 1.25 \cdot 10^{-3}$m	Convergence Type	$\mathcal{U}$
0.225	$7.848 \cdot 10^{-2}$N	$7.777 \cdot 10^{-2}$N	$7.812 \cdot 10^{-2}$N	Oscillatory	0.7%
Temporal					
Δx	$Co_{\text{max}} = 0.45$	$Co_{\text{max}} = 0.225$	$Co_{\text{max}} = 0.1125$	Convergence Type	$\mathcal{U}$
$2.50 \cdot 10^{-3}$m	$7.828 \cdot 10^{-2}$N	$7.777 \cdot 10^{-2}$N	$7.826 \cdot 10^{-2}$N	Oscillatory	0.5%

9.1.3 Results and discussion

This section presents the results for the two tested case $\#1$ and $\#2$, with KC numbers of 0.47 and 1.47, respectively.

Case #1: $KC = 0.47$

Figure 9.4 shows the phase averaged, experimental and numerical, heave force for case $\#1$ with $KC = 0.47$. The results indicate relatively good agreement in phase and magnitude for the forces. Note that the traces have been aligned based on the first zero–down crossing (circular marker in Figure 9.4).

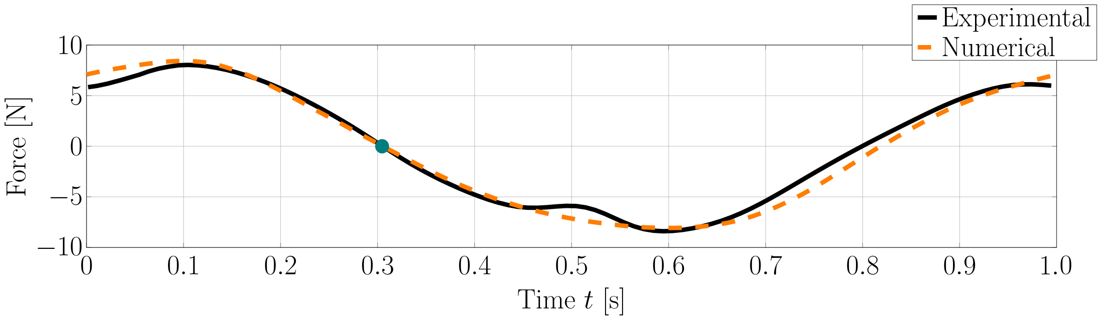

Figure 9.4: Time trace of the experimental and numerical heave force.

Considering the flow field data, Figures 9.5 (a)–(l) show screen shots of the absolute y–vorticity field around the heave plate for $KC = 0.47$ from the numerical simulations, for 11 different time instances. The figures also includes the normalised position of the heave plate for the different time instances for reference[2]. For a qualitative comparison to the experimental reference data, Figures 9.5 (a)–(f) are overlaid with transparent photographs from the flow visualisation experiments. The same experimental data are included in Figures 9.5 (g)–(l) as mirrors of the numerical field of view.

---

[2] Note that the normalised position in Figure 9.5 is idealised and does not reflect a physically or numerically measured quantity.

From Figure 9.5, it can be seen that the main characteristics of the flow field around the heave plate are captured well by the numerical model. At $t_r = 1$, 6, and 11, the heave plate is moving upwards from its mean position (i.e. $z = 0$) and a vortex is visible underneath the edge of the rim. From the numerical data, it can be seen that the shape of this vortex is slightly different at the different time steps, indicating imperfect steady state behaviour, likely induced by vortex–vortex interactions.

Moving upwards towards the peak position ($t_r = 2$ and 7), the vortex moves away from the heave plate and looses strength. Again, the numerical data shows slightly different behaviour for the two time instances, but the location of the vortex is still captured reasonably well, compared with the experimental reference.

Moving downwards past the peak ($t_r = 3$ and 8), the vortex changes direction and is now located above the rim of the heave plate, showing a relatively small size. For these two time instances, the numerical results show good agreement in terms of location and size of the vortex, compared with the experimental reference. Furthermore, the numerical data show a second vortex, left of the heave plate, which is not visible in the experimental photograph.

Approaching the minimum position ($t_r = 4$ and 9), the vortex is stretched and moves away from the rim of the heave plate. These characteristics are well captured in the numerical model, taking into account the visible differences between the time steps.

Just after the minimum position ($t_r = 5$ and 10), a small vertex forms again below the rim of the heave plate. The numerical data show a more concentrated vortex, compared to the experimental reference.

Overall, the results show agreement comparable with the force data in Figure 9.4, highlighting the capabilities of the numerical model to replicated the flow field around the heave plate for $KC = 0.47$, even under the assumption laminar flow conditions.

Case #2: $KC = 1.47$

For the case $KC = 1.47$, Figure 9.6 shows the phase averaged, experimental and numerical, heave force. Compared to $KC = 0.47$, more significant differences, predominantly in the phase, can be observed. In particular the trough is misaligned by ~ 0.1s. The peak shows a shift of ~ 0.05s. Since the KC number for this case lies above 1, it may be possible that turbulence effects play a more significant role (see Section 5.6.2), compared to the previous case, thus leading to the larger deviations.

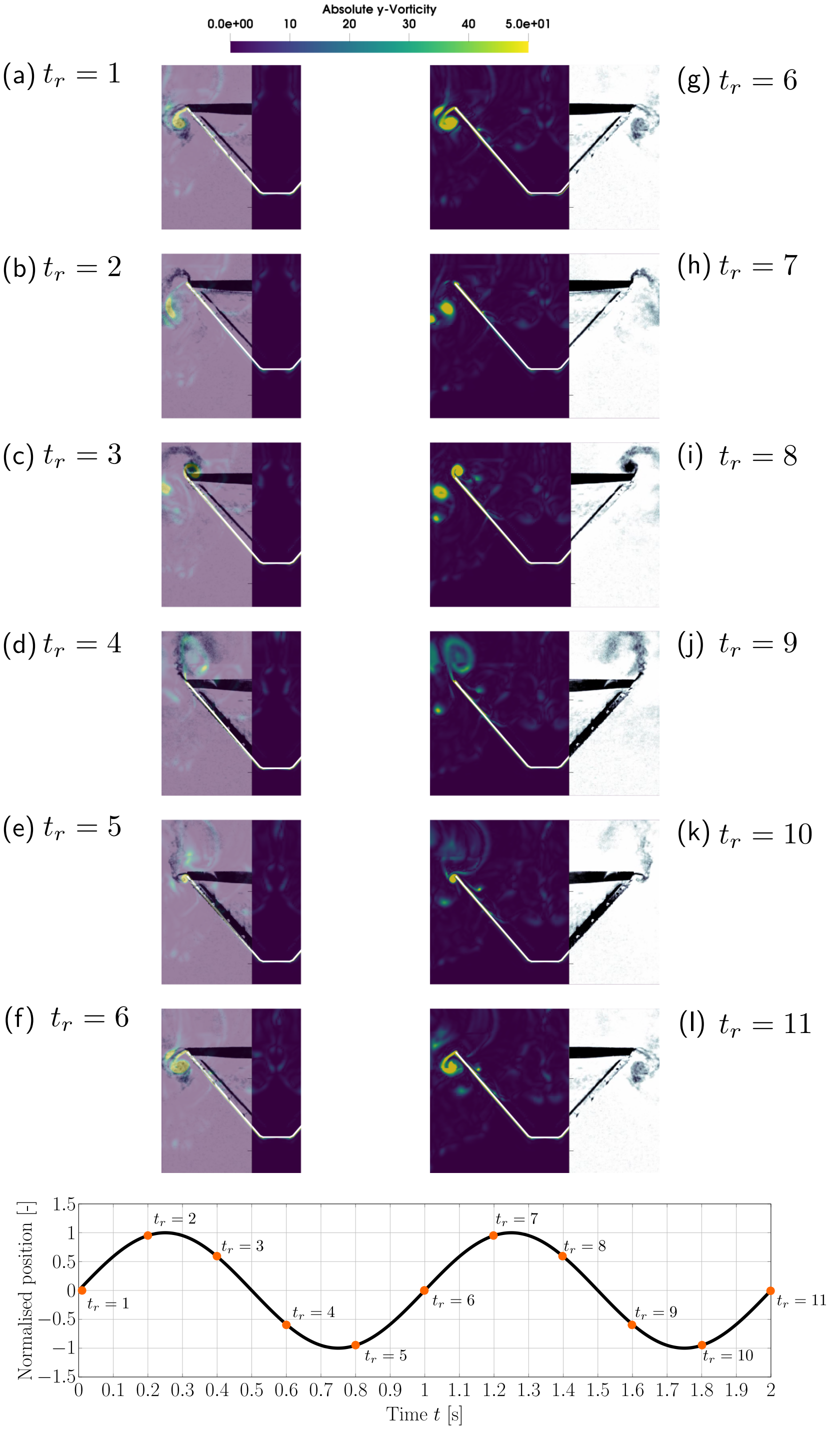

Figure 9.5: Screen shots of the absolute y–vorticity field around the heave plate for $KC = 0.47$ from the numerical simulations for 11 time instances. For a qualitative comparison to the experimental, (a)–(f) are overlaid with transparent photographs from the flow visualisation experiments. The same experimental data are included in (g)–(l) as mirrors of the numerical field of view. For reference, the normalised position of the heave plate for the different time instances is included in the figure.

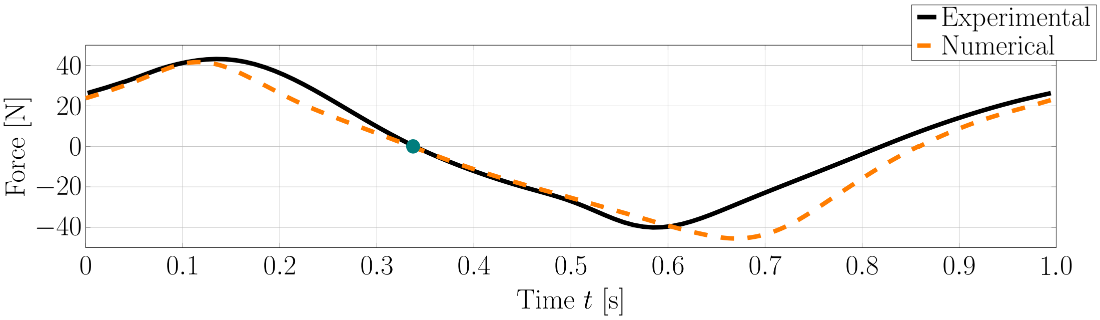

Figure 9.6: Time trace of the experimental and numerical heave force.

For the qualitative analysis of the flow field around the heave plate, Figures 9.7 (a)–(l) show screen shots of the absolute y–vorticity field for $KC = 1.47$ from the numerical simulations for 11 different time instances. The figure also includes the normalised position of the heave plate for the different time instances for reference. For a qualitative comparison to the experimental, Figures 9.7 (a)–(f) are overlaid with transparent photographs from the flow visualisation experiments. The same experimental data are included in Figures 9.7 (g)–(l) as mirrors of the numerical field of view.

For $KC = 1.47$, the general characteristics of the flow field are similar to the characteristics observed for $KC = 0.47$. At $t_r = 1$, 6, and 11, the heave plate passes the mean position, moving upwards, and a vortex can be observed below the rim of the plate. Approaching the peak ($t_r = 2$ and 7), the vortex increases in size. At $t_r = 3$ and 8, the heave plate moves downwards and a vortex is visible above the rim, losing strength when the plate approaches the minimum position ($t_r = 4$ and 9). Just after the minimum position, a vortex is again formed below the rim ($t_r = 5$ and 10) which grows in size when approaching the mean position.

As for the case of $KC = 0.47$, the overall characteristics are captured with reasonable accuracy by the numerical model. Significant differences between the experimental and numerical data can be observed at time instances $t_r = 2$ and 7. Here, the locations of the vortex below the rim of the plate do not agree and the vortex, visible in the experimental photograph above the rim of the plate, is not visible in the numerical data. In addition, more significant differences can be observed between equivalent time instances, e.g., for $t_r = 2/7$, $t_r = 3/8$, $t_r = 4/9$, and $t_r = 6/11$.

With the currently available numerical data set, it can not finally be concluded if the inclusion of turbulence modelling in the numerical model will lead to better agreement with the experimental reference for $KC = 1.47$. However, in the light of the relatively strong assumption of laminar flow in the numerical model, the results for both $KC = 0.47$ and $KC = 1.47$ can be declared as acceptable, indicating that the main flow feature around the heave plate can be captured without including turbulence modelling.

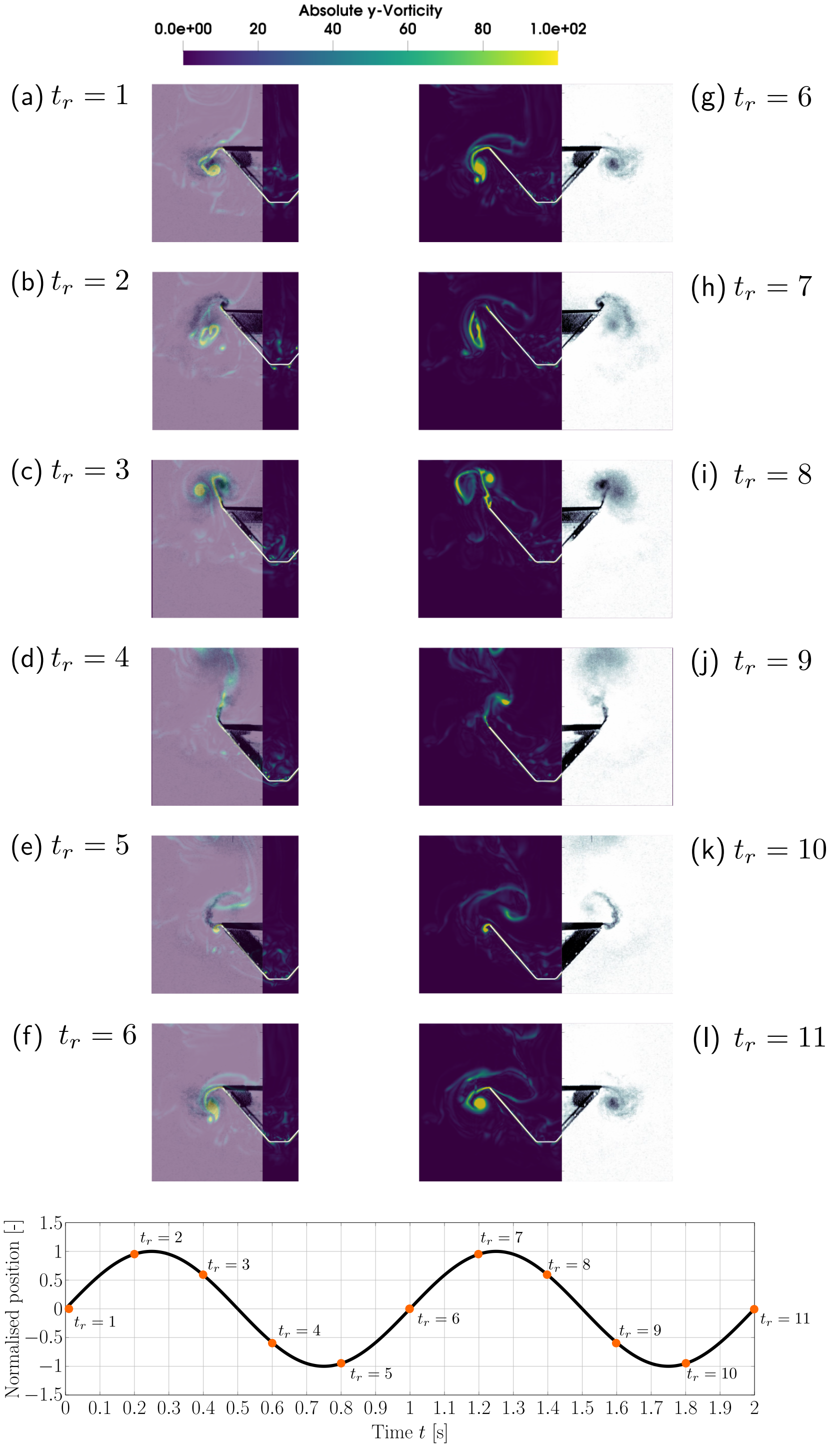

Figure 9.7: Screen shots of the absolute y–vorticity field around the heave plate for $KC = 1.47$ from the numerical simulations for 11 time instances. For a qualitative comparison to the experimental, (a)–(f) are overlaid with transparent photographs from the flow visualisation experiments. The same experimental data are included in (g)–(l) as mirrors of the numerical field of view. For reference, the normalised position of the heave plate for the different time instances is included in the figure.

9.2 Point absorber–type WECs

After analysing the flow field around a heave plate for WEC applications, finding acceptable agreement for the main flow characteristics between the experimental reference data and the numerical model, with a laminar flow assumption, this section concerns the influence of turbulence models on the free surface elevation, the wave excitation forces, and the WEC dynamics. To that end, inviscid, viscous laminar, and viscous turbulent simulations are performed and results are compared for four different test cases. Furthermore, for the turbulent simulations, the effect of the initial turbulence intensity T_i is investigated by considering three different values, i.e. $T_i = 1\%$, 5%, 10%. The study is based on two representative WEC structures, for which the numerical model (with a laminar flow assumption) is validated in Section 7.3.

9.2.1 Case study

This section presents the case study used to investigate the influence of turbulence modelling on the WEC dynamics. First, the WEC structures are introduced, followed by a description of the input waves.

9.2.2 WEC structures

The two different WEC structures, W1 and W2, based on the systems considered during the validation study in Section 7.3, are considered in the following. To recall, the structures resemble moored, point absorber–type devices with axisymmetric, cylindrical, geometries. For this study, device motion is constrained to 3–DoF (i.e. heave, surge, pitch) and single DoF (i.e. heave) motion. Furthermore, a PTO system, as in Chapter 8, with a PTO force f_u is implemented for the single DoF case.

Schematics of the two structures including all relevant dimensions are shown in Figures 7.65 (a) and (b). The physical properties (mass, inertia, etc.) are listed in Table 7.26. Note that, here, the nominal cases with $\pm 0\%$ measurement uncertainty are considered.

9.2.3 Input waves

In this study, an irregular JONSWAP wave train with a significant wave height of $H_s = 0.10$m and a peak period of $T_p = 1.94$s is considered, representing realistic, scaled, conditions at the AMETS test site in Bellmullet, Co. Mayo, off the West Coast of Ireland [591]. A time trace of the recorded free surface elevation, measured in the CFD–based NWT at the intended WEC location, during a preliminary wave–only simulation, is shown in Figure 9.8.

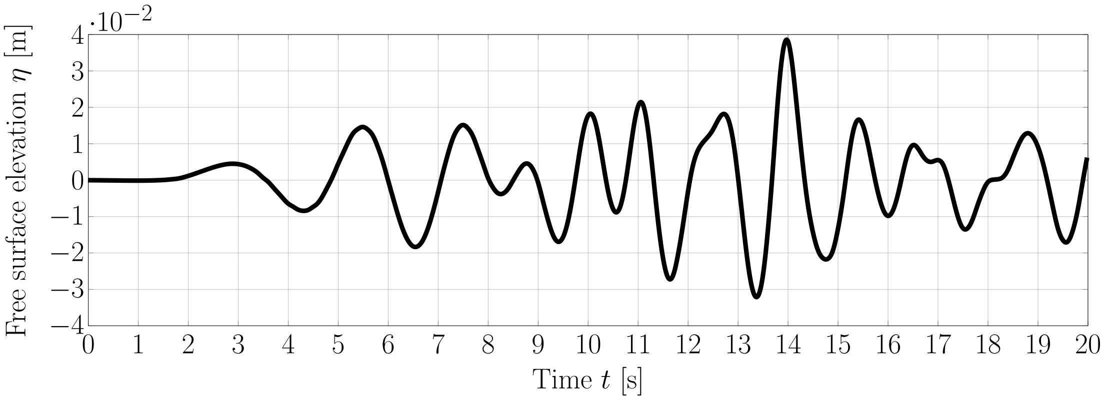

Figure 9.8: Time trace of the incident, irregular wave train measured in the CFD–based NWT at the intended WEC location.

9.2.4 Test cases

In this study, four different test cases are considered, following an incremental approach: (1) wave–only; (2) wave excitation (static device); (3) wave–induced motion (single DoF); (4) wave–induced motion (3–DoF). Throughout the test cases, simulations are performed assuming inviscid (Euler) and viscous (laminar and turbulent) flow conditions. For the turbulent simulations, the $k-\omega$ SST and the $k-\epsilon$ turbulence models (see Section 4.3.5) are employed with varying turbulence intensity of $T_i = 1\%$, 5%, 10%.

Waves–only

To investigate the effect of the inclusion of viscosity (i.e. Euler versus laminar simulations) and the use of turbulence models (i.e. wave damping, as shown in [568]), wave–only test cases are performed and results are compared by means of the normalised RMS, nRMS, following

$$\mathsf{nRMS} = \frac{\mathsf{RMS}\,(\Pi) - \mathsf{RMS}\left(\hat{\Pi}\right)}{\mathsf{RMS}\left(\hat{\Pi}\right)} 100\% \tag{9.1}$$

Here, $\mathsf{RMS}\,(\Pi)$ is the RMS of the free surface elevation from the inviscid or viscous turbulent simulation and $\mathsf{RMS}\left(\hat{\Pi}\right)$ is the RMS of the free surface elevation from the viscous laminar simulation. Throughout this study, the results from the viscous laminar simulations are the reference, since the numerical model has been successfully validated in Section 7.3, with the assumption of laminar flow.

Wave excitation

During the wave excitation force test, the device is held fixed in its equilibrium position, while exposed to the irregular wave train depicted in Figure 9.8. For the comparison between viscous laminar, viscous turbulent, and inviscid simulations, the wave excitation force is post–processed and compared.

Wave–induced motion – Heave–only

Introducing mobile WEC structures, wave–induced motion tests are considered. First, the structures are constrained to move in the heave DoF only. For this particular case, the influence of WEC control is included in the study by considering both controlled (see Section 8.1.2 and Chapter 11 for more details on the WEC control) and uncontrolled devices. In the controlled case, $\mathscr{H}_{\mathrm{W1}} = [-1318\mathrm{N\,m^{-1}}\ 64\mathrm{N\,s\,m^{-1}}]$ and $\mathscr{H}_{\mathrm{W2}} = [-1385\mathrm{N\,m^{-1}}\ 33\mathrm{N\,s\,m^{-1}}]$. For the comparison between viscous laminar, viscous turbulent, and inviscid simulations, the WEC's heave motion is post–processed and compared.

Wave–induced motion – 3–DoF

Finally, wave–induced motion of structures, constrained to move in the heave, surge, and pitch DoF, are considered. For this test case, only the uncontrolled case is considered[3]. For the comparison between viscous laminar, viscous turbulent, and inviscid simulations, the WEC's heave, surge, and pitch motion is post–processed and compared.

9.2.5 Numerical wave tank

For this study, the numerical wave tank in Chapter 8, employed for the mesh morphing method, is adapted (see Figure 8.3). However, some changes to the discretisation and the boundary conditions are implemented.

Computational domain

The overall domain and spatial discretisation layout is adapted from the setup in Chapter 8 (see Figure 8.3). However, when using turbulence modelling, the discretisation around the WEC is important to capture the boundary layer by means of wall functions (see Chapter 4). As stated in Chapter 4 and shown in Section 7.3, the condition on the y^+ value (i.e. $30 < y^+ < 300$) poses some challenges for oscillating flows.

---

[3] Note that no EMCS is available for the 3–DoF model due to a lacking control design model for this case

During the setup of the numerical domain, preliminary (wave excitation force) studies have been conducted to monitor the achieved y^+ value. During these preliminary tests, problems were encountered indicating that larger first–layer thicknesses would be required to obey the $30 < y^+ < 300$ criterion; however, the background grid size (leading to converged solutions, see Table 8.1) does not allow arbitrarily large first–layer thicknesses. Thus, a trade–off has to be accepted with a first–layer thickness of $5 \cdot 10^{-3}$m, leading to y^+ values of 30 or lower. These preliminary studies highlight the complexity of achieving an acceptable grid layout, complying with the condition on y^+.

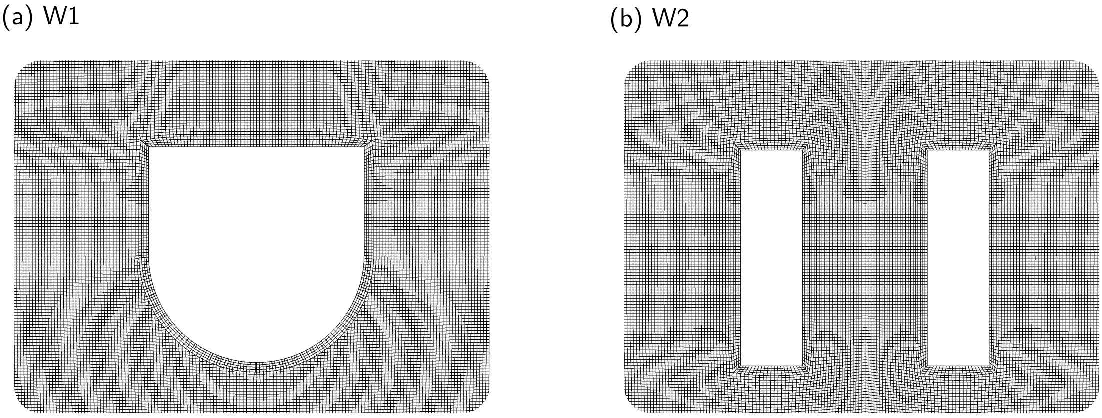
(a) W1

(b) W2

Figure 9.9: Screen shots of the spatial discretisation around the two WEC structures (a) W1 and (b) W2.

Since the achieved spatial discretisation does not strictly obey the aforementioned y^+ condition, a preliminary sensitivity analysis on the use of wall functions is conducted based on the single DoF, heave–only, test case. Simulations with the $k - \omega$ SST and $k - \epsilon$ turbulence model and $T_i = 5\%$ are conducted using no wall functions (i.e. under–resolving the boundary layer), as well as standard and low–Re wall functions. Table 9.3 lists the nRMS between the different viscous and inviscid flow simulations for a controlled, heave–only, test case. For the computation of the nRMS, RMS (Π) is the RMS of the heave displacement from the inviscid or viscous turbulent simulation and RMS $\left(\hat{\Pi}\right)$ is the RMS of the heave displacement from the viscous laminar simulation.

Table 9.3: Influence of wall function: nRMSD between the different viscous and inviscid flow simulations for controlled, heave–only, test cases

		No WFs[†]		**Standard WFs**		**Low Re WFs**	
		W1	W2	W1	W2	W1	W2
$k - \omega$ SST	$(T_i = 5\%)$	-5.85%	-7.01%	-1.13%	-0.43%	-1.02%	-0.32%
$k - \epsilon$	$(T_i = 5\%)$	-7.94%	-11.53%	-0.96%	-0.47%	-0.82%	-0.32%

[†] WFs: wall functions

The results in Table 9.3 clearly indicate that the nRMS values are increased (by approx. an order of magnitude) when omitting wall function on an under–resolved grid. Given the successful validation of the numerical model under the assumption of laminar flow (see Section 7.3), it can be assumed that these large nRMS values indicate unrealistic results. It should be pointed out, however, that no direct validation of the turbulence model will be conducted here, due to the lack of appropriate, high–fidelity, reference data. Finally, for all subsequent simulations, standard wall functions are used.

9.2.6 Results and discussion

This section presents the results of the four different test cases outlined in Section 9.2.4.

Waves–only

For a qualitative comparison, Figure 9.10 shows the time traces of the free surface elevation, measured at the intended device position, from the inviscid and viscous (laminar and turbulent) simulations. Visually, a relatively small deviation between the results can be observed. It can be seen in the zoom box in Figure 9.10 that, by considering turbulence modelling and with increasing turbulence intensity, the numerical wave damping increases.

The quantitative analysis based on the nRMS is shown in Table 9.4, listing the results including the two turbulence models and the different turbulence intensities. For the inviscid simulation, negligible differences of $<< 0.1\%$ are calculated, indicating marginal larger free surface elevation amplitudes, compared to the laminar case. Similarly, for the $k-\omega$ SST turbulence model with $T_i = 1\%$, the deviation between the viscous turbulent and viscous laminar simulation is marginal; however, the negative sign indicates wave damping due to the inclusion of turbulence modelling. With increasing turbulence intensity, the deviation increases. For $T_i = 5\%$ and 10% the two turbulence models show relatively similar deviations, with maximum values of the order of -6%.

Table 9.4: nRMS between the different viscous and inviscid flow simulations for the wave–only test case

	Euler	**Turbulent**					
		$k-\omega$ SST			$k-\epsilon$		
		$T_i = 1\%$	$T_i = 5\%$	$T_i = 10\%$	$T_i = 1\%$	$T_i = 5\%$	$T_i = 10\%$
nRMS	0.02%	-0.19%	-2.72%	-6.62%	-1.45%	-1.89%	-6.32%

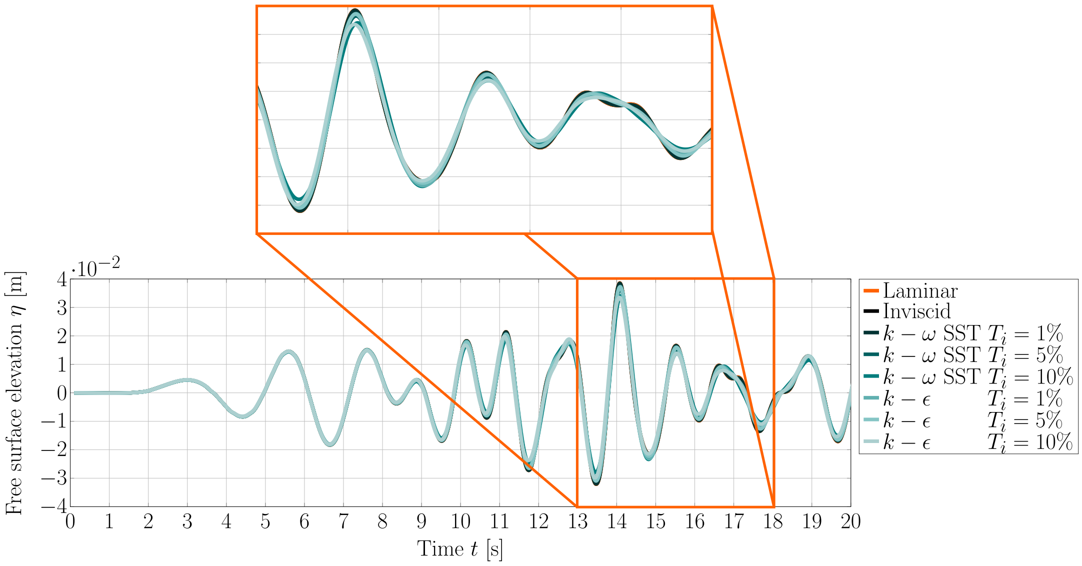

Figure 9.10: Time trace of the free surface elevation measured at the intended device location during wave–only tests.

Wave excitation

Figures 9.11 (a)–(d) show the nRMS of the heave and surge wave excitation forces for W1 and W2 compared to the nRMS of the free surface elevation. The plots include the data points for the viscous (laminar), viscous (turbulent), and inviscid simulations. In Figures 9.11 (a)–(d), the nRMS for the inviscid simulations indicates that the heave and surge excitation forces are slightly larger compared with the viscous laminar simulation. For all viscous turbulent simulations, the nRMS suggests lower excitation forces, compared with the laminar case.

Furthermore, the results indicate similar trends in the nRMS for W1 and W2. While, for both structures, the nRMS in the heave force shows maximum values $> -4\%$, the nRMS in the surge force shows maximum values $> -10\%$, which are similar values as the nRMS in the free surface elevation. Increased viscous effects in the surge DoF, compared to the other DoFs, has also been highlighted in [455]. Comparing the results for W1 and W2, it can be seen that the (significant) difference in the shape of the two structures is not reflected in the calculated nRMS values, which are of similar magnitude for W1 and W2.

For both heave and surge forces, the nRMS increases with increasing turbulence intensity T_i. Comparing the results for the $k-\omega$ SST (square markers in Figure 9.11) and the $k-\epsilon$ turbulence model (diamond markers in Figure 9.11), larger nRMS values can be observed for the $k-\omega$ SST model with $T_i = 5\%$ and 10%.

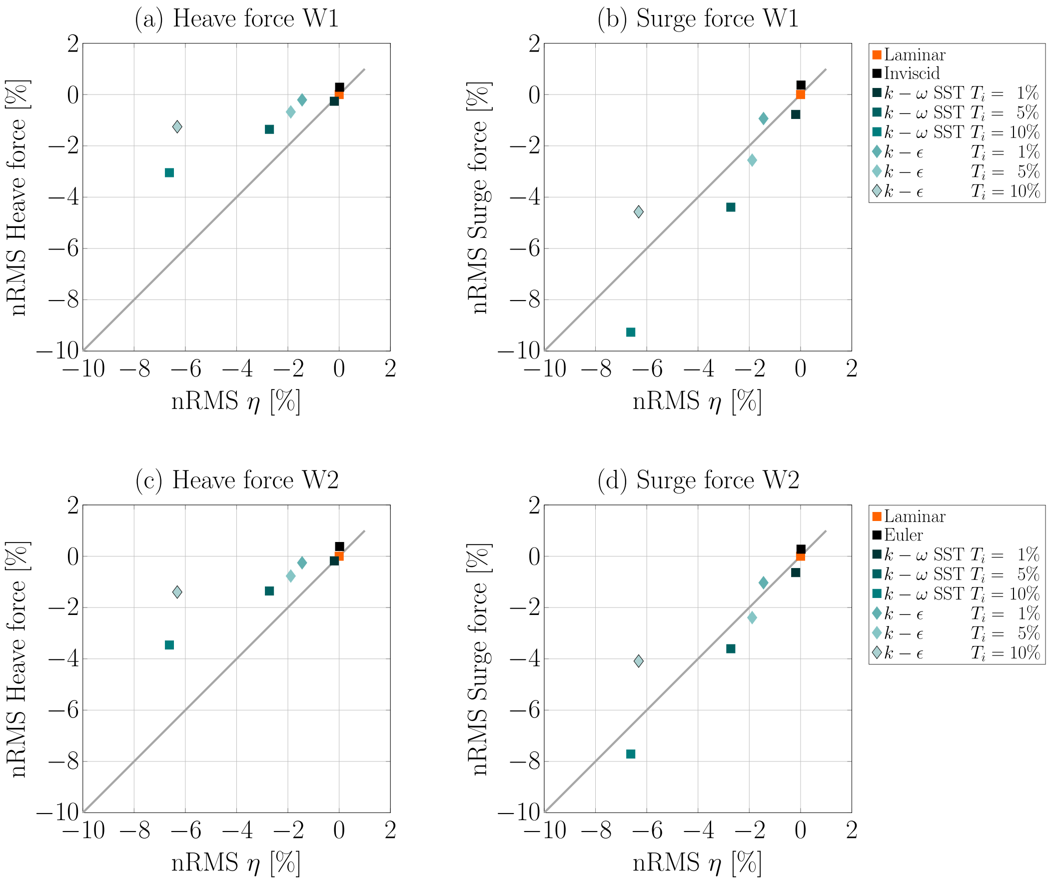

Figure 9.11: nRMS of the heave and surge wave excitation forces over the nRMS of the free surface elevation for (a)/(b) W1 and (c)/(d) W2.

Wave–induced motion – Heave–only

For the case of wave–induced motion and structures constrained to the heave DoF, Figures 9.12 (a) and (b) show the nRMS of the heave displacement for W1 and W2 over the nRMS of the free surface elevation, respectively. At first sight, it can be seen that the heave motion nRMS follows the trend of the heave excitation force nRMS. Furthermore, both WEC structures show similar results. Relatively small maximum nRMS of $> -3\%$ and $> -2\%$ can be found for W1 and W2 with the $k-\omega$ SST turbulence model and $T_i = 10\%$, respectively.

To investigate the effect of WEC control and, thus, exaggerated device motion (see Chapter 8) on the influence of turbulence modelling, simulations of an uncontrolled device, constrained to the heave DoF, are performed. Note that, for brevity, only cases with $T_i = 5\%$ are considered.

Figures 9.13 (a) and (b) show the time trace of the heave displacement of controlled and uncontrolled WEC structures W1 and W2, respectively. The time traces clearly indicate the enhanced device motion under controlled conditions.

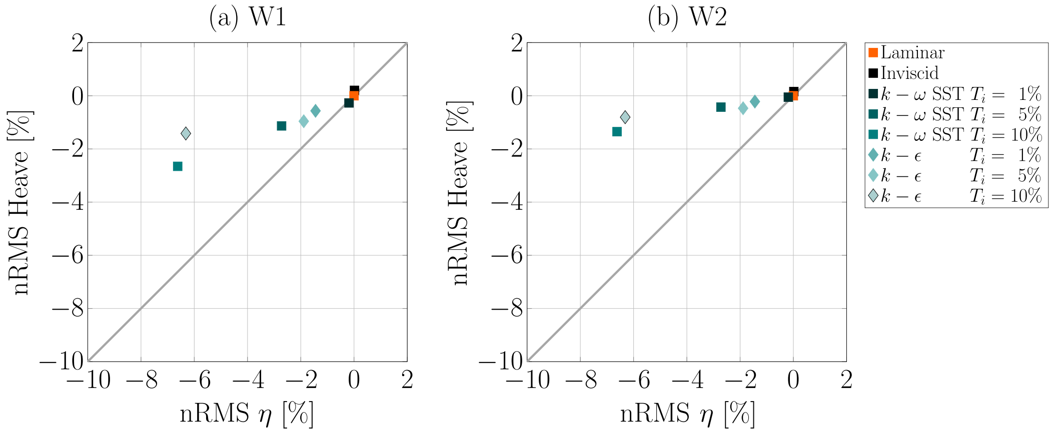

Figure 9.12: nRMSD of the heave displacement over the nRMSD of the free surface elevation for (a) W1 and (b) W2.

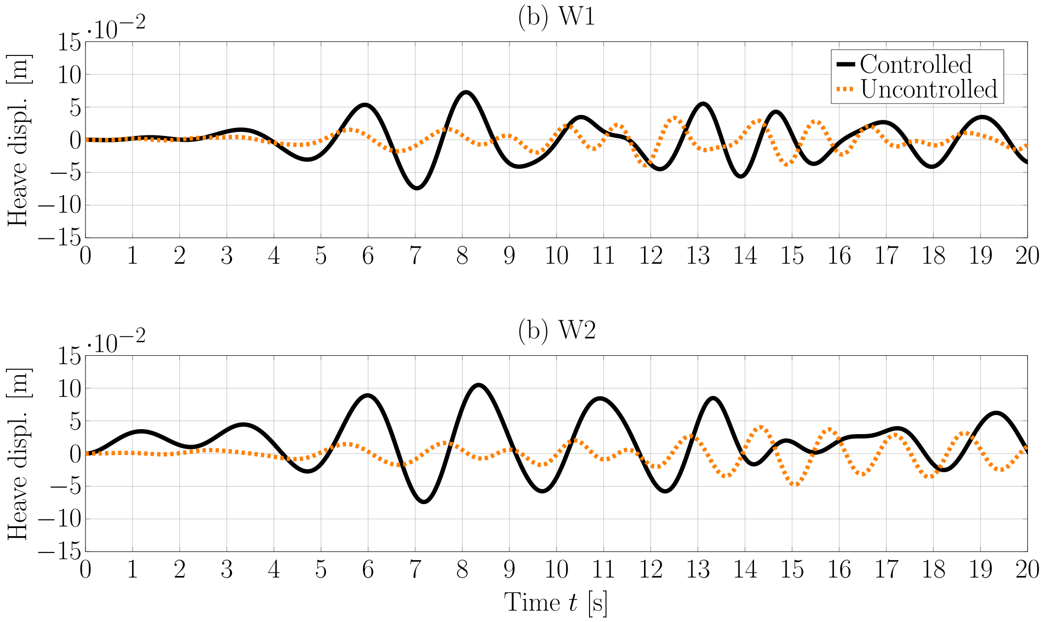

Figure 9.13: Time trace of the heave displacement of a controlled and uncontrolled WEC structures (a) W1 and (b) W2.

Based on the time traces in Figures 9.13 (a) and (b), Figures 9.14 (a) and (b) show the nRMS of the heave displacement over the nRMS of the free surface elevation for W1 and W2, respectively, for both the controlled and uncontrolled cases. The results indicate an increased nRMS for the uncontrolled WECs, compared to the controlled cases, most significantly for W1. These results are somewhat unexpected, since the enhanced device motion in the controlled case is assumed to 'trigger' turbulence effects. However, due to the coupling between the effect of turbulence modelling on the device motion and the free surface elevation, an exact determination of the differences between the viscous laminar and turbulent simulations is not straightforward and requires additional analysis (see Chapter 12).

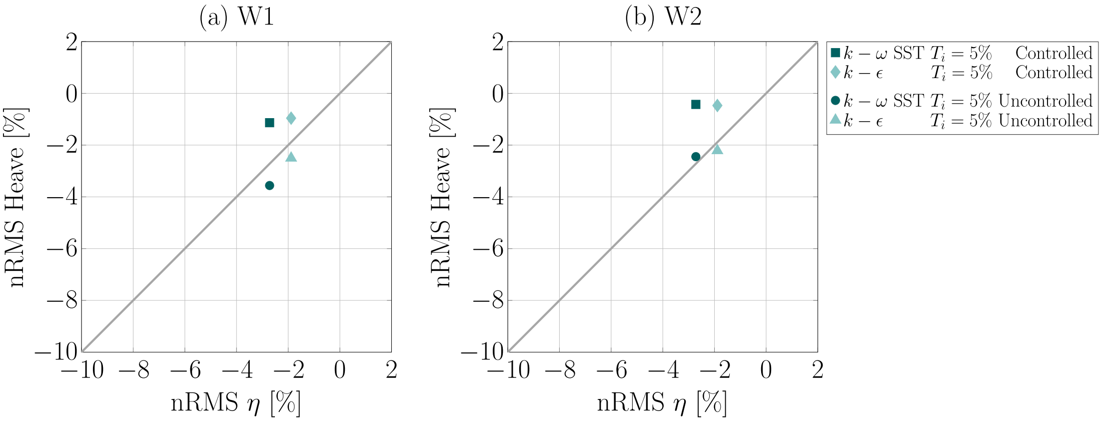

Figure 9.14: nRMSD of the heave displacement over the nRMSD of the free surface elevation for (a) W1 and (b) W2.

Wave–induced motion – 3–DoF

Finally, wave–induced motion of the uncontrolled structures W1 and W2, constrained to move in the heave, surge, and pitch DoFs only, is considered. Figures 9.15 (a)–(f) show the nRMS of the heave, surge, and pitch displacements over the nRMS of the free surface elevation, for both W1 and W2. The corresponding time traces of the device motion are plotted in Figures 9.16 (a)–(f). Note that, again for brevity, only results of the $k-\omega$ SST and the $k-\epsilon$ turbulence model with $T_i = 5\%$ are considered in the following.

For the heave DoF (Figures 9.15 (a) and (b)), similar values of the nRMS are found for W1 and W2 as for the uncontrolled heave–only test case (see Figure 9.14), where overall larger nRMS values are found for structure W1.

Similar results are found for the pitch DoF (Figures 9.15 (e) and (f)). Again, slightly larger nRMS values are visible for W1, compared to W2, and the nRMS for the $k-\omega$ SST turbulence model is larger compared to the $k-\epsilon$ turbulence model. Overall, for both the heave and pitch displacement, relatively small maximum nRMS values of -4% are found.

More significant differences can be seen for the surge DoF (Figures 9.15 (c) and (d)). For both W1 and W2, the nRMS of the device motion is significantly larger, compared to the displacement in the heave or pitch DoF, with maximum values of up to -16%. The results are consistent with the results for the heave and pitch DoF, such that the $k-\omega$ SST turbulence model shows larger deviations compared to the $k-\epsilon$ turbulence model. These observations are underlined by the time traces shown in Figures 9.16 (c) and (d).

To some extent, the results for the surge displacement of the mobile WEC structures W1 and W2 are consistent with the findings for the wave excitation force test (see Figure 9.11 (b) and (d)), where the wave excitation forces in the surge DoF are also notably larger than for the heave DoF.

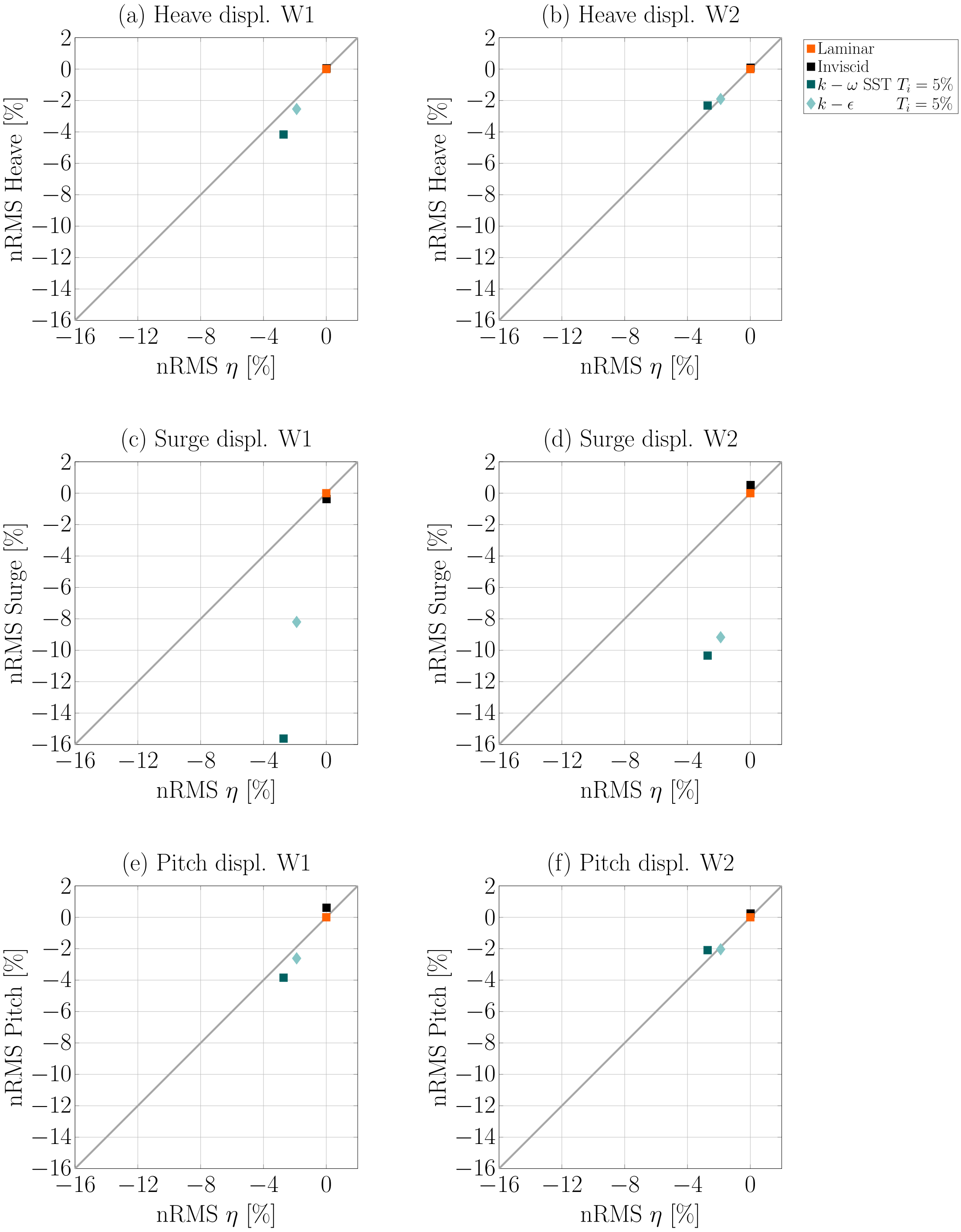

Figure 9.15: nRMSD of the heave, surge, and pitch displacement over the nRMSD of the free surface elevation for (a)/(c)/(e) W1 and (b)/(d)/(f) W2.

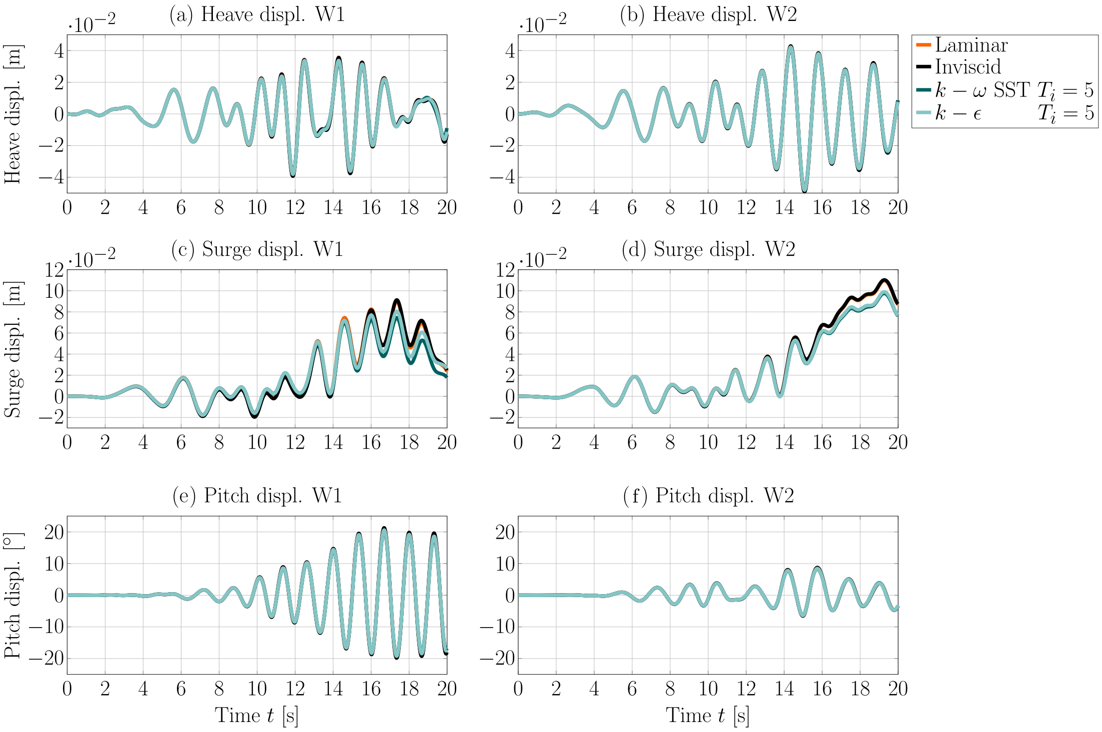

Figure 9.16: Time trace of the heave, surge, and pitch displacement of WEC structures (a)/(c)/(e) W1 and (b)/(d)/(f) W2.

In summary, it can be stated that the use of turbulence models has a significant influence on the free surface elevation, the wave excitation forces, and the device dynamics. The presented results suggest that the degree of the influence depends on the specific turbulence model, as well as the turbulence intensity, employed in the NWT. While, for all tested WSI cases, the excitation forces or device motion in the heave DoF show relatively small nRMS values of $> -4\%$, the excitation forces and device motion in the surge DoF shows larger nRMS values of up to -16%. These results are, to some extend, consistent with findings in [455].

However, more in depth analysis is required to get a better understanding of the effect and the accuracy of turbulence modelling for WEC applications. In future work, e.g., cases with regular wave excitation should be considered and the recently proposed, modified, turbulence models by Devolder *et al.* [568, 569] should be considered to separate the influence of artificial wave damping and the behaviour of the WSI, when turbulence modelling is included in the CFD–based NWT.

9.3 Concluding remarks

This chapter analyses the flow field around WEC structures. Initially, in Section 9.1, forced oscillation tests for a heave plate in WEC applications are modelled numerically and results are compared to experimental reference data. Assuming laminar flow, the numerical results of the force and the characteristic flow features (by means of the y-vorticity field) are captured reasonably well, indicating that CFD–based NWTs can capture the main characteristics of the flow field around WECs, even under the assumption of laminar flow.

In Section 9.2, two representative WEC structures are considered for the analysis of the effect of turbulence modelling on the free surface elevation, wave excitation force, and device dynamics. The results indicate an influence of the specific turbulence model and the initial turbulence intensity on the free surface elevation, wave excitation forces, and device motion. However, without a more in–depth investigation, including dedicated, high quality, validation data (including e.g. pressure measurements or PIV data), there remains an uncertainty regarding the inclusion and capabilities of 'industry standard' turbulence models. Under the light of the successful validation of a number of different WEC devices for a range of different test cases assuming laminar flow conditions, such assumptions for the flow conditions may be suitable, avoiding uncertainty in the selection of a 'correct' turbulence model.

10

Analysis of scaling effects on WECs

Contents

Scale model tests in the open ocean, or in physical and numerical wave tanks (see Chapter 7), are commonly used to evaluate and optimise the performance of WECs. From relatively small scale model tests (e.g. $1/50$th–$1/5$th), researchers and developers extrapolate the full scale performance of devices by applying well–known scaling laws, i.e. Froude and Reynolds scaling [24], to scale dimensions of the structure, the considered wave characteristics, and/or the loads exerted on the structure.

Although the applied scaling laws are well established, errors are inherently induced due to the discrepancy between Froude and Reynolds scaling within physical wave tanks, stemming from the difficulty to correctly scale fluid viscosity [536, 387]. To overcome this issue during physical testing, full scale testing can be considered; however, such tests require extensive capital expenditure and pose difficulties regarding the control and monitoring of the test condition, as well as the accuracy and resolution of the instrumentation [607].

To get a better understanding of hydrodynamic scaling effects, and the implications for performance estimation of the full scale WEC device, NWTs are powerful tools, allowing the analysis of WECs at different scales at virtually no additional cost. Specifically, CFD–based NWTs, accounting for all relevant hydrodynamic non-linearities, can deliver valuable information on the near flow field around WEC structures and/or the WEC performance, depending on the scale. Thus, as shown in Chapter 5, a number of studies can be found in the literature, investigating the effect of different scales during model testing. From the reviewed literature, two observations can be made:

1) CFD-based NWTs generally require experimental validation to ensure the accuracy of the numerical model. However, an existing lack of validated CFD-based NWTs models of the same device across different scales can be observed. Only [373, 516, 518] include cross–scale validation: Mundon *et al.* [373] investigate only the identification of drag coefficients, while Dai *et al.* [516] consider a fixed OWC, and Zabala *et al.* [518] only provide qualitative validation. There is a need to investigate the scale effects on the performance of a WEC system, in operational conditions, based on validated numerical models.
2) CFD-based NWTs provide the capability of by-passing the well known discrepancy between Froude and Reynolds scaling by allowing alteration of the transport properties of the involved fluid. However, while Schmitt *et al.* [387] only consider scaling of the fluid viscosity and e.g. Palm *et al.* [454] only consider scaling of the geometric dimensions, CFD–based NWT allow the analysis of the scaling effects by including cases considering Froude scaling only, as well as Froude and Reynolds scaling.

This chapter presents the analysis of the hydrodynamic scaling effects for the Wavestar WEC in operational conditions, based on a validated numerical model, introduced in Chapter 7. In particular, this study considers scaling of the geometric dimensions with full scale fluid viscosities, as well as scaling both the fluid viscosities and geometric dimensions, to analyse the effect of different model scales on the WEC response.

The case of scaled geometric dimensions with full scale fluid viscosity represents the typical model setup in a physical wave tank. Hence, this study investigates the hydrodynamic scaling errors in such test conditions. For the analysis, three different scales, i.e. $1/20$th, $1/5$th, and $1/1$, are considered, where the CFD-based NWT for the small scale WECs has been validated in Chapter 7. A suite of test cases with increasing complexity is considered, ranging from regular wave–only test cases to wave–induced WEC motion in irregular waves.

10.1 Model scaling

For scaling of the relevant physical properties, the Froude scaling law is applied throughout this study. Froude scaling is based on maintaining a consistent Froude number (see Equation (10.1)) between scales, which represents the ratio between inertia (f_{in}) and gravity forces (f_g). Hence, when the Froude number remains constant between scales, the ratio between inertial forces and gravitational forces is also constant.

$$Fr = \left(\frac{f_{in}}{f_g}\right)^{1/2} \tag{10.1}$$

To achieve Froude scaling, the physical parameters are simply scaled by the corresponding scaling factor, $\varkappa$, listed in Table 10.1.

As mentioned above, special attention must be paid to the scaling of the (kinematic) fluid viscosity ν, not only to comply with the Froude scaling law but also with the Reynolds scaling law. Reynolds scaling is based on maintaining a consistent Reynolds number (see Equation (10.2)) between scales, which represents the ratio between inertia and viscous forces (f_v). Hence, when the Reynolds number remains constant between scales, the ratio between inertial forces and viscous forces is also constant.

$$Re = \frac{f_{in}}{f_v} \tag{10.2}$$

In physical wave tanks, viscosity cannot be scaled easily, whereas in CFD–based NWTs, the required adjustment can be made simply by changing the transport properties of the fluids involved. Based on the units of ν, i.e. [$\mathrm{m^2\,s^{-1}}$], and the scaling factors given in Table 10.1, the viscosity can be scaled accordingly:

$$\nu_{\mathsf{MS}} = \nu_{\mathsf{FS}} \cdot \frac{\varkappa^2}{\sqrt{\varkappa}}\,, \tag{10.3}$$

where the subscript $_{\mathsf{MS}}$ refers to the model scale and $_{\mathsf{FS}}$ refers to full scale.

In this study, three different scales, i.e. $1/1$ (FS), $1/5$th (MS), and $1/20$th (MS), are analysed, such that $\varkappa = [1/1,\ 1/5,\ 1/20]$, respectively. Furthermore, at $1/5$th and $1/20$th scale, two cases are considered, representing:

1) Froude and Reynolds similarity, i.e. scaling geometric properties, mass, forces, inertial properties, as well as fluid viscosity. Such cases are henceforth referred to as $1/5_{\mathsf{FaR}}$ and $1/20_{\mathsf{FaR}}$.
2) Only Froude similarity, i.e. scaling geometric properties, mass, forces, inertial properties, but using full scale fluid viscosity, thereby showing the same properties as small scale physical wave tank tests. Such cases are henceforth referred to as $1/5_{\mathsf{F}}$ and $1/20_{\mathsf{F}}$.

Table 10.1: Froud scaling factors

Physical parameter	Unit	Scaling factor
Length	[m]	$\varkappa$
Mass	[kg]	$\varkappa^3$
Force	[N]	$\varkappa^3$
Torque	[N m]	$\varkappa^4$
Acceleration	[m s^{-2}]	1
Time	[s]	$\sqrt{\varkappa}$
Pressure	[Pa]	$\varkappa$

10.2 Case study

For the analysis of hydrodynamic scaling effects, the Wavestar WEC is considered. This section gives a brief overview of the device specifics (see Section 10.2.1) and the particular numerical reference case is detailed in Section 10.2.2.

10.2.1 The Wavestar WEC

As stated in Chapter 7, the Wavestar WEC consists of several hemispherical hulls, each with a single operational DoF, rotating around a hinge on an fixed structure, rigidly connected to the hull. A photograph of the $1/1$ scale model is shown in Figure 10.1 (a). Experimental test campaigns have been conducted in two different test facilities, at two different scales: Experiments of a $1/5$th scale device (see Figure 10.1 (b)) are documented in [583], while the test campaign of a $1/20$th scale device (see Figure 10.1 (c)) is documented in [SMD] and Section 7.2. The experimental data has been used for independent numerical model validation in Chapter 7.

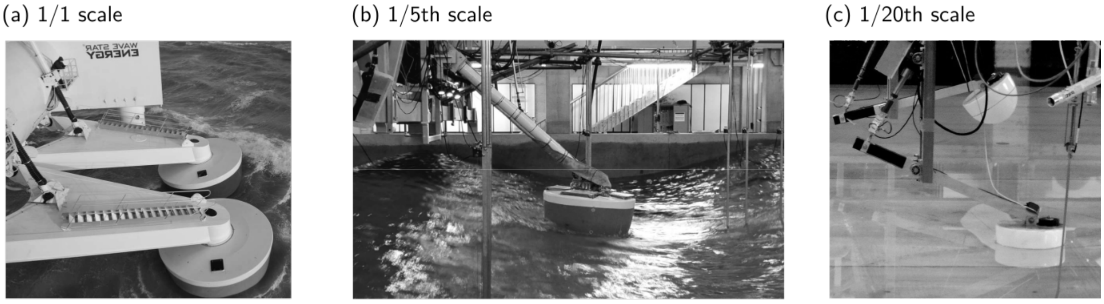
(a) 1/1 scale (b) 1/5th scale (c) 1/20th scale

Figure 10.1: Photographs of the Wavestar WEC at different scales. (a) Full scale (from from [608]); (b) $1/5$th scale at the University of Plymouth (from from [582]); (c) $1/20$th scale at Aalborg University.

10.2.2 Numerical WEC model

The current study establishes the numerical model of the $1/20$th scale WEC (see Figure 7.41 (b)), validated in Section 7.2, as a reference case and applies the scaling laws to this model. The system characteristics are listed in Table 7.1 for the $1/20$th, $1/5$th, and $1/1$ scale models.

It is important to note that the numerical solvers, solution schemes, and relative discretisation sizes in Section 7.2 are consistent with the setting for the numerical $1/5$th scale WEC model in Section 7.1, thus the model can be considered validated across different scales. Differences between the $1/20$th scale model and the $1/5$th scale model occur in terms of the physical properties, such as mass and inertia, which is a characteristic of the underlying physical prototype. The physical WEC model at $1/5$th and $1/20$th scale are correctly scaled (relative to the $1/1$ model) in terms of the floater geometry; however, due to the difference in the mechanical PTO system, as well as in the required sub–structures, the mass and inertial values do not strictly follow scaling laws. The mass of the complete system (floater and PTO), for instance, is adjusted between the physical $1/5$th and $1/20$th scale model such that the draft of the floater is scaled correctly. Such difficulties, induced by applying scaling laws, can be bypassed in CFD–based NWTs, allowing the analysis of purely hydrodynamic scaling effects.

10.3 Test cases

Similarly to the validation studies in Chapter 7, the present analysis of the hydrodynamic scaling effects for the Wavestar WEC follows an incremental approach:

- Initially, to investigate the influence of scaling on the incident waves, wave–only test cases are considered (see Section 10.3.1).

Table 10.2: Physical properties of the $1/20$th, $1/5$th, and $1/1$ scale Wavestar model. The hinge notation can be extracted from Figure 7.41 (b)

Property	**Unit**	**Value**		
Scale		$1/20_{\mathsf{FaR}}$ ($1/20_{\mathsf{F}}$)	$1/5_{\mathsf{FaR}}$ ($1/5_{\mathsf{F}}$)	$1/1$
Mass (float & arm)	[kg]	4.10	262.40	32800
Inertia (float & arm)	[kg m^2]	0.43	440.32	1376000
Floater diameter (at SWL)	[m]	0.25	1.00	5.00
Submergence (in equilibrium)	[m]	0.10	0.40	2.00
Water depth d	[m]	0.90	3.60	18.00
Hinge **A**:				
x	[m]	-0.45	-1.80	-9.00
y	[m]	0.00	0.00	0.00
z	[m]	0.23	0.92	4.60
Hinge **B**:				
x	[m]	-0.45	-1.80	-9.00
y	[m]	0.00	0.00	0.00
z	[m]	0.64	2.56	12.80
Hinge **C**:				
x	[m]	-0.64	-2.54	-12.80
y	[m]	0.00	0.00	0.00
z	[m]	0.30	1.20	6.00
Centre of mass:				
x	[m]	-0.05	-0.20	-1.00
y	[m]	0.00	0.00	0.00
z	[m]	0.11	0.44	2.20

- To introduce WSI, but still keep the complexity of the model relatively low, wave excitation force tests are examined (see Section 10.3.2).
- To develop a preliminary understanding of the scaling effects on the system dynamics, free decay tests are investigated (see Section 10.3.3).
- Progressively increasing the complexity of the test cases, forced oscillation tests are studied (see Section 10.3.4).
- Finally, wave–induced motion tests, under regular and irregular wave excitation, are analysed (see Section 10.3.5).

10.3.1 Waves–only

For the wave–only test cases, the waves propagate through the tank undisturbed. The long crested plane waves, considered in the present study, allow simulation in a two–dimensional domain, since such waves are invariant in the lateral direction. For scale analysis, both a regular wave and an irregular wave train are considered. The characteristics of the waves, i.e. (significant) wave height $H\,(H_s)$, (peak) wave period $T\,(T_p)$, (peak) wave frequency $f\,(f_p)$, (peak) wave length $\lambda\,(\lambda_p)$, and wave steepness $^{H}\!/_{\lambda}\,(^{H_s}\!/_{\lambda_p})$, are based on the test cases in Section 7.2 and are listed in Table 10.3. For the regular wave and the irregular wave train, simulations are run for 20 and 100 (peak) periods, respectively. Free surface elevation measurements are extracted at four different locations, depicted in Figure 10.2.

Table 10.3: Characteristics of the regular and irregular wave train for the considered model scales

		$H\,(H_s)$	$T\,(T_p)$	$f\,(f_p)$	$\lambda\,(\lambda_p)$	$^{H}\!/_{\lambda}\,(^{H_s}\!/_{\lambda_p})$
$1/1$		1.20m	6.26s	0.16Hz	58.60m	0.02
$1/5_{\text{FaR}}$	$(1/5_{\text{F}})$	0.24m	2.80s	0.36Hz	11.72m	0.02
$1/20_{\text{FaR}}$	$(1/20_{\text{F}})$	0.06m	1.40s	0.71Hz	2.93m	0.02

10.3.2 Wave excitation

During the wave excitation force tests, the WEC is locked in its equilibrium position, while being exposed to the regular and irregular wave trains. The wave excitation torque T_{ex}, about pivot point **A** (see Figure 7.41 (b)), is monitored and compared across the scales. The wave excitation torque T_{ex} can be easily extracted from each CFD simulation during post-processing, and the pressure and viscous shear force components can be separately quantified.

10.3.3 Free decay

For the free decay tests, the initial position of the body is displaced from equilibrium, resulting in an exponentially decaying oscillation returning to its rest state. The WEC motion and the hydrodynamic force on the WEC hull are monitored and compared across scales. The motion of the WEC is measured from the displacement of the PTO translator shaft, L_{PTO}.

10.3.4 Forced oscillation

The forced oscillation tests involve using the PTO system to apply a defined input force F_{PTO} on the WEC, without any input waves in the tank. The resulting WEC motion is monitored and compared across the scales. Two different types of input force signals are employed:

Single–frequency excitation

For the single–frequency excitation cases, a simple sinusoidal force signal is used to drive the system. The force amplitude is set to 5N (at $1/20$th scale) and the frequency corresponds to the wave frequency in Table 10.3. Simulations are run for 20 oscillation periods.

Multi–frequency excitation

The multi–frequency excitation experiments, realised through up-chirp force signals, are commonly performed for system identification purposes [336, 319]. The input force is defined as a linear frequency sweep with a fixed amplitude and the characteristics listed in Table 10.4.

Table 10.4: Characteristics of the multi–frequency excitation input for the considered model scales

		Frequency range	Force amplitude
$1/1$		[0.02, 1.07] Hz	80000N
$1/5_{\mathsf{FaR}}$	$(1/5_{\mathsf{F}})$	[0.06, 2.39] Hz	640N
$1/20_{\mathsf{FaR}}$	$(1/20_{\mathsf{F}})$	[0.11, 4.77] Hz	10N

10.3.5 Wave–induced WEC motion

Finally, for the wave–induced WEC motion tests, the WEC is exposed to the incident regular and irregular wave trains. The motion and hydrodynamic forces on the WEC hull are monitored and compared across the scales.

10.4 Numerical wave tanks

The setup of the numerical wave tank follows the setup for the validation study in Section 7.2; however, some adjustments have to be implemented for the different scales of the considered device.

10.4.1 Numerical wave generation and absorption

For numerical wave generation and absorption, the static boundary wave generation method [102] is used in conjunction with a numerical beach for wave absorption [110]. The optimal beach length, and the maximum damping factor, within the numerical beach $s_{b,\mathsf{Max}}$ are determined in Section 7.2 and set to 4.5m and 2.5s^{-1} at $1/20$th scale, respectively. For the NWTs at $1/5$th and $1/1$ scale, the beach length and the maximum damping factor are scaled according to Froude scaling and Table 10.5 lists the values for L_B and $s_{b,\mathsf{Max}}$ for all scales.

Table 10.5: Numerical beach lengths and maximum damping factors for the considered model scales

		$1/20_{\mathsf{FaR}}$ ($1/20_{\mathsf{F}}$)	$1/5_{\mathsf{FaR}}$ ($1/5_{\mathsf{F}}$)	$1/1$
L_B	[m]	4.50	18.00	90.00
$s_{b,\mathsf{Max}}$	[s^{-1}]	2.50	1.25	0.56

10.4.2 Computational domain

The same computational domain is used for all the different test cases outlined in Section 10.3. Figures 10.2 (a) and (b) show the top and side views of the numerical domain, respectively. The relevant dimensions of the computational domain at the three different scale are indicated in Figures 10.2 (a) and (b) and listed in Table 10.6.

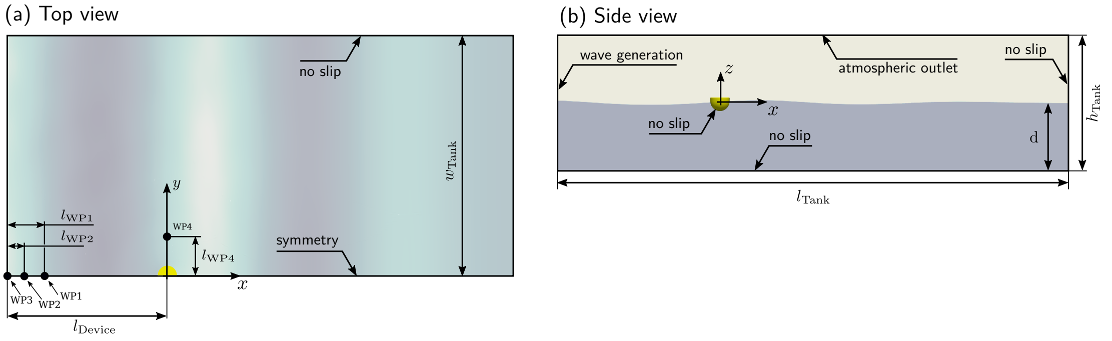
(a) Top view

(b) Side view

Figure 10.2: Schematic of the numerical wave tank: Side view (a) and top view (b).

The choices of the spatial and temporal discretisation sizes follow Section 7.2. Spatially, the interface region in the simulation zone and region around the body are discretised with cells of a (vertical) size of 10CPH and a maximum aspect ratio of 4 in the horizontal and lateral direction, resulting in 116 cells per λ. For the temporal discretisation, a fixed time step size of 0.001s is used at the $1/20$th scale and scaled according to Froude scaling. To analyse the influence of a scaled time step size on the results of the surface elevation and the WEC dynamics, simulations with a time step of 0.001s for all scales, as well as with scaled time steps, are performed.

Figures 10.3 (a) and (b) show the time traces of the free surface elevation at wave probe WP4, for a fixed time step size of 0.001s and a scaled time step size at $1/1$

Table 10.6: Dimensions of the numerical wave tanks for the considered model scales

		$1/20_{\mathsf{FaR}}$ ($1/20_{\mathsf{F}}$)	$1/5_{\mathsf{FaR}}$ ($1/5_{\mathsf{F}}$)	$1/1$
d	[m]	0.90	3.60	18.00
h_{Tank}	[m]	1.80	7.20	36.00
w_{Tank}	[m]	3.25	13.00	65.00
l_{Tank}	[m]	6.81	27.24	136.20
l_{Device}	[m]	2.16	8.64	43.20
l_{WP1}	[m]	0.45	1.80	9.0
l_{WP2}	[m]	0.20	0.80	4.0
l_{WP4}	[m]	0.86	3.44	17.2

scale and $1/5_{\mathsf{FaR}}$ scale, respectively. The same data is plotted for the irregular wave train in Figures 10.4 (a) and (b). Finally, Figures 10.5 (a) and (b) show the time traces of the WEC displacement and the excitation torque, respectively, during a multi–frequency excitation force test for a fixed time step size of 0.001s and a scaled time step size at $1/1$ scale. Form the plotted results, no influence of the time step size on the simulation results can be identified. Thus, for computational efficiency, scaled time step sizes are used throughout this study.

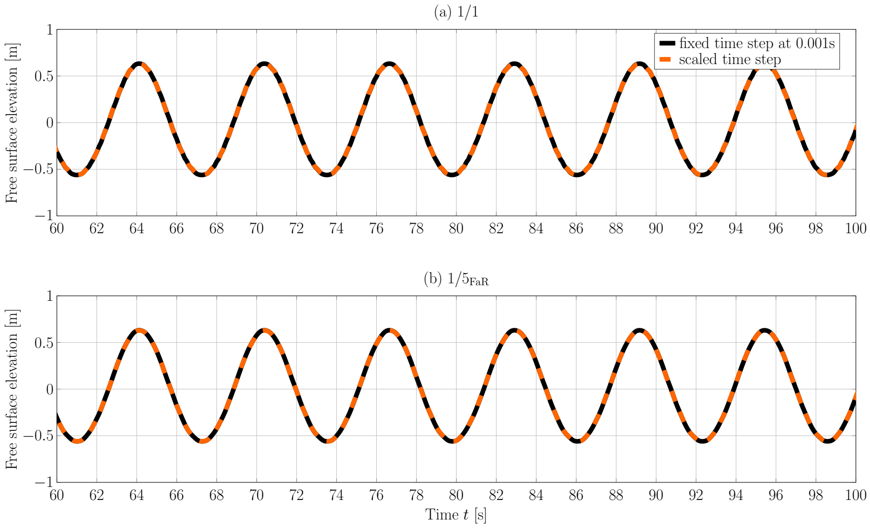

Figure 10.3: Time traces of the free surface elevation at wave probe WP4 for a fixed time step size of 0.001s and a scaled time step size at (a) $1/1$ scale and (b) $1/5_{\mathsf{FaR}}$ scale.

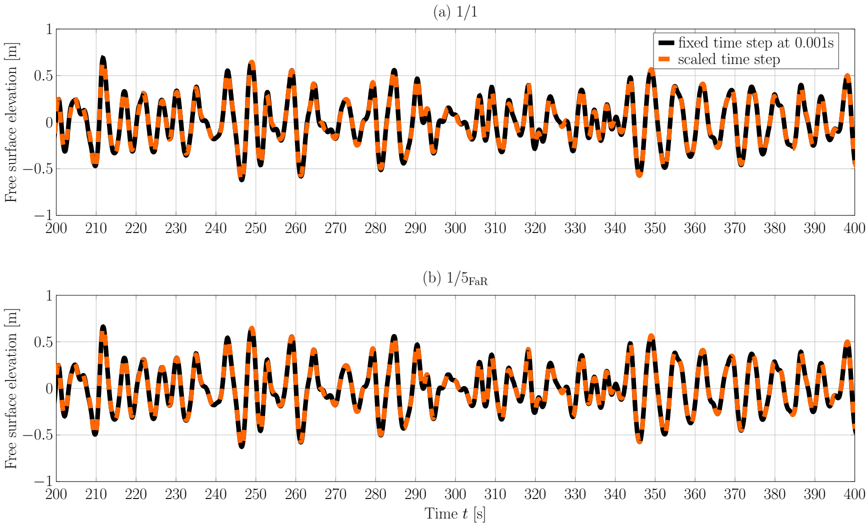

Figure 10.4: Time traces of the free surface elevation at WP4 for a fixed time step size of 0.001s and a scaled time step size for (a) $1/1$ scale and (b) $1/5_{\mathsf{FaR}}$ scale.

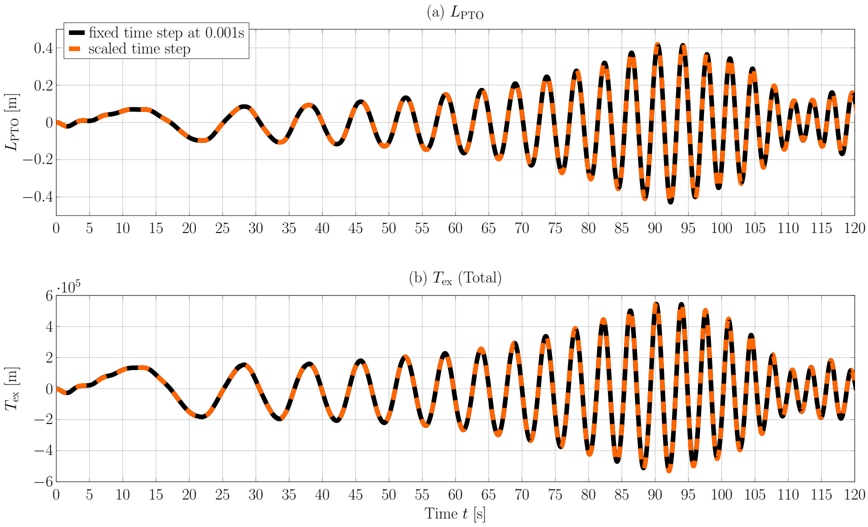

Figure 10.5: Time traces of the (a) WEC displacement and (b) the excitation torque for a fixed time step size of 0.001s and a scaled time step size at $1/1$ scale.

10.4.3 Viscosity

To achieve Froude and Reynolds scaling in the $1/5_{\mathsf{FaR}}$th and $1/20_{\mathsf{FaR}}$th scale case, the fluid viscosity needs to be scaled, using the relationship shown in Equation (10.3). For the $1/5_{\mathsf{F}}$th and $1/20_{\mathsf{F}}$th scale, fluid viscosities of the $1/1$ scale case are used. Table 10.7 lists the different fluid viscosities, of water and air, for all scales.

Table 10.7: Kinematic fluid viscosities for the considered model scales

Scale	Water viscosity [m^2 s^{-1}]	Air viscosity [m^2 s^{-1}]
$1/1$	$1.00 \cdot 10^{-6}$	$1.48 \cdot 10^{-5}$
$1/5_{\mathsf{F}}$	$1.00 \cdot 10^{-6}$	$1.48 \cdot 10^{-5}$
$1/5_{\mathsf{FaR}}$	$8.94 \cdot 10^{-8}$	$1.32 \cdot 10^{-6}$
$1/20_{\mathsf{F}}$	$1.00 \cdot 10^{-6}$	$1.48 \cdot 10^{-5}$
$1/20_{\mathsf{FaR}}$	$1.12 \cdot 10^{-8}$	$1.65 \cdot 10^{-7}$

10.5 Results and discussion

This section presents the results for the different test cases introduced in Section 10.3. All results are compared at full scale, requiring scaling of the $1/5$th and $1/20$th results, using the scaling factors in Table 10.1. The results are analysed qualitatively and quantitatively. For the former, plots of the relevant quantities are shown across the scales. For the quantitative comparison, the nRMSD is evaluated, following:

$$\mathsf{nRMSD}_{kl} = \sqrt{\frac{\sum_{i=1}^{n} \left[\varpi_k(i) - \varpi_l(i)\right]^2}{n}} \frac{100\%}{\mathcal{N}} , \tag{10.4}$$

where ϖ denotes the considered quantity (e.g. surface elevation, excitation torque, etc.), and the subscript $_k$ and $_l$ indicate a specific scale, i.e. $1/1$, $1/5_{\mathsf{F}}$, $1/5_{\mathsf{FaR}}$, $1/20_{\mathsf{F}}$, $1/20_{\mathsf{FaR}}$. The normalisation factor, $\mathcal{N}$, is defined as $\mathcal{N} = \max(\varpi_{(1/1)}) + |\min(\varpi_{(1/1)})|$. Following the above calculations, the 'deviation matrix' (e.g. Table 10.8) can be calculated, showing the contrasts between the different scales. Comparing the results between $1/5_{\mathsf{FaR}}$ and $1/5_{\mathsf{F}}$, as well as $1/20_{\mathsf{FaR}}$ and $1/20_{\mathsf{F}}$, highlighted in orange in the 'deviation matrix', potential scaling errors due to the mismatch between Froude and Reynolds scaling can be seen.

10.5.1 Wave–only tests

Following the incremental procedure outlined in Section 10.3, first, the wave–only cases are compared across the different scales.

Regular waves

Starting with regular waves, Figures 10.6 (a)–(d) show the phase–averaged time traces of the free surface elevation at the four wave probes WP1–WP4, respectively (the wave probe locations are marked in Figure 10.2). Visual inspection of the results allows a qualitative comparison, indicating that negligible differences can be observed between the scales at all wave probe locations.

Table 10.8 shows the 'deviation matrix' for the results at wave probe WP4, with all symmetric entries blanked out. Overall, relatively small deviations ($< 0.25\%$) can be observed between the various scales. For the regular wave–only case, virtually no difference (nRMSD $< 0.01\%$) between $1/5_{\mathsf{FaR}}$ and $1/5_{\mathsf{F}}$, as well as $1/20_{\mathsf{FaR}}$ and $1/20_{\mathsf{F}}$, are found, highlighting the negligible effect of fluid viscosity for this particular case. Furthermore, the agreement between the free surface elevation across all scales allows any deviations in the following test cases to be attributed to the WSI.

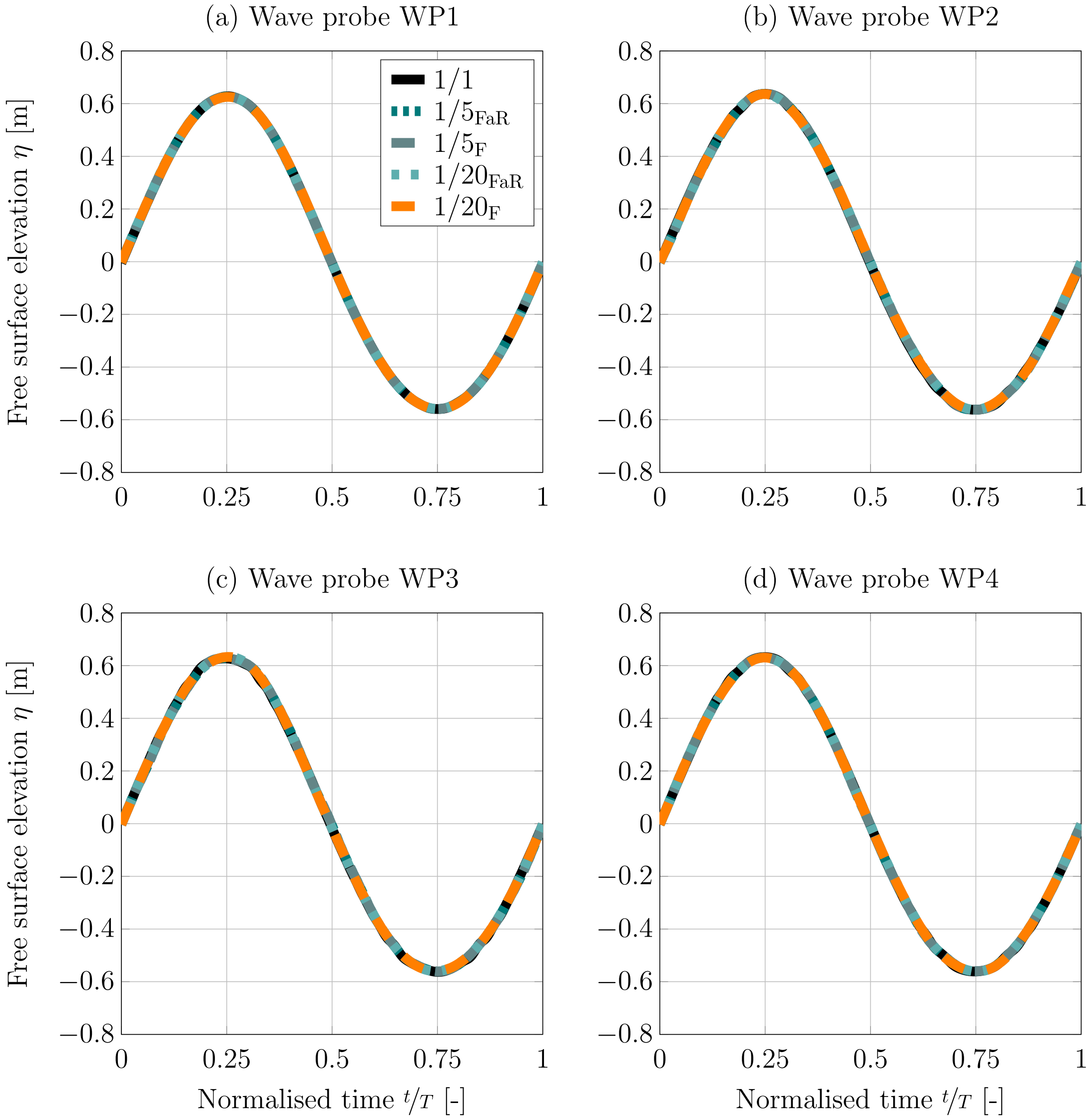

Figure 10.6: Time trace of the phase–averaged free surface elevation measured at wave probes WP1, WP2, WP3, and WP4.

Table 10.8: nRMSD [%] between the scales for the free surface elevation at wave probe WP4

	$1/5_{\mathsf{F}}$	$1/5_{\mathsf{FaR}}$	$1/20_{\mathsf{F}}$	$1/20_{\mathsf{FaR}}$
$1/1$	0.24	0.24	0.24	0.24
$1/5_{\mathsf{F}}$		0.00	0.15	0.15
$1/5_{\mathsf{FaR}}$			0.15	0.15
$1/20_{\mathsf{F}}$				0.00

Irregular wave train

For the irregular wave train, the deviation across the scales is analysed in both the time and frequency domains. By way of example, Figure 10.7 (a) shows the time traces for the free surface elevation (measured at wave probe WP4) at $1/1$ scale. Based on the free surface elevation time traces, the SDF is plotted in Figure 10.7 (b). From the plot in Figure 10.7 (b), no qualitative difference can be observed between scales. The results for the irregular wave train are therefore consistent with the results for the regular wave.

(a) Free surface elevation at wave probe WP4

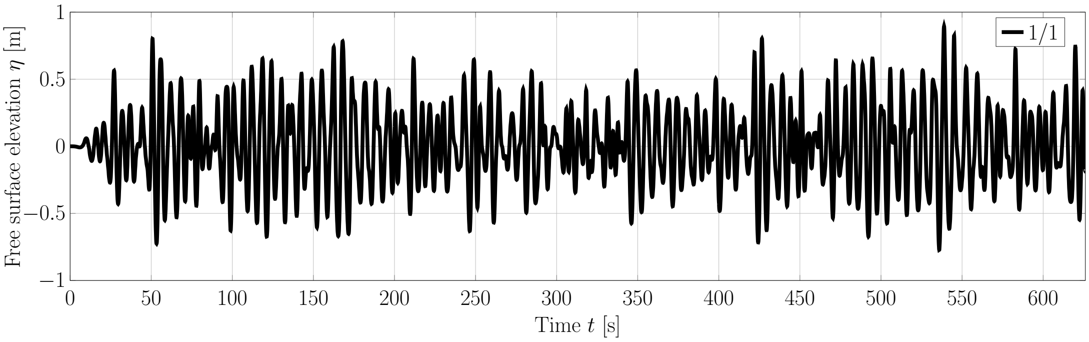

(b) SDF

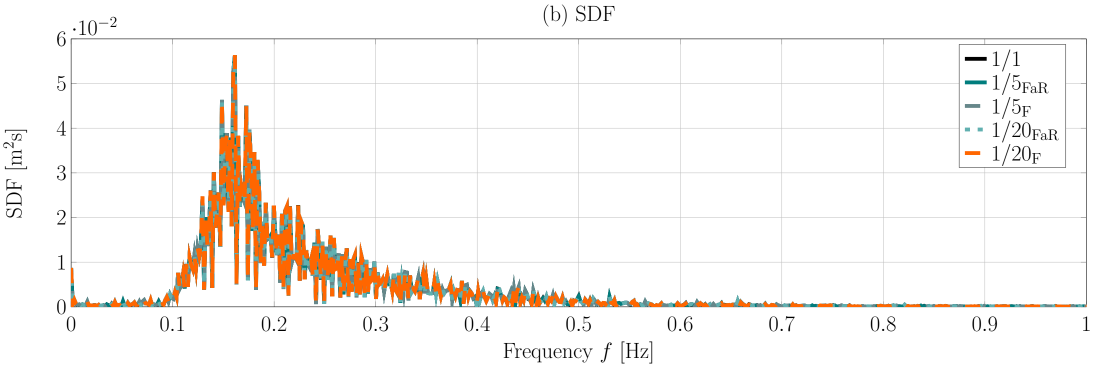

Figure 10.7: (a) Time trace of the irregular wave for the $1/1$ scale measured at wave probe WP4; (b) SDF for all scales based on the free surface elevation measured at wave probe WP4.

Tables 10.9 and 10.10 show the nRMSD between scales for the free surface elevation, measured at wave probe WP4, and the corresponding SDF, respectively. Overall, similar deviations are calculated for the irregular wave train, compared to the regular wave, for both the free surface elevation (nRMSD $\leq 0.20\%$) and the SDF (nRMSD $<< 0.10\%$). In particular, comparing the nRMSD for the $1/5_{\mathsf{FaR}}$ and $1/5_{\mathsf{F}}$ cases, as well as the $1/20_{\mathsf{FaR}}$ and $1/20_{\mathsf{F}}$ scales, deviations of less than 0.07% are evident, indicating a slightly larger, compared to the regular wave–only case, but still negligible influence of viscosity.

Table 10.9: nRMSD [%] between the scales for the free surface elevation at WP4

	$1/5_{\mathsf{F}}$	$1/5_{\mathsf{FaR}}$	$1/20_{\mathsf{F}}$	$1/20_{\mathsf{FaR}}$
$1/1$	0.16	0.16	0.20	0.19
$1/5_{\mathsf{F}}$		0.01	0.14	0.12
$1/5_{\mathsf{FaR}}$			0.14	0.12
$1/20_{\mathsf{F}}$				0.07

Table 10.10: nRMSD [%] between the scales for the SDF

	$1/5_{\mathsf{F}}$	$1/5_{\mathsf{FaR}}$	$1/20_{\mathsf{F}}$	$1/20_{\mathsf{FaR}}$
$1/1$	0.03	0.03	0.04	0.03
$1/5_{\mathsf{F}}$		0.00	0.03	0.03
$1/5_{\mathsf{FaR}}$			0.03	0.02
$1/20_{\mathsf{F}}$				0.01

10.5.2 Wave excitation tests

Introducing WSI, wave excitation force tests are initially considered for regular waves, followed by irregular wave excitation.

Regular wave

Figures 10.8 (a)–(c) show the total, phase–averaged, wave excitation torque and the contributing components due to pressure and viscous shear, respectively.
Inspection of the force magnitudes in Figures 10.8 (a)–(c) reveals a clear dominance of pressure induced wave excitation torque on the WEC hull, with torques of the order of $1 \cdot 10^5$ N m for the pressure component and $1 \cdot 10^2$ N m for the viscous component. Furthermore, for the pressure component and, thus, the total wave excitation torque, no qualitative difference can be observed between the scales. Conversely, the viscous component of T_{ex} shows significant difference between the scales, where the viscous shear forces for the $1/20_{\mathsf{F}}$ scale are largely over–predicted, compared to the $1/1$ scale.

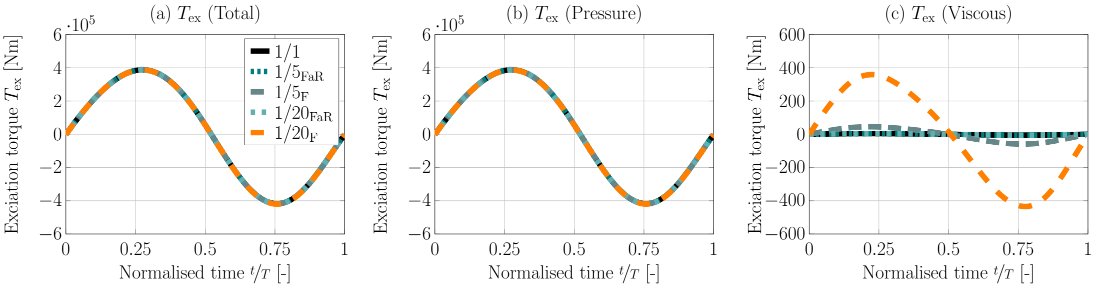

Figure 10.8: Time trace of the phase–averaged excitation torque across all scales

The qualitative analysis is underlined by the quantitative analysis, based on the nRMSD, listed in Tables 10.11–10.13. The values of the nRMSD for the total T_{ex}, and its pressure component, show similar values which are, in fact, in accordance with the nRMSD values calculated for the regular wave–only case, i.e. nRMSD $\leq 0.20\%$. Conversely, for the viscous component of T_ex, nRMSD values of up to $\sim 2900\%$ are calculated. Of particular interest are the deviations between the $1/5$ and $1/5_\text{F}$, as well as $1/20_\text{FaR}$ and $1/20_\text{F}$ scale. For the deviation between the $1/5_\text{FaR}$ and $1/5_\text{F}$, a nRMSD of 352% is calculated, highlighting over–prediction of the viscous forces in the $1/5_\text{F}$ case. This is expected, since the fluid viscosity at $1/5_\text{F}$ is over–predicated (by a factor of 11, see Table 10.7), compared to the $1/5$ scale. Similarly, the deviation between the $1/20_\text{FaR}$ and $1/20_\text{F}$ scale shows a deviation of 2912% which can, again, be attributed to over–prediction of the fluid viscosity (by a factor of 89, see Table 10.7) at $1/20_\text{F}$, compared to the $1/20_\text{FaR}$ scale. For the $1/1$, $1/5_\text{FaR}$, and $1/20_\text{FaR}$ cases, the nRMSD falls into the same range as for the total T_ex and its pressure component, i.e. $\leq 0.22\%$. Even though significant deviations can be observed for the viscous components of T_ex, the comparison between scales for the total T_ex is unaffected by these deviations, being dominated by the pressure component, which may be specific to the investigated case. If the problem at hand is dominated by viscous forces, more significant deviations between the total T_ex at various scales may be expected.

Table 10.11: nRMSD [%] between the scales for the total excitation torque

	$1/5_\text{F}$	$1/5_\text{FaR}$	$1/20_\text{F}$	$1/20_\text{FaR}$
$1/1$	0.07	0.07	0.16	0.13
$1/5_\text{F}$		0.02	0.20	0.19
$1/5_\text{FaR}$			0.21	0.19
$1/20_\text{F}$				0.11

Table 10.12: nRMSD [%] between the scales for the pressure excitation torque

	$1/5_\text{F}$	$1/5_\text{FaR}$	$1/20_\text{F}$	$1/20_\text{FaR}$
$1/1$	0.07	0.07	0.15	0.13
$1/5_\text{F}$		0.02	0.19	0.19
$1/5_\text{FaR}$			0.20	0.19
$1/20_\text{F}$				0.09

Table 10.13: nRMSD [%] between the scales for the viscous excitation torque

	$1/5_\text{F}$	$1/5_\text{FaR}$	$1/20_\text{F}$	$1/20_\text{FaR}$
$1/1$	352.73	0.14	2912.60	0.11
$1/5_\text{F}$		352.73	2560.70	352.67
$1/5_\text{FaR}$			2912.60	0.22
$1/20_\text{F}$				2912.50

Irregular wave train

For the wave excitation test under irregular wave excitation, overall similar results as for the previous cases are found. By way of example, Figures 10.9 (a)–(c) show the time traces for the total wave excitation torque T_{ex} and its pressure and viscous shear components, respectively. As for the case of regular wave excitation, the total T_{ex} is dominated by the pressure component, while the viscous component of T_{ex} is several orders of magnitude lower.

The SDF of the total T_{ex}, and its viscous component, are shown in Figures 10.10 (a) and (b), respectively. As expected from the regular wave excitation results, no qualitative differences can be observed for the total T_{ex}, while the viscous component of T_{ex} at $1/20_{\text{F}}$ scale is significantly over–predicted.

These results are underpinned by the quantitative analysis based on the nRMSD. Results for the the nRMSD between the total and viscous excitation torque (in the time domain) are listed in Tables 10.14 and 10.15.

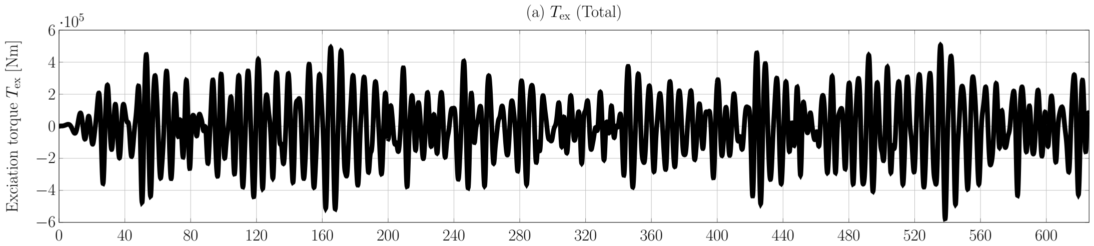
(a) T_{ex} (Total)

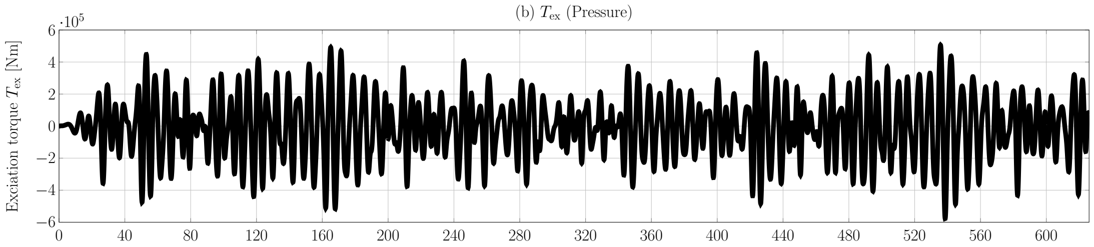
(b) T_{ex} (Pressure)

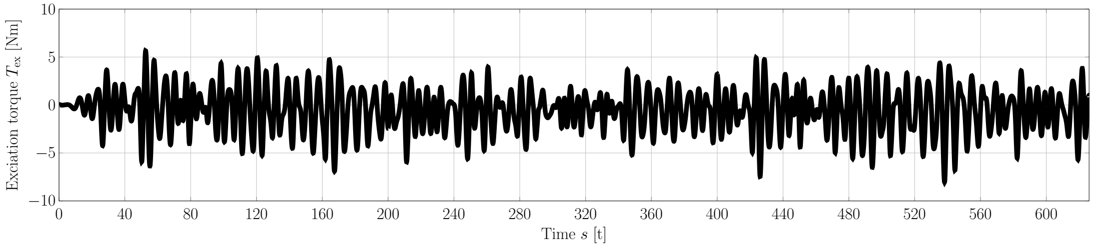
(c) T_{ex} (Viscous)

Figure 10.9: Time trace of the excitation torque for the irregular sea state at 1/1 scale: (a) Total T_{ex}; (b) Pressure T_{ex}; (c) Viscous T_{ex}.

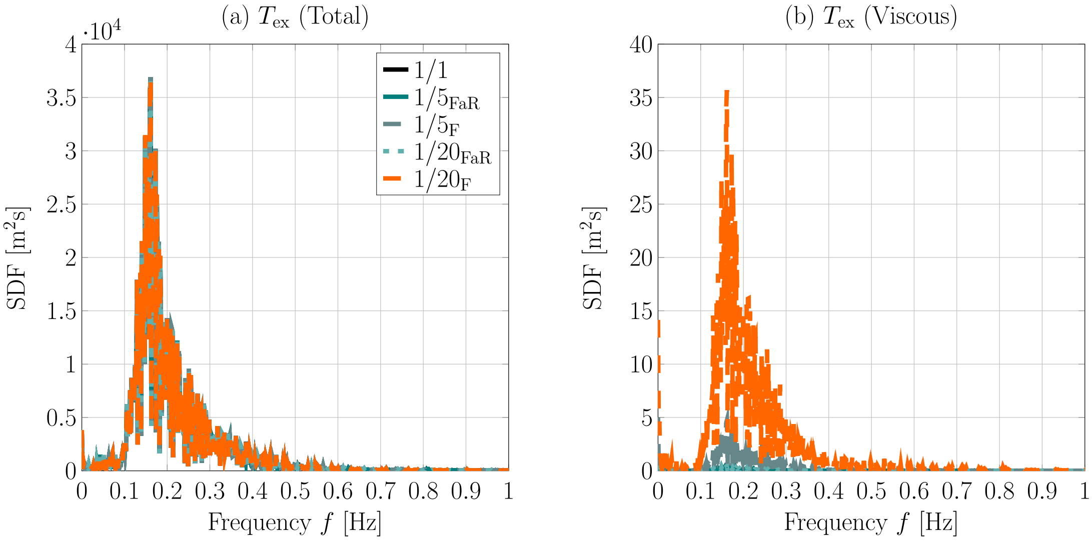

Figure 10.10: SDF of the excitation torque for the irregular sea state: (a) Total T_{ex}; (b) Viscous T_{ex}.

For the total excitation torque, the results are consistent with the previous results, showing nRMSD values of $< 0.10\%$. For the viscous component of T_{ex}, relatively large values of up to $\sim 1900\%$ are calculated for the nRMSD. Inspection of the deviation between scales reveals the same phenomena as for the regular wave excitation test, whereby the viscosity, and thus the according T_{ex}, is over–predicted at the Froude scales. Good agreement between the viscous T_{ex} is achieved, when Reynolds and Froude scaling is obeyed. Ultimately, the influence of the viscous component on the total T_{ex} is negligible.

Table 10.14: nRMSD [%] between the scales for the total excitation torque

	$1/5_{\text{F}}$	$1/5_{\text{FaR}}$	$1/20_{\text{F}}$	$1/20_{\text{FaR}}$
$1/1$	0.05	0.04	0.08	0.04
$1/5_{\text{F}}$		0.05	0.06	0.04
$1/5_{\text{FaR}}$			0.07	0.04
$1/20_{\text{F}}$				0.06

Table 10.15: nRMSD [%] between the scales for the viscous excitation torque

	$1/5_{\text{F}}$	$1/5_{\text{FaR}}$	$1/20_{\text{F}}$	$1/20_{\text{FaR}}$
$1/1$	168.25	0.40	1363.25	0.55
$1/5_{\text{F}}$		168.32	1974.03	168.27
$1/5_{\text{FaR}}$			1363.62	0.46
$1/20_{\text{F}}$				1363.58

10.5.3 Free decay test

Figures 10.11 (a)–(b) show the free decay results for the WEC displacement (by means of the displacement of the PTO translator shaft L_{PTO}), the total hydrodynamic torque, T_{Hyd}, and its viscous component, as well as the SDF based on L_{PTO}, respectively. For the quantitative analysis, nRMSD values are listed in Tables 10.16–10.19.

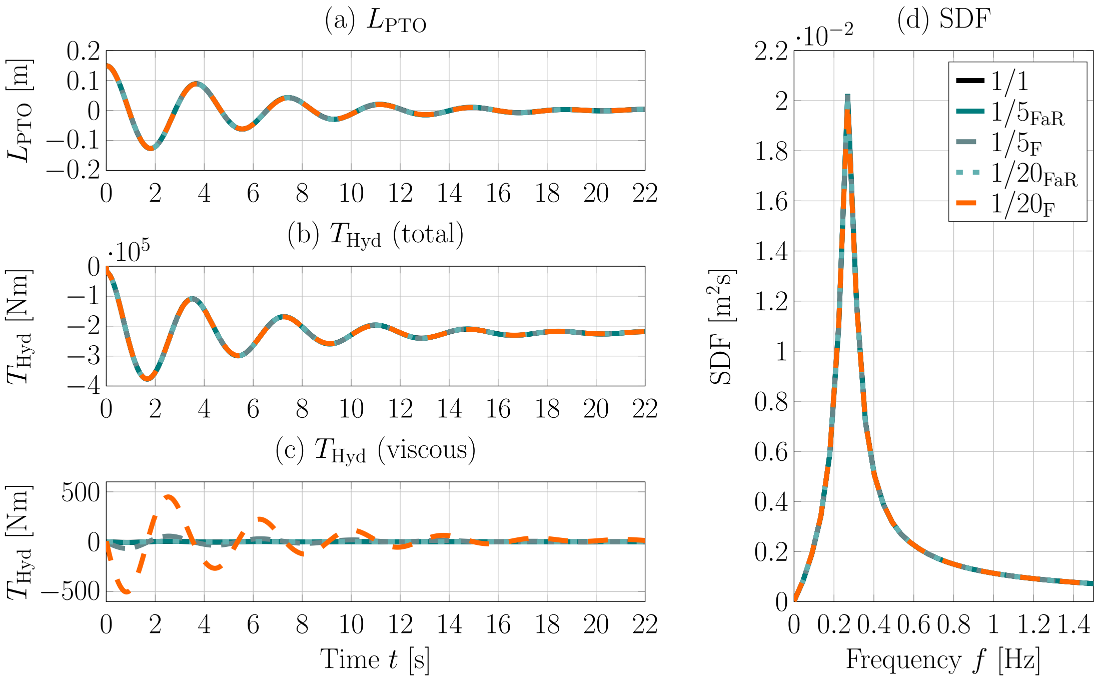

Figure 10.11: Time trace of (a) the WEC displacement, (b) the total hydrodynamic torque and (c) the viscous component of the hydrodynamic torque. (d) shows the SDF based on L_{PTO}.

As for the previous cases, the largest qualitative and quantitative deviations between scales can be observed for the viscous component of the hydrodynamic force (nRMSD up to $\sim 1400\%$). From the free decay test, it can be observed that the deviation in the viscous component of the hydrodynamic torque has not only a negligible influence on the total hydrodynamic torque (max. nRMSD $\leq 0.21\%$) but also, as expected, negligible influence on the device motion (max. nRMSD for $L_{\mathrm{PTO}} < 0.25\%$ and $<< 0.10\%$ for the SDF).

Table 10.16: nRMSD [%] between the scales for L_{PTO}

	$1/5_{\mathrm{F}}$	$1/5_{\mathrm{FaR}}$	$1/20_{\mathrm{F}}$	$1/20_{\mathrm{FaR}}$
$1/1$	0.14	0.15	0.12	0.00
$1/5_{\mathrm{F}}$		0.02	0.22	0.14
$1/5_{\mathrm{FaR}}$			0.24	0.15
$1/20_{\mathrm{F}}$				0.12

Table 10.17: nRMSD [%] between the scales for the total T_{Hyd}

	$1/5_{\mathrm{F}}$	$1/5_{\mathrm{FaR}}$	$1/20_{\mathrm{F}}$	$1/20_{\mathrm{FaR}}$
$1/1$	0.11	0.12	0.11	0.00
$1/5_{\mathrm{F}}$		0.01	0.20	0.11
$1/5_{\mathrm{FaR}}$			0.21	0.12
$1/20_{\mathrm{F}}$				0.11

Table 10.18: nRMSD [%] between the scales for the viscous T_{Hyd}

	$1/5_{\mathsf{F}}$	$1/5_{\mathsf{FaR}}$	$1/20_{\mathsf{F}}$	$1/20_{\mathsf{FaR}}$
$1/1$	170.70	2.80	1389.83	0.03
$1/5_{\mathsf{F}}$		170.13	1221.74	170.67
$1/5_{\mathsf{FaR}}$			1389.64	2.80
$1/20_{\mathsf{F}}$				1389.80

Table 10.19: nRMSD [%] between the scales for the SDF based on L_{PTO}

	$1/5_{\mathsf{F}}$	$1/5_{\mathsf{FaR}}$	$1/20_{\mathsf{F}}$	$1/20_{\mathsf{FaR}}$
$1/1$	0.02	0.03	0.03	0.00
$1/5_{\mathsf{F}}$		0.00	0.05	0.02
$1/5_{\mathsf{FaR}}$			0.05	0.03
$1/20_{\mathsf{F}}$				0.03

10.5.4 Forced oscillation tests

In the following, forced oscillation tests with single– and multi–frequency excitation are discussed.

Single–frequency excitation

Figures 10.12 (a)–(c) show the time trace of the phase–averaged WEC displacement, the total hydrodynamic torque, and the viscous component of the total hydrodynamic torque, respectively. The corresponding ‘deviation matrices’ are shown in Tables 10.20–10.22. Overall, similar results as for all previous test cases are found for the single–frequency forced oscillation test. If Froude and Reynolds similarity is achieved, all considered quantities scale correctly (nRMSD $< 0.60\%$, see Table 10.20–10.22). If only Froude similarity is achieved, viscous forces on the WEC hull are over–predicted (nRMSD $> 345\%$, see Table 10.22), but with no significant effect on the overall loads on the WEC hull or WEC motion.

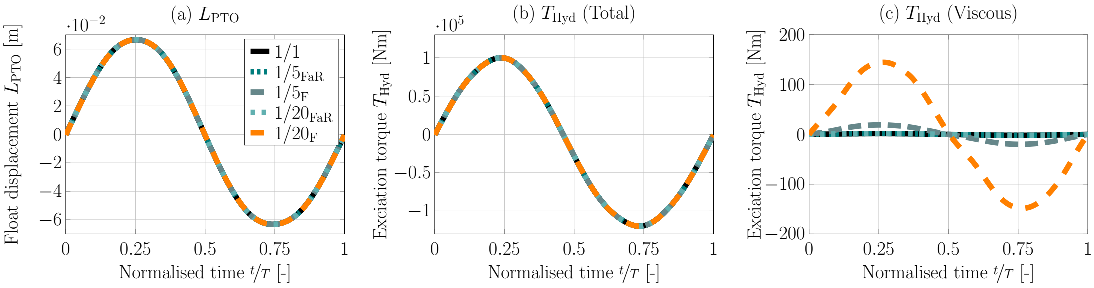

Figure 10.12: Time trace of the phase–averaged (a) the WEC displacement, (b) the total hydrodynamic torque, and (c) the viscous component of the total hydrodynamic torque.

Table 10.20: nRMSD [%] between the scales for the WEC displacement

	$1/5_{\text{F}}$	$1/5_{\text{FaR}}$	$1/20_{\text{F}}$	$1/20_{\text{FaR}}$
$1/1$	0.03	0.02	0.08	0.02
$1/5_{\text{F}}$		0.01	0.06	0.01
$1/5_{\text{FaR}}$			0.07	0.01
$1/20_{\text{F}}$				0.07

Table 10.21: nRMSD [%] between the scales for the total hydrodynamic torque

	$1/5_{\text{F}}$	$1/5_{\text{FaR}}$	$1/20_{\text{F}}$	$1/20_{\text{FaR}}$
$1/1$	0.04	0.03	0.05	0.03
$1/5_{\text{F}}$		0.00	0.02	0.01
$1/5_{\text{FaR}}$			0.02	0.01
$1/20_{\text{F}}$				0.02

Table 10.22: nRMSD [%] between the scales for the viscous hydrodynamic torque

	$1/5_{\text{F}}$	$1/5_{\text{FaR}}$	$1/20_{\text{F}}$	$1/20_{\text{FaR}}$
$1/1$	346.02	0.59	2825.42	0.43
$1/5_{\text{F}}$		346.07	2480.00	346.00
$1/5_{\text{FaR}}$			2825.45	0.19
$1/20_{\text{F}}$				2825.80

Multi–frequency excitation

Figures 10.13 (a)–(d) show the time trace of the WEC displacement, the total hydrodynamic torque, the viscous component of the total hydrodynamic torque, L_{PTO}, and the SDF of L_{PTO}, respectively. The corresponding 'deviation matrices' are shown in Tables 10.23–10.26.

From inspection of Figures 10.13 (a)–(c), larger displacement and force magnitudes can be observed, compared to the single–frequency excitation (multiplication factor ~ 7) case. Regardless of the increased displacement and force magnitudes, the observed scaling effects are consistent with the results for the single–frequency forced oscillation test and, in fact, with all previous results. Negligible deviations between the scales can be observed for L_{PTO} (and the according SDF) and the total hydrodynamic torques.

Table 10.23: nRMSD [%] between the scales for the PTO piston length

	$1/5_{\text{F}}$	$1/5_{\text{FaR}}$	$1/20_{\text{F}}$	$1/20_{\text{FaR}}$
$1/1$	0.20	0.20	0.67	0.16
$1/5_{\text{F}}$		0.02	0.67	0.05
$1/5_{\text{FaR}}$			0.67	0.05
$1/20_{\text{F}}$				0.66

Table 10.24: nRMSD [%] between the scales for the total excitation torque

	$1/5_{\text{F}}$	$1/5_{\text{FaR}}$	$1/20_{\text{F}}$	$1/20_{\text{FaR}}$
$1/1$	0.19	0.19	0.18	0.15
$1/5_{\text{F}}$		0.02	0.15	0.04
$1/5_{\text{FaR}}$			0.17	0.05
$1/20_{\text{F}}$				0.14

Table 10.25: nRMSD [%] between the scales for the viscous excitation torque

	$1/5_{\text{F}}$	$1/5_{\text{FaR}}$	$1/20_{\text{F}}$	$1/20_{\text{FaR}}$
$1/1$	157.18	0.25	1322.90	0.20
$1/5_{\text{F}}$		157.19	1165.80	157.17
$1/5_{\text{FaR}}$			1322.89	0.10
$1/20_{\text{F}}$				1322.85

Table 10.26: nRMSD [%] between the scales for the SDF

	$1/5_{\text{F}}$	$1/5_{\text{FaR}}$	$1/20_{\text{F}}$	$1/20_{\text{FaR}}$
$1/1$	0.08	0.08	0.21	0.06
$1/5_{\text{F}}$		0.00	0.21	0.02
$1/5_{\text{FaR}}$			0.22	0.02
$1/20_{\text{F}}$				0.21

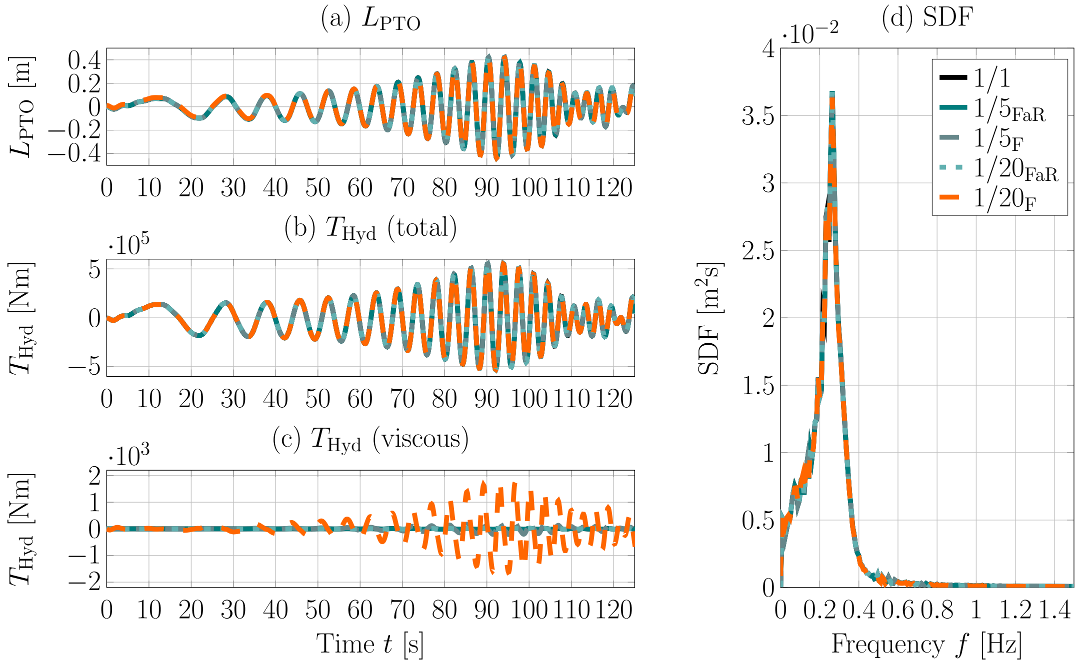

Figure 10.13: Time trace of (a) the WEC displacement, (b) the total hydrodynamic torque and (c) the viscous component of the hydrodynamic torque. (d) shows the L_{PTO} SDF

10.5.5 Wave–induced WEC motion tests

Finally, wave–induced WEC motion, under regular and irregular wave excitation, is analysed.

Regular wave

Figures 10.14 (a)–(c) show the time trace of the phase–averaged WEC displacement, the total excitation torque, and the viscous component of the total excitation torque. The 'deviation matrices' are shown in Tables 10.27–10.29.

The magnitude of the WEC displacement (Figures 10.14 (a)) is of a similar order as for the multi–frequency forced oscillation test, while the total excitation torque (Figures 10.14 (b)) is slightly lower. Similarly, the viscous component of the excitation torque (Figures 10.14 (c)) is slightly lower, compared to the multi–frequency forced oscillation test. Overall, qualitatively and quantitatively, the deviations between the scales are consistent with the previous test cases.

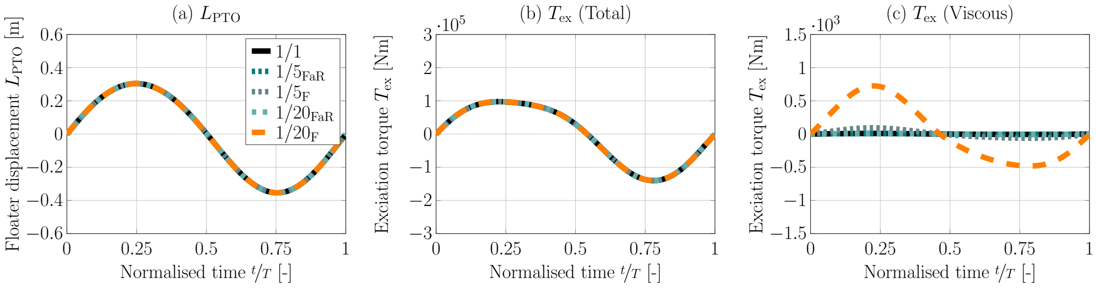

Figure 10.14: Time trace of the phase–averaged (a) WEC displacement, (b) total hydrodynamic torque, and (c) viscous component of the total hydrodynamic torque

Table 10.27: nRMSD [%] between the scales for the WEC displacement

	$1/5_{\text{F}}$	$1/5_{\text{FaR}}$	$1/20_{\text{F}}$	$1/20_{\text{FaR}}$
1/1	0.03	0.04	0.08	0.01
$1/5_{\text{F}}$		0.02	0.10	0.03
$1/5_{\text{FaR}}$			0.12	0.04
$1/20_{\text{F}}$				0.08

Table 10.28: nRMSD [%] between the scales for the total excitation torque

	$1/5_{\text{F}}$	$1/5_{\text{FaR}}$	$1/20_{\text{F}}$	$1/20_{\text{FaR}}$
1/1	0.07	0.15	0.11	0.06
$1/5_{\text{F}}$		0.11	0.14	0.08
$1/5_{\text{FaR}}$			0.22	0.12
$1/20_{\text{F}}$				0.14

Table 10.29: nRMSD [%] between the scales for the viscous excitation torque

	$1/5_{\text{F}}$	$1/5_{\text{FaR}}$	$1/20_{\text{F}}$	$1/20_{\text{FaR}}$
1/1	354.47	0.09	2968.60	0.12
$1/5_{\text{F}}$		354.45	2641.10	354.42
$1/5_{\text{FaR}}$			2968.50	0.16
$1/20_{\text{F}}$				2968.51

Regular waves – Resonance

Under controlled conditions, the WEC dynamics are pushed towards resonance with the incident waves, thereby enhancing WEC motion and power production. It is well known that, due to the enhanced WEC motion, hydrodynamic non–linear effects are introduced [17].

To analyse the hydrodynamic scaling effects in resonance conditions, the wave period of the regular wave is chosen to match the natural frequency of the device, taken from the peak of the SDF plot in Figure 10.11 (d). The results of the phase–averaged WEC displacement, the total excitation torque, and the viscous component of the total excitation torque are shown in Figures 10.15 (a)–(c).

Comparing the results shown in Figures 10.15 (a)–(c) for the resonance case with the results shown in Figures 10.14 (a)–(c), it can readily be seen that the device motion, indicated by L_{PTO}, as well as the excitation torques, is increased. Furthermore, from a qualitative inspection, slightly different trajectories in the excitation torque can be observed. However, in qualitative terms, the deviations between scales for the WEC displacement and the excitation torque, for the case of resonant excitation follow the same trend as in the previous test cases.

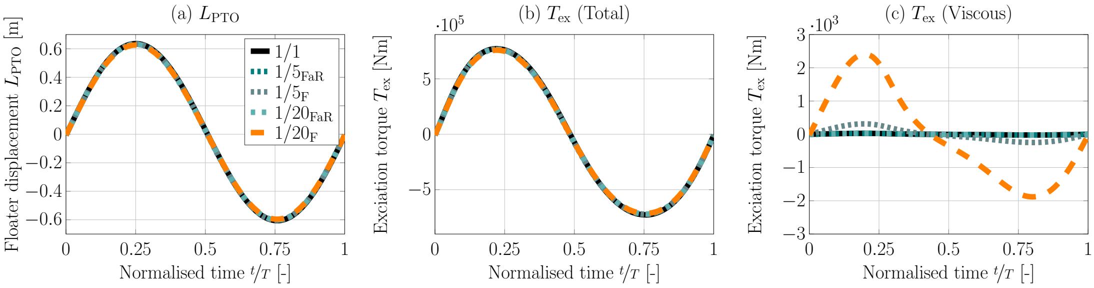

Figure 10.15: Time trace of the phase–averaged (a) the WEC displacement, (b) the total hydrodynamic torque, and (c) the viscous component of the total hydrodynamic torque

For a quantitative analysis, Tables 10.30–10.32 list the nRMSD values for the WEC displacement, the total excitation force, and its viscous component, respectively. Comparing the quantitative results for the resonance excitation case with the results for regular excitation (see Tables 10.27–10.29), it can be observed that, for the viscous component of the excitation torque, similar differences between scales can be observed for the resonant and non–resonant excitation cases. For the total excitation torque, differences between the scales are approximately twice as large for the case of resonant excitation, compared with the non–resonant excitation test. Regarding WEC displacement, the differences between the scales are approximately one order of magnitude larger for the case of resonant excitation, compared with the non–resonant excitation test. However, the values for the nRMSD remain below 0.7%, and can be considered negligible.

Table 10.30: nRMSD [%] between the scales for the WEC displacement

	$1/5_{\text{F}}$	$1/5_{\text{FaR}}$	$1/20_{\text{F}}$	$1/20_{\text{FaR}}$
$1/1$	0.21	0.23	0.60	0.30
$1/5_{\text{F}}$		0.03	0.43	0.13
$1/5_{\text{FaR}}$			0.43	0.15
$1/20_{\text{F}}$				0.30

Table 10.31: nRMSD [%] between the scales for the total excitation torque

	$1/5_{\text{F}}$	$1/5_{\text{FaR}}$	$1/20_{\text{F}}$	$1/20_{\text{FaR}}$
$1/1$	0.26	0.28	0.64	0.33
$1/5_{\text{F}}$		0.04	0.45	0.18
$1/5_{\text{FaR}}$			0.46	0.21
$1/20_{\text{F}}$				0.33

Table 10.32: nRMSD [%] between the scales for the viscous excitation torque

	$1/5_{\mathsf{F}}$	$1/5_{\mathsf{FaR}}$	$1/20_{\mathsf{F}}$	$1/20_{\mathsf{FaR}}$
$1/1$	329.75	0.39	2752.20	0.17
$1/5_{\mathsf{F}}$		329.53	2422.50	329.67
$1/5_{\mathsf{FaR}}$			2752.00	0.23
$1/20_{\mathsf{F}}$				2752.10

Regular waves – Cylinder

From the previous results for the WSI test cases, it has been seen that the scaling effects, in particular when Froude and Reynolds similarity are not obeyed simultaneously, affect viscous excitation torque; however, the scaling effect does not significantly affect the total excitation torque or the WEC displacement, due to its small relative magnitude. To trigger (shaped induced) viscous effects, the shape of the floater has been changed to a cylindrical float with sharp edges (see Figure 10.16), while retaining the bounding box of the original float. Furthermore, the mass of the float has been adjusted to retain the draft of the original float. The cylindrical float is excited with the regular waves listed in Table 7.17 and, as for the previous cases, the WEC displacement and the excitation torques are analysed.

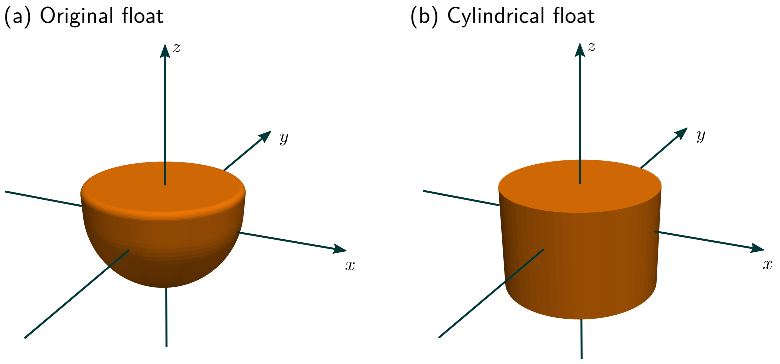
(a) Original float

(b) Cylindrical float

Figure 10.16: Considered float geometries

Figures 10.17 (a)–(c) show the time traces of the phase–averaged WEC displacement, the total excitation torque, and the viscous component of the total excitation torque. From a qualitative perspective, the observed behaviour of T_{ex} and L_{PTO} for the original floater in the previous WSI test cases can also be observed for the case of the cylindrical float. Only significantly different torque trajectories can be observed, compared with the original float.

For a quantitative analysis, the 'deviation matrices' are listed in Tables 10.33–10.35 for the WEC displacement, the total excitation torque, and the viscous component of the total excitation torque, respectively. Compared with the results for the original

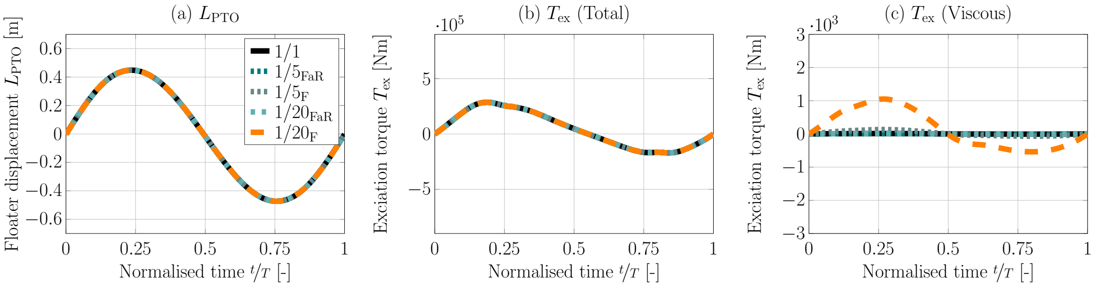

Figure 10.17: Time trace of the phase–averaged (a) the WEC displacement, (b) the total hydrodynamic torque, and (c) the viscous component of the total hydrodynamic torque

float, similar values of the nRMSD between the scales can be observed for the WEC displacement and the total excitation torque. Specifically for the viscous component of the excitation torque, slightly larger values of the nRMSD, in particular for the interesting cases of $1/5_{\text{FaR}}$ vs $1/5_{\text{F}}$ ($\sim 354\%$ for the original float, $\sim 370\%$ for the cylinder) and $1/20_{\text{FaR}}$ vs $1/20_{\text{F}}$ ($\sim 2968\%$ for the original float, $\sim 3185\%$ for the cylinder), can be observed. This is expected, due to geometry–induced viscous effects. However, as for all previous cases, the differences between scales for the viscous component of the excitation torque does not significantly effect the total excitation torque or the WEC displacement.

Table 10.33: nRMSD [%] between the scales for the WEC displacement

	$1/5_{\text{F}}$	$1/5_{\text{FaR}}$	$1/20_{\text{F}}$	$1/20_{\text{FaR}}$
1/1	0.07	0.07	0.02	0.02
$1/5_{\text{F}}$		0.04	0.07	0.08
$1/5_{\text{FaR}}$			0.07	0.08
$1/20_{\text{F}}$				0.01

Table 10.34: nRMSD [%] between the scales for the total excitation torque

	$1/5_{\text{F}}$	$1/5_{\text{FaR}}$	$1/20_{\text{F}}$	$1/20_{\text{FaR}}$
1/1	0.28	0.20	0.08	0.07
$1/5_{\text{F}}$		0.13	0.27	0.32
$1/5_{\text{FaR}}$			0.18	0.22
$1/20_{\text{F}}$				0.10

Table 10.35: nRMSD [%] between the scales for the viscous excitation torque

	$1/5_{\text{F}}$	$1/5_{\text{FaR}}$	$1/20_{\text{F}}$	$1/20_{\text{FaR}}$
1/1	369.39	0.52	3185.20	0.19
$1/5_{\text{F}}$		369.67	815.80	369.44
$1/5_{\text{FaR}}$			3185.50	0.37
$1/20_{\text{F}}$				3185.20

Irregular wave train

Finally, wave–induced motion for the case of irregular wave excitation is considered. Figures 10.18 (a)–(d) show the SDF of the WEC displacement, the total excitation torque, the viscous component of the excitation torque, and a snippet (between

300–400s) of the time trace for the WEC displacement, respectively. The results of the corresponding quantitative analysis are shown in Tables 10.36–10.38. Overall, the qualitative and quantitative results are consistent with the findings of all previous WSI test cases shown in this section.

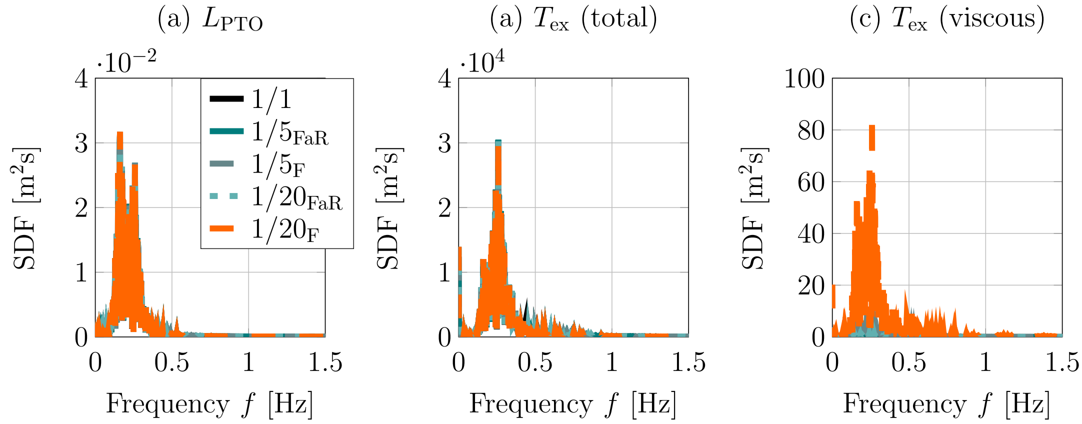
(a) L_{PTO} (a) T_{ex} (total) (c) T_{ex} (viscous)

(d) L_{PTO}

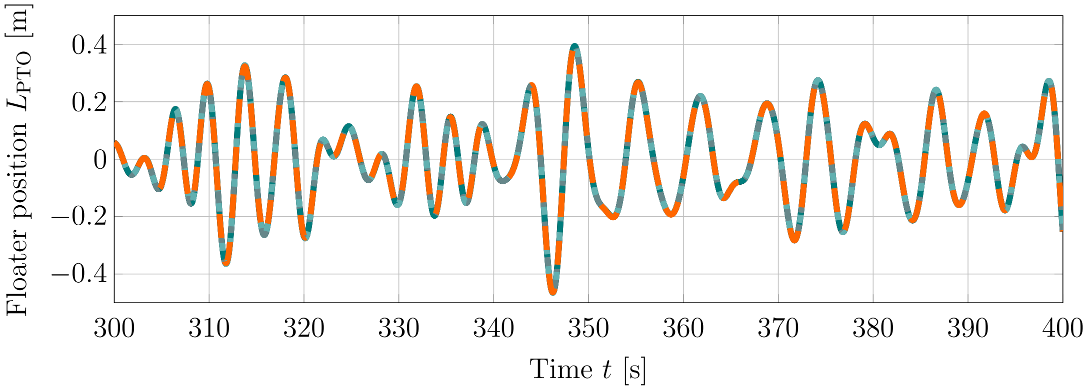

Figure 10.18: SDF of (a) the WEC displacement, (b) the total excitation torque, and (c) the viscous component of the excitation torque. (d) Shows a snippet (between 300–400s) of the time trace of the WEC displacement.

Table 10.36: nRMSD [%] between the scales for the WEC displacement

	1/5$_{\mathrm{F}}$	1/5$_{\mathrm{FaR}}$	1/20$_{\mathrm{F}}$	1/20$_{\mathrm{FaR}}$
1/1	0.01	0.01	0.01	0.01
1/5$_{\mathrm{F}}$		0.00	0.02	0.01
1/5$_{\mathrm{FaR}}$			0.02	0.01
1/20$_{\mathrm{F}}$				0.01

Table 10.37: nRMSD [%] between the scales for the total excitation torque

	1/5$_{\mathrm{F}}$	1/5$_{\mathrm{FaR}}$	1/20$_{\mathrm{F}}$	1/20$_{\mathrm{FaR}}$
1/1	0.01	0.03	0.03	0.02
1/5$_{\mathrm{F}}$		0.02	0.03	0.02
1/5$_{\mathrm{FaR}}$			0.02	0.01
1/20$_{\mathrm{F}}$				0.02

Table 10.38: nRMSD [%] between the scales for the viscous excitation torque

	$1/5_{\text{F}}$	$1/5_{\text{FaR}}$	$1/20_{\text{F}}$	$1/20_{\text{FaR}}$
$1/1$	25.98	2.34	200.91	2.34
$1/5_{\text{F}}$		23.64	174.94	23.64
$1/5_{\text{FaR}}$			198.58	0.04
$1/20_{\text{F}}$				198.57

10.6 Concluding remarks

Avoiding mechanical scaling effects, such as excessive friction, and providing the ability to achieve Froude and Reynold similarity, CFD–based NWTs are powerful tools to analyse the hydrodynamic scaling effects on WEC devices. Based on a validated numerical model, this chapter analyses hydrodynamic scale effects for the Wavestar WEC device. Following an incremental procedure with progressively increasing complexity of the considered test cases, the study covers the full range of relevant test cases for WEC applications.

From the results, the straightforward conclusion can be drawn that, for the Wavestar device, and likely all similar devices with hemispherical bottom shapes and a single operational DoF, hydrodynamic scaling effects are negligible for the overall WEC dynamics and total loads on the hull. Even when Froude and Reynolds similarity are not obeyed simultaneously, the deviations across scales fall well below 1%. Only the viscous shear component of the excitation torque shows significant deviations across scales (in particular when 'adding' sharp corners to the device geometry) and only when Froude and Reynolds similarity are obeyed simultaneously, can scaling effects be ruled out for the viscous component. However, as stated throughout the study, the observed deviations do not significantly affect the total load and WEC displacement. Thus, for devices whose dynamics and loads are mainly driven by pressure induced forces, hydrodynamic scaling effects can likely be assumed negligible.

11

Assessment of WEC controllers

Contents

As stated in Chapter 1, to push WECs towards commercial viability, allowing the conversion of energy at a competitive LCoE, EMCSs for WECs are under development [539]. Since the objective of WEC control is to 'drive' the system towards resonance with the incoming wave field, the operational space of the WEC is enhanced (see Figure 1.4), and, if performed correctly, power conversion is optimised.

During the design and evaluation of EMCSs, control engineers rely on numerical modelling, typically based on linear hydrodynamic models, either stemming from linear potential flow theory or data–driven system identification techniques (see [540] for further detail on dynamical models considered in the WEC control literature). In classical control applications, the mathematical models used for control design are often linearised around a desired operational point, according to the process under analysis. The controller is subsequently synthesised to drive the system towards this set point and, thus, in the neighbourhood of this operational point, the linearising assumption is inherently obeyed.

However, the large amplitude motions, induced by a reactive WEC control action, may result in viscous drag, flow separation, vortex shedding, and other non-linear hydrodynamic effects [541]. Thus, in contrast to the aforementioned classical control applications, energy–maximising operating conditions and objectives do not comply with the linearising assumptions in the control design model. The contradiction between the control objective and the associated (usually linear) underlying mathematical model questions if the common practice of designing a controller in a linear design environment can deliver optimal reactive controllers for application in physical, non–linear, operational conditions.

It is shown, in previous chapters, that high–fidelity CFD–based NWTs are useful tools in WEC R&D. Inherently capturing all relevant hydrodynamic non–linearities, these virtual test–beds are particularly valuable for the realistic evaluation of EMCSs for WEC applications, allowing investigation of the contradiction between the control design model assumptions and the resulting operational conditions.

In the literature of CFD–based NWTs for wave energy applications (see Chapter 5), only a few studies (i.e. [327, 417]) are found, investigating the effect of the modelling environment on the performance assessment of EMCSs for WEC applications. This chapter extends the existing literature by evaluating the performance of three different EMCSs, designed with a linear model, stemming from data–driven system identification, in both a linear and non-linear hydrodynamic modelling framework. The different EMCSs, considered in this study, are as follows:

1. resistive (i.e. velocity feedback only) controller,
2. reactive (i.e. displacement and velocity feedback) controller, and
3. the recently published energy-maximising moment-based controller [609, 610].

These control strategies, which are described in detail in Section 11.3, show varying levels of aggressiveness, in terms of control action.

The non–linear hydrodynamic model in the evaluation stage is based on a CFD–based NWT, while the linear hydrodynamic model in the evaluation stage is the same as the model used for control design. For this study, two different moored, heaving, point absorber–type WEC structures are considered. Based on this comprehensive case study, the paper aims to highlight the importance of non–linear hydrodynamic WEC models during the evaluation stage of EMCSs for WEC applications.

11.1 Case study

This section introduces the WEC structures and incident sea state considered throughout this study.

11.1.1 WEC structures

Two different WEC structures are considered, W1 and W2, resembling moored, point absorber–type devices with axisymmetric geometries. The WECs are based on the systems considered during the validation study in Section 7.3 and structure W2 is also considered in Chapter 8. In contrast to the numerical setup documented in Section 7.3, for this study, device motion is constrained to a single DoF, i.e. heave. Furthermore, a PTO system, as in Chapter 8, with a PTO control force f_{u} is implemented. Schematics of the two structures including all relevant dimensions are shown in Figures 7.65 (a) and (b). The physical properties (mass, inertia, etc.) are listed in Table 7.26. Note that, here, the nominal cases with $\pm 0\%$ measurement uncertainty in the inertia and location of the CoM are considered.

11.1.2 Input waves

In this study, an irregular, JONSWAP, sea state with a significant wave height of $H_s = 0.10$m and a peak period of $T_p = 1.94$s is considered, representing realistic, scaled, conditions at the AMETS test site in Bellmullet, Co. Mayo, off the West Coast of Ireland [591] (see Chapter 8). A time trace of the recorded free surface elevation, measured in the CFD–based NWT at the intended WEC location, during a preliminary wave–only simulation is shown in Figure 11.1.

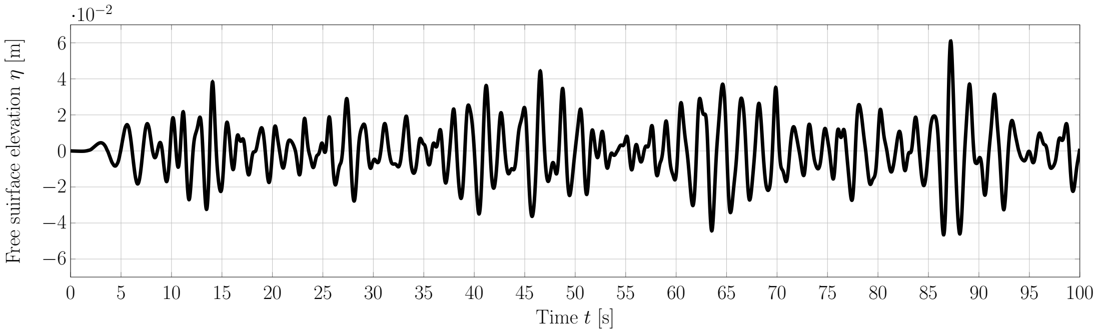

Figure 11.1: Time trace of the incident, irregular wave train measured in the CFD–based NWT at the intended WEC location.

11.2 System identification

As previously discussed, the vast majority of WEC control strategies, proposed to optimise energy absorption from incoming waves, are *model–based*: a mathematical structure, i.e. a model Σ describing the dynamics of the WEC system, is required to compute the corresponding energy–maximising control law. Naturally, there is a limit to the complexity of these mathematical models for which an optimal energy–maximising control solution can be effectively found in real–time, either algebraically or numerically (see, for instance, [540, 611]).

Motivated by the above requirements, linear WEC systems are virtually always used, reflecting both their simplicity and associated computational convenience. Such linear models are often written in terms of a state–space (parametric) representation. A number of methods can be used to obtain a WEC model Σ, ranging from the (pure) use of physical principles (i.e. *white–box* modelling), to determining a mathematical structure and parameters purely from input–output data (i.e. *black–box* modelling) [538].

In this study, the linear control design model for each corresponding WEC system, W1 and W2, is obtained via classical system identification techniques, following a frequency–domain black–box identification methodology[1], i.e. using input–output system identification techniques. In particular, the WEC structure, implemented in the CFD–based NWT, is driven by a finite set of $\underline{N}$ sufficiently exciting [538] input signals, $\mathscr{U} = \{f_i\}_{i=1}^{\underline{N}}$, generating a corresponding set of outputs $\mathscr{Y} = \{y_i\}_{i=1}^{\underline{N}}$ (which, in this case, are heave velocities). Aiming to identify the so-called *force–to–velocity* mapping, i.e. the map $f_i \mapsto y_i$, each input force f_i in the set $\mathscr{U}$ is chosen as an up-chirp signal (see, for instance, [538]), with $\underline{N}$ different amplitudes.

Let (f_i, y_i) denote an input–output pair of signals for the WEC system. Following standard frequency–domain techniques, the so–called empirical transfer function estimate (ETFE) $\underline{H}_i(j\omega)$, can be readily computed, for each input–output pair, using the expression

$$\underline{H}_i(j\omega) = \frac{Y_i(j\omega)}{F_i(j\omega)}, \tag{11.1}$$

with $i \in \{1, 2, ..., \underline{N}\}$, and where Y_i and F_i denote the Fourier transform of y_i and f_i, respectively.

---

[1] Note that frequency–domain methods are based on the superposition principle, i.e. inherently assume linear conditions.

Once the set $\{\underline{H}_i\}_{i=1}^{N}$ is obtained, the average empirical transfer function estimate, $\bar{\underline{H}}$, is computed, aiming to build a low–variance set, used as the input to the frequency–domain identification algorithm [538]. The explicit expression of $\bar{\underline{H}}$ is simply given by:

$$\bar{\underline{H}}(j\omega) = \frac{1}{\underline{N}} \sum_{i=1}^{N} \underline{H}_i(j\omega). \tag{11.2}$$

The final objective of this system identification procedure is to obtain a parametric form approximating the behaviour of the WEC system under analysis, which, in this case, is characterised by the average ETFE (11.2), computed explicitly using the CFD-based NWT. The technique used to achieve such a parametric form is the *moment–matching–based* identification framework presented in [612, 613], which provides an approximation of $\bar{\underline{H}}$ in terms of a state–space representation Σ. In particular, Σ is a deterministic, finite–dimensional system, given by the set of differential equations,

$$\bar{\underline{H}}(j\omega) \approx \Sigma : \begin{cases} \dot{x} = A_{ss}x + B_{ss}(f_{\mathsf{e}} - f_{\mathsf{u}}), \\ \tilde{y} = C_{ss}x = \dot{z}, \end{cases} \tag{11.3}$$

where x is the state–vector of a particular order n_{ss}, f_{e} is the wave excitation force, and the output $\tilde{y} = \dot{z}$ corresponds to the heave velocity of the WEC system. Note that the system identification technique, presented in [612, 613], guarantees preservation of both internal stability (in the Lyapunov sense [614]), and passivity (see, for instance, [615]). The latter is an input–output property which stems from the underlying physical principles associated with the WEC, and is required to guarantee existence and uniqueness of a globally optimal solution for the moment–based energy–maximising controller [609, 610] (presented in Section 11.3.1).

11.3 WEC control

The main objective of a wave energy device is to harvest energy from the incoming wave field.[2] Therefore, the optimal control objective is to maximise the absorbed energy over a time interval $\mathcal{T} = [0, T']$, written in terms of the objective function E_{WEC},

$$E_{\mathsf{WEC}}(f_{\mathsf{u}}) = \frac{1}{T'} \int_{\mathcal{T}} f_{\mathsf{u}}(\tau)\dot{z}(\tau)\, d\tau = \frac{1}{T'} \int_{\mathcal{T}} P_{\mathsf{WEC}}(\tau)\, d\tau, \tag{11.4}$$

where P_{WEC} denotes the instantaneous absorbed power. Note that this energy–maximising control objective does not fit into a traditional (reference tracking) control

---

[2] Note that, here, the incoming wave field is measured in an empty CFD–based NWT, i.e. no device present, at the intended device position. It is then assumed that the incoming wave field is not influenced when placing the device in the CFD–based NWT. This approach bears some inherent errors; however, is common practice.

problem, i.e. the performance objective is strictly related to the maximisation of energy absorption. Consequently, the energy–maximising control objective can be formulated in terms of an optimal control problem (OCP), i.e. find f_{u}, such that

$$\begin{aligned} f_{\text{u}}^{\text{opt}} &= \arg\max_{f_{\text{u}}} \; E_{\text{WEC}}(f_{\text{u}}) \\ &\text{subject to:} \\ &\text{WEC dynamics given by } \Sigma \text{ in (11.3).} \end{aligned} \tag{11.5}$$

Note that, although not considered in this study, state and input constraints can also be directly incorporated to the OCP (11.5) [540].

11.3.1 Moment-based optimal control

The moment-based energy–maximising control strategy presented in [609, 610] provides an efficient and convenient way to parametrise the input and state variables in terms of the system–theoretic concept of *moments* (see [616]). Moments are intrinsically connected to the steady–state response characteristics of the (WEC) system under analysis, allowing for a parametrisation of problem (11.5) in terms of the steady–state response of a suitably defined interconnected system.

In particular, given the harmonic nature of ocean waves [609, 610], the excitation force f_{e} and control input f_{u} are expressed as the solution of a signal generator, $\mathcal{G}$, described by the set of equations

$$\mathcal{G} : \begin{cases} \dot{\xi}_{\mathcal{G}} = S_{\mathcal{G}} \xi_{\mathcal{G}}, \\ f_{\text{e}} = L_{\text{e}} \xi_{\mathcal{G}}, \\ f_{\text{u}} = L_{\text{u}} \xi_{\mathcal{G}}, \end{cases} \tag{11.6}$$

where the dynamic matrix $S_{\mathcal{G}}$ is such that the solution vector $\xi_{\mathcal{G}}$ is composed of harmonic functions of a fundamental frequency ω_0, with $\omega_0 = {}^{2\pi}/_{T'}$. L_{e} and L_{u} are the moment domain equivalents of f_{e} and f_{u}, respectively. In other words, both the excitation force f_{e}, and control input f_{u}, are expressed as a linear superposition of harmonic functions.

With the parametrisation of Equation (11.6), and the state-space WEC system (11.3), the OCP (11.5) can be mapped into a quadratic program (QP), i.e. the energy–maximising control input $f_{\text{u}}^{\text{opt}}$ can be computed as the unique global solution of a *concave* quadratic optimisation problem in L_u. Figure 11.2 shows a block–diagram of the feedforward control architecture.

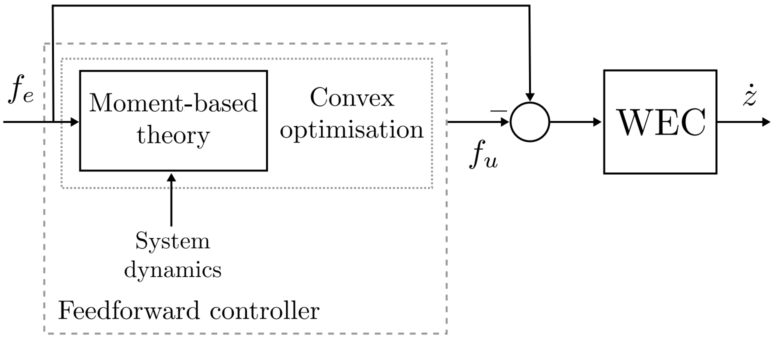

Figure 11.2: Moment–based control structure.

11.3.2 Reactive and resistive feedback controllers

In addition to the moment–based controller, less 'aggressive' EMCSs, i.e. reactive and resistive feedback controllers, are considered as reference cases. Both reactive and resistive strategies are varieties of 'traditional' output feedback WEC controllers (see, for instance, [615]), as detailed in the following. For the reactive control case, the PTO force follows from an output feedback technique, involving both displacement and velocity of the WEC system, i.e.

$$f_{\mathsf{u}} = k_{\mathsf{u},1} z + b_{\mathsf{u},1} \dot{z}, \tag{11.7}$$

where the matrix $\mathscr{H}_1 = [k_{\mathsf{u}} \; b_{\mathsf{u}}]$ is the optimal reactive feedback gain.
Similarly, for the resistive control case, the PTO force follows from an output feedback technique, but only involving the velocity of the WEC system, i.e.

$$f_{\mathsf{u}} = b_{\mathsf{u},2} \dot{z}, \tag{11.8}$$

where the scalar value $\mathscr{H}_2 = b_{\mathsf{u},2}$ is the optimal resistive feedback gain.
Both optimal gains, i.e. $\mathscr{H}_1$ and $\mathscr{H}_2$, are commonly computed following exhaustive search procedures, explicitly using the dynamical model obtained via system identification techniques, i.e. system Σ in Equation (11.3). A block-diagram of both reactive and resistive control strategies, is illustrated in Figures 11.3 (a) and (b), respectively.

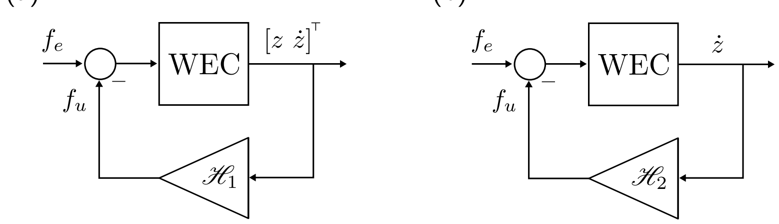

Figure 11.3: (a) Reactive and (b) resistive control structures.

11.4 Test cases

The present study is divided into three main steps, requiring specific sets of test cases. The steps are:

1. System identification and control design,
2. model validation, and
3. performance evaluation.

The specific test cases are detailed in the following.

11.4.1 System identification and control design

Initially, system identification chirp test cases are simulated to provide the required data for the system identification procedure outlined in Section 11.2. Subsequently, wave excitation force tests are required to produce the required data for the control synthesis, outlined in Section 11.3.

Multi–frequency forced oscillation

For the up-chirp tests, each element f_i in the set of input forces $\mathscr{U}$ (see Section 11.2) is defined as a linear frequency sweep in the range $[0.1,\, 60.0]$ rad s^{-1}, with 3 different amplitudes, i.e. $\underline{N} = 3$ in Equation (11.2), i.e. $10.5\,$N, $12.55\,$N, and $15\,$N (see Figure 11.4). Note that several force amplitudes are considered to cater for the computation of the average empirical transfer function estimate $\bar{\underline{H}}$, aiming to build a low–variance set, used as the input to the frequency-domain identification algorithm. Each of these forces is fed to the system through the motion solver of the CFD–based NWT (see Section 11.5). The input forces f_i, and the post–processed device motions y_i, are then directly used within the system identification procedure, described in Section 11.2.

Wave excitation force tests

As stated in Section 11.3, with the identified linear WEC model, the three EMCSs can be synthesised under the assumption of perfect knowledge of the wave excitation force. To acquire the required wave excitation force signals for controller synthesis, wave excitation force tests are simulated, where the WEC structures are held fixed in their equilibrium position and are exposed to the incident irregular wave train depicted in Figure 11.1. The wave excitation force is extracted from the numerical data in a post–processing step.

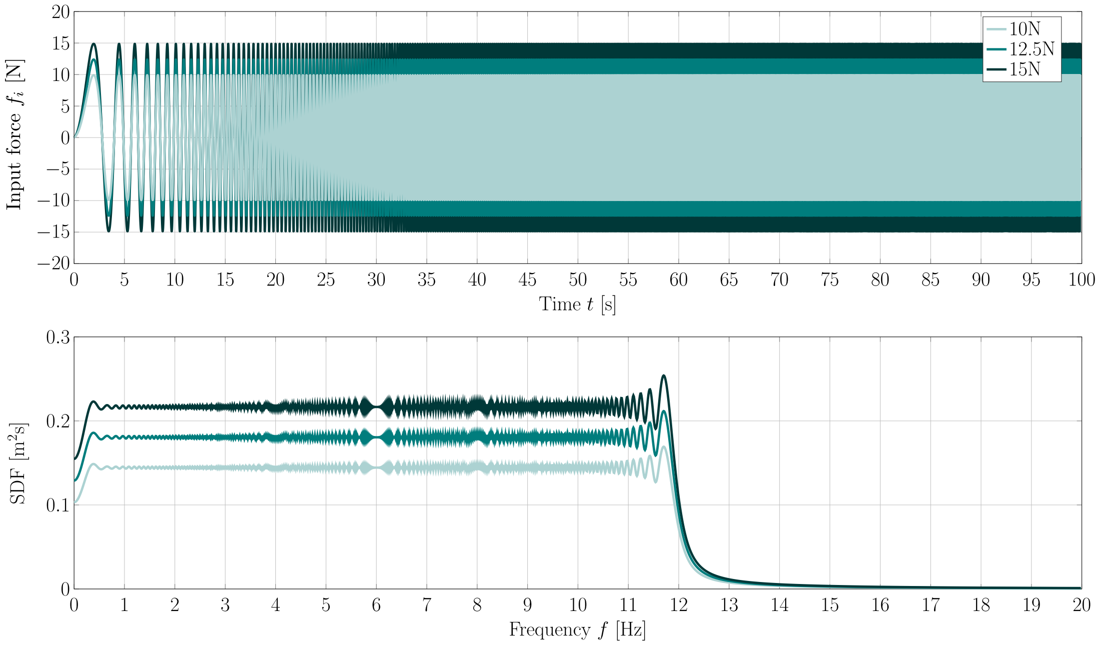

Figure 11.4: Time traces and spectral density distributions of the input forces f_i for the multi–frequency forced oscillation.

11.4.2 Model validation

To ensure and assess the quality of the identified linear WEC models, validation test cases are considered. The motion of the WEC structures, exposed to the linear irregular wave train, is simulated in the CFD–based and linear modelling framework under *un*controlled conditions. In such conditions, the two models (linear and CFD–based) are expected to deliver similar results, thereby ensuring a fair comparison during the controller evaluation step.

11.4.3 Controller performance evaluation

Finally, in the performance evaluation step, the motion of the WEC structures, exposed to the irregular wave train, is simulated in the CFD–based and linear modelling framework under controlled conditions, using the three different EMCSs detailed in Section 11.3. Comparing time traces of the WEC motion and control force, as well as absorbed energy, allows a comprehensive evaluation of the controller performance, predicted in both the linear and CFD–based modelling frameworks.

11.5 Numerical wave tank

For this study, the numerical wave tank in Chapter 8 for the mesh morphing method is directly adapted (see Figure 8.3). To avoid numerical instability and allow the use of the mesh morphing method, instead of the computationally more costly overset grid method, the outer radius in the mesh morphing method is expanded to 3m. Furthermore, the spatial discretisation is adapted to comply with the required 10CPH cell size in the vertical direction for the slightly smaller wave height in this study (0.10m instead of 0.12m).

11.6 Results and discussion

This section presents and discusses the results of the three different steps: System identification and control design, model validation, and controller evaluation.

11.6.1 System identification and control design

Using the data generated with the CFD–based NWT, i.e. the set of chirp inputs $\mathscr{U} = \{f_i\}_{i=1}^{3}$, and their corresponding outputs (velocities) $\mathscr{Y} = \{y_i\}_{i=1}^{3}$ (see Figure 11.5), the system identification procedure, described in Section 11.2, can be readily considered, to compute a mathematical (parametric) representation for each WEC system W1 and W2. In particular, two 8th-order[3] nominal linear models, Σ_1 and Σ_2 (as in Equation (11.3)), are obtained for the force–to–velocity mappings associated with W1 and W2, respectively. The frequency responses of Σ_1 and Σ_2, along with each corresponding average ETFE $\underline{\bar{H}}$ (see Equation (11.2)), are shown in the Bode plots in Figures 11.6 (a) and (b), respectively.

With the identified linear WEC model, the three EMCSs are synthesised under the assumption of perfect knowledge of the wave excitation force. Optimal control parameters (stiffness and damping) for the feedback controllers (see Table 11.1), as well as optimal control force time traces for the feedforward (moment–based) controller (see Figure 11.7) are now determined based on the identified control design models.

Table 11.1: Optimal stiffness and damping coefficients of the feedback controller

WEC structure	**Reactive**		**Resistive**
	$k_{\text{u},1}$ [N m^{-1}]	$b_{\text{u},1}$ [N s m^{-1}]	$b_{\text{u},2}$ [N s m^{-1}]
W1	-1318	64	23
W2	-1385	33	59

---

[3] The expression '8th-order' refers to $n_{ss} = 8$.

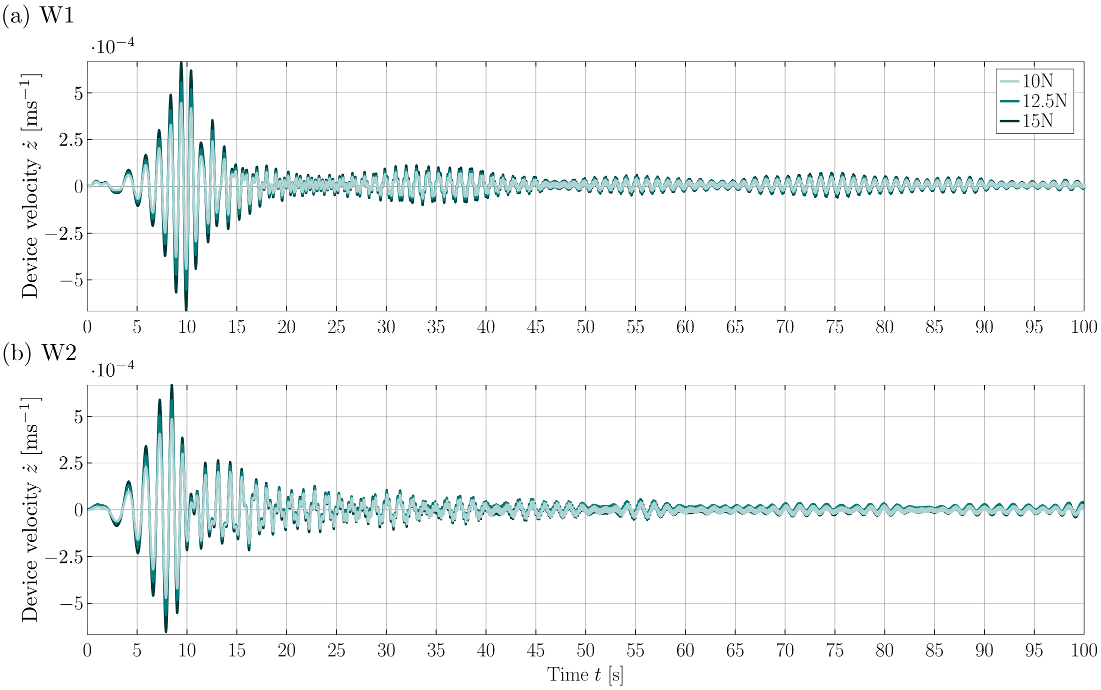

Figure 11.5: Time traces of the the WEC velocity $\dot{z}$ of (a) W1 and (b) W2, for the multi–frequency (chirp) forced oscillation test.

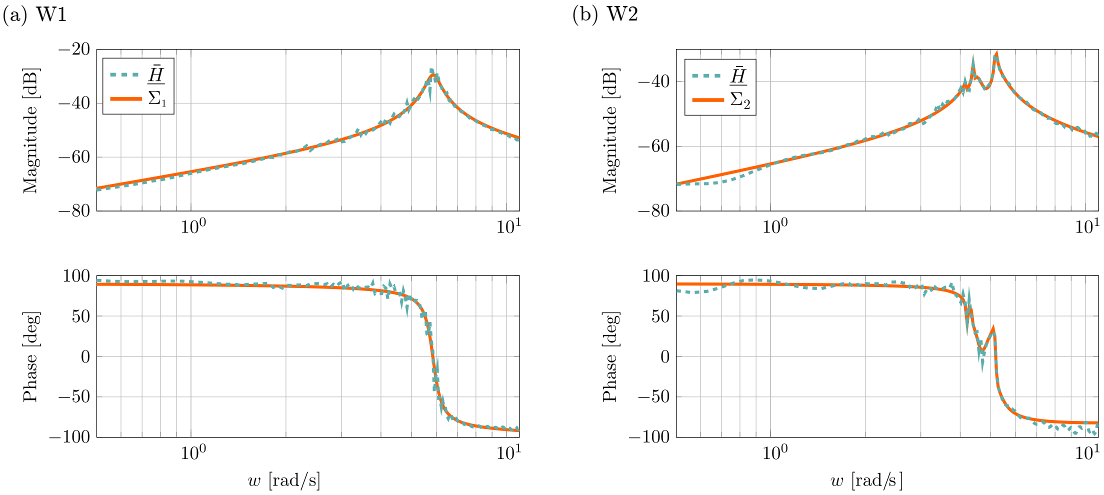

Figure 11.6: Bode plot for the force-to-velocity frequency response associated with structure (a) W1 and (b) W2, including the average ETFE and the approximating system Σ_1 and Σ_2.

11.6.2 Model validation

To ensure and assess the quality of the identified linear WEC models, simulations under uncontrolled conditions are performed in the CFD–based and linear modelling framework.

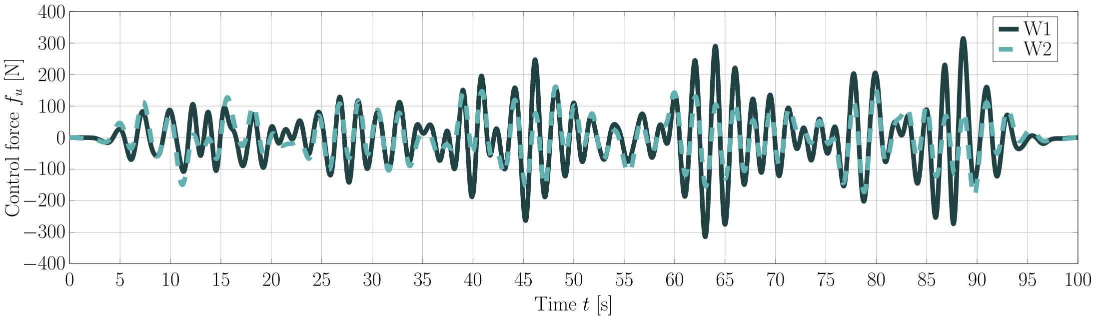

Figure 11.7: Time trace of the control force f_u for the feedforward controller for WEC structures W1 and W2.

W1

Figure 11.8 shows the time traces of the (a) WEC displacement and (b) velocity for W1 for the case of an uncontrolled device from the CFD–based and linear modelling framework. Excellent agreement between the different models is achieved with a nRMSD, following Equation (8.3), of 1.4% and 1.6% for the device displacement and velocity, respectively. For the calculation of the nRMSD following Equation (8.3), here, ϖ denotes the quantity from the CFD–based NWT, while $\hat{\varpi}$ is the corresponding quantity from the linear model. Normalisation in Equation (8.3) is achieved by $\mathcal{N} = \max(\varpi) + |\min(\varpi)|$.

W2

Figure 11.9 shows the time traces of the (a) WEC displacement and (b) velocity for W2 for the case of an uncontrolled device from the CFD–based and linear modelling framework. As in the case of W1, excellent agreement between the different models is achieved with a nRMSD of 2.4% and 2.7% for the device displacement and velocity, respectively.

Overall, the results of the validation step highlight the accuracy of the identified, linear WEC models (under the specified uncontrolled conditions), thereby forming the basis of a fair comparison in the subsequent controller evaluation step.

(a) Displacement

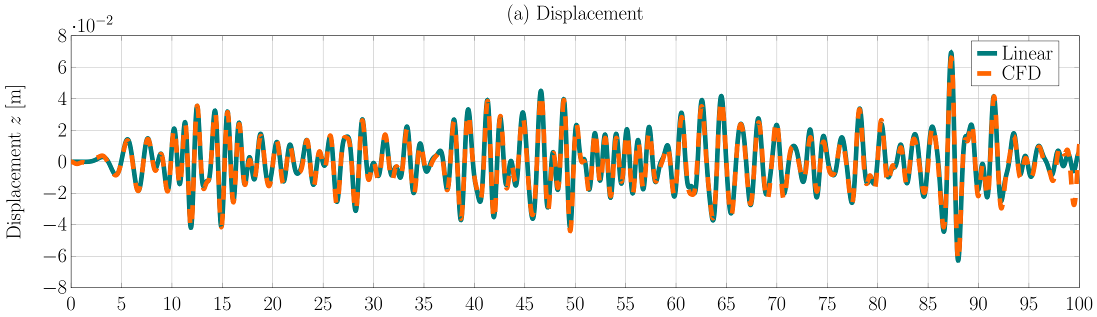

(b) Velocity

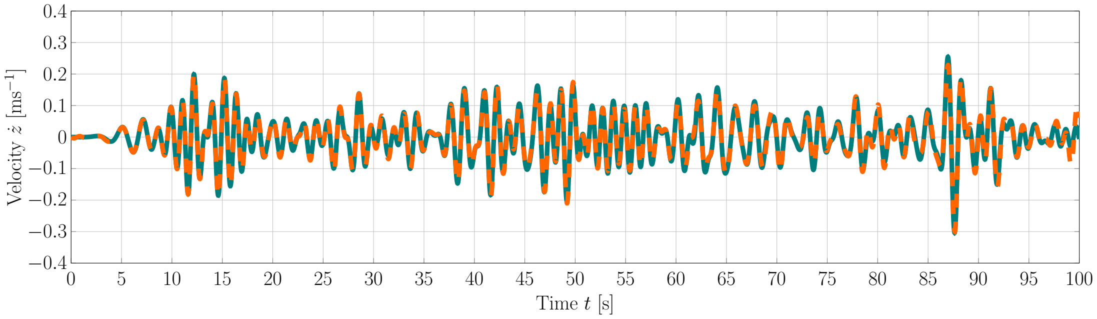

Figure 11.8: Time traces of the WEC (a) displacement and (b) velocity for W1.

(a) Displacement

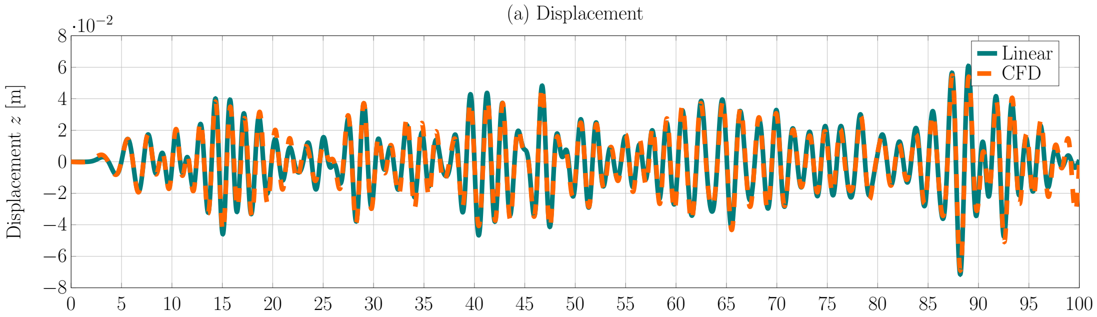

(b) Velocity

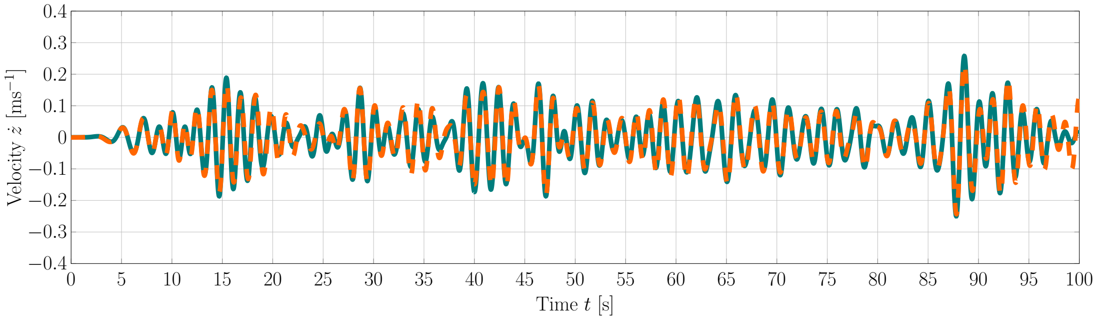

Figure 11.9: Time trace of the WEC (a) displacement and (b) velocity for W2.

11.6.3 Controller performance evaluation

In the performance evaluation step, the results of the device displacement z and velocity $\dot{z}$ data, as well as the control force f_u and the instantaneous power P_WEC, are compared between the CFD–based and linear modelling frameworks. Furthermore, the cumulative absorbed energy, $\mathcal{E}$, and the deviation rate of the absorbed energy, $\mathscr{D}$, following Equation (11.9), are compared.

$$\mathscr{D} = \left(1 - \frac{E_\mathsf{WEC,CFD}}{E_\mathsf{WEC,Lin}}\right) \cdot 100\% \,, \tag{11.9}$$

where E_CFD follows:

$$E_\mathsf{WEC,CFD} = \frac{1}{t_\mathsf{s}} \int_{t_\mathsf{s}} P_\mathsf{WEC,CFD} \, \mathsf{d}t_\mathsf{s} \,, \tag{11.10}$$

and

$$E_\mathsf{WEC,Lin} = \frac{1}{t_\mathsf{s}} \int_{t_\mathsf{s}} P_\mathsf{WEC,Lin} \, \mathsf{d}t_\mathsf{s} \,, \tag{11.11}$$

where the simulated time $t_\mathsf{s} = 100$s. Consequently, a deviation rate $> 0\%$ indicates over–prediction of the absorbed energy with the linear WEC model, thereby highlighting the importance of an accurate EMCS evaluation framework.

W1

Figures 11.10 – 11.12 show the time traces of the device displacement and velocity data, the control force, and the instantaneous power of W1 for the three different EMCSs: moment–based feedforward, reactive feedback, and resistive feedback, respectively. It can readily be seen that all quantities follow the same trend: more aggressive controllers increase the magnitude of displacement, velocity, control force, and instantaneous power. Furthermore, it can clearly be seen that the moment–based feedforward and reactive feedback EMCS generate, at times, negative instantaneous power, which is a characteristic of reactive control. The instantaneous power for the resistive feedback controller is continuously positive, as expected.

For a quantitative assessment of the difference between the linear and CFD–based model predictions for the different EMCSs, Table 11.2 lists the nRMSD for the device displacement and velocity, the control force, and the instantaneous power. Table 11.2 also contains the values of $\mathscr{D}$.

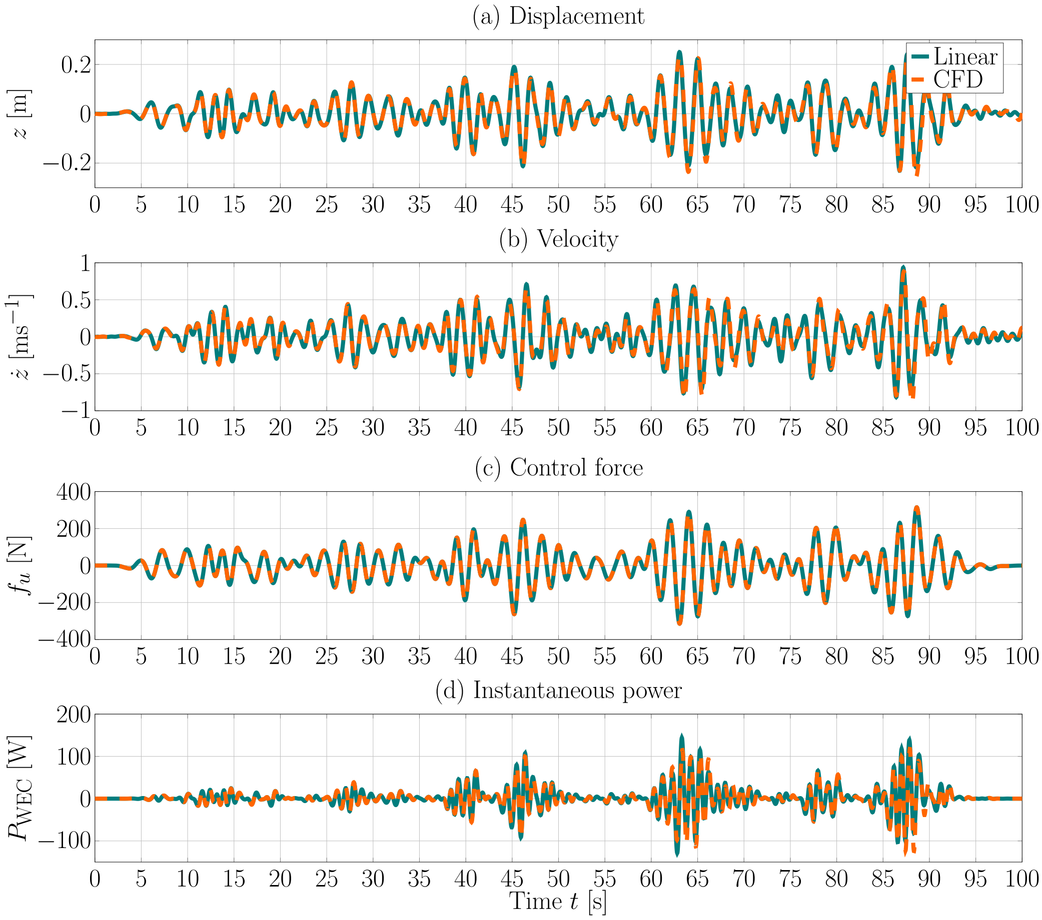

Figure 11.10: Time trace of the device (a) displacement, (b) velocity, (c) control force, and (d) instantaneous power for W1 with the moment–based feedforward controller.

For the resistive feedback controller, relatively small values, of the order of 2%, are computed for the nRMSDs for the displacement, velocity, control force, and instantaneous power, indicating relatively linear device behaviour. These values of the nRMSDs increase relative consistently (to $\sim 5\%$) for all the considered data for the reactive feedback controller. The increased nRMSDs suggest a stronger influence of hydrodynamic non–linearities due to the enhanced WEC motion. Interestingly, for the most aggressive controller in this study, the moment–based feedforward EMCS, the nRMSDs lie between the calculated values for the resistive and reactive feedback controller ($\sim$ 3%)[4].

---

[4] Note that the nRMSD for the control force is 0% since the exact same control force is applied to the system in the linear and CFD–based modelling framework.

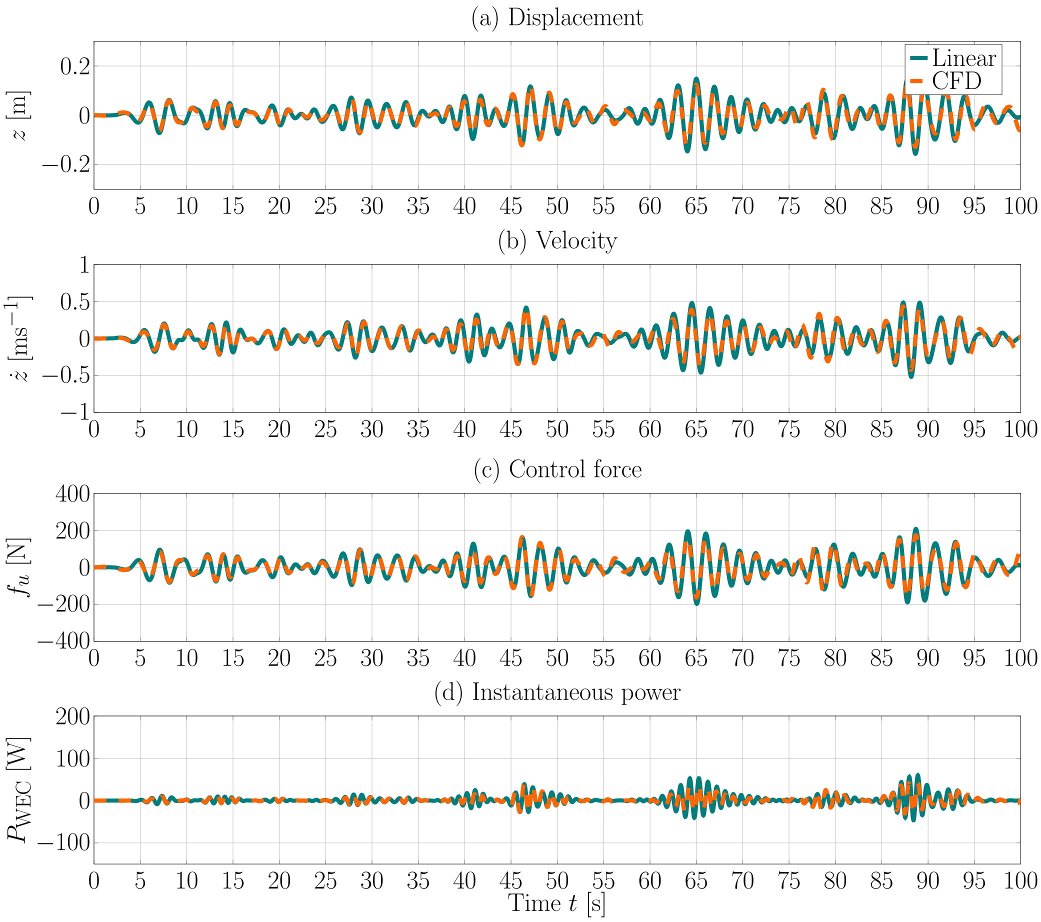

Figure 11.11: Time trace of the device (a) displacement, (b) velocity, (c) control force, and (d) instantaneous power for W1 with the reactive feedback controller.

The fact that the reactive feedback controller presents the highest nRMSD value, despite not being the most aggressive controller, is simply related to its feedback nature: both displacement and velocity, computed from the fully nonlinear CFD-NWT, are directly utilised to modify the internal dynamics of the WEC in a closed-loop fashion. This, in turn, generates a more pronounced difference with respect to its fully linear counterpart, specifically in terms of time traces.

Table 11.2: Deviation between the linear and CFD model for the controller evaluation of W1

	Feedback Resistive	**Feedback Reactive**	**Feedforward Moment–based**
Displacement z	1.4%	5.0%	2.1%
Velocity $\dot{z}$	1.8%	5.2%	2.8%
Control force f_{u}	1.8%	5.0%	0%
Instantaneous power P_{WEC}	1.7%	6.3%	3.0%
$\mathscr{D}$	1.7%	5.2%	22.4%

(a) Displacement

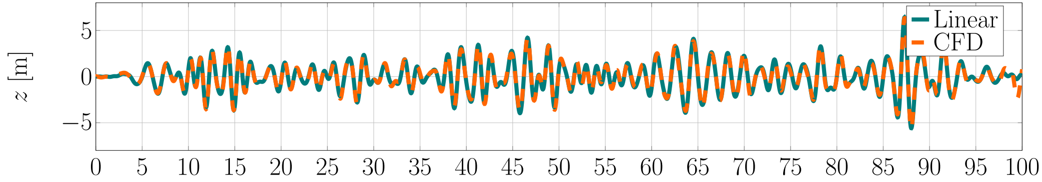

(b) Velocity

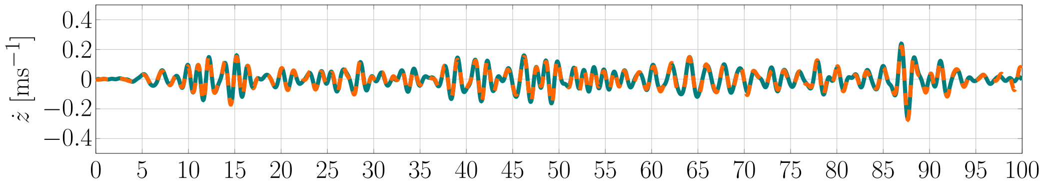

(c) Control force

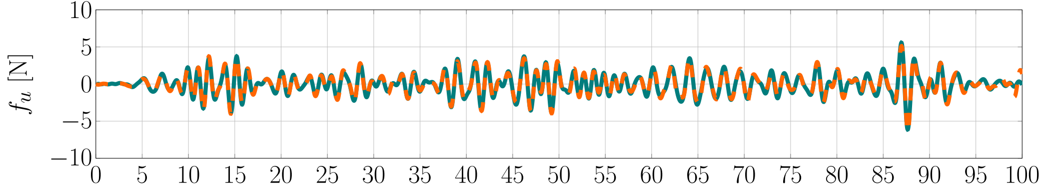

(d) Instantaneous power

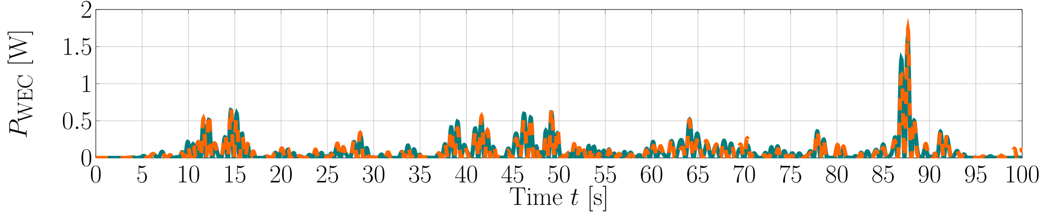

Figure 11.12: Time trace of the device (a) displacement, (b) velocity, (c) control force, and (d) instantaneous power for W1 with the resistive feedback controller.

Regarding $\mathscr{D}$, for the resistive case, the realistic performance of the EMCS in the CFD–based model, by means of the absorbed energy, is evaluated to be 98.3% of the predicted performance from the linear hydrodynamic model (i.e. $\mathscr{D} = 1.7\%$). For the reactive feedback controller $\mathscr{D} = 5.2\%$, again indicating that the accuracy of the linear model deteriorates under more aggressive control action. The trend of $\mathscr{D}$ is consistent with the findings for the nRMSDs and is indirectly visualised in Figure 11.13, showing the time trace of the cumulative absorbed energy. Finally, for the reactive feedforward controller, a deviation rate of 22.4% is calculated, thereby following the trend of reduced accuracy of the linear model under increased control action. Again, the observed deviation between the linear and the CFD–based model is visualised in Figure 11.13. However, as stated in the previous paragraph, relatively small values of the nRMSDs are calculated for the moment–based feedforward controller.

By way of example, Figure 11.14 shows a close up of the time traces in Figure 11.10, between 58s and 72s. In this time window, relatively large (compared to the preceding and succeeding part of the time trace) deviation in the device velocity between

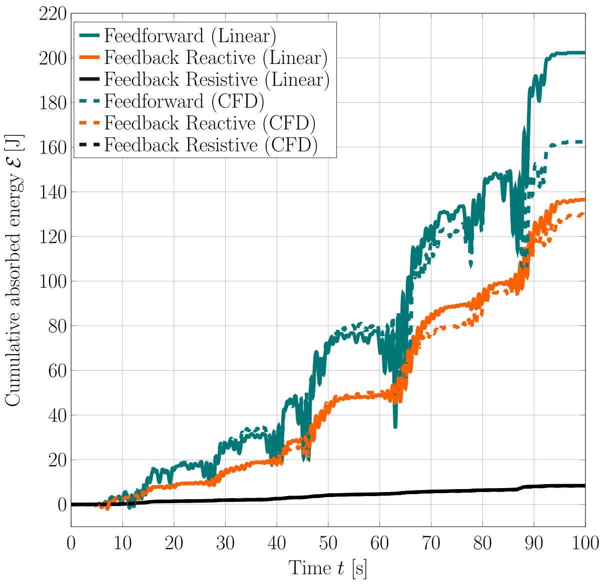

Figure 11.13: Time trace of the cumulative absorbed energy for W1 with the three different EMCSs.

the linear and CFD–based model can be observed, specifically with respect to the instantaneous phase synchronisation between signals, which is known to be a key factor in the energy-maximising optimality principle [34]. Given that the control force is the same in both models, the deviations in the simulated velocity are the sole cause for the deviations in the instantaneous power. Even though the deviations in the instantaneous power appear, qualitatively, to be relatively moderate (as suggested by the nRMSD), cumulatively, such deviations have, as shown here, a potentially significant influence on the performance assessment of EMCSs. Thus, the results for the reactive feedforward controller highlight the importance of a complete analysis of all data influencing the performance assessment of an EMCS.

W2

For W2, the values of the nRMSD for the device displacement, velocity, control force, and instantaneous power, as well as the cumulative absorbed energy, and the deviation rate of the absorbed energy follow the same trend as previously observed for W1. Table 11.3 lists the nRMSDs of the relevant quantities between the linear and CFD–based model for the three different EMCSs, as well as the deviation rate of the absorbed energy. Figure 11.15 shows the corresponding time traces of the cumulative absorbed energy.

For the resistive feedback controller, the values of the nRMSDs, as well as $\mathscr{D}$, are almost identical, compared with W1, highlighting the linearity of this case even when a structure whose geometry, i.e. sharp edges, is likely to induce non–linear hydrodynamic

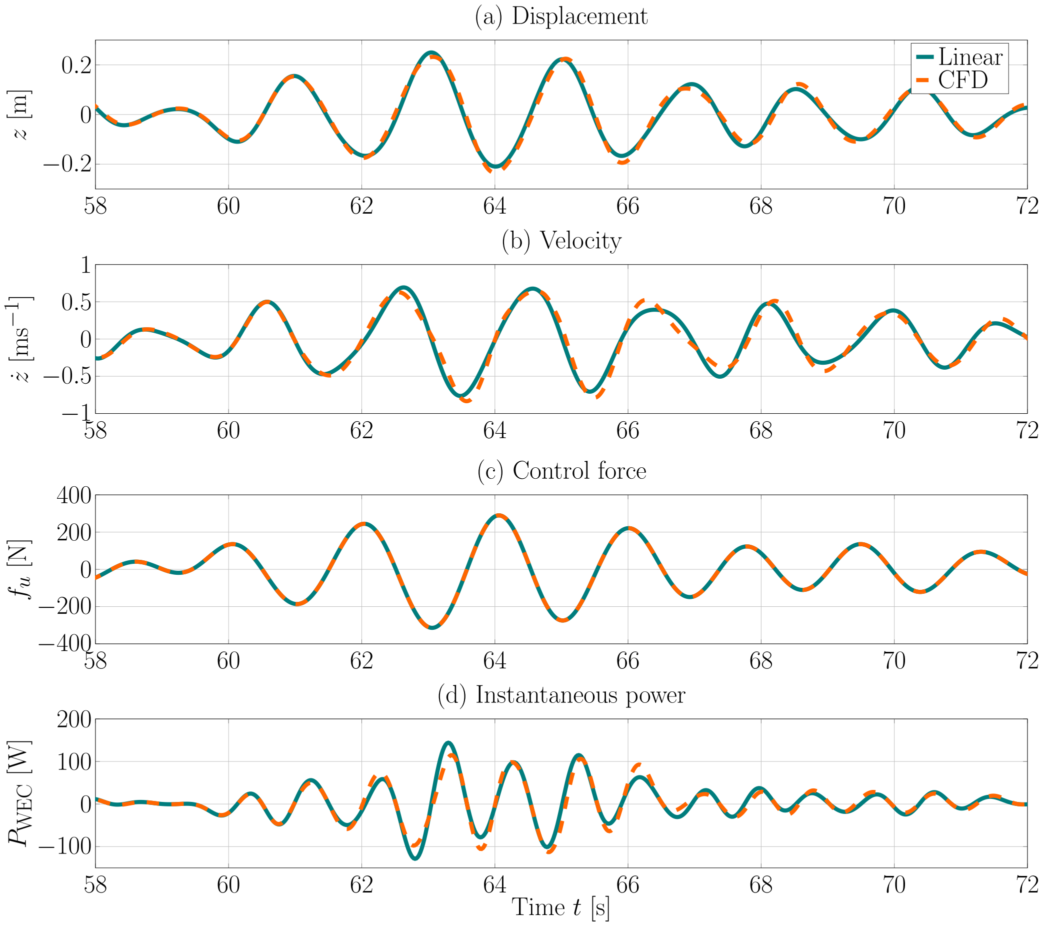

Figure 11.14: Close up of the time trace of the device (a) displacement, (b) velocity, (c) control force, and (d) instantaneous power for W1 with the moment–based feedforward controller.

effects, such as vortex shedding, are considered. The effects of geometry–induced non–linearities are clearly highlighted by the deviation rate of the absorbed energy $\mathscr{D}$ for the cases of more aggressive control action. For the case of the reactive feedback controller, only 57.4% of the absorbed energy, predicted by the linear model, are absorbed in the CFD–model (i.e. $\mathscr{D} = 42.6\%$). An even further reduction ($\mathscr{D} = 52.8\%$) can be calculated for the moment–based feedforward controller. Given the similarity of the test cases (i.e. incident sea state), the structural dimensions, and the excellent validation of the linear model under uncontrolled conditions for both WEC structures, the observed effects can be confidently put down to shape–induced viscous non–linearities.

Table 11.3: Deviation between the linear and CFD–based model for the controller evaluation of W2

	Feedback Resistive	Feedback Reactive	Feedforward Moment–based
Displacement z	1.6%	5.7%	2.7%
Velocity $\dot{z}$	1.8%	5.4%	3.7%
Control force f_u	1.9%	5.7%	0.0%
Instantaneous power P_WEC	2.6%	6.9%	3.1%
$\mathscr{D}$	1.9%	42.6%	52.8%

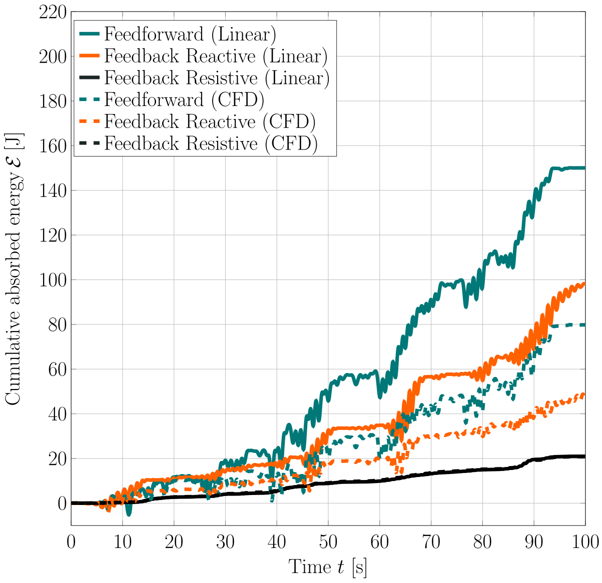

Figure 11.15: Time trace of the cumulative absorbed energy for W2 with the three different EMCSs.

11.7 Concluding remarks

This chapter investigates the influence of different modelling frameworks (linear and CFD–based) on the performance assessment of EMCSs. Considering three different controllers of varying aggressiveness, implemented in two different WEC structures, the presented results allow a comprehensive assessment of the effects of the fidelity–imbalance between the design and evaluation framework of EMCSs.

Based on the results presented in this chapter, it can be stated that the performance evaluation of linear reactive controllers requires a high–fidelity evaluation framework for realistic performance estimation. Power production estimation is significantly over–predicted by the linear simulation model when more aggressive controllers are employed. Since linear models will likely be the first choice for control design, it is important to evaluate the performance of the designed controller under realistic, non–linear conditions.

Finally, it should be noted that the linear hydrodynamic models used within this study are based on system identification, thereby are likely to be more representative of the average system dynamics compared to linear models based on BEM–based potential flow solutions. Hence, the deterioration in the performance of BEM–based models compared to CFD–based models may be even more severe than the deterioration observed in this study. Thus, for controllers designed on BEM–based models, a rigorous evaluation of the performance under realistic conditions is vital.

12

Conclusions and outlook

Contents

12.1 Conclusions

Pushing WECs towards commercial viability via extensive R&D is required to transform wave energy from an untapped energy source to a significant contributor to the global renewable energy mix. During this R&D process, numerical modelling is an integral part. Being available at different levels of fidelity and different associated levels of computational cost (see Figure 1.3), the relative strengths of different numerical models can be leveraged at different stages of the WEC R&D process (see Chapters 1 and 2). This thesis focusses on the high–fidelity end of the numerical modelling spectrum by means of CFD–based NWTs (see Chapter 4). The literature review in Chapter 5 shows that CFD–based NWTs are employed for various WEC applications, including different WEC sub–system models of varying fidelity. However, the literature review also reveals knowledge gaps of which some are filled in Chapters 6 – 11 of this thesis. In particular, this thesis investigates the aspects of numerical wave generation and absorption, model validation, dynamic mesh motion methods, the flow field around WECs, scaling effects, and the assessment of WEC controllers. From the presented work, the following conclusions can be drawn for the individual aspects:

- **Numerical wave makers:** For the generation and absorption of ocean waves (see Chapter 3), different numerical wave makers are available (see Chapter 4) and used (see Chapter 5) within CFD–based NWTs. Extending the set of available numerical wave makers in OpenFOAM, Chapter 6 presents the efficient application of an impulse source wave maker including a calibration method for the tuning of the wave maker input. While the proposed calibration procedure ensures that the target wave is created at the desired position in space and time, the formulation of the source term enables a simple implementation in OpenFOAM's VOF framework, showing potential to be extended to other solvers, as shown in [SMF].

  Tackling the assessment of numerical wave makers, Chapter 6 furthermore presents a suite of methodologies and metrics for the quantitative assessment of the available numerical wave makers, aiding in the choice of 'the best' wave maker for a given problem. While the presented illustrative example proves the applicability of the proposed metrics and methodologies to a variety of wave makers and wave conditions, the example also highlights the complexity of a general and fair comparison of different numerical wave makers. Independently investigating implementations for wave generation and absorption, the results ultimately suggest a computationally efficient, flexible, and relatively accurate numerical wave maker to be composed of a static boundary method for wave generation and a numerical beach implementation for wave absorption.

- **Model validation:** To ensure accuracy of a CFD–based NWT, validation of the numerical setup is required. Employing data from experimental test campaigns as reference, Chapter 7 presents the successful validation of numerical models of four different WECs, i.e. a 1/5th and 1/20th scale Wavestar device, as well as two different taut–moored point absorber–type WECs. From the presented results, it can be concluded that the exact numerical replication of a physical model is a challenging task, requiring often unavailable properties of the physical model, such as mechanical friction. However, it remains up to the user to define the required level of accuracy of the numerical model, relative to the chosen reference. Relative deviations between the reference and the referent model of the order of 10% are commonly found in conjunction with the declaration of model validity in the WEC literature (see Chapter 5). Such orders of errors are also achieved throughout the validation studies presented in this thesis.

- **Evaluation of the overset grid methods:** As for the numerical wave makers, different dynamic mesh motion methods are available (see Chapter 4) and used (see Chapter 5) within CFD–based NWTs. While mesh morphing is the classical approach (in particular in OpenFOAM–based NWTs), recently, the overset grid method has gained more attraction. In Chapter 8, the performance of the overset grid method is evaluated by comparing results of single– and multi–phase problems, simulated using the overset grid against simulations using the mesh morphing method. It can be concluded that the overset grid methods, available in OpenFOAM, are equivalent to the mesh morphing method regarding accuracy. However, given the significant increase in run–time for the overset grid method, CFD users are advised to assess beforehand, if the mesh morphing method exceeds the limits of numerical stability, to avoid unnecessary computational cost.

- **Flow field around WECs:** The analysis of the flow field around WEC structures is considered in Chapter 9 of this thesis, based on two test cases. Modelling forced oscillation tests for a heave plate in WEC applications, it can be concluded that, even under the assumption of laminar flow conditions, the numerical results of the hydrodynamic forces and the characteristic flow features are captured reasonably well, compared to the experimental reference. Thereby, the results raise the question to what extend turbulence effects, by means of turbulence modelling, are relevant in CFD–based NWT WEC experiments.

  To that end, two representative WEC structures are considered for the analysis of the effect of turbulence modelling on the free surface elevation, wave excitation force, and device dynamics. While indicating a dependency of the considered quantities on the inclusion/exclusion of turbulence modelling, no final conclusions on the ‘correct’ turbulence model can be drawn from the presented results. The study rather suggests the need of a more in–depth investigation, including dedicated, high quality, validation data (including e.g. pressure measurements and/or PIV data), to answer the question whether or not turbulence effects are significant for CFD–based NWT experiments (see Section 12.2).

- **Analysis of scaling effects:** Exploiting the ability of a CFD–based NWT to achieve Froude and Reynolds similarity by tuning the properties of the involved fluids, Chapter 10 investigates the hydrodynamic scaling effects based on the validated numerical model of the Wavestar WEC. The results of the considered (incremental) test cases allow the conclusion that the specific device (and likely other devices with similar operational DoFs and pressure driven dynamics) is independent of hydrodynamic scaling effects.

This observation has implications for the design of physical wave tank tests. Since the well–known problem of correct Froude *and* Reynolds scaling in physical wave tanks does not seem to affect the overall device dynamics, scaling effects in physical wave tanks are mainly driven by mechanical artefacts, such are exaggerated friction in bearings or PTO components. Thus, to avoid scaling effects in physical tests, effort should be made to reduce such mechanical artefacts.

- **Assessment of WEC controllers:** While, in classical control applications, the control design model is linearised around a desired set point of the considered system, EMCSs for WEC applications drive the system away from the linearising assumptions (small wave height and body motion) of the controller design model. However, due to their computational efficiency, linear models, either based on SID techniques or BEM–based potential flow solutions, are preferred during control design.

  Chapter 11 aims to answer the question if linear reactive controller are limited by inherently violating the underlying assumptions within the (linear) design model through the control objective function. Based on the results the answer to this question is: Yes, linear reactive controllers are inherently limited by the WEC control paradox, such that power production estimation is significantly over–predicted by the control design model when more aggressive controllers are employed.

Overall, this thesis highlights the potential of high–fidelity numerical modelling by means of CFD–based NWT experiments for WEC R&D (Chapters 7, 8, 10, and 11) but also shows the complexity of this modelling framework (Chapters 2, 4, 6, 7, and 9). With the additional knowledge regarding high–fidelity WEC modelling, gained through the work presented in this thesis, together with advances in the numerical modelling of WEC sub–systems in, e.g., [379] and [617], [JPA], steps towards truly high–fidelity, wave–to–wire, WEC models can be taken to support the development and commercialisation of WECs by means of, for instance:

- Design–of–experiment methodologies,
- Generation of benchmark data for the assessment of lower–fidelity NWTs,
- Generation of input data for data–driven system identification procedures,
- Evaluation of the WEC performance under realistic conditions.

However, future work is still required to develop such a high–fidelity, wave–to–wire, WEC model.

12.2 Future work

Based on the findings in Chapters 6 – 11, the following can be identified as pertinent future work to enhance the capabilities of CFD–based NWTs for WEC applications and, furthermore, increase confidence in such high–fidelity modelling frameworks:

- **Impulse source wave maker:** To further enhance the performance of the presented impulse source wave maker, the possibility of using non-constant acceleration inputs along the water column should be assessed. Such non-constant inputs can be realised by either imposing a depth–varying acceleration profile within a single impulse source or by implementation numerous impulse sources along the water column, which can be individually calibrated. Furthermore, a non–linear calibration method is desired to extend the wave maker's range of applicability.
- **Model validation:** To increase confidence in CFD–based NWT experiments and truly exploit the capabilities of a high–fidelity modelling framework, more general validation studies should be performed, aiming at an independent analysis of relevant aspects of high–fidelity WEC modelling, such as turbulence effects (see below). Such studies require dedicated high–fidelity reference data sets, including e.g. PIV data (see [SMH]).
- **Turbulence modelling:** To gain more confidence in the capabilities of available turbulence models and address the question as to whether turbulence effects are significant for WEC applications, high–quality reference data are required in conjunction with comprehensive numerical analysis. It should be noted here that the acquisition of dedicated (experimental) validation data, as well as the numerical analysis of turbulence effects within CFD–based NWTs is challenging in itself, due to the vast number of influential parameters, e.g. device shape, scale, as well as operational principle and conditions.

  As a first step, follow–up studies can be deduced from the presented studies in Chapter 9. Including turbulence models in the numerical model of the heave plate will help to assess the model capabilities for $KC > 1$. Regarding the modelling of point absorber–type WECs, including regular wave cases and more recent turbulence models (e.g. [568, 569, 618]) will help to understand cause and effect of turbulence models on the WEC dynamics.
- **Holistic WEC modelling:** To extend holistic modelling capabilities, the study in [JPA] should be extended, based on the knowledge gained throughout the chapters of this thesis. Applying the non–linear PTO model in [JPA] in conjunction with sophisticated EMCSs, used in Chapter 11, to a validated CFD–based hydrodynamic model of a full scale WEC device, such as the Wavestar, allows WEC performance assessment in a fully non–linear wave–to–wire modelling framework.

References

[1] G. Mork, S. Barstow, A. Kabuth, and M.T. Pontes. Assessing the global wave energy potential. In *Proceedings of the 28th International Conference on Ocean, Offshore and Arctic Engineering (OMAE), Shanghai, China*, pages 447–454, 2010.

[2] Wave Energy Scotland. *Direct contact dielectric elastomer*, 2020. `https://www.waveenergyscotland.co.uk/programmes/details/power-take-off/direct-contact-dielectric-elastomer/`, Last accessed 03/03/2020.

[3] Our World in Data. *Average temperature anomaly, Global*, 2020. `https://ourworldindata.org/grapher/temperature-anomaly`, Last accessed 01/03/2020.

[4] C. Kost, S. Shammugam, V. Jülch, H. Nguyen, and T. Schlegl. Stromgestehungskosten erneuerbare energien. Technical report, Fraunhofer-Institut für Solare Energiesysteme ISE, 2018.

[5] Sea Power Ltd. *Cost of energy*, 2020. `http://www.seapower.ie/cost-of-energy/`, Last accessed 01/03/2020.

[6] J. C. Mankins. Technology readiness levels. Technical report, Office of Space Access and Technology, NASA, 1995.

[7] K. Tanizawa and S. Naito. A study on parametric roll motions by fully nonlinear numerical wave tank. In *Proceedings of the 7th International Offshore and Polar Engineering Conference, Honolulu, HI, USA*, 1997.

[8] C. H. Kim, A. H. Clement, and K. Tanizawa. Recent research and development of numerical wave tanks – a review. *International Journal of Offshore and Polar Engineering*, 9, 1999.

[9] J. W. Kim, H. Jang, A. Baquet, J. O'Sullivan, S. Lee, B. Kim, and H. Jasak. Technical and economic readiness review of CFD-based numerical wave basin for offshore floater design. In *Proceedings of the Offshore Technology Conference, Houston, TX, USA*, pages 1–17, 2016.

[10] Our World in Data. *Moore's Law: Transistors per microprocessor*, 2020. `https://ourworldindata.org/grapher/transistors-per-microprocessor?time=1971..2017`, Last accessed 26/02/2020.

[11] R. Guanche. On the importance of calibration and validation procedures: hybrid modeling. In *Proceedings of the BCAM Workshop Hydrodynamics of Wave Energy Converters 2017, Bilbao, Basque Country*, 2017.

[12] O. M. Faltinsen. *Sea loads on ships and offshore structures*. Cambridge University Press, 1990.

[13] A.P. Engsig-Karup, H.B. Bingham, and O. Lindberg. An efficient flexible-order model for 3D nonlinear water waves. *Journal of computational physics*, 228(6):2100–2118, 2009.

[14] U. Bosi. *A unified spectral/hp element depth-integrated Boussinesq model for nonlinear wave-floating body interaction*. PhD thesis, Université de Bordeaux, France, 2019.

[15] J.R. Morison, J.W. Johnson, and S.A. Schaaf. The force exerted by surface waves on piles. *Journal of Petroleum Technology*, 2(5):149–154, 1950.

[16] A. Babarit, H. Mouslim, and P. Laporte-Weywada. On the numerical modelling of the non linear behaviour of a wave energy converter. In *Proceedings of the 28th International Conference on Ocean, Offshore and Arctic Engineering (OMAE), Shanghai, China*, pages 1045–1053, 2010.

[17] G. Giorgi and J.V. Ringwood. Nonlinear Froude-Krylov and viscous drag representations for wave energy converters in the computation/fidelity continuum. *Ocean Engineering*, 141:164–175, 2017.

[18] M. Penalba, G. Giorgi, and J. V. Ringwood. Mathematical modelling of wave energy converters: A review of nonlinear approaches. *Renewable and Sustainable Energy Reviews*, 78:1188–1207, 2017.

[19] H. G. Weller, G. Tabor, C. Jasak, and C. Fureby. A tensorial approach to computational continuum mechanics using object-oriented techniques. *Computers in Physic*, 12:620 – 631, 1998.

[20] P. Schmitt. *Investigation of the near flow field of bottom hinged flap type wave energy converters*. PhD thesis, School of Planning, Architecture and Civil Engineering, Queen's University Belfast, UK, 2013.

[21] Wavestar. *Wavestar*, 2020. `http://wavestarenergy.com/`, Last accessed 07/03/2020.

[22] CCP-WSI. *CCP–WSI Blind Test Series 2 website*, 2020. `http://www.ccp-wsi.ac.uk/data_repository/test_cases/test_case_004`, Last accessed 12/05/2020.

[23] CCP-WSI. *CCP–WSI Blind Test Series 3 website*, 2020. `http://www.ccp-wsi.ac.uk/data_repository/test_cases/test_case_005`, Last accessed 12/05/2020.

[24] V. Heller. Scale effects in physical hydraulic engineering models. *Journal of Hydraulic Research*, 49(3):293–306, 2011.

[25] R B. Bird, W. E Stewart, and E. N Lightfoot. *Transport phenomena*. Wiley New York, 1962.

[26] J. C Slattery. *Momentum, energy, and mass transfer in continua*. McGraw-Hill, 1972.

[27] D. J. Acheson. *Elementary Fluid Dynamics*. Clarendon Press, 1990.

[28] F. M. White. *Fluid mechanics*. Mc Graw-Hill, 2009.

[29] J. H. Ferziger and M. Peric. *Computational Methods for Fluid Dynamics*. Springer-Verlag GmbH, 2001.

[30] H. Versteeg and W. Malalasekra. *An Introduction to Computational Fluid Dynamics*. Prentice Hall, 2007.

[31] R. T Hudspeth. *Waves and wave forces on coastal and ocean structures*. World Scientific, 2006.

[32] P. K. Kundu, I. M. Cohen, and D. R Dowling. *Fluid Mechanics (Fifth Edition)*. Elsevier, 2012.

[33] S. Araya. *Divergence and Curl*, 2020. `https://www.slideserve.com/salali/9-7-divergence-and-curl`, Last accessed 24/02/2020.

[34] J. Falnes. *Ocean waves and oscillating systems*. Cambridge University Press, 2002.

[35] L. Birk. *Fundamentals of Ship Hydrodynamics: Fluid Mechanics, Ship Resistance and Propulsion*. Wiley, 2019.

[36] P. K. Banerjee and R. Butterfield. *Boundary element methods in engineering science*. McGraw-Hill London, 1981.

[37] M. Folley. *Numerical modelling of wave energy converters: state-of-the-art techniques for single devices and arrays*. Academic Press, 2016.

[38] P.P. Wegener. *What makes airplanes fly?: history, science, and applications of aerodynamics*. Springer, 1997.

[39] S. B. Pope. *Turbulent Flows*. Cambridge University Press, 2000.

[40] C. L. Fefferman. Existence and smoothness of the Navier-Stokes equation. *The millennium prize problems – Clay Mathematics Institute*, 57:67, 2006.

[41] B. Le Méhauté. *An introduction to hydrodynamics and water waves*. Springer Science & Business Media, 1969.

[42] R.G. Dean and R.A. Dalrymple. *Water Wave Mechanics for Engineers and Scientists*. World Scientific, 1991.

[43] M. K. Ochi. *Ocean Waves – The Stochastic Approach*. Cambridge University Press, 1998.

[44] S. K. Chakrabarti. *Handbook of Offshore Engineering*. Elsevier, 2005.

[45] A. Pecher and J. P. Kofoed. *Handbook of ocean wave energy*. Springer, 2017.

[46] J. D. Fenton. Lecture notes in coastal and ocean engineering, 2020. Institute of Hydraulic Engineering and Water Resources Management, Vienna University of Technology.

[47] G. G. Stokes. On the theory of oscillatory waves. *Transactions of the Cambridge Philosophical Society*, 1880.

[48] J. D. Fenton. A fifth-order stokes theory for steady waves. *Journal of waterway, port, coastal, and ocean engineering*, 111(2):216–234, 1985.

[49] C. L. Bretschneider. Wave variability and wave spectra for wind-generated gravity waves. Technical Report 118, Beach Erosion Board, US Army, Corps of Engineers, Washington D.C., 1959.

[50] K. Hasselmann, T. Barnett, E. Bouws, H. Carlson, D. Cartwright, K. Enke, J. Ewing, H. Gienapp, D. Hasselmann, P. Kruseman, A. Meerburg, P. Müller, D. Olbers, K. Richter, W. Sell, and H. Walden. Measurements of wind-wave growth and swell decay during the Joint North Sea Wave Project (JONSWAP). Technical Report A8 12, Ergänzungsheft zur Deutschen Hydrographischen Zeitschrift, 1973.

[51] W. J. Pierson Jr. and L. Moskowitz. A proposed spectral form for fully developed wind seas based on the similarity theory of SA Kitaigorodskii. *Journal of Geophysical Research*, 69(24):5181–5190, 1964.

[52] D.Z. Ning, J. Zang, S.X. Liu, R. Eatock Taylor, B. Teng, and P.H. Taylor. Free-surface evolution and wave kinematics for nonlinear uni-directional focused wave groups. *Ocean Engineering*, 36(15):1226–1243, 2009.

[53] R. A. Gingold and J. J. Monaghan. Smoothed particle hydrodynamics: theory and application to non-spherical stars. *Monthly notices of the royal astronomical society*, 181(3):375–389, 1977.

[54] A.J.C. Crespo, J. M Domínguez, B. D. Rogers, M. Gómez-Gesteira, S. Longshaw, R.J.F.B. Canelas, R. Vacondio, A. Barreiro, and O. García-Feal. DualSPHysics: Open-source parallel CFD solver based on Smoothed Particle Hydrodynamics (SPH). *Computer Physics Communications*, 187:204–216, 2015.

[55] S. Koshizuka and Y. Oka. Moving-particle semi-implicit method for fragmentation of incompressible fluid. *Nuclear science and engineering*, 123(3):421–434, 1996.

[56] C.G. Koh, M. Gao, and C. Luo. A new particle method for simulation of incompressible free surface flow problems. *International journal for numerical methods in engineering*, 89(12):1582–1604, 2012.

[57] S. J. Cummins and M. Rudman. An SPH projection method. *Journal of computational physics*, 152(2):584–607, 1999.

[58] M. S. Shadloo, A. Zainali, M. Yildiz, and A. Suleman. A robust weakly compressible SPH method and its comparison with an incompressible SPH. *International Journal for Numerical Methods in Engineering*, 89(8):939–956, 2012.

[59] C. Grossmann, H.-G. Roos, and M. Stynes. *Numerical treatment of partial differential equations*, volume 154. Springer, 2007.

[60] F. H. Harlow. The particle-in-cell computing method for fluid dynamics. *Methods Comput. Phys.*, 3:319–343, 1964.

[61] Q. Chen, J. Zang, A. S. Dimakopoulos, D. M. Kelly, and C.J.K. Williams. A cartesian cut cell based two-way strong fluid–solid coupling algorithm for 2D floating bodies. *Journal of Fluids and Structures*, 62:252–271, 2016.

[62] Q. Chen, J. Zang, D. Ning, C. Blenkinsopp, and J. Gao. A 3D parallel particle-in-cell solver for extreme wave interaction with floating bodies. *Ocean Engineering*, 179:1–12, 2019.

[63] F. Moukalled, L. Mangani, and M. Darwish. *The finite volume method in computational fluid dynamics*, volume 113. Springer, 2016.

[64] B.P. Leonard. A stable and accurate convective modelling procedure based on quadratic upstream interpolation. *Computer methods in applied mechanics and engineering*, 19(1):59–98, 1979.

[65] B. Van Leer. Towards the ultimate conservative difference scheme. II. Monotonicity and conservation combined in a second-order scheme. *Journal of computational physics*, 14(4):361–370, 1974.

[66] B. Van Leer. Towards the ultimate conservative difference scheme III. Upstream-centered finite-difference schemes for ideal compressible flow. *Journal of Computational Physics*, 23(3):263–275, 1977.

[67] B. Van Leer. Towards the ultimate conservative difference scheme. IV. A new approach to numerical convection. *Journal of computational physics*, 23(3):276–299, 1977.

[68] B. Van Leer. Towards the ultimate conservative difference scheme. V. A second-order sequel to godunov's method. *Journal of computational Physics*, 32(1):101–136, 1979.

[69] B. E. Larsen, D. R. Fuhrman, and J. Roenby. Performance of interfoam on the simulation of progressive waves. *Coastal Engineering Journal*, 61(3):380–400, 2019.

[70] S. Send, C. Monroy, and S. Malencia. On the use of Euler and Crank-Nicolson time-stepping schemes for seakeeping simulations in OpenFOAM. In *Proceedings of the VII International Conference on Computational Methods in Marine Engineering (MARINE), Nantes, France*, pages 1–16, 2017.

[71] S.V. Patankar and D.B. Spalding. A calculation procedure for heat, mass and momentum transfer in three-dimensional parabolic flows. *International Journal of Heat and Mass Transfer*, 15(10):1787–1806, 1972.

[72] R.I. Issa. Solution of the implicitly discretised fluid flow equation by operator-splitting. *Journal of Computational Physics*, 1986.

[73] T. Holzmann. *Mathematics, Numerics, Derivations and OpenFOAM*. Holzmann CFD, 2016.

[74] P.-H. Musiedlak. *Numerical modelling of responses of offshore wave energy converters in extreme waves*. PhD thesis, University of Plymouth, 2019.

[75] S. Patankar. *Numerical heat transfer and fluid flow*. Taylor & Francis, 2018.

[76] J.P. Van Doormaal and G.D. Raithby. Enhancements of the SIMPLE method for predicting incompressible fluid flows. *Numerical heat transfer*, 7(2):147–163, 1984.

[77] CFD Direct. *OpenFOAM v6 user Guide: 5.2. Boundaries*, 2020. `https://cfd.direct/openfoam/user-guide/v6-boundaries/`, Last accessed 03/04/2020.

[78] C. W. Hirt and B. D. Nichols. Volume of Fluid (VOF) Method for the Dynamics of Free Boundaries. *Journal of Computational Physics*, 39:201–225, 1981.

[79] S. Muzaferija and M. Peric. Computation of free-surface flows using the finite-volume method and moving grids. *Numerical Heat Transfer*, 32(4):369–384, 1997.

[80] O. Ubbink and R.I. Issa. A method for capturing sharp fluid interfaces on arbitrary meshes. *Journal of Computational Physics*, 153(1):26–50, jul 1999.

[81] H. Rusche. *Computational Fluid Dynamics of Dispersed Two-Phase Flows at High Phase Fractions*. PhD thesis, Imperial College of Science, Technology & Medicine London, 2002.

[82] E. Berberović, N. P. van Hinsberg, S. Jakirlić, I. V. Roisman, and C. Tropea. Drop impact onto a liquid layer of finite thickness: Dynamics of the cavity evolution. *Physical Review E*, 79:036306–1 – 036306–15, 2009.

[83] S. S. Deshpande, L. Anumolu, and M.F. Trujillo. Evaluating the performance of the two-phase flow solver interfoam. *Computational science & discovery*, 5(1):014016, 2012.

[84] B. Devolder, P. Troch, and P. Rauwoens. Accelerated numerical simulations of a heaving floating body by coupling a motion solver with a two-phase fluid solver. *Computers & Mathematics with Applications*, 77(6):1605–1625, 2019.

[85] OpenFOAM Foundation. *OpenFOAM 2.3.0: Multiphase Modelling*, 2020. `https://openfoam.org/release/2-3-0/multiphase/`, Last accessed 24/03/2020.

[86] J. Roenby, H. Bredmose, and H. Jasak. A computational method for sharp interface advection. *Royal Society open science*, 3(11):160405, 2016.

[87] V. Vukčević, H. Jasak, and I. Gatin. Implementation of the ghost fluid method for free surface flows in polyhedral finite volume framework. *Computers & fluids*, 153:1–19, 2017.

[88] P. Roache. Quantification of uncertainty in computational fluid dynamics. *Annual Reviews in Fluid Mechanics*, 29:123–160, 1997.

[89] P. Roache. *Verification and validation in computational science and engineering*, volume 895. Hermosa Publisher Albuquerque, NM, 1998.

[90] I. B. Celik, U. Ghia, P. J. Roache, C. J. Freitas, H. Coleman, and P. E. Raad. Procedure for estimation and reporting of uncertainty due to discretization in CFD applications. *Journal of Fluids Engineering*, 130:078001–1–4, 2008.

[91] R. Courant, K. Friedrichs, and H. Lewy. über die partiellen Differenzengleichungen der mathematischen Physik. *Mathematische Annalen*, 1928.

[92] F. Stern, R.V. Wilson, H.W. Coleman, and E.G. Paterson. Comprehensive approach to verification and validation of CFD simulations – Part 1: Methodology and procedures. *Journal of Fluids Engineering*, 123:793–802, 2001.

[93] V. Vukčević. *Numerical Modelling of Coupled Potential and Viscous Flow for Marine Applications*. PhD thesis, University of Zagreb Faculty of Mechanical Engineering and Naval Architecture, 2016.

[94] V. Vukčević, H. Jasak, and Š. Malenica. Decomposition model for naval hydrodynamic applications, Part II: Verification and validation. *Ocean Engineering*, 121:76–88, 2016.

[95] L. F. Richardson and J Arthur Gaunt. J.A. VIII. the deferred approach to the limit. *Phil. Trans. R. Soc. Lond. A*, 226:299–361, 1927.

[96] M. A. Afshar. Numerical wave generation in OpenFOAM. Master's thesis, Department of Shipping and Marine Technology, Chalmers University of Technology, 2010.

[97] N.G. Jacobsen, D. R. Fuhrmann, and J. Fredsø. A wave generation toolbox for the open-source CFD library: OpenFoam(R). *International Journal for Numerical Methods in Fluids*, 70:1073 – 1088, 2012.

[98] J. Hrvoje, V. Vukčević, and I. Gatin. Numerical simulation of wave loading on static offshore structures. In *Springer Tracts in Mechanical Engineering*, pages 95–105. Springer International Publishing, 2015.

[99] R. Perić, V. Vukčević, M. Abdel-Maksoud, and H. Jasak. Tuning the case-dependent parameters of relaxation zones for flow simulations with strongly reflecting bodies in free-surface waves. *arXiv preprint arXiv:1806.10995*, 2018.

[100] Q. Chen, D.M. Kelly, and J. Zang. On the relaxation approach for wave absorption in numerical wave tanks. *Ocean Engineering*, 187:106210, 2019.

[101] P. Troch and J. De Rouck. An active wave generating–absorbing boundary condition for VOF type numerical model. *Coastal Engineering*, 38(4):223–247, 1999.

[102] P. Higuera, J. L. Lara, and I. J. Losada. Realistic wave generation and active wave absorption for Navier–Stokes models application to OpenFOAM. *Coastal Engineering*, 71:102 – 118, 2013.

[103] P. Higuera. *Application of Computational Fluid Dynamics to Wave Action on Structures*. PhD thesis, University of Cantabria, School of Civil Engineering, 2015.

[104] P. Lin and P. L.-F. Liu. Internal wave-maker for navier-stokes equations models. *Journal of Waterway, Port, Coastal, and Ocean Engineering*, 125:207 – 215, 1999.

[105] R. Perić and M. Abdel-Maksoud. Generation of free-surface waves by localized source terms in the continuity equation. *Ocean Engineering*, 109:567–579, 2015.

[106] G. Wei, J.T. Kirby, and A. Sinha. Generation of waves in Boussinesq models using a source function method. *Coastal Engineering*, 36(4):271–299, 1999.

[107] J. Choi and S.B. Yoon. Numerical simulations using momentum source wave-maker applied to RANS equation model. *Coastal Engineering*, 56(10):1043–1060, 2009.

[108] T. Ha, P. Lin, and Y.-S. Cho. Generation of 3D regular and irregular waves using Navier-Stokes equations model with an internal wave maker. *Coastal Engineering*, 76:55 – 67, 2013.

[109] S. Saincher and J. Banerjee. On wave damping occurring during source-based generation of steep waves in deep and near-shallow water. *Ocean Engineering*, 135:98–116, 2017.

[110] P. Schmitt and B. Elsäeßer. A review of wave makers for 3D numerical simulations. In *Proceedings of the VI International Conference on Computational Methods in Marine Engineering (MARINE), Rome, Italy*, pages 437–446, 2015.

[111] L.F. Chen, J. Zang, A.J. Hillis, G.C.J. Morgan, and A.R. Plummer. Numerical investigation of wave-structure interaction using OpenFOAM. *Ocean Engineering*, 88:91–109, 2014.

[112] R. Perić and M. Abdel-Maksoud. Analytical prediction of reflection coefficients for wave absorbing layers in flow simulations of regular free-surface waves. *Ocean Engineering*, 147:132–147, 2018.

[113] W. Finnegan and J. Goggins. Numerical simulation of linear water waves and wave–structure interaction. *Ocean Engineering*, 43:23–31, 2012.

[114] I. López, B. Pereiras, F. Castro, and G. Iglesias. Optimisation of turbine-induced damping for an OWC wave energy converter using a RANS–VOF numerical model. *Applied Energy*, 127:105–114, 2014.

[115] Z. Chen, P.M. Singh, and Y.-D. Choi. Structural analysis on the arm and floater structure of a wave energy converter. *The KSFM Journal of Fluid Machinery*, 18:5–11, 2015.

[116] J. Davidson, M. Cathelain, L. Guillemet, T. Le Huec, and J.V. Ringwood. Implementation of an openfoam numerical wave tank for wave energy experiments. In *Proceedings of the 11th European Wave and Tidal Energy Conference (EWTEC), Nantes, France*, pages 09B1–1–1–10, 2015.

[117] H.A. Schäffer and G. Klopman. Review of multidirectional active wave absorption methods. *Journal of Waterway, Port, Coastal, and Ocean Engineering*, 126:88–97, 2000.

[118] P. Higuera. Enhancing active wave absorption in RANS models. *Applied Ocean Research*, 94:102000, 2020.

[119] C.J.J. Galvin. Wave-height prediction for wave generatros in shallow water. Technical report, US Army Coastal Engineering Research Center, 1964.

[120] S.A. Hughes. *Physical models and laboratory techniques in coastal engineering*, volume 7. World Scientific, 1993.

[121] J. Spinneken and C. Swan. Second-order wave maker theory using force-feedback control. Part I: A new theory for regular wave generation. *Ocean Engineering*, 36(8):539–548, 2009.

[122] J. Spinneken and C. Swan. Second-order wave maker theory using force-feedback control. Part II: An experimental verification of regular wave generation. *Ocean engineering*, 36(8):549–555, 2009.

[123] J. Westphalen, D. M. Greaves, A. Raby, Z. Z. Hu, D. M. Causon, C. G. Mingham, P. Omidvar, P. K. Stansby, and B. D. Rogers. Investigation of wave-structure interaction using state of the art CFD techniques. *Open Journal of Fluid Dynamics*, 4:18–43, 2014.

[124] D.M Causon, D.M. Ingram, C.G. Mingham, G. Yang, and R.V. Pearson. Calculation of shallow water flows using a cartesian cut cell approach. *Advances in Water Resources*, 23:545–562, 2000.

[125] D.M. Ingram, D.M. Causon, and C.G. Mingham. Developments in cartesian cut cell methods. *Mathematics and Computers in Simulation*, 61:561–572, 2003.

[126] N. Sharma and N.A. Patankar. A fast computation technique for the direct numerical simulation of rigid particulate flows. *Journal of Computational Physics*, 205:439–457, 2005.

[127] Flow 3D. *No Loss with FAVOR*, 2020. `https://www.flow3d.com/resources/cfd-101/modeling-techniques/no-loss-with-favor/`, Last accessed 25/03/2020.

[128] G. Wei. A fixed-mesh method for general moving objects in fluid flow. *Modern Physics Letters B*, 19(28n29):1719–1722, 2005.

[129] B. Devolder, P. Schmitt, O. Rauwoens, B. Elsäßer, and P. Troch. A review of the implicit motion solver algorithm in OpenFOAM to simulate a heaving buoy. In *Proceedings of the 18th Numerical Towing Tank Symposium, Marstrand, Sweden*, pages 1–6, 2015.

[130] OpenFOAM Foundation. *OpenFOAM 2.3.0 Release Notes: Mesh Motion*, 2014. `https://openfoam.org/release/2-3-0/mesh-motion/`, Last accessed 25/03/2020.

[131] J.F. Thompson. *Handbook of Grid Generation*. CRC Press LLC, 1999.

[132] Z. Shen, D. Wan, and P.M. Carrica. Dynamic overset grids in OpenFOAM with application to KCS self-propulsion and manoeuvring. *Ocean Engineering*, 108:287–306, 2015.

[133] D.D.J. Chandar. On overset interpolation strategies and conservation on unstructured grids in openfoam. *Computer Physics Communications*, 239:72–83, 2019.

[134] J. Boussinesq. *Essai sur la théorie des eaux courantes*. Impr. nationale, 1877.

[135] P. Sagaut. *Large eddy simulation for incompressible flows: An introduction*. Springer Science & Business Media, 2006.

[136] J. Smagorinsky. General circulation experiments with the primitive equations: I. The basic experiment. *Monthly weather review*, 91(3):99–164, 1963.

[137] D. K. Lilly. On the application of the eddy viscosity concept in the inertial sub-range of turbulence. *NCAR manuscript*, 123, 1966.

[138] D. K Lilly. The representation of small-scale turbulence in numerical simulation experiments. In *Proceedings of the IBM Scientific Computing Symposium on Environmental Science, Yorktown Heights, NY, USA*, pages 195–210, 1967.

[139] B.E. Launder and D.B. Spalding. The numerical computation of turbulent flows. *Computer Methods in applied Mechanics and Engineering*, 3:269 – 289, 1974.

[140] T.-H. Shih, W.W. Liou, A. Shabbir, Z. Yang, and J. Zhu. A new $k - \varepsilon$ eddy viscosity model for high Reynolds number turbulent flows. *Computers & Fluids*, 24(3):227–238, 1995.

[141] T.-H. Shih, W.W. Liou, A. Shabbir, Z. Yang, and J. Zhu. A new $k - \varepsilon$ eddy viscosity model for high Reynolds number turbulent flows – Model development and validation. Technical report, NASA Technical Memorandum 106721, 1994.

[142] cfd online. *Relisable k-epislon model*, 2020. `https://www.cfd-online.com/Wiki/Realisable_k-epsilon_model`, Last accessed 30/03/2020.

[143] V. Yakhot, S. A. Orszag, S. Thangam, T. B. Gatski, and C. G. Speziale. Development of turbulence models for shear flows by a double expansion technique. *Physics of Fluids A: Fluid Dynamics*, 4:1510–1520, 1992.

[144] cfd online. *Relisable RNG k-epislon model*, 2020. `https://www.cfd-online.com/Wiki/RNG_k-epsilon_model`, Last accessed 30/03/2020.

[145] ANSYS, Inc. *ANSYS Fluent Theory Guide v16.1*, 2015.

[146] D. C. Wilcox. Reassessment of the scale-determining equation for advanced turbulence models. *American Institute of Aeronautics and Astronautics AIAA Journal*, 26:1299–1310, 1988.

[147] D. C. Wilcox. Comparison of two-equation turbulence models for boundary layers with pressure gradient. *American Institute of Aeronautics and Astronautics AIAA Journal*, 31:1414–1421, 1993.

[148] D. C. Wilcox. Simulation of transition with a two-equation turbulence model. *American Institute of Aeronautics and Astronautics AIAA Journal*, 32:247–255, 1994.

[149] F.R. Menter. Performance of popular turbulence model for attached and separated adverse pressure gradient flows. *American Institute of Aeronautics and Astronautics AIAA Journal*, 30(8):2066–2072, 1992.

[150] F.R. Menter. Improved Two-equation k–ω Turbulence Models for Aerodynamic Flows. Technical report, NASA Technical Memorandum TM-103975, 1992.

[151] F.R. Menter. Two-equation eddy-viscosity turbulence models for engineering applications. *American Institute of Aeronautics and Astronautics AIAA Journal*, 32(8):1598–1605, 1994.

[152] F.R. Menter. Eddy viscosity transport equations and their relation to the $k - \varepsilon$ model. *Journal of Fluids Engineering*, 119(4):876–884, 1997.

[153] H. Schlichting. *Boundary layer theory*. Springer, 1960.

[154] D.V. Evans. Power from water waves. *Annual review of Fluid mechanics*, 13(1):157–187, 1981.

[155] Y. Li and Y.-H. Yu. A synthesis of numerical methods for modelling wave energy converter-point absorbers. *Renewable and Sustainable Energy Reviews*, 16:4352–4364, 2012.

[156] M. Folley, A. Babarit, B. Child, D. Forehand, L. O'Boyle, K. Silverthorne, J. Spinneken, V. Stratigaki, and P. Troch. A review of numerical modelling of wave energy converter arrays. In *Proceedings of the 31st International Conference on Ocean, Offshore and Arctic Engineering (OMAE), Rio de Janeiro, Brazil*, pages 1–11, 2012.

[157] R. G. Coe and V. S. Neary. Review of methods for modelling wave energy converter survival in extreme sea states. In *Proceedings of the 2nd Marine Energy Technology Symposium (METS), Seattle, WA, USA*, 2014.

[158] H. Bouhrim and A. El Marjani. On numerical modeling in OWC systems for wave energy conversion. In *Proceedings of the 2014 Internation Renewable and Sustainable Energy Conference (IRSEC), Ouarzazate, Morocco*, 2014.

[159] A. H. Day, A. Babarit, A. Fontaine, Y.-P. He, M. Karaskowski, M. Murai, I. Penesis, F. Salvatore, and H.-K. Shin. Hydrodynamic modelling of marine renewable energy devices: A state of the art review. *Ocean Engineering*, 108:46–69, 2015.

[160] H. A. Wolgamot and C. J. Fitzgerald. Nonlinear hydrodynamic and real fluid effects on wave energy converters. *Proceedings of the Institution of Mechanical Engineers, Part A: Journal of Power and Energy*, 229:772 – 794, 2015.

[161] S. Saincher and J. Banerjee. Influence of wave breaking on the hydrodynamics of wave energy converters: A review. *Renewable and Sustainable Energy Reviews*, 58:704–717, 2016.

[162] F. Dias, E. Renzi, S. Gallagher, D. Sarkar, Y. Wei, T. Abadie, C. Cummins, and A. Rafiee. Analytical and computational modelling for wave energy systems: the example of oscillating wave surge converters. *Acta Mechanica Sinica*, 33(4):647–662, 2017.

[163] M.A. Zullah and Y.-H. Lee. Review of fluid structure interaction methods application to floating wave energy converter. *International Journal of Fluid Machinery and Systems*, 11(1):63–76, 2018.

[164] J. Davidson and R. Costello. Efficient nonlinear hydrodynamic models for wave energy converter design—a scoping study. *Journal of Marine Science and Engineering*, 8(1):35, 2020.

[165] L. Qian, C.G. Mingham, D.M. Causon, and D.M. Ingram. Numerical simulation of a wave driven rotating vane using a two-fluid solver. In *Proceedings of the IASTED International Conference on Environmental Modelling and Simulation, St. Thomas, US Virgin Islands*, 2004.

[166] G. F. Clauss, C. E. Schmittner, and R. Stueck. Numerical wave tank simulation of extreme waves for the investigation of structural responses. In *Proceedings of the ASME 24th International Conference on Offshore Mechanics and Arctic Engineering (OMAE), Halkidiki, Greece*, pages 785–792, 2005.

[167] L. Qian, C. Mingham, D. Causon, D. Ingram, M. Folley, and T. Whittaker. Numerical simulation of wave power devices using a two-fluid free surface solver. *Modern Physics Letters B*, 19:1479–1482, 2005.

[168] M. Alves and A. Sarmento. Non-linear and viscous analisys of the diffraction flow in OWC wave power plants. In *Proceedings of the 16th International Offshore and Polar Engineering Conference (ISOPE), Lisbon, Portugal*, pages 179–184, 2006.

[169] D.M. Greaves. Viscous waves and wave-structure interaction in a tank using adapting quadtree grids. *Journal of Fluids and Structures*, 23(8):1149–1167, 2007.

[170] Z. Liu, B.-S. Hyun, and J.Y. Jin. Numerical wave tank using two-phase VOF model. In *Proceedings of the KOSMEE Fall Annual Meeting*, pages 153–159, 2007.

[171] E. B. Agamloh, A. K. Wallace, and A. von Jouanne. Application of fluid-structure interaction simulation of an ocean wave energy extraction device. *Renewable Energy*, 33:748–757, 2008.

[172] Z. Liu, B.-S. Hyun, and K.-Y. Hong. Application of numerical wave tank to OWC air chamber for wave energy conversion. In *Proceedings of the 18th International Offshore and Polar Engineering Conference (ISOPE), Vancouver, BC, Canada*, pages 1–7, 2008.

[173] Z. Liu, B.-S. Hyun, and J. Jin. Numerical prediction for overtopping performance of OWEC. In *Proceedings of the Oceans'08 MTS/IEEE, Kobe, Japan*, pages 35–41, 2008.

[174] Z. Liu, B.-S. Hyun, and J. Jin. Numerical analysis of wave field in OWC chamber using VOF model. *Journal of Ocean Engineering and Technology*, 22:1 – 6, 2008.

[175] B. W. Nam, S. H. Shin, K. Y. Hong, and S. W. Hong. Numerical simulation of wave flow over the spiral reef overtopping device. In *Proceedings of the 8th ISOPE Pacific/Asia Offshore Mechanics Symposium, Bangkok, Thailand*, pages 262–267, 2008.

[176] L. Victor, P. Troch, and D. Vanneste. Experimental and numerical study of the hydrodynamic behaviour of wave energy converters based on wave overtopping. In *Proceedings of the 2nd International Conference on Ocean Energy, Brest, France*, pages 1–9, 2008.

[177] M. A. Bhinder, C. G. Mingham, D. M. Causon, M. T. Rahmati, G. A. Aggidis, and R.V. Chaplin. A joint numerical and experimental study of a surging point absorbing wave energy converter (WRASPA). In *Proceedings of the 28th International*

Conference on Ocean, Offshore and Arctic Engineering (OMAE), Honolulu, HI, USA, pages 1–10, 2009.

[178] M. A. Bhinder, C. G. Mingham, D. M. Causon, M. T. Rahmati, G. A. Aggidis, and R.V. Chaplin. Numerical and experimental study of a surging point absorber wave energy converter. In *Proceedings of the 8th European Wave and Tidal Energy Conference (EWTEC), Uppsala, Sweden*, pages 973–978, 2009.

[179] M. A. Bhinder, C. G. Mingham, D. M. Causon, M. T. Rahmati, G. A. Aggidis, and R.V. Chaplin. Numerical and experimental study of a point absorbing wave energy converter in regular waves. In *Proceedings of the 2009 International Conference on Clean Electrical Power, Capri, Italy*, pages 599–603, 2009.

[180] A. Babarit, H. Mouslim, A. Clement, and P. Laporte-Weywada. On the numerical modelling of the non linear behaviour of a wave energy converter. In *Proceedings of the 28th International Conference on Ocean, Offshore and Arctic Engineering (OMAE), Honolulu, HI, USA*, pages 1–10, 2009.

[181] M. Gomes, L.A. Isoldi, C.R. Olinto, L.A.O. Rocha, and J.A. Souza. Computational modeling of a regular wave tank. In *Proceedings of the Third Southern Conference on Computational Modelling,Rio Grande, Brazil*, pages 60 – 65, 2009.

[182] Z.Z. Hu, D.M. Causon, C.G. Mingham, and L. Qian. Numerical wave tank study of a wave energy converter in heave. In *Proceedings of the 19th International Offshore and Polar Engineering Conference (ISOPE), Osaka, Japan*, pages 383–388, 2009.

[183] Z. Liu, H. Shi, and B.-S. Hyun. Practical design and investigation of the breakwater OWC facility in China. In *Proceedings of the 8th European Wave and Tidal Energy Conference (EWTEC), Uppsala, Sweden*, pages 304–308, 2009.

[184] Z. Liu, B.-S. Hyun, K.-Y. Hong, and Y.-Y. Lee. Investigation on integrated system of chamber and turbine for OWC wave energy convertor. In *Proceedings of the 19th International Offshore and Polar Engineering Conference (ISOPE), Osaka, Japan*, pages 1–7, 2009.

[185] L. Victor, P. Troch, and J.P. Kofoed. Prediction of the individual wave overtopping volumes of a wave energy converter using experimental testing and first numerical model results. In *Proceedings of the 8th European Wave and Tidal Energy Conference (EWTEC), Uppsala, Sweden*, pages 999–1008, 2009.

[186] J. Westphalen, D.M. Greaves, C.K. Williams, P.H. Taylor, D.M. Causon, C.G. Mingham, Z.Z. Hu, P.K. Stansby, B.D. Rogers, and P. Omidvar. Extreme wave loading on offshore wave energy devices using CFD: A hierarchical team approach. In *Proceedings of the 8th European Wave and Tidal Energy Conference (EWTEC), Uppsala, Sweden*, pages 500–509, 2009.

[187] D.P. Davyt, R. Ramalhais, and E. Didier. Numerical analysis of regular waves over an onshore oscillating water column. In *Proceedings of the 13th Brazilian Congress of Thermal Sciences and Engineering, Uberlandia, MG, Brazil*, pages 1–10, 2010.

[188] Z.Z. Hu, D.M. Causon, C.G. Mongham, and L. Qian. Numerical simulation of nonlinear wave interactions with a wave energy converter. In *Proceedings of The 20th International Offshore and Polar Engineering Conference (ISOPE), Beijing, China*, pages 1–6, 2010.

[189] Y. Li and M. Lin. Wave-body interactions for a surface-piercing body in water of finite depth. *Journal of Hydrodynamics, Ser. B*, 22:745–752, 2010.

[190] Z. Liu, B.-S. Hyun, H. Shi, and K. Hong. Practical simulation of oscillating water column chamber for wave energy conversion. *International Journal of Green Energy*, 7:337–346, 2010.

[191] D. Prasad, M.A. Zullah, M.R. Ahmed, and Y.-H. Lee. Effect of front guide nozzle shape on the flow characteristics in an augmentation channel of a direct drive turbine for wave power generation. *Science in China Series E: Technological Sciences*, 53:46–51, 2010.

[192] J. Sanders, J.E. Dolbow, P.J. Mucha, and T.A. Laursen. A new method for simulating rigid body motion in incompressible two-phase flow. *International Journal for Numerical Methods in Fluids*, 67(6):713–732, 2010.

[193] J. Westphalen, D.M. Greaves, A. Hunt-Raby, C.J.K. Williams, P.K. Stansby, and T. Stallard. Numerical simulation of a floating body in multiple degrees of freedom. In *Proceedings of Marine Renewable and Offshore Wind Energy, London, UK*, pages 81–88, 2010.

[194] Y. Zhang, Q. Zou, D.M. Greaves, D.E. Reeve, A. Raby, D. Graham, and P. James. An investigation of the hydrodynamic characteristics of an oscillating water column device using a level set immersed boundary model. In *Proceedings of The 20th International Offshore and Polar Engineering Conference (ISOPE), Beijing, China*, pages 843–849, 2010.

[195] M.A. Zullah, D. Prasad, M.R. Ahmed, and Y.H. Lee. Performance analysis of a wave energy converter using numerical simulation technique. *Science in China Series E: Technological Sciences*, 53:13–18, 2010.

[196] M.A Bhinder, A. Babarit, L. Gentaz, and P. Ferrant. Assessment of viscous damping via 3D-CFD modeling of a floating wave energy device. In *Proceedings of the 9th European Wave and Tidal Energy Conference (EWTEC), Southampton, UK*, pages 1–6, 2011.

[197] J.M.P Conde, P.R.F. Teixeira, and E. Didier. Numerical simulation of an oscillating water column wave energy converter: Comparison of two numerical codes. In *Proceedings of the 21st International Offshore and Polar Engineering Conference (ISOPE), Maui, HI, USA*, pages 668–674, 2011.

[198] Z. Z. Hu, D. M. Causon, C. G. Mingham, and L. Qian. Numerical simulation of floating bodies in extreme free surface waves. *Natural Hazards and Earth System Science*, 11:519–527, 2011.

[199] U. Şentürk and A. Özdamar. Modelling the interaction between water waves and the oscillating water column wave energy device. *Mathematical and Computational Applications*, 16:630–640, 2011.

[200] O. Thilleul, V. Baudry, P.M. Guilcher, Y.-M. Scolan, E. Jacquin, A. Babarit, P. Locuratolo, and Larivain A. Complementary use of linear potential code, a RANS and a SPH solver for the optimisation of a wave energy converter. In *Proceedings of the 9th European Wave and Tidal Energy Conference, Southampton, UK*, pages 1–10, 2011.

[201] Z. Liu, B.-S. Hyun, and K. Hong. Numerical study of air chamber for oscillating water column wave energy convertor. *China Ocean Engineering*, 25(1):169–178, 2011.

[202] J. Westphalen. *Extreme Wave Loading on Offshore Wave Energy Devices using CFD*. PhD thesis, Univeristy of Plymouth, 2011.

[203] J.D.L. Winchester, A.P. McCabe, and G.A. Aggidis. CFD analysis of a multi-axis wave energy converter with novel geometry. In *Proceedings of the 9th European Wave and Tidal Energy Conference, Southampton, UK*, pages 1–8, 2011.

[204] Y. Yu and Y. Li. A RANS simulation of the heave response of a two-body floating point absorber. In *Proceedings of the 21st International Offshore and Polar Engineering Conference (ISOP), Maui, HI, USA*, pages 565–571, 2011.

[205] Y. Yu and Y. Li. Preliminary results of a RANS simulation for a floating point absorber wave energy system under extreme wave conditions. In *Proceeding of the 30th International Conference on Ocean, Offshore, and Arctic Engineering (OMAE), Rotterdam, The Netherlands*, pages 1–8, 2011.

[206] M.A. Bhinder, A. Babarit, L. Gentaz, and P. Ferrant. Effect of viscous forces on the performance of a surging wave energy converter. In *Proceedings of the 22nd International Offshore and Polar Engineering Conference (ISOPE), Rhodes, Greece*, pages 545–549, 2012.

[207] Y. J. Cho, M. A. Zullah, M. Faizal, Y. D. Choi, and Y. H. Lee. A study on the flow characteristics of a direct drive turbine for energy conversion generation by experiment and CFD. *IOP Conference Series: Earth and Environmental Science*, 15:042040–1–8, 2012.

[208] M.N. Gomes, C.D. Nascimento, B.L. Bonafini, E.D. Santos, L.A. Isoldi, and L.A.O Rocha. Two-dimensional geometric optimization of an oscillating water column converter in laboratory scale. *Revista de Engenharia Térmica*, 11(1-2):30–36, 2012.

[209] J. Grimmler, N. Lopes, J.A. Souza, E.D. dos Santos, L.A. Isoldi, M. Gomes, and L.A.P. Rocha. Numerical study about the shape influence of the hydropneumatic chamber in an OWC wave energy converter. In *Proceedings of the 14th Brazilian Congress of Thermal Sciences and Engineering, Rio de Janeiro, Brazil*, 2012.

[210] J. Jin, Z. Liu, K. Hong, and B.-S. Hyun. 3D numerical investigation on reservoir system for an overtopping wave energy convertor. *Journal of Navigation and Port Research*, 36:97–103, 2012.

[211] J. Jin, Z. Liu, B.-S. Hyun, and K. Hong. Effects of wave direction on performance of oscillating water column type wave energy convertor. In *Proceedings of the 22nd International Offshore and Polar Engineering Conference (ISOPE), Rhodes, Greece*, pages 582–587, 2012.

[212] L. Li, M. Tan, and J. Blake. OpenFOAM simulation of regular wave and wave load on cylinder. In *Proceedings of the 15th Numerical Towing Tank Symposium, Cortona, Italy*, pages 146 – 151, 2012.

[213] Z. Liu, J.-Y. Jin, Hyun B.-S., and K. Hong. Review of application of VOF-based NWT on integrated OWC system. *Journal of the Korean Society for Marine Environmental Engineering*, 15(2):111 – 117, 2012.

[214] I. Lopez, G. Iglesias, M. Lopez, F. Castro, and M.A. Rodríguez. Turbine-chamber coupling in an OWC wave energy converter. *Coastal Engineering Proceedings*, 1:1–7, 2012.

[215] I. Mirzaii and M. Passandideh-Fard. Modeling free surface flows in presence of an arbitrary moving object. *International Journal of Multiphase Flow*, 39:216–226, 2012.

[216] O. Puolakka and T. Mikkola. Radiation moment on vertical bottom-hinged flap. In *Proceedings of the 15th Numerical Towing Tank Symposium, Cortona, Italy*, pages 146 – 151, 2012.

[217] D. Prasad, M. R. Ahmed, and Y.-H. Lee. Performance studies on a direct drive turbine for wave power generation in a numerical wave tank. In *Proceedings of the 1st Asian Wave and Tidal Energy Conference, Jeju Island, Korea*, pages 185–192, 2012.

[218] P. Schmitt, S. Bourdier, D. Sarkar, E. Renzi, F. Dias, K. Doherty, T. Whittaker, and J. van 't Hoff. Hydrodynamic loading on a bottom hinged oscillating wave surge converter. In *Proceedings of the 22nd International Offshore and Polar Engineering Conference (ISOPE), Rhodes, Greece*, pages 550–557, 2012.

[219] P. Schmitt, K. Doherty, D. Clabby, and T. Whittaker. The opportunities and limitations of usinf CFD in the development of wave energy converters. In *Proceedings of the International Conference on Marine & Offshore Renewable Energy, London, UK*, pages 1–9, 2012.

[220] J. A. Souza, L. A. Isoldi, E. D. dos Santos, M. das Neves Gomes, and L. A. O. Rocha. Numerical simulation of sea wave energy converters using the OpenFOAM software. In *Proceedings of the 14th Brazilian Congress of Thermal Sciences and Engineering, Rio de Janeiro, Brazi*, 2012.

[221] J. P. Thaker and J. Banerjee. Numerical simulation of periodic motion of two phases in a two-dimensional channel: Application to wave energy converter. In *Proceedings of the 39th National Conference on Fluid Mechanics and Fluid Power, Surat, India*, pages 1–8, 2012.

[222] J. Westphalen, D.M. Greaves, C.J.K. Williams, A.C. Hunt-Raby, and J. Zang. Focused waves and wave-structure interaction in a numerical wave tank. *Ocean Engineering*, 45:9 – 21, 2012.

[223] Y. Zhang, Q.-P. Zou, and D.M Greaves. Air-water two-phase flow modelling of hydrodynamic performance of an oscillating water column device. *Renewable Energy*, 41:159 – 170, 2012.

[224] H. Akimoto and K. Tanaka. Conceptual study of a drag type water turbine for electricity generation from wave power. In *Proceedings of the 12th International Symposium on Fluid Control, Measurement and Visualization, Nara, Japan*, pages 1–6, 2013.

[225] M. Anbarsooz, M. Passandideh-Fard, and M. Moghiman. Fully nonlinear viscous wave generation in numerical wave tanks. *Ocean Engineering*, 59:73–85, 2013.

[226] B. Bouali and S. Larbi. Contribution to the geometry optimization of an oscillating water column wave energy converter. *Energy Procedia*, 36:565–573, 2013.

[227] C. Caskey and T. Jeans. Analysis of a cycloidal wave energy converter using unsteady Reynolds-Averaged Navier-Stokes simulation. In *Proceedings of the 10th European Wave and Tidal Energy Conference (EWTEC), Aalborg, Denmark*, pages 740–1–10, 2013.

[228] J. Davidson, S. Giorgi, and J.V. Ringwood. Linear parametric hydrodynamic models based on numerical wave tank experiments. In *Proceedings of the 10th European Wave and Tidal Energy Conference (EWTEC), Aalborg, Denmark*, pages 1–10, 2013.

[229] A. Iturrioz, R. Guanche, J.A. Armesto, C. Vidal, and I.J. Losada. Experimental and numerical development of a floating multi-chamber OWC device. In *Proceedings of the 10th European Wave and Tidal Energy Conference (EWTEC), Aalborg, Denmark*, pages 581–1–10, 2013.

[230] N. Li, K.-M.and Parthasarathy, Y.H. Choi, and Y.W. Lee. Study on wave energy generation of floating bodies for energy absorption by CFD. In *Proceedings of the 23rd International Offshore and Polar Engineering Conference (ISOPE), Anchorage, AK, USA*, 2013.

[231] R. Nicholls-Lee, A. Walker, S. Hindley, and R. Argall. Coupled multi-phase CFD and transient mooring analysis of the floating wave energy converter OWEL. In *Proceedings of the 32nd International Conference on Ocean, Offshore and Arctic Engineering (OMAE), Nantes, France*, pages 1–10, 2013.

[232] J. Palm, C. Eskilsson, G.M. Paredes, and L. Bergdahl. CFD simulation of a moored floating wave energy converter. In *Proceedings of the 10th European Wave and Tidal Energy Conference (EWTEC), Aalborg, Denmark*, pages 554–1–9, 2013.

[233] G.M. Paredes, J. Palm, C. Eskilsson, L. Bergdahl, and F. Taveira-Pinto. Numerical modelling of mooring systems for floating wave energy converters. *8as Jornadas De Hidráulica, Recursos Hídricos E Ambiente*, pages 41–48, 2013.

[234] E. Ransley, M. Hann, D.M. Greaves, A. Raby, and D. Simmonds. Numerical and physical modeling of extreme waves at Wave Hub. *Journal of Coastal Research*, 165:1645–1650, 2013.

[235] E. Ransley, M. Hann, D.M. Greaves, A. Raby, and D. Simmonds. Numerical and physical modelling of extreme wave impacts on a fixed truncated circular cylinder. In *Proceedings of the 10th European Wave and Tidal Energy Conference (EWTEC), Aalborg, Denmark*, pages 789–1–9, 2013.

[236] P. Schmitt, K. Doherty, and T. Whittaker. Shape optimisation of a bottom hinged flap type wave energy converter. In *Proceedings of the Conference on Maritime Energy, Hamburg, Germany*, pages 1–15, 2013.

[237] J. A. Souza, E. D. dos Santos, and L. A. Isoldi. Numerical simulation of an OWC device. In *Proceedings of the 22nd International Congress of Mechanical Engineering, Rio de Janeiro, Brazil*, pages 3563–3570, 2013.

[238] O. Thilleul, A. Babarit, A. Drouet, and S. Le Floch. Validation of CFD for the determination of damping coefficients for the use of wave energy converters modelling. In *Proceedings of the 32nd International Conference on Ocean, Offshore and Arctic Engineering (OMAE), Nantes, France*, pages 1–10, 2013.

[239] P.R.F Teixeira, D.P. Davyt, E. Didier, and R. Ramalhais. Numerical simulation of an oscillating water column device using a code based on Navier–Stokes equations. *Energy*, 61:513–530, 2013.

[240] T. Vyzikas, E. Ransley, M. Hann, D. Magagna, D.M. Greaves, D. Simmonds, V. Magar, and D. Conley. Integrated numerical modelling system for extreme wave events at the wave hub site. In *Proceedings of the ICE conference on coasts, marine structures and breakwaters 2013, Edinburgh, UK*, pages 1–10, 2013.

[241] Y. Wei, A. Rafiee, and F. Dias. On the viscous effects in the interaction of water waves with an oscillating wave surge converter. In *Proceedings of the 10th European Wave and Tidal Energy Conference (EWTEC), Aalborg, Denmark*, pages 808–1–9, 2013.

[242] Y. Wei, A. Rafiee, B. Elsäßer, and F. Dias. Numerical simulation of an oscillating wave surge converter. In *Proceedings of the 32nd International Conference on Ocean, Offshore and Arctic Engineering, Nantes, France*, pages 1–7, 2013.

[243] Y.-H. Yu and Y. Li. Reynolds-Averaged Navier–Stokes simulation of the heave performance of a two-body floating-point absorber wave energy system. *Computers & Fluids*, 73:104–114, 2013.

[244] M.A. Zullah and Y.-H. Lee. Performance evaluation of a direct drive wave energy converter using CFD. *Renewable Energy*, 49:237–241, 2013.

[245] M. Anbarsooz, M. Passandideh-Fard, and M. Moghiman. Numerical simulation of a submerged cylindrical wave energy converter. *Renewable Energy*, 64:132–143, 2014.

[246] H. Akimoto, Y. Y. Kim, and K. Tanaka. Performance prediction of the rotational wave energy converter using single-bucket drag type turbine. In *Proceedings of the 33rd International Conference on Ocean, Offshore and Arctic Engineering (OMAE), San Francisco, CA, USA*, pages 1–8, 2014.

[247] H. Akimoto, Y. Y. Kim, and K. Tanaka. Configuration of the single-bucket wave turbine for the direct utilization of orbital fluid motion. In *Proceedings of the GRAND RENEWABLE ENERGY 2014, Tokyo, Japan*, pages 1–7, 2014.

[248] J.A. Armesto, R. Guanche, A. Iturrioz, C. Vidal, and I.J. Losada. Identification of state-space coefficients for oscillating water columns using temporal series. *Ocean Engineering*, 79:43–49, 2014.

[249] H. Asmuth, P. Schmitt, B. Elsäßer, and A. Henry. Determination of non-linear damping coefficients of bottom–hinged oscillating wave surge converters using numerical free decay tests. In *Proceedings of the 1st International Conference on Renewable Energies Offshore (RENEW), Lisbon, Portugal*, pages 507–513, 2014.

[250] A. Bøckmann, C. Pâkozdi, T. Kristiansen, H. Jang, and J. Kim. An experimental and computational development of a benchmark solution for the validation of numerical wave tanks. In *Proceedings of the 33rd International Conference on Ocean, Offshore and Arctic Engineering (OMAE), San Francisco, CA, USA*, pages 1–14, 2014.

[251] L.F. Chen, L. Sun, J. Zang, and A. Hillis. Numerical simulation of wave-induced roll of a 2-D rectangular barge using OpenFOAM. In *Proceedings of the 29th International Workshop on Water Waves and Floating Bodies (iwwwfb), Osaka, Japan*, pages 1–4, 2014.

[252] J. Davidson, S. Giorgi, and J.V. Ringwood. Numerical wave tank identification of nonlinear discrete time hydrodynamic models. In *Proceedings of the 1st International Conference on Renewable Energies Offshore (RENEW), Lisbon, Portugal*, pages 279–286, 2014.

[253] C. Eskilsson, J. Palm, J. Kofoed, and E. Friis-Madsen. CFD study of the overtopping discharge of the Wave dragon wave energy converter. In *Proceedings of the 1st International Conference on Renewable Energies Offshore (RENEW), Lisbon, Portugal*, pages 287–294, 2014.

[254] A. Ghasemi, A. Pathak, and M. Raessi. Computational simulation of the interactions between moving rigid bodies and incompressible two-fluid flows. *Computers & Fluids*, 94:1–13, 2014.

[255] A. Henry, A. Rafiee, P. Schmitt, F. Dias, and T. Whittaker. The characteristics of wave impacts on a oscillating wave surge converter. *Journal of Ocean and Wind Energy*, 1:101 – 110, 2014.

[256] A. Iturrioz, R. Guanche, J.A. Armesto, M.A. Alves, C. Vidal, and I.J. Losada. Time-domain modeling of a fixed detached oscillating water column towards a floating multi-chamber device. *Ocean Engineering*, 76:65–74, 2014.

[257] A.J.C. King. Numerical modelling of the Bombora wave energy conversion device. In *Proceedings of the 19th Australasian Fluid Mechanics Conference, Melbourne, Australia*, pages 1–4, 2014.

[258] Y. Luo, J.-R. Nader, P. Cooper, and S.-P. Zhu. Nonlinear 2D analysis of the efficiency of fixed oscillating water column wave energy converters. *Renewable Energy*, 64:255–265, 2014.

[259] Y. Luo, Z. Wang, G. Peng, Y. Xiao, L. Zhai, X. Liu, and Q. Zhang. Numerical simulation of a heave-only floating OWC (oscillating water column) device. *Energy*, 76:799–806, 2014.

[260] D.D. Prasad, R.R Ahmed, and Y.-H. Lee. Flow and performance characteristics of a direct drive turbine for wave power generation. *Ocean Engineering*, 81:39–49, 2014.

[261] J. Palm, C. Eskilsson, L. Bergdahl, and G.M. Paredes. CFD study of a moored floating cylinder: Comparison with experimental data. In *Proceedings of the 1st International Conference on Renewable Energies Offshore, Lisbon (RENEW), Portugal*, pages 913–921, 2014.

[262] I. Simonetti, L. Cappietti, H. El Safi, and H. Oumeraci. 3D numerical modelling of oscillating water column wave energy conversion devices: current knowledge and OpenFOAM implementation. In *Proceedings of the 1st International Conference on Renewable Energies Offshore, Lisbon (RENEW), Portugal*, pages 497–504, 2014.

[263] V. Stratigaki. *Experimental Study and Numverical Modelling of Intra-Array Interactions and Extra-Array Effects of Wave Energy Converter Arrays*. PhD thesis, Faculteit Ingenieurswetenschappen en Architectuur, Universiteit Gent, 2014.

[264] F.M. Seibt, M. Letzow, M. Gomes, J.A. Souza, L.A.O. Rocha, E.D. dos Santos, and L.A. Isoldi. Computational modeling applied to the study of wave energy converters (WEC). *Marine Systems & Ocean Technology*, 9:77 – 84, 2014.

[265] F.M Seibt, E.C. Couto, E.D. dos Santos, L.A. Isoldi, L.A.O. ocha, and P.R.d.F. Teixeira. Numerical study on the effect of submerged depth on the horizontal plate wave energy converter. *China Ocean Engineering*, 28:687–700, 2014.

[266] F.M. Seibt, M. Letzow, M. Gomes, J.A. Souza, L.A.O. Rocha, E.D. dos Santos, and L.A. Isoldi. Numerical analysis of the fluid-dynamic behavior of a submerged plate wave energy converter. *Computational Thermal Sciences: An International Journal*, 6:525–534, 2014.

[267] E.D. dos Santos, B.N. Machado, M.M. Zanella, M.N. Gomes, J.A. Souza, L.A. Isoldi, and L.A.O. Rocha. Numerical study of the effect of the relative depth on the overtopping wave energy converters according to constructal design. *Defect and Diffusion Forum*, 348:232–244, 2014.

[268] Y. Wei, A. Henry, O. Kimmoun, and F. Dias. Numerical study of wave slamming on an oscillating flap. In *Proceedings of the 33rd International Conference on Ocean, Offshore and Arctic Engineering, San Francisco, CA, USA*, pages 1–9, 2014.

[269] L. Zaoui, B. Bouali, S. Larbi, and A. Benchatti. Performance analysis of a 3D axisymmetric oscillating water column. *Energy Procedia*, 50:246–254, 2014.

[270] L. Chen. *Modelling of Marine Renewable Energy*. PhD thesis, University of Bath, Department of Architecture and Civil Engineering, 2015.

[271] H. Akimoto, K. Tanaka, and Y.Y. Kim. Drag-type cross-flow water turbine for capturing energy from the orbital fluid motion in ocean wave. *Renewable Energy*, 76:196 – 203, 2015.

[272] M. Bergmann, G. Bracco, F. Gallizio, E. Giorcelli, A. Iollo, G. Mattiazzo, and M. Ponzetta. A two-way coupling CFD method to simulate the dynamics of a wave energy converter. In *Proceedings of the Oceans'15 MTS/IEEE, Genoa, Italy*, pages 1–6. IEEE, 2015.

[273] M. A. Bhinder, A. Babarit, L. Gentaz, and P. Ferrant. Potential time domain model with viscous correction and CFD analysis of a generic surging flaoting wave energy converter. *International Journal of Marine Energy*, 10:70–96, 2015.

[274] M. Buccino, F. Dentale, D. Salerno, and D. Vicinanza. CFD numerical simulation and experiments on Seawave slot-cone generator in random wave. In *Proceedings of the 11th European Wave and Tidal Energy Conference (EWTEC), Nantes, France*, pages 07B1–3–1–8, 2015.

[275] L. Chen, J. Zang, A. J. Hillis, and A. R. Plummer. Hydrodynamics performance of a flap-type wave energy converter in viscous flow. In *Proceedings of the 25th International Ocean and Polar Engineering Conference (ISOPE), Kona, HI, USA*, pages 1–8, 2015.

[276] B. Chenari, S. S. Saadatian, and A.D. Ferreira. Numerical modelling of regular waves propagation and breaking using Waves2Foam. *Journal of Clean Energy Technologies*, 3:276–281, 2015.

[277] J. Davidson, S. Giorgi, and J.V. Ringwood. Linear parametric hydrodynamic models for ocean wave energy converters identified from numerical wave tank experiments. *Ocean Engineering*, 103:31–39, 2015.

[278] J. Davidson, M. Cathelain, L. Guillemet, T. Le Huec, and J.V. Ringwood. Implementation of an OpenFOAM numerical wave tank for wave energy experiments. In *Proceedings of the 11th European Wave and Tidal Energy Conference (EWTEC), Nantes, France*, pages 09B1–1–1–10, 2015.

[279] L. Ding, L. Zhang, C. Wu, X. Mao, and D. Jiang. Flow induced motion and energy harvesting of bluff bodies with different cross sections. *Energy Conversion and Management*, 91:416–426, 2015.

[280] A.S. Dimakopoulos, M.J. Cooker, E.M. Lopez, D. Longo, and R. Pinguet. Flow characterisation and numerical modelling of OWC wave energy converters. In *Proceedings of the 11th European Wave and Tidal Energy Conference (EWTEC), Nantes, France*, pages 09P2–2–1–8, 2015.

[281] C. Eskilsson, J. Palm, A. P. Engsig-Karup, U. Bosi, and M. Ricchiuto. Wave induced motions of point-absorbers: A hierarchical investigation of hydrodynamic models. In *Proceedings of the 11th European Wave and Tidal Energy Conference (EWTEC), Nantes, France*, pages 08B1–3–1–8, 2015.

[282] L. Di Fresco, A. Traverso, S. Barberis, E. Guglielmino, and M. Garrone. Off-shore wave energy harvesting: A WEC-microturbine system: Harvesting and storing energy for off-shore applications. In *Proceedings of the Oceans'15 MTS/IEEE, Genoa, Italy*, pages 1–6, 2015.

[283] W. Finnegan and J. Goggins. Linear irregular wave generation in a numerical wave tank. *Applied Ocean Research*, 52:188–200, 2015.

[284] S. Giorgi, J. Davidson, and J.V. Ringwood. Identification of nonlinear excitation force kernels using numerical wave tank experiments. In *Proceedings of the 11th European Wave and Tidal Energy Conference (EWTEC), Nantes, France*, pages 09C1–1–1–10, 2015.

[285] M.N. Gomes, E.D. dos Santos, L.A. Isoldi, and L.A.O. Rocha. Numerical analysis including pressure drop in oscillating water column device. *Open Engineering*, 5:229–237, 2015.

[286] M.N. Gomes, M. F. Espinel Lara, S. L. P. Iahnke, B. Neves Machado, M. Moraes Goulart, F. M. Seibt, E. D. dos Santos, L.A. Isoldi, and L.A.O. Rocha. Numerical approach of the main physical operational principle of several wave energy converters: oscillating water column, overtopping and submerged plate. *Defect and Diffusion Forum*, 362:115–171, 2015.

[287] N. F. Heilskov. Structural design of wave energy converters - State-of-the-Art and implementation of design tools for floating wave energy converters. Technical report, Danish Hydraulic Institute DHI, 2015.

[288] A. Iturrioz, R. Guanche, J.L. Lara, C. Vidal, and I.J. Losada. Validation of OpenFOAM for oscillating water column three-dimensional modeling. *Ocean Engineering*, 107:222–236, 2015.

[289] B.H. Kim, J. Wata, M.A. Zullah, M.R. Ahmed, and Y.-H. Lee. Numerical and experimental studies on the PTO system of a novel floating wave energy converter. *Renewable Energy*, 79:111–121, 2015.

[290] A. Kamath, H. Bihs, and O.A. Arntsen. Numerical investigations of the hydrodynamics of an oscillating water column device. *Ocean Engineering*, 102:40–50, 2015.

[291] A. Kamath, H. Bihs, and O.A. Arntsen. Numerical modeling of power take-off damping in an oscillating water column device. *International Journal of Marine Energy*, 10:1–16, 2015.

[292] L. Li, M. Tan, and J. Blake. Numerical simulation of multi-body wave energy converter. In *Proceedings of the 25th International Ocean and Polar Engineering Conference (ISOPE), Kona, HI, USA*, pages 1–7, 2015.

[293] V. Mishra, S. Beatty, B. Buckham, P. Oshkai, and C. Crawford. Application of an arbitrary mesh interface fo CFD simulation of an oscillating wave energy converter. In *Proceedings of the 11th European Wave and Tidal Energy Conference (EWTEC), Nantes, France*, pages 07B1–4–1–10, 2015.

[294] E. Medina-Lopez, W. Allsop, D. Dimakopoulos, and T. Bruce. Conjectures on the failure of the OWC breakwater at Mutriku. In *Proceedings of the Coastal Structures & Solution to Coastal Disasters Joint Conference, Boston, MA, USA*, pages 1–12, 2015.

[295] E. Mendoza, X. Chávez, J.C. Alcérreca-Huerta, and R. Silva. Hydrodynamic behavior of a new wave energy convertor: The Blow-Jet. *Ocean Engineering*, 106:252–260, 2015.

[296] A. Nematbakhsh, C. Michailides, Z. Gao, and T. Moan. Comparison of experimental data of a moored multibody wave energy device with a hybrid CFD and BIEM numerical analysis framework. In *Proceedings of the 34th International Conference on Ocean, Offshore and Arctic Engineering (OMAE), St. John's, Newfoundland, Canada*, pages 1–10, 2015.

[297] M.T. Reis, E. Didier, J. Dias, A. Mendonca, J.M.P. Conde, M.G. Neves, C.J.E.M. Fortes, and P.R.F. Teixeira. Development of an integrated tool for numerical modelling of OWC-WECs in vertical breakwaters. In *Proceedings of the 2nd International Workshop on Hydraulic Structures, Coimbra, Portugal*, pages 186–195, 2015.

[298] J.V. Ringwood, J. Davidson, and S. Giorgi. Optimising numerical wave tank tests for the parametric identification of wave energy device models. In *Proceedings of the 34th International Conference on Ocean, Offshore and Arctic Engineering (OMAE), St. John's, Newfoundland, Canada*, pages 1–10, 2015.

[299] E.J. Ransley. *Survivability of Wave Energy Converter and Mooring Coupled System using CFD*. PhD thesis, School of Marine Science and Engineeting, Univeristy of Plymouth, 2015.

[300] A. Rafiee and J. Fievez. Numerical prediction of extreme loads on the CETO wave energy converter. In *Proceedings of the 11th European Wave and Tidal Energy Conference (EWTEC), Nantes, France*, pages 09A1–2–1–10, 2015.

[301] P. Schmitt and B. Elsäßer. On the use of OpenFOAM to model oscillating wave surge converters. *Ocean Engineering*, 108:98–104, 2015.

[302] I. Simonetti, L. Cappietti, H. El Safti, G. Manfrida, H. Matthies, and H. Oumeraci. The use of OpenFOAM as a virtual laboratory to simulate oscillating water column wave energy converters. In *Proceedings of the VI International Conference on Computational Methods in Marine Engineering (MARINE), Rome, Italy*, pages 1–12, 2015.

[303] I. Simonetti, L. Cappietti, H. El Safti, and H. Oumeraci. Numerical modelling of fixed oscillating water column wave energy conversion devices: toward geometry hydraulic optimization. In *Proceedings of the 34th International Conference on Ocean, Offshore and Arctic Engineering (OMAE), St. John's, Newfoundland, Canada*, pages 1–10, 2015.

[304] P. Stansby, H. Gu, E. C. Moreno, and T. Stallard. Drag minimisation for high capture width with three float wave energy converter M4. In *Proceedings of the 11th European Wave and Tidal Energy Conference (EWTEC), Nantes, France*, pages 08B3–3–1–6, 2015.

[305] F. Scarpetta, G. Martina, M. Torresi, and S.M. Camporeale. CFD analysis of the wave interaction with both a submerged impermeable breakwater and one embedding an OWC device. In *Proceedings of the 11th European Wave and Tidal Energy Conference (EWTEC), Nantes, France*, pages 10B–2–5–1–10, 2015.

[306] O. Thilleul, R. Menard, F. Surmont, C. Berhault, J. C. Poirier, F. Cany, A. S. Dubois, and J. Bossard. Evaluation of response bases design method and validation of wave loads computations in CFD. In *Proceedings of the 11th European Wave and Tidal Energy Conference (EWTEC), Nantes, France*, pages 08P2–5–1–10, 2015.

[307] D. Vicinanza, F. Dentale, D. Salerno, and M. Buccino. Structural response of seawave slot-cone generator (SSG) from random wave CFD simulations. In *Proceedings of the 25 International Ocean and Polar Engineering Conference (ISOPE), Kona, HI, USA*, pages 985–991, 2015.

[308] M.G. Verduzco-Zapata and F.J. Ocampo-Torres. Study of a 6 DOF wave energy converter interacting with regular waves using 3D CFD. In *Proceedings of the 11th European Wave and Tidal Energy Conference (EWTEC), Nantes, France*, pages 08B3–5–1–6, 2015.

[309] Y. Wei, A. Rafiee, A. Henry, and F. Dias. Wave interaction with an oscillating wave surge converter, Part I: Viscous effects. *Ocean Engineering*, 104:185 – 203, 2015.

[310] Y. Wei and F. Dias. Numerical study of three dimensional effects of wave impact on an oscillating wave surge converter. In *Proceedings of the 34th International Conference on Ocean, Offshore and Arctic Engineering (OMAE), St. John's, Newfoundland, Canada*, pages 1–10, 2015.

[311] T. Abadie and F. Dias. Numerical study of wave interaction with a modular oscillating wave surge converter. In *Proceedings of the 26th International Ocean and Polar Engineering Conference (ISOPE), Rhodes, Greece*, pages 1021–1028, 2016.

[312] M. Anbarsooz, A. Faramarzi, and A. Ghasemi. A numerical study on the performance of fixed oscillating water column wave energy converter at steep waves. In *Proceedings of the ASME 2016 Power Conference, Charlotte, NA, USA*, pages 1–7, 2016.

[313] V. Anvesh, D. Karmakar, and C.G. Soarse. Performance of oscillating water column wave energy converters integrated in breakwaters. In *Proceedings of the 2nd International Conference on Renewable Energies Offshore (RENEW), Lisbon, Portugal*, pages 295–302, 2016.

[314] A. Büchner, T. Knapp, M. Bednarz, P. Sinn, and A. Hildebrandt. Loads and dynamic response of a floating wave energy converter due to regular waves from CFD simulations. In *Proceedings of the 35th International Conference on Ocean, Offshore and Arctic Engineering (OMAE), Busan, South Korea*, pages 1–10, 2016.

[315] A. Bharath, I. Penesis, J.-R. Nader, and G. Macfarlane. Non-linear CFD modelling of a submerged sphere wave energy converter. In *Proceedings of the 3rd Asian Wave and Tidal Energy Conference (AWTEC), Singapore*, pages 320–329, 2016.

[316] L. Chen, L. Sun, J. Zang, A.J. Hillis, and A.R. Plummer. Numerical study of roll motion of a 2-D floating structure in viscous flow. *Journal of Hydrodynamics, Ser. B*, 28:544–563, 2016.

[317] W.C. Chen, Y.L. Zhang, and H.F. Yu. Numerical study on the performance of a twin-raft wave energy dissipator in a stilling basin. *Journal of Fluids and Structures*, 66:170–182, 2016.

[318] D.P. Coiro, G. Troise, G. Calise, and N. Bizzarrini. Wave energy conversion through a point pivoted absorber: Numerical and experimental tests on a scaled model. *Renewable Energy*, 87:317–325, 2016.

[319] J. Davidson, S. Giorgi, and J.V. Ringwood. Identification of wave energy device models from numerical wave tank data—Part 1: Numerical wave tank identification tests. *IEEE Transactions on Sustainable Energy*, 7(3):1012–1019, 2016.

[320] B. Devolder, O. Rauwoens, and P. Troch. Numerical simulation of a single floating point absorber wave energy converter using OpenFOAM. In *Proceedings of the 2nd International Conference on Renewable Energies Offshore (RENEW), Lisbon, Portugal*, pages 197–205, 2016.

[321] A. Elhanafi. Prediction of regular wave loads on a fixed offshore oscillating water column-wave energy converter using CFD. *Journal of Ocean Engineering and Science*, 1(4):268–283, 2016.

[322] A. Elhanafi, A. Fleming, G. Macfarlane, and Z. Leong. Numerical energy balance analysis for an onshore oscillating water column–wave energy converter. *Energy*, 116:539–557, 2016.

[323] P. Filianoti and L. Gurnari. A CFD analysis of the wave field in front of a U-OWC breakwater. In *Proceedings of the 2nd International Conference on Renewable Energies Offshore (RENEW), Lisbon, Portugal*, pages 327–334, 2016.

[324] P.J.M Ferrer, D.M. Causon, L. Qian, C.G. Mingham, and Z.H. Ma. A multi-region coupling scheme for compressible and incompressible flow solvers for two-phase flow in a numerical wave tank. *Computers & Fluids*, 125:116–129, 2016.

[325] P.J.M Ferrer, D.M. Causon, L. Qian, C.G. Mingham, and Z.H. Ma. Numerical simulation of wave slamming on a flap type oscillating wave energy device. In *Proceedings of the 26th International Ocean and Polar Engineering Conference (ISOPE), Rhodes, Greece*, pages 672–677, 2016.

[326] W. Guo, X. Zheng, W. Zhang, and L. Zhang. Performance evaluation and optimization of a slack-moored two-floating WEC using CFD. In *Proceedings of the 26th International Ocean and Polar Engineering Conference (ISOPE), Rhodes, Greece*, pages 602–608, 2016.

[327] G. Giorgi and J. V. Ringwood. Implementation of latching control in a numerical wave tank with regular waves. *Journal of Ocean Engineering and Marine Energy*, 2:211–226, 2016.

[328] G. Giorgi, M. Penalba, and J. V. Ringwood. Nonlinear hydrodynamic models for heaving buoy wave energy converters. In *Proceedings of the 3rd Asian Wave and Tidal Energy Conference (AWTEC), Singapore*, pages 144–153, 2016.

[329] S. Giorgi, J. Davidson, and J.V. Ringwood. Identification of wave energy device models from numerical wave tank data—Part 2: Data-based model determination. *IEEE Transactions on Sustainable Energy*, 7:1020–1027, 2016.

[330] Z.Z. Hu, D.M. Greaves, and A. Raby. Numerical wave tank study of extreme waves and wave-structure interaction using OpenFOAM. *Ocean Engineering*, 126:329–342, 2016.

[331] A.J.C. King, C. Algie, S. Ryan, and R. Ong. Modelling of fluid structure interactions in submerged flexible membranes for the bombora wave energy converter. In *Proceedings of the 20th Australasian Fluid Mechanics Conference, Perh, Australia*, pages 1–4, 2016.

[332] H. Li, H.Z. He, S.H. Yang, J. Zhang, J. Liang, and W. Sheng. Numerical and experimental studies of water impact on conical point absorber buoys. In *Proceedings of the 2nd International Conference on Renewable Energies Offshore (RENEW), Lisbon, Portugal*, pages 215–226, 2016.

[333] T. Tan Loh, D.M. Greaves, T. Maeki, M. Vuorinen, D. Simmonds, and A. Kyte. Numerical modelling of the WaveRoller device using OpenFOAM. In *Proceedings of the 3rd Asian Wave and Tidal Energy Conference (AWTEC), Singapore*, pages 134–143, 2016.

[334] J. Palm, C. Eskilsson, G.M. Paredes, and L. Bergdahl. Coupled mooring analysis for floating wave energy converters using CFD: Formulation and validation. *International Journal of Marine Energy*, 16:83–99, 2016.

[335] K. Rajagopalan and G. Nihous. Study of the force coefficients on plates using an open source numerical wave tank. *Ocean Engineering*, 118:187–203, 2016.

[336] J.V. Ringwood, J. Davidson, and S. Giorgi. Identifying models using recorded data. In *Numerical Modelling of Wave Energy Converters*, pages 123–147. Elsevier, 2016.

[337] P. Schmitt, H. Asmuth, and B. Elsäßer. Optimising power take-off of an oscillating wave surge converter using high fidelity numerical simulations. *International Journal of Marine Energy*, 16:196–208, 2016.

[338] L. Sjökvist and M. Götman. The effect of overtopping waves on peak forces on a point absorbing WEC. In *Proceedings of the 3rd Asian Wave and Tidal Energy Conference (AWTEC), Singapore*, pages 11–16, 2016.

[339] M. Torresi, F. Scarpetta, G. Martina, P.F. Filianoti, and S.M. Camporeale. Numerical prediction of the natural frequency of an oscillating water column operating under resonant conditions. *The International Journal of Ocean and Climate Systems*, 7:100–107, 2016.

[340] F.R. Torres, P.R.F. Teixeira, and E. Didier. Study of the turbine power output of an oscillating water column device by using a hydrodynamic – Aerodynamic coupled model. *Ocean Engineering*, 125:147–154, 2016.

[341] C. Windt, J. Tchoufag, and M.-R. Alam. Numerical investigation of three-dimensional effects on wave excitation forces on a submerged rigid board. In *Proceedings 2nd International Conference on Offshore Renewable Energy, Glasgow, UK*, pages 1–9, 2016.

[342] Y. Wei, T. Abadie, A. Henry, and F. Dias. Wave interaction with an oscillating wave surge converter. Part II: Slamming. *Ocean Engineering*, 113:319 – 334, 2016.

[343] Y. Wei, Y. Abadie, and F. Dias. A cost-effective method for modelling wave-OWSC interaction. In *Proceedings of the 26th International Ocean and Polar Engineering Conference (ISOPE), Rhodes, Greece*, pages 658–664, 2016.

[344] E. Quon, A. Platt, Y.-H. Yu, and M. Lawson. Application of the most likely extreme response method for wave energy converters. In *Proceedings of the 35th International Conference on Ocean, Offshore and Arctic Engineering (OMAE), Busan, South Korea*, pages 1–10, 2016.

[345] G. Palma, S.M. Formentin, B. Zanuttigh, P. Contestabile, and D. Vicinanza. Design optimization of a multifunctional wave energy device. In *Proceedings of the 2nd International Conference on Renewable Energies Offshore (RENEW), Lisbon, Portugal*, pages 235–240, 2016.

[346] J. Allen, K. Samapanis, J. Wan, J. Miles, D.M. Greaves, and G. Iglesias. Laboratory tests and numerical modelling in the development of WaveCat. In *Proceedings of the 12th European Wave and Tidal Energy Conference (EWTEC), Cork, Ireland*, pages 818–1–10, 2017.

[347] B. Bouali and S. Larbi. Sequential optimization and performance prediction of an oscillating water column wave energy converter. *Ocean Engineering*, 131:162 – 173, 2017.

[348] J.A. Bridgwater Court, D.R.S. Cahndel, A.R. Plummer, and A.J. Hillis. Modelling of array interactions for a curved OSWEC using OpenFOAM. In *Proceedings of the 12th European Wave and Tidal Energy Conference (EWTEC), Cork, Ireland*, pages 776–1–10, 2017.

[349] W.C. Chen, I. Dolguntseva, A. Savin, Y.L. Zhang, W. Li, O. Svensson, and M. Leijon. Numerical modelling of a point-absorbing wave energy converter in irregular and extreme waves. *Applied Ocean Research*, 63:90 – 105, 2017.

[350] J. Davidson, R. Genest, and J.V. Ringwood. Adaptive control of a wave energy converter simulated in a numerical wave tank. In *Proceedings of the 12th European Wave and Tidal Energy Conference (EWTEC), Cork, Ireland*, pages 747–1–10, 2017.

[351] B. Devolder, P. Rauwoens, and P. Troch. Numerical simulation of an array of heaving floating point absorber wave energy converters using OpenFOAM. In *Proceedings of the VII International Conference on Computational Methods in Marine Engineering (MARINE), Nantes, France*, pages 777–788, 2017.

[352] B. Devolder, P. Rauwoens, and P. Troch. Towards the numerical simulation of 5 floating point absorber wave energy converts installed in a line array using OpenFOAM. In *Proceedings of the 12th European Wave and Tidal Energy Conference (EWTEC), Cork, Ireland*, pages 739–1–10, 2017.

[353] A. Elhanafi, G. Macfarlane, A. Fleming, and Z. Leong. Investigations on 3D effects and correlation between wave height and lip submergence of an offshore stationary OWC wave energy converter. *Applied Ocean Research*, 64:203–216, 2017.

[354] A. Elhanafi, G. Macfarlane, A. Fleming, and Z. Leong. Numerical hydrodynamic analysis of an offshore stationary–floating oscillating water column–wave energy converter using CFD. *International Journal of Naval Architecture and Ocean Engineering*, 9:77–99, 2017.

[355] A. Elhanafi, G. Macfarlane, A. Fleming, and Z. Leong. Scaling and air compressibility effects on a three-dimensional offshore stationary OWC wave energy converter. *Applied Energy*, 189:1–20, 2017.

[356] A. Elhanafi, G. Macfarlane, A. Fleming, and Z. Leong. Underwater geometrical impact on the hydrodynamic performance of an offshore oscillating water column–wave energy converter. *Renewable Energy*, 105:209–231, 2017.

[357] A. Elhanafi, G. Macfarlane, A. Fleming, and Z. Leong. Experimental and numerical investigations on the intact and damage survivability of a floating-moored oscillating water column device. *Applied Ocean Research*, 68:276 – 292, 2017.

[358] A. Elhanafi, G. Macfarlane, A. Fleming, and Z. Leong. Intact and damaged survivability of an offshore floating-moored OWC device. In *Proceedings of the 27th International Ocean and Polar Engineering Conference (ISOPE), San Francisco, CA, USA*, pages 58–65, 2017.

[359] A. Elhanafi, G. Macfarlane, A. Fleming, and Z. Leong. Experimental and numerical measurements of wave forces on a 3D offshore stationary OWC wave energy converter. *Ocean Engineering*, 144:98 – 117, 2017.

[360] A. Elhanafi, G. Macfarlane, A. Fleming, and Z. Leong. Experimental and numerical investigations on the hydrodynamic performance of a floating-moored oscillating water column wave energy converter. *Applied Energy*, 205:369 – 390, 2017.

[361] C. Eskilsson, J. Palm, and L. Bergdahl. On numerical uncertainty of VOF-RANS simulations of wave energy converters through V&V technique. In *Proceedings of the 12th European Wave and Tidal Energy Conference (EWTEC), Cork, Ireland*, pages 1021–1–9, 2017.

[362] W. Wang, M. Wu, J. Palm, and C. Eskilsson. Estimation of numerical uncertainty in CFD simulations of a passivley controlled wave energy converter. *Proceedings of the Institution of Mechanical Engineers, Part M: Journal of Engineering for the Maritime Environment*, 232:71–84, 2017.

[363] H.T. Gao, J Zou, and B. Li. Simulating investigation on the motion and power response of double raft wave energy capturer with different shapes. In *Proceeding of the International Conference on Energy, Power and Environmental Engineering (ICEPEE 2017), Shanghai, China*, pages 161–167, 2017.

[364] A. Ghasemi, M. Anbarsooz, A. Malvandi, A. Ghasemi, and F. Hedayati. A nonlinear computational modeling of wave energy converters: A tethered point absorber and a bottom-hinged flap device. *Renewable Energy*, 103:774–785, 2017.

[365] G. Giorgi and J.V. Ringwood. Consistency of viscous drag identification tests for wave energy applications. In *Proceedings of the 12th European Wave and Tidal Energy Conference (EWTEC), Cork, Ireland*, pages 643–1–8, 2017.

[366] V. Gnanaruban and M. Folley. Computational fluid dynamic modelling of a lift-based wave energy converter. In *Proceeding of the 28th International Symposium on Transport Phenomena, Peradeniya, Sri Lanka*, pages 1–4, 2017.

[367] S. Jin and R. Patton. Geometry influence on hydrodynamic response of a heaving point absorber wave energy converter. In *Proceedings of the 12th European Wave and Tidal Energy Conference (EWTEC), Cork, Ireland*, pages 957–1–8, 2017.

[368] S. Jungrungruengtaworn and B.-S. Hyun. Influence of slot width on the performance of multi-stage overtopping wave energy converters. *International Journal of Naval Architecture and Ocean Engineering*, 9(6):668–676, 2017.

[369] G.S. Kanchak, S. Saincher, and J. Banerjee. Numerical investigations on hydrodynamic efficiency of oscillating water column. In *Proceeding of the 6th Asian Symposium on Computational Heat Transfer and Fluid Flow, Chennai, India*, pages 1–7, 2017.

[370] D.C. Lo, T.-W. Hsu, and C.-D. Yang. Hydrodynamic performances of wave pass two buoys-type wave energy converter. In *Proceedings of the 27th International Ocean and Polar Engineering Conference, ISOPE, San Francisco, CA, USA*, pages 133–139, 2017.

[371] T. Tan Loh, D. Pizer, D. Simmonds, A. Kyte, and D.M. Greaves. Simulation and analysis of wave-structure interactions for a semi-immersed horizontal cylinder. *Ocean Engineering*, 145:676–689, 2017.

[372] F. Meng, A. Rafiee, B. Cazzolato, B. Ding, Arjomandi M., J. D. Piper, N. Sergiienko, and Q. Hu. Numerical simulation of a submerged spherical point absorber with asymmetric mass distribution. In *Proceedings of the 12th European Wave and Tidal Energy Conference (EWTEC), Cork, Ireland*, pages 1128–1–8, 2017.

[373] T. R. Mundon, B. J. Rosenberg, and J. van Rij. Reaction body hydrodynamics for a multi-DOF point-absorbing WEC. In *Proceedings of the 12th European Wave and Tidal Energy Conference (EWTEC), Cork, Ireland*, pages 997–1–10, 2017.

[374] M. A. Musa, A. Y. Maliki, M. F. Ahmad, W. N. Sani, O. Yaakob, and K.B. Samo. Numerical simulation of wave flow over the overtopping breakwater for energy conversion (OBREC) device. *Procedia engineering*, 194:166–173, 2017.

[375] A. Y. Maliki, M. A. Musa, M. F. Ahmad, and O. Yaakob. Numerical simulation of wave flow over the overtopping breakwater for energy conversion (OBREC) device. *Journal of Engineering Science and Technology*, 12(5):1337–1353, 2017.

[376] P.-H. Musiedlak, E.J. Ransley, D.M. Greaves, M. Hann, G. Iglesias, and B. Child. Investigation of model validity for numerical survivability testing of WECs. In *Proceedings of the 12th European Wave and Tidal Energy Conference (EWTEC), Cork, Ireland*, pages 796–1–8, 2017.

[377] H.R. Mottahedi, M. Anbarsooz, and M. Pasandide-Fard. Numerical study of the performance of an oscillating wave surge converter using volume of fluid method. *Modares Mechanical Engineering*, 17(6):265–276, 2017.

[378] K. O Connell, A. Cashman, F. Thiebaut, and G. Kelly. Development of a free heaving OWC model with non-linear PTO interaction. *Renewable Energy*, 205:369 – 390, 2017.

[379] J. Palm. *Mooring dynamics for wave energy applications*. PhD thesis, Chalmers University of Technology, Gothenburg, Sweden, 2017.

[380] A. Pilechi, S. Baker, and A. Cornett. Validation of a CFD tool for studying the behaviour of wave energy converters. In *Proceedings of the 12th European Wave and Tidal Energy Conference (EWTEC), Cork, Ireland*, pages 654–1–10, 2017.

[381] D.D. Prasad, M.R. Ahmed, Y.-H. Lee, and R.N. Sharma. Validation of a piston type wave-maker using numerical wave tank. *Ocean Engineering*, 131:57–67, 2017.

[382] E.J. Ransley, D.M. Greaves, A. Raby, Simmonds D., and M. Hann. Survivability of wave energy converters using CFD. *Renewable Energy*, 109:235–247, 2017.

[383] E.J. Ransley, D.M. Greaves, A. Raby, Simmonds D., M.M. Jakobsen, and M. Kramer. RANS-VOF modelling of the wavestar point absorber. *Renewable Energy*, 109:49–65, 2017.

[384] J. van Rij, Y.-H. Yu, and Y. Guo. Structural loads analysis for wave energy converters. In *Proceeding of the 36th International Conference on Ocean, Offshore, and Arctic Engineering (OMAE), Trondheim, Norway*, pages 1–10, 2017.

[385] F. Scarpetta, M. Torresi, S.M. Camporeale, and P.F. Filianoti. CFD simulation of the unsteady flow in an Oscillating Water Column: comparison between numerical and experimental results for a small scale experimental device. In *Proceedings of the 12th European Wave and Tidal Energy Conference (EWTEC), Cork, Ireland*, pages 988–1–7, 2017.

[386] F. Scarpetta, L. Gurnari, M. Torresi, and S.M. Camporeale. A CFD simulation of a full-scale U-OWC breakwater. In *Proceedings of the 12th European Wave and Tidal Energy Conference (EWTEC), Cork, Ireland*, pages 1014–1–9, 2017.

[387] P. Schmitt and B. Elsäßer. The application of Froude scaling to model tests of Oscillating Wave Surge Converters. *Ocean Engineering*, 141:108–115, 2017.

[388] I. Simonetti and L. Cappietti. A CFD study on the balance of energy in a fixed bottom-detached oscillating water column wave energy converter. In *Proceedings of the 12th European Wave and Tidal Energy Conference (EWTEC), Cork, Ireland*, pages 937–1–7, 2017.

[389] I. Simonetti, L. Cappietti, H. Elsafti, and Oumeraci. H. Optimization of the geometry and the turbine induced damping for fixed detached and asymmetric OWC devices: a numerical study. *Energy*, 139:1197 – 1209, 2017.

[390] I. Simonetti, L. Cappietti, H. Elsafti, and Oumeraci. H. Evaluation of air compressibility effects on the performance of fixed OWC wave energy converters using CFD modelling. *Renewable Energy*, 119:741 – 753, 2017.

[391] L. Sjökvist, M. Göteman, and M. Leijon. Survivability of a point absorbing wave energy converter impacted by tsunami waves. In *Proceedings of the 12th European Wave and Tidal Energy Conference (EWTEC), Cork, Ireland*, pages 653–1–9, 2017.

[392] L. Sjökvist, J. Wu, E.J. Ransley, J. Engström, M. Eriksson, and M. Göteman. Numerical models for the motion and forces of point-absorbing wave energy converters in extreme waves. *Ocean Engineering*, 145:1 – 14, 2017.

[393] L. Sjökvist and M. Göteman. Peak forces on wave energy linear generators in tsunami and extreme waves. *Energies*, 10(9):1323, 2017.

[394] T. Vyzikas, S. Deshoulieres, O. Giroux, M. Barton, and D.M. Greaves. Numerical study of fixed oscillatin water column with RANS-type two-phase CFD model. *Renewable Energy*, 102:294 – 305, 2017.

[395] D. Wang, K. Xia, and D. Wan. Numerical investigation of hydrodynamic responses of point absorbing wave energy device. In *Proceeding of the 3rd International Conference for Innovation and Coorperation of Naval Architecture and Marine Engineering (ICNAME), Qingdao, China*, pages 64–70, 2017.

[396] H.I. Yamaç and A. Koca. Numerical wave tank analysis for energy harvesting with oscillating water column. In *Proceedings of the 2017 International Conference Mechatronics, Gliwice, Poland*, pages 726–734. Springer, 2017.

[397] Y.-S. Kuo, C.-Y. Chung, S.-C. Hsiao, and Y.-K. Wang. Hydrodynamic characteristics of oscillating water column caisson breakwaters. *Renewable Energy*, 103:439–447, 2017.

[398] A. Moñino, E. Medina-López, M. Clavero, and S. Benslimane. Numerical simulation of a simple OWC problem for turbine performance. *International journal of marine energy*, 20:17–32, 2017.

[399] E. Medina-López, R.J. Bergillos, A. Moñino, M. Clavero, and M. Ortega-Sánchez. Effects of seabed morphology on oscillating water column wave energy converters. *Energy*, 135:659–673, 2017.

[400] A. Pathak, C. Freniere, and M. Raessi. Advanced computational simulations of water waves interacting with wave energy converters. *European Journal of Computational Mechanics*, 26(1-2):172–204, 2017.

[401] F. Mahnamfar and A. Altunkaynak. Comparison of numerical and experimental analyses for optimizing the geometry of OWC systems. *Ocean Engineering*, 130:10–24, 2017.

[402] C. Worden Hodge, W. Bateman, Z. Yuan, P.R. Thies, and T. Bruce. Performance analysis of the CCell wave energy device. In *Proceedings of the 12th European Wave and Tidal Energy Conference (EWTEC), Cork, Ireland*, pages 959–1–10, 2017.

[403] D.V.E. Barbosa, A.L.G. Santos, E.D. dos Santos, and J.A. Souza. Overtopping device numerical study: Openfoam solution verification and evaluation of curved ramps performances. *International Journal of Heat and Mass Transfer*, 131:411–423, 2018.

[404] A. Bharath, J.-R. Nader, I. Penesis, and G. Macfarlane. Nonlinear hydrodynamic effects on a generic spherical wave energy converter. *Renewable Energy*, 118:56–70, 2018.

[405] M. Buccino, M. Daliri, F. Dentale, and A. Di Leo. A CFD study on impact wave loadings exerted behind overtopping type WECs. In *Proceeding of the 28th International Ocean and Polar Engineering Conference (ISOPE), Saporo, Japan*, pages 1349–1354, 2018.

[406] Z.-F. Chen, B.-Z. Zhou, L. Zhang, W.-C. Zhang, S.-Q. Wang, and J. Zang. Geometrical evaluation on the viscous effect of point-absorber wave-energy converters. *China Ocean Engineering*, 32(4):443–452, 2018.

[407] S.A. Brown, P.-H. Musiedlak, E.J Ransley, and D.M. Greaves. Numerical simulation of focused wave interactions with a fixed FPSO using OpenFOAM 4.1. In *Proceeding of the 28th International Ocean and Polar Engineering Conference (ISOPE), Saporo, Japan*, pages 1498–1503, 2018.

[408] Z. Xie, S. Yan, Q. Ma, and T. Stoesser. Numerical modelling of focusing wave impact on a fixed offshore structure. In *Proceeding of the 28th International Ocean and Polar Engineering Conference (ISOPE), Saporo, Japan*, pages 1451–1457, 2018.

[409] H. Chen, L. Qian, Z. Ma, D.M. Causon, and C. Mingham. Numerical simulation of phase-focused wave group interaction with an FPSO-Shaped body. In *Proceeding of the 28th International Ocean and Polar Engineering Conference (ISOPE), Saporo, Japan*, pages 1481–1485, 2018.

[410] Q. Chen and J. Zang. Numerical modelling of focused wave impact with a fixed FSPO-like structure using a particle-in-cell solver. In *Proceeding of the 28th International Ocean and Polar Engineering Conference (ISOPE), Saporo, Japan*, pages 1492–1497, 2018.

[411] I. Gatin, H. Jasak, and V. Vukčević. Focused wave loading on a fixed FPSO using naval hydro pack. In *Proceeding of the 28th International Ocean and Polar Engineering Conference (ISOPE), Saporo, Japan*, pages 1434–1442, 2018.

[412] P. Higuera, E. Buldakov, and D. Stagonas. Numerical modelling of wave interaction with an FPSO using a combination of OpenFOAM and Lagrangian models. In *Proceeding of the 28th International Ocean and Polar Engineering Conference (ISOPE), Saporo, Japan*, pages 1486–1491, 2018.

[413] Q. Li, Y. Zhuang, D. Wan, and G. Chen. Numerical analysis of the interaction between a fixed FPSO benchmark model and focused waves. In *Proceeding of the 28th International Ocean and Polar Engineering Conference (ISOPE), Saporo, Japan*, pages 1420–1427, 2018.

[414] Q. Li, S. Yan, J. Wang, Q.W. Ma, Z. Xie, and V. Sriram. Numerical simulation of focusing wave interaction with FPSO-like structure using FNPT-NS solver. In *Proceeding of the 28th International Ocean and Polar Engineering Conference (ISOPE), Saporo, Japan*, pages 1458–1464, 2018.

[415] H. Wu, T. Li, L. Ma, X. Song, D.A. Hudson, P. Temarel, and W.G. Price. Numerical simulation of FPSO-like structure in waves by RANS method. In *Proceeding of the 28th International Ocean and Polar Engineering Conference (ISOPE), Saporo, Japan*, pages 1428–1433, 2018.

[416] Y. Zhuang, Q. Li, and D. Wan. Numerical study of a fixed FPSO-shaped body under focused waves with different headings. In *Proceeding of the 28th International Ocean and Polar Engineering Conference (ISOPE), Saporo, Japan*, pages 1257–1263, 2018.

[417] J. Davidson, R. Genest, and J.V. Ringwood. Adaptive control of a wave energy converter. *IEEE Transactions on Sustainable Energy*, 9(4):1588–1595, 2018.

[418] S. Jin, R. Patton, and B. Guo. Viscosity effect on a point absorber wave energy converter hydrodynamics validated by simulation and experiment. *Renewable energy*, 129:500–512, 2018.

[419] L. Yang, Z. Lyu, P. Yang, D. Pavlidis, F. Fang, J. Xiang, J.-P. Latham, and C. Pain. Numerical simulation of attenuator wave energy converter using one-fluid formulation. In *Proceeding of the 28th International Ocean and Polar Engineering Conference (ISOPE), Saporo, Japan*, pages 602–607, 2018.

[420] A. Elhanafi and C. J. Kim. Experimental and numerical investigation on wave height and power take–off damping effects on the hydrodynamic performance of an offshore–stationary OWC wave energy converter. *Renewable energy*, 125:518–528, 2018.

[421] A. Elhanafi, G. Macfarlane, and D. Ning. Hydrodynamic performance of single–chamber and dual–chamber offshore–stationary oscillating water column devices using CFD. *Applied Energy*, 228:82–96, 2018.

[422] F. Yang, W. Shi, X. Zhou, B. Guo, and D. Wang. Numerical investigation of a wave glider in head seas. *Ocean engineering*, 164:127–138, 2018.

[423] C. Xu and Z. Huang. An OpenFOAM–based two–phase flow model for simulating three–dimensional oscillating–water–column devices: Model verification and validation. In *Book of abstracts of the 13th OpenFOAM Workshop (OFW13), Shanghai, China*, pages 366–368, 2018.

[424] M. Wu, W. Wang, J. Palm, and C. Eskilsson. CFD simulation of a passively controlled point absorber wave energy converter. In *Trends and Challenges in Maritime Energy Management*, pages 499–511. Springer, 2018.

[425] C.-P. Tsai, C.-H. Ko, and Y.-C. Chen. Investigation on performance of a modified breakwater-integrated OWC wave energy converter. *Sustainability*, 10(3):643, 2018.

[426] K. Rezanejad, J.F.M. Gadelho, and C.G. Soares. Hydrodynamic analysis of an oscillating water column wave energy converter in the stepped bottom condition using CFD. *Renewable Energy*, 135:1241–1259, 2018.

[427] D.D. Prasad, M. R. Ahmed, and Y.-H. Lee. Studies on the performance of savonius rotors in a numerical wave tank. *Ocean Engineering*, 158:29–37, 2018.

[428] A. Rafiee and A. Valizadeh. Non-linear hydrodynamics of bluff bodies oscillating near free-surface. In *Proceedings of the 28th International Ocean and Polar Engineering Conference (ISOPE), Sapporo, Japan*, pages 307–315, 2018.

[429] S.K. Poguluri, Y.H. Bae, and I.H. Cho. Effect of viscous damping on the performance of a pitch-type WEC rotor. In *Proceedings of the 28th International Ocean and Polar Engineering Conference (ISOPE), Sapporo, Japan*, pages 733–740, 2018.

[430] H.S.K Ko, Y.H. Bae, I.H. Cho, J. Kim, and C.H. Ko. Numerical and experimental study for a cylindrical wave energy converter with different rotational axes. In *Proceedings of the 28th International Ocean and Polar Engineering Conference (ISOPE), Sapporo, Japan*, pages 685–689, 2018.

[431] H. Kim, N. Parthasarathy, K.M. Li, Y.H. Choi, N. Oshima, and Y.W. Lee. The effect of wavelength on a floating body and its location for wave energy absorption using CFD. In *Proceedings of the 28th International Ocean and Polar Engineering Conference (ISOPE), Sapporo, Japan*, pages 741–746, 2018.

[432] H.R. Mottahedi, M. Anbarsooz, and M. Passandideh-Fard. Application of a fictitious domain method in numerical simulation of an oscillating wave surge converter. *Renewable energy*, 121:133–145, 2018.

[433] P. Mohapara, A. Bhattacharyya, and T. Sahoo. Performance of a floating oscillating water column wave energy converter in the presence of a sloping bed. In *Proceedings of the 37th International Conference on Ocean, Offshore and Arctic Engineering (OMAE), Madrid, Spain*, pages 1–8, 2018.

[434] C.-C. Lin, Y.-C. Cho, S.-Y. Tzang, C.-Y. Chiou, and Y.-Y. Huang. Numerical study on the geometric and inertial parameters for oscillating wave surge converters. In *Proceedings of the 37th International Conference on Ocean, Offshore and Arctic Engineering (OMAE), Madrid, Spain*, pages 1–9, 2018.

[435] C.-C. Lin, Y.-C. Chow, and S.-Y. Tzang. The viscous effect in power capture of bottom–hinged oscillating wave surge converters. In *Proceedings of the 4rd Asian Wave and Tidal Energy Conference (AWTEC), Taipei, Taiwan*, pages 423–1–7, 2018.

[436] C. Worden Hodge, W. Bateman, Z. Yuan, P.R. Thies, and T. Bruce. Coupled modelling of a non-linear wave energy converter and hydraulic PTO. In *Proceedings of the 28th International Ocean and Polar Engineering Conference (ISOPE), Sapporo, Japan*, pages 634–640, 2018.

[437] S.C. Lee, S. Park, S. Song, and S.M. Jeong. Development of platform 6-DOF motion-mooring system coupled solver using open source libraries. In *Proceedings of the 28th International Ocean and Polar Engineering Conference (ISOPE), Sapporo, Japan*, pages 1237–1241, 2018.

[438] S. Park, K.-H. Kim, B.W. Nam, J.-S. Kim, and K. Hong. Numerical study on performance analysis for OWC WEC applicable to breakwater. In *Proceedings of the 4rd Asian Wave and Tidal Energy Conference (AWTEC), Taipei, Taiwan*, pages 466–1–5, 2018.

[439] B.W. Schubert, F. Meng, N.Y. Sergiienko, W. Robertson, B.S. Cazzolato, Ghayesh M.H., A. Rafiee, B. Ding, and M. Arjomandi. Pseudo-nonlinear hydrodynamic coefficients for modelling point absorber wave energy converters. In *Proceedings of the 4rd Asian Wave and Tidal Energy Conference (AWTEC), Taipei, Taiwan*, pages 442–1–10, 2018.

[440] J.C. Martins, M.M. Goulart, M.d.N. Gomes, J.A. Souza, L.A.O. Rocha, L.A. Isoldi, and E.D. Dos Santos. Geometric evaluation of the main operational principle of an overtopping wave energy converter by means of constructal design. *Renewable Energy*, 118:727–741, 2018.

[441] T. Martin, H. Bihs, A. Kamath, and Ø. A. Arntsen. Simulation of floating bodies in waves and mooring in a 3D numerical wave tank using REEF3D. In *Proceedings of the Fourth International Conference in Ocean Engineering (ICOE2018), Chennai, India*, pages 673–683. Springer, 2018.

[442] I.P. Johannesen and G.T. Brockhaus. Simulation of motions and forces for a generic wave energy converter using RANS CFD. In *Proceedings of the 3rd International Conference on Renewable Energies Offshore (RENEW), Lisbon, Portugal*, pages 447–453, 2018.

[443] H. Islam, S.C. Mohapatra, and C.G. Soares. Comparisons of CFD, experimental and analytical simulations of a heaving box-type floating structure. In *Proceedings of the 3rd International Conference on Renewable Energies Offshore (RENEW), Lisbon, Portugal*, pages 633–639, 2018.

[444] J.F.M. Gadelho, S.C. Mohapatra, and C.G. Soares. CFD analysis of a fixed floating box-type structure under regular waves. In *Proceedings of the 3rd International Conference on Renewable Energies Offshore (RENEW), Lisbon, Portugal*, pages 513–520, 2018.

[445] C. Eskilsson and J. Palm. Simulations of floating wave energy devices using adaptive mesh refinement. In *Proceedings of the 3rd International Conference on Renewable Energies Offshore (RENEW), Lisbon, Portugal*, pages 431–438, 2018.

[446] P.-H. Musiedlak, E. Ransley, S.A. Brown, B.F.M. Child, M. Hann, G. Idlesias, and D. Greaves. Starting a wave structure interaction CFD simulation from an advance time: Hot–start. In *Proceedings of the 7th European Conference on Computational Fluid Dynamics (ECFD 7), Glasgow, UK*, pages 431–438, 2018.

[447] Q. Chen, J. Zang, X. Zhao, and D. Ning. Numerical study of the hydrodynamic performance of a pile-restrained WEC-type floating breakwater. In *Proceedings of the 33rd International Workshop on Water Waves and Floating Bodies, Guidel-Plage, France*, pages 1–4, 2018.

[448] E. Di Lauro, M. Maza, J.L. Lara, I.J. Losada, and D. Vicinanza. Numerical modeling of wave interaction with a non-conventional breakwater for wave energy conversion. *Coastal Engineering Proceedings*, (36):64–64, 2018.

[449] P.G.F. Filianoti, L. Gurnari, M. Torresi, and S.M. Camporeale. CFD analysis of the energy conversion process in a fixed oscillating water column (OWC) device with a wells turbine. *Energy Procedia*, 148:1026–1033, 2018.

[450] P.G.F. Filianoti and L. Gurnari. Wave pressure distributions on a U-OWC breakwater: Experimental data vs CFD model. *Coastal Engineering Proceedings*, (36):15–15, 2018.

[451] W. Guo, Y.-H. Zhou, W.-C. Zhang, and Q.-S. Zhao. Hydrodynamic analysis and power conversion for point absorber WEC with two degrees of freedom using CFD. *China Ocean Engineering*, 32(6):718–729, 2018.

[452] B. Devolder, P. Troch, and P. Rauwoens. Survivability simulation of a wave energy converter in a numerical wave tank. In *Book of abstracts of the 13th OpenFOAM Workshop (OFW13), Shanghai, China*, pages 308–3011, 2018.

[453] B. Devolder, V. Stratigaki, P. Troch, and P. Rauwoens. CFD simulations of floating point absorber wave energy converter arrays subjected to regular waves. *Energies*, 11(3):641, 2018.

[454] J. Palm, L. Bergdahl, and C. Eskilsson. Parametric excitation of moored wave energy converters using viscous and non-viscous CFD simulations. In *Proceedings of the 3rd International Conference on Renewable Energies Offshore (RENEW), Lisbon, Portugal*, pages 455–462, 2018.

[455] J. Palm, C. Eskilsson, L. Bergdahl, and R. E. Bensow. Assessment of scale effects, viscous forces and induced drag on a point-absorbing wave energy converter by CFD simulations. *Journal of Marine Science and Engineering*, 6(4):124, 2018.

[456] H. Gu, P. Stansby, T. Stallard, and E.C. Moreno. Drag, added mass and radiation damping of oscillating vertical cylindrical bodies in heave and surge in still water. *Journal of Fluids and Structures*, 82:343–356, 2018.

[457] M.S. Bazli, O. Yaakob, and K.H. Siang. Validation study of U-Oscillating water column device using computational fluid dynamic (CFD) simulation. In *Proceedings of the 1st International Conference on Marine Technology (MARTEC), Utmki, Malaysia*, pages 18–25, 2018.

[458] A.M.A. Rahim, O. Yaakob, and C.L. Siow. Modelling on numerical wave tank for application of OWC simulation. In *Proceedings of the 1st International Conference on Marine Technology (MARTEC), Utmki, Malaysia*, pages 45–53, 2018.

[459] A. Subramanian. Prediction of diffraction forces on a wave energy converter using BEM and CFD approach. Master's thesis, The University of North Carolina at Charlotte, 2018.

[460] J. Van Rij, Y.-H. Yu, and R.G. Coe. Design load analysis for wave energy converters. In *Proceedings of the 37th International Conference on Ocean, Offshore and Arctic Engineering (OMAE), Madrid, Spain*, pages 1–10, 2018.

[461] S.C. Mohapatra, H. Islam, and C.G. Soares. Wave diffraction by a floating fixed truncated vertical cylinder based on Boussinesq equations. In *Proceedings of the 3rd International Conference on Renewable Energies Offshore (RENEW), Lisbon, Portugal*, pages 281–289, 2018.

[462] A.M. Miquel, A. Kamath, M. Alagan Chella, R. Archetti, and H. Bihs. Analysis of different methods for wave generation and absorption in a CFD-based numerical wave tank. *Journal of Marine Science and Engineering*, 6(2):73, 2018.

[463] E.J. Ransley, Se Yan, S. A. Brown, T. Mai, D. Graham, Q. Ma, P.-H. Musiedlak, A. P. Engsig-Karup, C. Eskilsson, and Q. Li. A blind comparative study of focused wave interactions with a fixed FPSO-like structure (CCP-WSI Blind Test Series 1). *International Journal of Offshore and Polar Engineering*, 29(2):113–127, 2019.

[464] S. Jin, R. Patton, and B. Guo. Enhancement of wave energy absorption efficiency via geometry and power take-off damping tuning. *Energy*, 169:819–832, 2019.

[465] S.A. Brown, E.J. Ransely, P.-H. Musiedlak, and D. Greaves. Numerical investigation of focused wave impacts on floating wave energy converters using OpenFOAM. In *Proceedings of the 29th International Offshore and Polar Engineering Conference (ISOPE), Honolulu, HI, USA*, pages 3044–3050, 2019.

[466] S.A. Brown, E.J. Ransely, and D. Greaves. CCP-WSI Blind Test Series 2: Assessment of focused wave impacts on floating WECs using OpenFOAM. In *Proceedings of the 13th European Wave and Tidal Energy Conference (EWTEC), Naples, Italy*, pages 1294–1–9, 2019.

[467] H. Chen, L. Qian, Z. Ma, and Z. Lin. CCP-WSI Blind Test Series 3: OpenFOAM simulation of focused wave interaction with a simplified wave energy converter. In *Proceedings of the 29th International Offshore and Polar Engineering Conference (ISOPE), Honolulu, HI, USA*, pages 3096–3101, 2019.

[468] Z. Lin, L. Qing, Z. Ma, H. Chen, D. Causon, and C. Mingham. Simulation of focused wave impact on point absorber wave energy converters - CCP-WSI Blind Test Series 2. In *Proceedings of the 13th European Wave and Tidal Energy Conference (EWTEC), Naples, Italy*, pages 1463–1–6, 2019.

[469] L. Cheng, J. Zheng, H. Gu, and X. Gong. Focused wave interaction with floating structures by in-house codes. In *Proceedings of the 29th International Offshore and Polar Engineering Conference (ISOPE), Honolulu, HI, USA*, pages 3102–3107, 2019.

[470] Z. Liu, Y. Zhang, D. Wan, and G. Chen. Numerical study on focused wave interactions with a moored floating structure. In *Proceedings of the 29th International Offshore and Polar Engineering Conference (ISOPE), Honolulu, HI, USA*, pages 3081–3088, 2019.

[471] J. Wang, J. Wang, S. Yan, Q. Ma, and G. Xia. An improved passive wave absorption technique for FNPT-NS solver. In *Proceedings of the 29th International Offshore and Polar Engineering Conference (ISOPE), Honolulu, HI, USA*, pages 3066–3072, 2019.

[472] S. Yan, J. Wang, J. Wang, Q. Ma, and Z. Xie. Numerical simulation of wave structure interaction using qaleFOAM. In *Proceedings of the 29th International Offshore and Polar Engineering Conference (ISOPE), Honolulu, HI, USA*, pages 3089–3095, 2019.

[473] S. Yan, J. Wang, Q. Ma, J. Wang, and Z. Xie. Numerical simulation of focused wave interaction with WECs using a hybrid FNPT/NS solver. In *Proceedings of the 13th European Wave and Tidal Energy Conference (EWTEC), Naples, Italy*, pages 1452–1–9, 2019.

[474] Q. Chen, H. Ding, and J. Zang. Application of a hybrid Eulerian-Lagrangian PIC model to focused wave interaction with WEC-type floating buoys. In *Proceedings of the 13th European Wave and Tidal Energy Conference (EWTEC), Naples, Italy*, pages 1480–1–6, 2019.

[475] J. van Rij, Y.-H. Yu, and N. Tom. Validation of simulated wave energy converter responses to focused waves for CCP-WSI Blind Test Series 2. In *Proceedings of the 13th European Wave and Tidal Energy Conference (EWTEC), Naples, Italy*, pages 1483–1–10, 2019.

[476] Z. Huang, C. Xu, and S. Huang. A CFD simulation of wave loads on a pile-type oscillating-water-column device. *Journal of Hydrodynamics*, 31(1):41–49, 2019.

[477] C. Xu and Z. Huang. Three-dimensional CFD simulation of a circular OWC with a nonlinear power-takeoff: Model validation and a discussion on resonant sloshing inside the pneumatic chamber. *Ocean Engineering*, 176:184–198, 2019.

[478] U. Izquierdo, G. A. Esteban, J. M. Blanco, I. Albaina, and A. Peña. Experimental validation of a CFD model using a narrow wave flume. *Applied Ocean Research*, 86:1–12, 2019.

[479] L. Galera, U. Izquierdo, G. A. Esteban, J. M. Blanco, I. Albaina, and A. Aristondo. Experimental validation of a RANS-VOF numerical model of the wave generation and propagation in a 2D wave flume. In *Proceedings of the VIII International Conference on Computational Methods in Marine Engineering (MARINE), Gothenburg, Sweden*, pages 134–144, 2019.

[480] F. M. Seibt, E.D. Dos Santos, G. M. Das Neves, L.A.O. Rocha, L.A. Isoldi, and C. Fragassa. Numerical evaluation on the efficiency of the submerged horizontal plate type wave energy converter. *FME Transactions*, 47(3):543–551, 2019.

[481] Q. Xu, Y. Li, Y.-H. Yu, B. Ding, Z. Jiang, Z. Lin, and B. Cazzolato. Experimental and numerical investigations of a two-body floating-point absorber wave energy converter in regular waves. *Journal of Fluids and Structures*, 91:102613, 2019.

[482] Z. Yuan, L. Zhang, B. Zhou, P. Jin, and X. Zheng. Analysis of the hydrodynamic performance of an oyster wave energy converter using Star-CCM+. *Journal of Marine Science and Application*, 18(2):153–159, 2019.

[483] E. Zhao, J. Sun, H. Jiang, and L. Mu. Numerical study on the hydrodynamic characteristics and responses of moored floating marine cylinders under real-world tsunami-like waves. *IEEE Access*, 7:122435–122458, 2019.

[484] X. Zhang, Q. Zeng, and Z. Liu. Hydrodynamic performance of rectangular heaving buoys for an integrated floating breakwater. *Journal of Marine Science and Engineering*, 7(8):239, 2019.

[485] J. Wu, Y. Yao, D. Sun, Z. Ni, and M. Göteman. Numerical and experimental study of the solo duck wave energy converter. *Energies*, 12(10):1941, 2019.

[486] M.G. Verduzco-Zapata, F.J. Ocampo-Torres, R.O. Jimenez-Betancourt, and E. Torres-Orozco. Submerged horizontal plate used for wave energy extraction and as a potential coastal defence alternative. In *Proceedings of the 13th European wave and tidal energy conference (EWTEC), Naples, Italy*, pages 1703–1—6, 2019.

[487] A. Feichtner, E.B.L. Mackay, G. Tabor, P.R. Thies, and L. Johanning. Modelling wave interaction with thin porous structures using OpenFOAM. In *Proceedings of the 13th European wave and tidal energy conference (EWTEC), Naples, Italy*, pages 1415–1—10, 2019.

[488] D.T. Nguyen, Y.-C. Chow, J.-H. Chen, and Lin C.-C. Performance assessment of different RANS turbulence models in numerical simulations for BH-OWSC. In *Proceedings of the 13th European wave and tidal energy conference (EWTEC), Naples, Italy*, pages 1519–1—6, 2019.

[489] G. Palma, S.M. Formentin, P. Contestabile, B. Zanuttigh, and D. Vicinanza. Wave loads on the OBREC device in a real wave climate. In *Proceedings of the 13th European wave and tidal energy conference (EWTEC), Naples, Italy*, pages 1791–1—8, 2019.

[490] G. Palma, M.S. Formentin, B. Zanuttigh, P. Contestabile, and D. Vicinanza. Numerical simulations of the hydraulic performance of a breakwater-integrated overtopping wave energy converter. *Journal of Marine Science and Engineering*, 7(2):38, 2019.

[491] M.F. Roslan, M.F. Ahmad, and M.A. Musa. Investigation on reflected wave by different geometrical ramp shape of overtopping break water for energy conversions using experimental and simulation. In *IOP Conference Series: Materials Science and Engineering*, volume 676, pages 012019–1–10. IOP Publishing, 2019.

[492] M. Kharati-Koopaee and M. Kiali-Kooshkghazi. Assessment of plate-length effect on the performance of the horizontal plate wave energy converter. *Journal of Waterway, Port, Coastal, and Ocean Engineering*, 145(1):04018037–1–14, 2019.

[493] H. Islam, S.C. Mohapatra, J. Gadelho, and C. G. Soares. Openfoam analysis of the wave radiation by a box-type floating structure. *Ocean Engineering*, 193:1065321–13, 2019.

[494] Z. Ma, Y. Mao, Y. Cheng, and G. Zhai. Effect of the PTO damping force on the 2D oscillating buoy wave energy converter integrated into a pile-restrained floating breakwater. *Iranian Journal of Science and Technology, Transactions of Mechanical Engineering*, pages 1–13, 2019.

[495] R. Reabroy, X. Zheng, L. Zhang, J. Zang, Z. Yuan, M. Liu, K. Sun, and Y. Tiaple. Hydrodynamic response and power efficiency analysis of heaving wave energy converter integrated with breakwater. *Energy Conversion and Management*, 195:1174–1186, 2019.

[496] S. K. Poguluri, I.-H. Cjo, and Y. H. Bae. Performance assessment of pitch-type WEC–rotor based on time domain simulations. In *Proceedings of the 29th International Offshore and Polar Engineering Conference (ISOPE), Honolulu, HI, USA*, pages 195–201, 2019.

[497] S. K. Poguluri, H. S. Ko, and Y. H. Bae. CFD investigation of pitch-type wave energy converter-rotor based on RANS simulations. *Ships and Offshore Structures*, pages 1–13, 2019.

[498] H.S. Ko, I.-H. Cho, and Y. H. Bae. Numerical and experimental study for nonlinear dynamic behavior of an asymmetric wave energy converter. In *Proceedings of the 29th International Offshore and Polar Engineering Conference (ISOPE), Honolulu, HI, USA*, pages 182–186, 2019.

[499] H.S. Ko, I.-H. Cho, and Y. H. Bae. Numerical and experimental study of a horizontal cylinder-type wave energy converter with off-centered axes of rotation. *International Journal of Offshore and Polar Engineering*, 29(04):429–436, 2019.

[500] H. Li and E.E. Bachynski. Numerical simulation of fully nonlinear interaction between regular and irregular waves and a 2D floating body. In *Proceedings of the 38th International Conference on Ocean, Offshore and Arctic Engineering (OMAE), Glasgow, UK*, pages 1–10, 2019.

[501] T.T. Tran, A.M. Krueger, B. Gunawan, and M.R. Alam. Predicting the dynamic characteristics of a fully submerged wave energy converter subjected to a power take-off failure using a high-fidelity computational fluid dynamics model. In *Proceedings of the 13th European wave and tidal energy conference (EWTEC), Naples, Italy*, pages 1392–1—9, 2019.

[502] R.G. Coe, B.J. Rosenberg, E.W. Quon, C.C. Chartrand, Y.-H. Yu, J. van Rij, and T.R. Mundon. CFD design-load analysis of a two-body wave energy converter. *Journal of Ocean Engineering and Marine Energy*, 5(2):99–117, 2019.

[503] B.J. Rosenberg, T.R. Mundon, R.G. Coe, E.W. Quon, C.C. Chartrand, Y.-H. Yu, and J. Can Rij. Development of WEC design loads: A comparison of numerical and experimental approaches. In *Proceedings of the 13th European wave and tidal energy conference (EWTEC), Naples, Italy*, pages 1682–1—8, 2019.

[504] J. van Rij, Y.-H. Yu, Y. Guo, and R.G. Coe. A wave energy converter design load case study. *Journal of Marine Science and Engineering*, 7(8):250, 2019.

[505] J. van Rij, Y.-H. Yu, A. McCall, and R.G. Coe. Extreme load computational fluid dynamics analysis and verification for a multibody wave energy converter. In *Proceedings of the 38th International Conference on Ocean, Offshore and Arctic Engineering (OMAE), Glasgow, UK*, pages 1–10, 2019.

[506] E. Medina-López, A. Moñino, R.J. Bergillos, M. Clavero, and M. Ortega-Sánchez. Oscillating water column performance under the influence of storm development. *Energy*, 166:765–774, 2019.

[507] Y.-X. Lin, D.-W. Chen, and J.-H. Chen. Simulation of a resonance-amplified floater oscillation in an open-type circular caisson. In *Proceedings of the 13th European wave and tidal energy conference (EWTEC), Naples, Italy*, pages 1612–1—6, 2019.

[508] Z. Luan, G. He, Z. Zhang, P. Jing, R. Jin, B. Geng, and C. Liu. Study on the optimal wave energy absorption power of a float in waves. *Journal of Marine Science and Engineering*, 7(8):269, 2019.

[509] S. Park, K.-H. Kim, B.-W. Nam, J.-S. Kim, and K. Hong. Experimental and numerical analysis of performance of oscillating water column wave energy converter applicable to breakwaters. In *Proceedings of the 38th International Conference on Ocean, Offshore and Arctic Engineering (OMAE), Glasgow, UK*, pages 1–8, 2019.

[510] M.G. Hassanabad and M. Shegeft. Numerical simulation study on the offshore oscillating water column OWC integrated into a floating breakwater using CFD. In *Proceedings of the 13th European wave and tidal energy conference (EWTEC), Naples, Italy*, pages 1747–1—7, 2019.

[511] M. Shalby, A. Elhanafi, P. Walker, and D.G. Dorrell. CFD modelling of a small–scale fixed multi–chamber OWC device. *Applied Ocean Research*, 88:37–47, 2019.

[512] L. Gurnari, P. Filianoti, S.M. Camporeale, and M. Torresi. Hydrodynamic analysis of a full-scale U-OWC breakwater: comparison between analytical models and CFD simulation. In *Proceedings of the 13th European wave and tidal energy conference (EWTEC), Naples, Italy*, pages 1465–1—10, 2019.

[513] Z. Deng, C. Wang, P. Wang, P. Higuera, and R. Wang. Hydrodynamic performance of an offshore-stationary OWC device with a horizontal bottom plate: Experimental and numerical study. *Energy*, 187:115941, 2019.

[514] B. Ding, P.-Y. Wuillaume, F. Meng, A. Babarit, B. Schubert, N. Sergiienko, and B. Cazzolato. Comparison of wave-body interaction modelling methods for the study of reactively controlled point absorber wave energy converter. In *Proceedings of the 34th International Workshop on Water Waves and Floating Bodies, Newcastle, Australia*, pages 1–4, 2019.

[515] C. Jiang, O. el Moctar, and T.E. Schellin. Prediction of hydrodynamic damping of moored offshore structures using CFD. In *Proceedings of the 38th International Conference on Ocean, Offshore and Arctic Engineering (OMAE), Glasgow, UK*, pages 1–13, 2019.

[516] S. Dai, S. Day, Z. Yuan, and H. Wang. Investigation on the hydrodynamic scaling effect of an OWC type wave energy device using experiment and CFD simulation. *Renewable energy*, 142:184–194, 2019.

[517] Z. Li, G. Deng, P. Queutey, B. Bouscasse, G. Ducrozet, L. Gentaz, D. Le Touzé, and P. Ferrant. Comparison of wave modeling methods in CFD solvers for ocean engineering applications. *Ocean Engineering*, 188:106237, 2019.

[518] I. Zabala, J.C.C. Henriques, J.M. Blanco, A. Gomez, L.M.C. Gato, I. Bidaguren, A.F.O. Falcão, A. Amezaga, and R.P.F. Gomes. Wave-induced real-fluid effects in marine energy converters: Review and application to OWC devices. *Renewable and Sustainable Energy Reviews*, 111:535–549, 2019.

[519] H. Chen, L. Qian, Z. Ma, W. Bai, Y. Li, D. Causon, and C. Mingham. Application of an overset mesh based numerical wave tank for modelling realistic free-surface hydrodynamic problems. *Ocean Engineering*, 176:97–117, 2019.

[520] P. Gunawardane, S. Rathnayake, B.-H. Kim, and Y.-H. Lee. Hydrodynamics of top hinged owsc wave energy device the "pendulor" with a bottom gap. *Journal of Advanced Marine Engineering and Technology*, 44(1):75–81, 2020.

[521] T. Martin, A. Kamath, and H. Bihs. Modeling and simulation of moored-floating structures using the tension element method. *Journal of Offshore Mechanics and Arctic Engineering*, 142(1), 2020.

[522] H. Zhang, B. Zhou, C. Vogel, R. Willden, J. Zang, and L. Zhang. Hydrodynamic performance of a floating breakwater as an oscillating-buoy type wave energy converter. *Applied Energy*, 257:113996, 2020.

[523] H. Zhang, B. Zhou, C. Vogel, R. Willden, J. Zang, and J. Geng. Hydrodynamic performance of a dual-floater hybrid system combining a floating breakwater and an oscillating-buoy type wave energy converter. *Applied Energy*, 259:114212, 2020.

[524] F. Meng, A. Rafiee, B. Ding, B. Cazzolato, and M. Arjomandi. Nonlinear hydrodynamics analysis of a submerged spherical point absorber with asymmetric mass distribution. *Renewable Energy*, 147:1895–1908, 2020.

[525] A. Çelik and A. Altunkaynak. Determination of hydrodynamic parameters of a fixed OWC by performing experimental and numerical free decay tests. *Ocean Engineering*, page 106827, 2020.

[526] Q. Chen, J. Zang, J. Birchall, D. Ning, X. Zhao, and J. Gao. On the hydrodynamic performance of a vertical pile-restrained WEC-type floating breakwater. *Renewable Energy*, 146:414–425, 2020.

[527] L.A. Gaspar, P.R.F. Teixeira, and E. Didier. Numerical analysis of the performance of two onshore oscillating water column wave energy converters at different chamber wall slopes. *Ocean Engineering*, 201:107119, 2020.

[528] L. Gurnari, P.G.F. Filianoti, M. Torresi, and S.M. Camporeale. The wave-to-wire energy conversion process for a fixed U-OWC device. *Energies*, 13(1):283, 2020.

[529] B. Hafsa, E.M. Abdellatif, and H. Mounir. Wave generation in an OWC system for wave energy conversion. In *MATEC Web of Conferences*, volume 307, pages 01012–1–4. EDP Sciences, 2020.

[530] B.W. Schubert, W.S.P. Robertson, B.S. Cazzolato, and M.H. Ghayesh. Linear and nonlinear hydrodynamic models for dynamics of a submerged point absorber wave energy converter. *Ocean Engineering*, 197:106828, 2020.

[531] Jie-Min Zhan, Qing Fan, Wen-Qing Hu, and Ye-Jun Gong. Hybrid realizable k-ε/laminar method in the application of 3D heaving OWCs. *Renewable Energy*, 155:691–702, 2020.

[532] A. Clément, P. McCullen, A. Falcão, A. Fiorentino, F. Gardner, K. Hammarlund, G. Lemonis, T. Lewis, K. Nielsen, S. Petroncini, M.-T. Pontes, P. Schild, B.O. Sjöström, H.C. Sørensen, and T. Thorpe. Wave energy in europe: current status and perspectives. *Renewable and Sustainable Energy Reviews*, 6(5):405–431, 2002.

[533] European Marine Energy Centre (EMEC). *Wave Devices*, 2020. `http://www.emec.org.uk/marine-energy/wave-devices/`, Last accessed 09/04/2020.

[534] Sandia National Laboratories. *WEC-Sim (Wave Energy Converter SIMulator)*, 2020. `https://wec-sim.github.io/WEC-Sim/`, Last accessed 08/05/2020.

[535] Orcina. *OrcaFlex product website*, 2020. `https://www.orcina.com/orcaflex/`, Last accessed 14/04/2020.

[536] Norske Veritas. *Environmental conditions and environmental loads*. Det Norske Veritas, 2000.

[537] ANSYS. *ANSYS AQWA product website*, 2020. `https://www.ansys.com/products/structures/ansys-aqwa`, Last accessed 14/04/2020.

[538] L. Ljung. *System Identification - Theory for the User*. Prentice Hall, 1999.

[539] J.V. Ringwood, G. Bacelli, and F. Fusco. Energy-maximizing control of wave-energy converters: The development of control system technology to optimize their operation. *IEEE Control Systems*, 34:30–55, 2014.

[540] N. Faedo, S. Olaya, and J.V. Ringwood. Optimal control, MPC and MPC-like algorithms for wave energy systems: An overview. *IFAC Journal of Systems and Control*, 1:37–56, 2017.

[541] M Penalba and J V Ringwood. Linearisation-based nonlinearity measures for wave-to-wire models in wave energy. *Ocean Engineering*, 171:496–504, 2019.

[542] Mathworks. *Simscape Fluids product website*, 2020. `https://www.mathworks.com/products/simscape-fluids.html`, Last accessed 12/05/2020.

[543] J. Davidson and J.V. Ringwood. Mathematical modelling of mooring systems for wave energy converters – a review. *Energies*, 10(5):666, 2017.

[544] M. Hall, B. Buckham, and C. Crawford. Evaluating the importance of mooring line model fidelity in floating offshore wind turbine simulations. *Wind energy*, 17(12):1835–1853, 2014.

[545] H. Bihs, A. Kamath, M. A. Chella, A. Aggarwal, and Ø.A. Arntsen. A new level set numerical wave tank with improved density interpolation for complex wave hydrodynamics. *Computers & Fluids*, 140:191–208, 2016.

[546] B.T. Paulsen, H. Bredmose, and H.B. Bingham. An efficient domain decomposition strategy for wave loads on surface piercing circular cylinders. *Coastal Engineering*, 86:57–76, 2014.

[547] Q. Li, J. Wang, S. Yan, J. Gong, and Q. Ma. A zonal hybrid approach coupling FNPT with OpenFOAM for modelling wave-structure interactions with action of current. *Ocean Systems Engineering*, 8(4):381–407, 2018.

[548] Siemens. *Simcenter STAR–CCM+ product website*, 2020. `https://www.plm.automation.siemens.com/global/de/products/simcenter/STAR-CCM.html`, Last accessed 14/04/2020.

[549] Numeca. *FINE/Marine product website*, 2020. `https://www.numeca.com/en_eu/product/finemarine`, Last accessed 14/04/2020.

[550] P. Ferrant, L. Gentaz, B. Alessandrini, and D. Le Touzé. A potential/RANSE approach for regular water wave diffraction about 2-D structures. *Ship Technology Research*, 50(4):165–171, 2003.

[551] DNV-GL. *WaveDyn product website*, 2020. `https://renewableenergysoftwareportal.dnvgl.com/Home/ProductDownloads?productID=5`, Last accessed 14/04/2020.

[552] W. S. Atkins Concultants, Sirehna, HSVA, FLOWTECH, VVT, Imperial College of Science & Technology, Germanischer Lloyd, and Astilleros Espanoles. Best practice guidelines for marine applications of computational fluid dynamics. Technical report, MARINET CFD, 2002.

[553] L. Eça, S. Toxopeus, T. v. Terwisga, and H. Streckwall. Best practice guidelines for the application of computational fluid dynamics in marine hydrodynamics. Technical report, VIRTUE - The Virtuel Tank Utility in Europe, Affiliation: VIRTUE Project, 2009.

[554] ITTC. Practical Guidelines for Ship CFD Applications. Technical report, International Towing Tank Conference, 2011.

[555] J. Oberhagemann, V. Shigunov, and O. el Moctar. Application of CFD in long-term extreme value analyses of wave loads. *Ship Technology Research*, 59(3):4–22, 2012.

[556] L. Eça, G. Vaz, and M. Hoekstra. A verification and validation exercise for the flow over a backward facing step. In *Proceedings of the V European Conference on Computational Fluid Dynamics*, 2010.

[557] L. Eça and M. Hoekstra. A procedure for the estimation of the numerical uncertainty of CFD calculations based on grid refinement studies. *Journal of Computational Physics*, 262:104–130, 2014.

[558] ANSYS. *ANSYS Fluent product website*, 2020. `https://www.ansys.com/products/fluids/ansys-fluent`, Last accessed 14/04/2020.

[559] J. Kim, J. O'Sullivan, and A. Read. Ringing analysis of a vertical cylinder by Euler overlay method. In *Proceedings of the 31th International Conference on Ocean, Offshore and Arctic Engineering (OMAE), Rio de Janeiro, Brazil*, pages 855–866. American Society of Mechanical Engineers Digital Collection, 2012.

[560] A. Sommerfeld. *Partial Differential Equations in Physics*. Academic Press, 1949.

[561] E.P.D. Mansard and E.R. Funke. The measurement of incident and reflected spectra using a least squares method. In *Coastal Engineering 1980*, pages 154–172. 1980.

[562] P. B. Garcia-Rosa, R. Costello, F. Dias, and J. V. Ringwood. Hydrodynamic modelling competition - Overview and approach. In *Proceedings of the 34th International Conference on Ocean, Offshore and Arctic Engineering (OMAE), St. John's, Newfoundland, Canada*, pages 1–10, 2015.

[563] FLOW Science. *FLOW–3D product website*, 2020. `https://www.flow3d.com/`, Last accessed 14/04/2020.

[564] ESI. *OpenFOAM v1706 Release Notes: New and improved numerics*, 2014. `https://www.openfoam.com/releases/openfoam-v1706/numerics.php#numerics-overset`, Last accessed 10/05/2020.

[565] B.M. Sumer and J. Fredsoe. *Hydrodynamics Around Cylindrical Structures*, volume 26. World Scientific, 2006.

[566] P.R. Spalart, S. Deck, M.L. Shur, K.D. Squires, M. K. Strelets, and A. Travin. A new version of detached-eddy simulation, resistant to ambiguous grid densities. *Theoretical and computational fluid dynamics*, 20(3):181, 2006.

[567] ANSYS. *ANSYS Fluent V2F Turbulence Model Manual*, 2013.

[568] B. Devolder, P. Rauwoens, and P. Troch. Application of a buoyancy-modified k-ω SST turbulence model to simulate wave run-up around a monopile subjected to regular waves using OpenFOAM. *Coastal Engineering*, 125:81–94, 2017.

[569] B. Devolder, P. Troch, and P. Rauwoens. Performance of a buoyancy-modified k-ω and k-ω SST turbulence model for simulating wave breaking under regular waves using OpenFOAM. *Coastal Engineering*, 138:49–65, 2018.

[570] ITTC. Recommended procedures and guidelines: Uncertainty analyssis instrument calibration. Technical report, ITTC, 2008.

[571] ANSYS. *ANSYS CFX product website*, 2020. `https://www.ansys.com/products/fluids/ansys-cfx`, Last accessed 14/04/2020.

[572] A. P. Engsig-Karup. *Unstructured nodal DG-FEM solution of high-order Boussinesq-type equations*. PhD thesis, Technical Univeristy of Denmark, 2006.

[573] S.R. Masterton and C. Swan. On the accurate and efficient calibration of a 3D wave basin. *Ocean Engineering*, 35(8-9):763–773, 2008.

[574] J. Cruz. *Ocean wave energy: current status and future perspectives*. Springer Science & Business Media, 2007.

[575] J. Roenby, B. E. Larsen, H. Bredmose, and H. Jasak. A new volume-of-fluid method in OpenFOAM. In *Proceedings of the VII International Conference on Computational Methods in Marine Engineering (MARINE), Nantes, France*, pages 1–12, 2017.

[576] P. Schmitt, L. Danisch, P. Lamont-Kane, and B. Elsäßer. Designing short-term wave traces to assess wave power devices. *International Journal of Offshore and Polar Engineering*, 28(01):46–53, 2018.

[577] OpenFOAM Foundation. *OpenFOAM 6 Release Notes*, 2018. `https://openfoam.org/release/6/`, Last accessed 19/05/2020.

[578] N. Jacobsen. waves2Foam Manual. Technical report, Deltares, 2017.

[579] P. Higuera. *OlaFlow website*, 2020. `https://olaflow.github.io/`, Last accessed 21/05/2020.

[580] OpenFOAM Foundation. *C++ Source Code Guide: InterfaceHeight class reference*, 2018. `https://cpp.openfoam.org/v6/classFoam_1_1functionObjects_1_1interfaceHeight.html#details`, Last accessed 19/05/2020.

[581] J. Hals, A. Babarit, J.R. Krokstad, M. J. Muliawan, A. Kurniawan, and T. Moan. The NumWEC project. Numerical estimation of energy delivery from a selection of wave energy converters. Technical report, Norwegian University of Science and Technology, 2015.

[582] M. M. Jakobsen. Wave-Structure interations on point absorber. Technical report, Aalborg University Denmark, 2014.

[583] M. M. Jakobsen, S. Beatty, G. Iglesias, and M. M. Kramer. Characterization of loads on a hemispherical point absorber wave energy converter. *International Journal of Marine Energy*, 13:1–15, 2016.

[584] OpenFOAM Foundation. *OpenFOAM 4.1 Sources*, 2016. `https://openfoam.org/download/4-1-source/`, Last accessed 30/05/2020.

[585] J.V. Ringwood, F. Ferri, K. Ruehl, Y.-H. Yu, R.G. Coe, G. Bacelli, J. Weber, and M.M. Kramer. A competition for WEC control systems. In *Proceedings of the 12th European Wave and Tidal Energy Conference (EWTEC), Cork, Ireland*, pages 831–1–9, 2017.

[586] N. Tom, K. Ruehl, and F. Ferri. Numerical model development and validation for the WECCCOMP control competition. In *Proceedings of the 37th International Conference on Ocean, Offshore and Arctic Engineering (OMAE), Madrid, Spain*, pages 1–10, 2018.

[587] M.S. Jung and O.J. Kwon. *A Parallel Unstructured Overset Mesh Technique for Unsteady Flow Simulations*. Springer, 2009.

[588] ESI. OpenFOAM v1712 Release Notes: New and improved numerics, 2017. `https://www.openfoam.com/releases/openfoam-v1712/numerics.php#numerics-overset`, Last accessed 05/06/2020.

[589] ESI. OpenFOAM v1812 Release Notes: New and improved numerics, 2018. `https://www.openfoam.com/releases/openfoam-v1812/numerics.php#numerics-overset`, Last accessed 05/06/2020.

[590] R. Atan, J. Goggins, and S.n Nash. A detailed assessment of the wave energy resource at the Atlantic Marine Energy Test Site. *Energies*, 9(11):967, 2016.

[591] F. Sharkey, E. Bannon, M. Conlon, and K. Gaughan. Dynamic electrical ratings and the economics of capacity factor for wave energy converter arrays. In *Proceedings of the 9th European Wave and Tidal Energy Conference (EWTEC), Southampton, UK*, pages 1–8, 2011.

[592] G.C. Goodwin, S.F. Graebe, and M.E. Salgado. *Control system design*, volume 240. Prentice Hall New Jersey, 2001.

[593] ESI. OpenFOAM v1812 Release Notes, 2018. `https://www.openfoam.com/releases/openfoam-v1812/`, Last accessed 05/06/2020.

[594] P. Balitsky, G. Bacelli, and J.V. Ringwood. Control-influenced layout optimization of arrays of wave energy converters. In *Proceedings of the 33rd International Conference on Ocean, Offshore and Arctic Engineering (OMAE), San Francisco, CA, USA*, pages 1–10, 2014.

[595] P.B. Garcia-Rosa, G. Bacelli, and J.V. Ringwood. Control-informed optimal array layout for wave farms. *IEEE Transactions on Sustainable Energy*, 6(2):575–582, 2015.

[596] OpenFOAM Wiki. *checkMesh*, 2015. `https://openfoamwiki.net/index.php/CheckMesh`, Last accessed 14/06/2020.

[597] H.M. Blackburn and R.D. Henderson. A study of two-dimensional flow past an oscillating cylinder. *Journal of Fluid Mechanics*, 385:255–286, 1999.

[598] C. J. Rusch, B.L. Polagye, and B.D. Maurer. Experimental visualisation of heave plate flow regimes. In *Proceedings of the 13th European Wave and Tidal Energy Conference (EWTEC), Naples, Italy*, pages 1533–1—10, 2019.

[599] S. Holmes, S. Bhat, P. Beynet, A. Sablok, and I. Prislin. Heave plate design with computational fluid dynamics. *J. Offshore Mech. Arct. Eng.*, 123(1):22–28, 2000.

[600] W.-J. Shen, Y.-G. Tang, and L.-G. Liu. Research on the hydrodynamic characteristics of heave plate structure with different form edges of a spar platform. *China Ocean Engineering*, 26(1):177–184, 2012.

[601] C.N. Phan, M. Aureli, and M. Porfiri. Finite amplitude vibrations of cantilevers of rectangular cross sections in viscous fluids. *Journal of Fluids and Structures*, 40:52–69, 2013.

[602] C.A. Garrido-Mendoza, K.P. Thiagarajan, A. Souto-Iglesias, A. Colagrossi, and B. Bouscasse. Computation of flow features and hydrodynamic coefficients around heave plates oscillating near a seabed. *Journal of Fluids and Structures*, 59:406–431, 2015.

[603] C. Lopez-Pavon and A. Souto-Iglesias. Hydrodynamic coefficients and pressure loads on heave plates for semi-submersible floating offshore wind turbines: A comparative analysis using large scale models. *Renewable Energy*, 81:864–881, 2015.

[604] S. Zhang and T. Ishihara. Numerical study of hydrodynamic coefficients of multiple heave plates by large eddy simulations with volume of fluid method. *Ocean Engineering*, 163:583–598, 2018.

[605] ANSYS. *ANSYS Fluent 12.0 Theory guide*, 2009. `https://www.afs.enea.it/project/neptunius/docs/fluent/html/th/node99.htm`, Last accessed 22/06/2020.

[606] S. Zhang and T. Ishihara. Numerical study of distributed hydrodynamic forces on a circular heave plate by large-eddy simulations with volume of fluid method. *Ships and Offshore Structures*, pages 1–13, 2019.

[607] L. O'Boyle, K. Doherty, J. van't Hoff, and J. Skelton. The value of full scale prototype data-testing Oyster 800 at EMEC, Orkney. In *Proceedings of the 11th European Wave and Tidal Energy Conference (EWTEC), Nantes, France*, pages 08D–1–1–11, 2015.

[608] J. Tougaard. Underwater noise from a wave energy converter is unlikely to affect marine mammals. *PloS one*, 10(7), 2015.

[609] N. Faedo, G. Scarciotti, A. Astolfi, and J.V. Ringwood. Energy-maximising control of wave energy converters using a moment-domain representation. *Control Engineering Practice*, 81:85–96, 2018.

[610] N. Faedo, G. Scarciotti, A. Astolfi, and J.V. Ringwood. Moment-based constrained optimal control of an array of wave energy converters. In *Proceedings of the 2019 American Control Conference (ACC), Philadelphia, PA, USA*, pages 4797–4802, 2019.

[611] M. Penalba and J.V. Ringwood. Systematic Complexity Reduction of Wave-to-Wire Models for Wave Energy System Design. *Ocean Engineering*, Under review, 2020.

[612] N. Faedo, Y. Peña-Sanchez, and J.V. Ringwood. Finite-order hydrodynamic model determination for wave energy applications using moment-matching. *Ocean Engineering*, 163:251 – 263, 2018.

[613] N. Faedo, Y. Peña-Sanchez, and J.V. Ringwood. Passivity preserving moment-based finite-order hydrodynamic model identification for wave energy applications. In *Proceedings of the 3rd International Conference on Renewable Energies Offshore (RENEW), Lisbon, Portugal*, pages 351–359, 2018.

[614] I. Goldhirsch, P.-L. Sulem, and S.A. Orszag. Stability and Lyapunov stability of dynamical systems: A differential approach and a numerical method. *Physica D: Nonlinear Phenomena*, 27(3):311–337, 1987.

[615] H.K. Khalil. *Noninear Systems*. Prentice-Hall, New Jersey, 1996.

[616] A. Astolfi. Model reduction by moment matching for linear and nonlinear systems. *IEEE Transactions on Automatic Control*, 55(10):2321–2336, 2010.

[617] M. Penalba. *Design, validation and application of wave-to-wire models for heaving point absorber wave energy converters*. PhD thesis, Maynooth University, 2018.

[618] B.E. Larsen and D.R. Fuhrman. On the over-production of turbulence beneath surface waves in Reynolds-averaged Navier–Stokes models. *Journal of Fluid Mechanics*, 853:419–460, 2018.